PEREGRINE SOLITON AND BREATHERS IN WAVE PHYSICS: ACHIEVEMENTS AND PERSPECTIVES

EDITED BY: Bertrand Kibler, Amin Chabchoub and Heremba Bailung

PUBLISHED IN: Frontiers in Physics

frontiers Research Topics

ISSN 1664-8714
ISBN 978-2-88974-111-3
DOI 10.3389/978-2-88974-111-3

About Frontiers

Frontiers is more than just an open-access publisher of scholarly articles: it is a pioneering approach to the world of academia, radically improving the way scholarly research is managed. The grand vision of Frontiers is a world where all people have an equal opportunity to seek, share and generate knowledge. Frontiers provides immediate and permanent online open access to all its publications, but this alone is not enough to realize our grand goals.

Frontiers Journal Series

The Frontiers Journal Series is a multi-tier and interdisciplinary set of open-access, online journals, promising a paradigm shift from the current review, selection and dissemination processes in academic publishing. All Frontiers journals are driven by researchers for researchers; therefore, they constitute a service to the scholarly community. At the same time, the Frontiers Journal Series operates on a revolutionary invention, the tiered publishing system, initially addressing specific communities of scholars, and gradually climbing up to broader public understanding, thus serving the interests of the lay society, too.

Dedication to Quality

Each Frontiers article is a landmark of the highest quality, thanks to genuinely collaborative interactions between authors and review editors, who include some of the world's best academicians. Research must be certified by peers before entering a stream of knowledge that may eventually reach the public - and shape society; therefore, Frontiers only applies the most rigorous and unbiased reviews.
Frontiers revolutionizes research publishing by freely delivering the most outstanding research, evaluated with no bias from both the academic and social point of view. By applying the most advanced information technologies, Frontiers is catapulting scholarly publishing into a new generation.

What are Frontiers Research Topics?

Frontiers Research Topics are very popular trademarks of the Frontiers Journals Series: they are collections of at least ten articles, all centered on a particular subject. With their unique mix of varied contributions from Original Research to Review Articles, Frontiers Research Topics unify the most influential researchers, the latest key findings and historical advances in a hot research area! Find out more on how to host your own Frontiers Research Topic or contribute to one as an author by contacting the Frontiers Editorial Office: frontiersin.org/about/contact

PEREGRINE SOLITON AND BREATHERS IN WAVE PHYSICS: ACHIEVEMENTS AND PERSPECTIVES

Topic Editors:
Bertrand Kibler, UMR6303 Laboratoire Interdisciplinaire Carnot de Bourgogne (ICB), France
Amin Chabchoub, The University of Sydney, Australia
Heremba Bailung, Ministry of Science and Technology (India), India

Citation: Kibler, B., Chabchoub, A., Bailung, H., eds. (2022). Peregrine Soliton and Breathers in Wave Physics: Achievements and Perspectives.
Lausanne: Frontiers Media SA. doi: 10.3389/978-2-88974-111-3

Table of Contents

frontiers in Physics

EDITORIAL
published: 02 December 2021
doi: 10.3389/fphy.2021.795983

Editorial: Peregrine Soliton and Breathers in Wave Physics: Achievements and Perspectives

Bertrand Kibler[1]*, *Amin Chabchoub*[2,3,4] *and Heremba Bailung*[5]

[1]Laboratoire Interdisciplinaire Carnot de Bourgogne (ICB), UMR 6303 CNRS-Université Bourgogne Franche-Comté, Dijon, France, [2]Hakubi Center for Advanced Research, Kyoto University, Kyoto, Japan, [3]Disaster Prevention Research Institute, Kyoto University, Kyoto, Japan, [4]Centre for Wind, Waves and Water, School of Civil Engineering, The University of Sydney, Sydney, NSW, Australia, [5]Plasma Physics Laboratory, Physical Sciences Division, Institute of Advanced Study in Science and Technology, Guwahati, India

Keywords: nonlinear waves, hydrodynamics, optics, plasma physics, breathers and rogue waves, nonlinear Schrodinger equation

Editorial on the Research Topic

Peregrine Soliton and Breathers in Wave Physics: Achievements and Perspectives

The field of rogue wave physics has been extended well beyond the hydrodynamics community during the last decade, in particular, due to the analogy drawn through the one-dimensional nonlinear Schrödinger equation (NLSE) and related nonlinear wave theory. More specifically, breather solutions to the NLSE, whose entire space-time evolution is analytically described, are now considered as the simplest nonlinear prototypes of possible eminent hydrodynamic rogue waves, which are responsible for many maritime catastrophes. A special focus has been placed on doubly localized Peregrine-type breathers. Breathers exhibit unique pulsating on a nonzero background and localization properties directly linked to the ubiquitous modulation instability phenomenon in one-dimensional wave propagation scenarios.

It is worth mentioning that since their discovery in the late 70s, breather solutions on a finite background and notably those manifesting double localization [1] have remained untested experimentally, for almost 30 years, until their emergence into the light in 2010 [2]. Following the observation in optics, two experimental observations in other distinct fields of wave physics, namely, fluids dynamics [3] and plasma [4], followed within a few months after. All of them confirmed the controlled generation of doubly localized and strongly nonlinear Peregrine-type waves in real physical systems. These have now been among the highly cited studies in nonlinear wave physics during the last decade. The proof of existence and control of this class of nonlinear waves have been of fundamental significance for extreme wave dynamics control in laboratory environments and are now driving numerous experimental studies in various wave systems and mathematical and engineering developments worldwide.

This multidisciplinary research topic commemorates the 10th anniversary of the observation of the Peregrine breather (also commonly called the Peregrine soliton or the rational breather). A collection of fourteen original research, four brief research report, three mini-review, and three review articles are presented, featuring some of the latest advances in theoretical, numerical, and experimental studies of breather waves and modulation instability processes.

As an introduction to this research topic, we first refer the reader to four articles that review some of the theoretical foundations of breather waves. Karjanto discussed the relationship between periodic first-order breather solutions and their limiting behavior toward the Peregrine breather. Alejo et al. recalled the unstable properties of these nonlinear Schrödinger-type breathers, according

OPEN ACCESS

Edited and reviewed by:
José S. Andrade Jr,
Federal University of Ceara, Brazil

***Correspondence:**
Bertrand Kibler
bertrand.kibler@u-bourgogne.fr

Specialty section:
This article was submitted to Mathematical and Statistical Physics, a section of the journal Frontiers in Physics

Received: *15 October 2021*
Accepted: *04 November 2021*
Published: *02 December 2021*

Citation:
Kibler B, Chabchoub A and Bailung H (2021) Editorial: Peregrine Soliton and Breathers in Wave Physics: Achievements and Perspectives. Front. Phys. 9:795983. doi: 10.3389/fphy.2021.795983

to a standard definition of stability. The work by Akhmediev focused on the Peregrine breather as an "elementary particle" of more complicated patterns resulting from its higher-order combination. Such solutions are characterized by "triangular numbers," defined as the total number of Peregrine waves in a regular pattern, while Osborne elaborated on how to determine the general breather solutions by means of Riemann theta functions.

Next, more recent and specific theoretical findings can be found in the following seven articles addressing complex wave propagation problems. The study by Pelinovsky provided a methodology to compute the instability rates for the standing periodic waves and the double-periodic solutions of the NLSE. Ye et al. presented exact explicit coupled Peregrine solutions on a periodic-wave background caused by the interference in the vector cubic-quintic nonlinear Schrödinger equation. Uthayakumar et al. reviewed the Peregrine-type solutions appearing under the framework of extended versions of the NLSE describing the diverse nonlinear systems. In addition, Peng et al. looked into the dynamics of pole trajectories in the complex plane for rational solutions of the NLSE and its extensions. El-Tantawy et al. investigated breather waves in a linear damped nonlinear Schrödinger equation. Schober and Islas explored the effects of dissipation and higher-order nonlinearities on the stability of breather solutions, whilst Singh and Saini examined modulation instability and breathers in a dusty plasma.

In parallel, the reader can find four articles with detailed numerical investigations of both fundamental and applied problems, for which no analytical development is yet available. The contribution of Agafontsev and Gelash analyzed the spontaneous emergence of rogue waves for two different initial wave systems, namely, the unstable plane wave and the bound-state multi-soliton. Coulibaly et al. reported on the possible persistence of Peregrine-type waves in systems outside of the equilibrium, as described by the driven and damped nonlinear Schrödinger equation. From a more applied perspective, Shou and Huang proposed a scheme to actively control optical Peregrine breathers in a coherent atomic gas *via* electromagnetically induced transparency, while Wang et al. investigated the probability of extreme waves in deep crossing random seas in response to the variation of initial spectral bandwidth.

Furthermore, the reader will be able to discover eight articles providing recent experimental observations and characterizations of breather or rogue wave dynamics using distinct laboratory facilities to generate water, ion-acoustic, and light waves. Chabchoub et al. showed the possible observation of the degenerate soliton interaction, also demonstrated to be a Peregrine breather on the zero-background limit. The brief report by Hsu et al. demonstrated that the Peregrine breather traveling at the free surface of a shear current of slowly varying vorticity may transform into gray solitons. Using a multidipole double plasma device, Pathak analyzed the effect of Landau damping on the evolution of the ion-acoustic Peregrine breather. Naveau et al. described a novel optical fiber experimental setup based on a heterodyne optical time-domain reflectometer. Here, breather and recurrence dynamics can be evidenced by monitoring the power and relative phase evolutions of spectral components. Tikan et al. reviewed optical fiber experiments involving either single pulse or partially coherent waves that show the spontaneous and local emergence of the Peregrine breather. Xu et al. reported the observation of a novel type of breather interaction in telecommunication optical fibers, namely, ghost-like breather interaction dynamics, in which two identical breathers propagate with opposite group velocities. The work of Finot stressed and illustrated that great care must be taken when trying to identify the nature of coherent structures in an experimental record. An example of a highly peaked structure over a continuous background is shown to have any connection with a Peregrine breather, despite possessing similar key features. Jauberteau et al. showed the possible boosting or taming of spatio-temporal beam instabilities and the possible formation of rogue optical filaments in quadractic crystals.

Last but not least, it is worth to highlight the original research of Waseda et al. in a real sea environment, making use of a stereo image sequence of the ocean surface. With the help of a nonlinear phase resolving wave model, they evidenced a coherent wave group, compact in both propagating and transverse directions and oriented obliquely to the propagation direction, similarly to the recently discovered directional solitons and breathers.

In conclusion, this research topic contains 24 articles devoted to the multifaceted development of ongoing studies in the field of nonlinear Schrödinger breathers and related modulation instability. We strongly hope that this "research topic" will serve as a useful collection of state-of-the-art accomplishments of the research community to date. As such, we anticipate that these contributions will lead to a growing interest, research inspiration, and significant advances, which will be benefiting a wide range of theoretical and applied scientists.

AUTHOR CONTRIBUTIONS

All authors listed have made a substantial, direct, and intellectual contribution to the work and approved it for publication.

FUNDING

This work has received funding from the French National Research Agency (PIA2/ISITE-BFC, Grant No. ANR-15-IDEX-03, "Breathing Light" project).

ACKNOWLEDGMENTS

The Research Topic editors thank all of our contributing authors for their dedication to the Research Topic and the reviewers for their constructive comments and suggestions.

REFERENCES

1. Peregrine DH. Water Waves, Nonlinear Schrödinger Equations and Their Solutions. *J Aust Math Soc Ser B, Appl. Math* (1983) 25(1):16–43. doi:10.1017/s0334270000003891
2. Kibler B, Fatome J, Finot C, Millot G, Dias F, Genty G, et al. The Peregrine Soliton in Nonlinear Fibre Optics. *Nat Phys* (2010) 6(10):790–5. doi:10.1038/nphys1740
3. Amin C, Hoffmann NP, Akhmediev N. Rogue Wave Observation in a Water Wave Tank. *Phys Rev Lett* (2011) 106(20):204502.
4. Bailung H, Sharma SK, Nakamura Y. Observation of Peregrine Solitons in a Multicomponent Plasma with Negative Ions. *Phys Rev Lett* (2011) 107(25):255005. doi:10.1103/physrevlett.107.255005

Conflict of Interest: The authors declare that the research was conducted in the absence of any commercial or financial relationships that could be construed as a potential conflict of interest.

frontiers in Physics

ORIGINAL RESEARCH
published: 22 October 2020
doi: 10.3389/fphy.2020.581662

The Dynamics of Pole Trajectories in the Complex Plane and Peregrine Solitons for Higher-Order Nonlinear Schrödinger Equations: Coherent Coupling and Quintic Nonlinearity

*Ning N. Peng, Tin L. Chiu and Kwok W. Chow**

Department of Mechanical Engineering, University of Hong Kong, Pokfulam, Hong Kong

The Peregrine soliton is an exact, rational, and localized solution of the nonlinear Schrödinger equation and is commonly employed as a model for rogue waves in physical sciences. If the transverse variable is allowed to be complex by analytic continuation while the propagation variable remains real, the poles of the Peregrine soliton travel down and up the imaginary axis in the complex plane. At the turning point of the pole trajectory, the real part of the complex variable coincides with the location of maximum height of the rogue wave in physical space. This feature is conjectured to hold for at least a few other members of the hierarchy of Schrödinger equations. In particular, evolution systems with coherent coupling or quintic (fifth-order) nonlinearity will be studied. Analytical and numerical results confirm the validity of this conjecture for the first- and second-order rogue waves.

Keywords: quintic nonlinearity, coherent coupling, pole trajectories, rogue waves, nonlinear Schrödinger equations

OPEN ACCESS

Edited by:
Bertrand Kibler, UMR6303 Laboratoire Interdisciplinaire Carnot de Bourgogne (ICB), France

Reviewed by:
Dumitru Mihalache, Horia Hulubei National Institute for Research and Development in Physics and Nuclear Engineering (IFIN-HH), Romania
Shihua Chen, Southeast University, China

****Correspondence:***
Kwok W. Chow
kwchow@hku.hk

Specialty section:
This article was submitted to Mathematical and Statistical Physics, a section of the journal Frontiers in Physics

Received: *09 July 2020*
Accepted: *21 August 2020*
Published: *22 October 2020*

Citation:
Peng NN, Chiu TL and Chow KW (2020) The Dynamics of Pole Trajectories in the Complex Plane and Peregrine Solitons for Higher-Order Nonlinear Schrödinger Equations: Coherent Coupling and Quintic Nonlinearity. Front. Phys. 8:581662. doi: 10.3389/fphy.2020.581662

1. INTRODUCTION

The Peregrine soliton is an exact, rational solution of the nonlinear Schrödinger equation (NLSE) [1]. The NLSE is widely used to model wave packet dynamics in various disciplines in physical science, e.g., fluid mechanics and optics [2, 3]. Arising from this algebraically localized nature, the Peregrine soliton is frequently employed in engineering applications to describe rogue waves, unexpectedly large displacements from equilibrium configurations or a tranquil background [4–6].

The Peregrine soliton is non-singular if the NLSE is in the focusing regime, where second-order dispersion and cubic nonlinearity are of the same sign. Analytically, the properties of the Peregrine soliton have been studied intensively, e.g.,

(a) an amplitude three times the plane wave background,
(b) a wave profile with a central maximum and two minima on the sides, and
(c) the modulation instability of the background plane wave and the energy cascade phenomena being closely related.

Experimentally, the occurrence of rogue waves is realized through wave channels in hydrodynamics and fiber laser setting in optics [7]. Our goal is to provide still another perspective, namely, utilizing the dynamics of pole trajectories in the complex plane to elucidate the properties of rogue waves [8–10].

Employing the concept of poles and singularities in the complex plane had actually been initiated in the field of nonlinear waves earlier. Specifically, the elastic collisions of solitons for the Korteweg–de Vries equation (KdV) had been investigated through this technique [11, 12]. More precisely, the time coordinate of KdV is permitted to be complex by analytic continuation. The trajectories of the poles of the exact two-soliton solution are then traced in the complex plane.

The objective now is to apply this concept to the NLSE,

$$iA_t + A_{xx} + \sigma |A|^2 A = 0, \tag{1}$$

and the higher-order members of this hierarchy, where A is a slowly varying, complex-valued envelope of the wave packet and σ is a real parameter. The variables t and x will represent slow time (spatial coordinate) and group velocity frame (retarded time) in the setting of fluid mechanics (optics), respectively. We shall adopt the terminology of fluid mechanics in the present work. Mathematically, time t of Equation (1) is often termed the propagation variable, while space x can be labeled as the transverse variable.

A preliminary attempt to look into the properties of poles for rational solutions of NLSE was started earlier in the literature [13], where the distribution of poles in the complex plane was tabulated at a specific time (or, more precisely, at $t = 0$). Here a full effort is invested to study the trajectories of poles as time evolves.

The sequence of presentation of results can now be explained. A conjecture on pole trajectories for the nonlinear Schrödinger equation (Equation 1) is first explained (Section 2). A correlation on the locations of maximum height of a rogue wave in the physical space and the real parts of the poles in the complex plane is proposed. How this conjecture can also be verified for the more complicated case of coherently coupled Schrödinger equations is then elucidated (Section 3). We then illustrate the same scenario for a Schrödinger equation with quintic nonlinearity (Section 4). Finally, we discuss physical insights and draw conclusions (Section 5).

2. THE PEREGRINE SOLITON

Analytically, the Peregrine soliton of Equation (1) is given by

$$A = \alpha \exp\left(i\sigma\alpha^2 t\right)\left\{1 - \frac{2\left(1 + 2i\sigma\alpha^2 t\right)}{\sigma\alpha^2\left(x^2 + 2\sigma\alpha^2 t^2 + \frac{1}{2\sigma\alpha^2}\right)}\right\} \tag{2}$$

and thus non-singular solution occurs only for $\sigma > 0$. The free parameter α measures the amplitude of the background plane wave. The maximum height is three times the background plane wave and occurs at $x = t = 0$. If the variable x in Equation (2) is allowed to be complex by analytic continuation, poles will occur at

$$x = \pm\left[2\sigma\alpha^2 t^2 + 1/\left(2\sigma\alpha^2\right)\right]^{1/2} i.$$

As time t evolves from "negative infinity" to "positive infinity," the pole in the upper half plane moves down the imaginary axis of the complex x plane for negative t, changes direction at the "turning point" at $t = 0$, and travels up the imaginary axis again for positive t. The maximum height of the rogue wave (Peregrine soliton) in the physical space occurs at the location $x = 0$, which is the real part of the turning point in the pole trajectories in the complex x plane.

Hence, we can formulate a conjecture:

Conjecture

The spatial locations of the points of maximum heights of a rogue wave in physical space will coincide, or closely correlate, with the real parts of the poles of the rogue wave solutions in the complex plane at points where the pole trajectories reverse directions.

For the Peregrine soliton of the nonlinear Schrödinger equation, this conjecture holds trivially from consideration of Equations (2) and (3). The challenge now is to test this conjecture for more complicated higher members of nonlinear Schrödinger hierarchy. In this work, we select systems with coherent coupling and quintic (fifth-order) nonlinearity as test cases.

As second- and higher-order rogue waves typically have four or more trajectories for poles in the complex plane, not all turning points will correspond to the maximum heights of rogue waves. The precise necessary and sufficient conditions for this matching still require intensive research efforts in the future.

3. SYSTEM OF SCHRÖDINGER EQUATIONS WITH COHERENT COUPLING

3.1. Verification of the Conjecture

In systems with multiple waveguides, e.g., optical fibers with birefringence [3], phase-sensitive or coherent coupling can occur. More precisely, for fibers with strong birefringence, the phase-sensitive portion of the four-wave process oscillates rapidly and can be eliminated on averaging. On the other hand, in the regime of weak birefringence, coherent coupling cannot be ignored and forms a critical component of the dynamics. More precisely, the Schrödinger equations with coherent coupling (* = complex conjugate; A, B = slowly varying envelopes) are:

$$\begin{aligned} i\frac{\partial A}{\partial t} + \frac{\partial^2 A}{\partial x^2} + 2(|A|^2 + 2|B|^2)A - 2B^2A^* = 0\,, \\ i\frac{\partial B}{\partial t} + \frac{\partial^2 B}{\partial x^2} + 2(|B|^2 + 2|A|^2)B - 2A^2B^* = 0\,. \end{aligned} \tag{3}$$

Terms of the forms $|A|^2A$, $|B|^2A$, B^2A^* will measure the physical effects of self-phase modulation, cross-phase modulation, and coherent coupling, respectively. Partial derivatives of t and x will indicate the rates of change with respect to the propagation and transverse variables, respectively. We shall still refer to them as "time" and "spatial coordinate," slightly bending their meaning from the original optical context. The algebraically localized, exact rogue wave solutions are given in the literature earlier as [14]

$$\begin{aligned} A = \frac{N_1 \exp(2it)}{D_{00}}\,, \\ B = \frac{N_2 \exp(2it)}{D_{00}} \end{aligned} \tag{4}$$

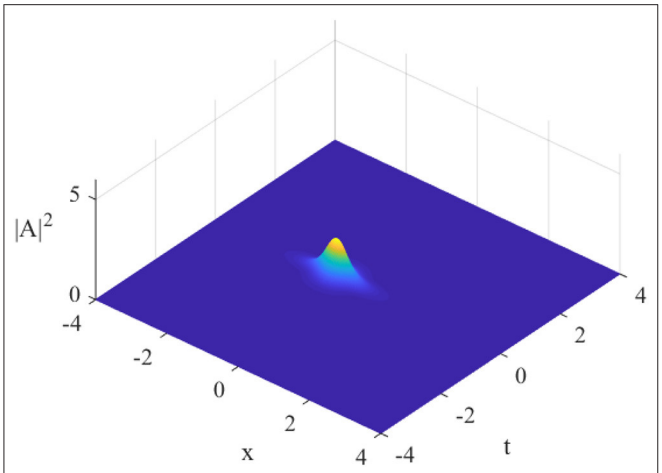

FIGURE 1 | Wave profile of the intensity of the wave envelope in physical space, $|A|^2$ (Equation 4 through Equation 7), vs. spatial coordinate x and time t, $b = 1.5$. The rogue wave has one single maximum. The profile for $|B|^2$ is similar.

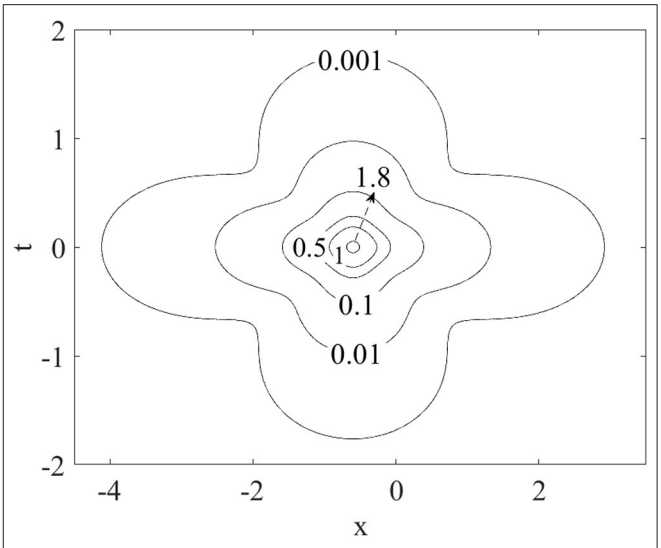

FIGURE 2 | Planar plot of the wave intensity $|A|^2$ in physical space vs. the spatial coordinate x for one particular instant in time t, Equation (4) through Equation (7), $b = 1.5$. The maximum height occurs at the spatial location of $x = -0.600$.

where ($b =$ a free parameter)

$$\begin{aligned} N_1 &= 8(-1+b)(5-2b+2b^2+20it-40t^2 \\ &\quad +6x+4bx+10x^2)\,, \end{aligned} \tag{5}$$

$$\begin{aligned} D_{00} &= 25-20b+24b^2-8b^3+4b^4+144t^2 \\ &\quad +352bt^2-96b^2t^2+1600t^4+60x+16bx \\ &\quad +8b^2x+16b^3x+480t^2x+320bt^2x \\ &\quad +136x^2+8bx^2+56b^2x^2+800t^2x^2+120x^3 \\ &\quad +80bx^3+100x^4\,, \end{aligned} \tag{6}$$

$$\begin{aligned} N_2 &= -25+4b^2-8b^3+4b^4-72it-176ibt \\ &\quad +48ib^2t-256t^2+352bt^2-96b^2t^2 \\ &\quad -1600it^3+1600t^4-24bx+8b^2x+16b^3x \\ &\quad -240itx-160ibtx+480t^2x \\ &\quad +320bt^2x+36x^2+8bx^2+56b^2x^2-400itx^2 \\ &\quad +800t^2x^2+120x^3+80bx^3+100x^4\,. \end{aligned} \tag{7}$$

We can now describe how the conjecture in Section 2 can be verified in the present case:

3.1.1. Physical Space

The wave profile will depend critically on parameter b, which creates a one-dimensional degree of freedom for the system. For a typical value, say $b = 1.500$, the wave intensities, $|A|^2$ and $|B|^2$, will exhibit one single maximum in a three-dimensional plot of intensity vs. space (x) and time (t) (**Figure 1**). This feature is also vividly highlighted in a planar contour plot (**Figure 2**). Of particular relevance to the present study is that this maximum occurs in physical space at the location $x = -0.600$.

3.1.2. Complex Plane

If we now consider the transverse variable x in Equation (3) as complex by analytic continuation, singularities or poles will occur when the denominator D_{00} of Equation (4) vanishes. The numerical values can be readily found by Newton's or other standard methods. As D_{00} is a polynomial of degree four in x for any given t, there will be four poles. For the present case of $b = 1.500$, a plot of the imaginary parts of the poles vs. time t is illustrated in **Figure 3**. At the "turning point," where the movement of the poles (with respect to time) changes direction, the real part is again -0.600.

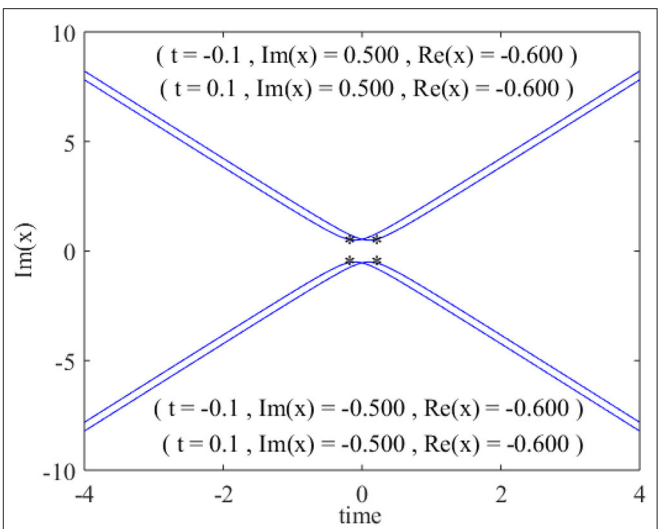

FIGURE 3 | The trajectories of poles in the complex x plane, i.e., zeros of the denominator D_{00} of Equation (4) to Equation (6): imaginary part of the poles vs. time t. At the turning points of the curves, the real part of the pole is -0.600, which is the spatial location of the point of maximum height in physical space.

Other than an apparently fortunate coincidence, this rather amazing match also touches a deeper theoretical question. In principle, the locations of maximum intensities ($|A|^2$, $|B|^2$) can

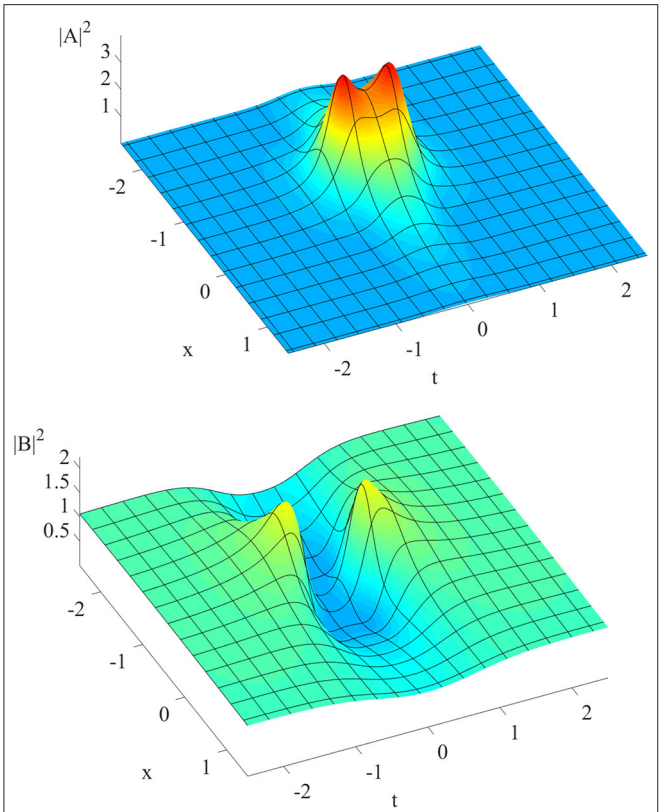

FIGURE 4 | Wave intensities $|A|^2$ (top) and $|B|^2$ (bottom) vs. space x and time t, clearly illustrating the "double peak" structure.

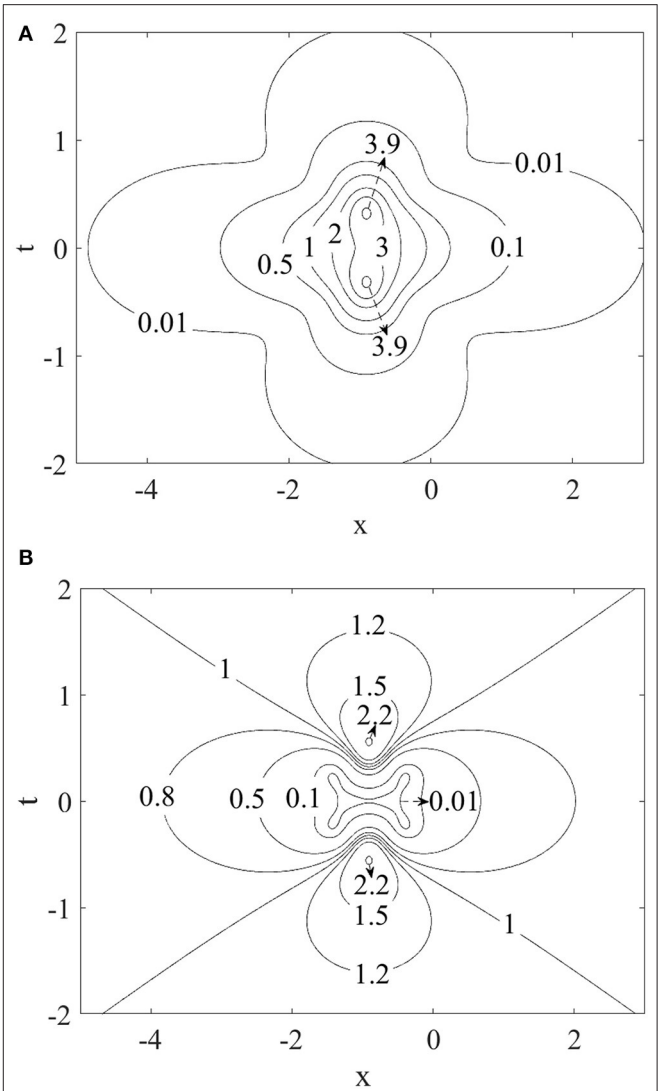

FIGURE 5 | (A) Planar contour plot of the wave intensities $|A|^2$, illustrating the "double peak" structure. **(B)** Planar contour plot of the wave intensities $|B|^2$, illustrating the "double peak" structure.

be determined by calculus using the expressions of Equation (4) through Equation (7). However, the present conjecture does propose another route. More precisely, we only need to select a portion of the complete analytical solution, namely, D_{00} in the present case, and determine the location of the poles in the complex plane by extending the transverse variable by analytic continuation. On the other hand, not all points involving a change of direction of pole trajectories will automatically correspond to peaks of rogue waves. The precise necessary and sufficient conditions are still not clear. On a broader question, whether this association between maximum heights in the physical space and pole trajectories in the complex plane will hold generally for all "soliton equations" remains open. Further investigative efforts are required.

3.2. Rogue Waves With "Double Peaks"

3.2.1. Physical Space

While the rogue wave of the nonlinear Schrödinger equation always displays one single maximum for all input parameters, the present case of coherent coupling may exhibit two peaks as we increase parameter b. As an illustrative example, we select $b = 3.040$. The rogue wave for $|A|^2$ possesses two maxima (**Figure 4**). The intensity first rises to a peak, subsides slightly, and then grows to another peak before decaying into the background again. Similarly, the rogue wave for $|B|^2$ also first rises to a peak, drops to a deeper "valley," and gains strength to attain another peak before disappearing into the background (**Figure 4**). Numerically, this maximum height occurs at the spatial location of $x = -0.908$. This whole feature can also be illustrated through planar contour plots (**Figure 5**).

3.2.2. Complex Plane

If we now allow variable x to be complex by analytic continuation, the poles arise from the zeros of D_{00} (Equation 6). For any given time t, D_{00} is a fourth-order polynomial, and hence there will be four pole trajectories (**Figure 6**). If we trace the imaginary part of the poles as a function of time, the real parts of the poles at the turning points of these trajectories attain the value

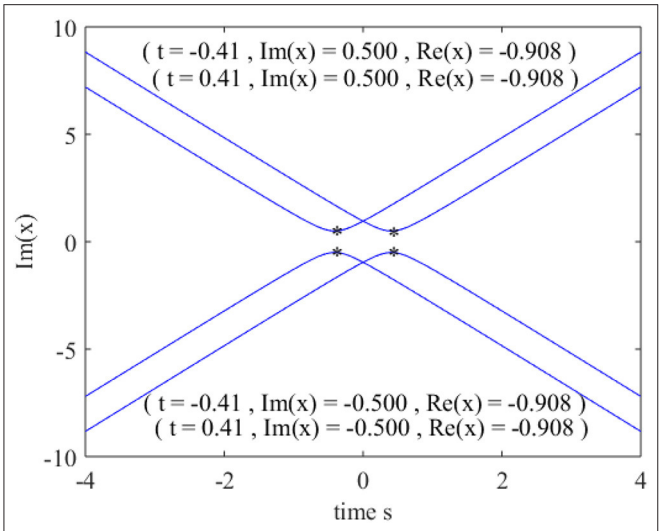

FIGURE 6 | Pole trajectories in the complex plane by allowing the variable x to be complex by analytic continuation. Poles occur at the zeros of D_{00} of Equation (6). The real parts of the poles at the turning points of the trajectories coincide with the locations of maximum heights of the rogue wave in physical space.

of −0.908, identical to the spatial locations of maximum heights in physical space.

To ensure that the phenomenon just displayed is not a fortunate coincidence, we test other values of b (**Table 1**). The remarkable correlations between the real parts of the poles and the locations of maximum heights in physical space are again confirmed.

From these data, we can propose an empirical, linear relation connecting the real part of the poles and parameter b (**Figure 7**).

4. A SCHRÖDINGER EQUATION WITH QUINTIC NON-LINEARITY

To establish further support for the conjecture outlined in Section 2, we consider a Schrödinger equation with quintic (fifth-order) nonlinearity (u = complex valued, slowly varying wave envelope):

$$i\frac{\partial u}{\partial t} = \frac{\partial^2 u}{\partial x^2} \pm ia|u|^2\frac{\partial u}{\partial x} \pm i\beta u^2\frac{\partial u^*}{\partial x} + c|u|^4 u \pm d|u|^2 u\,. \quad (8)$$

The parameters a, β, and d can be arbitrary, but c must be given by

$$c = \frac{\beta(2\beta - a)}{4} \quad (9a)$$

The first- and second-order rogue waves, denoted by u_1 and u_2, respectively, can be established by Darboux transformation. One special case has been given earlier in the literature as [15]

$$a = d = -1, \beta = 1, \quad (9b)$$

TABLE 1 | Correlating the real parts of the poles in the complex x plane and locations of maximum heights in physical space.

Value of parameter b	Maximum of $\|A\|$ in physical space	Turning points of trajectories of imaginary parts in the complex x plane
0.760	−0.452	−0.452
1.520	−0.604	−0.604
3.040	−0.908	−0.908
6.080	−1.516	−1.516
12.160	−2.732	−2.732
24.320	−5.164	−5.164

$$u_1 = \rho_1^2\frac{(40t^2 + 4t(4x + 5i) + 8x^2 - 4ix - 3)\exp(-7it/4)}{40t^2 + 4t(4x - 3i) + 8x^2 - 4ix + 1}\,, \quad (10)$$

$$\begin{aligned}
u_2 =& \rho_2^2[(64000t^6 + 19200t^5(4x + 5i)\\
&+192t^4(360x^2 + 300ix - 133)\\
&+128t^3(272x^3 + 300ix^2 - 282x + 375i)\\
&+72t^2(192x^4 + 64ix^3 - 336x^2\\
&+144ix - 175) + 12t(256x^5 + 64ix^4 + 64x^3\\
&-288ix^2 - 468x - 123i)\\
&+512x^6 - 768ix^5 - 960x^4 + 384ix^3 - 792x^2\\
&+180ix + 45)\exp(-7it/4)]/(64000t^6\\
&+19200t^5(4x - 3i) + 192t^4(360x^2\\
&-340ix + 127) + 128t^3(272x^3\\
&-372ix^2 - 306x - 99i) + 24t^2(576x^4\\
&-832ix^3 - 816x^2 + 336ix\\
&+483) + 12t(256x^5 - 448ix^4 - 192x^3\\
&-96ix^2 + 108x - 75i)\\
&+512x^6 - 768ix^5 - 192x^4 - 384ix^3\\
&+360x^2 - 108ix + 9)\,. \quad (11)
\end{aligned}$$

The parameters ρ_1 and ρ_2 can be obtained from the derivations outlined in earlier references [15]. They may also be readily determined by examining the far field condition [$|x|$, $|t| \to \infty$] of Equations (10) and (11), i.e., they are the roots of the algebraic equation:

$$7/4 = c(\rho_n)^8 \pm d(\rho_n)^4, n = 1,\ 2.$$

As we are concentrating on the *location* of the maximum height of rogue waves and the correlation with pole trajectories, we shall just consider a "normalized" height of the rogue wave $u_n/(\rho_n)^2$ (**Figures 8**, **9**).

The first-order rogue wave displays one single maximum and two "valleys," resembling the properties of the well-known Peregrine soliton (**Figure 8**). The second-order rogue wave exhibits three peaks, one large peak in the center of the three-dimensional plot and two smaller peaks at the sides (**Figure 9**). These two smaller peaks are symmetrically placed and have the same amplitude but are smaller than that of the central maximum.

The locations of the points of maximum height in the physical space are again strongly correlated with the real parts of the poles in

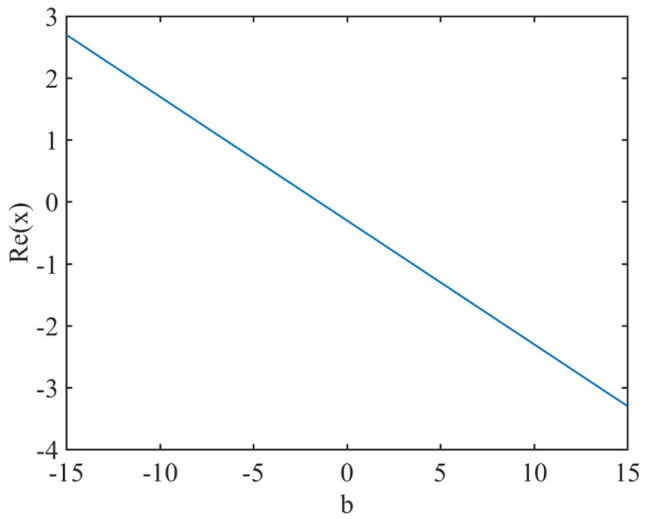

FIGURE 7 | An empirical linear relation between the real parts of the poles at the turning points and parameter b.

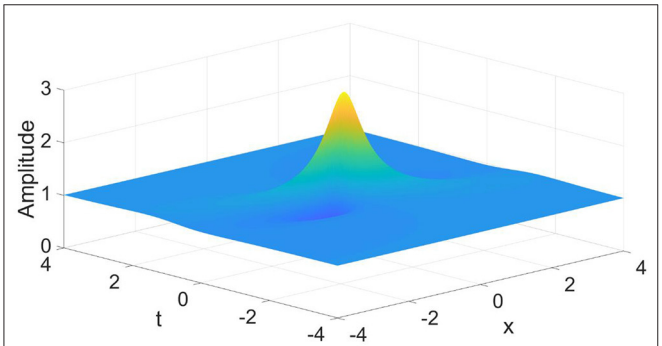

FIGURE 8 | The amplitude of the normalized first-order rogue wave of the complex valued wave envelope u governed by a nonlinear Schrödinger equation with quintic nonlinearity, Equation (8). The profile resembles a classical Peregrine soliton.

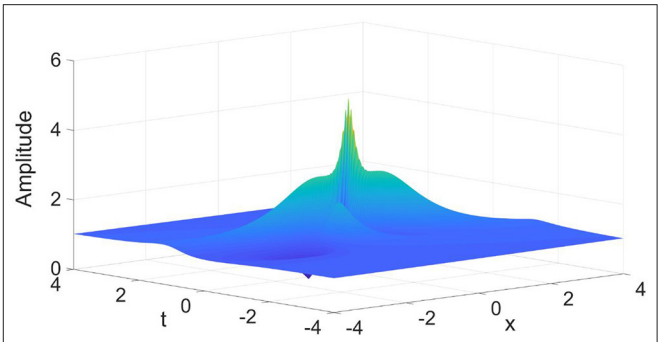

FIGURE 9 | The amplitude of the normalized second-order rogue wave of the complex valued wave envelope u governed by a nonlinear Schrödinger equation with quintic nonlinearity, Equation (8). There is a central maximum with two smaller peaks on the sides.

TABLE 2 | Correlating the real parts of the poles in the complex plane and locations of maximum heights in physical space.

(A) First-order rogue wave	
Physical space: maximum height occurs at $x = 0$	Complex plane (by regarding x as complex): Poles are located at $i/4 - t \pm \{[4(t - i/8)^2 + 1/4]^{1/2}\}i$ As time t evolves, the turning point of the trajectory occurs at $t = 0$
(B) Second-order rogue wave	
Physical space: (1) Central maximum occurring at $x = 0$ at time $t = 0$ (2) Two smaller maxima occurring at the sides, i.e., $x = \pm\ 0.4514$ at time $t = \pm\ 0.2075$	Complex plane (by regarding x as complex): Poles of $u_2 =$ zeros of the denominator of Equation (7): (1) At $t = 0$, pole is located at 0–0.687i (2) At $t = \pm\ 0.2075$, pole is located at 0.4526 – 0.3285i

the complex plane. The matching is exact for the first-order rogue wave and the central maximum for the second-order rogue wave. For the smaller peaks on the sides, the correlation is correct up to two decimal places (**Table 2**).

While this matching alone cannot predict the occurrence of rogue waves, as we need the information on the time t, nevertheless this surprising link might constitute a predictive feature on the extraordinary analytical structures these evolution equations might possess.

5. DISCUSSIONS AND CONCLUSIONS

The Peregrine soliton is an exact, algebraically localized solution of the nonlinear Schrödinger equation and is commonly employed as a model for rogue waves. Higher-order rational solutions also exist for this general hierarchy of evolution equations. Naturally, the algebra becomes increasingly complicated as the order increases. Schemes to locate the maxima in physical space thus become a practical necessity in addition to being of theoretical interest as the families of Schrödinger equations are widely applicable to physical sciences, e.g., fluid mechanics, optics, and plasma.

We proposed a conjecture (Section 2) which will hopefully provide an important step in this direction [8–10]. If the transverse variable of the Schrödinger equation is allowed to be complex, the real parts of the pole trajectories at the turning points will be identical to or will closely correlate with the locations of maximum heights of the rogue wave in physical space. Concurrently, this conjecture highlights deeper issues which might reveal the analytic structures of exact solutions of the family of nonlinear Schrödinger systems, as a portion of the analytic solution appears to be sufficient to give a reasonable prediction on the maximum amplitude of the wave profile.

To substantiate our earlier works [8, 10], we study further examples of Schrödinger equations here, namely, those with coherent coupling [14, 16] and quintic (fifth-order) nonlinearities [15]. The conjecture is again verified for the first and second-order rogue waves of these models.

Many challenges remain ahead. It would be fruitful to investigate other evolution systems which admit unexpectedly large displacements, e.g., rogue waves on a periodic background [17–19] and rogue waves for discrete equations [20, 21].

DATA AVAILABILITY STATEMENT

The original contributions presented in the study are included in the article/supplementary material, further inquiries can be directed to the corresponding author.

AUTHOR CONTRIBUTIONS

KWC proposed the theoretical framework. NNP performed the calculation for the case of coherent coupling, while TLC was responsible for the quintic case. All authors contributed to the article and approved the submitted version.

FUNDING

Partial financial support has been provided by the Research Grants Council General Research Fund contract HKU17200718.

REFERENCES

1. Peregrine, DH. Water-waves, nonlinear Schrödinger-equations and their solutions. *J Aust Math Soc B*. (1983) **25**:16–43. doi: 10.1017/S0334270000003891
2. Craik ADD. *Wave Interactions and Fluid Flows*. Cambridge: Cambridge University Press (1985). doi: 10.1017/CBO9780511569548
3. Kivshar Y, Agrawal G. *Optical Solitons: From Fibers to Photonic Crystals*. San Diego, CA: Academic Press (2003). doi: 10.1016/B978-012410590-4/50012-7
4. Dysthe K, Krogstad HE, Müller P. Oceanic rogue waves. *Annu Rev Fluid Mech*. (2008) **40**:287–310. doi: 10.1146/annurev.fluid.40.111406.102203
5. Kharif C, Pelinovsky E, Slunyaev A. *Rogue Waves in the Ocean*. Berlin: Springer (2009).
6. Onorato M, Residori S, Bortolozzo U, Montina A, Arecchi FT. Rogue waves and their generating mechanisms in different physical contexts. *Phys Rep*. (2013) **528**:47–89. doi: 10.1016/j.physrep.2013.03.001
7. Chen, SH, Baronio F, Soto-Crespo, JM, Grelu P, Mihalache D. Versatile rogue waves in scalar, vector, and multidimensional nonlinear systems. *J Phys A Math Theor*. (2017) **50**:463001. doi: 10.1088/1751-8121/aa8f00
8. Chung WC, Chiu TL, Chow KW. Employing the dynamics of poles in the complex plane to describe properties of rogue waves: case studies using the Boussinesq and complex modified Korteweg–de Vries equations. *Nonlinear Dyn*. (2020) **99**:2961–70. doi: 10.1007/s11071-020-05475-z
9. Chiu TL, Liu TY, Chan HN, Chow KW. The dynamics and evolution of poles and rogue waves for nonlinear Schrödinger equations. *Commun Theor Phys*. (2017) **68**:290–4. doi: 10.1088/0253-6102/68/3/290
10. Liu TY, Chiu TL, Clarkson PA, Chow KW. A connection between the maximum displacements of rogue waves and the dynamics of poles in the complex plane. *Chaos*. (2017) **27**:091103. doi: 10.1063/1.5001007
11. Konno K, Ito H. Nonlinear interactions between solitons in complex t-plane 1. *J Phys Soc Jpn*. (1987) **56**:897–904. doi: 10.1143/JPSJ.56.897
12. Konno K. Nonlinear interactions between solitons in complex t-plane 2. *J Phys Soc Jpn*. (1987) **56**:1334–9. doi: 10.1143/JPSJ.56.1334
13. Ankiewicz A, Clarkson PA, Akhmediev N. Rogue waves, rational solutions, the patterns of their zeros and integral relations. *J Phys A Math Theor*. (2010) **43**:122002. doi: 10.1088/1751-8113/43/12/122002
14. Sun WR, Tian B, Jiang Y, Zhen HL. Optical rogue waves associated with the negative coherent coupling in an isotropic medium. *Phys Rev E*. (2015) **91**:023205. doi: 10.1103/PhysRevE.91.023205
15. Wang L, Jiang DY, Qi FH, Shi YY, Zhao YC. Dynamics of the higher-order rogue waves for a generalized mixed nonlinear Schrödinger model. *Commun Nonlinear Sci Numer Simulat*. (2017) **42**:502–19. doi: 10.1016/j.cnsns.2016.06.011
16. Zhang CR, Tian B, Liu L, Chai HP, Du Z. Vector breathers with the negatively coherent coupling in a weakly birefringent fiber. *Wave Motion*. (2019) **84**:68–80. doi: 10.1016/j.wavemoti.2018.09.003
17. Peng WQ, Tian SF, Wang XB, Zhang TT. Characteristics of rogue waves on a periodic background for the Hirota equation. *Wave Motion*. (2020) **93**:102454. doi: 10.1016/j.wavemoti.2019.102454
18. Li M, Fu HM, Wu CF. General soliton and (semi-)rational solutions to the nonlocal Mel'nikov equation on the periodic background. *Stud Appl Math*. (2020) **145**:97–136. doi: 10.1111/sapm.12313
19. Chen JB, Pelinovsky DE, White RE. Rogue waves on the double-periodic background in the focusing nonlinear Schrödinger equation. *Phys Rev E*. (2019) **100**:052219. doi: 10.1103/PhysRevE.100.052219
20. Ortiz AK, Prinari B. Inverse scattering transform for the defocusing Ablowitz-Ladik system with arbitrarily large nonzero background. *Stud Appl Math*. (2019) **143**:373–403. doi: 10.1111/sapm.12282
21. Wang HT, Wen XY. Soliton elastic interactions and dynamical analysis of a reduced integrable nonlinear Schrödinger system on a triangular-lattice ribbon. *Nonlinear Dyn*. (2020) **100**:1571–87. doi: 10.1007/s11071-020-05587-6

Conflict of Interest: The authors declare that the research was conducted in the absence of any commercial or financial relationships that could be construed as a potential conflict of interest.

frontiers in Physics

ORIGINAL RESEARCH
published: 17 November 2020
doi: 10.3389/fphy.2020.596950

Peregrine Solitons on a Periodic Background in the Vector Cubic-Quintic Nonlinear Schrödinger Equation

Yanlin Ye[1], *Lili Bu*[1], *Wanwan Wang*[1], *Shihua Chen*[1]*, *Fabio Baronio*[2]* and *Dumitru Mihalache*[3]

[1]School of Physics and Quantum Information Research Center, Southeast University, Nanjing, China, [2]INO CNR and Dipartimento di Ingegneria Dell'Informazione, Università di Brescia, Brescia, Italy, [3]Department of Theoretical Physics, Horia Hulubei National Institute for Physics and Nuclear Engineering, Măgurele, Romania

We present exact explicit Peregrine soliton solutions based on a periodic-wave background caused by the interference in the vector cubic-quintic nonlinear Schrödinger equation involving the self-steepening effect. It is shown that such periodic Peregrine soliton solutions can be expressed as a linear superposition of two fundamental Peregrine solitons of different continuous-wave backgrounds. Because of the self-steepening effect, some interesting Peregrine soliton dynamics such as ultrastrong amplitude enhancement and rogue wave coexistence are still present when they are built on a periodic background. We numerically confirm the stability of these analytical solutions against non-integrable perturbations, i.e., when the coefficient relation that enables the integrability of the vector model is slightly lifted. We also demonstrate the interaction of two Peregrine solitons on the same periodic background under some specific parameter conditions. We expect that these results may shed more light on our understanding of the realistic rogue wave behaviors occurring in either the fiber-optic telecommunication links or the crossing seas.

Keywords: peregrine soliton, rogue wave, vector nonlinear Schrödinger equation, self-steepening, cubic-quintic nonlinearity

OPEN ACCESS

Edited by:
Bertrand Kibler, UMR6303 Laboratoire Interdisciplinaire Carnot de Bourgogne (ICB), France

Reviewed by:
Gennady El, Northumbria University, United Kingdom
Alberto Molgado, Autonomous University of San Luis Potosí, Mexico

***Correspondence:**
Shihua Chen
cshua@seu.edu.cn
Fabio Baronio
fabio.baronio@unibs.it

Specialty section:
This article was submitted to Mathematical and Statistical Physics, a section of the journal Frontiers in Physics

Received: *20 August 2020*
Accepted: *05 October 2020*
Published: *17 November 2020*

Citation:
Ye Y, Bu L, Wang W, Chen S, Baronio F and Mihalache D (2020) Peregrine Solitons on a Periodic Background in the Vector Cubic-Quintic Nonlinear Schrödinger Equation. Front. Phys. 8:596950. doi: 10.3389/fphy.2020.596950

1 INTRODUCTION

Originally, rogue waves refer to the surface gravity waves occurring in the open ocean whose wave heights are at least twice as high as the significant wave height of the surrounding waves [1]. Under extreme conditions, they soar like a wall of water that can dwarf even the largest of modern ships, and then disappear into the sea as if all this does not happen [2, 3]. As these massive waves usually possess a devastating power and behave unpredictably, they are hard to observe and study. Historically, the first scientific observation that proved the existence of rogue waves was made at the Draupner oil platform in the North Sea on January 1, 1995, hence named "New Year Wave" afterward [4]. Since then, rogue waves became an active multidisciplinary area of research, ranging from hydrodynamics to optics and photonics [5–8].

Despite the extensive studies, there is still a lot of debate over the physical mechanisms behind rogue waves [9, 10]. While the linear theory based on the superposition of random waves or the inhomogeneity has prevailed for some time [11, 12], the nonlinear viewpoint gains increasing

popularity, as in a stricter sense only the superposition process of nonlinear waves could bring about extreme waves higher than the sum of the wave heights involved [13]. Actually, the most accepted mechanisms—integrable turbulence [14, 15] and modulation instability (MI) [16, 17] are of nonlinear nature, by which irregular extreme wave events could be created. This is easily understood within the MI framework, where the periodic perturbations on a continuous-wave (cw) background tend to undergo exponential growth initially, and then evolve into a multiplicity of waves, from which rogue waves may arise [18–20]. Therefore, using nonlinear Schrödinger (NLS) equation or other relevant equations to model realistic rogue waves is not only possible but also fascinating, as done in the current rogue wave investigations [21–23].

Mathematically, one can associate rogue waves to the rational solutions of the integrable nonlinear wave equation, which are localized on both time and space [18]. A typical example is the Peregrine soliton, which is a fundamental rational solution of the celebrated NLS equation [24]. This type of soliton solution exhibits a single doubly-localized peak on a finite background, with its peak position and constant phase all undetermined, hence matching well the fleeting and transient wave characteristics of rogue waves as witnessed in real world. For this reason, the Peregrine soliton was thought of as a promising prototype of rogue wave events seen in nature [25]. Its importance and universality have been confirmed by a succession of well-designed experiments, with physical settings spanning from the water-wave tanks [26] to optical fibers [21, 27], and from the deep ocean [28] to plasmas [29]. Moreover, in a multicomponent (or vector) nonlinear system, some variants of Peregrine solitons such as dark Peregrine solitons [30] and anomalous Peregrine solitons [31, 32] have come to light, opening new perspectives on the versatility of Peregrine solitons as an essential prototype in rogue wave science. Here, in a broad sense, we still term the fundamental rogue waves in a multicomponent system Peregrine solitons or Peregrine solitary waves, provided that they inherit the basic wave features of the Peregrine soliton in the original NLS equation [33, 34].

Recently, there has also been an intense research on the so-called periodic Peregrine soliton, by which we mean a Peregrine soliton formed on a periodic background [35–41]. Normally, when a multicomponent nonlinear system is confronted, it may occur to us that an interference would occur when two or more monochromatic waves of different frequencies are simultaneously present in the same region. The appearance of interference fringes, which was ever instrumental in establishing the wave nature of light in the history, is a direct evidence of such interference effects. As interference effects are inherent to the vector nonlinear system consisting of continuous waves, it is therefore reasonable for us to inspect the possibility of the existence of Peregrine solitons on a periodic background caused by interference.

In this paper, we present an in-depth study of the formation of Peregrine solitons on a periodic background, within the framework of the vector cubic-quintic NLS (CQ-NLS) equation, which is a two-component version of the scalar NLS-type Gerdjikov–Ivanov equation [42]. As will be shown, this model has included the necessary ingredients such as group-velocity dispersion (GVD), Kerr nonlinearity, quintic nonlinearity, and self-steepening, which could provide more accurate descriptions for realistic rogue waves met in complex systems, as compared to the simple Manakov model [43, 44] and to the vector Gerdjikov–Ivanov equation [45]. We will show that in this vector nonlinear system, a periodic background could form as a result of an interference between two continuous waves. Further, we present explicitly the general Peregrine soliton solutions built on such a periodic background, which were not reported previously, to the best of our knowledge. The robustness of these analytical solutions against non-integrable perturbations has been numerically confirmed, by lifting the integrality condition of the above vector CQ-NLS model. With these exact solutions, the dynamics of the coexisting and anomalous Peregrine solitons, as well as their interactions, of course occurring on a periodic background, are exhibited. The underlying mechanisms responsible for the generation of such periodic Peregrine solitons are also discussed.

2 THEORETICAL FRAMEWORK

In the context of fiber optics, we write the vector CQ-NLS equation as

$$\mathrm{i}u_{1z}+\frac{1}{2}u_{1tt}+\sigma u_1\left(|u_1|^2+|u_2|^2\right)+\gamma^2 u_1\left(|u_1|^2+|u_2|^2\right)^2-\mathrm{i}\gamma u_1\left(u_1u_{1t}^*+u_2u_{2t}^*\right)=0, \quad (1)$$

$$\mathrm{i}u_{2z}+\frac{1}{2}u_{2tt}+\sigma u_2\left(|u_1|^2+|u_2|^2\right)+\gamma^2 u_2\left(|u_1|^2+|u_2|^2\right)^2-\mathrm{i}\gamma u_2\left(u_1u_{1t}^*+u_2u_{2t}^*\right)=0, \quad (2)$$

where $u_{1,2}(z,t)$ are the normalized complex envelopes of two optical components, and z and t are the distance and retarded time, respectively. Subscripts z and t stand for partial derivatives. While the constant coefficient 1/2 points to the GVD effect and the coefficient σ to the self-phase modulation, γ accounts for the pulse self-steepening effect [46], and γ^2 relates to the quintic nonlinearity, which was often found in highly nonlinear materials such as chalcogenide fibers [47]. Here, in terms of the anomalous and normal dispersion cases, the parameter σ can be normalized to 1 and −1, respectively, which have an otherwise interpretation of self-focusing and self-defocusing in the context of beam optics, when the independent variable t is interpreted as the transversal spatial coordinate [48]. Besides, the combination of cubic and quintic nonlinearity is a conventional consideration in the design of mode-locked fiber lasers [49] or in stabilizing the soliton propagation in nonlinear media [50]. With the above ingredients included, this vector model represents an important generalization of the Manakov system [43, 44], although the former involves a specific relation between the coefficients for quintic nonlinearity and self-steepening terms. Therefore, from a mathematical perspective, it can provide a

more accurate description of the propagation of ultrashort optical pulses in highly nonlinear birefringent fibers. The physical relevance of this integrable model can be seen by inspecting the stability of its solutions against non-integrable perturbations, i.e., when the above mentioned specific relation is lifted. We should point out that, to weigh the nonlinearity factors that affect the rogue wave dynamics, we have excluded the higher-order dispersion terms from **Eqs 1** and **2**, which usually appear when pulses are driven in the few-cycle regime [47] or in the microstructure fiber [51].

Obviously, the above vector system could be reproduced from the compatibility condition, $\mathbf{R}_{tz} = \mathbf{R}_{zt}$ (which can read $\mathbf{U}_z - \mathbf{V}_t + \mathbf{UV} - \mathbf{VU} = 0$), of the following 3×3 linear eigenvalue problem:

$$\mathbf{R}_t = \mathbf{UR}, \ \mathbf{R}_z = \mathbf{VR}, \tag{3}$$

where $\mathbf{R} = [r, s, w]^T$ is the eigenfunction (T means a matrix transpose, and r, s, and w are functions of the variables z, t, and the complex spectral parameter λ), and

$$\mathbf{U} = -\frac{\mathrm{i}(\lambda - \sigma)\sigma_3}{2\gamma} + \sqrt{\lambda}\mathbf{Q} - \mathrm{i}\gamma\sigma_3\mathbf{Q}^2,$$

$$\mathbf{V} = -\frac{\mathrm{i}(\lambda - \sigma)^2\sigma_3}{4\gamma^2} + \frac{\sqrt{\lambda}}{2}\left(\frac{\lambda - \sigma}{\gamma}\mathbf{Q} - \mathrm{i}\sqrt{\lambda}\,\sigma_3\mathbf{Q}^2 + \mathrm{i}\sigma_3\mathbf{Q}_t\right)$$

$$+\frac{\mathrm{i}\gamma^2\sigma_3}{2}\mathbf{Q}^4 - \frac{\gamma}{2}(\mathbf{QQ}_t - \mathbf{Q}_t\mathbf{Q}),$$

with $\sigma_3 = \mathrm{diag}(1, -1, -1)$ being the diagonal matrix, and

$$\mathbf{Q} = \begin{pmatrix} 0 & u_1 & u_2 \\ -u_1^* & 0 & 0 \\ -u_2^* & 0 & 0 \end{pmatrix}.$$

We should point out that the Lax pair **Eq. 3** takes the same form as used in the scalar CQ-NLS equation [42], except that the **Q** is now defined by a 3×3 matrix. The subsequent Darboux dressing operation is straightforward. In simple terms, let first $u_{1,2}$ be the seeding solutions and substitute them into the Lax pair **Eq. 3** to yield the eigenfunction **R**. Then, in terms of **R** at given spectral parameter, a dress operator **D** can be properly constructed, by which **R** will be dressed into $\mathbf{R}'$ (i.e., $\mathbf{R}' = \mathbf{DR}$). It requires that $\mathbf{R}'$ must satisfy the Lax pair **Eq. 3** of the same form, but with a new pair of potentials u_1' and u_2' in **U** and **V**. Lastly, the Darboux transformation formulas that relate the new solutions $u_{1,2}'$ to the seeding solutions $u_{1,2}$ can be found. As concerns this standard procedure, one can refer to Refs. 52–56 for more details. Intended for rogue wave states only, a generalized or nonrecursive Darboux transformation method can be developed, which can give the nth-order rogue wave solutions without any iteration operation [42, 57, 58, 59].

For our present purposes, we are merely concerned with the fundamental rogue wave solutions, which evolve directly from the MI of continuous wave fields. It is easily shown that the initial plane-wave solutions u_{j0} $(j = 1, 2)$ of the vector CQ-NLS equation, defined by the amplitudes a_j, wavenumbers k_j, frequencies ω_j, and initial constant phases ϕ_j, all of which are real, can be expressed as

$$u_{j0} = a_j \exp\left[\mathrm{i}\left(k_j z + \omega_j t + \phi_j\right)\right], \tag{4}$$

under the dispersion relations:

$$k_j = A(\sigma + \gamma^2 A) - \gamma(\omega_1 a_1^2 + \omega_2 a_2^2) - \frac{\omega_j^2}{2}.$$

Here and in what follows, we define $A = a_1^2 + a_2^2$ for the sake of brevity. Also, we will assume below the initial constant phases ϕ_j to be zero, without loss of generality. Then, with the help of the Darboux transformation technique outlined above [42, 58, 59] followed by tedious algebraic manipulations, we obtain the exact fundamental rogue wave solutions on a periodic background, expressed by

$$u_1 = \frac{\sqrt{2}}{2}(Uu_{10} + Vu_{20}), \ u_2 = \frac{\sqrt{2}}{2}(Uu_{10} - Vu_{20}), \tag{5}$$

where u_{10} and u_{20} are initial plane-wave solutions denoted by **Eq. 4**, and U(z,t) and $V(z, t)$ are the complex rational polynomials given by

$$U = 1 - \frac{2\mathrm{i}\alpha\left[\nu^2 z - (A\gamma + \mu + \omega_1)\theta\right] + \eta(A\gamma^2 - \gamma\omega_1 + \sigma)}{\left[(A\gamma + \mu + \omega_1)^2 + \nu^2\right](M + \mathrm{i}N)}, \tag{6}$$

$$V = 1 - \frac{2\mathrm{i}\alpha\left[\nu^2 z - (A\gamma + \mu + \omega_2)\theta\right] + \eta(A\gamma^2 - \gamma\omega_2 + \sigma)}{\left[(A\gamma + \mu + \omega_2)^2 + \nu^2\right](M + \mathrm{i}N)}, \tag{7}$$

with

$$\theta = t + (A\gamma + \mu)z, \tag{8}$$

$$\eta = 2A\gamma^2 + \mu\gamma + \sigma, \ \alpha = \nu^2\gamma^2 + \eta^2, \tag{9}$$

$$M = \alpha(\theta^2 + \nu^2 z^2) + \frac{\eta^2}{4\nu^2}, \ N = \gamma(\nu^2\gamma z - \eta\theta). \tag{10}$$

The parameters μ and ν in **Eqs 6–10** are the real and imaginary parts of the root χ $(= \mu + \mathrm{i}\nu)$ of the algebraic equation:

$$1 + \frac{a_1^2(A\gamma^2 - \gamma\omega_1 + \sigma)}{(A\gamma + \chi + \omega_1)^2} + \frac{a_2^2(A\gamma^2 - \gamma\omega_2 + \sigma)}{(A\gamma + \chi + \omega_2)^2} = 0. \tag{11}$$

We would like to emphasize that our solutions given by **Eq. 5** entail the most general closed form for a pair of Peregrine rogue waves on a periodic background, and their existence relies on the algebraic condition given by **Eq. 11**. Generally, the real-coefficient quartic **Eq. 11** admits two different pairs of complex roots and hence the solutions (**Eq. 5**) may exhibit two different Peregrine soliton structures for the same set of initial parameters. Moreover, in our solutions, the rational polynomials U and V have been well separated by real and imaginary parts, and their peaks have been translated to locate on the origin so that their peak-to-background ratios read $|f_U|$ and $|f_V|$, respectively, where

$$f_U \equiv U(0, 0) = 1 - \frac{4(A\gamma^2 - \gamma\omega_1 + \sigma)\nu^2}{\eta\left[(A\gamma + \mu + \omega_1)^2 + \nu^2\right]}, \tag{12}$$

$$f_V \equiv V(0, 0) = 1 - \frac{4(A\gamma^2 - \gamma\omega_2 + \sigma)\nu^2}{\eta\left[(A\gamma + \mu + \omega_2)^2 + \nu^2\right]}. \tag{13}$$

Once the real parameters μ and ν are known from **Eq. 11**, the intriguing rogue wave dynamics on a periodic background, defined by **Eq. 5**, could be uncovered. As a matter of fact, the conventional rogue wave dynamics on a cw background, which are known as $u_1 = Uu_{10}$ and $u_2 = Vu_{20}$, can be understood as well, and one can refer to [59] for more information.

Let us now consider the special case where the quartic **Eq. 11** admits two pairs of equal complex roots. In this situation, one can find that, when the plane-wave parameters satisfy

$$A\left(2A\gamma^2 - \kappa\gamma + 2\sigma\right)^2 - \left(9A\gamma^2 - 4\kappa\gamma + 8\sigma\right)\delta^2 = 0, \tag{14}$$

$$B = \frac{A\delta\gamma}{2A\gamma^2 - \kappa\gamma + 2\sigma}, \tag{15}$$

where $\kappa = \omega_1 + \omega_2$, $\delta = \omega_1 - \omega_2$, and $B = a_1^2 - a_2^2$ (the same below, for the sake of brevity), the real and imaginary parts of the root χ would take the following simple form

$$\mu = -A\gamma - \frac{\kappa}{2}, \quad \nu = \frac{\sqrt{3}}{2}\delta. \tag{16}$$

Substituting **Eq. 16** into **Eqs 6** and **7** yields (noting now that $\alpha = \frac{3}{4}\delta^2\gamma^2 + \eta^2$)

$$U = 1 - \frac{\mathrm{i}\left(\frac{3}{2}\delta z - \theta\right)\delta\alpha + \eta\left(\eta - \frac{1}{2}\delta\gamma\right)}{\delta^2\alpha\left(\frac{3}{4}\delta^2 z^2 + \theta^2\right) + \frac{1}{3}\eta^2 - \mathrm{i}\delta^2\gamma\left(\eta\theta - \frac{3}{4}\delta^2\gamma z\right)}, \tag{17}$$

$$V = 1 - \frac{\mathrm{i}\left(\frac{3}{2}\delta z + \theta\right)\delta\alpha + \eta\left(\eta + \frac{1}{2}\delta\gamma\right)}{\delta^2\alpha\left(\frac{3}{4}\delta^2 z^2 + \theta^2\right) + \frac{1}{3}\eta^2 - \mathrm{i}\delta^2\gamma\left(\eta\theta - \frac{3}{4}\delta^2\gamma z\right)}, \tag{18}$$

which result in the special type of deterministic Peregrine rogue wave solutions denoted by **Eq. 5**, for any given set of parameters that meets **Eqs 14** and **15**. As there is only one pair of (μ, ν) value given by **Eq. 16**, no rogue wave coexistence [23] would occur any more in this special case.

Further, we find that when the parameter conditions given by **Eqs 14** and **15** are satisfied, there would exist a pair of two-Peregrine-soliton states that can describe the interaction between two Peregrine rogue waves on the periodic background. After some algebra, we can express this special kind of two-Peregrine-soliton solutions by the same **Eq. 5**, but let the complex rational polynomials U and V be denoted by

$$U = 1 - \frac{3\sqrt{3}\delta\gamma R S^* \beta\phi^*}{\gamma\left(|\beta|^2|R|^2 + \lambda_0 a_1^2|S|^2 + \lambda_0 a_2^2|W|^2\right)}, \tag{19}$$

$$V = 1 + \frac{3\sqrt{3}\delta\gamma R W^* \beta\phi}{\gamma\left(|\beta|^2|R|^2 + \lambda_0 a_1^2|S|^2 + \lambda_0 a_2^2|W|^2\right)}, \tag{20}$$

where

$$R = \gamma_1 + \gamma_2\xi + \gamma_3\left(\frac{3\xi^2}{2} - \frac{\mathrm{i}\sqrt{3}\xi}{\delta} - \frac{\mathrm{i}3z}{2}\right), \tag{21}$$

$$S = R + \frac{\gamma a_2^2 - \delta\phi}{\delta\left(\delta + \gamma B\right)}\left[\gamma_2 + \gamma_3\left(3\xi + \frac{\mathrm{i}\sqrt{3}}{\delta\phi}\right)\right], \tag{22}$$

$$W = R + \frac{\gamma a_1^2 + \delta\phi^*}{\delta\left(\delta + \gamma B\right)}\left[\gamma_2 + \gamma_3\left(3\xi + \frac{\mathrm{i}\sqrt{3}}{\delta\phi^*}\right)\right], \tag{23}$$

with $\xi = \frac{\sqrt{3}}{2}\delta z - \mathrm{i}(t - \kappa z/2)$, $\phi = \frac{1}{2} - \frac{\mathrm{i}\sqrt{3}}{2}$, $\lambda_0 = \sigma - \frac{\gamma\kappa}{2} + \frac{\mathrm{i}3\sqrt{3}}{2}\delta\gamma$, $\beta = \frac{\sqrt{3}}{2}\gamma A + \frac{\mathrm{i}}{2}(\gamma B - 2\delta)$, and γ_1, γ_2 and $\gamma_3\,(\neq 0)$ being three arbitrary complex constants (not confused with the system parameter γ). It should be noted that, as $\gamma_3 = 0$, the above polynomials U and V can reduce to **Eqs 17** and **18**, and then the two-soliton dynamics would disappear.

3 INTRIGUING ROGUE WAVE DYNAMICS ON A PERIODIC BACKGROUND

For given initial parameters, our analytical solutions **Eqs 5–7** may exhibit intriguing rogue wave characteristics, including periodic background hallmark, rogue wave coexistence, anomalous peak amplitude, and applicability for both normal and anomalous dispersions. In the following, we proceed to uncover these interesting features as well as their underlying generation mechanisms.

First of all, it is obvious that the periodic Peregrine soliton solutions of the vector CQ-NLS equation can be generally expressed as a linear superposition of two fundamental Peregrine solitons of different cw backgrounds, provided that the continuous waves involve a nonvanishing frequency difference. In fact, as one might check, when the frequency difference meets $\delta = \omega_1 - \omega_2 = 0$, the two field components u_1 and u_2 would take the form of conventional Peregrine solitons, with a three-fold peak amplitude but without any periodicity on the amplitude of the background, as seen in **Figures 1A,B**, where the Peregrine solitons defined by **Eq. 5** are demonstrated in the anomalous dispersion regime ($\sigma = 1$), with the initial parameters $\omega_1 = \omega_2 = 3/2$, $\gamma = 1$, $a_1 = \sqrt{3/2}$, and $a_2 = \sqrt{1/2}$. However, once $\delta \neq 0$, the background fields that support the rogue waves would feature the periodic or amplitude-modulated waves defined by

$$\left|u_1^{\mathrm{bg}}\right| = \sqrt{\frac{A}{2} + a_1 a_2 \cos\left[\delta\left(t - z\kappa/2\right)\right]}, \tag{24}$$

$$\left|u_2^{\mathrm{bg}}\right| = \sqrt{\frac{A}{2} - a_1 a_2 \cos\left[\delta\left(t - z\kappa/2\right)\right]}. \tag{25}$$

It follows easily that the characteristic periodicity results from the interference effects of two plane waves (see the second terms in the radicals), and that the background waves will be modulated at a temporal beat frequency equal to δ, with their patterns moving at a transversal velocity equal to $v = t/z = \kappa/2$. **Figures 1C–F** show two pairs of Peregrine solitons formed on such periodic backgrounds, using otherwise identical initial parameters as in **Figures 1A,B** except $\omega_2 = -3/2$, which means $\delta \neq 0$ and $\kappa = 0$. These two pairs of periodic Peregrine solitons are caused by two different (μ, ν) values (see caption) that are obtained by substituting the same set of initial parameters into the quartic **Eq. 11**. This means that on the same periodic background would occur the pair of Peregrine soliton states shown in **Figures 1C,D** or the other pair shown in **Figures 1E,F**, or both pairs simultaneously. This is what we meant the rogue wave coexistence first proposed for multi-component long-wave–short-wave resonance [23].

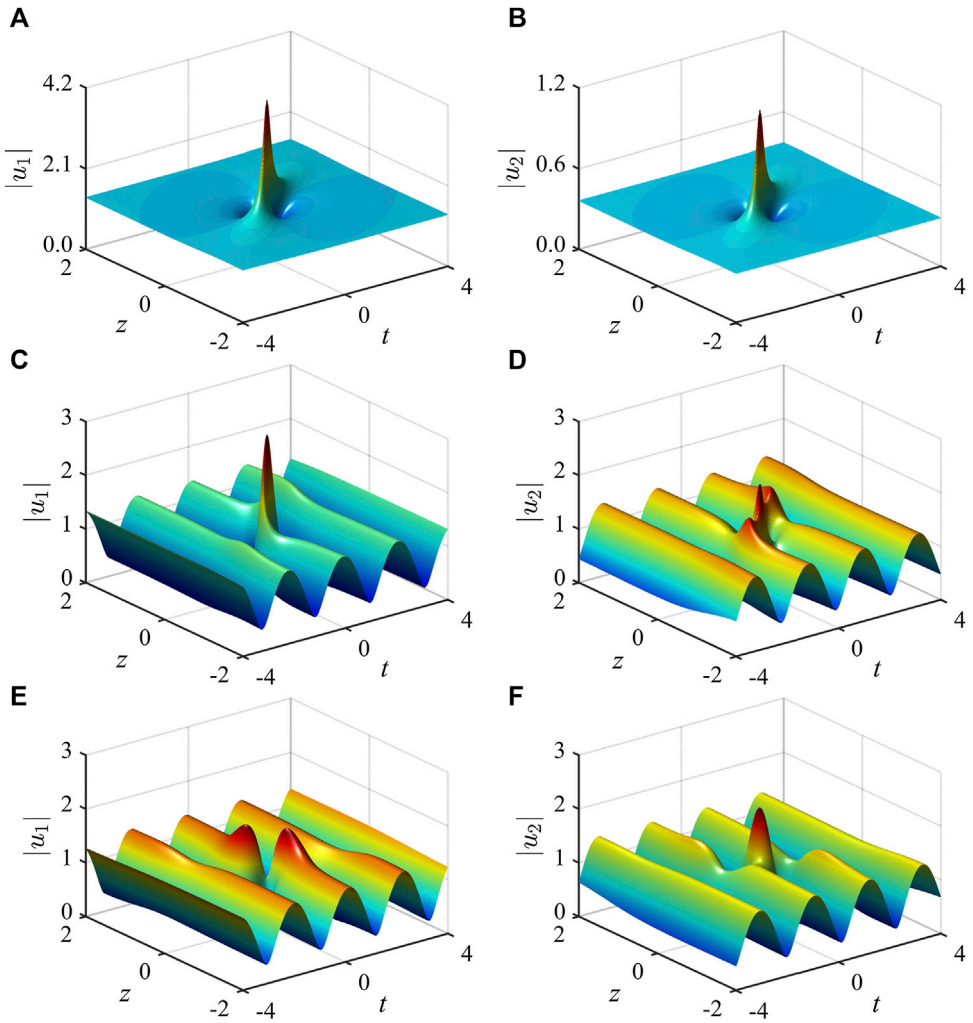

FIGURE 1 | Peregrine soliton states formed on **(A),(B)** the cw backgrounds when $\delta = 0$ and **(C)–(F)** the periodic-wave backgrounds when $\delta \neq 0$, in the anomalous dispersion regime ($\sigma = 1$), under the same parameters $a_1 = \sqrt{3/2}$, $a_2 = \sqrt{1/2}$, and $\gamma = 1$. The other parameters are specified by **(A),(B)**: $\omega_1 = \omega_2 = 3/2$, $\mu = -7/2$, $\nu = \sqrt{3}$; **(C),(D)**: $\omega_1 = 3/2$, $\omega_2 = -3/2$, $\mu = -2 - \frac{3}{4}\sqrt{2\sqrt{3}}$, $\nu = \frac{3}{4}\sqrt{2\sqrt{3}}$; and **(E),(F)**: $\omega_1 = 3/2$, $\omega_2 = -3/2$, $\mu = -2 + \frac{3}{4}\sqrt{2\sqrt{3}}$, $\nu = \frac{3}{4}\sqrt{2\sqrt{3}}$.

Further, we find that the Peregrine solitons formed will possess the following enhancement factors, relative to the average amplitude, $\sqrt{A/2}$, of the periodic background:

$$f_{u_1} = \frac{|u_1(0,0)|}{\sqrt{A/2}} = \frac{|f_U a_1 + f_V a_2|}{\sqrt{A}}, \tag{26}$$

$$f_{u_2} = \frac{|u_2(0,0)|}{\sqrt{A/2}} = \frac{|f_U a_1 - f_V a_2|}{\sqrt{A}}, \tag{27}$$

where $f_{U,V}$ are defined by **Eqs 12** and **13**. According to the above definitions, one can find that the Peregrine solitons shown in **Figures 1C–F** are actually enhanced in the center position up to 2.91 [**Figure 1C**], 1.80 [**Figure 1D**], 0.89 [**Figure 1E**], and 2.18 [**Figure 1F**] times as high as the average height of the periodic backgrounds, respectively. These enhancement values are all below 3 and do not seem to be different from what we observed in Manakov systems [43, 44].

However, there is more to our story intended for the vector CQ-NLS system, which involves the self-steepening effect denoted by the parameter γ. It is found that due to the presence of the self-steepening effect, the enhancement factors of periodic Peregrine solitons, defined by **Eqs 26** and **27**, can also be larger than 3, when an appropriate set of initial parameters is selected [32]. To show this, we demonstrate in **Figures 2A,B** the periodic Peregrine solitons in the same anomalous dispersion regime, but using another set of initial parameters $\gamma = 1$, $a_1 = \sqrt{7/6}$, $a_2 = \sqrt{5/6}$, $\omega_1 = 1/2$, and $\omega_2 = -1/2$, which, according to **Eq. 11**, can give rise to $\mu = -2$ and $\nu = \sqrt{96 + 3\sqrt{805}}/6$. It is seen that one Peregrine soliton component shown in **Figure 2A** has an enhancement value of around 3.9, while the other one shown in **Figure 2B** has a much smaller value, 0.56 or so. For comparison, we also provide in **Figures 2C,D** the surface plots of the rational polynomials $|U|$ and $|V|$ obtained under the same parameter condition, which

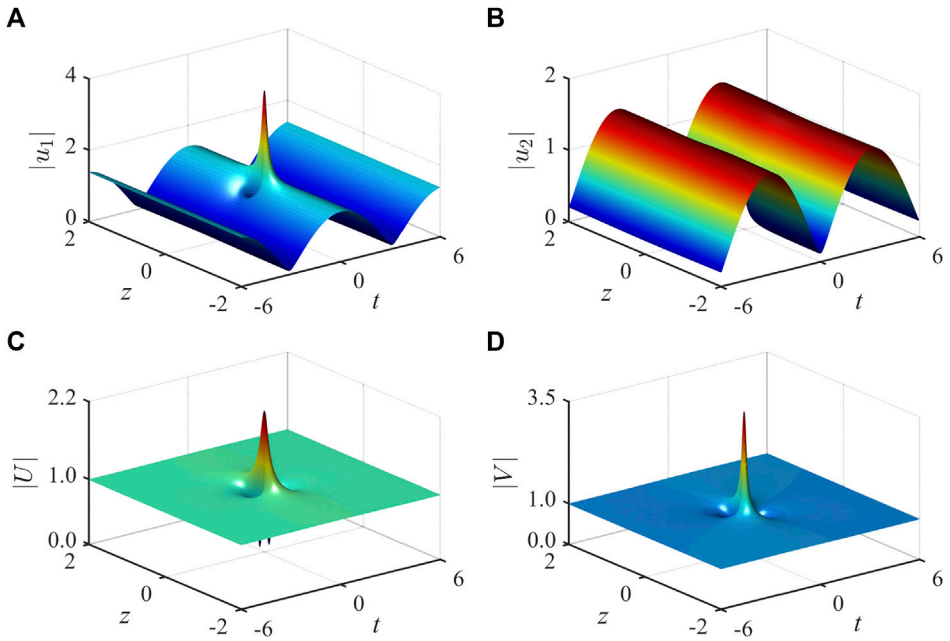

FIGURE 2 | Peregrine soliton states on a periodic background, with **(A)** an anomalous amplitude enhancement on the u_1 field component, and **(B)** a heavy falling-off on the u_2 field component, formed in the anomalous dispersion regime ($\sigma = 1$). The initial parameters are specified by $\gamma = 1$, $a_1 = \sqrt{7/6}$, $a_2 = \sqrt{5/6}$, $\omega_1 = 1/2$, $\omega_2 = -1/2$, $\mu = -2$, and $\nu = \frac{1}{6}\sqrt{96 + 3\sqrt{805}}$. For comparison, the surface plots of the rational polynomials $|U|$ and $|V|$ are shown in **(C)** and **(D)**, respectively.

correspond to the conventional bright-bright Peregrine soliton solutions of the vector CQ-NLS equation, each involving the peak-to-background ratios $|f_U| \approx 2.18$ and $|f_V| \approx 3.45$, respectively. It is hence obvious that the ultrastrong peak shown in **Figure 2A** results from the constructive interference of such bright-bright Peregrine soliton components, while the peak in **Figure 2B** may almost disappear due to the destructive interference, as implied in **Eqs 26** and **27**.

Of most concern is the case of the combination of negative cubic nonlinearity and positive quintic nonlinearity in our vector model, which admits the existence of periodic Peregrine solitons as well. One may recall that such a competing nonlinearity can often be used to support the formation of stable dissipative solitons in mode-locked fiber lasers [49] or to stabilize the soliton propagation in nonlinear media [50]. A study of MI of the background fields reveals that such a competing nonlinearity, which actually means $\sigma = -1$ (i.e., normal dispersion in the context of fiber optics), may favor the generation of Peregrine solitons, with larger transient wave-packet size, as compared to the anomalous dispersion case discussed above [59]. **Figure 3** shows the formation of periodic Peregrine solitons in the normal dispersion regime, which is a linear superposition of the given U and V distributions shown in **Figures 3A,B**. For simplicity, we used a special set of initial parameters that meets **Eqs 14** and **15** and thus used **Eqs 17** and **18** for U and V in **Eq. 5**. Clearly, using this set of parameters, we can obtain $|f_U| = 4$ and $|f_V| = 0$, as indicated in **Figures 3A,B**. Hence, both periodic Peregrine soliton components shown in **Figures 3C,E** would involve an enhancement value 1.63 in the center position, despite that they have a different amplitude distribution, as indicated by the contour plots in **Figures 3D,F**. As compared with **Figure 1**, the periodic Peregrine solitons shown in **Figure 3** exhibit a larger spatiotemporal dimension and thus a larger transient wave-packet size.

Now a natural question arises as to whether these periodic-background Peregrine soliton solutions are robust against numerical noises or even against strong "non-integrable" perturbations by which we mean that the specific relation between the coefficients for quintic nonlinearity and self-steepening terms can be lifted. To answer this question, we perform extensive numerical simulations with respect to our analytical solutions (**Eq. 5**), using an efficient code based on the exponential time differencing Crank–Nicolson (ETDCN) scheme with Padé approximation [60, 61]. Here we present merely two sets of numerical results, for a typical set of system parameters $\sigma = 1$, $\gamma = 1/4$, $a_1 = 8/9$, $a_2 = 4\sqrt{5}/9$, $\omega_1 = -40/81$, and $\omega_2 = 40/81$, which would lead to $\mu = -4/9$ and $\nu = -40\sqrt{3}/81$. First, for the purpose of comparison, we integrated the original integrable CQ-NLS **Eqs 1** and **2** numerically, with the analytical solutions at $z = -4$ as initial conditions. Simulation results are shown in **Figures 4A,B**. It is clear that our numerical code gave precisely the whole solution profiles as predicted by the analytical solutions (**Eq. 5**) till $z = 4$, despite the intrinsic numerical noises. Second, we violate the integrability of the governed model by solely changing the coefficient $i\gamma$ of the self-steepening term to $i\gamma(1 + 10\%)$ in the model, and simulate again the Peregrine soliton solutions under otherwise identical parameter conditions, with results given in **Figures 4C,D**. It is clearly seen that the whole Peregrine soliton profiles on a periodic background can still be well maintained till $z = 2$ (see the region before the white dashed line), almost the same as shown in **Figures 4A,B**, implying that our analytical solutions (**Eq. 5**) are still robust against such strong non-integrable perturbations. After $z = 2$, due to the onset of MI, there would

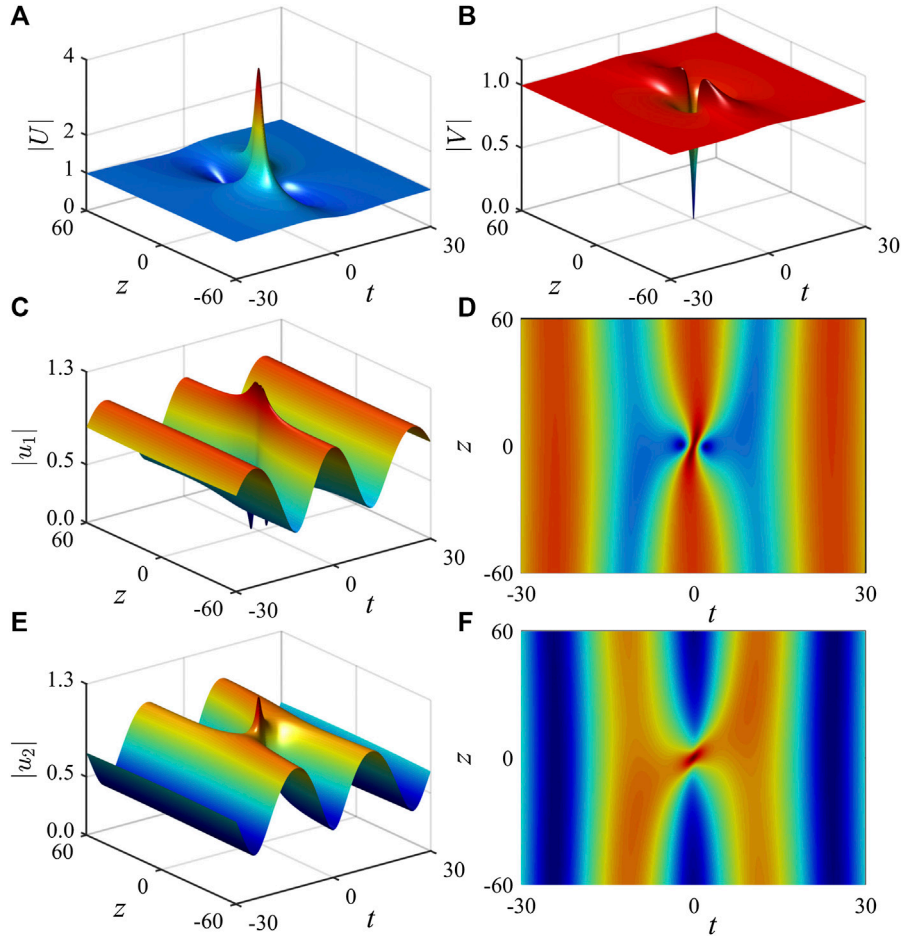

FIGURE 3 | Peregrine solitons on a periodic background formed in the normal dispersion regime ($\sigma = -1$), defined by the solutions **Eqs 5**, **17**, and **18**, under the parameters $\gamma = 1$, $a_1 = 4/9$, $a_2 = 4\sqrt{5}/9$, $\omega_1 = -10/81$, $\omega_2 = 10/81$, $\mu = -32/27$, and $\nu = -10\sqrt{3}/81$. While **(A)** and **(B)** display the surface plots for $|U|$ and $|V|$, **(C)** and **(E)** show the surface plots of Peregrine solitons for the u_1 and u_2 fields, respectively, with their corresponding contour plots given in **(D)** and **(F)**.

appear complex wave structures, which tend to interfere with the trailing edge of Peregrine soliton profiles. The above simulations also confirm, to an extent, the physical relevance of our analytical solutions obtained with the coupled CQ-NLS **Eqs 1** and **2**, although the model involves a special parameter relation between the quintic nonlinearity and the self-steepening terms in order to enable integrability.

Finally, we would like to point out that our solution form defined by **Eq. 5** is universal and can be applied to the higher-order rogue wave hierarchy built on a periodic background, only when Uu_{10} and Vu_{20} are the corresponding conventional higher-order solutions of the underlying vector model. Here for our current purpose, we provide the periodic two-Peregrine-soliton solutions defined by **Eqs 5**, **19**, and **20**, which describe the interaction between two Peregrine soliton constituents, for any set of initial parameters that meets **Eqs 14** and **15**. Typical results are demonstrated in **Figure 5**, where we used the same system parameters as in **Figure 3**, and three extra parameters $\gamma_1 = 60$, $\gamma_2 = 8\mathrm{i}$, and $\gamma_3 = 1$. It is shown that on a periodic background, there appear two well-separated Peregrine soliton states on each field component; one may behave like a spike, while the other is weaker in peak amplitude. Of course, there would occur other complex patterns on the periodic background, when the free parameters γ_s (s=1,2,3) are changed. However, it is due to the inclusion of these extra parameters that our general solutions presented above can be used to model the multivariant rogue wave events met in practical conditions.

4 CONCLUSIONS

In conclusion, we presented exact Peregrine soliton solutions built on a periodic background caused by the interference in the vector CQ-NLS equation involving self-steepening. It is revealed that such periodic Peregrine soliton solutions are indeed a linear superposition of two fundamental Peregrine solitons of different cw backgrounds, provided that the continuous waves possess a nonvanishing frequency difference. With these exact solutions, we demonstrated the

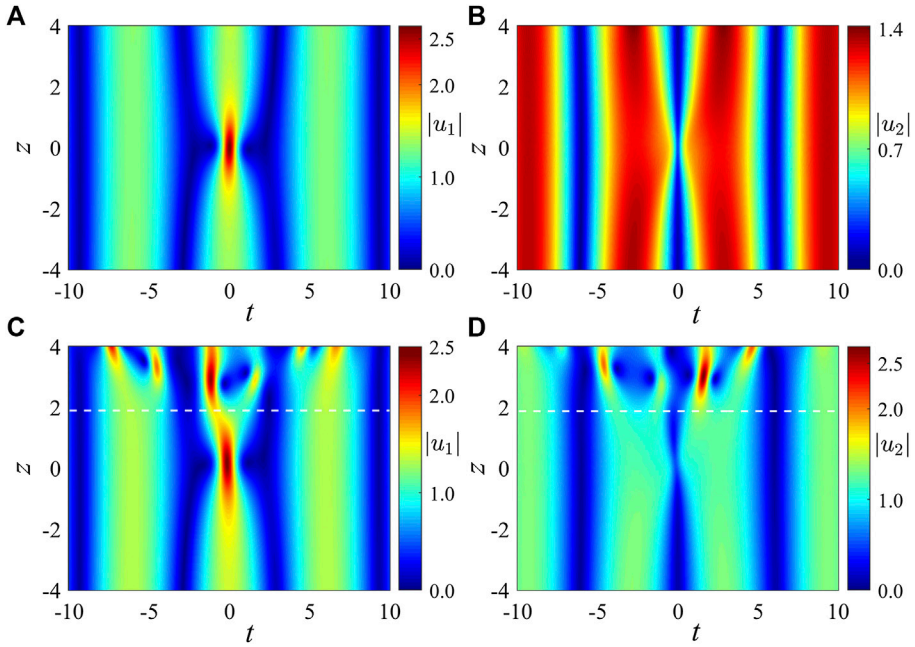

FIGURE 4 | Typical simulations of the periodic Peregrine soliton solutions (**Eq. 5**) for given parameters $\sigma = 1$, $\gamma = 1/4$, $a_1 = 8/9$, $a_2 = 4\sqrt{5}/9$, $\omega_1 = -40/81$, $\omega_2 = 40/81$, $\mu = -4/9$, and $\nu = -40\sqrt{3}/81$, under **(A)**,**(B)** the original integrable CQ-NLS **Eqs 1** and **2**, and **(C)**,**(D)** the same CQ-NLS model but with the coefficient $i\gamma$ of the self-steepening term being changed to $i\gamma(1 + 10\%)$, respectively.

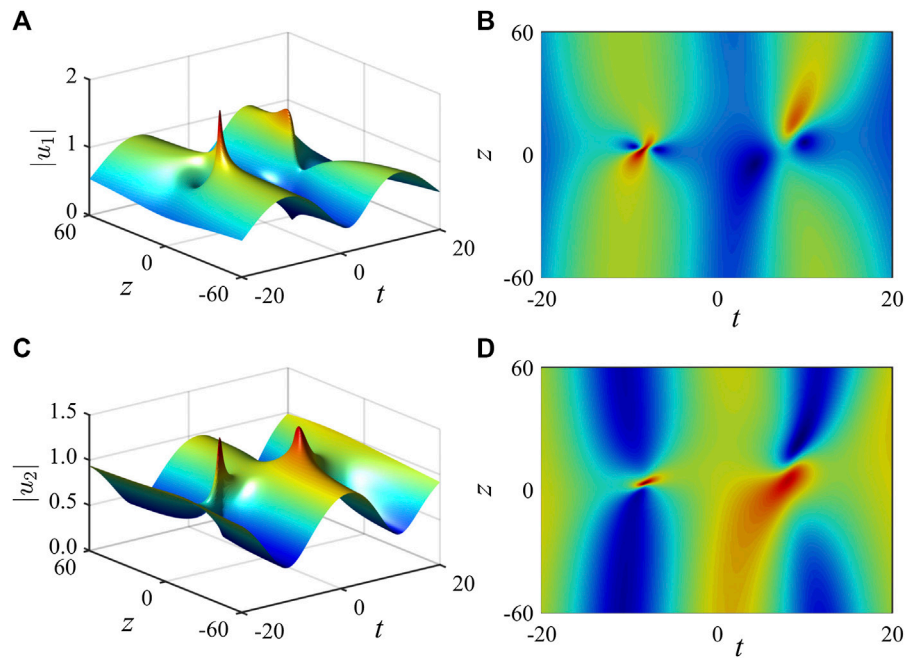

FIGURE 5 | Interaction of two Peregrine solitons on a periodic background, under the same initial parameters as in **Figure 3**. The three extra parameters in **Eqs 19** and **20** are given by $\gamma_1 = 60$, $\gamma_2 = 8i$, and $\gamma_3 = 1$.

coexistence of Peregrine solitons on the same periodic background, under certain parameter conditions. Further, the ultrastrong amplitude enhancement was proved to occur on the periodic background as well, due to the presence of the self-steepening effect. We numerically confirm the stability of these analytical solutions against significant non-integrable

perturbations. We also showed the interaction of two Peregrine solitons on the periodic background, which are still a linear superposition of those on the cw background. Basically, such simple superposition rule can be applied to the higher-order rogue wave hierarchy on a periodic background. As one might expect, these findings may shed more light on our understanding of the realistic rogue wave behaviors occurring in either the fiber-optic telecommunication links [7] or the crossing seas [9].

DATA AVAILABILITY STATEMENT

The original contributions presented in the study are included in the article/supplementary materials, further inquiries can be directed to the corresponding authors.

AUTHOR CONTRIBUTIONS

YY, LB, and WW performed the derivations and plotted the figures. SC, FB, and DM proposed the theoretical framework, performed simulations, and wrote and revised the manuscript. All authors contributed to the article and approved the submitted version.

FUNDING

This work was supported by the National Natural Science Foundation of China (Grants No. 11474051 and No. 11974075) and by the Scientific Research Foundation of Graduate School of Southeast University (Grant No. YBPY1872).

REFERENCES

1. Dysthe K, Krogstad HE, Müller P. Oceanic Rogue waves. *Annu Rev Fluid Mech* (2008) 40:287–310. doi:10.1146/annurev.fluid.40.111406.102203.
2. Adcock TAA, Taylor PH, Draper S. Nonlinear dynamics of wave-groups in random seas: unexpected walls of water in the open ocean. *Proc R Soc A* (2015) 471:20150660. doi:10.1098/rspa.2015.0660.
3. Akhmediev N, Ankiewicz A, Taki M. Waves that appear from nowhere and disappear without a trace. *Phys Lett* (2009) 373:675–8. doi:10.1016/j.physleta.2008.12.036
4. Kharif C, Pelinovsky E, Slunyaev A. *Rogue waves in the ocean* Berlin, Germany: Springer (2009) 216 p.
5. Solli DR, Ropers C, Koonath P, Jalali B. Optical rogue waves. *Nature* (2007) 450:1054–7. doi:10.1038/nature06402.
6. Shats M, Punzmann H, Xia H. Capillary rogue waves *Phys Rev Lett* (2010) 104:104503. doi:10.1103/PhysRevLett.104.104503.
7. Wabnitz S. *Nonlinear guided wave optics: a testbed for extreme waves* Bristol, UK: IOP Publishing (2017) 387 p.
8. Malomed BA, Mihalache D. Nonlinear waves in optical and matter-wave media: a topical survey of recent theoretical and experimental results. *Rom J Phys* (2019) 64:106.
9. Onorato M, Residori S, Bortolozzo U, Montina A, Arecchi FT. Rogue waves and their generating mechanisms in different physical contexts. *Phys Rep* (2013) 528:47–89. doi:10.1016/j.physrep.2013.03.001.
10. Pisarchik AN, Jaimes-Reátegui R, Sevilla-Escoboza R, Huerta-Cuellar G, Taki M. Rogue waves in a multistable system. *Phys Rev Lett* (2011) 107:274101. doi:10.1103/PhysRevLett.107.274101.
11. Vergeles S, Turitsyn SK. Optical rogue waves in telecommunication data streams. *Phys Rev A* (2011) 83:061801. doi:10.1103/PhysRevA.83.061801.
12. Arecchi FT, Bortolozzo U, Montina A, Residori S. Granularity and inhomogeneity are the joint generators of optical rogue waves. *Phys Rev Lett* (2011) 106:153901. doi:10.1103/PhysRevLett.106.153901.
13. Dudley JM, Dias F, Erkintalo M, Genty G. Instabilities, breathers and rogue waves in optics. *Nat Photon* (2014) 8:755–64. doi:10.1038/NPHOTON.2014.220.
14. Walczak P, Randoux S, Suret P. Optical rogue waves in integrable turbulence. *Phys Rev Lett* (2015) 114:143903. doi:10.1103/PhysRevLett.114.143903.
15. Soto-Crespo JM, Devine N, Akhmediev N. Integrable turbulence and rogue waves: breathers or solitons? *Phys Rev Lett* (2016) 116:103901. doi:10.1103/PhysRevLett.116.103901.
16. Onorato M, Osborne AR, Serio M. Modulational instability in crossing sea states: a possible mechanism for the formation of freak waves. *Phys Rev Lett* (2006) 96:014503. doi:10.1103/PhysRevLett.96.014503.
17. Baronio F, Conforti M, Degasperis A, Lombardo S, Onorato M, Wabnitz S. Vector rogue waves and baseband modulation instability in the defocusing regime. *Phys Rev Lett* (2014) 113:034101. doi:10.1103/PhysRevLett.113.034101.
18. Chen S, Baronio F, Soto-Crespo JM, Grelu P, Mihalache D. Versatile rogue waves in scalar, vector, and multidimensional nonlinear systems. *J Phys Math Theor* (2017) 50:463001. doi:10.1088/1751-8121/aa8f00.
19. Grinevich PG, Santini PM. The exact rogue wave recurrence in the NLS periodic setting via matched asymptotic expansions, for 1 and 2 unstable modes. *Phys Lett A* (2018) 382:973–9. doi:10.1016/j.physleta.2018.02.014.
20. Grinevich PG, Santini PM. The finite-gap method and the periodic NLS Cauchy problem of anomalous waves for a finite number of unstable modes. *Russ Math Surv* (2019) 74:211–63. doi:10.1070/RM9863.
21. Kibler B, Fatome J, Finot C, Millot G, Dias F, Genty G, et al.. The Peregrine soliton in nonlinear fibre optics. *Nat Phys* (2010) 6:790–5. doi:10.1038/NPHYS1740.
22. Chen S, Baronio F, Soto-Crespo JM, Liu Y, Grelu P. Chirped Peregrine solitons in a class of cubic-quintic nonlinear Schrödinger equations. *Phys Rev E* (2016) 93:062202. doi:10.1103/PhysRevE.93.062202.
23. Chen S, Soto-Crespo JM, Grelu P. Coexisting rogue waves within the (2+1)-component long-wave-short-wave resonance. *Phys Rev E* (2014) 90:033203. doi:10.1103/PhysRevE.90.033203.
24. Peregrine DH, Water waves, nonlinear Schrödinger equations and their solutions. *J Aust Math Soc Ser B Appl Math* (1983) 25:16–43. doi:10.1017/S0334270000003891.
25. Shrira VI, Geogjaev VV. What makes the Peregrine soliton so special as a prototype of freak waves? *J Eng Math* (2010) 67:11–22. doi:10.1007/s10665-009-9347-2.
26. Chabchoub A, Hoffmann NP, Akhmediev N. Rogue wave observation in a water wave tank. *Phys Rev Lett* (2011) 106:204502. doi:10.1103/PhysRevLett.106.204502.
27. Tikan A, Billet C, El G, Tovbis A, Bertola M, Sylvestre T, et al.. Universality of the peregrine soliton in the focusing dynamics of the cubic nonlinear schrödinger equation. *Phys Rev Lett* (2017) 119:033901. doi:10.1103/PhysRevLett.119.033901.
28. Dudley JM, Genty G, Mussot A, Chabchoub A, Dias F. Rogue waves and analogies in optics and oceanography. *Nat Rev Phys* (2019) 1:675–89. doi:10.1038/s42254-019-0100-0.
29. Bailung H, Sharma SK, Nakamura Y. Observation of Peregrine solitons in a multicomponent plasma with negative ions. *Phys Rev Lett* (2011) 107:255005. doi:10.1103/PhysRevLett.107.255005.
30. Frisquet B, Kibler B, Morin P, Baronio F, Conforti M, Millot G, et al.. Optical dark rogue wave. *Sci Rep* (2016) 6:20785. doi:10.1038/srep20785.
31. Chen S, Ye Y, Soto-Crespo JM, Grelu P, Baronio F. Peregrine solitons beyond the threefold limit and their two-soliton interactions. *Phys Rev Lett* (2018) 121:104101. doi:10.1103/PhysRevLett.121.104101.
32. Chen S, Pan C, Grelu P, Baronio F, Akhmediev N. Fundamental Peregrine solitons of ultrastrong amplitude enhancement through self-steepening in

vector nonlinear systems. *Phys Rev Lett* (2020) 124:113901. doi:10.1103/PhysRevLett.124.113901.
33. Baronio F. Akhmediev breathers and Peregrine solitary waves in a quadratic medium. *Opt Lett* (2017) 42:1756–9. doi:10.1364/OL.42.001756.
34. Baronio F, Chen S, Mihalache D. Two-color walking Peregrine solitary waves. *Opt Lett* (2017) 42:3514–7. doi:10.1364/OL.42.003514.
35. Liu W, Zhang Y, He J. Rogue wave on a periodic background for Kaup–Newell equation. *Rom Rep Phys* (2018) 70:106.
36. Andral U, Kibler B, Dudley JM, Finot C. Akhmediev breather signatures from dispersive propagation of a periodically phase-modulated continuous wave. *Wave Motion* (2020) 95:102545. doi:10.1016/j.wavemoti.2020.102545.
37. Zhao L-C, Duan L, Gao P, Yang Z-Y, Vector rogue waves on a double-plane wave background. *Europhys Lett* (2019) 125:40003. doi:10.1209/0295-5075/125/40003.
38. Rao J, He J, Mihalache D, Cheng Y. PT-symmetric nonlocal Davey-Stewartson I equation: general lump-soliton solutions on a background of periodic line waves. *Appl Math Lett* (2020) 104:106246. doi:10.1016/j.aml.2020.106246.
39. Chen J, Pelinovsky DE, Rogue periodic waves of the focusing nonlinear Schrödinger equation. *Proc R Soc A* (2018) 474:20170814. doi:10.1098/rspa.2017.0814.
40. Chen J, Pelinovsky DE, White RE. Rogue waves on the double-periodic background in the focusing nonlinear Schrödinger equation. *Phys Rev E* (2019) 100:052219. doi:10.1103/PhysRevE.100.052219.
41. Xu G, Chabchoub A, Pelinovsky DE, Kibler B. Observation of modulation instability and rogue breathers on stationary periodic waves. *Phys Rev Res* (2020) 2:033528. doi:10.1103/PhysRevResearch.2.033528.
42. Chen S, Zhou Y, Bu L, Baronio F, Soto-Crespo JM, Mihalache D. Super chirped rogue waves in optical fibers. *Optic Express* (2019) 27:11370–84. doi:10.1364/OE.27.011370.
43. Baronio F, Degasperis A, Conforti M, Wabnitz S. Solutions of the vector nonlinear schrödinger equations: evidence for deterministic Rogue waves. *Phys Rev Lett* (2012) 109:044102. doi:10.1103/PhysRevLett.109.044102.
44. Chen S, Mihalache D. Vector rogue waves in the Manakov system: diversity and compossibility. *J Phys Math Theor* (2015) 48:215202. doi:10.1088/1751-8113/48/21/215202.
45. Zhang Y, Cheng Y, He J. Riemann-Hilbert method and N-soliton for two-component Gerdjikov-Ivanov equation. *J Nonlinear Math Phys* (2017) 24:210–23. doi:10.1080/14029251.2017.1313475.
46. Kodama Y, Hasegawa A. Nonlinear pulse propagation in a monomode dielectric guide. *IEEE J Quant Electron* (1987) 23:510–24. doi:10.1109/JQE.1987.1073392.
47. Agrawal GP. *Nonlinear fiber optics* 4th ed. San Diego, CA: Academic (2007) 529 p.
48. Kivshar YS, Agrawal GP. *Optical solitons: from fibers to photonic crystals* San Diego, CA: Academic (2003) 557 p.
49. Grelu P. *Nonlinear optical cavity dynamics: from microresonators to fiber lasers* Weinheim, Germany: Wiley VCH (2016) 785 p.
50. Mihalache D, Mazilu D, Crasovan L-C, Towers I, Buryak AV, Malomed BA, et al. Stable spinning optical solitons in three dimensions. *Phys Rev Lett* (2002) 88:073902. doi:10.1103/PhysRevLett.88.073902.
51. Dudley JM, Genty G, Coen S. Supercontinuum generation in photonic crystal fiber. *Rev Mod Phys* (2006) 78:1135–84. doi:10.1103/RevModPhys.78.1135.
52. Chen S, Song L-Y. Rogue waves in coupled Hirota systems. *Phys Rev E* (2013) 87:032910. doi:10.1103/PhysRevE.87.032910.
53. Degasperis A, Lombardo S. Rational solitons of wave resonant-interaction models. *Phys Rev E* (2013) 88:052914. doi:10.1103/PhysRevE.88.052914.
54. Degasperis A, Lombardo S. Multicomponent integrable wave equations: I. Darboux-dressing transformation. *J Phys Math Theor* (2007) 40:961–77. doi:10.1088/1751-8113/40/5/007.
55. Degasperis A, Lombardo S. Multicomponent integrable wave equations: II. soliton solutions. *J Phys Math Theor* (2009) 42:385206. doi:10.1088/1751-8113/42/38/385206.
56. Degasperis A, Lombardo S, Sommacal M. Rogue wave type solutions and spectra of coupled nonlinear schrödinger equations. *Fluids* (2019) 4:57. doi:10.3390/fluids4010057.
57. Guo B, Ling L, Liu QP. Nonlinear Schrödinger equation: generalized Darboux transformation and rogue wave solutions. *Phys Rev E* (2012) 85:026607. doi:10.1103/PhysRevE.85.026607.
58. Ye Y, Zhou Y, Chen S, Baronio F, Grelu P. General rogue wave solutions of the coupled Fokas-Lenells equations and non-recursive Darboux transformation. *Proc R Soc A* (2019) 475:20180806. doi:10.1098/rspa.2018.0806.
59. Ye Y, Liu J, Bu L, Pan C, Chen S, Mihalache D. Rogue waves and modulation instability in an extended Manakov system. *Nonlinear Dyn* (2020) doi:10.1007/s11071-020-06029-z.
60. Kleefeld B, Khaliq AQM, Wade BA. An ETD Crank-Nicolson method for reaction-diffusion systems. *Numer Methods Part Differ Equ* (2012) 28:1309–35. doi:10.1002/num.20682.
61. Chen S, Ye Y, Baronio F, Liu Y, Cai X-M, Grelu P. Optical Peregrine rogue waves of self-induced transparency in a resonant erbium-doped fiber. *Optic Express* (2017) 25:29687–98. doi:10.1364/OE.25.029687.

Conflict of Interest: The authors declare that the research was conducted in the absence of any commercial or financial relationships that could be construed as a potential conflict of interest.

frontiers in Physics

MINI REVIEW
published: 24 November 2020
doi: 10.3389/fphy.2020.591995

Review on the Stability of the Peregrine and Related Breathers

Miguel A. Alejo[1], *Luca Fanelli*[2†] *and Claudio Muñoz*[3*]

[1]Departamento de Matemáticas, Universidad de Córdoba, Córdoba, Spain, [2]Dipartimento di Matematica "Guido Castelnuovo", Universitá di Roma "La Sapienza", Roma, Italy, [3]CNRS and Departamento de Ingeniería Matemática DIM, Universidad de Chile, Santiago, Chile

In this note, we review stability properties in energy spaces of three important nonlinear Schrödinger breathers: Peregrine, Kuznetsov-Ma, and Akhmediev. More precisely, we show that these breathers are *unstable* according to a standard definition of stability. Suitable Lyapunov functionals are described, as well as their underlying spectral properties. As an immediate consequence of the first variation of these functionals, we also present the corresponding nonlinear ODEs fulfilled by these nonlinear Schrödinger breathers. The notion of global stability for each breather mentioned above is finally discussed. Some open questions are also briefly mentioned.

Keywords: Peregrine breather, Kuznetsov-Ma breather, Akhmediev breather, stability, nonlinear Schrodinger equation

OPEN ACCESS

Edited by:
Bertrand Kibler,
UMR6303 Laboratoire Interdisciplinaire Carnot de Bourgogne (ICB), France

Reviewed by:
Dmitry Pelinovsky,
McMaster University, Canada
Christian Klein,
Université de Bourgogne, France

***Correspondence:**
Claudio Muñoz
cmunoz@dim.uchile.cl

†Present address:
Luca Fanelli,
Dipartimento di Matematica "Guido Castelnuovo", Universitá di Roma "La Sapienza", Roma, Italy

Specialty section:
This article was submitted to Mathematical and Statistical Physics, a section of the journal Frontiers in Physics

Received: *05 August 2020*
Accepted: *19 August 2020*
Published: *24 November 2020*

Citation:
Alejo MA, Fanelli L and Muñoz C (2020) Review on the Stability of the Peregrine and Related Breathers. Front. Phys. 8:591995. doi: 10.3389/fphy.2020.591995

1. INTRODUCTION

In this short review, we describe a series of mathematical results related to the stability of the Peregrine breather and other explicit solutions to the cubic nonlinear Schrödinger (NLS) equation, an important candidate to modelize rogue waves. The mentioned model is NLS posed on the real line

$$i\partial_t u + \partial_x^2 u + |u|^2 u = 0, \quad u(t,x) \in \mathbb{C}, \quad (t,x) \in \mathbb{R}^2. \tag{1}$$

We assume a nonzero boundary value condition (BC) at infinity, in the form of a *Stokes wave* e^{it}: for all $t \in \mathbb{R}$,

$$\left|u(t,x) - e^{it}\right| \to 0 \quad \text{as} \quad x \to \pm\infty. \tag{2}$$

It is well known that **Eq. 1** possesses a huge family of complex solutions. Among them, a fundamental role in the dynamics is played by *breathers*. We shall say that a particular smooth solution to **Eqs 1** and **2** is a breather if, up to the invariances of the equation, its dynamics show the evolution of some concentrated quantity in an oscillatory fashion. NLS has scaling, shifts, phase, and Galilean invariances: namely, if u solves **Eq. 1**, another solution to **Eq. 1** is

$$u_{c,v,\gamma,x_0,t_0}(t,x) := \sqrt{c}\, u\big(c(t-t_0), \sqrt{c}\,(x - vt - x_0)\big)\exp\left(ict + \frac{i}{2}xv - \frac{i}{4}v^2 t + i\gamma\right). \tag{3}$$

In this paper, we review the known results about stability in Sobolev spaces of the Peregrine (P) breather[1] [1]:

[1]Or Peregrine soliton, but because of the nature of its variational formulation, it is more a breather than a soliton.

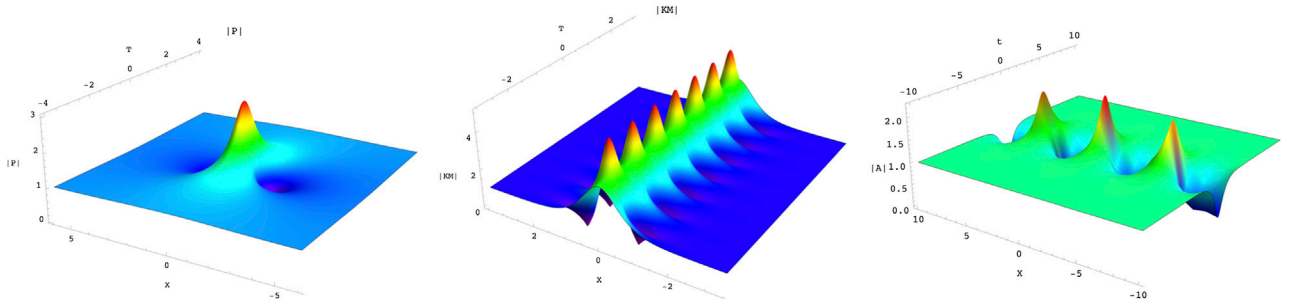

FIGURE 1 | Left: absolute value $|B_P|$ of the Peregrine breather **Eq. 4**. Center: $|B_{KM}|$, **Eq. 5**. Right: $|B_A|$ **Eq. 6**.

$$B_P(t,x) := e^{it}\left(1 - \frac{4(1+2it)}{1+4t^2+2x^2}\right); \tag{4}$$

and we will also present, with less detail, the analogous properties of the Kuznetsov-Ma (KM) and Akhmediev (A) breathers: (i) if $a > 1/2$, the Kuznetsov-Ma (KM) breather is as follows [2–4] (see **Figure 1** for details):

$$B_{KM}(t,x) := e^{it}\left(1 - \sqrt{2}\,\beta\,\frac{(\beta^2\cos(\alpha t) + i\alpha\sin(\alpha t))}{\alpha\cosh(\beta x) - \sqrt{2}\beta\cos(\alpha t)}\right),$$
$$\alpha := (8a(2a-1))^{1/2}, \quad \beta := (2(2a-1))^{1/2}, \tag{5}$$

and (ii) for $a \in (0, 1/2)$, the Akhmediev breather is as follows [2]:

$$B_A(t,x) := e^{it}\left(1 + \frac{\alpha^2\cosh(\beta t) + i\beta\sinh(\beta t)}{\sqrt{2a}\cos(\alpha x) - \cosh(\beta t)}\right),$$
$$\beta := (8a(1-2a))^{1/2}, \quad \alpha := (2(1-2a))^{1/2}. \tag{6}$$

Notice the oscillating character of the three above examples. In addition, also notice that B_{KM} is time-periodic, while B_A is space-periodic. Although the Peregrine breather is not periodic in time, it is a particular limiting "degenerate" case of the two last cases.

NLS **Eq. 1** with nonzero BC **Eq. 2** is believed to describe the emergence of rogue or freak waves in the deep sea [1, 5, 6]. Peregrine waves were experimentally observed 10 years ago in Ref. 7. The model itself is also a well-known example of the mechanism known as modulational instability [5, 8]. For an alternative explanation to the rogue wave phenomenon which is stable under perturbations, see Refs. 9, 10.

Along these lines, we will explain that Peregrine and two other breathers are unstable according to a standard definition of stability. It could be the case that a less demanding definition of stability, involving infinite energy solutions, could repair this problem. However, such a question is still an open problem.

This paper is organized as follows. In **Section 2**, we recall some standard results for NLS with zero and nonzero background and the notion of modulational instability and local well-posedness. **Section 3** is devoted to the conservation laws of NLS, and **Section 4** to the notion of stability. **Sections 5** and **6** review the Peregrine, Kuznetsov-Ma, and Akhmediev breathers' stability properties. Finally, **Section 7** is devoted to a discussion, final comments, and conclusions.

2. MODULATIONAL INSTABILITY

2.1. A Quick Review of the Literature

Let us briefly review the main results involving **Eq. 1** in the zero and nonzero BC cases. A much more complete description of the current literature can be found in the papers present in this volume and in Refs. 11–13.

NLS **Eq. 1** is a well-known integrable model (see Ref. 14) and describes the propagation of pulses in nonlinear media and gravity waves in the ocean [12]. The local and global well-posedness theory for NLS with zero BC at infinity was initiated by Ginibre and Velo [15]; see also Tsutsumi [16] and Cazenave and Weissler [17]. Finally, see Cazenave [11] for a complete account of the different NLS equations. One should have in mind that **Eq. 1** is globally well-posed in $L^2(\mathbb{R})$, which has been proved by Tsutsumi in Ref. 16 and ill-posed in $H^s(\mathbb{R})$, $s < 0$, as shown in Ref. 18, where the authors prove the lack of uniform continuity of the solution map.

In the zero background cases, one has standard solitons for **Eq. 1**:

$$Q(t,x) := \sqrt{c}\,\mathrm{sech}\left(\sqrt{c}\,(x - vt - x_0)\right)e^{i\left(ct + \frac{1}{2}xv - \frac{1}{4}v^2t + \gamma_0\right)},$$
$$c > 0, v, x_0, \gamma_0 \in \mathbb{R}. \tag{7}$$

These are time-periodic, spatially localized solutions of **Eq. 1** and orbitally stable; see Cazenave-Lions [19], Weinstein [20], and Grillakis-Shatah-Strauss [21]. See also Refs. 22–24 for the case of several solitons.

2.2. Some Heuristics

NLS with nonzero boundary conditions, represented in **Eqs 1** and **2**, is characteristic of the *modulational instability* phenomenon, which—roughly speaking—says that small perturbations of the exact Stokes solution e^{it} are unstable and grow quickly. This unstable behavior leads to a nontrivial competition with the (focusing) nonlinearity, time at which the solution is apparently stabilized.

There are plenty of works in the literature dealing with this phenomenon, not only in the NLS case. Usually also called Benjamin-Feir mechanism [25], the NLS case has been described in a series of papers [2, 8, 26–28]. See also references therein for more details on the physical literature. Here, we present the standard, simple, but formal explanation of

this phenomenon, in terms of a frequency analysis of the linear solution.

To this aim, consider *localized* perturbations of **Eqs 1** and **2** of the form

$$u(t,x) = e^{it}\,(1 + w(t,x)), \quad w \text{ unknown.} \tag{8}$$

Notice that this ansatz is motivated by **Eq. 4**. Then **Eq. 1** becomes a modified NLS equation with a zeroth-order term, which is real-valued and has the wrong sign:

$$i\partial_t w + \partial_x^2 w + 2\,\mathrm{Re}w + 2|w|^2 + w^2 + |w|^2 w = 0. \tag{9}$$

The associated linearized equation for **Eq. 9** is just

$$\partial_t^2\phi + \partial_x^4\phi + 2\partial_x^2\phi = 0, \qquad \phi = \mathrm{Re}w. \tag{10}$$

This problem has some instability issues, as a standard frequency analysis reveals: looking for a formal standing wave $\phi = e^{i(kx-\omega t)}$solution to **Eq. 10**, one has $\omega(k) = \pm\,|k|\sqrt{k^2-2}$, which shows that, for small wavenumbers ($|k| < \sqrt{2}$), the linear equation behaves in an "elliptic" fashion, and exponentially (in time) growing modes are present from small perturbations of the vacuum solution. A completely similar conclusion is obtained working in the Fourier variable. This singular behavior is not present when the equation is defocusing, that is, **Eq. 1** with nonlinearity $-|u|^2u$.

This phenomenon is similar to the one present in the *bad Boussinesq* equation; see Kalantarov and Ladyzhenskaya [29]. However, in the latter case, the situation is even more complicated, since the linear equation is ill-posed for all large frequencies, unlike NLS **Eqs 1** and **2**, which is only badly behaved at small frequencies.

2.3. Local Well-Posedness

The above heuristics could lead to thinking that the model **Eqs 1** and **2** is not well-posed (in the Hadamard sense [30]) in standard Sobolev spaces (appealing to physical considerations, we will only consider solutions to these models with *finite energy*). Recall that, for $s \in \mathbb{R}$, the vector space $H^s(\mathbb{R}\ \ \mathbb{C})$ corresponds to the Hilbert space of complex-valued functions $u : \mathbb{R} \to \mathbb{C}$, such that $\int (1+\xi^2)^s|\widehat{u}(\xi)|^2 d\xi < +\infty$, endowed with the standard norm (with the hat $\widehat{\cdot}$, we denote the Fourier transform). Also, $H^s_\sharp := H^s_\sharp((0, 2\pi/a))$denotes the Sobolev space $H^s$of $2\pi/a$-space-periodic functions. In Refs. 31, 32, it was shown that even if there is no time decay for the linear dynamics due to the modulationally unstable regime, the equation is still locally well-posed.

Theorem 2.1. Let $s > 1/2$ and $a > 0$. The NLS with nonzero background **Eq. 9** is locally well-posed in H^s, in the aperiodic case, and in $H^s_\sharp$in the periodic case.

The main feature in the proof of Theorem 2.1 is the fact that if we work in Sobolev spaces, in principle, *there are no* $L^1 - L^\infty$ *decay estimates for the linear dynamics*. Moreover, one has exponential growth in time of the L^2 norm, and therefore, no suitable Strichartz estimates seem to be available, unless one cuts off some bad frequencies. Consequently, Theorem 2.1 is based on the fact that we work in dimension one and that for $s > 1/2$, we have the inclusion $H^s \hookrightarrow$. See Ref. 2 for early results on the Cauchy problem for **Eq. 1** in the periodic case, at high regularity (H^2 global weak solutions).

Note that P in **Eq. 4** is always well-defined and has essentially no loss of regularity, confirming in some sense the intuition and the conclusions in Theorem 2.1. Also, note that, using the symmetries of the equation, we have LWP for any solution of **Eq. 1** of the form $u(t,x) = u_{c,v,\gamma}(t,x) + w(t,x)$, for $w \in H^s$, and $s > 1/2$, with $u_{c,v,\gamma}$ defined in **Eq. 3**.

Two interesting questions are still open: global existence vs. blow-up and ill-posedness of the flow map for lower regularities. Since **Eq. 1** is integrable, it can be solved, at least formally, by inverse scattering methods. Biondini and Mantzavinos [33] showed the existence and long-time behavior of a global solution to **Eq. 1** in the integrable case, under certain exponential decay assumptions at infinity and a *no-soliton* spectral condition. In this paper, we have decided to present the results stated just in some energy space, with no need for extra decay conditions.

3. CONSERVED QUANTITIES

Being an integrable model, **Eqs 1** and **2** possess an infinite number of conserved quantities [14]. Here, we review the most important for the question of stability: mass, energy, and momentum. For both *KM* and *P*, one has the mass, momentum, and energy,

$$\begin{aligned} M[u] &:= \int (|u|^2 - 1), \quad P[u] := \mathrm{Im}\int (\overline{u} - e^{-it})u_x, \\ E[u] &:= \int |u_x|^2 - \frac{1}{2}\int (|u|^2-1)^2, \end{aligned} \tag{11}$$

and the Stokes wave + H^2 perturbations conserved energy:

$$F[u] := \int\Big(|u_{xx}|^2 - 3(|u|^2-1)|u_x|^2 - \frac{1}{2}\Big((|u|^2)_x\Big)^2 + \frac{1}{2}(|u|^2-1)^3\Big). \tag{12}$$

In Ref. 34, the mass, energy, and momentum of the *P* **Eq. 4** and *KM* **Eq. 5** breathers were computed. Indeed, one has [34, 35]

$$\begin{aligned} M[B_P] = E[B_P] = P[B_P] = F[B_P] = P[B_{KM}] = 0, \\ M[B_{KM}] = 4\beta, \quad E[B_{KM}] = -\frac{8}{3}\beta^3, \quad F[B_{KM}] = \frac{4}{5}\beta^5. \end{aligned}$$

We conclude that *KM* and *P* breathers are zero speed solutions. Note instead that, under a suitable Galilean transformation, they must have nonzero momentum. Note also that *P* has the same energy and mass as the Stokes wave solution (the nonzero background), a property not satisfied by the standard soliton on zero background. Also, compare the mass and energy of the Kuznetsov-Ma breather with the ones obtained in Ref. 36 for the mKdV breather.

Assume now that $u = u(t,x)$ is a $2\pi/a$-periodic solution to **Eq. 1**. Two standard conserved quantities for **Eq. 1** in the periodic setting are mass and energy

$$M_A[u] := \int_0^{\frac{2\pi}{a}} (|u|^2 - 1), \qquad E_A[u] := \int_0^{\frac{2\pi}{a}} \left(|u_x|^2 - \frac{1}{2}(|u|^2 - 1)^2 \right). \tag{13}$$

A third one, appearing from the integrability of the equation, is given by Ref. 35.

$$F_A[u] := \int_0^{\frac{2\pi}{a}} \left(|u_{xx}|^2 - 3(|u|^2 - 1)|u_x|^2 - \frac{1}{2}\left((|u|^2)_x \right)^2 + \frac{1}{2}(|u|^2 - 1)^3 \right). \tag{14}$$

4. ORBITAL STABILITY

From a physical and mathematical point of view, understanding the stability properties of candidates to rogue waves is of uttermost importance because not all the observed patterns bear the same qualitative and quantitative information.

Since the equation is locally well-posed and does have continuous-in-time solutions, it is possible to define a notion of orbital stability for the Peregrine, Kuznetsov-Ma, and Akhmediev breathers. To study the stability properties of such waves is key to validate them as candidates for explaining rogue waves; see Ref. 36. First, we consider the aperiodic case.

Mathematically speaking, the notion of orbital stability is the one to have in mind. Fix $s > 1/2$ and $t_0 \in \mathbb{R}$. We say that a particular globally defined solution $U = e^{it}(1 + W)$ of **Eq. 1** is *orbitally stable* in H^s if there are constants $C_0, \varepsilon_0 > 0$ such that, for any $0 < \varepsilon < \varepsilon_0$, if $w_0 - W(t_0)_{H^s} < \varepsilon$, then

$$\sup_{t \in \mathbb{R}} \inf_{y \in \mathbb{R}} \left\| w(t) - W(t, x - y) \right\|_{H^s} < C_0 \, \varepsilon. \tag{15}$$

Here, $w(t)$ is the solution to the IVP **Eq. 9** with initial datum $w(t_0) = w_0$, constructed in Theorem 2.1, and $x_0(t)$ can be assumed continuous because the IVP is well-posed in a continuous-in-time Sobolev space.

Note that no phase correction is needed in **Eq. 15**: **Eq. 9** is no longer $U(1)$ invariant, and any phase perturbation of a modulationally unstable solution $u(t)$ in **Eq. 1**, of the form $u(t)e^{i\gamma}$, $\gamma \in \mathbb{R}$, *requires an infinite amount of energy*. The same applies for Galilean transformations. If **Eq. 15** is not satisfied, we will say that U is unstable. Note additionally that condition **Eq. 15** requires w globally defined; otherwise, U is trivially unstable, since U is globally defined.

Recall that NLS solitons on a zero background **Eq. 7** satisfy **Eq. 15** (with an additional phase correction) for $s = 1$; see, e.g., Refs. 19–21. Some breather solutions of canonical integrable equations such as mKdV and Sine-Gordon have been shown stable using Lyapunov functional techniques; see Refs. 36, 38–41. See also Refs. 42, 43 for a rigorous treatment using IST, Refs. 12, 13, 43 for more results for other canonical models, and Refs. 45, 46 for the stability of periodic waves and kinks for the defocusing NLS. For several years, a proof of stability/instability of NLS breathers was open, due to the difficult character (no particular sign) of conservation laws.

Now, we consider an adapted version of stability for dealing with the Akhmediev breather **Eq. 6**. We must fix a particular spatial period, which for the latter case will be settled as $L = 2\pi/a$; for some fixed $a \in (0, 1/2)$, see **Eq. 6**.

By stability in this case, we mean the following. Fix $s > 1/2$ and $t_0 \in \mathbb{R}$. We say that a particular $2\pi/a$-periodic globally defined solution $U = e^{it}(1 + W)$of **Eq. 1** is *orbitally stable* in $H^s_\sharp(2\pi/a)$if there are constants $C_0, \varepsilon_0 > 0$ such that, for any $0 < \varepsilon < \varepsilon_0$, if $u_0 - U(t_0)_{H^s_\sharp} < \varepsilon$, then

$$\sup_{t \in \mathbb{R}} \inf_{y, s \in \mathbb{R}} \left\| u(t) - e^{is} U(t, x - y) \right\|_{H^s_\sharp} < C_0 \, \varepsilon. \tag{16}$$

If **Eq. 16** is not satisfied, we will say that U is unstable. Note how in this case phase corrections are allowed. This is because they are finite energy perturbations in the periodic case. In other words, any change of the form $B_A(t, x)e^{i\gamma}$, $\gamma \in \mathbb{R}$, of the Akhmediev breather $B_A(t, x)$ is a finite energy perturbation. The remaining sections of this review are devoted to showing that all breathers considered in the introduction are unstable according to the previously introduced definitions.

5. THE PEREGRINE BREATHER

Recall the Peregrine breather introduced in **Eq. 4**. Note that it is a polynomially decaying (in space and time) perturbation of the nonzero background given by the Stokes wave e^{it}. Using a simple argument coming from the modulational instability of **Eq. 1**, in Ref. 39 it was proved that B_P is unstable with respect to perturbations in Sobolev spaces H^s, $s > 1/2$. Previously, Haragus and Klein [3] showed numerical instability of the Peregrine breather, giving a first hint of its unstable character.

Theorem 5.1. The Peregrine breather **Eq. 4** is unstable under small H^s perturbations, $s > 1/2$.

The proof of this result uses the fact that Peregrine breathers are in some sense converging to the background final state (i.e., they are asymptotically stable) in the whole space norm $H^s(\mathbb{R})$, a fact forbidden in Hamiltonian systems with conserved quantities and stable solitary waves.

Theorem 5.1 is in contrast with other positive results involving breather solutions [36, 38, 47]. In those cases, the involved equations (mKdV, Sine-Gordon) were globally well-posed in the energy space (and even in smaller subspaces), with uniform in time bounds. Several physical and computational studies on the Peregrine breather can be found in Refs. 27, 48 and references therein. A recent stability analysis was performed in Ref. 49 in the case of complex-valued Ginzburg-Landau models. The proof of Theorem 5.1 is in some sense a direct application of the notion of modulational instability together with an asymptotic stability property.

5.1. Sketch of Proof of Theorem 5.1

This proof is not difficult, and it is based on the notion of *asymptotic stability*, namely, the convergence at infinity of perturbations of the breather. Fix $s > 1/2$. Let us assume that the Peregrine breather P in **Eq. 4** is orbitally stable, as in **Eq. 15**. Write

$$P(t,x) = e^{it}(1 + Q(t,x)), \qquad Q(t,x) := -\frac{4(1+2it)}{1+4t^2+2x^2}. \quad (17)$$

Now consider, as a perturbation of the Peregrine breather, the Stokes wave **Eq. 2**. One has (Ref. 34)

$$\lim_{t\to+\infty} \left\| e^{it} - P(t) \right\|_{H^s} = \lim_{t\to+\infty} \|Q(t)\|_{H^s} = 0.$$

Therefore, we have two modulationally unstable solutions to **Eq. 1** that converge to the same profile as $t \to +\infty$. This fact contradicts the orbital stability, since for $y = x_0(t) \in \mathbb{R}$ given in **Eq. 15**, $0 < c_0 := \|Q(0, x - x_0(0))\|_{H^s}$ is a fixed number, but if $t_0 = T$ is taken large enough, $\|Q(T)\|_{H^s}$ can be made arbitrarily small. This proves Theorem 5.1.

Although Theorem 5.1 clarifies the stability/instability question for the Peregrine breather, other questions remain unsolved. Is the Peregrine breather stable under less restrictive assumptions on the perturbed data? A suitable energy space for the Peregrine breather could be

$$\mathcal{E} := \{u \in L^\infty(\mathbb{R}), \quad |u|^2 - 1 \in L^2(\mathbb{R}), \quad u_x \in L^2(\mathbb{R})\}$$

endowed with the metric $d(u_1,u_2) := \|u_1 - u_2\|_{L^\infty} + \|u_{1,x} - u_{2,x}\|_{L^2} + \||u_1|^2 - |u_2|^2\|_{L^2}$. This space is standard for the study of kink structures in Gross-Pitaevski [50, 51]. However, even in this space, the argument used in Theorem 5.1 works, giving instability as well. In other words, the asymptotic stability property *in the whole space* is key for the instability.

5.2. Variational Characterization

In the following lines, we discuss some improvements of the previous result. In particular, we discuss the variational characterization of the Peregrine breather. For an introduction to this problem in the setting of breathers, see, e.g., Ref. 32. In Ref. 35, the authors quantified in some sense the instability of the Peregrine breather.

Theorem 5.2 (Variational characterization of Peregrine). Let $B = B_P$ be any Peregrine breather. Then B is a critical point of a real-valued functional $F[u]$ **Eq. 12**, in the sense that

$$F'[B](z) = 0, \quad \text{for all } z \in H^2(\mathbb{R} \ \ \mathbb{C}). \quad (18)$$

Moreover, B satisfies the nonlinear ODE

$$B_{(4x)} + 3B_x^2\overline{B} + \left(4|B|^2 - 3\right)B_{xx} + B^2\overline{B}_{xx} + 2|B_x|^2B + \frac{3}{2}\left(|B|^2 - 1\right)^2 B = 0. \quad (19)$$

Theorem 5.2 reveals that Peregrine breathers are, in some sense, degenerate. More precisely, contrary to other breathers, the characterization of P does not require the mass and the energy, respectively. The absence of these two quantities may be related to the fact that $M[B_P] = E[B_P] = 0$, meaning a particular form of instability (recall that mass and energy are convex terms aiding to the stability of solitonic structures). We would like to further stress the fact that the variational characterization of the famous Peregrine breather is in H^2, since mass and energy are useless.

The proof of Theorem 5.2 is simple and variational and follows previous ideas presented in Ref. 36 for the case of mKdV breathers and Ref. 39 for the case of the Sine-Gordon breather (see also Ref. 47 for a recent improvement of this last result, based in Ref. 38). The main differences are in the complex-valued nature of the involved breathers and the nonlocal character of the *KM* and *P* breathers.

The following result gives a precise expression for the lack of stability in Peregrine breathers. Recall that $\sigma_c(\mathscr{L})$ stands for the continuum spectrum of a densely defined unbounded linear operator $\mathscr{L}$. Essentially, the continuous spectrum of the second derivative of the Lyapunov functional F" stays below zero.

Theorem 5.3 (Direction of instability of the Peregrine breather). Let $B = B_P$ be a Peregrine breather, critical point of the functional F_P defined in **Eq. 12**. Then, the following is satisfied: let $z_0 \in H^2$ be any sufficiently small perturbation and $w = w(t) := e^{-it}\partial_x z_0 \in H^1$. Then, as $t \to +\infty$,

$$F''[B_P](z_0,z_0) = \frac{1}{2}\int \left(|w_x|^2 - |w|^2 - w^2\right)(t) + O\left(\|z_0\|_{H^1}^3\right) + o_{t\to+\infty}(1). \quad (20)$$

From **Eq. 20**, one can directly check that $F''[B_P](z_0,z_0) < 0$ for a continuum of small z_0 and large times. The proof of Theorem 5.3 is a consequence of the following identity. For each $z \in H^2(\mathbb{R})$, we have

$$F[B_P + z] = F[B_P] + \mathcal{G}[z] + \mathcal{Q}[z] + \mathcal{N}[z], \quad (21)$$

where $F[B_P] = 0$, $\mathcal{G}[z] = 2\mathrm{Re}\int \overline{z}G[B_P] = 0$, with $G[B_P] = (5.3)$, and $\mathcal{Q}[z]$ is a quadratic functional of the form $\mathcal{Q}[z] := \mathrm{Re}\int \overline{z}\mathscr{L}_P[z]\mathrm{dx}$, where $\mathscr{L}_P[z]$ is a matrix linear operator [35]. Finally, assuming $\|z\|_{H^1}$ small enough, the term $|\mathcal{N}[z]|$ is of cubic order and small.

6. THE KUZNETSOV-MA AND AKHMEDIEV BREATHERS

Here, we describe the stability properties of the other two important breathers for NLS: the Kuznetsov-Ma (KM) breather **Eq. 5** (see **Figure 1** and Refs. 2, 4, 52 for details) and the Akhmediev breather **Eq. 6** [2].

6.1. Kuznetsov-Ma

Most of the results obtained in the Peregrine case are also available for the Kuznetsov-Ma breather. We start by noticing that B_{KM} is, unlike Peregrine, a Schwartz perturbation of the Stokes wave e^{it} and therefore a smooth classical solution of **Eq. 1**. It has been also observed in optical fiber experiments; see Kibler et al. [53]. This reference and references therein are a nearly complete background for the mathematical problem and its physical applications.

Using a similar argument as in the proof of Theorem 5.1 for the Peregrine case, one can show that Kuznetsov-Ma breathers are unstable [39]. The (formally) unstable character of Peregrine and Kuznetsov-Ma breathers was well known in the physical and fluids literature (they arise from modulational instability); therefore, the conclusions from previous results are not surprising. In water tanks and optic fiber experiments, researchers were able to reproduce these waves [7, 27, 53], if, e.g., the initial setting or configuration is close to the exact theoretical solution.

Floquet analysis has been recently done for the KM breather in Ref. 54. Concerning the variational structure of the KM breather, it is slightly more complicated than the one for Peregrine, but it has the same flavor.

Theorem 6.1 [35]. *Let* $B = B_{KM}$ be a Kuznetsov-Ma breather **Eq. 5**. Then,

$$B_{(4x)} + 3B_x^2\overline{B} + \left(4|B|^2 - 3\right)B_{xx} + B^2\overline{B}_{xx} + 2|B_x|^2B + \frac{3}{2}\left(|B|^2 - 1\right)^2B - \beta^2\left(B_{xx} + \left(|B|^2 - 1\right)B\right) = 0. \tag{22}$$

Note that the elliptic equation for the *P* breather **Eq. 19** is directly obtained by the formal limit $\beta \to 0$ in the *KM* elliptic **Eq. 22**. This is concordance with the expected behavior of the *KM* breather as $a \to (1/2)^+$; see **Eq. 5**.

The variational structure of B_{KM} goes as follows. Define

$$\mathscr{H}[u] := F[u] + \beta^2 E[u]. \tag{23}$$

Here, *E* and *F* are given by **Eqs 11** and **12**, respectively. Then, for any $z \in H^2(\mathbb{R} \ \mathbb{C})$, $\mathscr{H}'[B_{KM}](z) = 0$. One has the following.

Theorem 6.2 (Absence of spectral gap and instability of the KM breather [35]). Let $B = B_{KM}$ be a Kuznetsov-Ma breather **Eq. 5**, critical point of the functional $\mathscr{H}$ defined in **Eq. 23**. Then,

$$\mathscr{H}'[B_{KM}] = 0, \quad \mathscr{H}''[B_{KM}](\partial_x B_{KM}) = 0, \quad \text{and} \quad \inf\sigma_c\left(\mathscr{H}''[B_{KM}]\right) < 0. \tag{24}$$

Note that classical stable solitons or solitary waves *Q* **Eq. 7** easily satisfy the estimate $\inf\sigma_c(\mathscr{H}''_Q[Q]) > 0$, where $\mathscr{H}''_Q$ is the standard quadratic form associated with the energy-mass-momentum variational characterization of *Q* [20]. Even in the cases of the mKdV breather B_{mKdV} [36] or Sine-Gordon breather B_{SG} [39], one has the gap $\inf\sigma_c(\mathscr{H}''_{mKdV}[B_{mKdV}]) > 0$ and $\inf\sigma_c(\mathscr{H}''_{SG}[B_{SG}]) > 0$. The *KM* breather does not follow this property at all, giving another hint of its unstable character.

The above theorem shows that the *KM* linearized operator $\mathscr{H}''$ has at least one *embedded eigenvalue*. This is not true in the case of linear, real-valued operators with fast decaying potentials, but since $\mathscr{H}''$ is a matrix operator, this is perfectly possible. Recall that if $\inf\sigma_c(\mathscr{H}''[B_{KM}]) > 0$, then the KM could perfectly be stable, a contradiction.

6.2. The Akhmediev Breather

Recall the Akhmediev breather **Eq. 6**. Note that B_A is a $2\pi/a$-periodic in space, localized in time smooth solution to **Eq. 1**, with some particular properties at spatial infinity. In the limiting case $a\uparrow 1/2$, one can recover the Peregrine soliton **Eq. 4**. Moreover, one has

$$\lim_{t \to \pm\infty} \left\| B_A(t,x) - e^{\pm i\theta}e^{it} \right\|_{H^1_\sharp} = 0, \qquad e^{i\theta} = 1 - \alpha^2 - i\beta. \tag{25}$$

The instability of B_A goes as follows. Once again, being B_A unstable, it does not mean that it has no structure at all.

Theorem 6.3 [31]. The Akhmediev breather **Eq. 6** is unstable under small perturbations in $H^s_\sharp$, $s > 1/2$. Also, it is a critical point of the functional $\mathscr{H}[u] := F_A[u] - \alpha^2 E_A[u]$, i.e., $\mathscr{H}'[B_A][w] = 0$ for all $w \in H^2_\sharp$. In particular, for each $t \in \mathbb{R}$, $B_A = A$ satisfies the nonlinear ODE:

$$A_{(4x)} + 3A_x^2\overline{A} + \left(4|A|^2 - 3\right)A_{xx} + A^2\overline{A}_{xx} + 2|A_x|^2A + \frac{3}{2}\left(|A|^2 - 1\right)^2A + \alpha^2\left(A_{xx} + \left(|A|^2 - 1\right)A\right) = 0. \tag{26}$$

The proof of Theorem 6.3 uses **Eq. 25** in a crucial way: a modified Stokes wave is an attractor of the dynamics around the Akhmediev breather for a large time.

Remark 6.1. We finally remark that the three above discussed breathers, B_P, B_{KM}, B_A, are all related to the two-soliton solutions of NLS on the plane-wave background (see Chapter 3 in Ref. 55). Indeed, the stationary Lax-Novikov equations for all breathers belong to the same family **Eqs 19**, **22**, and **26** (see the recent paper [56] for a detailed discussion about the stationary Lax-Novikov equations). Similar conclusions are expressed in Ref. 35.

7. CONCLUSION

We have reviewed the stability properties of three NLS solutions with nonzero background: Peregrine, Kuznetsov-Ma, and Akhmediev breathers. Working in associated energy spaces, with no additional decay condition, this review also characterizes the spectral properties of each of them. According to the definition of stability, no NLS **Eq. 1** breather seems to be stable, not even in larger spaces. The instability is easily obtained from the fact that each breather converges on the whole line, as time tends to infinity, toward the Stokes wave. If the solutions were stable, this would imply that each breather is the Stokes wave itself. Some deeper connections between the stability of breathers and the nonzero background (modulational instability) are highly expected, but it seems that no proof of this fact is in the literature. Maybe Bäcklund transformations, in the spirit of Refs. 38, 41, 47, could help to give preliminary answers, and rigorous IST methods such as the ones in Refs. 42, 43 may help to solve this question. Finally, the dichotomy blow-up/global well-posedness and ill-posedness for large data in NLS **Eq. 1** with nonzero background are interesting mathematical open problems to be treated elsewhere.

AUTHOR CONTRIBUTIONS

The three authors contributed equally to the conception, research, and writing of the manuscript.

FUNDING

We have received partial funding from CMM Conicyt PIA AFB170001 and Fondecyt 1191412.

ACKNOWLEDGMENTS

We thank both referees for several comments, criticisms, and the addition of several unattended references that led to an important improvement of a previous version of this manuscript.

REFERENCES

1. Peregrine DH. Water waves, nonlinear Schrödinger equations and their solutions. *J Austral Math Soc Ser B.* (1983) 25:16–43. doi:10.1016/j.anihpc.2018.10.005
2. Akhmediev N, Korneev VI. Modulation instability and periodic solutions of the nonlinear Schrödinger equation. *Theor Math Phys.* (1986) 69:1089–93. 10.1007/BF01037866
3. Klein C, Haragus M. Numerical study of the stability of the Peregrine breather. *Ann Math Sci Appl.* (2017) 2:217–39.
4. Kuznetsov E. Solitons in a parametrically unstable plasma. *Sov Phys Dokl.* (1977) 22:507–508.
5. Akhmediev N, Ankiewicz A, Taki M. Waves that appear from nowhere and disappear without a trace. *Phys Lett.* (2009) 373:675–8. doi:10.1016/j.physleta.2008.12.036
6. Shrira VI, Geogjaev YV. What make the Peregrine soliton so special as a prototype of freak waves? *J Eng Math.* (2010) 67:11–22. doi:10.1007/s10665-009-9347-2
7. Kibler B, Fatome J, Finot C, Millot G, Dias F, Genty G, et al. The Peregrine soliton in nonlinear fibre optics. *Nature Phys.* (2010) 6:790–95. doi:10.1038/nphys1740.
8. Zakharov VE, Dyachenko AI, Prokofiev AO. Freak waves as nonlinear stage of stokes wave modulation instability. *Eur J Mech B Fluids.* (2006) 5:677–92.
9. Bona JL, Ponce G, Saut JC, Sparber C. Dispersive blow-up for nonlinear Schrödinger equations revisited. *J Math Pures Appl.* (2014) 102:782–811. doi:10.1016/j.matpur.2014.02.006
10. Bona JL, Saut JC. Dispersive blowup of solutions of generalized Korteweg-de vries equations. *J Differ Equations.* (1993) 103:3–57. doi:10.1006/jdeq.1993.1040
11. Cazenave T. *Semilinear Schrödinger equations.* New York, NY; American Mathematical Society (2003) 323 p.
12. Dauxois T, Peyrard M. *Physics of solitons.* Cambridge, UK: Cambridge University Press (2006) 435 p.
13. Yang J. *Nonlinear waves in integrable and nonintegrable systems*. Philadelphia, PA: SIAM Mathematical Modeling and Computation, (2010) 430 p.
14. Zakharov VE, Shabat AB. Exact theory of two-dimensional self-focusing and one-dimensional self-modulation of waves in nonlinear media. *J Exp Theor Phys Lett.* (1970) 34:62–9.
15. Ginibre J, Velo G. On a class of nonlinear Schrödinger equations I: the Cauchy problem. *J Funct Anal.* (1979) 32:1–32. doi:10.1016/0022-1236(79)90076-4
16. Tsutsumi Y. L^2-solutions for nonlinear Schrödinger equations and nonlinear groups. *Funkcial Ekvac.* (1987) 30:115–25.
17. Cazenave T, Weissler F. The Cauchy problem for the critical nonlinear Schrödinger equation in H^s. *Non Anal.* (1990) 14:807–36. doi:10.1016/0362-546X(90)90023-A
18. Kenig C, Ponce G, Vega L. On the ill-posedness of some canonical dispersive equations. *Duke Math J.* (2001) 106:617–33. 10.1215/S0012-7094-01-10638-8
19. Cazenave T, Lions PL. Orbital stability of standing waves for some nonlinear Schrödinger equations. *Comm Math Phys.* (1982) 85:549–61. doi:10.1007/BF01403504
20. Weinstein MI. Lyapunov stability of ground states of nonlinear dispersive evolution equations. *Comm Pure Appl Math.* (1986) 39:51–68. 10.1002/cpa.3160390103
21. Grillakis M, Shatah J, Strauss W. Stability theory of solitary waves in the presence of symmetry. *I J Funct Anal.* (1987) 74:160–97. doi:10.1016/0022-1236(87)90044-9
22. Kapitula T. On the stability of N-solitons in integrable systems. *Nonlinearity.* (2007) 20:879–907. 10.1088/0951-7715/20/4/005
23. Martel Y, Merle F. Multi-solitary waves for nonlinear Schrödinger equations. *Ann IHP Anal Non.* (2006) 23:849–64. doi:10.1016/j.anihpc.2006.01.001
24. Martel Y, Merle F, Tsai TP. Stability in H^1 of the sum of K solitary waves for some nonlinear Schrödinger equations. *Duke Math J.* (2006) 133:405–466. 10.1215/S0012-7094-06-13331-8
25. Bridges TJ, Mielke A. A proof of the Benjamin-Feir instability. *Arch Rat Mech Anal.* (1995) 133:145–98. doi:10.1007/BF00376815
26. Achilleos V, Diamantidis S, Frantzeskakis DJ, Karachalios NI, Kevrekidis PG. Conservation laws, exact traveling waves and modulation instability for an extended nonlinear Schrödinger equation. *J Phys A Math Theor.* (2015) 48:355205. 10.1088/1751-8113/48/35/355205
27. Brunetti M, Marchiando N, Betti N, Kasparian J. Modulational instability in wind-forced waves. *Phys Lett.* (2014) 378:3626–30. doi:10.1016/j.physleta.2014.10.017
28. Al Khawaja U, Bahlouli H, Asad-uz-zaman M, Al-Marzoug SM. Modulational instability analysis of the Peregrine soliton. *Comm Nonlinear Sci Num Simul.* (2014) 19:2706–2714. doi:10.1016/j.cnsns.2014.01.002
29. Kalantarov VK, Ladyzhenskaya OA. The occurrence of collapse for quasilinear equations of parabolic and hyperbolic types, *J Math Sci.* (1978) 10:53. doi:10.1007/BF01109723.
30. Hadamard J. Sur les problèmes aux dérivées partielles et leur signification physique. *Princeton Univ. Bull.* (1902) 13:49–52.
31. Alejo MA, Fanelli L, Muñoz C. The Akhmediev breather is unstable. *Sao Paulo J Math Sci.* (2019) 13:391–401. 10.1007/s40863-019-00145-4
32. Muñoz C. Stability of integrable and nonintegrable structures. *Adv Differ Equations.* (2014) 19:947–996.
33. Biondini G, Mantzavinos D. Long-time asymptotics for the focusing nonlinear Schrödinger equation with nonzero boundary conditions at infinity and asymptotic stage of modulational instability. *Comm Pure Appl Math.* (2017) 70:2300–65. doi:10.1002/cpa.21701
34. Muñoz C. Instability in nonlinear Schrödinger breathers. *Proyecciones.* (2017) 36:653–83. 10.4067/S0716-09172017000400653
35. Alejo MA, Fanelli L, Muñoz C. Stability and instability of breathers in the $U(1)$ Sasa-Satsuma and nonlinear Schrödinger models. Preprint repository name [Preprint] (2019) Available from: https://arxiv.org/abs/1901.10381.
36. Alejo MA, Muñoz C. Nonlinear stability of mKdV breathers. *Comm Math Phys.* (2013) 324:233–62. doi:10.1007/s00220-013-1792-0
37. Calini A, Schober CM. Dynamical criteria for rogue waves in nonlinear Schrödinger models. *Nonlinearity.* (2012) 25:R99–R116. 10.1088/0951-7715/25/12/R99
38. Alejo MA, Muñoz C. Dynamics of complex-valued modified KdV solitons with applications to the stability of breathers. *Anal Partial Differ Equation.* (2015) 8:629–74. 10.2140/apde.2015.8.629
39. Alejo MA, Muñoz C, Palacios JM. On the variational structure of breather solutions I: Sine-Gordon equation. *J Math Anal Appl.* (2017) 453:1111–38. doi:10.1016/j.jmaa.2017.04.056.
40. Alejo MA, Muñoz C, Palacios JM. On the variational structure of breather solutions II: Periodic mKdV equation. *Electron J Differ Equations.* (2017) 2017:56.
41. Alejo MA, Muñoz C, Palacios JM. On asymptotic stability of the Sine-Gordon kink in the energy space. Preprint repository name [Preprint] (2020) Available from: https://arxiv.org/abs/2003.09358
42. Cheng G, Liu J. Long-time asymptotics of the modified KdV equation in weighted Sobolev spaces. Preprint repository name [Preprint] (2019) Available from: https://arxiv.org/abs/1903.03855
43. Cheng G, Liu J. Soliton resolution for the modified KdV equation. Preprint repository name [Preprint] (2019) Available from: https://arxiv.org/abs/1907.07115
44. Pelinovsky D, Yang J. Stability analysis of embedded solitons in the generalized third-order nonlinear Schrödinger equation. *Chaos.* (2005) 15:037115. 10.1063/1.1929587
45. Gallay T, Pelinovsky DE. Orbital stability in the cubic defocusing NLS equation: I. Cnoidal periodic waves. *J Differ Equation.* (2015) 258:3607–38. 10.1016/j.jde.2015.01.018
46. Gallay T, Pelinovsky DE. Orbital stability in the cubic defocusing NLS equation: II. The black soliton. *J Differ Equation.* (2015) 258:3639–60. doi:10.1016/j.jde.2015.01.019
47. Muñoz C, Palacios JM. Nonlinear stability of 2-solitons of the Sine-Gordon equation in the energy space. *Ann IHP Anal Non.* (2019) 36:977–1034.
48. Dysthe K, Trulsen K. Note on breather type solutions of the NLS as models for freak waves. *Phys Scr.* (1999) T82:48–52. 10.1238/Physica.Topical.082a00048
49. Zweck J, Latushkin Y, Marzuola JL, Jones CKRT. The essential spectrum of periodically-stationary solutions of the complex Ginzburg-Landau equation. Preprint repository name [Preprint] (2020) Available from: https://arxiv.org/abs/2005.09176.
50. Gallo C. The Cauchy problem for defocusing nonlinear Schrödinger equations with non-vanishing initial data at infinity. *Comm Partial Differ Equation.* (2008) 33:729–71. doi:10.1080/03605300802031614

51. Gérard P. The Cauchy problem for the Gross-Pitaevskii equation *Ann I H Poincaré AN*. (2006) 23:765–79. doi:10.1016/j.anihpc.2005.09.004
52. Ma YC. The perturbed plane-wave solutions of the cubic Schrödinger equation. *Stud Appl Math*. (1979) 60:43–58. 10.1002/sapm197960143
53. Kibler B, Fatome J, Finot C, Millot G, Genty G, Wetzel B, et al. Observation of Kuznetsov-Ma soliton dynamics in optical fibre. *Sci Rep*. (2012) 2:463. doi:10.1038/srep00463.
54. Cuevas-Maraver J, Kevrekidis PG, Frantzeskakis DJ, Karachalios NI, Haragus M, James G. Floquet analysis of Kuznetsov-Ma breathers: A path towards spectral stability of rogue waves. *Phys Rev E*. (2017) 96:012202. doi:10.1103/PhysRevE.96.012202
55. Ablowitz MJ, Clarkson PA. *Solitons, nonlinear evolution equations and inverse scattering*. Cambridge, UK: Cambridge University Press (1991) 516 p.
56. Chen J, Pelinovsky DE, White R. Rogue waves on the double-periodic background in the focusing nonlinear Schrödinger equation. *Phys Rev E*. (2019) 100:052219. doi:10.1103/PhysRevE.100.052219

Conflict of Interest: The authors declare that the research was conducted in the absence of any commercial or financial relationships that could be construed as a potential conflict of interest.

frontiers in Physics

ORIGINAL RESEARCH
published: 26 November 2020
doi: 10.3389/fphy.2020.602229

Breather Structures and Peregrine Solitons in a Polarized Space Dusty Plasma

Kuldeep Singh and N. S. Saini**

Department of Physics, Guru Nanak Dev University, Amritsar, India

In this theoretical investigation, we have examined the combined effects of nonthermally revamped polarization force on modulational instability *MI* of dust acoustic waves *DAWs* and evolution of different kinds of dust acoustic (DA) breathers in a dusty plasma consisting of negatively charged dust as fluid, Maxwellian electrons, and ions obeying Cairns' nonthermal distribution. The nonthermality of ions has considerably altered the strength of polarization force. By employing the multiple-scale perturbation technique, the nonlinear Schrödinger equation *NLSE* is derived to study modulational *MI* instability of dust acoustic waves *DAWs*. It is noticed that influence of the polarization force makes the wave number domain narrow where MI sets in. The rational solutions of nonlinear Schrödinger equation illustrate the evolution of DA breathers, namely, Akhmediev breather, Kuznetsov–Ma breather, and Peregrine solitons (rogue waves). Further, the formation of super rogue waves due to nonlinear superposition of DA triplets rogue waves is also discussed. It is analyzed that combined effects of variation in the polarization force and nonthermality of ions have a comprehensive influence on the evolution of different kinds of DA breathers. It is remarked that outcome of present theoretical investigation may provide physical insight into understanding the role of nonlinear phenomena for the generation of various types of DA breathers in experiments and different regions of space (e.g., the planetary spoke and cometary tails).

Keywords: dust acoustic waves, breather wave, Peregrine soliton, polarization force, rogue wave, Cairns nonthermal distribution

OPEN ACCESS

Edited by:
Bertrand Kibler, UMR6303 Laboratoire Interdisciplinaire Carnot de Bourgogne (ICB), France

Reviewed by:
R. Sabry, Prince Sattam Bin Abdulaziz University, Saudi Arabia
Douglas Alexander Singleton, California State University, Fresno, United States

****Correspondence:***
N. S. Saini
nssaini.phy@gndu.ac.in;
nssaini@yahoo.com
Kuldeep Singh
singh.kdeep07@gmail.com

Specialty section:
This article was submitted to Mathematical and Statistical Physics, a section of the journal Frontiers in Physics

Received: *02 September 2020*
Accepted: *05 October 2020*
Published: *26 November 2020*

Citation:
Singh K and Saini NS (2020) Breather Structures and Peregrine Solitons in a Polarized Space Dusty Plasma. Front. Phys. 8:602229. doi: 10.3389/fphy.2020.602229

1 INTRODUCTION

The plasma physicists have rejuvenated the research in the dusty plasma after the confirmation of presence of dust grains in Saturnian rings by Cassini and Voyager space missions [1]. It has been remarkably reported that such kind of dusty plasma is extremely abundant in various space/astrophysical environments (e.g., solar nebulae and comet tails) [2–6] and laboratory (e.g., manufacturing and processing of semiconductor devices) [7, 8]. The characteristic features of different nonlinear wave excitations in various space dusty plasma environments have been explored by numerous researchers. Prolific literature has confirmed the existence of extremely massive (i.e., nearly 10^6 to $10^{12} m_i$) and excessively charged dust due to its momentous role for generation of DA nonlinear waves in space dusty plasma environments. Numerous theoretical and experimental investigations [9–11] have reported that charged dust reacts with electromagnetic as well as gravitational fields and gives rise to new low frequency modes like dust ion acoustic (DIA) waves [12], dust acoustic waves [13], and other modes. In low frequency dust acoustic waves,

dust mass provides the inertia and pressure of electrons/ions provides the restoring force. Over the last few decades, many researchers have studied the variety of DA nonlinear structures such as solitons, shocks, double layers, and rogue waves, in magnetized/unmagnetized dusty plasmas in the framework of non-Maxwellian distributions [14–18]. Amin et al. [14] studied the MI of dust acoustic and dust ion acoustic waves and found that both DA and DIA waves are modulationally unstable. Shukla et al. [16] derived the dispersion relation for DAWs in a nonuniform dusty magnetoplasma. Labany et al. [17] studied the combined effects of adiabatic dust charge fluctuations and inhomogeneity on the salient features of DA solitons in a magnetized dusty plasma consisting of negatively charged dust, Boltzmann ions, and nonextensive electrons. They noticed the significant variation in the characteristics of DA solitary waves under the influence of dust charge fluctuations. El-Taibany and Sabry [18] illustrated the 3D DA solitary waves and double layers in the presence of magnetic field and nonthermal ions. It is believed that dust grains embedded in a dusty plasma are responsible for various kind of forces. Hamaguchi and Farouki [19] explored one of such forces as polarization force which occurs due to the deformation of the Debye sphere around the dust in nonuniform plasma. They found that difference in positive ion density on either side of negative dust leads to occurrence of the polarization force. The direction of polarization force is opposite to the electrostatic force and independent of sign of charge on dust [20]. Further, the polarization force has a great impact on the characteristics of DA waves. Numerous investigations have also been reported to demonstrate the variety of nonlinear structures by varying the polarization force in the framework of Maxwellian and non-Maxwellian distributions in various space plasma environments [21–27]. Singh et al. [26] illustrated that the superthermality of ions and polarization force have intense influence on the characteristics of DA periodic (cnoidal) waves in a superthermal polarized dusty plasma. In the recent past, Singh et al. [27] investigated the head-on collision among DA multisolitons in a dusty plasma having ions following the hybrid distribution in the presence of polarization force. It was found that rarefactive DA multisolitons are formed and phase shifts are strongly influenced by the polarization force.

Over the last few decades, the study of modulational instability and evolution of nonlinear envelope solitons in the context of nonlinear Schrödinger equation (NLSE) becomes an intriguing area of research in different plasma systems. The rational solutions of NLSE describe broad range of spatially and temporally localized sets of soliton solutions. One of such rational solutions is called Peregrine soliton [28] or prototype of the rogue waves resulting from counterbalance between nonlinearity and group velocity dispersion. The investigation of rogue waves has enhanced comprehensive understanding of evolution and formation of these mysterious waves in the ocean [29, 30]. It is demonstrated that the Peregrine breather plays a pivotal role for exclusive study of rogue waves [31]. It is reported that rogue waves are usually singular and large amplitude waves with draconian effects on living creatures. The rogue waves are known for their sudden appearance as a deep hole and huge crest in a serial pattern. Rogue waves have extremely large amplitude waves that evolve suddenly and then collapse without clue. Such kinds of waves are also observed in nonlinear optics, superfluids, and Bose–Einstein condensates [32, 33]. Further, it is also illustrated that the breather solutions of NLSE can be categorized as Kuznetsov–Ma breathers (space localized patterns and periodic in time) [34, 35] and the second class of breathers is the Akhmediev breather (which is periodic in space and localized in time) [36]. An experimental investigation of the formation of Peregrine solitons was reported by Bailung et al. [37] in a multicomponent plasma composed of negative ions. They illustrated that wave becomes modulationally unstable for critical value of negative ions density. Pathak et al. [38] have experimentally illustrated the occurrence of higher-order Peregrine breathers with amplitude five times the background carrier wave in multispecies plasma and verified their findings with second-order rational solution of breathers obtained from NLSE. Numerous researchers [39, 40] have also studied the evolutionary dynamics of such kind of nonlinear coherent solutions in different plasma environments. The nonlinear superposition of first-order rogue waves yields a complex and localized nonlinear structure with excessively large amplitude known as higher-order rogue waves and becomes a fascinating area of research. Such kind of pecking-order of higher-order breather solutions with a huge amplitude is called SRWs. Moreover, the rogue waves are first-order rational solution while SRWs are higher-order solution of NLSE. The nonlinear superposition of these TRWs forms the SRWs. The amplitude of SRWs goes on rising as triplets are replaced by sextets and so on [41, 42]. The observation of these higher- (second-) order rogue waves (RWs) has been verified in laboratory experiment including theoretical investigation [37, 38]. Numerous investigations of dust acoustic rogue waves have been reported in different plasma environments [43–50]. Singh and Saini [49] have observed that polarization force controls the MI domain of DA waves in a superthermal dusty plasma. They have also illustrated the evolutionary transition of DARW triplets to SRWs in a space dusty plasma. Recently, Jahan et al. [50] have studied the MI and DA rogue waves in a four-component dusty plasma having inertial two fluids of heavy as well as light negatively charged dust grains, superthermal electrons, and nonthermal ions. It is remarked that the conditions for the existence of DARWs are strongly altered under the influence of nonthermality of ions and superthermality of electrons.

Various satellite observations have disseminated the prevalence and abundance of energetic charged particles that exhibit nonthermal tails in the planetary magnetospheres and solar wind [51, 52]. Cairns et al. [53] introduced a new kind of distribution referred to as Cairns distribution in order to explore the concept of negative potential electrostatic wave structures observed by the Freja satellite [54]. They illustrated that the occurrence of charged particles obeying nonthermal distribution can appreciably change the propagation properties of ion acoustic waves in conformity with observations of Freja [54] and Viking [55] satellites. Nonthermal charged particles have been found in the Earth's bow-shock [56], Mar's ionosphere [57], lunar vicinity [58], and the Jupiter and Saturn environments [59]. A large

number of studies have focused on the characteristics of different nonlinear waves in the framework of nonthermal Cairns distribution in various plasma systems [27, 60–62]. Singh [60] studied the propagation of ion acoustic waves (IAWs) in an inhomogeneous electron-ion plasma having nonthermal electrons obeying Cairns distribution. The characteristics of nonlinear IAWs are strongly affected by the density inhomogeneities as well as nonthermality of electrons. Kalita and Kalita [61] studied the dust acoustic waves in a dusty plasma composed of weakly relativistic electrons, nonthermal ions (obeying Cairns distribution), and negatively charged dust. They found that the variation in nonthermal parameter of ions significantly modifies the amplitude of both compressive and rarefactive solitons. Shan et al. [62] studied the influence of nonthermality of electrons as well as protons on the formation of electrostatic ion acoustic waves in an ionospheric plasma.

In our present investigation, we have explored the MI of DAWs and hierarchy of DA breathers, Peregrine solitons, TRWs, and SRWs in a nonthermally polarized space dusty plasma having Cairns distributed nonthermal ions, Maxwellian electrons, and negatively charged dust fluid. Our present optimum knowledge authenticates that no such type of investigation has been carried out yet. We have used multiple-scale perturbation technique to obtain NLSE to study the MI and from its solution, the full class of *DA* breathers and TRWs as well as SRWs are illustrated. The basic fluid model of *DAWs* is given in **Section 2**. In **Section 3**, we have presented the derivation of NLSE. In **Section 4**, modulational instability, analytical solutions of NLSE for study of DA breathers (Akhmediev breather, Kuznetsov–Ma breather, and Peregrine solitons), TRWs, and SRWs are discussed. In **Section 5**, conclusions are presented.

2 FLUID MODEL

In this present investigation, we have examined the influence of polarization force and nonthermality of ions, on the evolution of dust acoustic rogue waves, breathers, and Peregrine solitons in a polarized space dusty plasma having negative dust fluid, Boltzmann electrons, and ions obeying Cairns nonthermal distribution. The modified expression for polarization force under the effect of nonthermal ions can be written as [27]

$$F_p = -Z_d e R C_{\alpha 0}\left[1 - C_{\alpha 1}\left(\frac{e\phi}{k_B T_i}\right) + C_{\alpha 2}\left(\frac{e\phi}{k_B T_i}\right)^2\right]^{1/2,} \tag{1}$$

where $R = Z_d e^2/4k_B T_i \lambda_{Di0}$, $\lambda_{Di0} = \sqrt{\epsilon_0 k_B T_i/n_i e^2 C_{\alpha 1}}$, $C_{\alpha 0} = (C_{\alpha 1} - 2C_{\alpha 2}\phi)$, $C_{\alpha 1} = 1 - \Lambda$, $C_{\alpha 2} = 1/2$, and $\Lambda = \frac{4\alpha}{1+3\alpha}$. α measures the energy spectrum of nonthermal ions. **Equation 1** illustrates that the polarization force is significantly revamped by nonthermality of ions (for more details, see Ref. 27). The expression for polarization force in Maxwellian limit ($\alpha \to 0$) agrees exactly with the expression in Asaduzzaman et al. [25]. Numerically, it is found that the polarization parameter R is decreased with rise in α (i.e., increase in nonthermality of ions) and temperature of ions.

The normalized expression for number density of nonthermally distributed ions by using Taylor's expansion can be written as [27]

$$n_i = \delta_i\left(1 - C_{\alpha 1}\phi + C_{\alpha 2}\phi^2 - C_{\alpha 3}\phi^3 + \cdots\right), \tag{2}$$

where α is the spectral index of nonthermally distributed ions. For low effect of nonthermality of ions, α is small. We have considered the normalized number density of electrons which is given as $n_e = \delta_e \exp(\sigma\phi)$ [49].

The nonthermally modified polarization force term is used in the dust momentum equation to examine the role of polarization force and nonthermality of ions on *DARWs*, breathers, and Peregrine solitons. At equilibrium, the charge neutrality yields $n_{e0} + Z_{d0} n_{d0} = n_{i0}$, where n_{j0} for $(j = e, i, d)$ are unperturbed densities of different species (i.e., electrons, ions, and dust), respectively. The set of normalized fluid model equations governs the dynamics of DAWs is written in the following form [27]:

$$\frac{\partial n_d}{\partial t} + \frac{\partial (n_d u_d)}{\partial x} = 0, \tag{3}$$

$$\frac{\partial u_d}{\partial t} + u_d \frac{\partial u_d}{\partial x} = \chi_p \frac{\partial \phi}{\partial x}, \tag{4}$$

and

$$\frac{\partial^2 \phi}{\partial x^2} = n_d - \delta_i\left[1 - C_{\alpha 1}\phi + C_{\alpha 1}\phi^2 - C_{\alpha 3}\phi^3 + \cdots\right] + \delta_e \exp(\sigma\phi), \tag{5}$$

where $\chi_p = [1 - R \cdot \Xi]$ and $\Xi = (C_{\alpha 1} - 2C_{\alpha 2}\phi + 1/2C_{\alpha 1}^2\phi)$. The n_d is normalized by n_{d0} and u_d is normalized by dust sound speed $C_d = (Z_{d0} k_B T_i/\mathrm{m_d})^{1/2}$. The electrostatic potential $\boldsymbol{\phi}$ is normalized by $k_B T_i/e$. The spatial and time coordinates are also normalized by dust Debye radius (i.e., $\lambda_{Dd} = (k_B T_i/4\pi e^2 \mathrm{Z_{d0} n_{d0}})^{1/2}$) and inverse of dust plasma frequency (i.e., $\omega_{pd}^{-1} = (m_d/4\pi Z_{d0}^2 e^2 n_{d0})^{1/2}$), respectively. Also, $\sigma = T_i/T_e$, $\delta_e = n_e/Z_{d0} n_{d0} = 1/(\rho - 1)$ and $\delta_i = n_i/Z_{d0} n_{d0} = \rho/(\rho - 1)$, and $\rho = n_{i0}/n_{e0}$.

3 DERIVATION OF THE NONLINEAR SCHRÖDINGER EQUATION

To analyze the characteristics of modulated DAWs in nonthermally polarized space dusty plasma, NLSE is derived from **Eqs 3–5** by employing expansion of dependent state variables and following stretching coordinates:

$$\zeta = \epsilon\left(x - \Lambda_g t\right) \quad \text{and} \quad \tau = \epsilon^2 t, \tag{6}$$

where finite parameter $\epsilon \ll 1$ and Λ_g represents the group velocity of envelope. The dependent state variables can be expanded as

$$\Upsilon = \Upsilon_0 + \sum_{m=1}^{\infty} \epsilon^{(m)} \sum_{\ell=-\infty}^{\infty} \Upsilon_\ell^{(m)}(\zeta, \tau) e^{i\ell(\mathrm{kx} - \omega \mathrm{t})}, \tag{7}$$

where $\Upsilon_\ell^{(m)} = [n_d u_d \phi]'$ and $\Upsilon_0 = [100]'$. By adopting multiscale technique, we have taken the fast scale in the phase via $(kx - \omega t)$

with slow scaling via (ζ, τ) in terms of ℓ^{th} harmonics. Further, $n_\ell^{(m)}$, $u_\ell^{(m)}$, and $\phi_\ell^{(m)}$ are real, such that $\Upsilon_{-\ell}^{(m)} = \Upsilon_\ell^{\star(m)}$, the star shows the complex conjugate.

By putting **Eqs 6** and **7** into **Eqs 3–5** and equating terms of first-order $(m, \ell) = (1, 1)$, the first-order quantities are obtained as.

$$n_1^{(1)} = \frac{k^2\chi_1}{\omega^2}\phi_1^{(1)} \quad and \quad u_1^{(1)} = -\frac{k\chi_1}{\omega^2}\phi_1^{(1)}. \tag{8}$$

Further, we obtain

$$\frac{\omega}{k} = \sqrt{\frac{\chi_1}{k^2 + \varrho_1}}, \tag{9}$$

where $\chi_1 = 1 - RC_{\alpha 1}$ and $\varrho_1 = \delta_e\sigma + \delta_i C_{\alpha 1}$. **Equation 9** represents the dispersion relation of DAWs. Now, equating terms for $(m, \ell) = (2, 1)$ and the analogy condition can be written as

$$\Lambda_g = \frac{d\omega}{dk} = \frac{\omega}{k}\left(1 - \frac{\omega^2}{\chi_1}\right). \tag{10}$$

Equation 10 represents the group velocity of the *DAWs*.

From the expressions corresponding to third harmonics $(m, \ell) = (3, 1)$ and with some algebraic manipulations, the final expression for NLSE is obtained as follows:

$$\imath\frac{\partial\Phi}{\partial\tau} + P\frac{\partial^2\Phi}{\partial\zeta^2} + Q\Phi|\Phi|^2 = 0, \tag{11}$$

where P and Q are dispersion and nonlinear coefficients, respectively. Expressions for these coefficients and other steps involved in the derivation of NLSE are illustrated in **Appendix**.

4 MODULATIONAL INSTABILITY AND BREATHERS SOLUTIONS

In this section, we have performed numerical analysis to examine the MI of DAWs and dynamics of DA breathers, Peregrine solitons, and evolution of DA-TRWs to SRWs in a nonthermal polarized dusty plasma. For numerical analysis, we have used MATHEMATICA-10 based program. We have discussed the combined influence of different plasma parameters (e.g., ρ, σ, R, and α) on the characteristics of different kinds of *DA* breathers, RW triplets, and super rogue waves. We have used data for numerical analysis for physical parametric ranges associated with planetary rings [65] in dusty plasma: $n_{i0} = 5 \times 10^7$, $n_{e0} = 4 \times 10^7$, $Z_d = 3 \times 10^3$, $n_d = 10^7\text{cm}^{-3}$, $T_i = 0.05$, $T_e = 50\,\text{eV}$, and $R = 0 - 0.155$. The experimental parametric ranges are as follows [21]: $n_{i0} = 7 \times 10^7$, $n_{e0} = 4 \times 10^7\text{cm}^{-3}$, $Z_d = 3 \times 10^3$, $n_d = 10^7\text{cm}^{-3}$, $T_i = 0.3$, $T_e = 8\text{eV}$, and $R = 0 - 0.155$.

4.1 Modulational Instability

We ensure that **Eq. 11** represents a plane wave solution $\Phi = \Phi_0\exp(\imath\mathbf{Q}|\Phi_0|^2\tau)$ which can be linearized by employing $\Phi = \Phi_0 + \varepsilon\Phi_{(1,0)}\cos(\tilde{\mathbf{k}}\zeta - \tilde{\omega}\tau)$ (i.e., the perturbed wave number $(\tilde{k})$ associated with the frequency $(\tilde{\omega})$ is different from its homologue). The dispersion relation in this perturbed case can be written as [63]

$$\tilde{\omega}^2 = P\tilde{k}^2\left(P\tilde{k}^2 - 2Q|\widetilde{\Phi_0}|^2\right) \tag{12}$$

It is noted that when the ratio of P to Q is positive (i.e., $P/Q > 0$), unstable modulated envelope is observed for $\tilde{k} < \tilde{k_c} = (2Q|\widetilde{\Phi_0}|^2/P)^{1/2}$. The growth rate (Γ_g) of DAWs is determined as follows [63]:

$$\Gamma_g = P\tilde{k}^2\left(\frac{\tilde{k_c}^2}{\tilde{k}^2} - 1\right)^{1/2} \tag{13}$$

It is observed that MI gets stabilized by developing a train of envelope in the form of bright solitons. When the ratio of P to Q is negative (i.e., $P/Q < 0$), stable modulated envelope is formed in the given plasma system.

The stability profile of DAWs is examined in **Figure 1A** which illustrates the variation of critical wave number $k(= k_c)$ with polarization parameter (R). The shaded (white) region associates with modulationally unstable (stable) regime of modulated DA carrier wave. The boundary line which separates the shaded area $(P/Q > 0)$ and the white area $(P/Q < 0)$ gives k_c at fixed value of R. An increase in R yields the deviation of k_c for higher values (i.e., impact of polarization force is to contract the wave number region). **Figure 1B** shows the variation of $k(= k_c)$ with the nonthermality parameter of ions (α). An increase in α moves the k_c in smaller value region. It is seen that the impact of nonthermality of ions is to broaden the wave number domain, where unstable region shows MI growth rate. **Figure 3C** highlights the influence of R and α on the growth rate of MI of DAWs. An increase in both R and α shrinks the maximum growth rate of DAWs. It is discerned that the polarization parameter and nonthermality of ions play pivotal role to change the growth rate of MI. It is stressed that the impact of nonthermality of ions and polarization force (via R) have strong influence on the MI of DAWs.

Now, the main focus of our investigation is to analyze solutions for $PQ > 0$ (i.e., for modulational unstable region). In this regime, nonlinear structures under study are rogue waves (localized in space as well as time), Akhmediev breather (localized in time but periodic in space), Kuznetsov–Ma breather (localized in space but periodic in time), TRWs, and SRWs. The detailed study of different kinds of breathers and other nonlinear structures is summarized as follows.

4.2 Peregrine Solitons

The Peregrine structure [28] as a prototype model for rogue waves has been adopted as a single rogue profile whose amplitude reduces in both time and space. The Peregrine solitons have been examined experimentally in water wave tank [40] and also in

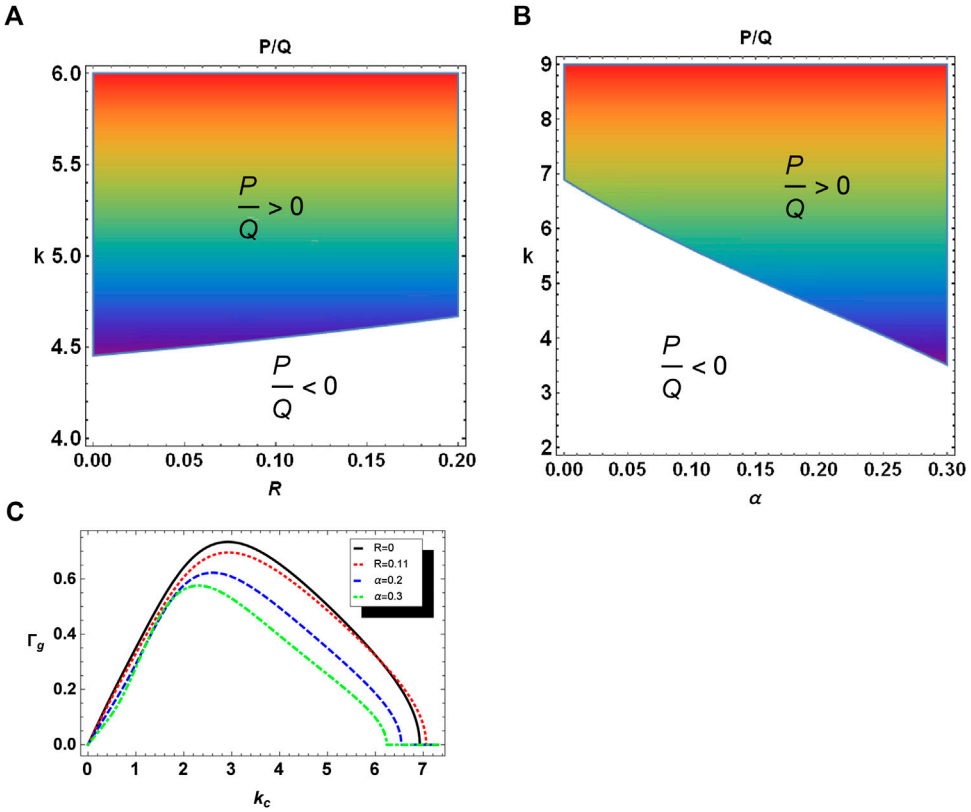

FIGURE 1 | The contour plot of P/Q in plane of **(A)** $k - R$ and **(B)** $k - \alpha$. **(C)** The variation of growth rate (Γ_g) of MI vs. k_c for different values of polarization parameter R and nonthermality parameter α.

plasma [37] situations. The NLS **Eq. 11** provides a first-order rational solution confined in both τ and ζ-plane given by

$$\Phi_{RW} = \sqrt{\frac{P}{Q}}\left[\frac{4(1+2\imath P\tau)}{1+4P^2\tau^2+4\zeta^2}-1\right]\exp(\imath P\tau). \tag{14}$$

Here, we have presented the standard solution of Peregrine solitons (i.e., rogue waves). In the limiting case, when both $R = 0$ and $\alpha = 0$,t the findings of our study agree with results for Maxwellian case of Ref. 64. The RWs are characterized as several times larger in amplitude than their surrounding waves and are more unpredictable. The profile of RWs formation in many experiments can be illustrated as the train of solitons developed due to the modulational instability of monochromatic wave packets which superimpose and suck energy from neighboring waves which further yields extremely large amplitude rogue waves (Peregrine solitons).

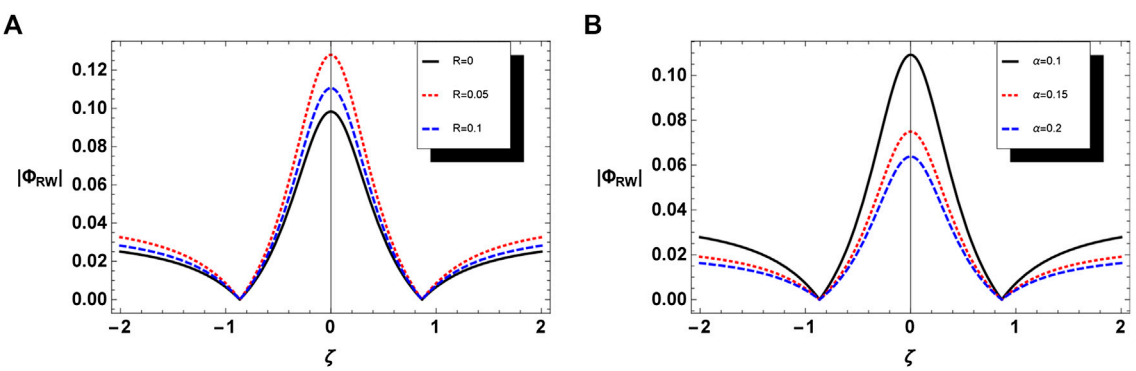

FIGURE 2 | The variation of DARW portrait with respect to ζ **(A)** for different values of R and **(B)** for different values of α at fixed values of $\sigma = 0.01$ and $\rho = 1.11$.

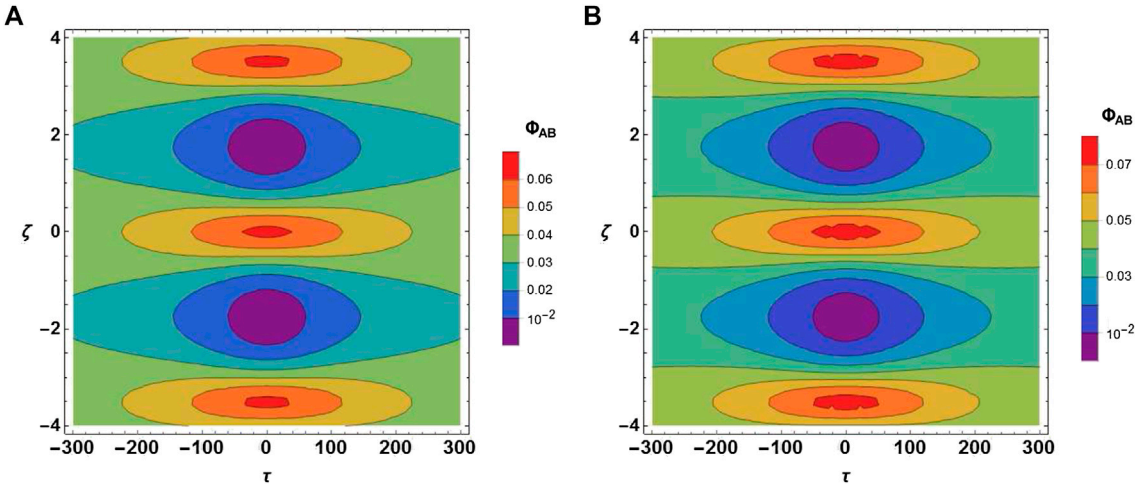

FIGURE 3 | The variation of DA Akhmediev breathers profile in ζ-τ plane **(A)** for $R = 0.1$ and **(B)** $R = 0.11$ at fixed values of $\alpha = 0.1$ and $\rho = 1.11$.

Figure 2A depicts the absolute of amplitude profile of DARWs for distinct values of polarization parameter *R*. It is seen that rise in *R* leads to escalating the amplitude of DARWs, whereas **Figure 2B** shows that increase in α (i.e., nonthermality of ions) reduces the amplitude of DARWs. Consequently, the polarization parameter increases the nonlinearity which leads to enhancing the amplitude of DARWs whereas nonlinearity decreases with the increase in nonthermality of ions and hence amplitude enervates.

4.3 Akhmediev Breather

The Akhmediev breather [36] is an exact solution of the NLSE **Eq. 11** which illustrates the MI regime. The associated waveforms (periodic in space and confined in time) are given by

$$\Phi_{AB} = \sqrt{\frac{P}{Q}}\left[1 + \frac{2(1-2\aleph)\cosh[\wp P\tau] + \iota\wp\sinh[\wp P\tau]}{\sqrt{2\aleph}\cos[\varsigma\zeta] - \cosh[\wp P\tau]}\right]\exp(\iota P\tau). \tag{15}$$

Here, free parameter "ℵ" measures the physical nature of the solution with relations $\varsigma = \sqrt{4(1-2\aleph)}$ and $\wp = \sqrt{2\aleph}\varsigma$. For $0 < \aleph < 0.5$ (i.e., the spatial frequency of wave modulation) "ς" and "℘" must be real such that $0 < \wp, \varsigma < 2$, and the solution demonstrates the AB which is confined in time and has a periodicity in space ζ with period $2\pi/\varsigma$. This solution can be reduced to the confined solution (in space as well as time) with the rise in the converter parameter ℵ up to the limit $\aleph \to 0.5$. Hence, the maximum amplitude of the AB is given by

$$|\Phi|_{AB(max)} = \sqrt{\frac{P}{Q}}(1 + 2\sqrt{2}\,\aleph); \quad \aleph \in (0, 0.5). \tag{16}$$

Figures 3A,B illustrate the variation of DA-AB for distinct values of polarization parameter (via *R*). It is observed that amplitude of DA-AB escalates with rise in polarization parameter. **Figures 4A,B** show the variation of DA Akhmediev breather for distinct values of nonthermality parameter (via α). It is found that amplitude of DA-AB reduces with rise in nonthermality of ions.

4.4 Kuznetsov–Ma Breather

Kuznetsov [34] and Ma [35] introduced one of the breather solutions which is named Kuznetsov–Ma (KM) breather. On the contrary to the AB, KM breather is periodic in time and confined in space and is given by [34, 35]

$$\Phi_{KM} = \sqrt{\frac{P}{Q}}\left[1 + \frac{2(1-2\aleph)\cos[\wp P\tau] - \iota\wp\sin[\wp P\tau]}{\sqrt{2\aleph}\cosh[\varsigma\zeta] - \cos[\wp P\tau]}\right]\exp(\iota P\tau). \tag{17}$$

Here, $0.5 < \aleph < \infty$; the variables "ς "and "℘ " are imaginary. Moreover, the hyperbolic functions are changed into the circular trigonometric functions and vice versa. Such solutions are periodic in time domain with periodicity $2\pi/(\wp P)$. The maximum amplitude of the DA-KM breather is given by

$$|\Phi|_{KM(max)} = \sqrt{\frac{P}{Q}}(1 + 2\sqrt{2}\,\aleph); \quad \aleph \in (0.5, \infty). \tag{18}$$

Figures 5A,B depict the variation in DA-KM breather for distinct values of polarization parameter (via *R*). It is observed that amplitude of DA-KM breather increases with increase in polarization parameter. **Figures 6A,B** show the variation in DA-KM breather for distinct values of nonthermal parameter (via α). It is found that the absolute amplitude of DA-KM breather decreases with rise in nonthermality of ions.

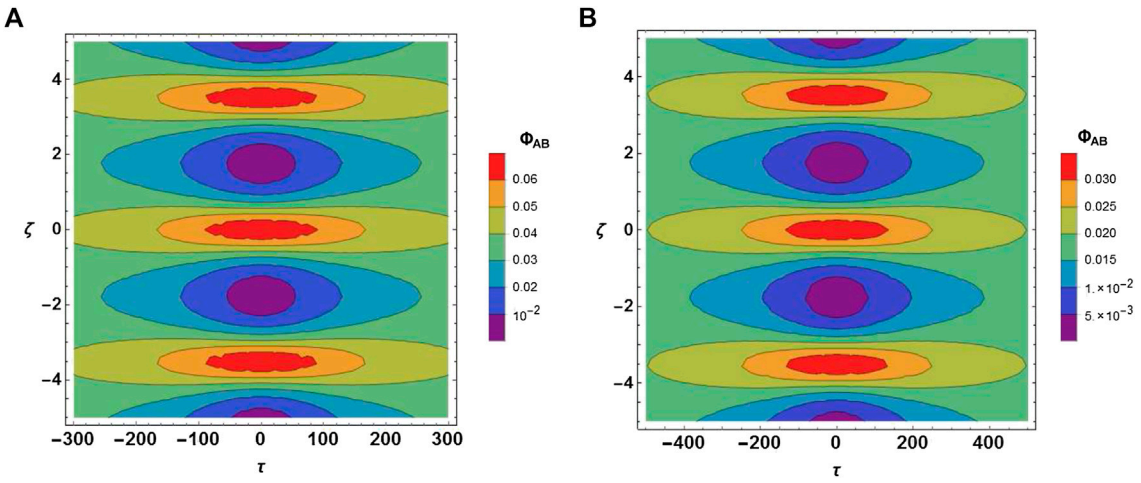

FIGURE 4 | The variation of DA Akhmediev breathers profile in ζ-τ plane **(A)** for $\alpha = 0.2$ and **(B)** $\alpha = 0.3$ at fixed values of $R = 0.11$ and $\rho = 1.11$.

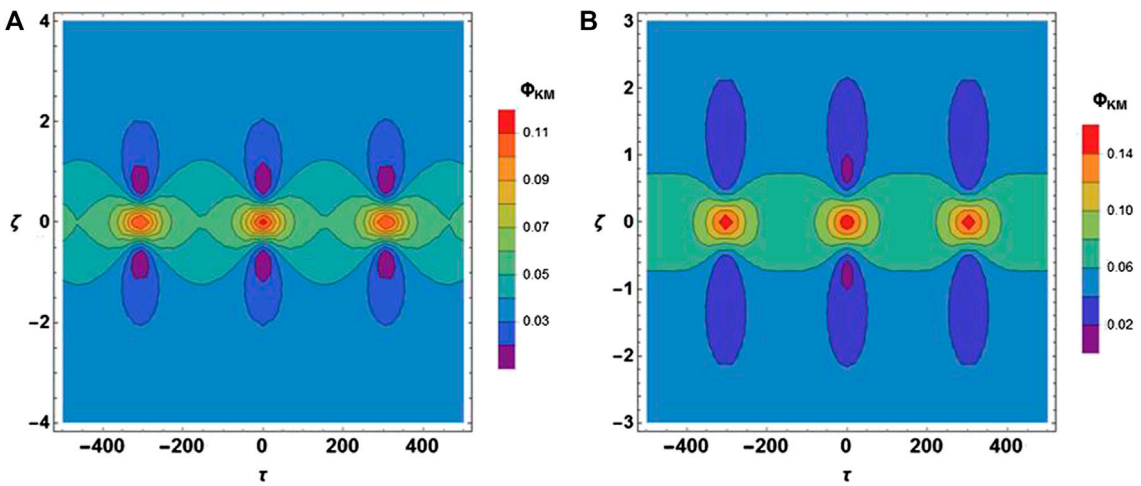

FIGURE 5 | The variation of DA Kuznetsov–Ma breather profile in ζ - τ plane **(A)** for $R = 0.1$ and **(B)** $R = 0.11$ at fixed values of $\alpha = 0.1$ and $\rho = 1.11$.

The maximum amplitude of breathers can be recapitulated as

$$\left.\begin{aligned} |\Phi|_{AB(max)} &= <3\sqrt{\frac{P}{Q}} \quad for \quad \aleph<\frac{1}{2}, \\ |\Phi|_{RW(max)} &= \sqrt{\frac{P}{Q}}\left(1+2\sqrt{2}\,\aleph\right)=3\sqrt{\frac{P}{Q}} \quad for \quad \aleph=\frac{1}{2}, \\ |\Phi|_{KM(max)} &= >3\sqrt{\frac{P}{Q}} \quad for \quad \aleph>\frac{1}{2}, \end{aligned}\right\} \tag{19}$$

Figures 7A–C illustrate the evolution of DA-AB, DA-KM breather, and DARWS for different ℵ values. It is important to note that the maximum amplitude of DARWs is higher than AB and lower than KM (i.e., $|\Phi|_{\mathbf{KM(max)}} > |\Phi|_{\mathbf{RW(max)}} > |\Phi|_{\mathbf{AB(max)}}$). It is also seen that, for AB, the spatial gap of neighboring peaks increases with the rise in ℵ which leads to suppressing the wave frequency and consequently strongly localized structures in both space and time dimensions until ℵ = 0.5 which evolves the DARWs. On the other hand, for the KM breather, the temporal gap of the neighboring peaks shrank with the increment in ℵ (i.e., the wave frequency enhances).

4.5 Rogue Wave Triplets and Super Rogue Waves

Over the last many years, the rogue wave triplets and super RWs solutions of NLSE have been studied theoretically as well as experimentally by numerous researchers [38, 41, 42]. It is found that rogue wave triplets are second-order RWs, and the nonlinear superposition of these DA-TRWs can give birth to higher amplitude SRWs that are also confined in both time and space

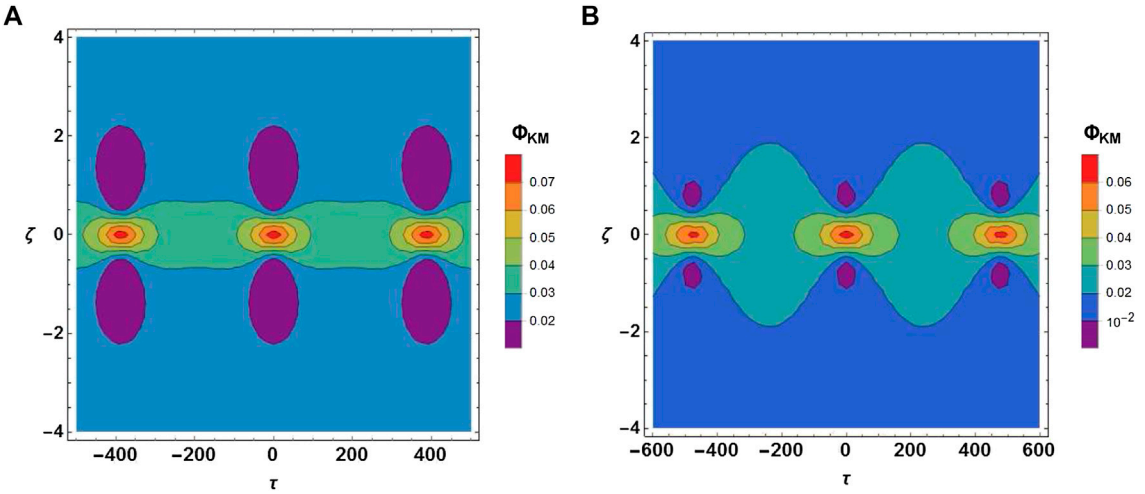

FIGURE 6 | The variation of DA Kuznetsov–Ma breather profile in ζ - τ plane **(A)** for $\alpha = 0.2$ and **(B)** $\alpha = 0.3$ at fixed values of $R = 0.11$ and $\rho = 1.11$.

domains. The higher-order rational solution of **Eq. 11** recognizes the DA-TRWs solution for unstable regime [41]:

$$\Phi = \sqrt{\frac{P}{Q}}\left[1 + \frac{(g_1 + \iota g_2)}{g_3}\right]\exp(\iota P\tau), \tag{20}$$

where

$$\left.\begin{aligned} g_1 &= \left[36 - 24\sqrt{2}\,\theta_1\zeta - 144\zeta^2\{4(P\tau)^2 + 1\} - 864(P\tau)^2 - 48\zeta^4 - 960(P\tau)^4 + 48\theta_2 P\tau\right],\\ g_2 &= 24\left[P\tau\{15 - 2\sqrt{2}\,\theta_1\zeta\} + \theta_2\left\{2(P\tau)^2 - \zeta^2 - \frac{1}{2}\right\} - 4\zeta^4 + 12\zeta^2 - 8(P\tau)^3\left(2\zeta^2 + 1\right) - 16(P\tau)^5\right],\\ g_3 &= \left[8\zeta^6 + 6\zeta^2\{3 - 4(P\tau)^2\}^2 + 64(P\tau)^6 + \theta_1\{\theta_1 + 2\sqrt{2}\,\zeta\left(12(P\tau)^2 + 396(P\tau)^2 - 2\zeta^2 + 3\right)\}\right.\\ &\left. + \theta_2\{4P\tau\left(6\zeta^2 - 4(P\tau)^2 - 9\right)\} + 12\zeta^4\{4(P\tau)^2 + 1\} + 432(P\tau)^4 + \theta_2 + 9\right] \end{aligned}\right\} \tag{21}$$

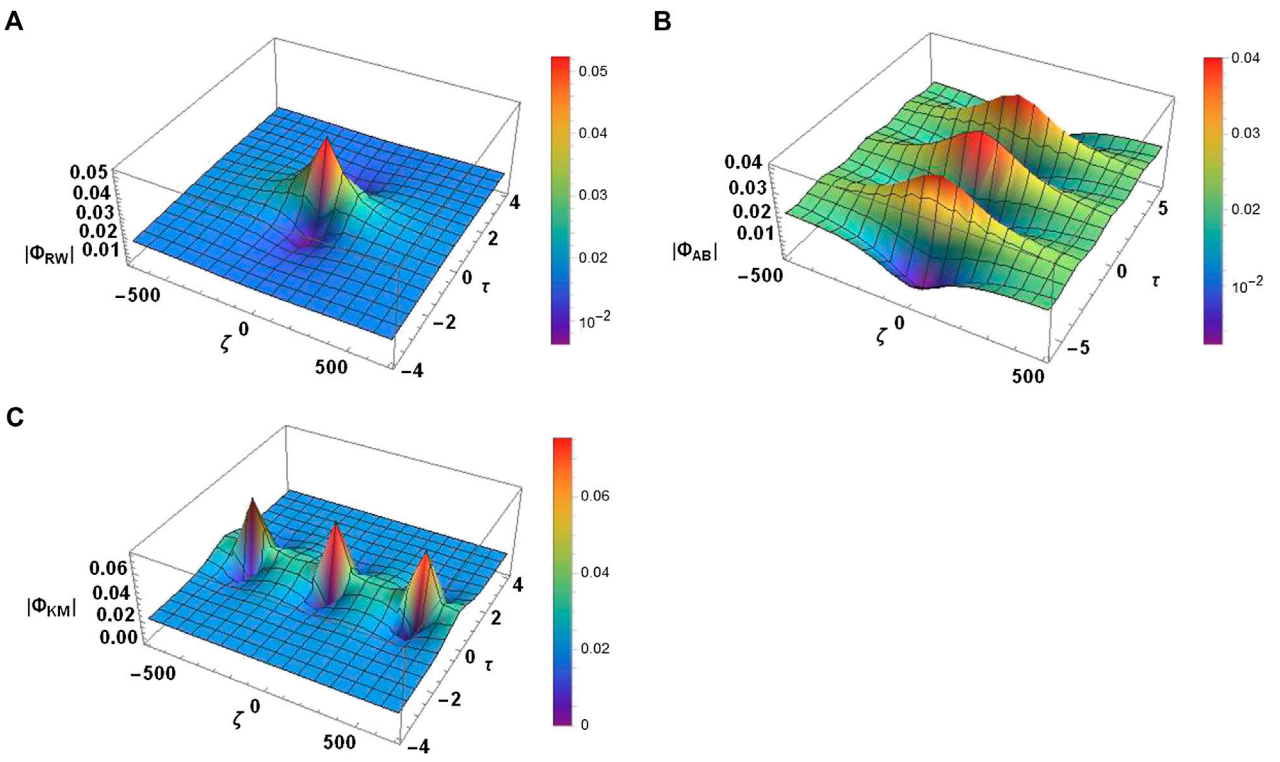

FIGURE 7 | The 3D profile of **(A)** DA rogue waves at $\aleph = 0.5$, **(B)** DA Akhmediev breather at $\aleph = 0.2$, and **(C)** DA Kuznetsov–Ma breather at $\aleph = 2$ with respect to ζ and τ whereas $R = 0.11$, $\alpha = 0.2$, and $\rho = 1.11$ are fixed.

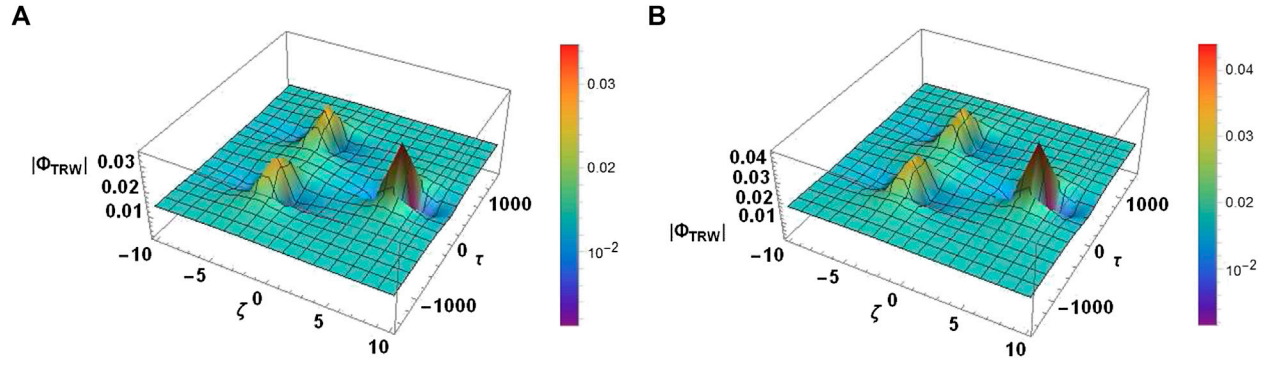

FIGURE 8 | The variation of DA-TRWs portrait in ζ-τ plane **(A)** for $R = 0.1$ and **(B)** $R = 0.13$ whereas $\alpha = 0.2$ and $\rho = 1.11$ are fixed.

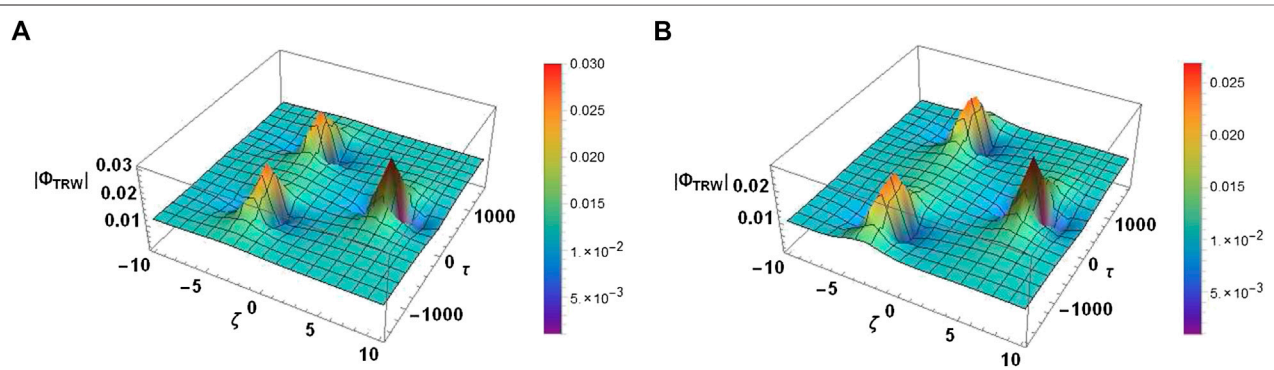

FIGURE 9 | The variation of DA-TRWs portrait in ζ-τ plane **(A)** for $\alpha = 0.2$ and **(B)** $\alpha = 0.3$, whereas $R = 0.11$ and $\rho = 1.11$ are fixed.

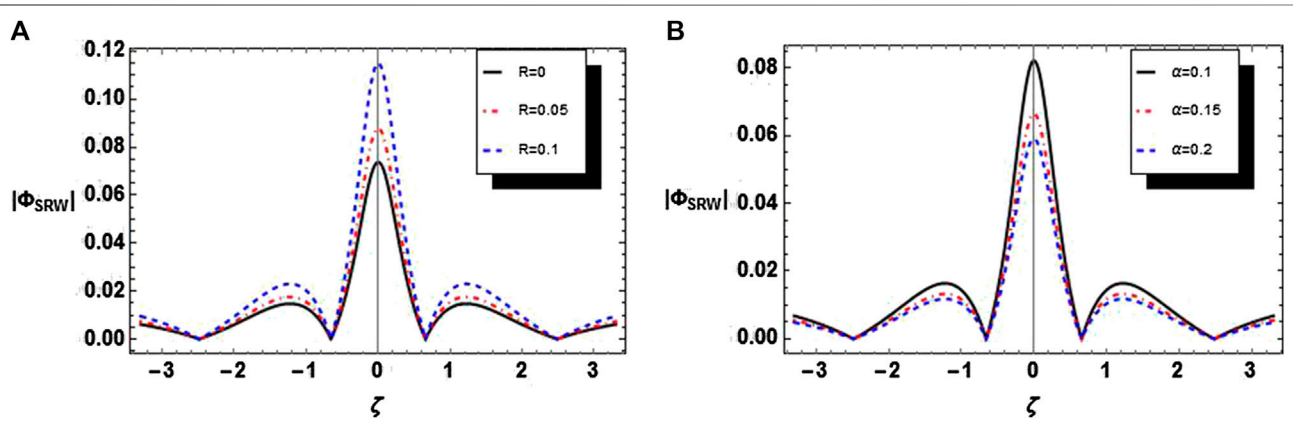

FIGURE 10 | The variation of DA-SRWs portrait vs. ζ **(A)** for different values of R and **(B)** for different values of α whereas $\sigma = 0.01$ and $\rho = 1.11$ are fixed.

Here, θ_1 and θ_2 represent the changeover of DA-TRWs to SRWs and also site of these triplets. We consider $\theta_1 = 1000$ and $\theta_2 = 0$ to portrait a qualitative fashion. Here, $A = (\theta_1^{1/3}/\sqrt{2}, 0)$, $B = (-\sqrt{2}\theta_1^{1/3}/4, \sqrt{3}\theta_1^{1/3}/4P)$, and $C = (-\sqrt{2}\theta_1^{1/3}/4, -\sqrt{3}\theta_1^{1/3}/4P)$ are the sites of DA-TRWs in $(\zeta - \tau)$. If we choose $\theta_1 = \theta_2 = 0$, then DA-SRWs are evolved after the overlapping of first-order DA-TRWs.

Figures 8A,B display the influence of absolute of the amplitude of DA-TRWs for distinct values of polarization force (R). An increase in R produces enhancement in the amplitude of DA-TRWs. **Figures 9A,B** demonstrate the absolute of the DA-TRWs profile for distinct values of α. It is remarked that with an increment in α (i.e., nonthermality of ions) the absolute amplitude DA-TRWs is enervated. The nonlinearity decreases as the

nonthermality of ions increases and consequently, the amplitude of DA-TRWs gets reduced. To demonstrate the evolutionary of DA-SRWs in space dusty plasma, we choose $\theta_1 = \theta_2 = 0$. The DA super rogue waves are evolved in the given plasma model due to nonlinear superposition of second-order DA-TRWs. **Figure 10A** depicts the variation of DA-SRWs for distinct values of polarization parameter R. It is noticed that the rise in R escalates the amplitude of DA-SRWs. **Figure 10B** illustrates that an increase in α leads to reducing the amplitude of DA-SRWs. It is conspicuous that rise in the value of R (α) enhances (reduces) the nonlinearity and increases (suppresses) the amplitude of DA-SRWs. It is remarked that the polarization force and nonthermality of ions substantially revamp the evolution of DA breathers, Peregrine solitons, and different rogue wave structures.

5 CONCLUSION

We have numerically studied the evolution of different kinds of DA breathers, Peregrine solitons, rogue wave triplets, and super rogue waves in a dusty plasma containing negatively charged dust fluid, Maxwellian electrons, and nonthermal ions (obeying Cairns distribution) in the presence of polarization force. First, the role of nonthermality of ions on the polarization force is discussed. By applying the multiple-scale perturbation technique, the NLSE is derived to analyze the MI of the DAWs. It is conspicuous that the polarization parameter controls the wave number domain whereas nonthermality of ions broadens the instability regime. The evolution of dust acoustic AB, KM breather, Peregrine solitons, DA-TRWs, and higher-order SRWs has been illustrated under the impact of nonthermal polarization force. Furthermore, an epoch-making role of all physical parameters like nonthermality of ions and polarization force on the characteristics of dust acoustic AB, KM breather, and first- as well as second-order RWs has been studied. The paramount findings of this study might provide the physical insight of nonlinear coherent structures in planetary rings where nonthermal ions are prevalent in different space environments. We propose to perform a dusty plasma experiment to validate our theoretical predications as formation of IA freak waves has already been examined experimentally by the researchers [37, 38].

DATA AVAILABILITY STATEMENT

The original contributions presented in the study are included in the article; further inquiries can be directed to the corresponding authors.

AUTHOR CONTRIBUTIONS

All authors have contributed equally.

ACKNOWLEDGMENTS

The authors acknowledge the support by DRS-II (SAP) No. F 530/17/DRS-II/2015(SAP-I) UGC and DST-PURSE.

REFERENCES

1. Goertz CK. Dusty plasmas in the solar system. *Rev Geophys* (1989) 27:271–92. doi:10.1029/rg027i002p00271.
2. Horanyi M, Mendis DA. The effects of electrostatic charging on the dust distribution at Halley's Comet. *Astrophys J* (1986) 307:800–7. doi:10.1086/164466.
3. Northrop TG. Dusty plasmas. *Phys Scripta* (1992) 45:475–90. doi:10.1088/0031-8949/45/5/011.
4. Mendis DA, Rosenberg M. Cosmic dusty plasma. *Annu Rev Astron Astrophys* (1994) 32:419–63. doi:10.1146/annurev.aa.32.090194.002223.
5. Thomas H, Morfill GE, Demmel V, Goree J, Feuerbacher B, Möhlmann D. Plasma crystal: coulomb crystallization in a dusty plasma. *Phys Rev Lett* (1994) 73:652–55. doi:10.1103/physrevlett.73.652.
6. Bouchoule A, Plain A, PH-Blondeau L, Laure C. Particle generation and behavior in a silane-argon low-pressure discharge under continuous or pulsed radio-frequency excitation. *J Appl Phys* (1991) 70:1991–2000. doi:10.1063/1.349484.
7. Laure AA, James BW, Vladimirov SV, Cramer NF. Self-excited vertical oscillations in an rf-discharge dusty plasma. *Phys Rev E* (2001) 64:025402. doi:10.1103/physreve.64.025402.
8. Adhikary NC, Bailung H, Pal AR, Chutia J, Nakamura Y. Observation of sheath modification in laboratory dusty plasma. *Phys Plasmas* (2007) 14:103705. doi:10.1063/1.2798046.
9. Mamun AA, Shukla PK. Electrostatic solitary and shock structures in dusty plasmas. *Phys Scripta* (2002) T98:107–14.
10. Shukla PK. Nonlinear waves and structures in dusty plasmas. *Phys Plasmas* (2003) 10:1619–27. doi:10.1063/1.1557071.
11. Shukla PK, Mamum AA. *Introduction to dusty plasma physics* Bristol, England: Institute of Physics Publishing (2002)
12. Shukla PK, Silin VP. Dust ion-acoustic wave. *Phys Scripta* (1992) 45:508. doi:10.1088/0031-8949/45/5/015.
13. Rao NN, Shukla PK, Yu MY. Dust-acoustic waves in dusty plasmas. *Planet Space Sci* (1990) 38:543–6. doi:10.1016/0032-0633(90)90147-i.
14. Amin MR, Morfill GE, Shukla PK. Modulational instability of dust-acoustic and dust-ion-acoustic waves. *Phys Rev E* (1998) 58:6517–23. doi:10.1103/physreve.58.6517.
15. Verheest F. *Waves in dusty space plasma* Dordrecht: Kluwer (2000)
16. Shukla PK, Bharuthram R, Schlickeiser R. Instability of the Shukla mode in a dusty plasma containing equilibrium density and magnetic field inhomogeneities. *Phys Plasmas* (2004) 11:1732. doi:10.1063/1.1668643.
17. El-Labany SK, El-Bedwehy NA, Selim MM, Al-Abbasy OM. Effect of dust-charge fluctuations on dust acoustic solitary waves in an inhomogeneous dusty plasma with nonextensive electrons. *Phys Plasmas* (2015) 22:023711. doi:10.1063/1.4913649.
18. El-Taibany WF, Sabry R. Dust-acoustic solitary waves and double layers in a magnetized dusty plasma with nonthermal ions and dust charge variation. *Phys Plasmas* (2005) 12:082302. doi:10.1063/1.1985987.
19. Hamaguchi S, Farouki RT, Hamaguchi S, Farouki RT. Polarization force on a charged particulate in a nonuniform plasma. *Phys Rev E* (1994) 49:4430–4441. doi:10.1103/physreve.49.4430.
20. Khrapak SA, Ivlev AV, Yaroshenko VV, Morfill GE. Influence of a polarization force on dust acoustic waves. *Phys Rev Lett* (2009) 102:245004. doi:10.1103/physrevlett.102.245004.
21. Bandyopadhyay P, Prasad G, Sen A, Kaw PK. Experimental study of nonlinear dust acoustic solitary waves in a dusty plasma. *Phys Rev Lett* (2008) 101:065006. doi:10.1103/physrevlett.101.065006.
22. Bandyopadhyay P, Konopka U, Khrapak SA, Morfill GE, Sen A. Effect of polarization force on the propagation of dust acoustic solitary waves. *New J Phys* (2010) 12:073002. doi:10.1088/1367-2630/12/7/073002.
23. Mamun AA, Ashrafi KS, Shukla PK. Effects of polarization force and effective dust temperature on dust-acoustic solitary and shock waves in a strongly coupled dusty plasma. *Phys Rev E* (2010) 82:026405. doi:10.1103/physreve.82.026405.
24. Ashrafi KS, Mamun AA, Shukla PK. Time-dependent cylindrical and spherical dust-acoustic solitary and shock waves in a strongly coupled dusty plasma in

the presence of polarization force. *Europhys Lett* (2010) 92:15004. doi:10.1209/0295-5075/92/15004.
25. Asaduzzaman M, Mamun AA, Ashrafi KS. Dust-acoustic waves in nonuniform dusty plasma in presence of polarization force. *Phys Plasmas* (2011) 18:113704. doi:10.1063/1.3657432.
26. Singh K, Ghai Y, Kaur N, Saini NS. Effect of polarization force on dust acoustic cnoidal waves in dusty plasma. *Euro Phys J D* (2018) 72:160. doi:10.1140/epjd/e2018-90228-2.
27. Singh K, Sethi P, Saini NS. Effect of polarization force on head-on collision between multi-solitons in dusty plasma. *Phys Plasmas* (2018) 25:033705. doi:10.1063/1.5020194.
28. Peregrine DH. Water waves, nonlinear Schrödinger equations and their solutions. *J Aust Math Soc Ser B Appl Math* (1983) 25:16. doi:10.1017/s0334270000003891.
29. Pelinovsky E, Kharif C. *Extreme ocean waves* Berlin: Springer (2008)
30. Osborne AR. *Nonlinear ocean waves and the inverse scattering transform* Amsterdam: Elsevier (2010)
31. Akhmediev N, Ankiewicz A, Taki M. Waves that appear from nowhere and disappear without a trace. *Phys Lett A* (2009) 373:675–8. doi:10.1016/j.physleta.2008.12.036.
32. Kharif C, Pelinovsky E, Slunyae A. *Rogue waves in the ocean* Berlin: Springer-Verlag (2009)
33. Müller P, Garrett C, Osborne A. Meeting report|rogue waves-the fourteenth 'Aha Huliko'a Hawaiian winter workshop. *Oceanog* (2005) 18:66–75. doi:10.5670/oceanog.2005.30.
34. Kuznetsov EA. Solitons in a parametrically unstable plasma. *Sov Phys Dokl* (1977) 22:507–8.
35. Ma Y-C. The perturbed plane-wave solutions of the cubic Schrödinger equation. *Stud Appl Math* (1979) 60:43. doi:10.1002/sapm197960143.
36. Akhmediev NN, Eleonskii VM, Kulagin NE. Exact first-order solutions of the nonlinear Schrödinger equation. *Theor Math Phys* (1987) 72:809–18. doi:10.1007/bf01017105.
37. Bailung H, Sharma SK, Nakamura Y. Observation of Peregrine solitons in a multicomponent plasma with negative ions. *Phys Rev Lett* (2011) 107:255005. doi:10.1103/physrevlett.107.255005.
38. Pathak P, Sharma SK, Nakamura Y, Bailung H. Observation of second order ion acoustic Peregrine breather in multicomponent plasma with negative ions. *Phys Plasmas* (2016) 23:022107. doi:10.1063/1.4941968.
39. Ankiewicz A, Kedziora DJ, Akhmediev N. Rogue wave triplets. *Phys Lett A* (2011) 375:2782–5. doi:10.1016/j.physleta.2011.05.047.
40. Chabchoub A, Hoffmann N, Onorato M, Akhmediev N. Super rogue waves: observation of a higher order breather in water waves. *Phys Rev X* (2012) 2:011015. doi:10.1103/physrevx.2.011015.
41. Guo S, Mei L, Shi W. Rogue wave triplets in an ion-beam dusty plasma with superthermal electrons and negative ions. *Phys Lett A* (2013) 377:2118–25. doi:10.1016/j.physleta.2013.06.015.
42. Guo S, Mei L, He Y, Li Y. Modulation instability and ion-acoustic rogue waves in a strongly coupled collisional plasma with nonthermal nonextensive electrons. *Plasma Phys Contr Fusion* (2016) 58:025014. doi:10.1088/0741-3335/58/2/025014.
43. Moslem WM, Sabry R, El-Labany SK, Shukla PK. Dust acoustic rogue waves in a nonextensive plasma. *Phys Rev* (2011) 84:066402. doi:10.1103/physreve.84.066402.
44. Zaghbeer SK, Salah HH, Sheta NH, El-Shewy EK, Elgarayh A. Effect of nonextensive electron and ion on dust acoustic rogue waves in dusty plasma of opposite polarity. *Astrophys Space Sci* (2014) 353:493. doi:10.1007/s10509-014-2081-x.
45. Bouzit O, Tribeche M. Dust-acoustic waves modulational instability and rogue waves in a polarized dusty plasma *Phys Plasmas*doi:10.1063/1.4933006.
46. Singh K, Kaur N, Saini NS. Head-on collision between two dust acoustic solitary waves and study of rogue waves in multicomponent dusty plasma. *Phys Plasmas* (2017) 24:063703. doi:10.1063/1.4984996.
47. Kaur N, Singh K, Ghai Y, Saini NS. Nonplanar dust acoustic solitary and rogue waves in an ion beam plasma with superthermal electrons and ions. *Plasma Sci Technol* (2018) 20:074009. doi:10.1088/2058-6272/aac37a.
48. Shikha RK, Chowdhury NA, Mannan A, Mamun AA. Dust acoustic rogue waves in an electron depleted plasma. *Eur Phys J D* (2019) 73:177. doi:10.1140/epjd/e2019-100158-8.
49. Singh K, Saini NS. The evolution of rogue wave triplets and super rogue waves in superthermal polarized space dusty plasma. *Phys Plasmas* (2019) 26:113702. doi:10.1063/1.5119894.
50. Jahan S, Mannan A, Chowdhury NA, Mamun AA. Dust-acoustic rogue waves in four-component plasmas. *Plasma Phys Rep* (2020) 46:90–6. doi:10.1134/s1063780x20010110.
51. Christon SP, Mitchell DG, Williams DJ, Frank LA, Huang CY, Eastman TE. Energy spectra of plasma sheet ions and electrons from ~50 eV/eto ~1 MeV during plasma temperature transitions. *J Geophys Res* (1988) 93:2562. doi:10.1029/JA093iA04p02562.
52. Pierrard V, Lamy H, Lemaire J. Exospheric distributions of minor ions in the solar wind. *J Geophys Res* (2004) 109:A02118. doi:10.1029/2003JA010069.
53. Cairns RA, Mamum AA, Bingham R, Boström R, Dendy RO, Nairn CMC, et al.. Electrostatic solitary structures in non-thermal plasmas. *Geophys Res Lett* (1995) 22:2709. doi:10.1029/95GL02781.
54. Bostrom R. Observations of weak double layers on auroral field lines. *IEEE Trans Plasma Sci* (1992) 20:756. doi:10.1109/27.199524.
55. Dovner PO, Eriksson AI, Boström R, Holback B. Freja Multiprobe observations of electrostatic solitary structures. *Geophys Res Lett* (1994) 21:1827–30. doi:10.1029/94GL00886.
56. Asbridge JR, Bame SJ, Strong IB. Outward flow of protons from the Earth's bow shock. *J Geophys Res* (1968) 73:5777. doi:10.1029/JA073i017p05777.
57. Lundlin R, Zakharov A, Pellinen R, Borg H, Hultqvist B, Pissarenko N, et al.. First measurements of the ionospheric plasma escape from Mars. *Nature (London)* (1989) 341:609–12.
58. Futaana Y., Machida S, Saito Y, Matsuoka A, Hayakawa H. Moon-related nonthermal ions observed by Nozomi: species, sources, and generation mechanisms. *J Geophys Res* (2003) 108:1025. doi:10.1029/2002JA009366.
59. Krimigis SM, Carbary JF, Keath EP, Armstrong TP, Lanzerotti LJ, Gloeckler G. General characteristics of hot plasma and energetic particles in the saturnian magnetosphere: results from the voyager spacecraft. *J Geophys Res* (1983) 88:8871. doi:10.1029/JA088iA11p08871.
60. Singh SV. Nonlinear ion acoustic waves in an inhomogeneous plasma with non-thermal distribution of electrons. *J Plasma Phys* (2015) 81:905810315. doi:10.1017/s0022377815000094.
61. Kalita BC, Kalita R. Implicit role of Cairns distributed ions and weak relativistic effects of electrons in the formation of dust acoustic waves in plasma. *J Plasma Phys* (2016) 82:905820201. doi:10.1017/s0022377816000167.
62. Shan SA, Hassan I, Saleem H. Electrostatic wave instability and soliton formation with non-thermal electrons in O–H plasma of ionosphere. *Phys Plasmas* (2019) 26:022114. doi:10.1063/1.5079841.
63. Saini NS, Kourakis I. 000Dust-acoustic wave modulation in the presence of superthermal ions. *Phys Plasmas* (2008) 15:123701. doi:10.1063/1.3033748.
64. Misra AP, Roy Chowdhury A. Modulational instability of dust acoustic waves in a dusty plasma with nonthermal electrons and ions. *Eur Phys J D* (2006) 39:49. doi:10.1140/epjd/e2006-00079-1.
65. Goertz CK, Linhua-Shan S, Havnes O. Electrostatic forces in planetary rings. *Geophys Res Lett* (1988) 15:84. doi:10.1029/gl015i001p00084.

Conflict of Interest: The authors declare that the research was conducted in the absence of any commercial or financial relationships that could be construed as a potential conflict of interest.

Appendix

Main Steps for the Derivation of Nonlinear Schrödinger Equation

From second harmonics $(m, \ell) = (2, 1)$, we obtain

$$\left.\begin{aligned} n_1^{(2)} &= -\frac{k^2\chi_1}{\omega^2}\Phi_1^{(2)} + 2\imath k\frac{\partial\Phi_1^{(1)}}{\partial\zeta} \\ u_1^{(2)} &= -\frac{k\chi_1}{\omega}\Phi_1^{(2)} - \imath\frac{k\chi_1\Lambda_g}{\omega^2}\frac{\partial\Phi_1^{(1)}}{\partial\zeta} - \imath\frac{\chi_1}{\omega}\frac{\partial\Phi_1^{(1)}}{\partial\zeta} \end{aligned}\right\} \tag{A1}$$

Further, the second harmonics $(m, \ell) = (2, 2)$ are given due to the self nonlinear interactions of the carrier waves as

$$\left.\begin{aligned} \phi_2^{(2)} &= b_1\left(\phi_1^{(1)}\right)^2 \\ u_2^{(2)} &= b_2\left(\phi_1^{(1)}\right)^2 \\ n_2^{(2)} &= b_3\left(\phi_1^{(1)}\right)^2 \end{aligned}\right\} \tag{A2}$$

These self-interactions provide the zeroth-order harmonics which can be analytically obtained by collecting $(m, \ell) = (3, 0)$:

$$\left.\begin{aligned} \phi_0^{(2)} &= a_1\left|\phi_1^{(1)}\right|^2 \\ u_0^{(2)} &= a_2\left|\phi_1^{(1)}\right|^2 \\ n_0^{(2)} &= a_3\left|\phi_1^{(1)}\right|^2 \end{aligned}\right\} \tag{A3}$$

Equating the third harmonics $(m, \ell) = (3, 1)$, we get the following set of equations:

$$\begin{aligned} &-\imath\omega n_1^{(3)} + \imath k u_1^{(3)} - \Lambda_g\frac{\partial n_1^{(2)}}{\partial\zeta} + \frac{\partial u_1^{(2)}}{\partial\zeta} + \frac{\partial n_1^{(1)}}{\partial\tau} \\ &+ \imath k\left(n_1^{(1)}u_0^{(2)} + u_1^{(1)}n_0^{(2)}\right) + \imath k\left(n_2^{(2)}u_{-1}^{(1)} + u_2^{(2)}n_{-1}^{(1)}\right) = 0 \end{aligned} \tag{A4}$$

$$\begin{aligned} &-\imath\omega u_1^{(3)} - \imath k\chi_1\Phi_1^{(3)} - \Lambda_g\frac{\partial u_1^{(2)}}{\partial\zeta} - \chi_1\frac{\partial\Phi_1^{(2)}}{\partial\zeta} + \frac{\partial u_1^{(1)}}{\partial\tau} \\ &+ \imath k\left(u_1^{(1)}u_0^{(2)}\right) + \imath k\left(u_2^{(2)}u_{-1}^{(1)}\right) + \imath k\chi_2\left(u_1^{(1)}u_0^{(2)}\right) = 0 \end{aligned} \tag{A5}$$

$$\begin{aligned} &-\left(k^2 + \varrho_1\right)\Phi_1^{(3)} + 2\imath k\frac{\partial\Phi_1^{(2)}}{\partial\zeta} + \frac{\partial^2\Phi_1^{(1)}}{\partial\zeta^2} \\ &+ 3\varrho_3\Phi_{-1}^{(1)}\Phi_1^{(1)}\Phi_1^{(1)} + 2\varrho_2\left(\Phi_1^{(1)}\Phi_0^{(2)} + \Phi_{-1}^{(1)}\Phi_2^{(2)}\right) - n_1^{(3)} = 0. \end{aligned} \tag{A6}$$

Now, substituting **Eqs 8**, **A2**, and **A3** along with **Eq. A1** in **Eqs A4–A6**, we get

$$\begin{aligned} &-\imath\omega n_1^{(3)} + \imath k u_1^{(3)} + \frac{\Lambda_g k^2\chi_1}{\omega^2}\frac{\partial\Phi_1^{(2)}}{\partial\zeta} - 2\imath k\Lambda_g\frac{\partial^2\Phi_1^{(1)}}{\partial\zeta^2} - \frac{k^2\chi_1}{\omega^2}\frac{\partial\Phi_1^{(1)}}{\partial\tau} \\ &- \imath\frac{\Lambda_g k\chi_1}{\omega^2}\frac{\partial^2\Phi_1^{(1)}}{\partial\zeta^2} - \frac{k\chi_1}{\omega}\frac{\partial\Phi_1^{(2)}}{\partial\zeta} + \imath\frac{\chi_1}{\omega}\frac{\partial^2\Phi_1^{(1)}}{\partial\zeta^2} \\ &- \imath\frac{k^3\chi_1}{\omega^2}(a_2 + b_2)\left|\Phi_1^{(1)}\right|^2\Phi_1^{(1)} - \imath\frac{k^2\chi_1}{\omega}(a_3 + b_3)\left|\Phi_1^{(1)}\right|^2\Phi_1^{(1)} = 0 \end{aligned} \tag{A7}$$

$$\begin{aligned} &-\imath\omega u_1^{(3)} - \imath k\chi_1\Phi_1^{(3)} - \frac{k\chi_1}{\omega}\frac{\partial\Phi_1^{(1)}}{\partial\tau} + \imath\frac{\Lambda_g^2 k\chi_1}{\omega^2}\frac{\partial^2\Phi_1^{(1)}}{\partial\zeta^2} + \frac{\Lambda_g k\chi_1}{\omega}\frac{\partial\Phi_1^{(2)}}{\partial\zeta} \\ &- \imath\frac{\Lambda_g\chi_1}{\omega}\frac{\partial^2\Phi_1^{(1)}}{\partial\zeta^2} - \chi_1\frac{\partial\Phi_1^{(2)}}{\partial\zeta} \\ &- \imath\frac{k^2\chi_1}{\omega}(a_2 + b_2)\left|\Phi_1^{(1)}\right|^2\Phi_1^{(1)} + \imath k\chi_2(a_1 + b_1)\left|\Phi_1^{(1)}\right|^2\Phi_1^{(1)} = 0 \end{aligned} \tag{A8}$$

$$\begin{aligned} &-\left(k^2 + \varrho_1\right)\Phi_1^{(3)} + 2\imath k\frac{\partial\Phi_1^{(2)}}{\partial\zeta} + \frac{\partial^2\Phi_1^{(1)}}{\partial\zeta^2} - n_1^{(3)} + 2\varrho_2(a_1 + b_1) \\ &\times\left|\Phi_1^{(1)}\right|^2\Phi_1^{(1)} + 3\varrho_3\left|\Phi_1^{(1)}\right|^2\Phi_1^{(1)} = 0. \end{aligned} \tag{A9}$$

Now, eliminating the $n_1^{(3)}$, $u_1^{(3)}$, and $\Phi_1^{(3)}$ and after some algebraic manipulations, we obtain the known NLS equation given by **Eq. 11**.

The expressions for dispersion coefficient (P) and nonlinear coefficient (Q) are given as

$$\left.\begin{aligned} P &= \frac{3}{2}\frac{\omega^3}{\chi_1 k^2}\left(\frac{\omega^2 - \chi_1}{\chi_1}\right) \\ Q &= \left(-\frac{\omega^3}{2k^2\chi_1}\right)\left[\frac{2k^3\chi_1}{\omega^3}(a_2 + b_2) + \frac{k^2\chi_1}{\omega^2}(a_3 + b_3) + 2\varrho_2(a_1 + b_1) - 3\varrho_3 - \frac{k^2\chi_2}{\omega^2}(a_1 + b_1)\right] \\ a_1 &= \left(\frac{\chi_1 k}{\chi_1 - \Lambda_g^2\varrho_1}\right)\left[\frac{\chi_1 k}{\omega^2} + \frac{2\chi_1 k^2\Lambda_g}{\omega^2} - \frac{\varrho_2\Lambda_g^2}{\chi_1 k} + \frac{\chi_2}{\chi_1 k}\right] \\ a_2 &= \frac{\chi_1}{\Lambda_g}\left[\frac{\chi_1 k^2}{\omega^2} + \frac{\chi_2}{\chi_1} - a_1\right] \\ a_3 &= \frac{1}{\Lambda_g}\left[a_2 + \frac{2k^3\chi_1^2}{\omega^3}\right] \\ b_1 &= \frac{\chi_1}{\omega}\left(\frac{\omega\varrho_2}{3\chi_1 k^2} - \frac{k^2\chi_1}{2\omega^3} + \frac{\chi_2}{6\omega\chi_1}\right) \\ b_2 &= \frac{k\chi_1}{\omega}\left(\frac{\chi_1 k^2}{2\omega^2} + \frac{\chi_2}{2\chi_1} - b_1\right) \\ b_3 &= \frac{k}{\omega}\left(b_2 + \frac{k^3\chi_1^2}{\omega^3}\right) \\ \varrho_2 &= \frac{1}{2}\left[\delta_i C_{\alpha 2} - \delta_e\sigma^2\right] \\ \varrho_3 &= \frac{1}{6}\left[\delta_i C_{\alpha 3} + \delta_e\sigma^3\right] \end{aligned}\right\} \tag{A10}$$

frontiers in Physics

REVIEW
published: 03 December 2020
doi: 10.3389/fphy.2020.596886

Peregrine Solitons of the Higher-Order, Inhomogeneous, Coupled, Discrete, and Nonlocal Nonlinear Schrödinger Equations

*T. Uthayakumar, L. Al Sakkaf and U. Al Khawaja**

Physics Department, United Arab Emirates University, Al-Ain, United Arab Emirates

This study reviews the Peregrine solitons appearing under the framework of a class of nonlinear Schrödinger equations describing the diverse nonlinear systems. The historical perspectives include the various analytical techniques developed for constructing the Peregrine soliton solutions, followed by the derivation of the general breather solution of the fundamental nonlinear Schrödinger equation through Darboux transformation. Subsequently, we collect all forms of nonlinear Schrödinger equations, involving systematically the effects of higher-order nonlinearity, inhomogeneity, external potentials, coupling, discontinuity, nonlocality, higher dimensionality, and nonlinear saturation in which Peregrine soliton solutions have been reported.

Keywords: Peregrine solitons, rogue waves, nonlinear Schrödinger equation, higher order and inhomogeneous nonlinear Schrödinger equation, coupled and discrete nonlinear Schrödinger equation, nonlocal nonlinear Schrödinger equation, higher dimensional nonlinear Schrödinger equation, saturable nonlinear Schrödinger equation

OPEN ACCESS

Edited by:
Amin Chabchoub,
The University of Sydney, Australia

Reviewed by:
Haci Mehmet Baskonus,
Harran University, Turkey
Andreas Gustavsson,
University of Seoul, South Korea

****Correspondence:***
U. Al Khawaja
u.alkhawaja@uaeu.ac.ae

Specialty section:
This article was submitted to Mathematical and Statistical Physics, a section of the journal Frontiers in Physics

Received: *20 August 2020*
Accepted: *30 September 2020*
Published: *03 December 2020*

Citation:
Uthayakumar T, Al Sakkaf L and Al Khawaja U (2020) Peregrine Solitons of the Higher-Order, Inhomogeneous, Coupled, Discrete, and Nonlocal Nonlinear Schrödinger Equations. Front. Phys. 8:596886. doi: 10.3389/fphy.2020.596886

1 INTRODUCTION

In 1834, the British engineer J. S. Russell observed a hump of water propagating in a narrow canal created by a boat that maintained its speed and shape for several miles. Unlike a repeated pattern of sinusoidal waves or a spreading out of water wave pulses, the most remarkable feature of the observed single hump is that it was not a series of peaks and troughs wave; instead, it has a "solitary wave" structure with only one peak oscillating with a constant velocity and unchanging profile with time which led him to advert it a "wave of translation". He followed his observations by intensive experiments in a water wave tank leading to demonstrating that, in contrast with the linear case where increasing the amplitude has nothing to do with the wave speed, the speed of the solitary wave is related to its height through $v = \sqrt{g(d+h)}$ and its envelope profile can take the form of $h\,\mathrm{sech}^2[k(x-vt)]$, where h, d, k, g, x, and t denote the wave height, the tank depth, the wavenumber, the gravitational acceleration, the propagation direction, and the time, respectively [1].

The conclusions made by Russell were argued by many mathematical theories such as the wave theory of G. B. Airy which indicates that the crest of a wave of a finite amplitude propagates faster than its remaining structure and eventually breaks [2] and G. G. Stokes theory which states that only the periodic waves can be in a finite and permanent profile [3]. In contrast to these mathematical arguments, in 1895 the Dutch mathematician D. Korteweg and his student G. de Vries came up with a model that describes the propagation of long surface waves in a narrow water channel [4]. A considerable conclusion of Korteweg and de Vries's model was its admissibility of a special solution that travels with constant speed and amplitude, which was in an exact match with Russel's

description. Currently, this model is known as the Korteweg–de Vries (KdV) equation. Disappointedly, the significance of this solution and Russell's observations were overlooked and not understood until 1965 when N. J. Zabusky and M. D. Kruskal pioneered numerical solutions to the KdV equation [5] and observed solitary wave pulses interact between themselves elastically as if they are real particles and return to their initial properties after the collision, except for some phase shifts. This results in a localized solution that remains stable and constant during the propagation which is now referred to as a bright soliton or briefly as a soliton. Nowadays, it is well known that solitons are constructed due to a dynamic balance between the group velocity dispersion and the nonlinearity of the system.

Nonlinear systems have attracted increasing interest after C. S. Gardner and his colleagues J. M. Greene, M. D. Kruskal, and R. M. Miura in 1967 introduced a method [6] now known as the inverse scattering transform (IST) that yields a solution to initial value problems (IVPs) for nonlinear partial differential equations (NPDEs). The IST method may be seen as an extension to the Fourier transform for NPDEs. The integrability of the nonlinear Schrödinger equation (NLSE) was discovered in 1972 when V. Zakharov and A. B. Shabat generalized the IST method and derived, for the first time, its soliton solution upon associating the NLSE to a linear system of differential equations [7]. The integrable NLSE equation is, in principle, admitting infinitely many independent solutions. Later on, the IST method was adopted to find a wide class of solutions to the NLSE and its various versions. Recently, all known solutions of the fundamental NLSE and its different versions were collected by [8].

The first breather type solution on a finite background of the NLSE was achieved in 1977 by E. A. Kuznetsov [9] and independently by Y. C. Ma [10] in 1979; now it is accordingly named Kuznetsov-Ma breather. Such a solution is periodic in time and localized in space. The Kuznetsov-Ma breather was derived by solving the initial value problem of the NLSE where the initial profile is a continuous wave (CW) on a background superposing with a soliton solution. The soliton profile in this context can be considered as a perturbation source on the CW. The modulational instability analysis is used to study the dynamics of the Kuznetsov-Ma breather when the amplitude of the soliton is much smaller than the background of the CW. The Kuznetsov-Ma breather solution can be also seen as a soliton on a finite background. In 1983, D. H. Peregrine [11] derived an exact solution to the focusing NLSE equation that is localized in both time and space domains, on a nonzero background. As a result of its dual localization which is the feature of a solitary wave, currently, this solution is known as Peregrine soliton. Physically, the Peregrine soliton models the closet prototype of rogue waves and thus usually takes the full name Peregrine rogue waves [12–14]. Rogue waves have been first studied in the context of oceanography [12, 15, 16]. Peregrine soliton is the lowest order rational solution of the NLSE that takes the form of one dominant peak, appears from "nowhere", causes danger, and "disappears without a trace" [17, 18]. Its dominant peak is accompanied by two side holes that exist as a result of energy conservation. Due to its danger, oceanographers often call it using some other names such as the "freak waves", the "killer waves", the "monster waves", the "abnormal waves", and the "extreme waves" and rarely use the words "rogon waves", "giant waves", or "steep waves". The highest amplitude of the Peregrine soliton equals two to three times the amplitude of the surrounding background waves.

Shortly, after the revelation of the Peregrine soliton, N. Akhmediev et al., in 1985, found another breather type solution on a finite background to the NLSE which is, contrary to the Kuznetsov-Ma breather, breathing periodically in space and localized in time domain [19]. This solution is now referred to as Akhmediev breather. In relation to the modulational instability analysis, when the frequency of the applied perturbation tends to zero (the soliton's frequency approaches zero), the Kuznetsov-Ma breather tends to a Peregrine soliton. More precisely, taking the temporal period of the Kuznetsov-Ma breather solution to infinity results in a Peregrine soliton. Interestingly, the Akhmediev breather solution also turns out into a Peregrine soliton when the spacial period tends to infinity.

Together with the Kuznetsov-Ma and the Akhmediev breathers, the Peregrine soliton belongs to the family of the solitons on a nonzero background. This family can be represented in one general breather solution form in which the Peregrine soliton can be recovered. The Peregrine soliton, particularly, is considered as the first-order rational solution of a series of infinite recurrence orders of rational solutions. The second-order Peregrine soliton appears with a higher amplitude than the first-order Peregrine soliton [17, 20]. Higher-order of rational solutions and Peregrine soliton hierarchy are also revealed in Refs. 21 and 22.

Although the formation of Peregrine soliton requires ideal mathematical conditions which could be practically impossible, earlier intensive experiments are performed to randomly observe optical rogue waves [23, 24], acoustic rogue waves [25], and rogue waves in parametrically excited capillary waves [26]. In 2010, B. Kibler et al. succeeded for the first time in demonstrating experimentally the dynamics of the Peregrine soliton in nonlinear fiber optics under nonideal excitation condition modeled by the NLSE [27]. Soon after, Peregrine solitons have been observed in deep water wave tanks [28].

Rogue waves can be naturally created via various generating mechanisms. From the perspective of the MI analysis, there is always a chance for these modulations on the CW background to create multiple breathers that are scattering in random directions. Collisions between these grown breathers probably proceed a formation of wave amplification. Higher peaks than the ones associated with the breathers can be generated from the growth of Akhmediev breathers [18, 29–31]. A similar result can be obtained when the collided breathers are Kuznetsov-Ma breathers [20]. Another possible mechanism for the rogue waves' creation is when the collision occurs between multiple solitons carrying different heights and propagating with different phases [32–36]. At the collision point, the amplitude of the peak becomes higher than the solitons individually, thanks to the nonlinear interaction between them. For other scenarios, see also [20, 30, 37–42].

Considerable efforts have been directed toward testing the stability of the Peregrine soliton behavior, analytically and

numerically, against external perturbations [43–46, 46, 47, 47–54]. The stability issue is of important interest to experimentalists, as they seek to reproduce or generate solutions under a laboratory setting. Determining the stability of the solution allows the estimation of the range of practical applications that the solution can occupy. Generally, the studies reveal that, due to the high double localization and sharp structure associated with the Peregrine soliton solution, it, consequently, exhibits high sensitivity to small perturbations or changes in the initial conditions and thus reveals unstable characteristics. Other interesting works on the stability of the Peregrine soliton can be found for instance in [55–65].

Peregrine soliton is of crucial importance due to its doubly dimensional localization in space and time and because it defines a limit case of a wide range of solutions to the NLSE. Thus, it has received huge attention from mathematicians, physicists, and engineers. Its investigations have been rolled up through many contexts such as observation of Peregrine solitons in a multicomponent plasma with negative ions [66, 67], phase properties of Peregrine soliton in the hydrodynamic and optical domains [68], implementation of breather-like solitons extracted from the Peregrine rogue wave in the nonlinear fibers [69], demonstrating experimentally and numerically the generation and breakup of the Peregrine soliton in telecommunications fiber [70], optical rogue waves in an injected semiconductor laser [71], and Peregrine solution in the presence of wind forcing in deep water wave tank laboratories [72].

Besides the experimental observations, numerous numerical simulations and theoretical studies have been performed to demonstrate and predict the occurrence of such a unique type of soliton on a finite background in diverse physical media, for example, in Bose-Einstein condensates [73], freak waves as limiting Stokes waves in the ocean [74], in a mode-locked fiber laser [75], in singly resonant optical parametric oscillators [76], Peregrine solitons and algebraic soliton pairs in Kerr nonlinear media [77], the interaction of two in-phase and out-of-phase Peregrine solitons in a Kerr nonlinear media [41], and recently in lattice systems [78]. For other studies, see also [18, 21, 29, 79–85].

In this work, we aim at reviewing the theoretical studies that have been performed for Peregrine solitons of NLSEs with different setups and conditions. The work is arranged as follows. In **Section 2**, we derive the general breather class of the NLSE via the Darboux transformation and Lax pair method. We show that the Peregrine soliton solution is a limiting case of the general breather solution. An alternative route is then presented where we implement a specific seed solution to derive directly the Peregrine soliton solution. **Section 3** is devoted to reviewing the Peregrine solitons of higher-order and inhomogeneous NLSEs. In **Section 4**, the Peregrine solitons of NLSEs with external constant and variable potentials are reviewed. **Section 5** discusses the Peregrine solitons in coupled NLSEs, known as the Manakov system or the vector NLSE (N-coupled NLSEs), the coupled Gross-Pitaevskii equations, the coupled Hirota equations, the coupled cubic-quintic NLSEs, the PT-symmetric coupled NLSEs, and the higher-order coupled NLSEs. In **Section 6**, we review the works done on Peregrine solitons of the discrete NLSEs, the Ablowitz-Ladik equations, the generalized Salerno equation, and the Hirota equations. In **Section 7**, the Peregrine solitons in nonlocal NLSEs are presented. The nonlocal NLSE is a non-Hermitian and PT-symmetric equation with the nonlinearity term potential $V(x,t)u(x,t) = u(x,t)u^*(-x,t)u(x,t)$, where $u(x,t)$ is the mean field wavefunction, satisfying the PT-symmetric condition, $V(x,t) = V^*(-x,t)$. The nonlocality can also be seen in the presence of the reverse time dependency where $V(x,t) = V^*(x,-t)$ or with the combination of spatial and temporal nonlocalities $V(x,t) = V^*(-x,-t)$. In **Section 8**, we discuss the Peregrine solitons of higher dimensional and mixed NLSEs. In **Section 9**, the Peregrine solitons in saturable NLSEs will be discussed. We end up in **Section 10** by the main conclusions and outlook for future work. The solutions for all the NLSEs considered are provided in the **Supplementary Material**.

2 ANALYTICAL DERIVATION OF THE FUNDAMENTAL PEREGRINE SOLITON

Various analytical methods are used to solve different versions of the NLSE such as the inverse scattering transform [86–93], the Adomian Decomposition method [94], the Homotopy Analysis method [95, 96], the similarity transformation method [97–102], and the Darboux transformation and Lax pair method [103–106], just to name a few. This section is devoted to deriving the general breather solution of the fundamental NLSE using the Darboux transformation and Lax pair method [107]. We show that, under certain limits, the general breather solution reduces to the Akhmediev breather, the Kuznetsov-Ma breather, the Peregrine soliton, the single bright soliton, or the continuous wave solution. The Darboux transformation method is an applicable method for solving only linear systems and cannot be directly applied for nonlinear systems. A crucial additional step is required to make it applicable for nonlinear systems as well. It is to search for an appropriate pair of matrices that associates the nonlinear equation to a linear system. This pair was introduced firstly in 1968 by P. D. Lax [108] and now named Lax pair. The Lax pair should be associated with the nonlinear system through what is called a compatibility condition. The next step is to solve the obtained linear system using a seed solution, which is a known exact solution to the nonlinear system. This technique gives remarkable merit which is the applicability to perform new exact solutions. Each seed solution performs another exact solution that belongs to the family of the seed solution. The latter obtained solution could be used as a new seed solution for the next performance round. All achieved solutions will belong to the same family of the initial seed solution. It is well known that using the trivial solution, $u(x,t) = 0$, as a seed in the Darboux transformation method for the NLSE will produce the single bright soliton solution. The single bright soliton solution can act as a seed solution in the next round to generate the two-soliton solution. Keeping on the same track, multisoliton solutions can be generated in this way. In order to generate the general breather

solution of the NLSE, a nontrivial seed solution is needed, namely, the continuous wave solution $u(x,t) = A\, e^{iA^2 t}$, where A is an arbitrary real amplitude of the wave. Here we include the final results. For the details of the mathematical derivation see **Supplementary Appendix**.

The fundamental NLSE can be written in dimensionless form as

$$iu_t + \frac{1}{2}u_{xx} + |u|^2 u = 0, \tag{1}$$

where $u = u(x,t)$ is the complex wave function and the subscripts denote partial derivatives with respect to t and x. The general breather solution of **Eq. 1** can be compactly written as*

$$u[1] = A\, e^{iA^2 t} \times \left\{ 1 - \frac{\sqrt{8}\,\lambda_{1r}}{A} \frac{\begin{matrix}(A^2+\Gamma^2)\cos(q_1) + i\,(A^2-\Gamma^2)\sin(q_1) \\ +2A\left[\Gamma_r \cosh(q_2) - i\,\Gamma_i \sinh(q_2)\right]\end{matrix}}{2A\,\Gamma_r \cos(q_1) + (\Gamma^2 + A^2)\cosh(q_2)} \right\}, \tag{2}$$

where

$$q_1 = \delta_1 + \sqrt{2}\left[\sqrt{2}\,x\,\Delta_i - 2\,t\,(\Delta_i\,\lambda_{1i} + \Delta_r\,\lambda_{1r})\right],$$
$$q_2 = \delta_2 + \sqrt{2}\left[\sqrt{2}\,x\,\Delta_r - 2\,t\,(\Delta_r\,\lambda_{1i} - \Delta_i\,\lambda_{1r})\right]$$
$$\Delta_r = \mathrm{Re}\left[\sqrt{2\,(\lambda_{1r} - i\,\lambda_{1i})^2 - A^2}\right], \Delta_i = \mathrm{Im}\left[\sqrt{2\,(\lambda_{1r} - i\,\lambda_{1i})^2 - A^2}\right]$$
$$\Gamma_r = \Delta_r + \sqrt{2}\,\lambda_{1r},\ \Gamma_i = \Delta_i - \sqrt{2}\,\lambda_{1i},\ \text{and}\ \Gamma = \sqrt{\Gamma_r^2 + \Gamma_i^2}$$

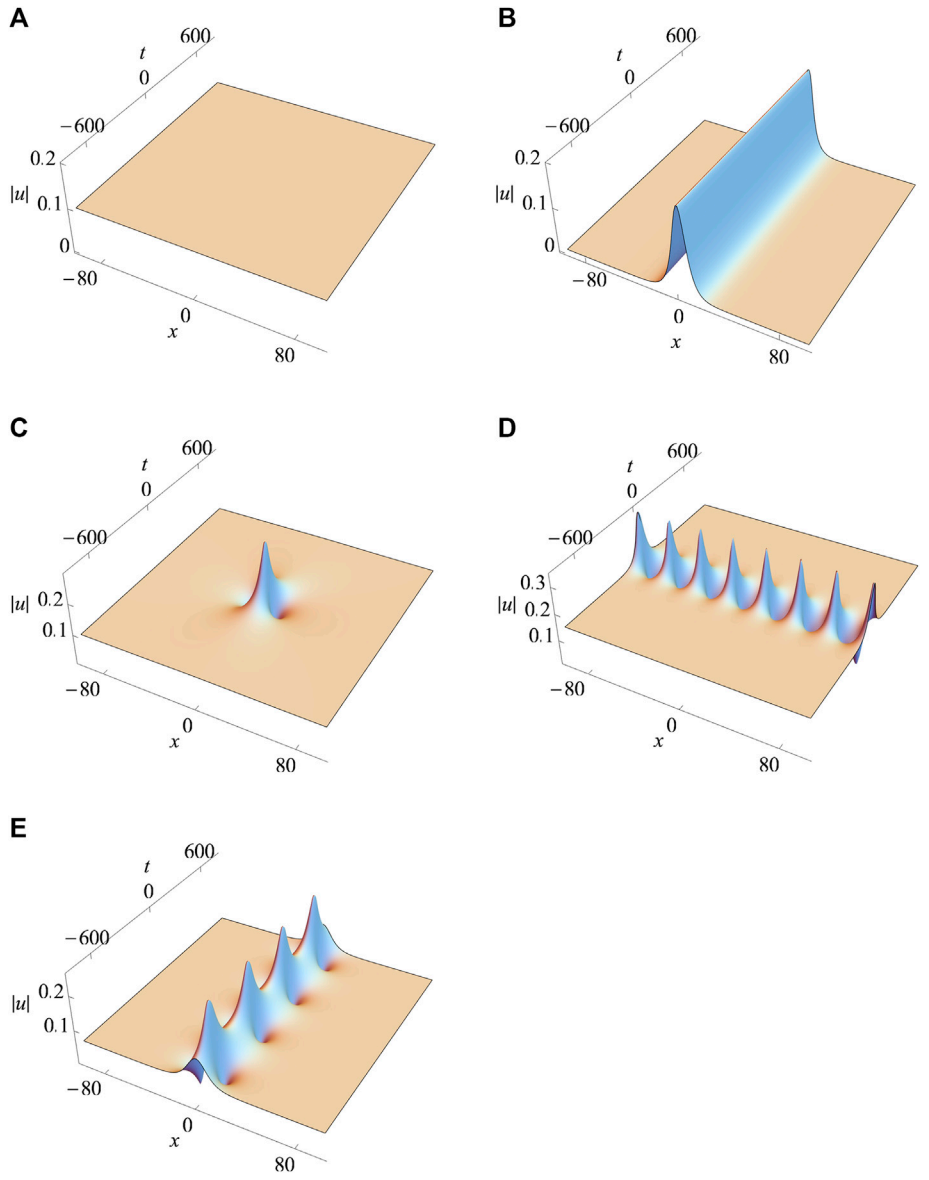

FIGURE 1 | The five members of the solution class (2) all at $\lambda_{1r} = 0.07$. **(A)** CW at $A = \sqrt{2}\lambda_{1r}$, **(B)** soliton at $A = 0$, **(C)** Peregrine soliton at $A = -\sqrt{2}\lambda_{1r}$, **(D)** Akhmediev breather at $A = 1.5\sqrt{2}\lambda_{1r}$, **(E)** Kuznetsov-Ma breather at $A = \sqrt{2}\lambda_{1r}/1.5$.

This is the general breather solution of the NLSE with five arbitrary real parameters, λ_{1r}, λ_{1i}, δ_1, δ_2, and A, which can be, with certain sets of parameter's values, reduced to different types of solutions within the same family. For the sake of obtaining the Akhmediev breather, the Kuznetsov-Ma breather, the Peregrine soliton, the single bright soliton, and the continuous wave solution as limiting cases of solution **Eq. 2**, the first four free parameters are held on $\lambda_{1r} = 0.05$, $\lambda_{1i} = 0$, $\delta_i = 0$, and $\delta_r = 0$, while we choose A to be the variable parameter.

(1) Continuous wave: In the limit $A \to \sqrt{2}\lambda_{1r}$, the general breather solution returns back to the seed solution with an amplitude $A = -\sqrt{2}\lambda_{1r}$ (**Figure 1A**)

$$u[1] = -\sqrt{2}\lambda_{1r}\, e^{2i\lambda_{1r}^2 t}. \tag{3}$$

(2) Soliton: In the trivial limit, when $A \to 0$, the general breather solution reduces to a soliton solution which is localized in x and does not change as it propagates, fixed shape along t direction (**Figure 1B**)

$$u[1] = -2\sqrt{2}\lambda_{1r}\, e^{4i\lambda_{1r}^2 t}\, \mathrm{sech}\left(2\sqrt{2}\,\lambda_{1r} x\right). \tag{4}$$

(3) Kuznetsov-Ma breather: When $|A| < \sqrt{2}\lambda_{1r}$ the general breather solution becomes periodic only in t and localized in x, which is referred to as a KM breather (**Figure 1E**).

(4) Akhmediev breather: When $|A| > \sqrt{2}\lambda_{1r}$ the general breather solution becomes periodic in x and localized in t, which is currently known as an Akhmediev breather (**Figure 1D**).

(5) Peregrine soliton: In the nontrivial limit, when $A \to -\sqrt{2}\lambda_{1r}$, the period goes to infinity and the breather solution reduces to the Peregrine soliton which is localized in both x and t and given by the rational expression (**Figure 1C**)

$$u[1] = \sqrt{2}\lambda_{1r}\, e^{2i\lambda_{1r}^2 t}\left(\frac{-3 - 16i\lambda_{1r}^2 t + 8\lambda_{1r}^2 x^2 + 16i\lambda_{1r}^4 t^2}{1 + 8\lambda_{1r}^2 x^2 + 16\lambda_{1r}^4 t^2}\right). \tag{5}$$

*There are different forms of the general breather solution in the literature. Three more expressions are listed in [8].

3 PEREGRINE SOLITONS OF HIGHER-ORDER AND INHOMOGENEOUS NLSES

This section is dedicated to review existing Peregrine soliton solutions of the inhomogeneous NLSE with higher-order effects and potentials reported in the literature. In general, the higher-order NLSE (HNLSE) encompasses the effects of the higher-order dispersion, the higher-order nonlinearity, the stimulated Raman self-frequency shift, and the self-steepening effects in addition to group velocity dispersion (GVD) and cubic nonlinearity of fundamental NLSE. Such HNLSEs play a significant role in describing the dynamics of the ultrashort pulse propagation, supercontinuum generation [109], Heisenberg spin chain [110], ocean waves [16], and so forth. However, our context will be adhering to the Peregrine soliton solutions realized for such HNLSEs with different higher-order dispersive and nonlinear effects under certain circumstances. Diverse HNLSEs have been reported in the literature, namely, the Hirota equation [111], the Lakshmanan-Porsezian-Daniel equation [110], the quintic NLSE [22], the sextic NLSE [112, 113], heptic NLSE [112], and octic NLSE [112]. This section attempts to review the occurrence of the Peregrine solution reported in the aforementioned HNLSEs. Additionally, the inhomogeneous NLSE which is commonly termed as variable coefficient NLSE is also explored for the occurrence of Peregrine solutions [114, 115]. Understanding such inhomogeneous NLSEs plays a significant role in describing the nonuniform, defective, and irregular space-time dependence of the physical systems as well as discovering the apt control parameters required for diverse complex systems [85, 116–118]. The higher-order and inhomogeneous NLSEs, in which Peregrine solutions are reported, are listed below.

3.1 The Interaction of the Optical Rogue Waves Described by a Generalized HNLSE With (Space-, Time-) Modulated Coefficients [118]

$$\begin{aligned} i\psi_z = {} & \beta(z,t)\psi_{tt} + \left[V(z,t) + i\gamma(z,t)\right]\psi + g(z,t)|\psi|^2\psi \\ & + i\left[\alpha_1(z)\psi_{ttt} + \alpha_2(z)\frac{\partial\left(|\psi|^2\psi\right)}{\partial t} + \alpha_3(z)\psi\frac{\partial|\psi|^2}{\partial t}\right] + \left[\mu(z)\right. \\ & \left. + i\sigma(z,t)\right]\psi_t. \end{aligned} \tag{6}$$

In the above equation, $\beta(z,t)$, $V(z,t)$, $\gamma(z,t)$, and $g(z,t)$ represent the (space-, time-) modulated coefficients of GVD, external potential, gain/loss, and SPM, respectively. $\alpha_1(z)$, $\alpha_2(z)$, and $\alpha_3(z)$ account for third-order dispersion, self-steepening, and stimulated Raman scattering coefficients, respectively. $\mu(z)$ and $\sigma(z,t)$ denote the coefficients of differential gain or loss parameter and (space-, time-) modulated walk-off, respectively. (Solutions: See S1 & S2.)

3.2 The Fourth-Order Integrable Generalized NLSE With Higher-Order Nonlinear Effects Describing the Propagation of Femtosecond Pulse Through a Nonlinear Silica Fiber [119]

$$\begin{aligned} & i\psi_t + \psi_{xx} + 2|\psi|^2\psi + \gamma_1\left(\psi_{xxxx} + 6\psi_x^2\psi^* + 4|\psi_x|^2\psi\right. \\ & \left. + 8|\psi|^2\psi_{xx} + 2\psi^2\psi_{xx}^* + 6|\psi|^4\psi\right) = 0. \end{aligned} \tag{7}$$

Here γ_1 indicates the strength of higher-order linear and nonlinear effects. (Solution: See S3.)

3.3 The Fifth-Order NLSE Describing One-Dimensional Anisotropic Heisenberg Ferromagnetic Spin Chain [120]

$$\begin{aligned} &i\psi_t + \frac{1}{2}\left(\psi_{xx} + 2|\psi|^2\psi\right) - i\alpha\left(\psi_{xxx} + 6|\psi|^2\psi_x\right) \\ &+ \gamma\Big[\psi_{xxx} + 6|\psi|^4\psi + 2\psi^2\psi^*_{xx} + 4\psi|\psi_x|^2 + 6\psi^*\left(\psi_x\right)^2 \\ &+ 8|\psi|^2\psi_{xx}\Big] - i\delta\Big[\psi_{xxxxx} + 30|\psi|^4\psi_x + 20\psi^*\psi_x\psi_{xx} \\ &+ 10|\psi|^2\psi_{xxx} + 10\left(\psi\left|\psi_x\right|^2\right)_x\Big] = 0, \end{aligned} \tag{8}$$

where the parameters α, γ, and δ are the coefficients of third-order dispersion, fourth-order dispersion, and fifth-order dispersion, respectively. (Solution: See S4.)

3.4 The Dynamics of Ultrashort Optical Pulses Propagating Through an Optical Fiber Described by a Higher-Order NLSE [121]

$$i\psi_x + \alpha_2 K_2(\psi) - i\alpha_3 K_3(\psi) + \alpha_4 K_4(\psi) - i\alpha_5 K_5(\psi) = 0, \tag{9}$$

where K_2, K_3, K_4, and K_5 are cubic, Hirota, Lakshmanan-Porsezian-Daniel, and quintic operators, respectively.

$$\begin{cases} K_2 = \psi_{tt} + 2\psi|\psi|^2, \\ K_3 = \psi_{ttt} + 6\psi_t|\psi|^2, \\ K_4 = \psi_{tttt} + 8|\psi|^2\psi_{tt} + 6|\psi|^4\psi + 4|\psi_t|^2\psi + 6\overline{\psi}\psi_t^2 + 2\psi^2\overline{\psi}_{tt}, \\ K_5 = \psi_{ttttt} + 10|\psi|^2\psi_{ttt} + 10\left(\psi|\psi_t|^2\right)_t + 20\overline{\psi}\psi_t\psi_{tt} + 30|\psi|^4\psi_t. \end{cases}$$

$\alpha_i\,(i = 1, 2, 3, 4, 5)$ are real constants. (Solution: See S5.)

3.5 The Sixth-Order NLSE With a Single Higher-Order Dispersion Term Describing the Dynamics of Modulation Instability, Rogue Waves, and Spectral Analysis [122]

$$i\psi_z + \delta_2\Gamma_2(\psi) + \delta_6\Gamma_6(\psi) = 0, \tag{10}$$

where δ_2 and δ_6 are the second- and sixth-order dispersion coefficients, respectively. Γ_2 and Γ_6 are cubic and sextic operator, respectively. In this analysis, the second-order dispersion coefficient value is fixed as $\delta_2 = 1/2$.

$$\begin{cases} \Gamma_2 = \psi_{tt} + 2\psi|\psi|^2, \\ \Gamma_6 = \psi_{tttttt} + \psi^2\left[60\left|\psi_t\right|^2\psi^* + 50\psi_{tt}\left(\psi^*\right)^2 + 2\psi^*_{tttt}\right] \\ \quad + \psi\left[12\psi^*\psi_{tttt} + 18\psi^*_t\psi_{ttt} + 8\psi_t\psi^*_{ttt} + 70\left(\psi^*\right)^2\psi_t^2 + 22\left|\psi_{tt}\right|^2\right] \\ \quad + 10\psi_t\left[3\psi^*\psi_{ttt} + 5\psi^*_t\psi_{tt} + 2\psi_t\psi^*_{tt}\right] + 10\psi^3\left[2\psi^*\psi^*_{tt} + \left(\psi^*_t\right)^2\right] \\ \quad + 20\psi^*\psi^2_{tt} + 20\psi\left|\psi\right|^6. \end{cases}$$

(Solution: See S6.)

3.6 An Infinite Hierarchy of the Integrable NLSE [112]

$$\begin{aligned} F[\psi(x,t)] &= i\psi_x + \alpha_2 K_2[\psi(x,t)] - i\alpha_3 K_3[\psi(x,t)] \\ &+ \alpha_4 K_4[\psi(x,t)] - i\alpha_5 K_5[\psi(x,t)] + \alpha_6 K_6[\psi(x,t)] \\ &- i\alpha_7 K_7[\psi(x,t)] + \alpha_8 K_8[\psi(x,t)] \\ &- i\alpha_9 K_9[\psi(x,t)] + \ldots = 0, \end{aligned} \tag{11}$$

where K_2, K_3, K_4, K_5, K_6, K_7, K_8, and K_9 are cubic, Hirota, Lakshmanan-Porsezian-Daniel, quintic, sextic, heptic, octic, and ninth-order operators, respectively. $\alpha_j\,(j = 1, 2, 3, 4, 5, 6, 7, 8, 9, \ldots)$ are real constants. The higher-order operators up to K_8 are provided below

$$\begin{cases} K_2 = \psi_{tt} + 2\psi|\psi|^2, \\ K_3 = \psi_{ttt} + 6\psi_t|\psi|^2, \\ K_4 = \psi_{tttt} + 8|\psi|^2\psi_{tt} + 6|\psi|^4\psi + 4|\psi_t|^2\psi + 6\psi_t^2\psi^* + 2\psi^2\psi^*_{tt}, \\ K_5 = \psi_{ttttt} + 10|\psi|^2\psi_{ttt} + 10\left(\psi|\psi_t|^2\right)_t + 20\psi^*\psi_t\psi_{tt} + 30|\psi|^4\psi_t, \\ K_6 = \psi_{tttttt} + \left[60\psi^*|\psi_t|^2 + 50\left(\psi^*\right)^2\psi_{tt} + 2\psi^*_{tttt}\right]\psi^2 \\ \quad + \psi\left[12\psi^*\psi_{tttt} + 8\psi_t\psi^*_{ttt} + 22|\psi_{tt}|^2\right] \\ \quad + \psi\left[18\psi_{ttt}\psi^*_t + 70\left(\psi^*\right)^2\psi_t^2\right] + 20\left(\psi_t\right)^2\psi^*_{tt} + 10\psi_t\left[5\psi_{tt}\psi^*_t\right. \\ \quad \left. + 3\psi^*\psi_{ttt}\right] + 20\psi^*\psi^2_{tt} + 10\psi^3\left[\left(\psi^*_t\right)^2 + 2\psi^*\psi^*_{tt}\right] + 20\psi|\psi|^6, \\ K_7 = \psi_{ttttttt} + 70\psi_{tt}^2\psi^*_t + 112\psi_t|\psi_{tt}|^2 + 98|\psi_t|^2\psi_{ttt} \\ \quad + 70\psi^2\left[\psi_t\left[(\psi)2 + 2\psi^*\psi^*_{tt}\right] + \psi^*\left(2\psi_{tt}\psi^*_t + \psi_{ttt}\psi^*\right)\right] \\ \quad + 28\psi_t^2\psi^*_{ttt} + 14\psi\left[\psi^*\left(20|\psi_t|^2\psi_t + \psi_{ttttt}\right) + 3\psi_{ttt}\psi^*_{tt}\right. \\ \quad \left. + 2\psi_{tt}\psi^*_{ttt} + 2\psi_{tttt}\psi^*_t + \psi_t\psi^*_{tttt} + 20\psi_t\psi_{tt}\left(\psi^*\right)^2\right] + 140|\psi|^6\psi_t \\ \quad + 70\psi_t^3\left(\psi^*\right)^2 + 14\left(5\psi_{tt}\psi_{ttt} + 3\psi_t\psi_{tttt}\right)\psi^*, \\ K_8 = \psi_{tttttttt} + 14\psi^3\left[40\,|\psi_t|^2\left(\psi^*\right)^2 + 20\psi_{tt}\left(\psi^*\right)^3 + 2\psi^*_{tttt}\psi^*\right. \\ \quad \left. + 3\left(\psi^*_{tt}\right)^2 + 4\psi^*_t\psi^*_{ttt}\right] + \psi^2\left[28\psi^*\left(14\psi_{tt}\psi^*_{tt} + 11\psi_{ttt}\psi^*_t\right.\right. \\ \quad \left.\left. + 6\psi_t\psi^*_{ttt}\right) + 238\psi_{tt}\left(\psi^*_t\right)^2 + 336|\psi_t|^2\psi^*_{tt} + 560\psi_t^2\left(\psi^*\right)^3\right. \\ \quad \left. + 98\psi_{tttt}\left(\psi^*\right)^2 + 2\psi^*_{tttttt}\right] + 2\psi\left\{21\psi_t^2\left[9\left(\psi^*_t\right)^2 + 14\psi^*\psi^*_{tt}\right]\right. \\ \quad \left. + \psi_t\left[728\psi_{tt}\psi^*_t\psi^* + 238\psi_{ttt}\left(\psi^*\right)^2 + 6\psi^*_{ttttt}\right] + 34|\psi_{ttt}|^2\right. \\ \quad \left. + 36\psi_{tttt}\psi^*_{tt} + 22\psi_{tt}\psi^*_{tttt} + 20\psi_{ttttt}\psi^*_t + 161\psi_{tt}^2\left(\psi^*\right)^2\right. \\ \quad \left. + 8\psi_{ttttttt}\psi^*\right\} + 182\psi_{tt}|\psi_{tt}|^2 + 308\psi_{tt}\psi_{ttt}\psi^*_t + 252\psi_t\psi_{ttt}\psi^*_{tt} \\ \quad + 196\psi_t\psi_{tt}\psi^*_{ttt} + 168\psi_t\psi_{tttt}\psi^*_t + 42\psi_t^2\psi^*_{tttt} + 14\psi^*\left(30\psi_t^3\psi^*_t\right. \\ \quad \left. + 4\psi_{ttttt}\psi_t + 5\psi_{ttt}^2 + 8\psi_{tt}\psi_{tttt}\right) + 490\psi_t^2\psi_{tt}\left(\psi^*\right)^2 \\ \quad + 140\psi^4\psi^*\left[\left(\psi^*_t\right)^2 + \psi^*\psi^*_{tt}\right] + 70\psi|\psi|^8. \end{cases}$$

(Solution: See S7.)

3.7 A Generalized Variable Coefficient Inhomogeneous NLSE With Varying Dispersion, Nonlinearity, Gain, and External Potentials [123]

$$i\psi_t + \frac{1}{2}\beta(t)\psi_{xx} + G(t)|\psi|^2\psi - \left(2\alpha(t)x + \frac{1}{2}\Omega(t)x^2\right)\psi = i\frac{\gamma(t)}{2}\psi. \tag{12}$$

Here, $\beta(t)$ and $G(t)$ are the dispersion and nonlinearity management parameters. $\alpha(t)$, $\Omega(t)$, and $\gamma(t)$ represent linear and harmonic oscillator potential and gain ($\gamma(t) < 0$) or loss ($\gamma(t) > 0$) coefficients, respectively. (Solutions: See S8 & S9.)

3.8 A Special Case of Eq. 12: The Variable Coefficient Inhomogeneous NLSE for Optical Signals [124]

$$i\psi_x + \frac{1}{2}\beta(x)\psi_{tt} + \chi(x)|\psi|^2\psi + \alpha(x)t^2\psi = i\gamma(x)\psi. \tag{13}$$

Here, $\beta(x)$, $\chi(x)$, $\alpha(x)$, and $\gamma(x)$ denote GVD, nonlinearity, normalized loss rate, and loss/gain coefficients, respectively. (Solutions: See S10 & S11.)

3.9 An Electron-Plasma Wave Packet With a Large Wavelength and Small Amplitude Propagating Through the Plasma Described by an Inhomogeneous NLSE With a Parabolic Density and Constant Damping Interaction [125]

$$i\psi_z + \psi_{tt} + 2|\psi|^2\psi - (\alpha t - \beta^2 t^2)\psi + i\beta\psi = 0, \tag{14}$$

where α and β are linear and damping coefficient, respectively. αt and $\beta^2 t^2$ account for the profiles of linear and parabolic density. (Solution: See S12.)

3.10 The Propagation of the Femtosecond Pulse Through an Inhomogeneous Fiber With Selective Linear and Nonlinear Coefficients Described by an Inhomogeneous Hirota Equation [126]

$$\psi_z = \alpha_1(z)\left(i\psi_{tt} + \frac{1}{3\delta}\psi_{ttt}\right) + \alpha_4(z)\left(i\delta\,\psi|\psi|^2 + |\psi|^2\psi_t\right) + \alpha_6(z)\psi, \tag{15}$$

where $\alpha_6 = \frac{\alpha_{1,z}\,\alpha_4 - \alpha_1\,\alpha_{4,z}}{2\alpha_1\,\alpha_4}$. Here $\alpha_1(z)$, $\alpha_2(z)$, and α_6 represent the contribution of the dispersion, nonlinearity, and gain/loss coefficient, respectively; δ is a constant. (Solution: See S13.)

3.11 The NLSE Describing the Water Waves in the Infinite Water Depth [127]

$$i\left(\psi_t + c_g\psi_x\right) - \frac{\omega_0}{8k_0^2}\psi_{xx} - \frac{1}{2}\omega_0 k_0^2|\psi|^2\psi = 0, \tag{16}$$

where $c_g = \partial\omega/\partial k$ is the group velocity. The angular frequency $\omega_0 = \sqrt{g\,k_0}$, where k_0 and g are the wave number and the acceleration due to gravity, respectively. (Solution: See S14.)

4 PEREGRINE SOLITONS WITH EXTERNAL POTENTIALS

This section deals with reviewing the Peregrine soliton solutions reported in the NLSE with diverse external potentials. In nonlinear dynamics, a waveform which can exhibit a localized translation resulting from the counteracting dispersive and nonlinear effects is coined as "soliton". Such classical soliton is also referred to as autonomous soliton, owing to the role of time as an independent variable and its absence in the nonlinear evolution equation. Those autonomous solitons can preserve their shape and velocity before and after collisions with an introduction of a phase shift [5]. However, in real circumstances, physical systems may be subjected to external space- and time-dependent forces. In such a case, these systems are known as nonautonomous systems and their corresponding solitons are known as nonautonomous solitons [128–130]. Furthermore, it is confirmed that solitons in such systems still have the ability to preserve their profile after collisions and adapt to the external potentials as well as to dispersive and nonlinear variations, but sacrificing the stability in amplitude, speed, and spectra [116, 131, 132]. In addition, such nonautonomous NLSEs can be generalized to describe the unusual phenomenon of rogue waves in different situations [85, 105, 123, 133–137]. Those rogue waves are characterized by spatiotemporal localization and possess the amplitudes greater than twice as that of the surrounding background [11, 13, 17, 18]. Further, dynamics of such rogue waves have been demonstrated experimentally in nonlinear optics [23, 24, 27, 138], plasma physics [139], Bose-Einstein condensation (BEC) [73], and atmospheric dynamics [140]. One of the basic waveforms of the rogue wave is the Peregrine soliton [11] whose appearance in the nonautonomous NLSEs under the influence of various external potentials will be presented below.

4.1 The Gross-Pitaevskii (GP) Equation Describing Matter Rogue Wave in BEC With Time-Dependent Attractive Interatomic Interaction in Presence of an Expulsive Potential [141]

$$i\psi_t - \frac{1}{2}\psi_{xx} + a(t)|\psi|^2\psi + \frac{1}{2}\lambda^2 x^2\psi = 0, \tag{17}$$

where $a(t)$ is the nonlinear coefficient, defined by $a(t) = |a_s(t)|/a_B$ with $a_s(t)$ the s-wave scattering length and a_B the Bohr radius. The aspect ratio is given by $\lambda = |\omega_0|/\omega_\perp$, where ω_0 and $\omega_\perp$ are oscillator frequencies in the direction of cigar and transverse axes, respectively. (Solution: See S15.)

4.2 A Generic (1 + 1)-Dimensional NLSE With Variable Coefficients in Dimensionless Form [142]

$$i\psi_t + \frac{D}{2}\psi_{xx} - g|\psi|^2\psi - V\psi = 0, \tag{18}$$

where D and g represent the coefficient of dispersion and nonlinearity and V is an external potential denoting the trap confining the atoms in BECs. (Solutions: See S16 & S17.)

4.3 NLSE Describing the Nonlinear Optical Systems With the Spatially Modulated Coefficients in Presence of a Special Quadratic External Potential in the Dimensionless Form [143]

$$i\psi_z + d(x)\psi_{xx} + 2\gamma(z,x)\left|\psi\right|^2\psi + V(z,x)\psi = 0. \tag{19}$$

Here, $d(x)$ and $\gamma(z,x)$ are the diffraction and the nonlinearity coefficients, respectively. $V(z,x) = d(x)(ax^2 + b)$ denotes the external potential modulated by the diffraction coefficient, with a and b being the real constants. (Solution: See S18.)

4.4 A GNLSE With Distributed Coefficients Describing the Amplification or Absorption of Optical Pulse Propagating Through a Monomode Optical Fiber [144]

$$i\psi_z - \frac{1}{2}\beta(z)\psi_{tt} + \gamma(z)|\psi|^2\psi + id(z)\psi = 0, \tag{20}$$

where $\beta(z)$, $\gamma(z)$, and $d(z)$ are GVD, nonlinearity, and amplification/absorption coefficients, respectively. (Solution: See S19.)

4.5 NLSE Describing the Rogue Wave Dynamics under a Linear Potential [105]

$$i\psi_t + \frac{1}{2}\psi_{xx} + \gamma(t)(x - x_0(t)) + |\psi|^2\psi = 0, \tag{21}$$

where $\gamma(t)$ and $x_0(t)$ are real arbitrary functions. (Solutions: See S20 & S21.)

4.6 NLSE Describing Rogue Wave Under a Quadratic Potential [105]

$$i\psi_t + \frac{1}{2}\psi_{xx} + \frac{1}{2}\left(\dot{\gamma}^2 - \ddot{\gamma}\right)x^2\psi + e^{\gamma}|\psi|^2\psi = 0, \tag{22}$$

where $\gamma(t)$ is an integrability condition of the above equation, relating the coefficients of the quadratic potential and the nonlinearity. (Solution: See S22.)

4.7 A GP Equation With an External Potential Describing the Mean Field Dynamics of a Quasi-One-Dimensional BEC [145]

$$i\psi_t + \frac{1}{2}\psi_{xx} + \gamma(t)|\psi|^2\psi + V(x,t)\psi - \frac{i}{2}g(t)\psi = 0, \tag{23}$$

where the nonlinearity parameter is defined by $\gamma(t) = \frac{a_s(t)}{a_B}$, with $a_s(t)$ the scattering length and a_B the Bohr radius. $V(x,t) = \frac{1}{2}\Omega^2(t)x^2 + h(t)x$ denotes the external potential, $\Omega^2(t) = -\frac{\omega_0^2(t)}{\omega_\perp^2}$ with ω_0 and $\omega_\perp$ representing the trap frequency in the axial direction and the radial trap frequency, respectively. $h(t)$ and $g(t)$ denote the linear potential and gain/loss coefficients for atomic and thermal cloud. (Solution: See S23.)

4.8 A GNLSE Describing the Pulse Propagation Through Tapered Graded-Index Nonlinear Waveguide Amplifier [146]

$$i\psi_z + \frac{1}{2}\psi_{xx} + F(z)\frac{x^2}{2}\psi - \frac{i}{2}G(z)\psi + |\psi|^2\psi = 0, \tag{24}$$

where $F(z)$ and $G(z)$ are the dimensionless tapering function and gain profile, respectively. (Solutions: See S24 & S25.)

4.9 The Propagation of Rogue Waves Described by a Nonautonomous NLSE With an External Harmonic Potential [147]

$$i\psi_t + \frac{\alpha(t)}{2}\psi_{xx} + \left(-i\gamma(t) + \frac{\omega(t)r^2}{2} + \beta(t)|\psi|^2\right)\psi = 0, \tag{25}$$

where $\alpha(t)$, $\gamma(t)$, and $\beta(t)$ represent the coefficients of the dispersion, the distributed gain/loss, and the Kerr nonlinearity, respectively. $\omega(t)r^2/2$ represents the harmonic potential. (Solutions: See S26 & S27.)

4.10 An Inhomogeneous NLSE With an External Potential to Tune the Width and Shape of the Pulse [148]

$$i\psi_t + \psi_{xx} + 2\left|\psi\right|^2\psi + \alpha^2x^2\psi + i\alpha\psi = 0, \tag{26}$$

where α is a real number. (Solution: See S28.)

4.11 The (1 + 1)-Dimensional Nonautonomous NLSE With a Linear Potential [149]

$$i\psi_z + \frac{\beta(z)}{2}\psi_{tt} + \chi(z)|\psi|^2\psi - 2\alpha(z)t\psi - i\gamma(z)\psi = 0, \tag{27}$$

where $\beta(z)$ and $\chi(z)$ are the coefficients of varying dispersion and nonlinearity, respectively. The term $2\alpha(z)t\psi$ denotes an approximate form of self-induced Raman effect. $\gamma(z)$ is the gain parameter. (Solutions: See S29 & S30.)

4.12 A Nonautonomous NLSE With Variable Coefficients in Presence of Varying Linear and Harmonic Potentials Describing the Optical Pulse Propagation [150]

$$\begin{aligned} i\psi_z(z,t) + \frac{d(z)}{2}\psi_{tt}(z,t) + r(z)|\psi(z,t)|^2\psi(z,t) \\ + \nu_1(z)t\psi(z,t) + \nu_2(z)t^2\psi(z,t) = 0, \end{aligned} \tag{28}$$

where $d(z)$ describes the varying dispersion. $r(z)$ is a transformation coefficient that relates the nonlinear coefficient with the gain/loss coefficient. $\nu_1(z)$ and $\nu_2(z)$ denote the varying linear and harmonic potential, respectively. (Solution: See S31.)

4.13 A NLSE Describing Varying Dispersion With an External Harmonic Oscillator Potential [151]

$$\begin{aligned} i\psi_z + \frac{D(z)}{2}\psi_{tt} + R(z)|\psi|^2\psi + i(\alpha(z) \\ + \delta D(z)P(z)t)\psi_t - \frac{i}{2}\Gamma(z)\psi = 0. \end{aligned} \tag{29}$$

Here $D(z)$, $R(z)$, $\alpha(z)$, $P(z)$, and $\Gamma(z)$ are varying dispersion in a harmonic oscillator potential form, varying nonlinearity, velocity of propagation, nonlinear focus length, and gain/loss coefficient, respectively. (Solutions: See S32 & S33.)

4.14 NLSE With Spatially Modulated Coefficients and a Special External Potential in the Dimensionless Form [39]

$$i\psi_z + \frac{1}{2}\beta(x)\psi_{xx} + \chi(x)|\psi|^2\psi + \frac{1}{2}\beta(x)\left(-\frac{1}{4}x^2 + m + \frac{1}{2}\right)\psi = 0. \tag{30}$$

Here, $\beta(x)$ and $\chi(x)$ denote coefficients of the diffraction and the nonlinearity, respectively. The external potential is a simple quadratic potential modulated by the diffraction coefficient, where m is a nonnegative integer referred to as the quantum modal parameter. (Solution: See S34.)

4.15 A Quasi-One-Dimension Gross-Pitaevskii Equation Describing BEC With Time-Dependent Quadratic Trapping Potential [152]

$$i\psi_t + \frac{1}{2}\psi_{xx} + \sigma\gamma(t)|\psi|^2\psi + f(t)\frac{x^2}{2}\psi + h(t)x\psi - \frac{i}{2}g(t)\psi = 0. \tag{31}$$

Here $\gamma(t) = 2a_s(t)/a_B$ with a_s and a_B being the atomic scattering length and the Bohr radius. Further, $f(t) = -\omega_0^2(t)/\omega_\perp^2$, $h(t) = -\alpha(t)/\omega_\perp^2 a_\perp$, and $g(t) = \eta(t)/\hbar\omega_\perp$ are the atoms confined in a cylindrical trap, time-dependent parabolic trap, and linear time-dependent potential, respectively, with $a_\perp = (\hbar/\mathrm{m}\omega_\perp)^{1/2}$. Here, $\sigma = +1(-1)$ corresponds to $a_s(t) < 0\,(>0)$ defining attractive (repulsive) time-dependent scattering length. ω_0 and $\omega_\perp$ are the trap frequency in the axial direction and the radial trap frequency, respectively. $\alpha(t)$ and $\eta(t)$ represent the interaction of linear time-dependent potential trap and gain/loss term incorporates the interaction of condensate with normal atomic cloud through three body interactions, respectively. (Solutions: See S35 & S36.)

5 PEREGRINE SOLITONS IN COUPLED NLSES

This section presents the Peregrine soliton solutions reported in the context of coupled NLSEs (CNLSEs), starting from basic vector NLSEs or the Manakov model [153] to the CNLSEs with the effects of higher-order dispersion/diffraction, self-focusing/defocusing, and other higher-order nonlinear effects [109, 154]. Such CNLSEs play a vital role in describing the interaction of multiple components of a vector wave or multiple scalar waves in numerous physical systems. In literature, several reports have demonstrated the significance of the CNLSEs in nonlinear science, namely, birefringent optical fibers [155], BEC [156], oceanic studies [157], biophysics [158], and even finance [159]. Recently, vector rogue waves featured with more than one component have been given special attention in nonlinear science, for their striking dynamics when compared to those of the scalar systems. A plethora of studies has been reported to understand such phenomena, which demonstrate new excitation patterns manifesting the vector rogue waves compared to that of the scalar rogue waves with well-known eye-shaped patterns [16, 160, 161]. Bludov et al. originally reported the numerical existence of the rogue waves in a two-component BEC described by the coupled GP equation with variable scattering lengths [162], followed with substantial analytical studies describing the spatiotemporal distribution of dark rogue waves [163], higher-order solutions [164], and baseband modulation stability featuring bright-dark and dark-dark rogue waves [165]. Furthermore a multi-rogue wave reveals four-petaled flower in

spatiotemporal distribution [166] and resonant interactions [167] in a three-component coupled NLSEs. In addition, these rogue waves have also been found to demonstrate unusual distribution of rogue waves in spatiotemporal distribution plane when compared to the scalar ones. Moreover, integrable mixed CNLSEs (M-CNLSEs) feature-rich solutions of the multi-rogue wave structures including rogue wave doublet, bright-dark composites, bright-dark triplet, and bright-bright and bright-dark quartets are also constructed to understand the rogue wave dynamics in multicomponent physical systems [168]. This section will be confined within our aim to present the Peregrine soliton solution under the framework of CNLSEs.

5.1 A Manakov Model [169–173]

$$\begin{aligned} &i\psi_{1t} + \psi_{1xx} + 2\left(|\psi_1|^2 + |\psi_2|^2\right)\psi_1 = 0,\\ &i\psi_{2t} + \psi_{2xx} + 2\left(|\psi_1|^2 + |\psi_2|^2\right)\psi_2 = 0, \end{aligned} \tag{32}$$

(solutions: See S37, S38, S39, S40, S41, S42 & S43.)

5.2 Special Cases of the Manakov System

i. The Manakov system of the form [174]

$$\begin{aligned} &i\psi_{1t} + \psi_{1xx} + 2\mu\left(|\psi_1|^2 + |\psi_2|^2\right)\psi_1 = 0,\\ &i\psi_{2t} + \psi_{2xx} + 2\mu\left(|\psi_1|^2 + |\psi_2|^2\right)\psi_2 = 0, \end{aligned} \tag{33}$$

where μ is a real constant. (Solution: See S44.)

ii. The two-coupled NLSE describing the wave evolution dynamics through a two-mode nonlinear fiber in dimensionless form [175]

$$\begin{aligned} &i\psi_{1z} + \psi_{1tt} + 2\left(|\psi_1|^2 + |\psi_2|^2\right)\psi_1 = 0,\\ &i\psi_{2z} + \psi_{2tt} + 2\left(|\psi_1|^2 + |\psi_2|^2\right)\psi_2 = 0. \end{aligned} \tag{34}$$

(Solution: See S45.)

iii. The Manakov model in the normal dispersion regime [63]

$$\begin{aligned} &i\psi_{1z} - \psi_{1tt} + \sigma\left(|\psi_1|^2 + |\psi_2|^2\right)\psi_1 = 0,\\ &i\psi_{2z} - \psi_{2tt} + \sigma\left(|\psi_1|^2 + |\psi_2|^2\right)\psi_2 = 0, \end{aligned} \tag{35}$$

where z, t, σ are the propagation distance, retarded time, and the strength of the cubic nonlinearity, respectively. (Solution: See S46.)

iv. The focusing CNLSE of the form [38, 164]

$$\begin{aligned} &i\psi_{1t} + \frac{1}{2}\psi_{1xx} + \left(|\psi_1|^2 + |\psi_2|^2\right)\psi_1 = 0,\\ &i\psi_{2t} + \frac{1}{2}\psi_{2xx} + \left(|\psi_1|^2 + |\psi_2|^2\right)\psi_2 = 0. \end{aligned} \tag{36}$$

(Solutions: See S47 & S48.)

v. The Manakov system [165]

$$\begin{aligned} &i\psi_{1t} + \psi_{1xx} - 2s\left(|\psi_1|^2 + |\psi_2|^2\right)\psi_1 = 0,\\ &i\psi_{2t} + \psi_{2xx} - 2s\left(|\psi_1|^2 + |\psi_2|^2\right)\psi_2 = 0, \end{aligned} \tag{37}$$

where the constant s takes the value -1 or $+1$ for focusing or defocusing regime, respectively. (Solution: See S49.)

vi. The Manakov system describing the propagation of optical pulses through the birefringent optical fibers [176]

$$\begin{aligned} &i\psi_{1x} + \frac{D}{2}\psi_{1tt} + \left(|\psi_1|^2 + |\psi_2|^2\right)\psi_1 = 0,\\ &i\psi_{2x} + \frac{D}{2}\psi_{2tt} + \left(|\psi_1|^2 + |\psi_2|^2\right)\psi_2 = 0. \end{aligned} \tag{38}$$

Dispersion (D) indicates the normal dispersion for ($D = -1$) and the anomalous dispersion for ($D = 1$). (Solution: See S50.)

5.3 The Three-Component CNLSE [177]

$$\begin{aligned} &i\psi_{1t} + \psi_{1xx} + 2\left(|\psi_1|^2 + |\psi_2|^2 + |\psi_3|^2\right)\psi_1 = 0,\\ &i\psi_{2t} + \psi_{2xx} + 2\left(|\psi_1|^2 + |\psi_2|^2 + |\psi_3|^2\right)\psi_2 = 0,\\ &i\psi_{3t} + \psi_{3xx} + 2\left(|\psi_1|^2 + |\psi_2|^2 + |\psi_3|^2\right)\psi_3 = 0. \end{aligned} \tag{39}$$

5.4 A Special Case of Eq. (39): The Three-Component CNLSE [178]

$$\begin{aligned} &i\psi_{1t} + \frac{1}{2}\psi_{1xx} + \left(|\psi_1|^2 + |\psi_2|^2 + |\psi_3|^2\right)\psi_1 = 0,\\ &i\psi_{2t} + \frac{1}{2}\psi_{2xx} + \left(|\psi_1|^2 + |\psi_2|^2 + |\psi_3|^2\right)\psi_2 = 0,\\ &i\psi_{3t} + \frac{1}{2}\psi_{3xx} + \left(|\psi_1|^2 + |\psi_2|^2 + |\psi_3|^2\right)\psi_3 = 0. \end{aligned} \tag{40}$$

(Solutions: See S51 & S52.)

5.5 The Three-Component Manakov System in the Defocusing Regime [179]

$$\begin{aligned} &i\psi_{1z} + i\delta\psi_{1t} + \psi_{1tt} - \sigma\left(|\psi_1|^2 + |\psi_2|^2 + |\psi_3|^2\right)\psi_1 = 0,\\ &i\psi_{2z} - i\delta\psi_{2t} + \psi_{2tt} - \sigma\left(|\psi_1|^2 + |\psi_2|^2 + |\psi_3|^2\right)\psi_2 = 0,\\ &i\psi_{3z} + \psi_{3tt} - \sigma\left(|\psi_1|^2 + |\psi_2|^2 + |\psi_3|^2\right)\psi_3 = 0, \end{aligned} \tag{41}$$

where δ denotes the group velocity mismatch and σ describes the coefficient of cubic nonlinearity. (Solution: See S53.)

5.6 The CNLSE Describing the Nonlinear Interaction of the Short Wave (A) and the Long Wave (U) [180]

$$\begin{aligned} &i\frac{\partial A}{\partial \xi} + \frac{1}{2}\frac{\partial^2 A}{\partial \tau^2} + UA = 0,\\ &\frac{\partial U}{\partial \xi} - \frac{\partial |A|^2}{\partial \tau} = 0. \end{aligned} \tag{42}$$

(Solution: See S54.)

5.7 The Integrable M-CNLSE [168]

$$i\psi_t^{(l)} + \psi_{xx}^{(l)} + \psi^{(l)} \sum_{j=1}^{M} \delta_j |\psi^{(j)}|^2 = 0,\ l = 1, 2, \ldots M. \tag{43}$$

Here δ_j s can be positive (negative) value defining focusing (defocusing) nonlinearity. (Solution: See S55.)

5.8 A Two-Coupled NLSE in Dimensionless Form [163]

$$\begin{aligned} i\psi_{1z} + \sigma_1\psi_{1tt} + \left[2g_1|\psi_1|^2 + 2g_2|\psi_2|^2\right]\psi_1 = 0, \\ i\psi_{2z} + \sigma_2\psi_{2tt} + \left[2g_1|\psi_1|^2 + 2g_2|\psi_2|^2\right]\psi_2 = 0, \end{aligned} \tag{44}$$

where σ_1 and σ_2 define the sign of GVD, taking the value +1 or −1 for anomalous or normal GVD, respectively. g_1 and g_2 are nonlinearity parameters determining the properties of Kerr medium with electrostriction mechanism. (Solution: See S56.)

5.9 The Coupled Derivative NLSE [181]

$$\begin{aligned} i\psi_{1t} + \psi_{1xx} - \frac{2}{3}i\epsilon\left[\left(|\psi_1|^2 + |\psi_2|^2\right)\psi_1\right]_x = 0, \\ i\psi_{2t} + \psi_{2xx} - \frac{2}{3}i\epsilon\left[\left(|\psi_1|^2 + |\psi_2|^2\right)\psi_2\right]_x = 0, \end{aligned} \tag{45}$$

where ϵ takes the value ± 1. (Solution: See S57.)

5.10 A CNLSE With Negative Coherent Coupling Describing the Propagation of Orthogonally Polarized Optical Waves in an Isotropic Medium [182]

$$\begin{aligned} i\psi_{1z} + \psi_{1tt} + 2\left(|\psi_1|^2 + 2|\psi_2|^2\right)\psi_1 - 2\psi_1^*\psi_2^2 = 0, \\ i\psi_{2z} + \psi_{2tt} + 2\left(2|\psi_1|^2 + |\psi_2|^2\right)\psi_2 - 2\psi_1^2\psi_2^* = 0. \end{aligned} \tag{46}$$

(Solutions: See S58 & S59.)

5.11 An Integrable Generalization of the CNLSE [183]

$$\begin{aligned} \psi_{1xt} + \alpha\beta^2\psi_1 - 2i\alpha\beta\psi_{1x} - \alpha\psi_{1xx} + i\alpha\beta^2\psi_1\psi_2\psi_{1x} = 0, \\ \psi_{2xt} + \alpha\beta^2\psi_2 - 2i\alpha\beta\psi_{2x} - \alpha\psi_{2xx} - i\alpha\beta^2\psi_1\psi_2\psi_{2x} = 0, \end{aligned} \tag{47}$$

where α and β are constants. (Solution: See S60.)

5.12 A Coupled NLSE With Special External Potential in a Parabolic Form [184]

$$\begin{aligned} i\psi_{1z} + \beta(x)\psi_{1xx} + 2\chi(x)\left(|\psi_1|^2 + |\psi_2|^2\right)\psi_1 + U(x)\psi_1 = 0, \\ i\psi_{2z} + \beta(x)\psi_{2xx} + 2\chi(x)\left(|\psi_1|^2 + |\psi_2|^2\right)\psi_2 + U(x)\psi_2 = 0, \end{aligned} \tag{48}$$

where $U(x) = \beta(x)(ax^2 + b)$ is a parabolic external potential modulated by the diffraction coefficient, with real constants a and b. $\beta(x)$ and $\chi(x)$ denote the effective diffraction coefficient and the nonlinearity coefficient, respectively. (Solution: See S61.)

5.13 The Gross-Pitaevskii Equations [185]

$$\begin{aligned} i\psi_{1t} = -\psi_{1xx} + \left(g_1|\psi_1|^2 + g|\psi_2|^2\right)\psi_1 + \beta(t)\psi_2, \\ i\psi_{2t} = -\psi_{2xx} + \left(g|\psi_1|^2 + g_2|\psi_2|^2\right)\psi_2 + \beta(t)\psi_1, \end{aligned} \tag{49}$$

where g_1 and g_2 are the dimensionless nonlinear coefficients for the quasi-one-dimensional condensate. The factor g can take two values $g = \pm 1$. The $\beta(t)$ in the last term can be used to switch between the two hyperfine states, originated from the external magnetic field. (Solution: See S62.)

5.14 A Coupled GNLSE [186]

$$\begin{aligned} i\psi_{1t} + \psi_{1xx} - 2\psi_1^2\psi_2 + 4\beta^2\psi_1^3\psi_2^2 + 4i\beta\left(\psi_1\psi_2\right)_x\psi_1 = 0, \\ i\psi_{2t} - \psi_{2xx} + 2\psi_1\psi_2^2 - 4\beta^2\psi_1^2\psi_2^3 + 4i\beta\left(\psi_1\psi_2\right)_x\psi_2 = 0, \end{aligned} \tag{50}$$

where β is a constant, describing the strength of higher-order terms. (Solution: See S63.)

5.15 A CNLSE [187]

$$\begin{aligned} i\psi_{1t} + \psi_{1xx} + 2\left(|\psi_1|^2 + 2|\psi_2|^2\right)\psi_1 - 2\psi_1^*\psi_2^2 = 0, \\ i\psi_{2t} + \psi_{2xx} + 2\left(|\psi_2|^2 + 2|\psi_1|^2\right)\psi_2 - 2\psi_2^*\psi_1^2 = 0. \end{aligned} \tag{51}$$

(Solution: See S64.)

5.16 The Two-Component CNLSE With Four-Wave Mixing Term [188]

$$\begin{aligned} i\psi_{1t} + \frac{1}{2}\psi_{1xx} + \sigma\left(|\psi_1|^2 + 2|\psi_2|^2\right)\psi_1 + \sigma\psi_2^2\psi_1^* = 0, \\ i\psi_{2t} + \frac{1}{2}\psi_{2xx} + \sigma\left(2|\psi_1|^2 + |\psi_2|^2\right)\psi_2 + \sigma\psi_1^2\psi_2^* = 0, \end{aligned} \tag{52}$$

where $\sigma = \pm 1$ accounts for attractive (+) or repulsive (−) interactions.

5.17 A Special Case of Eq. 52: An Integrable CNLSE [189]

$$\begin{aligned} i\psi_{1t} + \psi_{1xx} + 2|\psi_1|^2\psi_1 + 4|\psi_2|^2\psi_1 + 2\psi_2^2\psi_1^* = 0, \\ i\psi_{2t} + \psi_{2xx} + 2|\psi_2|^2\psi_2 + 4|\psi_1|^2\psi_2 + 2\psi_1^2\psi_2^* = 0. \end{aligned} \tag{53}$$

(Solutions: See S65 & S66.)

5.18 The Evolution of Two Orthogonally Polarized Components in an Isotropic Medium Described by the Normalized CNLSE [190, 191]

$$\begin{aligned} i\psi_{1z} + \psi_{1tt} + 2\left(|\psi_1|^2 - 2|\psi_2|^2\right)\psi_1 - 2\psi_1^*\psi_2^2 = 0, \\ i\psi_{2z} + \psi_{2tt} + 2\left(2|\psi_1|^2 - |\psi_2|^2\right)\psi_2 + 2\psi_2^*\psi_1^2 = 0. \end{aligned} \tag{54}$$

(Solutions: See S67 & S68.)

5.19 A System of Linearly Coupled NLSEs for Field Variables [60]

$$\begin{aligned} i\psi_{1z} &= -\psi_{1xx} + \left(\chi_1|\psi_1|^2 + \chi|\psi_2|^2\right)\psi_1 + i\gamma\psi_1 - \psi_2, \\ i\psi_{2z} &= -\psi_{2xx} + \left(\chi|\psi_1|^2 + \chi_1|\psi_2|^2\right)\psi_2 - i\gamma\psi_2 - \psi_1, \end{aligned} \tag{55}$$

where χ_1 and χ denote the SPM and XPM coefficients, respectively. γ represents the PT-balanced gain. (Solution: See S69.)

5.20 A CNLSE Describing the Dynamics of Light Propagation Through PT-Symmetric Coupled Waveguides [192]

$$\begin{aligned} i\psi_{1z} + \frac{1}{2}\psi_{1xx} + \left(\chi_1|\psi_1|^2 + \chi|\psi_2|^2\right)\psi_1 &= -\psi_2 + i\gamma\psi_1, \\ i\psi_{2z} + \frac{1}{2}\psi_{2xx} + \left(\chi|\psi_1|^2 + \chi_1|\psi_2|^2\right)\psi_2 &= -\psi_1 - i\gamma\psi_2, \end{aligned}$$

where the parameters χ (or $\chi_1 > 0$) and χ (or $\chi_1 < 0$) correspond to the focusing and defocusing case, respectively. The γ in the last term describes PT-balanced gain in the first and loss in the second waveguide. The relation $\psi_2(x,z) = \pm\,\psi_1(x,z)\exp(\pm i\theta)$ is used which casts above equations into the single equation of the form

$$i\psi_z + \frac{1}{2}\psi_{xx} + \left(\chi_1 + \chi|\right)\psi|^2\psi \pm \cos(\theta)\psi = 0. \tag{56}$$

(Solutions: See S70 & S71.)

5.21 A CNLSE With the Four-Wave Mixing Term Which Describes the Pulse Propagation in a Birefringent Fiber [193–196]

$$\begin{aligned} i\psi_{1t} + \psi_{1xx} + 2\left(a|\psi_1|^2 + c|\psi_2|^2 + b\psi_1\psi_2^* + b^*\psi_1^*\psi_2\right)\psi_1 = 0, \\ i\psi_{2t} + \psi_{2xx} + 2\left(a|\psi_1|^2 + c|\psi_2|^2 + b\psi_1\psi_2^* + b^*\psi_1^*\psi_2\right)\psi_2 = 0. \end{aligned} \tag{57}$$

Here a and c are real constants, describing the self-phase modulation and cross-phase modulation effects, respectively. b is a complex constant, describing the four-wave mixing effects. (Solutions: See S72, S73, S74 & S75.)

5.22 A Focusing-Defocusing Type CNLSE [197]

$$\begin{aligned} i\psi_{1t} + \psi_{1xx} + 2\gamma\left(|\psi_1|^2 - |\psi_2|^2\right)\psi_1 - \gamma\left(\psi_1^2 + \psi_2^2\right)\psi_1^* = 0, \\ i\psi_{2t} + \psi_{2xx} + 2\gamma\left(|\psi_1|^2 - |\psi_2|^2\right)\psi_2 + \gamma\left(\psi_1^2 + \psi_2^2\right)\psi_2^* = 0, \end{aligned} \tag{58}$$

where γ denotes the strength of nonlinearity. (Solution: See S76.)

5.23 A CNLSE With Variable Coefficients [198]

$$\begin{aligned} i\psi_{1t} + \psi_{1xx} + v(x,t)\psi_1 + g(t)\left(|\psi_1|^2 + |\psi_2|^2\right)\psi_1 + i\gamma(t)\psi_1 = 0, \\ i\psi_{2t} + \psi_{2xx} + v(x,t)\psi_2 + g(t)\left(|\psi_1|^2 + |\psi_2|^2\right)\psi_2 + i\gamma(t)\psi_2 = 0, \end{aligned} \tag{59}$$

where $v(x,t)$, $g(t)$, and $\gamma(t)$ are the coefficients of the external potential, nonlinearity, and gain, respectively. (Solutions: See S77 & S78.)

5.24 The Generalized CNLSE for Two Components [199]

$$\begin{aligned} &i\psi_{1z} + \alpha_1(z)\psi_{1xx} + \beta_1(z)|\psi_1|^2\psi_1 + \delta_1(z)|\psi_2|^2\psi_1 + \nu_1(x,z)\psi_1 \\ &\quad + i\gamma_1(z)\psi_1 = 0, i\psi_{2z} + \alpha_2(z)\psi_{2xx} + \beta_2(z)|\psi_1|^2\psi_2 \\ &\quad + \delta_2(z)|\psi_2|^2\psi_2 + \nu_2(x,z)\psi_2 + i\gamma_2(z)\psi_2 = 0, \end{aligned} \tag{60}$$

where $\alpha_1(z)$ and $\alpha_2(z)$ are diffraction (dispersion) coefficients. $\beta_1(z)$ and $\beta_2(z)$ are nonlinear coefficients. $\delta_1(z)$ and $\delta_2(z)$ are the coefficient of gain/loss. ν_1 and ν_2 are the two real valued functions of spatial coordinates x and z, describing the external potentials. γ_1 and γ_2 are real valued functions of the propagation distance z. (Solutions: See S79 & S80.)

5.25 The Coupled Inhomogeneous NLSE [200]

$$\begin{aligned} i\psi_{1t} + \psi_{1xx} + 2\left(|\psi_1|^2 + |\psi_2|^2\right)\psi_1 - \left(\alpha x - \beta^2 x^2\right)\psi_1 + i\beta\psi_1 = 0, \\ i\psi_{2t} + \psi_{2xx} + 2\left(|\psi_1|^2 + |\psi_2|^2\right)\psi_2 - \left(\alpha x - \beta^2 x^2\right)\psi_2 + i\beta\psi_2 = 0, \end{aligned} \tag{61}$$

where α denotes the coefficient of the linear density profile and β is the coefficient of damping. αx and $\beta^2 x^2$ correspond to the linear and parabolic density profiles. (Solution: See S81.)

5.26 The Higher-Order CNLSE With Variable Coefficients [201]

$$\begin{aligned} &i\psi_{jz} - \frac{1}{2}\beta_2(z)\psi_{jtt} - \gamma(z)\left(\sum_{n=1}^{2} a_{nj}|\psi_n|^2\right)\psi_j + i\beta_3(z)\psi_{jttt} \\ &\quad + i\chi(z)\left(\sum_{n=1}^{2} a_{nj}|\psi_n|^2\right)\psi_{jt} + i\delta(z)\left(\sum_{n=1}^{2} a_{nj}\psi_{nt}\psi_j^*\right)\psi_j \\ &\quad + i\Gamma(z)\psi_j = 0,\ j = 1,2. \end{aligned} \tag{62}$$

Here $\beta_2(z)$, $\gamma(z)$, $\beta_3(z)$, $\chi(z)$, $\delta(z)$, and $\Gamma(z)$ are coefficients of group velocity dispersion, nonlinearity (SPM and XPM), TOD, SS, SFS, and loss/gain, respectively. (Solution: See S82.)

5.27 The Coupled Hirota Equations [202]

$$\begin{aligned} &i\psi_{1t} + \frac{1}{2}\psi_{1xx} + \left(|\psi_1|^2 + |\psi_2|^2\right)\psi_1 + i\epsilon\left[\psi_{1xxx} + \left(6|\psi_1|^2 + 3|\psi_2|^2\right)\psi_{1x}\right. \\ &\left. + 3\psi_1\psi_2^*\psi_{2x}\right] = 0, i\psi_{2t} + \frac{1}{2}\psi_{2xx} + \left(|\psi_1|^2 + |\psi_2|^2\right)\psi_2 \\ &+i\epsilon\left[\psi_{2xxx} + \left(6|\psi_2|^2 + 3|\psi_1|^2\right)\psi_{2x} + 3\psi_2\psi_1^*\psi_{1x}\right] = 0, \end{aligned} \tag{63}$$

where ϵ is a constant that provides the strength of higher-order effects and scales the integrable perturbations of the simple Manakov system. (Solutions: See S83 & S84.)

5.28 A Coupled Cubic-Quintic NLSE Describing the Pulse Propagation in Non-Kerr Media [203]

$$\begin{aligned} &i\psi_{1z} + \psi_{1tt} + 2\left(|\psi_1|^2 + |\psi_2|^2\right)\psi_1 + \left(\rho_1|\psi_1|^2 + \rho_2|\psi_2|^2\right)^2\psi_1 \\ &- 2i\left[\left(\rho_1|\psi_1|^2 + \rho_2|\psi_2|^2\right)\psi_1\right]_t + 2i\left(\rho_1\psi_1^*\psi_{1t} + \rho_2\psi_2^*\psi_{2t}\right)\psi_1 \\ &= 0, i\psi_{2z} + \psi_{2tt} + 2\left(|\psi_1|^2 + |\psi_2|^2\right)\psi_2 + \left(\rho_1|\psi_1|^2 + \rho_2|\psi_2|^2\right)^2\psi_2 \\ &- 2i\left[\left(\rho_1|\psi_1|^2 + \rho_2|\psi_2|^2\right)\psi_2\right]_t + 2i\left(\rho_1\psi_1^*\psi_{1t} + \rho_2\psi_2^*\psi_{2t}\right)\psi_2 = 0, \end{aligned} \tag{64}$$

where ρ_1 and ρ_2 are the real parameters. (Solution: See S85.)

5.29 A Coupled Cubic-Quintic NLSE Describing the Effects of Quintic Nonlinearity on the Propagation of Ultrashort Pulse in a Non-Kerr Media [204]

$$\begin{aligned} &i\psi_{1t} + \psi_{1xx} + 2\left(|\psi_1|^2 + |\psi_2|^2\right)\psi_1 + \left(\rho_1|\psi_1|^2 + \rho_2|\psi_2|^2\right)^2\psi_1 \\ &- 2i\left[\left(\rho_1|\psi_1|^2 + \rho_2|\psi_2|^2\right)\psi_1\right]_x + 2i\left(\rho_1\psi_1^*\psi_{1x} + \rho_2\psi_2^*\psi_{2x}\right)\psi_1 \\ &= 0, i\psi_{2t} + \psi_{2xx} + 2\left(|\psi_1|^2 + |\psi_2|^2\right)\psi_2 + \left(\rho_1|\psi_1|^2 + \rho_2|\psi_2|^2\right)^2\psi_2 \\ &- 2i\left[\left(\rho_1|\psi_1|^2 + \rho_2|\psi_2|^2\right)\psi_2\right]_x + 2i\left(\rho_1\psi_1^*\psi_{1x} + \rho_2\psi_2^*\psi_{2x}\right)\psi_2 = 0, \end{aligned} \tag{65}$$

where ρ_1 and ρ_2 are real constants. (Solution: See S86.)

5.30 A Fourth-Order CNLSE Describing the Ultrashort Pulse Propagation in a Birefringent Optical Fiber [205]

$$\begin{aligned} &i\psi_{\alpha t} + \psi_{\alpha xx} + 2\psi_\alpha\sum_{\rho=1}^{2}|\psi_\rho|^2 + \gamma\left[\psi_{\alpha xxxx} + 2\psi_\alpha\sum_{\rho=1}^{2}|\psi_{\rho x}|^2\right. \\ &+ 2\psi_{\alpha x}\sum_{\rho=1}^{2}\psi_\rho\psi_{\rho x}^* + 6\psi_{\alpha x}\sum_{\rho=1}^{2}\psi_\rho^*\psi_{\rho x} + 4\psi_{\alpha xx}\sum_{\rho=1}^{2}|\psi_\rho|^2 \\ &+ 4\psi_\alpha\sum_{\rho=1}^{2}\psi_\rho^*\psi_{\rho xx} + 2\psi_\alpha\sum_{\rho=1}^{2}\psi_\rho\psi_{\rho xx}^* + 6\psi_\alpha\left(\sum_{\rho=1}^{2}|\psi_\rho|^2\right)^2\Bigg] \\ &= 0, \end{aligned} \tag{66}$$

where $\alpha = 1, 2$. γ is a real parameter that denotes the strength of higher-order linear and nonlinear effects. (Solution: See S87.)

5.31 A NLS-Type System With Self-Consistent Sources Associated With the Two-Component Homogeneous Plasma [206]

$$\begin{aligned} &\psi_{1t} - \frac{i\alpha}{2}\psi_{1xx} + i\alpha\,\sigma|\psi_1|^2\psi_1 - k_0\psi_2\psi_3^* = 0, \\ &\psi_{2x} - \psi_1\psi_3 = 0,\ \ \psi_{3x} - 2ik_0\psi_3 - \sigma\psi_1^*\psi_2 = 0, \end{aligned} \tag{67}$$

where α, σ, and k_0 denote the coefficients of dispersion, nonlinearity, and coupling, respectively. (Solution: See S88.)

6 PEREGRINE SOLITONS IN DISCRETE NLSE

This section delivers the Peregrine soliton solutions presented in the literature in the framework of discrete NLSEs. Since its origin from the mid-1960s, the general NLSE of continuous form plays a significant role in unraveling the physical phenomena and insights which lead to numerous scientific and technological applications in various nonlinear systems. Further, owing to its outstanding versatility, different forms of continuous NLSEs, namely, scalar and vector NLSEs, have been proposed with suitable additional terms to predict various dynamical situations in numerous nonlinear systems [90, 109, 207]. From the past three decades, apart from continuous nonlinear systems, considerable efforts have also been made to investigate the nonlinear discrete systems characterized by structural discontinuities and lattices. These systems find potential applications in electronic circuits [208, 209], optical waveguides

[210], nonlinear lattices [211], spatial energy concentrators [212], coupled nonlinear waveguide arrays [213], BEC trapped in periodic optical lattices [214], photorefractive crystals [215], and so forth. Those nonlinear discrete systems, discrete NLSEs, can be modeled through discretizing the continuous NLSE via appropriate transformations. In such discrete NLSEs, the energy evolution is in a semidiscrete form characterized by the spatial discretization and temporal continuity [90].

Additionally, the pioneering work by Ablowitz and Ladik led to a cutting-edge method for constructing a family of semidiscrete and doubly discrete nonlinear systems associated with their linear operator pairs, necessary for obtaining the solutions of the nonlinear systems via the inverse scattering transform (IST) [216]. Further, those formulations include an integrable semidiscretization of NLSE as well as doubly discrete integrable NLSE referred to as integrable discrete NLSE (IDNLSE) [217]. These equations form basic discrete equations which serve as a model for the plethora of applications where exact solutions can be realized through diverse methods such as Darboux and Bäcklund transformations in addition to the IST [86, 87, 89, 90, 93, 218]. Firstly, the DNLSE was reported by Christodoulides et al., in a nonlinear array of coupled waveguides displaying discrete self-focusing [219], followed by the experimental realization of discrete spatial solitons in AlGaAs nonlinear waveguide arrays [213]. Solitons resulting in these systems are due to the interplay between discreteness and self-trapping nonlinearity and coined as spatial discrete solitons or lattice solitons [220]. On the other hand, Peregrine solitons of DNLSEs display different dynamical behavior compared to that of the continuous counterpart and find interesting applications in spatial energy concentrators [212], photonic lattices [221], anharmonic lattices [222], Heisenberg spin chains [223], self-trapping on a dimer [224], and so forth. These Peregrine solitons that arise in discrete systems are studied in a broad category under the context of i) the DNLSEs [90, 219], ii) the Ablowitz-Ladik equations [90, 225], iii) the discrete Hirota equations (a combination of DNLSE and discrete complex modified KdV equations) [90, 226], and iv) the Salerno equation (an interpolation of the cubic DNLSE and the integrable Ablowitz-Ladik equation) [227]. Here, we present the class of DNLSEs where the Peregrine solitons were reported.

6.1 The Focusing and Defocusing Ablowitz-Ladik (AL) Equation [228]

$$i\frac{d\psi_n}{dt} = \left(1 \pm |\psi_n|^2\right)\left(\psi_{n+1} + \psi_{n-1}\right). \tag{68}$$

In the above AL equation, the term $|\psi_n|^2$ with + and − sign represents focusing and defocusing regimes, respectively. (Solution: See S89.)

6.2 The DNLSE Describing an Array of Coupled Nonlinear Waveguides [229]

$$i\frac{d\psi_n}{dt} + \psi_{n+1} + \psi_{n-1} - 2\psi_n + \sigma|\psi_n|^2\psi_n = 0. \tag{69}$$

Here, the constant σ takes the value " + 1" denoting the focusing nonlinearity and " − 1" denoting the defocusing nonlinearity. (Solution: See S90.)

6.3 An Optical Field Propagating Through a Tight Binding Waveguide Array Described by the DNLSE [230]

$$i\frac{d\psi_j}{dz} = -J_j\left(\psi_{j+1} + \psi_{j-1}\right) + V_j\psi_j + g|\psi_j|^2\psi_j, \tag{70}$$

where J_j is the coupling coefficient between j-th waveguide and adjacent waveguides. V_j is the propagation constant of the j-th waveguide. g is the constant describing nonlinear interaction. (Solution: See S91.)

6.4 The Discrete NLSE [231]

$$i\frac{d\psi_n}{dt} = \psi_{n+1} - 2\psi_n + \psi_{n-1} + \psi_n\psi_n^*\left(\psi_{n+1} + \psi_{n-1}\right). \tag{71}$$

(Solution: See S92.)

6.5 The Integrable AL Equation [232, 233]

$$i\frac{d\psi_n}{dt} + \left(\psi_{n-1} + \psi_{n+1}\right)\left(1 + |\psi_n|^2\right) - 2\psi_n = 0. \tag{72}$$

(Solutions: See S93 & S94.)

6.6 The Modified AL Equation [234]

$$i\frac{d\psi_n}{dt} + \left(\psi_{n-1} + \psi_{n+1}\right)\left(1 + |\psi_n|^2\right) - 2\left(q^2 + 1\right)\psi_n = 0. \tag{73}$$

(Solution: See S95.)

6.7 The Generalized Ablowitz-Ladik-Hirota Lattice Equation With Variable Coefficients [235]

$$i\psi_{n,t} + \left[\Lambda(t)\psi_{n+1} + \Lambda^*(t)\psi_{n-1}\right]\left(1 + g(t)|\psi_n|^2\right) - 2\nu_n(t)\psi_n + i\gamma(t)\psi_n = 0. \tag{74}$$

Here, the tunnel coupling constant between the sites is given by $\Lambda(t) = \alpha(t) + i\beta(t)$, with $\alpha(t)$ and $\beta(t)$ the differentiable real valued functions. $g(t)$, $\nu_n(t)$, and $\gamma(t)$ represent time-modulated interstice nonlinearity, space-time-modulated inhomogeneous frequency shift, and time-modulated effective gain/loss constants, respectively. (Solution: See S96.)

6.8 The Generalized Salerno Equation [64]

$$i\frac{d\psi_n}{dt} = -\frac{1}{2}\left(\psi_{n+1} - 2\psi_n + \psi_{n-1}\right) - \mu|\psi_n|^2\psi_n - \frac{1}{2}(1-\mu)|\psi_n|^2\left(\psi_{n+1} + \psi_{n-1}\right). \tag{75}$$

Above equation corresponds to the DNLSE, when $\mu = 1$, and reduces to the AL system, when $\mu = 0$, respectively. (Solution: See S97.)

6.9 The Discrete Hirota Equation [233]

$$i\frac{d\psi_n}{dt} + \left[(a-ib)\psi_{n-1} + (a+ib)\psi_{n+1}\right]\left(1+|\psi_n|^2\right) - 2\psi_n = 0. \tag{76}$$

(Solution: See S98.)

6.10 A Spatially Discrete Hirota Equation [236]

$$\frac{d\psi_n}{dt} = \alpha\left(1+|\psi_n|^2\right)\left[\psi_{n+2} - 2\psi_{n+1} + 2\psi_{n-1} - \psi_{n-2} + \psi_n^*\left(\psi_{n+1}^2 - \psi_{n-1}^2\right) - |\psi_{n-1}|^2\psi_{n-2} + |\psi_{n+1}|^2\psi_{n+2} + \psi_n\left(\psi_{n-1}^*\psi_{n+1} - \psi_{n+1}^*\psi_{n-1}\right)\right] - i\beta\left(1+|\psi_n|^2\right)\left(\psi_{n+1} + \psi_{n-1}\right) + 2i\beta\psi_n, \tag{77}$$

where α and β are real constants. (Solution: See S99.)

6.11 A Single Ablowitz-Ladik Equation With Only One Component [237]

$$i\frac{d\psi_n^{(1)}}{dt} + \frac{1}{2h^2}\left(\psi_{n-1}^{(1)} + \psi_{n+1}^{(1)} - 2\psi_n^{(1)}\right) + \frac{1}{2}\left(\psi_{n-1}^{(1)} + \psi_{n+1}^{(1)}\right)\left|\psi_n^{(1)}\right|^2 = 0, \tag{78}$$

where $1/h^2$ is a real coefficient. (Solution: See S100.)

6.12 The Discrete AL Equation [238]

$$i\frac{d\psi_n}{dt} = \frac{\psi_{n+1} + \psi_{n-1} - 2\psi_n}{h^2} + \sigma|\psi_n|^2\left(\psi_{n+1} + \psi_{n-1}\right). \tag{79}$$

Here $\sigma = +1$ and -1 for focusing and defocusing nonlinearity, respectively. h is a real parameter. (Solution: See S101.)

6.13 The Coupled AL Equations Describing the Coupled Discrete Nonlinear Wave Systems [51]

$$\begin{aligned}\psi_{n,t}^{(1)} &= -i\left(\sigma + |\psi_n^{(1)}|^2\right)\left(\psi_n^{(2)^*} + \psi_{n-1}^{(2)^*}\right),\\ \psi_{n,t}^{(2)} &= i\left(\sigma + |\psi_n^{(2)}|^2\right)\left(\psi_{n+1}^{(1)^*} + \psi_n^{(1)^*}\right).\end{aligned} \tag{80}$$

Here $\sigma = +1$ and -1 denote the focusing and defocusing nonlinearity, respectively. (Solution: See S102.)

6.14 The System of Differential-Difference Equations on the Doubly Infinite Lattice [239, 240]

$$\begin{aligned} i\frac{d\psi_n^{(1)}}{dt} &= \psi_{n+1}^{(1)} - 2\psi_n^{(1)} + \psi_{n-1}^{(1)} - \psi_n^{(1)}\psi_n^{(2)}\left(\psi_{n+1}^{(1)} + \psi_{n-1}^{(1)}\right),\\ -i\frac{d\psi_n^{(2)}}{dt} &= \psi_{n+1}^{(2)} - 2\psi_n^{(2)} + \psi_{n-1}^{(2)} - \psi_n^{(1)}\psi_n^{(2)}\left(\psi_{n+1}^{(2)} + \psi_{n-1}^{(2)}\right)\end{aligned} \tag{81}$$

with $\psi_n^{(2)} = \sigma\psi_n^{(1)^*}$. (Solutions: See S103 & S104.)

6.15 The Coupled AL Equation With Variable Coefficients Describing the Optical Field Through the Tight Binding Waveguide Array [241]

$$\begin{aligned} &i\frac{d\psi_n^{(1)}}{dt} + \left[1 + g_1(t)|\psi_n^{(1)}|^2 + g_2(t)|\psi_n^{(2)}|^2\right]\left[\Lambda_1(t)\psi_{n+1}^{(1)} + \Lambda_1^*(t)\psi_{n-1}^{(1)}\right]\\ &- 2\nu_1(n,t)\psi_n^{(1)} + i\gamma_1(t)\psi_n^{(1)}\\ &= 0, i\frac{d\psi_n^{(2)}}{dt} + \left[1 + g_1(t)|\psi_n^{(2)}|^2 + g_2(t)|\psi_n^{(1)}|^2\right]\left[\Lambda_2(t)\psi_{n+1}^{(2)}\right.\\ &\left. + \Lambda_2^*(t)\psi_{n-1}^{(2)}\right] - 2\nu_2(n,t)\psi_n^{(2)} + i\gamma_1(t)\psi_n^{(2)} = 0.\end{aligned} \tag{82}$$

Here the tunnel coupling coefficients between sites are given by $\Lambda_1(t) = a(t) + ib(t)$, $\Lambda_2(t) = c(t) + id(t)$ with $a(t)$, $b(t)$, $c(t)$, and $d(t)$ being differentiable functions. $g_1(t)$ and $g_2(t)$ denote the time-modulated interstice nonlinearity. The space-time-modulated inhomogeneous frequency shifts are denoted by $\nu_1(t)$ and $\nu_2(t)$. $\gamma_1(t)$ and $\gamma_2(t)$ represent the time-modulated effective gain and loss term. (Solution: See S105.)

7 PEREGRINE SOLITONS IN NONLOCAL NLSES

The objective of this section is to present the existing Peregrine soliton solutions reported in the literature under the context of nonlocal NLSEs. In nonlinear systems, NLSEs play a ubiquitous role in understanding the diverse nonlinear phenomena, finding potential applications from fundamental to advanced technologies [109]. Out of such diverse manifestations of NLSEs, the NLSE with parity-time symmetry has shown an extensive recent research interest. This equation displays invariance under the joint transformations of time $t \to -t$, space $x \to -x$ (both time and space reversal symmetry), and complex conjugation. Its original prediction was by Bender et al. in a class of non-Hermitian PT invariant Hamiltonians in quantum mechanics [242]. PT-symmetric systems have gained great attention in diverse fields

of research. Apart from the quantum mechanics, PT-symmetric systems have been investigated in many other physical systems, namely, nonlinear optics [243], plasmonics [244], BEC [245], electronics [246], and acoustics [247]. Such PT-symmetric systems allow the realization of a new class of gain/loss balanced dissipative as well as conservative systems which features unusual dynamics and control which cannot be realized in the conventional systems [248]. In the background of NLSEs, PT-symmetric systems involve two different models, namely, i) the nonlinear optical system where the optical potential is fixed PT-symmetric [243, 249–251] and ii) the coupled and multicomponent NLSE with a balance gain/loss [60, 252, 253].

Recently, Ablowitz et al. introduced an exactly integrable nonlocal PT-symmetric NLSE where the nonlinearity is nonlocal as well as PT-symmetric [254]. Furthermore, they constructed a discrete one-soliton solution via a left-right Riemann-Hilbert formulation in an exactly solvable PT-symmetric DNLSE which then discretized the above reported NLSE [255]. Since then, a numerous nonlocal integrable NLSEs have been reported such as the reverse time NLSE [93], the reverse space-time NLSE [93, 256], the nonlocal derivate NLSE [93, 257], PT-symmetric Davey-Stewartson equation [93, 258], and the reverse space-time complex modified KdV equation [93, 259, 260], to explore the exciting behaviors of nonlocal solutions in such systems. Recently, intense research investigations have been made in rogue waves to understand and control their appearance in nonlinear optics [155], BEC [156], hydrodynamics [157], biophysics [158], and so forth. In general, these rogue waves are mathematically expressed in a rational form which exhibits both spatial and temporal localization. Moreover, they possess interesting dynamical patterns and are found to be observed in a large number of local nonlinear integrable systems [17, 21, 173, 261, 262]. In the following, we list out the Peregrine soliton solution under the context of different nonlocal PT-symmetric NLSEs with space reversal, time reversal, and space-time reversal.

7.1 The Nonlocal NLSE With Parity-Time Symmetric Self-Induced Potential [263]

$$i\,\psi_z + \frac{1}{2}\psi_{xx} + \psi(x,z)\,\psi^*(-x,z)\,\psi(x,z) = 0. \tag{83}$$

(Solutions: See S106 & S107.)

7.2 The Reverse Time Nonlocal NLSE [256]

$$i\psi_t(x,t) = \psi_{xx}(x,t) + 2\psi^2(x,t)\psi(x,-t). \tag{84}$$

(Solution: See S108.)

7.3 A Nonlocal NLSE With the PT-Symmetric Potential [264]

$$i\psi_t(x,t) = \psi_{xx}(x,t) + 2\psi^2(x,t)\psi^*(-x,t). \tag{85}$$

(Solution: See S109.)

7.4 A Nonlocal NLSE [265]

$$i\psi_t(x,t) = \psi_{xx}(x,t) - 2\psi^2(x,t)\psi^*(-x,t). \tag{86}$$

(Solution: See S110.)

7.5 A Nonlocal NLSE With the Self-Induced PT-Symmetric Potential [266]

$$i\psi_t(x,t) + \psi_{xx}(x,t) + \frac{1}{2}\psi^2(x,t)\psi^*(-x,t) = 0. \tag{87}$$

(Solution: See S111.)

7.6 A Reverse Time Nonlocal NLSE [267]

$$i\psi_t(x,t) = \psi_{xx}(x,t) + 2\sigma\psi^2(x,t)\psi(x,-t). \tag{88}$$

Here, the constant σ takes the values +1 and −1 for focusing and defocusing nonlinearity, respectively. (Solution: See S112.)

7.7 A Nonlocal NLSE [268]

$$i\psi_t(x,t) = \psi_{xx}(x,t) + 2\sigma\psi^2(x,t)\psi^*(-x,t). \tag{89}$$

Here, σ takes the value +1 or −1 for focusing or defocusing nonlinearity, respectively. (Solution: See S113.)

7.8 A Nonlocal Derivative NLSE [269]

$$i\psi_t(x,t) + \psi_{xx}(x,t) + \sigma\left[\psi^2(x,t)\psi^*(-x,t)\right]_x = 0, \tag{90}$$

where σ takes the value +1 or −1 for focusing or defocusing nonlinearity, respectively. (Solution: See S114.)

7.9 A Nonlocal Third-Order NLSE [270]

$$\begin{aligned} &i\psi_t + ic\,\psi_x + \psi_{xx} + \sigma\psi\left[\psi(-x,t)\right]^*\psi + i\lambda\,\psi_{xxx} \\ &\quad + 3i\lambda\,\sigma\,\psi\left[\psi(-x,t)\right]^*\psi_x = 0, \end{aligned} \tag{91}$$

where λ, σ, and c are real constants. (Solution: See S115.)

7.10 An Integrable Three-Parameter Nonlocal Fifth-Order NLSE [271]

$$i\psi_t + S(\psi,r) + \alpha H(\psi,r) + \gamma P(\psi,r) + \delta Q(\psi,r) = 0, \tag{92}$$

where $\psi \equiv \psi(x,t)$, $r \equiv r(x,t)$ are complex fields; α, γ, and δ are all real parameters.

Here, a) $S(\psi,r)$ denotes the nonlocal NLS part

$$S(\psi, r) = \frac{1}{2}\psi_{xx} + \psi^2 r, \tag{93}$$

b) $H(\psi, r)$ represents the nonlocal Hirota part

$$H(\psi, r) = \psi_{xxx} + 6\psi\psi_x r, \tag{94}$$

c) $P(\psi, r)$ denotes the nonlocal Lakshmanan-Porsezian-Daniel (LPD) part

$$P(\psi, r) = \psi_{xxxx} + 8\psi\, r\psi_{xx} + 6\psi^3 r^2 + 4\psi\psi_x r_x + 6\psi_x^2 r + 2\psi^2 r_{xx}, \tag{95}$$

and d) $Q(\psi, r)$ is the nonlocal quintic part

$$Q(\psi, r) = \psi_{xxxxx} + 10\psi\, r\psi_{xxx} + 10\left(\psi\psi_x r_x\right)_x + 20r\,\psi_x\psi_{xx} + 30\psi^2 r^2\psi_x, \tag{96}$$

where $r(x,t) = \sigma\,\psi^*(-x,t)$ and $\sigma = \pm 1$. (Solutions: See S116, S117, S118 & S119.)

7.11 The Nonlocal Variant of the NLSE in a Dimensionless Form [272]

$$i\frac{\partial\psi}{\partial t} + \frac{1}{2}\frac{\partial^2\psi}{\partial x^2} + \theta\,\psi - \mu\,\psi = 0,$$
$$\nu\frac{\partial^2\theta}{\partial x^2} - 2q\,\theta = -2|\psi|^2, \tag{97}$$

where θ represents the optically induced deviation of the director angle, ν is the nonlocality parameter, μ is the propagation constant, and q is the parameter that represents the square of the applied static electric field that pretilts the nematic dielectric. Using Fourier transform θ can be rewritten as

$$\theta = F^{-1}\left[\frac{F\left[2|\psi|^2\right]}{\nu k^2 + 2}\right].$$

Here k is the wave number relevant to the Fourier variable. (Solution: See S120.)

7.12 The Generalized PT-Symmetric Nonlocal Coupled NLSE With Nonlocal SPM, XPM, and FWM of the Following Form [273]

$$i\frac{\partial\psi_1(x,t)}{\partial t} + \frac{\partial^2\psi_1(x,t)}{\partial x^2} + \Big[a\,\psi_1(x,t)\,\psi_1^*(-x,t) + b\,\psi_1(x,t)\,\psi_2^*(-x,t) + c\,\psi_2(x,t)\,\psi_2^*(-x,t) + d\,\psi_1^*(-x,t)\,\psi_2(x,t)\Big]\psi_1(x,t) = 0,$$
$$i\frac{\partial\psi_2(x,t)}{\partial t} + \frac{\partial^2\psi_2(x,t)}{\partial x^2} + \Big[a\,\psi_1(x,t)\,\psi_1^*(-x,t) + b\,\psi_1(x,t)\,\psi_2^*(-x,t) + c\,\psi_2(x,t)\,\psi_2^*(-x,t) + d\,\psi_1^*(-x,t)\,\psi_2(x,t)\Big]\psi_2(x,t) = 0, \tag{98}$$

where a and c correspond to the nonlocal SPM and XPM, respectively, while b, d represent the nonlocal FWM terms. (Solution: See S121.)

8 PEREGRINE SOLITONS IN HIGHER DIMENSIONAL AND MIXED NLSES

This section aims at presenting the Peregrine soliton solutions of higher dimensional and mixed NLSEs reported in the existing literature. The one-dimensional (1D) cubic NLSE or (1 + 1)-dimensional ((1 + 1)-D) cubic NLSE appears in diverse fields of physics, namely, nonlinear optics, plasma physics, BEC, condensed matter physics, and superfluids [109]. A successful first, completely integrable property of such (1 + 1)-D NLSE has been reported by Ablowitz et al., through the inverse scattering transform technique [87]. Higher dimensional NLSEs of such a basic (1 + 1)-D NLSE can be obtained by replacing the second spatial derivative through the Laplacian. Moreover, higher dimensional NLSEs are not integrable, but localized solutions are found to exist in two transverse directions [274, 275]. However, the obtained solutions are not robust against perturbations and found to be unstable after a finite distance. Also, the (3 + 1)-D NLSEs are not integrable, but localized solutions for these equations have been reported through the numerical simulations [6] and via the similarity transformations [275–277]. In particular, this section is related to the Peregrine soliton solution. The Peregrine solitons found profound interest in diverse areas of physics, namely, optical systems [278], BEC [73], hydrodynamics [12], and superfluids [25]. Originally, such Peregrine soliton solutions have been reported in the two-dimensional graded-index waveguides using the similarity transformation [279], followed by their appearance in a two-dimensional graded-index grating waveguide [280] and two-dimensional coupled NLSEs with distributed coefficients [281]. The Peregrine soliton solutions in a (3 + 1)-D inhomogeneous NLSE with variable coefficients [282] and a (3 + 1)-D higher-order coupled NLSE [283] have also been reported. These Peregrine solitons play an inevitable role in describing the dynamics of ocean waves, nonlinear optics, and BEC. Hence, this section considers reporting the Peregrine soliton solutions of various higher dimensional NLSEs and mixed NLSEs. Here, the mixed NLSEs refer to the higher dimensional NLSEs with other physical effects, namely, inhomogeneity, external potential, variable coefficient, and nonlocality. Such higher dimensional and mixed NLSEs in which Peregrine soliton solutions are reported will be listed in this section.

8.1 THE THREE-DIMENSIONAL INHOMOGENEOUS NLSE WITH VARIABLE COEFFICIENTS IN A DIMENSIONLESS FORM [282]

$$i\psi_t = -\frac{1}{2}\nabla^2\psi + v(r,t)\psi + g(t)|\psi|^2\psi + i\gamma(t)\psi. \tag{99}$$

8.2 A Special Case of Eq. 99 [284]

$$i\psi_t = -\frac{\beta(t)}{2}\nabla^2\psi + v(r,t)\psi + g(t)|\psi|^2\psi + i\gamma(t)\psi = 0, \quad (100)$$

where $\psi = \psi(\mathbf{r},t)$, $\mathbf{r} \in \mathbb{R}^3$, $\mathbf{r} = (x,y,z)$, $\nabla \equiv (\partial_x, \partial_y, \partial_z)$ with $\partial_x = \partial/\partial_x$. $v(\mathbf{r},t)$ is an external potential with a real valued function of time and spatial coordinates. $\beta(t)$, $g(t)$, and $\gamma(t)$ denote the coefficients of linearity, nonlinearity, and gain/loss, respectively. (Solutions: See S122, S123 & S124.)

8.3 A (2 + 1)-Dimensional NLSE With an External Potential [285]

$$i\psi_t + \psi_{xx} + \psi_{yy} - g(x,y,t)|\psi|^2\psi - V(x,y,t)\psi = 0, \quad (101)$$

where $g(x,y,t)$ is the coefficient of nonlinearity and $V(x,y,t)$ is an external potential. (Solutions: See S125 & S126.)

8.4 The 3D Variable Coefficient NLSE of the Form With Linear and Parabolic Potentials [286]

$$i\psi_t + \frac{\beta(t)}{2}\Delta\psi + \chi(t)|\psi|^2\psi + V(t,x,y,z)\psi = i\gamma(t)\psi, \quad (102)$$

where $\psi = \psi(t,x,y,z)$ is the order parameter in BECs or the complex envelope of the electric field in optical communication system. Here $\Delta = \partial_x^2 + \partial_y^2 + \partial_z^2$ is the 3-dimensional Laplacian operator. The functions $\beta(t)$, $\chi(t)$, and $\gamma(t)$ are the coefficients of the diffraction, nonlinearity, and gain/loss. Here, the potential $V = V_1(t)(x+y+z) + V_2(t)Y^2$, where $V_1(t)$ and $V_2(t)$ are linear and parabolic potential strengths and $Y^2 = x^2 + y^2 + z^2$. (Solution: See S127.)

8.5 A (2 + 1)-Dimensional NLSE With Variable Coefficients [287]

$$i\psi_t + \psi_{xy} + \alpha(x,y,t)\psi + \beta(t)\psi\,\partial_x^{-1}\partial_y|\psi|^2 + i\gamma(t)\psi = 0, \quad (103)$$

where $\psi = \psi(x,y,t)$, with the propagation variables x, y and transverse variable t. $\alpha(x,y,t)$ is an external potential which is the real valued function of space and time. $\beta(t)$ and $\gamma(t)$ are the coefficients of nonlinearity and gain/loss. The inverse d-bar operator, $\partial_x^{-1} = \partial_z^{-1} + \partial_{\bar{z}}^{-1}$, $z = x + iy$, $\partial_z = \frac{1}{2}(\partial_x - i\partial_y)$, $\partial_{\bar{z}} = \frac{1}{2}(\partial_x + i\partial_y)$, and $(\partial_{\bar{z}} f) = \frac{1}{\pi}\int_{\mathbb{R}^2} \frac{f(x_r,y_r)dx_r dy_r}{z - z_r}$. (Solution: See S128.)

8.6 A Two-Dimensional Nonlocal NLSE [288]

$$i\psi_t = -\psi_{xx} - \sigma\psi\int_{-\infty}^{+\infty}|\psi|^2 dy = 0, \quad (104)$$

where $\psi \equiv \psi(x,y,t)$ is a two-dimensional field envelope and σ (>0) is the nonlinearity coefficient. (Solution: See S129.)

8.7 A (2 + 1)-Dimensional Variable Coefficient NLSE With Partial Nonlocality [289]

$$i\psi_t + \beta(t)\psi_{xx} + \chi(t)\psi\int_{-\infty}^{+\infty}|\psi|^2 dy = 0, \quad (105)$$

where $\psi = \psi(t,x,y)$. $\beta(t)$ and $\chi(t)$ are the coefficients of diffraction and nonlinearity, respectively. (Solution: See S130.)

8.8 A (2 + 1)-Dimensional Variable Coefficient Partially Nonlocal NLSE [290]

$$i\frac{\partial\psi}{\partial z} + \beta(z)\frac{\partial^2\psi}{\partial x^2} + \chi(z)\psi\int_{-\infty}^{+\infty}|\psi|^2 dy + \gamma(z)x^2\psi = 0, \quad (106)$$

where $\psi = \psi(z,x,y)$ describing the optical field or wave function of condensate. $\beta(z)$ and $\gamma(z)$ are the coefficients of diffraction and tapering effect/harmonic trapping potential, respectively. The nonlinearity is localized in x-direction and nonlocalized in y-direction with the coefficient function $\chi(z)$. (Solution: See S131.)

8.9 A (2 + 1)-Dimensional (2D) Nonlocal NLSE Satisfying the Two-Dimensional Parity-Time-Symmetric Potential $\mathbf{V(x,y) = V^*(-x,-y)}$ [291, 292]

$$i\psi_t + \psi_{xy} + \psi r = 0,\ r_y = \left[\psi(x,y,t)\,\psi(-x,-y,t)^*\right]_x, \quad (107)$$

where $\psi = \psi(x,y,t)$ and $V(x,y,t) = \psi(x,y,t)\psi^*(x,y,t)$. (Solutions: See S132 & S133.)

8.10 A Two-Dimensional Nonlocal NLSE [293]

$$i\psi_t + \psi_{xx} + \psi_{yy} - 2\psi_{xy} + 2\psi V = 0,\ V = \psi(x,y,t)\psi^*(-x,-y,t), \quad (108)$$

where $\psi = \psi(x,y,t)$. (Solution: See S134.)

8.11 The Integrable "Reverse Space" 2D Nonlocal NLSE [294]

$$\left(i\partial_t + \partial_{xy}^2\right)\psi(x,y,t) - \frac{\lambda}{2}\psi(x,y,t)\left(\partial_z^{-1} + \partial_{\bar{z}}^{-1}\right)\partial_y\left[\psi(x,y,t)\psi^*(-x,-y,t)\right] = 0,\ \lambda = \pm 1. \quad (109)$$

8.12 A Reverse Space-Time Nonlocal NLSE [294]

$$\left(i\partial_t + \partial_{xy}^2\right)\psi(x,y,t) - \frac{\lambda}{2}\psi(x,y,t)\left(\partial_z^{-1} + \partial_{\bar{z}}^{-1}\right)\partial_y\left[\psi(x,y,t)\psi^*(-x,y,-t)\right] = 0,\ \lambda = \pm 1. \quad (110)$$

Here $z \equiv x + iy$ and $\partial_{z,\bar{z}}^{-1}$ are operators inverse to $\partial_z \equiv (1/2)(\partial_x - i\partial_y)$ and $\partial_{\bar{z}} \equiv (1/2)(\partial_x + i\partial_y)$. (Solutions: See S135 & S136.)

8.13 A Two-Dimensional Two-Coupled Variable Coefficient NLSE [281]

$$\begin{aligned} &i\psi_{1z} + \frac{\beta(z)}{2}\left(\psi_{1xx} + \psi_{1yy}\right) + R(z)\sum_{k=1}^{2}|\psi_k|^2\psi_1 = i\gamma(z)\psi_1, \\ &i\psi_{2z} + \frac{\beta(z)}{2}\left(\psi_{2xx} + \psi_{2yy}\right) + R(z)\sum_{k=1}^{2}|\psi_k|^2\psi_2 = i\gamma(z)\psi_2, \end{aligned} \tag{111}$$

where $\psi_j = \psi_j(x, y, z)$, $j = 1, 2$. The real analytic spatial functions, $\beta(z)$, $R(z)$, and $\gamma(z)$ represent the diffraction, nonlinearity, and gain/loss parameter, respectively. (Solution: See S137.)

8.14 The Variable Coefficient NLSE Describing the Inhomogeneous Nonlinear Waveguide [295]

$$\begin{aligned} &i\psi_{1z} + \frac{\beta}{2}\left(\psi_{1xx} + \psi_{1yy}\right) + \chi(z)\left(r_{11}|\psi_1|^2 + r_{12}|\psi_2|^2\right)\psi_1 \\ &+\frac{1}{2}f(z)\left(x^2 + y^2\right)\psi_1 = ig(z)\psi_1, i\psi_{2z} + \frac{\beta}{2}\left(\psi_{2xx} + \psi_{2yy}\right) \\ &+\chi(z)\left(r_{21}|\psi_1|^2 + r_{22}|\psi_2|^2\right)\psi_2 + \frac{1}{2}f(z)\left(x^2 + y^2\right)\psi_2 = ig(z)\psi_2, \end{aligned} \tag{112}$$

where $\psi_1(x, y, z)$ and $\psi_2(x, y, z)$ are the two normalized orthogonal components of electric fields. β, $\chi(z)$, g(z), and f(z) denote the dispersion, nonlinearity, gain, and geometry of tapered waveguide coefficients, respectively. r_{11} and r_{22} are the self-phase modulation coefficients for $\psi_1(x, y, z)$, $\psi_2(x, y, z)$ and r_{12} and r_{21} are the cross-phase modulation coefficients. (Solution: See S138.)

8.15 The Variable Coefficient CNLSE [296]

$$\begin{aligned} &i\psi_{1z} + \frac{1}{2}\left[\beta_1(z)\psi_{1xx} + \beta_2(z)\psi_{1yy} + \beta_3(z)\psi_{1tt}\right] + \chi(z)\left(\sigma_{11}|\psi_1|^2\right. \\ &\left.+\sigma_{12}|\psi_2|^2\right)\psi_1 = i\gamma(z)\psi_1, i\psi_{2z} + \frac{1}{2}\Big[\beta_1(z)\psi_{2xx} + \beta_2(z)\psi_{2yy} \\ &+\beta_3(z)\psi_{2tt}\Big] + \chi(z)\left(\sigma_{21}|\psi_1|^2 + \sigma_{22}|\psi_2|^2\right)\psi_2 = i\gamma(z)\psi_2, \end{aligned} \tag{113}$$

where $\psi_1(z, x, y, t)$ and $\psi_2(z, x, y, t)$ are the two normalized complex mode fields. $\beta_1(z)$ and $\beta_2(z)$ are the coefficients of diffractions along the x and y transverse coordinates. $\beta_3(z)$ is the coefficient of dispersion. $\chi(z)$ is the SPM, accounting for the self-focusing ($\chi > 0$) or the self-defocusing ($\chi < 0$) nonlinearity. The parameters σ_{11}, σ_{12}, σ_{21}, and σ_{22} determine the ratio of the coupling strengths of the cross-phase modulation to the SPM. For linearly polarized eigenmodes, $\sigma_{11} = \sigma_{22} = 1$, $\sigma_{12} = \sigma_{21} = 2/3$, in case of circularly polarized eigen modes, $\sigma_{11} = \sigma_{22} = 1, \sigma_{12} = \sigma_{21} = 2$ and for the elliptically polarized eigen modes, $\sigma_{11} = \sigma_{22} = 1$, $2 < \sigma_{12} = \sigma_{21} < 2/3$. The parameter $\gamma(z)$ represents the loss when $\gamma(z) < 0$ or gain when $\gamma(z) > 0$. (Solution: See S139.)

9 PEREGRINE SOLITONS IN SATURABLE NLSES

This section presents the Peregrine soliton solutions reported in the literature under the family of the saturable NLSEs. In nonlinear dynamics, the ultrashort optical pulse propagation through the dielectric waveguides like optical fibers is governed by the NLSEs. The key parameter that plays a decisive role in the nonlinear effects of such optical fibers is an intensity dependent variation of the refractive index, also known as the optical Kerr effect. The Kerr index induced refractive index results in the self-phase modulation which ultimately broadens the optical spectrum. Moreover, it is well known that the Kerr nonlinearity determines the nonlinear response of the optical medium up to a certain level of input power, but when input power level exceeds a certain value, the role of higher-order nonlinear susceptibility is inevitable. This eventually results in the saturation of the nonlinear response of the system. In general, all nonlinearities saturation is owing to the upper limit for change in the refractive index of the material medium and thereafter system does not display any change in the nonlinear index even at very high input power levels [109]. Also, it is demonstrated that the saturation in cubic nonlinearity is equivalent to the occurrence of the third-, fifth-, and seventh-order nonlinear susceptibility [297]. Such nonlinear index saturation has been originally observed in dual core nonlinear directional couplers by Stegeman et al. [298], followed by plethora of studies to understand the detrimental effects of nonlinear saturation in the coupling behaviors of directions couplers [299–302]. The propagation of solitons through the materials with nonlinear saturation has also been expressed through numerical and analytical methods. The dynamics of such system provide the evidence of the existence of bistable solitons of the same duration with different peak powers [303]. Moreover, the dynamics of ultrashort pulse propagation through the fibers with saturable nonlinearity in the normal dispersion regime has also been analyzed to determine the minimum duration of the output pulse of fiber-grating compressor [304]. In addition, the nonlinear saturation effects play a significant role in the MI gain spectrum of the ultrashort pulse propagation through the semiconductor doped fibers [305–307]. This section lists out the saturable NLSEs in which Peregrine soliton solutions were reported.

9.1 A NLSE Describes Quasi-1D Bose-Einstein Condensates [308]

$$i\psi_t = -\frac{1}{2}\psi_{xx} + V(x)\psi + \frac{1 - (3/2)|\psi|^2}{\sqrt{1 - |\psi|^2}}\psi, \tag{114}$$

where $V(x) = \frac{1}{2}\Omega^2 x^2$ is an external potential of harmonic form. Ω is the normalized trap strength. (Solution: See S140.)

10 SUMMARY AND OUTLOOK

The historical review of the discovery of the Peregrine soliton goes side by side with the mathematical steps of its derivation. We have adopted here the most common method of derivation, namely, the use of Lax pair and Darboux transformation. Employing the continuous wave as a seed solution, we have analytically derived the general breather solution of the NLSE through the Darboux transformation and Lax pair technique. We have shown that this class of solution turns out, under certain limits, into its five members, the Akhmediev breather, the Kuznetsov-Ma breather, the Peregrine soliton, the single bright soliton, and the continuous wave solution. When the temporal period of the Kuznetsov-Ma breather approaches infinity, it falls into the Peregrine soliton. A similar result is obtained when the spacial period of the Akhmediev breather tends to infinity. We have then collected all Peregrine soliton solutions of the NLSE and its various variations that are found in the literature. Particularly, we have recorded the Peregrine soliton solutions in higher-order and inhomogeneous NLSEs, in NLSE with external potentials, in coupled NLSEs, in discrete NLSEs, in nonlocal NLSEs, in higher dimensional and mixed NLSEs, and finally in saturable NLSEs. The Peregrine waves in saturable nonlinear systems are not sufficiently explored. Concerning studies in such systems will yield more information about modulation instability and new frequency generations, that will play a crucial role in nonlinear optical fields.

While studying the various nonlinear dynamics modeled by the NLSEs is a developing and attractive area of research, this work will be a useful guideline to keep track of new NLS frameworks that admit Peregrine soliton solutions, youthful stability investigations, up-to-date formation mechanisms, and fresh experimental observations. One future extension of this work is a deep exploration of the existence of Peregrine solitons in higher coupled NLSEs and higher dimensional systems. The accompanying features of these systems could support the robustness of the Peregrine soliton against different perturbations and initial conditions and thus generate more stable rogue wave structures. Additionally, it may be interesting to investigate numerically complex nonintegrable systems in order to achieve more stable rogue waves. Constructing such models experimentally allows for the monitorization of randomly many possible nonlinear dynamics. This opens the door to a better understanding of the preactions accomplished by extreme events such as rogue waves.

As the multisoliton interaction is one of the formation mechanisms of the rogue waves and it is recently reported in the bioenergy transport mechanism in the helical protein [32], this evidence may also be extended to different biomechanisms. Moreover, one of the not fully explored aspects, yet very important, is the knowledge of how a variety of initial conditions are influencing the rogue wave formation. In nonlinear optics, the knowledge of initial conditions plays an essential role in generating, on purpose, rogue waves in order to produce high energy light pulses. Last but not least, with regard to the dispersion and nonlinearity management, it may be interesting to consider interactions of multi-Peregrine solitons modeling by higher dimensional NLSEs. Recently, photonic rogue waves are analytically reported in lattice systems [78]. This will be useful in understanding wave interactions in diverse crystal structures.

AUTHOR CONTRIBUTIONS

All authors listed have made a substantial, direct, and intellectual contribution to the work and approved it for publication.

ACKNOWLEDGMENTS

The authors acknowledge the support of UAE University through grants UAEU-UPAR(1) 2019 and UAEU-UPAR(11) 2019.

SUPPLEMENTARY MATERIAL

The Supplementary Material for this article can be found online at: https://www.frontiersin.org/articles/10.3389/fphy.2020.596886/full#supplementary-material

REFERENCES

1. Russell JS, Taylor J. *Report on waves: made to the meetings of the british association*. Cambridge, MA: Harvard University (1845) p. 88.
2. Airy GB. *Tides and waves*. Munich, Germany: B. Fellows (1845) p. 396.
3. Stokes G. *On the theory of oscillatory waves*. Cambridge, UK: Pitt Press (1847) p. 15.
4. Korteweg DJ, de Vries G. Xli. on the change of form of long waves advancing in a rectangular canal, and on a new type of long stationary waves. *London, Edinburgh, Dublin Philos Mag J Sci* (1895) 39:422–43. doi:10.1080/14786449508620739.
5. Zabusky NJ, Kruskal MD. Interaction of "solitons" in a collisionless plasma and the recurrence of initial states. *Phys Rev Lett* (1965) 15:240–3. doi:10.1103/PhysRevLett.15.240.
6. Gardner CS, Greene JM, Kruskal MD, Miura RM. Method for solving the korteweg-devries equation. *Phys Rev Lett* (1967) 19:1095–7. doi:10.1103/PhysRevLett.19.1095.
7. Zakharov VE, Shabat AB. Exact theory of two-dimensional self-focusing and one-dimensional self-modulation of wave in nonlinear media. *Sov Phys JETP* (1972) 34:62–7.
8. Al Khawaja U, Al Sakkaf L. *Handbook of exact solutions to the nonlinear Schrödinger equations*. Bristol, UK: Institute of Physics Publishing (2019) 375 p.
9. Kuznetsov EA. Solitons in a parametrically unstable plasma. *Akad Nauk SSSR Doklady* (1977) 236:575–7.
10. Ma YC. The perturbed plane-wave solutions of the cubic schrödinger equation. *Stud Appl Math* (1979) 60:43–58. doi:10.1002/sapm197960143.
11. Peregrine DH. Water waves, nonlinear schrödinger equations and their solutions. *J Aust Math Soc* (1983) 25:16–43. doi:10.1017/S0334270000003891.
12. Kharif C, Pelinovsky E, Slunyaev A. *Rogue Waves in the ocean*. Berlin, Heidelberg: Springer-Verlag (2009) 216 p.
13. Shrira VI, Geogjaev VV. What makes the peregrine soliton so special as a prototype of freak waves? *J Eng Math* (2010) 67:11–22. doi:10.1007/s10665-009-9347-2.

14. Osborne A. Nonlinear ocean wave and the inverse scattering transform. In: R Pike P Sabatier, editors *Scattering*. Cambridge, MA: Academic Press (2002) p. 637–66.
15. Broad WJ. Rogue giants at sea. *The New York Times* (2006) 11.
16. Calini A, Schober CM. Rogue waves in higher order nonlinear schrödinger models. In: E Pelinovsky C Kharif, editors. *Extreme Ocean Waves*. Dordrecht, Netherlands: Springer (2008) p. 31–51.
17. Akhmediev N, Ankiewicz A, Taki M. Waves that appear from nowhere and disappear without a trace. *Phys Lett A* (2009) 373:675–8. doi:10.1016/j.physleta.2008.12.036.
18. Akhmediev N, Soto-Crespo JM, Ankiewicz A. Extreme waves that appear from nowhere: on the nature of rogue waves. *Phys Lett A* (2009) 373:2137–45. doi:10.1016/j.physleta.2009.04.023.
19. Akhmediev N, Eleonskii VM, Kulagin NE. Generation of periodic trains of picosecond pulses in an optical fiber: exact solutions. *Sov Phys JETP* (1985) 62: 894–9.
20. Kedziora DJ, Ankiewicz A, Akhmediev N. Second-order nonlinear schrödinger equation breather solutions in the degenerate and rogue wave limits. *Phys Rev E* (2012) 85:066601. doi:10.1103/PhysRevE.85.066601.
21. Akhmediev N, Ankiewicz A, Soto-Crespo JM. Rogue waves and rational solutions of the nonlinear schrödinger equation. *Phys Rev E* (2009) 80: 026601. doi:10.1103/PhysRevE.80.026601.
22. Chowdury A, Kedziora DJ, Ankiewicz A, Akhmediev N. Breather solutions of the integrable quintic nonlinear schrödinger equation and their interactions. *Phys Rev E* (2015) 91:022919. doi:10.1103/PhysRevE.91.022919.
23. Solli DR, Ropers C, Koonath P, Jalali B. Optical rogue waves. *Nature* (2007) 450:1054–7. doi:10.1038/nature06402.
24. Hammani K, Finot C, Dudley JM, Millot G. Optical rogue-wave-like extreme value fluctuations in fiber raman amplifiers. *Optic Express* (2008) 16:16467–74. doi:10.1364/OE.16.016467.
25. Ganshin AN, Efimov VB, Kolmakov GV, Mezhov-Deglin LP, McClintock PVE. Observation of an inverse energy cascade in developed acoustic turbulence in superfluid helium. *Phys Rev Lett* (2008) 101:065303. doi:10.1103/PhysRevLett.101.065303.
26. Shats M, Punzmann H, Xia H. Capillary rogue waves. *Phys Rev Lett* (2010) 104: 104503. doi:10.1103/PhysRevLett.104.104503.
27. Kibler B, Fatome J, Finot C, Millot G, Dias F, Genty G, et al. The peregrine soliton in nonlinear fibre optics. *Nat Phys* (2010) 6:790–5. doi:10.1038/nphys1740.
28. Chabchoub A, Hoffmann NP, Akhmediev N. Rogue wave observation in a water wave tank. *Phys Rev Lett* (2011) 106:204502. doi:10.1103/PhysRevLett.106.204502.
29. Akhmediev N, Soto-Crespo J, Ankiewicz A. How to excite a rogue wave. *Phys Rev A* (2009) 80:043818. doi:10.1103/PhysRevA.80.043818.
30. Frisquet B, Kibler B, Millot G. Collision of akhmediev breathers in nonlinear fiber optics. *Phys Rev X* (2013) 3:041032. doi:10.1103/PhysRevX.3.041032.
31. Chowdury A, Kedziora D, Ankiewicz A, Akhmediev N. Breather-to-soliton conversions described by the quintic equation of the nonlinear schrödinger hierarchy. *Phys Rev E* (2015) 91:032928. doi:10.1103/PhysRevE.91.032928.
32. Liu J, Jin DQ, Zhang XL, Wang YY, Dai CQ. Excitation and interaction between solitons of the three-spine α-helical proteins under non-uniform conditions. *Optik* (2018) 158:97–104. doi:10.1016/j.ijleo.2017.11.200.
33. Akhmediev N, Soto-Crespo J, Ankiewicz A. Could rogue waves be used as efficient weapons against enemy ships?. *Eur Phys J Spec Top* (2010) 185: 259–66. doi:10.1140/epjst/e2010-01253-8.
34. Taki M, Mussot A, Kudlinski A, Louvergneaux E, Kolobov M, Douay M. Third-order dispersion for generating optical rogue solitons. *Phys Lett A* (2010) 374:691–5. doi:10.1016/j.physleta.2009.11.058.
35. Genty G, de Sterke CM, Bang O, Dias F, Akhmediev N, Dudley JM. Collisions and turbulence in optical rogue wave formation. *Phys Lett A* (2010) 374: 989–96. doi:10.1016/j.physleta.2009.12.014.
36. Demircan A, Amiranashvili S, Brée C, Mahnke C, Mitschke F, Steinmeyer G. Rogue wave formation by accelerated solitons at an optical event horizon. *Appl Phys B* (2014) 115:343–54. doi:10.1007/s00340-013-5609-9.
37. Ablowitz MJ, Horikis TP. Interacting nonlinear wave envelopes and rogue wave formation in deep water. *Phys Fluids* (2015) 27:012107. doi:10.1063/1.4906770.
38. Wang XB, Han B. Characteristics of rogue waves on a soliton background in the general coupled nonlinear schrödinger equation. *Commun Theor Phys* (2019) 71:152. doi:10.1088/0253-6102/71/2/152.
39. Zhong WP, Belić M, Zhang Y. Second-order rogue wave breathers in the nonlinear schrödinger equation with quadratic potential modulated by a spatially-varying diffraction coefficient. *Optic Exp* (2015) 23:3708–16. doi:10.1364/OE.23.003708.
40. Wang Q, Li X. Collision properties of rogue waves in optical fiber. *Optic Commun* (2019) 435:255–64. doi:10.1016/j.optcom.2018.11.037.
41. Zhen-Kun W, Yun-Zhe Z, Yi H, Feng W, Yi-Qi Z, Yan-Peng Z. The interaction of peregrine solitons. *Chin Phys Lett* (2014) 31:090502. doi:10.1088/0256-307X/31/9/090502.
42. Ankiewicz A, Kedziora DJ, Akhmediev N. Rogue wave triplets. *Phys Lett A* (2011) 375:2782–5. doi:10.1016/j.physleta.2011.05.047.
43. Al Khawaja U, Bahlouli H, Asad-uz-zaman M, Al-Marzoug S. Modulational instability analysis of the peregrine soliton. *Commun Nonlinear Sci Num Simul* (2014) 19:2706–14. doi:10.1016/j.cnsns.2014.01.002.
44. Schober C, Strawn M. Stability analysis of the peregrine solution via squared eigenfunctions. *AIP Conf Proc* (2017) 1895:040004. doi:10.1063/1.5007371.
45. Calini A, Schober C. Observable and reproducible rogue waves. *J Optic* (2013) 15:105201. doi:10.1088/2040-8978/15/10/105201.
46. Islas A, Schober CM. Numerical investigation of the stability of the rational solutions of the nonlinear schrödinger equation. *Appl Math Comput* (2017) 305:17–26. doi:10.1016/j.amc.2017.01.060.
47. Calini A, Schober C. Numerical investigation of stability of breather-type solutions of the nonlinear schrödinger equation. *Nat Hazards Earth Syst Sci* (2014) 14:1431. doi:10.5194/nhess-14-1431-2014.
48. Calini A, Schober CM, Strawn M. Linear instability of the peregrine breather: numerical and analytical investigations. *Appl Numer Math* (2019) 141:36–43. doi:10.1016/j.apnum.2018.11.005.
49. Ankiewicz A, Devine N, Akhmediev N. Are rogue waves robust against perturbations?. *Phys Lett A* (2009) 373:3997–4000. doi:10.1016/j.physleta.2009.08.053.
50. Onorato M, Proment D. Approximate rogue wave solutions of the forced and damped nonlinear Schrödinger equation for water waves. *Phys Lett A* (2012) 376:3057–9. doi:10.1016/j.physleta.2012.05.063.
51. Wen XY, Yan Z, Malomed BA. Higher-order vector discrete rogue-wave states in the coupled Ablowitz-Ladik equations: exact solutions and stability. *Chaos* (2016) 26:123110. doi:10.1063/1.4972111.
52. Muñoz C. Instability in nonlinear schrödinger breathers. *Proyecciones* (2017) 36:653–83. doi:10.4067/S0716-09172017000400653.
53. Chen S, Soto-Crespo JM, Grelu P. Coexisting rogue waves within the (2 + 1)-component long-wave–short-wave resonance. *Phys Rev E* (2014) 90:033203. doi:10.1103/PhysRevE.90.033203.
54. Klein C, Haragus M. Numerical study of the stability of the peregrine breather. Preprint repository name [Preprint] (2015) Available from: https://arxiv.org/abs/1507.06766.
55. Chan HN, Chow KW, Kedziora DJ, Grimshaw RHJ, Ding E. Rogue wave modes for a derivative nonlinear schrödinger model. *Phys Rev E* (2014) 89: 032914. doi:10.1103/PhysRevE.89.032914.
56. Kharif C, Touboul J. Under which conditions the benjamin-feir instability may spawn an extreme wave event: a fully nonlinear approach. *Eur Phys J Spec Top* (2010) 185:159–68. doi:10.1140/epjst/e2010-01246-7.
57. Van Gorder RA. Orbital instability of the peregrine soliton. *J Phys Soc Jpn* (2014) 83:054005. doi:10.7566/JPSJ.83.054005.doi:10.1140/epjst/e2010-01246-7.
58. Cuevas-Maraver J, Malomed BA, Kevrekidis PG, Frantzeskakis DJ. Stabilization of the peregrine soliton and kuznetsov–ma breathers by means of nonlinearity and dispersion management. *Phys Lett A* (2018) 382: 968–72. doi:10.1016/j.physleta.2018.02.013.
59. El-Tantawy S, Shan SA, Akhtar N, Elgendy A. Impact of electron trapping in degenerate quantum plasma on the ion-acoustic breathers and super freak waves. *Chaos, Solit Fractals* (2018) 113:356–64. doi:10.1016/j.chaos.2018.04.037.
60. Bludov YV, Driben R, Konotop VV, Malomed B. Instabilities, solitons and rogue waves in -coupled nonlinear waveguides. *J Optic* (2013) 15:064010. doi:10.1088/2040-8978/15/6/064010.
61. Shin H. Deformation of a peregrine soliton by fluctuating backgrounds. *Phys Rev E* (2013) 88:032919. doi:10.1103/PhysRevE.88.032919.

62. Cuevas-Maraver J, Kevrekidis PG, Frantzeskakis DJ, Karachalios NI, Haragus M, James G. Floquet analysis of kuznetsov-ma breathers: a path towards spectral stability of rogue waves. *Phys Rev E* (2017) 96:012202. doi:10.1103/PhysRevE.96.012202.
63. Li JH, Chan HN, Chiang KS, Chow KW. Breathers and 'black' rogue waves of coupled nonlinear schrödinger equations with dispersion and nonlinearity of opposite signs. *Commun Nonlinear Sci Num Simul* (2015) 28:28–38. doi:10.1016/j.cnsns.2015.03.019.
64. Hoffmann C, Charalampidis E, Frantzeskakis D, Kevrekidis P. Peregrine solitons and gradient catastrophes in discrete nonlinear schrödinger systems. *Phys Lett A* (2018) 382:3064–70. doi:10.1016/j.physleta.2018.08.014.
65. Birem M, Klein C. Multidomain spectral method for schrödinger equations. *Adv Comput Math* (2016) 42:395–423. doi:10.1007/s10444-015-9429-9.
66. Bailung H, Sharma SK, Nakamura Y. Observation of peregrine solitons in a multicomponent plasma with negative ions. *Phys Rev Lett* (2011) 107:255005. doi:10.1103/PhysRevLett.107.255005.
67. Pathak P, Sharma SK, Nakamura Y, Bailung H. Observation of ion acoustic multi-peregrine solitons in multicomponent plasma with negative ions. *Phys Lett A* (2017) 381:4011–8. doi:10.1016/j.physleta.2017.10.046.
68. Xu G, Hammani K, Chabchoub A, Dudley JM, Kibler B, Finot C. Phase evolution of peregrine-like breathers in optics and hydrodynamics. *Phys Rev E* (2019) 99:012207.doi:10.1103/PhysRevE.99.012207.
69. Yang G, Wang Y, Qin Z, Malomed BA, Mihalache D, Li L. Breather like solitons extracted from the peregrine rogue wave. *Phys Rev E* (2014) 90:062909. doi:10.1103/PhysRevE.90.062909.
70. Hammani K, Kibler B, Finot C, Morin P, Fatome J, Dudley JM, et al. Peregrine soliton generation and breakup in standard telecommunications fiber. *Opt Lett* (2011) 36:112–4. doi:10.1364/OL.36.000112.
71. Zamora-Munt J, Garbin B, Barland S, Giudici M, Leite JRR, Masoller C, et al. Rogue waves in optically injected lasers: origin, predictability, and suppression. *Phys Rev A* (2013) 87:035802. doi:10.1103/PhysRevA.87.035802.
72. Chabchoub A, Hoffmann N, Branger H, Kharif C, Akhmediev N. Experiments on wind-perturbed rogue wave hydrodynamics using the peregrine breather model. *Phys Fluids* (2013) 25:101704. doi:10.1063/1.4824706.
73. Bludov YV, Konotop VV, Akhmediev N. Matter rogue waves. *Phys Rev A* (2009) 80:033610. doi:10.1103/PhysRevA.80.033610.
74. Dyachenko AI, Zakharov VE. Modulation instability of stokes wave freak wave. *J Exp Theor Phys Lett* (2005) 81:255–9. doi:10.1134/1.1931010.
75. Zaviyalov A, Egorov O, Iliew R, Lederer F. Rogue waves in mode-locked fiber lasers. *Phys Rev A* (2012) 85:013828. doi:10.1103/PhysRevA.85.013828.
76. Oppo GL, Yao AM, Cuozzo D. Self-organization, pattern formation, cavity solitons, and rogue waves in singly resonant optical parametric oscillators. *Phys Rev A* (2013) 88:043813. doi:10.1103/PhysRevA.88.043813.
77. Chen S, Song LY. Peregrine solitons and algebraic soliton pairs in kerr media considering space–time correction. *Phys Lett A* (2014) 378:1228–32. doi:10.1016/j.physleta.2014.02.042.
78. Rivas D, Szameit A, Vicencio RA. Rogue waves in disordered 1d photonic lattices. *Sci Rep* (2020) 10:1–8. doi:10.1038/s41598-020-69826-x.
79. Osborne AR, Onorato M, Serio M. The nonlinear dynamics of rogue waves and holes in deep-water gravity wave trains. *Phys Lett A* (2000) 275:386–93. doi:10.1016/S0375-9601(00)00575-2.
80. Osborne AR. The random and deterministic dynamics of 'rogue waves' in unidirectional, deep-water wave trains. *Mar Struct* (2001) 14:275–93. doi:10.1016/S0951-8339(00)00064-2.
81. Yan Z. Nonautonomous "rogons" in the inhomogeneous nonlinear schrödinger equation with variable coefficients. *Phys Lett A* (2010) 374:672–9. doi:10.1016/j.physleta.2009.11.030.
82. Dai CQ, Wang YY, Tian Q, Zhang JF. The management and containment of self-similar rogue waves in the inhomogeneous nonlinear schrödinger equation. *Ann Phys* (2012) 327:512–21. doi:10.1155/2016/7879517.
83. Xu S, He J, Wang L. Two kinds of rogue waves of the general nonlinear schrödinger equation with derivative. *Europhys Lett* (2012) 97:30007. doi:10.1209/0295-5075/97/30007.
84. Yang G, Li L, Jia S. Peregrine rogue waves induced by the interaction between a continuous wave and a soliton. *Phys Rev E* (2012) 85:046608. doi:10.1103/PhysRevE.85.046608.
85. Zhao LC. Dynamics of nonautonomous rogue waves in Bose–Einstein condensate. *Ann Phys* (2013) 329:73–9. doi:10.1016/j.aop.2012.10.010.
86. Ablowitz MJ. Lectures on the inverse scattering transform. *Stud Appl Math* (1978) 58:17–94. doi:10.1002/sapm197858117.
87. Ablowitz MJ, Segur H. *Solitons and the inverse scattering transform*. Philadelphia, PA: Siam (1981) 434 p.
88. Drazin PG, Johnson RS. *Solitons: an introduction*. Cambridge, UK: Cambridge University Press (1989) 226 p.
89. Ablowitz MJ, Ablowitz M, Clarkson P, Clarkson PA. Solitons, nonlinear evolution equations and inverse scattering. *Bull London Math Soc* (1993) 25:620–2. doi:10.1112/blms/25.6.620.
90. Ablowitz M, Prinari B, Trubatch A. *Discrete and continuous nonlinear schrödinger systems*. Cambridge, UK: Cambridge University Press (2005) 276 p.
91. Aktosun T. Inverse scattering transform and the theory of solitons. Preprint repository name [Preprint] (2009) Available from: https://arxiv.org/abs/0905.4746.
92. Ablowitz MJ. *Nonlinear dispersive waves: asymptotic analysis and solitons*. Cambridge, UK: Cambridge University Press (2011) 348 p.
93. Ablowitz MJ, Musslimani ZHF. Inverse scattering transform for the integrable nonlocal nonlinear schrödinger equation. *Nonlinearity* (2016) 29:915. doi:10.1088/0951-7715/29/3/915.
94. Adomian G. *Solving frontier problems of physics: the decomposition method; with a preface by yves cherruault*. Dordrecht, Netherlands: Kluwer Academic Publishers (1994) 12 p.
95. Liao SJ. An explicit, totally analytic approximate solution for blasius' viscous flow problems. *Int J Non Lin Mech* (1999) 34:759–78. doi:10.1016/S0020-7462(98)00056-0.
96. Liao S. On the homotopy analysis method for nonlinear problems. *Appl Math Comput* (2004) 147:499–513. doi:10.1016/S0096-3003(02)00790-7.
97. Ye J, Zheng C. Exact projective excitations of nonautonomous nonlinear schrödinger system in (1 + 1)-dimensions. *J Mod Phys* (2012) 3:702. doi:10.4236/jmp.2012.38095.
98. Zhao D, He XG, Luo HG. Transformation from the nonautonomous to standard nls equations. *Eur Phys J D* (2009) 53:213–6. doi:10.1140/epjd/e2009-00051-7.
99. Pérez-García VM, Torres PJ, Konotop VV. Similarity transformations for nonlinear schrödinger equations with time-dependent coefficients. *Phys Nonlinear Phenom* (2006) 221:31–6. doi:10.1016/j.physd.2006.07.002.
100. Kundu A. Integrable nonautonomous nonlinear schrödinger equations are equivalent to the standard autonomous equation. *Phys Rev E* (2009) 79:015601. doi:10.1103/PhysRevE.79.015601.
101. Kruglov V, Peacock A, Harvey J. Exact self-similar solutions of the generalized nonlinear schrödinger equation with distributed coefficients. *Phys Rev Lett* (2003) 90:113902. doi:10.1103/PhysRevLett.90.113902.
102. Al Khawaja U, Boudjemâa A. Binding energy of soliton molecules in time-dependent harmonic potential and nonlinear interaction. *Phys Rev E* (2012) 86:036606. doi:10.1103/PhysRevE.86.036606.
103. Al Khawaja U. Soliton localization in bose–einstein condensates with time-dependent harmonic potential and scattering length. *J Phys Math Theor* (2009) 42:265206. doi:10.1088/1751-8113/42/26/265206.
104. Guo B, Ling L, Liu Q. Nonlinear schrödinger equation: generalized darboux transformation and rogue wave solutions. *Phys Rev E* (2012) 85:026607. doi:10.1103/PhysRevE.85.026607.
105. Al Khawaja U, Taki M. Rogue waves management by external potentials. *Phys Lett A* (2013) 377:2944–9. doi:10.1016/j.physleta.2013.09.012.
106. Al Khawaja U. Exact solitonic solutions of the gross-pitaevskii equation with a linear potential. *Phys Rev E* (2007) 75:066607. doi:10.1103/PhysRevE.75.066607.
107. Matveev VB, Matveev V. *Darboux transformations and solitons*. Berlin, Germany: Springer (1991) p. 120.
108. Lax PD. Integrals of nonlinear equations of evolution and solitary waves. *Commun Pure Appl Math* (1968) 21:467–90. doi:10.1002/cpa.3160210503.
109. Agrawal G. *Nonlinear fiber optics*. 6th ed. Cambridge, MA: Academic Press (2019) p. 728.
110. Lakshmanan M, Porsezian K, Daniel M. Effect of discreteness on the continuum limit of the heisenberg spin chain. *Phys Lett A* (1988) 133:483–8. doi:10.1016/0375-9601(88)90520-8.
111. Hirota R. Exact envelope-soliton solutions of a nonlinear wave equation. *J Math Phys* (1973) 14:805–9. doi:10.1063/1.1666399.

112. Ankiewicz A, Kedziora DJ, Chowdury A, Bandelow U, Akhmediev N. Infinite hierarchy of nonlinear schrödinger equations and their solutions. *Phys Rev E* (2016) 93:012206. doi:10.1103/PhysRevE.93.012206.
113. Sun WR. Breather-to-soliton transitions and nonlinear wave interactions for the nonlinear schrödinger equation with the sextic operators in optical fibers. *Ann Phys* (2017) 529:1600227. doi:10.1002/andp.201600227.
114. Ruprecht PA, Holland MJ, Burnett K, Edwards M. Time-dependent solution of the nonlinear schrödinger equation for bose-condensed trapped neutral atoms. *Phys Rev A* (1995) 51:4704–11. doi:10.1103/PhysRevA.51.4704.
115. Dai CQ, Wang YY, Tian Q, Zhang JF. The management and containment of self-similar rogue waves in the inhomogeneous nonlinear schrödinger equation. *Ann Phys* (2012) 327:512–21. doi:10.1016/j.aop.2011.11.016.
116. Chen HH, Liu CS. Solitons in nonuniform media. *Phys Rev Lett* (1976) 37: 693–7. doi:10.1103/PhysRevLett.37.693.
117. Raghavan S, Agrawal GP. Spatiotemporal solitons in inhomogeneous nonlinear media. *Optic Commun* (2000) 180:377–382. doi:10.1016/S0030-4018(00)00727-6.
118. Yan Z, Dai C. Optical rogue waves in the generalized inhomogeneous higher-order nonlinear schrödinger equation with modulating coefficients. *J Optic* (2013) 15:064012. doi:10.1088/2040-8978/15/6/064012.
119. Wang LH, Porsezian K, He JS. Breather and rogue wave solutions of a generalized nonlinear schrödinger equation. *Phys Rev E* (2013) 87:053202. doi:10.1103/PhysRevE.87.053202.
120. Sun WR, Tian B, Zhen HL, Sun Y. Breathers and rogue waves of the fifth-order nonlinear schrödinger equation in the heisenberg ferromagnetic spin chain. *Nonlinear Dynam* (2015) 81:725–32. doi:10.1007/s11071-015-2022-4.
121. Wang XB, Zhang TT, Dong MJ. Dynamics of the breathers and rogue waves in the higher-order nonlinear schrödinger equation. *Appl Math Lett* (2018) 86:298–304. doi:10.1016/j.aml.2018.07.012.
122. Yue Y, Huang L, Chen Y. Modulation instability, rogue waves and spectral analysis for the sixth-order nonlinear schrödinger equation. *Commun Nonlinear Sci Numer Simulat* (2020) 89:105284. doi:10.1016/j.cnsns.2020.105284.
123. Wu X, Hua G, Ma Z. Novel rogue waves in an inhomogenous nonlinear medium with external potentials. *Commun Nonlinear Sci Numer Simulat* (2013) 18:3325–36. doi:10.1016/j.cnsns.2013.05.007.
124. Manzetti S. Mathematical modeling of rogue waves: a survey of recent and emerging mathematical methods and solutions. *Axioms* (2018) 7:1–19. doi:10.3390/axioms7020042.
125. Sun WR, Tian B, Jiang Y, Zhen HL. Double-wronskian solitons and rogue waves for the inhomogeneous nonlinear schrödinger equation in an inhomogeneous plasma. *Ann Phys* (2014) 343:215–27. doi:10.1016/j.aop.2014.01.018.
126. He J, Tao Y, Porsezian K, Fokas A. Rogue wave management in an inhomogeneous nonlinear fibre with higher order effects. *J Nonlinear Math Phys* (2013) 20:407–19. doi:10.1080/14029251.2013.855045.
127. Onorato M, Residori S, Bortolozzo U, Montina A, Arecchi F. Rogue waves and their generating mechanisms in different physical contexts. *Phys Rep* (2013) 528:47–89. doi:10.1016/j.physrep.2013.03.001.
128. Tappert FD, Zabusky NJ. Gradient-induced fission of solitons. *Phys Rev Lett* (1971) 27:1774–6. doi:10.1103/PhysRevLett.27.1774.
129. Ponomarenko SA, Agrawal GP. Do solitonlike self-similar waves exist in nonlinear optical media? *Phys Rev Lett* (2006) 97:013901. doi:10.1103/PhysRevLett.97.013901.
130. Serkin VN, Hasegawa A, Belyaeva TL. Nonautonomous solitons in external potentials. *Phys Rev Lett* (2007) 98:074102. doi:10.1103/PhysRevLett.98.074102.
131. Serkin VN, Hasegawa A. Novel soliton solutions of the nonlinear schrödinger equation model. *Phys Rev Lett* (2000) 85:4502–5. doi:10.1103/PhysRevLett.85.4502.
132. Serkin VN, Hasegawa A. Exactly integrable nonlinear schrödinger equation models with varying dispersion, nonlinearity and gain: application for soliton dispersion. *IEEE J Sel Top Quant Electron* (2002) 8:418–31. doi:10.1109/JSTQE.2002.1016344.
133. Yan Z, Konotop VV. Exact solutions to three-dimensional generalized nonlinear schrödinger equations with varying potential and nonlinearities. *Phys Rev E* (2009) 80:036607. doi:10.1103/PhysRevE.80.036607.
134. Kumar CN, Gupta R, Goyal A, Loomba S, Raju TS, Panigrahi PK. Controlled giant rogue waves in nonlinear fiber optics. *Phys Rev A* (2012) 86:025802. doi:10.1103/PhysRevA.86.025802.
135. Zhao LC. Dynamics of nonautonomous rogue waves in bose–einstein condensate. *Ann Phys* (2013) 329:73–9. doi:10.1016/j.aop.2012.10.010.
136. Chen HY, Zhu HP. Controllable behaviors of spatiotemporal breathers in a generalized variable-coefficient nonlinear schrödinger model from arterial mechanics and optical fibers. *Nonlinear Dynam* (2015) 81:141–9. doi:10.1007/s11071-015-1978-4.
137. Dai CQ, Wang YY. Controllable combined peregrine soliton and kuznetsov–ma soliton in PT-symmetric nonlinear couplers with gain and loss. *Nonlinear Dynam* (2015) 80:715–21. doi:10.1007/s11071-015-1900-0.
138. Erkintalo M, Genty G, Dudley JM. Rogue-wave-like characteristics in femtosecond supercontinuum generation. *Opt Lett* (2009) 34:2468–70. doi:10.1364/OL.34.002468.
139. Moslem WM. Langmuir rogue waves in electron-positron plasmas. *Phys Plasmas* (2011) 18:032301. doi:10.1063/1.3559486.
140. Stenflo L, Marklund M. Rogue waves in the atmosphere. *J Plasma Phys* (2010) 76:293–5. doi:10.1017/S0022377809990481.
141. Wen L, Li L, Li ZD, Song SW, Zhang XF, Liu WM. Matter rogue wave in bose-einstein condensates with attractive atomic interaction. *Euro Phys J D* (2011) 64:473–8. doi:10.1140/epjd/e2011-20485-4.
142. He JS, Charalampidis EG, Kevrekidis PG, Frantzeskakis DJ. Rogue waves in nonlinear schrödinger models with variable coefficients: application to bose-einstein condensates. *Phys Lett A* (2014) 378:577–83. doi:10.1016/j.physleta.2013.12.002.
143. Zhong W, Chen L, Belić M, Petrović N. Controllable parabolic-cylinder optical rogue wave. *Phys Rev E* (2014) 90:043201. doi:10.1103/PhysRevE.90.043201.
144. Sun Y, Tian B, Liu L, Wu X. Rogue waves for a generalized nonlinear schrödinger equation with distributed coefficients in a monomode optical fiber. *Chaos, Solit Fractals* (2018) 107:266–74. doi:10.1016/j.chaos.2017.12.012.
145. Loomba S, Pal R, Kumar CN. Controlling rogue wave triplets in Bose–Einstein condensate. *J Phys B Atom Mol Opt Phys* (2015) 48:105003. doi:10.1088/0953-4075/48/10/105003.
146. Goyal A, Gupta R, Loomba S, Kumar CN. Riccati parameterized self-similar waves in tapered graded-index waveguides. *Phys Lett A* (2012) 376:3454–7. doi:10.1016/j.physleta.2012.07.041. doi:10.1088/0953-4075/48/10/105003.
147. Ali S, Younis M. Rogue wave solutions and modulation instability with variable coefficient and harmonic potential. *Frontiers in Physics* (2020) 7:255. doi:10.3389/fphy.2019.00255.
148. Tao Y, He J, Porsezian K. Deformed soliton, breather, and rogue wave solutions of an inhomogeneous nonlinear schrödinger equation. *Chin Phys B* (2013) 22:074210. doi:10.1088/1674-1056/22/7/074210.
149. Dai CQ, Zheng CL, Zhu HP. Controllable rogue waves in the nonautonomous nonlinear system with a linear potential. *Eur Phys J D* (2012) 66:1. doi:10.1140/epjd/e2012-20718-0.
150. Jia H, Yang R, Tian J, Zhang W. Controllable excitation of higher-order rogue waves in nonautonomous systems with both varying linear and harmonic external potentials. *Optic Commun* (2018) 415:93–100. doi:10.1016/j.optcom.2018.01.026.
151. Loomba S, Gupta R, Kaur H, Rajan MSM. Self-similar rogue waves in an inhomogeneous generalized nonlinear schrödinger equation. *Phys Lett A* (2014) 378:2137–41. doi:10.1016/j.physleta.2014.05.028.
152. Panigrahi PK, Gupta R, Goyal A, Kumar CN. Riccati generalization of self-similar solutions of nonautonomous gross-pitaevskii equation. *Eur Phys J Spec Top* (2013) 222:655–63. doi:10.1140/epjst/e2013-01870-7.
153. Manakov S. On the theory of two-dimensional stationary self-focusing of electromagnetic waves. *J Exp Theor Phys Lett* (1974) 38:248
154. Kivshar YS, Malomed BA. Dynamics of solitons in nearly integrable systems. *Rev Mod Phys* (1989) 61:763–915. doi:10.1103/RevModPhys.61.763.
155. Radhakrishnan R, Lakshmanan M. Bright and dark soliton solutions to coupled nonlinear schrödinger equations. *J Phys Math Gen* (1995) 28: 2683–92. doi:10.1088/0305-4470/28/9/025.
156. Busch T, Anglin JR. Dark-bright solitons in inhomogeneous bose-einstein condensates. *Phys Rev Lett* (2001) 87:010401. doi:10.1103/PhysRevLett.87.010401.

157. Dhar AK, Das KP. Fourth-order nonlinear evolution equation for two stokes wave trains in deep water. *Phys Fluid A Fluid Dynam* (1991) 3:3021. doi:10.1063/1.858209.
158. Scott AC. Launching a davydov soliton: I. soliton analysis. *Phys Scripta* (1984) 29:279–83. doi:10.1088/0031-8949/29/3/016.
159. Yan Z. Vector financial rogue waves. *Phys Lett A* (2011) 375:4274–9. doi:10.1016/j.physleta.2011.09.026.
160. Akhmediev N, Pelinovsky E. Editorial - introductory remarks on "discussion debate: Rogue waves - towards a unifying concept?". *Eur Phys J Spec Top* (2010) 185:1–4. doi:10.1140/epjst/e2010-01233-0.
161. Kharif C, Pelinovsky E. Physical mechanisms of the rogue wave phenomenon. *Eur J Mech B Fluid* (2003) 22:603–34. doi:10.1016/j.euromechflu.2003.09.002.
162. Bludov YV, Konotop VV, Akhmediev N. Vector rogue waves in binary mixtures of bose-einstein condensates. *Eur Phys J Spec Top* (2010) 185:169–80. doi:10.1140/epjst/e2010-01247-6.
163. Zhao LC, Liu J. Localized nonlinear waves in a two-mode nonlinear fiber. *J Opt Soc Am B* (2012) 29:3119–27. doi:10.1364/JOSAB.29.003119.
164. Zhao LC, Guo2 B, Ling L. High-order rogue wave solutions for the coupled nonlinear schrödinger equations-ii. *J Math Phys* (2016) 57:043508. doi:10.1063/1.4947113.
165. Baronio F, Conforti M, Degasperis A, Lombardo S, Onorato M, Wabnitz S. Vector rogue waves and baseband modulation instability in the defocusing regime. *Phys Rev Lett* (2014) 113:034101. doi:10.1103/PhysRevLett.113.034101.
166. Zhao LC, Liu J. Rogue-wave solutions of a three-component coupled nonlinear schrödinger equation. *Phys Rev E* (2013) 87:013201. doi:10.1103/PhysRevE.87.013201.
167. Baronio F, Conforti M, Degasperis A, Lombardo S. Rogue waves emerging from the resonant interaction of three waves. *Phys Rev Lett* (2013) 111:114101. doi:10.1103/PhysRevLett.111.114101.
168. Rao J, Porsezian K, Kanna T, Cheng Y, He J. Vector rogue waves in integrable m-coupled nonlinear schrödinger equations. *Phys Scripta* (2019) 94:075205. doi:10.1088/1402-4896/ab1482.
169. Baronio F, Degasperis A, Conforti M, Wabnitz S. Solutions of the vector nonlinear schrödinger equations: evidence for deterministic rogue waves. *Phys Rev Lett* (2012) 109:044102. doi:10.1103/PhysRevLett.109.044102.
170. Mu G, Qin Z, Grimshaw R. Dynamics of rogue waves on a multisoliton background in a vector nonlinear schrödinger equation. *SIAM J Appl Math* (2015) 75:1–20. doi:10.1137/140963686.
171. Guo BL, Ling LM. Rogue wave, breathers and bright-dark-rogue solutions for the coupled schrödinger equations. *Chin Phys Lett* (2011) 28:110202. doi:10.1088/0256-307x/28/11/110202.
172. He J, Guo L, Zhang Y, Chabchoub A. Theoretical and experimental evidence of non-symmetric doubly localized rogue waves. *Proc R Soc A* (2014) 470:20140318. doi:10.1098/rspa.2014.0318.
173. Zhai BG, Zhang WG, Wang XL, Zhang HQ. Multi-rogue waves and rational solutions of the coupled nonlinear schrödinger equations. *Nonlinear Anal R World Appl* (2013) 14:14–27. doi:10.1016/j.nonrwa.2012.04.010.
174. Vishnu Priya N, Senthilvelan M, Lakshmanan M. Akhmediev breathers, ma solitons, and general breathers from rogue waves: a case study in the manakov system. *Phys Rev E* (2013) 88:022918. doi:10.1103/PhysRevE.88.022918.
175. Zhao LC, Xin GG, Yang ZY. Rogue-wave pattern transition induced by relative frequency. *Phys Rev E* (2014) 90:022918. doi:10.1103/PhysRevE.90.022918.
176. Chen S, Soto-Crespo JM, Grelu P. Dark three-sister rogue waves in normally dispersive optical fibers with random birefringence. *Optic Express* (2014) 22:27632–42. doi:10.1364/OE.22.027632.
177. Xu T, Chen Y. Localized waves in three-component coupled nonlinear schrödinger equation. *Chin Phys B* (2016) 25:090201. doi:10.1088/1674-1056/25/9/090201.
178. Wang XB, Han B. The three-component coupled nonlinear schrödinger equation: Rogue waves on a multi-soliton background and dynamics. *Europhys Lett* (2019) 126:15001. doi:10.1209/0295-5075/126/1500.
179. Chan HN, Chow KW. Rogue wave modes for the coupled nonlinear schrödinger system with three components: a computational study. *Appl Sci* (2017) 7(1–12):559. doi:10.3390/app7060559.
180. Chen S, Grelu P, Soto-Crespo JM. Dark- and bright-rogue-wave solutions for media with long-wave–short-wave resonance. *Phys Rev E* (2014) 89:011201. doi:10.1103/PhysRevE.89.011201.
181. Xu T, He G. The coupled derivative nonlinear schrödinger equation: conservation laws, modulation instability and semirational solutions. *Nonlinear Dynam* (2020) 100:2823–37. doi:10.1007/s11071-020-05679-3.
182. Sun WR, Tian B, Xie XY, Chai J, Jiang Y. High-order rogue waves of the coupled nonlinear schrödinger equations with negative coherent coupling in an isotropic medium. *Commun Nonlinear Sci Numer Simulat* (2016) 39:538–44. doi:10.1016/j.cnsns.2016.04.005.
183. Feng L, Zhang T. Breather wave, rogue wave and solitary wave solutions of a coupled nonlinear schrödinger equation. *Appl Math Lett* (2018) 78:133–40. doi:10.1016/j.aml.2017.11.011.
184. Zhong W, Beli M, Malomed BA. Rogue waves in a two-component manakov system with variable coefficients and an external potential. *Am Phys Soc* (2015) 92:053201. doi:10.1103/PhysRevE.92.053201.
185. Bludov YV, Konotop VV, Akhmediev N. Vector rogue waves in binary mixtures of bose–einstein condensates. *Eur Phys J Spec Top* (2010) 185:169–80. doi:10.1140/epjst/e2010-01247-6.
186. Mukam SPT, Souleymanou A, Kuetche VK, Bouetou TB. Generalized darboux transformation and parameter-dependent rogue wave solutions to a nonlinear schrödinger system. *Nonlinear Dynam* (2018) 93:373–83. doi:10.1007/s11071-018-4198-x.
187. Li ZD, Wang Y-Y, He PB. Formation mechanism of asymmetric breather and rogue waves in pair-transition-coupled nonlinear schrödinger equations. *Chin Phys B* (2019) 28:010504. doi:10.1088/1674-1056/28/1/010504.
188. Zhang G, Yan Z, Wen XY. Modulational instability, beak-shaped rogue waves, multi-dark-dark solitons and dynamics in pair-transition-coupled nonlinear schrödinger equations. *Proc R Soc A* (2017) 473:1–19. doi:10.1098/rspa.2017.0243.
189. Zhao LC, Ling L, Yang ZY, Liu J. Pair-tunneling induced localized waves in a vector nonlinear schrödinger equation. *Commun Nonlinear Sci Numer Simulat* (2015) 23:21–7. doi:10.1016/j.cnsns.2014.10.031.
190. Guo R, Liu YF, Hao HQ, Qi FH. Coherently coupled solitons, breathers and rogue waves for polarized optical waves in an isotropic medium. *Nonlinear Dynam* (2015) 80:1221–30. doi:10.1007/s11071-015-1938-z.
191. Chen SS, Tian B, Sun Y, Zhang CR. Generalized darboux transformations, rogue waves, and modulation instability for the coherently coupled nonlinear schrödinger equations in nonlinear optics. *Ann Phys* (2019) 531:1900011. doi:10.1002/andp.201900011.
192. Dai C, Huang W. Multi-rogue wave and multi-breather solutions in PT-symmetric coupled waveguides. *Appl Math Lett* (2014) 32:35–40. doi:10.1016/j.aml.2014.02.013.
193. Vishnu Priya N, Senthilvelan M. Generalized darboux transformation and nth order rogue wave solution of a general coupled nonlinear schrödinger equations. *Commun Nonlinear Sci Numer Simulat* (2015) 20:401–20. doi:10.1016/j.cnsns.2014.06.001.
194. Li HM, Tian B, Wang DS, Sun WR, Xie XY, Liu L. Rogue waves for a coupled nonlinear schrödinger system in a multi-mode fibre. *J Mod Optic* (2016) 63:1924–31. doi:10.1080/09500340.2016.1177617.
195. Vishnu Priya N, Senthilvelan M. On the characterization of breather and rogue wave solutions and modulation instability of a coupled generalized nonlinear schrödinger equations. *Wave Motion* (2015) 54:125–33. doi:10.1016/j.wavemoti.2014.12.001.
196. Vishnu Priya N, Senthilvelan M, Lakshmanan M. Dark solitons, breathers, and rogue wave solutions of the coupled generalized nonlinear schrödinger equations. *Phys Rev E* (2014) 89:062901. doi:10.1103/PhysRevE.89.062901.
197. Wang YF, Guo BL, Liu N. Optical rogue waves for the coherently coupled nonlinear schrödinger equation with alternate signs of nonlinearities. *Appl Math Lett* (2018) 82:38–42. doi:10.1016/j.aml.2018.01.007.
198. Yu F, Yan Z. New rogue waves and dark-bright soliton solutions for a coupled nonlinear schrödinger equation with variable coefficients. *Appl Math Comput* (2014) 233:351–8. doi:10.1016/j.amc.2014.02.023.
199. Cheng X, Wang J, Li J. Controllable rogue waves in coupled nonlinear schrödinger equations with varying potentials and nonlinearities. *Nonlinear Dynam* (2014) 77:545–52. doi:10.1007/s11071-014-1316-2.
200. Sun WR, Tian B, Liu RX, Liu DY. Triple wronskian vector solitons and rogue waves for the coupled nonlinear schrödinger equations in the inhomogeneous plasma. *J Math Anal Appl* (2015) 424:1006–20. doi:10.1016/j.jmaa.2014.11.056.

201. Li J, Han J, Du Y, Dai C. Controllable behaviors of peregrine soliton with two peaks in a birefringent fiber with higher-order effects. *Nonlinear Dynam* (2015) 82:1393–8. doi:10.1007/s11071-015-2246-3.
202. Wang X, Chen Y. Rogue-wave pair and dark-bright-rogue wave solutions of the coupled hirota equations. *Chin Phys B* (2014) 23:070203. doi:10.1088/1674-1056/23/7/070203.
203. Zhang Y, Nie X-J, Zha Z. Rogue wave solutions for the coupled cubic–quintic nonlinear schrödinger equations in nonlinear optics. *Phys Lett* (2014) 378:191–7. doi:10.1016/j.physleta.2013.11.010.
204. Xu T, Chen Y, Lin J. Localized waves of the coupled cubic–quintic nonlinear schrödinger equations in nonlinear optics. *Chin Phys B* (2017) 26:120201. doi:10.1088/1674-1056/26/12/120201.
205. Lan Z. Rogue wave solutions for a coupled nonlinear schrödinger equation in the birefringent optical fiber. *Appl Math Lett* (2019) 98:128–34. doi:10.1016/j.aml.2019.05.028.
206. Meng GQ, Qin JL, Yu GL. Breather and rogue wave solutions for a nonlinear schrödinger-type system in plasmas. *Nonlinear Dynam* (2015) 81:739–51. doi:10.1007/s11071-015-2024-2.
207. Askaryan GA. Effects of the gradient of a strong electromagnetic beam on electrons and atoms. *Sov Phys-JETP* (1962) 15:1088–90.
208. Marquié P, Bilbault JM, Remoissenet M. Observation of nonlinear localized modes in an electrical lattice. *Phys Rev E* (1995) 51:6127–33. doi:10.1103/PhysRevE.51.6127.
209. Bilbault JM, Marquié P. Energy localization in a nonlinear discrete system. *Phys Rev E* (1996) 53:5403–8. doi:10.1103/PhysRevE.53.5403.
210. Aceves AB, De Angelis C, Peschel T, Muschall R, Lederer F, Trillo S, et al. Discrete self-trapping, soliton interactions, and beam steering in nonlinear waveguide arrays. *Phys Rev E* (1996) 53:1172–89. doi:10.1103/PhysRevE.53.1172.
211. Hennig D, Tsironis G. Wave transmission in nonlinear lattices. *Phys Rep* (1999) 307:333–432. doi:10.1016/S0370-1573(98)00025-8.
212. Bludov YV, Konotop VV, Akhmediev N. Rogue waves as spatial energy concentrators in arrays of nonlinear waveguides. *Opt Lett* (2009) 34:3015–7. doi:10.1364/OL.34.003015.
213. Eisenberg HS, Silberberg Y, Morandotti R, Boyd AR, Aitchison JS. Discrete spatial optical solitons in waveguide arrays. *Phys Rev Lett* (1998) 81:3383–6. doi:10.1103/PhysRevLett.81.3383.
214. Anderson BP, Kasevich MA. Macroscopic quantum interference from atomic tunnel arrays. *Science* (1998) 282:1686–9. doi:10.1126/science.282.5394.1686.
215. Fleischer JW, Carmon T, Segev M, Efremidis NK, Christodoulides DN. Observation of discrete solitons in optically induced real time waveguide arrays. *Phys Rev Lett* (2003) 90:023902. doi:10.1103/PhysRevLett.90.023902.
216. Ablowitz MJ, Kaup DJ, Newell AC, Segur H. The inverse scattering transform-fourier analysis for nonlinear problems. *Stud Appl Math* (1974) 53:249–315. doi:10.1002/sapm1974534249.
217. Ablowitz MJ, Ladik JF. Nonlinear differential-difference equations. *J Math Phys* (1975) 16:598–603. doi:10.1063/1.522558.
218. Ablowitz MJ, Ladik JF. Nonlinear differential-difference equations and fourier analysis. *J Math Phys* (1976) 17:1011. doi:10.1063/1.523009.
219. Christodoulides DN, Joseph RI. Discrete self-focusing in nonlinear arrays of coupled waveguides. *Opt Lett* (1988) 13:794–6. doi:10.1364/OL.13.000794.
220. Chen Z, Segev M, Christodoulides DN. Optical spatial solitons: historical overview and recent advances. *Rep Prog Phys* (2012) 75:086401. doi:10.1088/0034-4885/75/8/086401.
221. Rivas D, Szameit A, Vicencio RA. Rogue waves in disordered 1d photonic lattices. *Sci Rep* (2020) 10:13064. doi:10.1038/s41598-020-69826-x.
222. Takeno S, Hori K. A propagating self-localized mode in a one-dimensional lattice with quartic anharmonicity. *J Phys Soc Jpn* (1990) 59:3037–40. doi:10.1143/JPSJ.59.3037.
223. Ishimori Y. An integrable classical spin chain. *J Phys Soc Jpn* (1982) 51:3417–8. doi:10.1143/JPSJ.51.3417.
224. Kenkre VM, Campbell DK. Self-trapping on a dimer: time-dependent solutions of a discrete nonlinear schrödinger equation. *Phys Rev B* (1986) 34:4959–61. doi:10.1103/PhysRevB.34.4959.
225. Ablowitz MJ. Nonlinear evolution equations-continuous and discrete. *Soc Ind Appl Math Rev* (1977) 19:663–84. doi:10.1137/1019105.
226. Hirota R. Nonlinear partial difference equations. I. a difference analogue of the Korteweg-De Vries equation. *J Phys Soc Jpn* (1977) 43:1424–33. doi:10.1143/JPSJ.43.1424.
227. Salerno M. Quantum deformations of the discrete nonlinear schrödinger equation. *Phys Rev A* (1992) 46:6856–9. doi:10.1103/PhysRevA.46.6856.
228. Ohta Y, Yang J. General rogue waves in the focusing and defocusing ablowitz–ladik equations. *J Phys Math Theor* (2014) 47:255201. doi:10.1088/1751-8113/47/25/255201.
229. Bludov YV, Konotop VV, Akhmediev N. Rogue waves as spatial energy concentrators in arrays of nonlinear waveguides. *Opt Lett* (2009) 34:3015–7. doi:10.1364/OL.34.003015.
230. Efe S, Yuce C. Discrete rogue waves in an array of waveguides. *Phys Lett A* (2015) 379:1251–5. doi:10.1016/j.physleta.2015.02.031.
231. Li M, Shui JJ, Xu T. Generation mechanism of rogue waves for the discrete nonlinear schrödinger equation. *Appl Math Lett* (2018) 83:110–5. doi:10.1016/j.aml.2018.03.018.
232. Ankiewicz A, Akhmediev N, Lederer F. Approach to first-order exact solutions of the ablowitz-ladik equation. *Phys Rev E* (2011) 83(6):056602. doi:10.1103/PhysRevE.83.056602.
233. Ankiewicz A, Akhmediev N, Soto-Crespo JM. Discrete rogue waves of the ablowitz-ladik and hirota equations. *Phys Rev E* (2010) 82(7):026602. doi:10.1103/PhysRevE.82.026602.
234. Akhmediev N, Ankiewicz A. Modulation instability, fermi-pasta-ulam recurrence, rogue waves, nonlinear phase shift, and exact solutions of the ablowitz-ladik equation. *Phys Rev E* (2011) 83:046603. doi:10.1103/PhysRevE.83.046603.
235. Yan Z, Jiang D. Nonautonomous discrete rogue wave solutions and interactions in an inhomogeneous lattice with varying coefficients. *J Math Anal Appl* (2012) 395:542–9. doi:10.1016/j.jmaa.2012.05.058.
236. Yang J, Zhu ZN. Higher-order rogue wave solutions to a spatial discrete hirota equation. *Chin Phys Lett* (2018) 35:090201. doi:10.1088/0256-307x/35/9/090201.
237. Ankiewicz A, Devine N, Ünal M, Chowdury A, Akhmediev N. Rogue waves and other solutions of single and coupled ablowitz–ladik and nonlinear schrödinger equations. *J Optic* (2013) 15:064008. doi:10.1088/2040-8978/15/6/064008.
238. Wen XY, Yan Z. Modulational instability and dynamics of multi-rogue wave solutions for the discrete ablowitz-ladik equation. *J Math Phys* (2018) 59:073511. doi:10.1063/1.5048512.
239. Prinari B. Discrete solitons of the focusing ablowitz-ladik equation with nonzero boundary conditions via inverse scattering. *J Math Phys* (2016) 57:083510. doi:10.1063/1.4961160.
240. Ortiz AK, Prinari B. Inverse scattering transform for the defocusing ablowitz–ladik system with arbitrarily large nonzero background. *Stud Appl Math* (2019) 143:373–403. doi:10.1111/sapm.12282.
241. Li L, Yu F. Optical discrete rogue wave solutions and numerical simulation for a coupled ablowitz–ladik equation with variable coefficients. *Nonlinear Dynam* (2018) 91:1993–2005. doi:10.1007/s11071-017-3998-8.
242. Bender CM, Boettcher S. Real spectra in non-hermitian hamiltonians having PT-symmetry. *Phys Rev Lett* (1998) 80:5243–6. doi:10.1103/PhysRevLett.80.5243.
243. Musslimani ZH, Makris KG, El-Ganainy R, Christodoulides DN. Optical solitons in PT periodic potentials. *Phys Rev Lett* (2008) 100:030402. doi:10.1103/PhysRevLett.100.030402.
244. Benisty H, Degiron A, Lupu A, Lustrac AD, Chénais S, Forget S, et al. Implementation of pt symmetric devices using plasmonics: principle and applications. *Optic Express* (2011) 19:18004. doi:10.1364/OE.19.018004.
245. Cartarius H, Wunner G. Model of a PT-symmetric bose-einstein condensate in a δ-function double-well potential. *Phys Rev A* (2012) 86:013612. doi:10.1103/PhysRevA.86.013612.
246. Schindler J, Li A, Zheng MC, Ellis FM, Kottos T. Experimental study of active lrc circuits with PT symmetries. *Phys Rev A* (2011) 84:040101. doi:10.1103/PhysRevA.84.040101.
247. Zhu X, Ramezani H, Shi C, Zhu J, Zhang X. PT-symmetric acoustics. *Phys Rev X* (2014) 4:031042. doi:10.1103/PhysRevX.4.031042.
248. Sinha D, Ghosh PK. Integrable nonlocal vector nonlinear schrödinger equation with self-induced parity-time-symmetric potential. *Phys Lett A* (2017) 381:124–8. doi:10.1016/j.physleta.2016.11.002.

249. Hu S, Ma X, Lu D, Yang Z, Zheng Y, Hu W. Solitons supported by complex -symmetric Gaussian potentials. *Phys Rev A* (2011) 84:043818. doi:10.1103/PhysRevA.84.043818.
250. Shi Z, Jiang X, Zhu X, Li H. Bright spatial solitons in defocusing kerr media with -symmetric potentials. *Phys Rev A* (2011) 84:053855. doi:10.1103/PhysRevA.84.053855.
251. Rüter CE, Makris KG, El-Ganainy R, Christodoulides DN, Segev M, Kip D. Observation of parity–time symmetry in optics. *Nat Phys* (2010) 6:192–5. doi:10.1038/nphys1515.doi:10.1103/PhysRevA.84.053855.
252. Barashenkov IV, Suchkov SV, Sukhorukov AA, Dmitriev SV, Kivshar YS. Breathers in -symmetric optical couplers. *Phys Rev A* (2012) 86:053809. doi:10.1103/PhysRevA.86.053809.
253. Konotop VV, Yang J, Zezyulin DA. Nonlinear waves in -symmetric systems. *Rev Mod Phys* (2016) 88:035002. doi:10.1103/RevModPhys.88.035002.
254. Ablowitz MJ, Musslimani ZH. Integrable nonlocal nonlinear schrödinger equation. *Phys Rev Lett* (2013) 110:064105. doi:10.1103/PhysRevLett.110.064105.
255. Ablowitz MJ, Musslimani ZH. Integrable discrete symmetric model. *Phys Rev E* (2014) 90:032912. doi:10.1103/PhysRevE.90.032912.
256. Yang B, Chen Y. Several reverse-time integrable nonlocal nonlinear equations: Rogue-wave solutions. *Chaos* (2018) 28:053104. doi:10.1063/1.5019754.
257. Zhou ZX. Darboux transformations and global solutions for a nonlocal derivative nonlinear schrödinger equation. *Commun Nonlinear Sci Numer Simulat* (2018) 62:480–8. doi:10.1016/j.cnsns.2018.01.008.
258. Fokas AS. Integrable multidimensional versions of the nonlocal nonlinear schrödinger equation. *Nonlinearity* (2016) 29:319–24. doi:10.1088/0951-7715/29/2/319.
259. Ma LY, Shen SF, Zhu ZN. Soliton solution and gauge equivalence for an integrable nonlocal complex modified korteweg-de vries equation. *J Math Phys* (2017) 58:103501. doi:10.1063/1.5005611.
260. Luo XD. Inverse scattering transform for the complex reverse space-time nonlocal modified korteweg-de vries equation with nonzero boundary conditions and constant phase shift. *Chaos* (2019) 29:073118. doi:10.1063/1.5090426.
261. Ankiewicz A, Clarkson PA, Akhmediev N. Rogue waves, rational solutions, the patterns of their zeros and integral relations. *J Phys Math Theor* (2010) 43:122002. doi:10.1088/1751-8113/43/12/122002.
262. Dubard P, Gaillard P, Klein C, Matveev V. On multi-rogue wave solutions of the nls equation and positon solutions of the kdv equation. *Eur Phys J Spec Top* (2010) 185:247–58. doi:10.1140/epjst/e2010-01252-9.
263. Gupta SK, Sarma AK. Peregrine rogue wave dynamics in the continuous nonlinear schrödinger system with parity-time symmetric kerr nonlinearity. *Commun Nonlinear Sci Numer Simulat* (2016) 36:141–7. doi:10.1016/j.cnsns.2015.11.017.
264. Yang B, Yang J. On general rogue waves in the parity-time-symmetric nonlinear schrödinger equation. *J Math Anal Appl* (2020) 487:124023. doi:10.1016/j.jmaa.2020.124023.
265. Sakthivinayagam P, Chen J. PT-symmetric cubic-quintic nonlinear schrödinger equation with dual power nonlinearities and its solitonic solutions. *Optik* (2020) 217:164665. doi:10.1016/j.ijleo.2020.164665.
266. Liu W. High-order rogue waves of the benjamin ono equation and the nonlocal nonlinear schrödinger equation. *Mod Phys Lett B* (2017) 31:1750269. doi:10.1142/S0217984917502694.
267. Yang B, Chen Y. General rogue waves and their dynamics in several reverse time integrable nonlocal nonlinear equations. Preprint repository name [Preprint] (2017) Available from: https://arxiv.org/abs/1712.05974.
268. Yang B, Yang J. Rogue waves in the nonlocal PT-symmetric nonlinear schrödinger equation. *Lett Math Phys* (2019) 109:945–73. doi:10.1007/s11005-018-1133-5.
269. Yang B, Yang J. Transformations between nonlocal and local integrable equations. *Stud Appl Math* (2018) 140:178–201. doi:10.1111/sapm.12195.
270. Xu Z, Chow K. Breathers and rogue waves for a third order nonlocal partial differential equation by a bilinear transformation. *Appl Math Lett* (2016) 56:72–7. doi:10.1016/j.aml.2015.12.016.
271. Yang Y, Wang X, Cheng X. Higher-order rational solutions for a new integrable nonlocal fifth-order nonlinear schrödinger equation. *Wave Motion* (2018) 77:1–11. doi:10.1016/j.wavemoti.2017.10.012.
272. Ward CB, Kevrekidis PG, Horikis TP, Frantzeskakis DJ. Rogue waves and periodic solutions of a nonlocal nonlinear schrödinger model. *Phys Rev Res* (2020) 2:013351. doi:10.1103/PhysRevResearch.2.013351.
273. Vinayagam P, Radha R, Al Khawaja U, Ling L. New classes of solutions in the coupled PT-symmetric nonlocal nonlinear schrödinger equations with four wave mixing. *Commun Nonlinear Sci Numer Simulat* (2018) 59:387–95. doi:10.1016/j.cnsns.2017.11.016.
274. Chiao RY, Garmire E, Townes CH. Self-trapping of optical beams. *Phys Rev Lett* (1964) 13:479–82. doi:10.1103/PhysRevLett.13.479.
275. Bergé L. Wave collapse in physics: principles and applications to light and plasma waves. *Phys Rep* (1998) 303:259–370. doi:10.1016/S0370-1573(97)00092-6.
276. Vlasov V, Petrishev I, Talanov V. Averaged description of wave beams in linear and nonlinear media. *Radiofiz* (1971) 14:1353–63. doi:10.1007/BF01029467.
277. Gagnon L. Exact solutions for optical wave propagation including transverse effects. *J Opt Soc Am B* (1990) 7:1098–102. doi:10.1364/JOSAB.7.001098.
278. Montina A, Bortolozzo U, Residori S, Arecchi FT. Non-Gaussian statistics and extreme waves in a nonlinear optical cavity. *Phys Rev Lett* (2009) 103:173901. doi:10.1103/PhysRevLett.103.173901.
279. Zhu HP. Nonlinear tunneling for controllable rogue waves in two dimensional graded-index waveguides. *Nonlinear Dynam* (2013) 72:873–82. doi:10.1007/s11071-013-0759-1.
280. Dai CQ, Zhu HP. Superposed kuznetsov-ma solitons in a two-dimensional graded-index grating waveguide. *J Opt Soc Am B* (2013) 30:3291–7. doi:10.1364/JOSAB.30.003291.
281. Manikandan K, Senthilvelan M, Kraenkel RA. On the characterization of vector rogue waves in two-dimensional two coupled nonlinear schrödinger equations with distributed coefficients. *Eur Phys J B* (2016) 89:218. doi:10.1140/epjb/e2016-70420-0.
282. Yan Z, Konotop VV, Akhmediev N. Three-dimensional rogue waves in nonstationary parabolic potentials. *Phys Rev E* (2010) 82:036610. doi:10.1103/PhysRevE.82.036610.
283. Yu F. Multi-rogue waves for the (3+1)-dimensional coupled higherorder nonlinear schrödinger equations in optical fiber. *Sci Sin Math* (2014) 44:151–63. doi:10.1360/012014-10.
284. Yu F. Nonautonomous rogue wave solutions and numerical simulations for a three-dimensional nonlinear schrödinger equation. *Nonlinear Dynam* (2016) 85:1929. doi:10.1007/s11071-016-2806-1.
285. Wang G. Symmetry analysis and rogue wave solutions for the (2+1)-dimensional nonlinear schrödinger equation with variable coefficients. *Appl Math Lett* (2016) 56:56–64. doi:10.1016/j.aml.2015.12.011.
286. Zhu H, Chen Y. Spatiotemporal superposed rogue-wave-like breathers in a (3+1)-dimensional variable-coefficient nonlinear schrödinger equation. *Nonlinear Anal Model Contr* (2016) 21:77–91. doi:10.15388/NA.2016.1.5.
287. Wang X, Han B. On the breathers and rogue waves to a (2+1)-dimensional nonlinear schrödinger equation with variable coefficients. *Waves Random Complex Media* (2019) 1–11. doi:10.1080/17455030.2019.1646944.
288. Yan Z. Rogon-like solutions excited in the two-dimensional nonlocal nonlinear schrödinger equation. *J Math Anal Appl* (2011) 380:689–96. doi:10.1016/j.jmaa.2011.01.071.
289. Dai CQ, Liu J, Fan Y, Yu DG. Two-dimensional localized peregrine solution and breather excited in a variable-coefficient nonlinear schrödinger equation with partial nonlocality. *Nonlinear Dynam* (2017) 88:1373–83. doi:10.1007/s11071-016-3316-x.
290. Chen YX, Xu FQ, Hu YL. Excitation control for three-dimensional peregrine solution and combined breather of a partially nonlocal variable-coefficient nonlinear schrödinger equation. *Nonlinear Dynam* (2019) 95:1957–64. doi:10.1007/s11071-018-4670-7.
291. Liu Y, Li B. Rogue waves in the (2+1)-dimensional nonlinear schrödinger equation with a parity-time-symmetric potential. *Chin Phys Lett* (2017) 34:010202. doi:10.1088/0256-307X/34/1/010202.
292. Peng WQ, Tian SF, Zhang TT, Fang Y. Rational and semi-rational solutions of a nonlocal (2 + 1)-dimensional nonlinear schrödinger equation. *Math Methods Appl Sci* (2019) 42:6865–77. doi:10.1002/mma.5792.
293. Liu W, Zhang J, Li X. Rogue waves in the two dimensional nonlocal nonlinear schrödinger equation and nonlocal klein-gordon equation. *PloS One* (2018) 13:e0192281. doi:10.1371/journal.pone.0192281.
294. Cao Y, Malomed BA, He J. Two (2+1)-dimensional integrable nonlocal nonlinear schrödinger equations: breather, rational and semi-rational solutions. *Chaos Solit Fractals* (2018) 114:99–107. doi:10.1016/j.chaos.2018.06.029.

295. De KK, Goyal A, Raju TS, Kumar CN, Panigrahi PK. Riccati parameterized self-similar waves in two-dimensional graded-index waveguide. *Optic Commun* (2015) 341:15–21. doi:10.1016/j.optcom.2014.11.101.
296. Wang YY, Dai CQ, Zhou GQ, Fan Y, Chen L. Rogue wave and combined breather with repeatedly excited behaviors in the dispersion/diffraction decreasing medium. *Nonlinear Dynam* (2017) 87:67–73. doi:10.1007/s11071-016-3025-5.
297. Chen YF, Beckwitt K, Wise FW, Aitken BG, Sanghera JS, Aggarwal ID. Measurement of fifth- and seventh-order nonlinearities of glasses. *J Opt Soc Am B* (2006) 23:347–52. doi:10.1364/JOSAB.23.000347.
298. Stegeman GI, Seaton CT. Effects of saturation and loss on nonlinear directional couplers. *Appl Phys Lett* (1987) 50:1035. doi:10.1063/1.97962.
299. Caglioti E, Trillo S, Wabnitz S, Daino B, Stegeman GI. Power-dependent switching in a coherent nonlinear directional coupler in the presence of saturation. *Appl Phys Lett* (1987) 51:293. doi:10.1063/1.98476.
300. Chen Y. Twin core nonlinear couplers with saturable nonlinearity. *Electron Lett* (1990) 26:1374. doi:10.1049/el:19900883.
301. Chen Y. Mismatched nonlinear couplers with saturable nonlinearity. *J Opt Soc Am B* (1991) 8:986–92. doi:10.1364/JOSAB.8.000986.
302. Khadzhi PI, Orlov OK. Light propagation in a directional coupler with saturable nonlinearity. *Tech Phys* (2000) 45:1164–9. doi:10.1134/1.1318103.
303. Gatz S, Herrmann J. Soliton propagation in materials with saturable nonlinearity. *J Opt Soc Am B* (1991) 8:2296–302. doi:10.1364/JOSAB.8.002296.
304. Herrmann J. Propagation of ultrashort light pulses in fibers with saturable nonlinearity in the normal-dispersion region. *J Opt Soc Am B* (1991) 8:1507–11. doi:10.1364/JOSAB.8.001507.
305. Coutaz JL, Kull M. Saturation of the nonlinear index of refraction in semiconductor-doped glass. *J Opt Soc Am B* (1991) 8:95–8. doi:10.1364/JOSAB.8.000095.
306. Hickmann JM, Cavalcanti SB, Borges NM, Gouveia EA, Gouveia-Neto AS. Modulational instability in semiconductor-doped glass fibers with saturable nonlinearity. *Opt Lett* (1993) 18:182–4. doi:10.1364/OL.18.000182.
307. da Silva GL, Gleria I, Lyra ML, Sombra ASB. Modulational instability in lossless fibers with saturable delayed nonlinear response. *J Opt Soc Am B* (2009) 26:183–8. doi:10.1364/JOSAB.26.000183.
308. Charalampidis EG, Cuevas-Maraver J, Frantzeskakis DJ, Kevrekidis PG. Rogue waves in ultracold bosonic seas. *Rom Rep Phys* (2018) 70:1–25.
309. Akhmediev N, Korneev V, Mitskevich N. N-modulation signals in a single-mode optical waveguide under nonlinear conditions. *Sov Phys JETP* (1988) 67:89–95. doi:10.1016/j.revip.2019.100037.

Conflict of Interest: The authors declare that the research was conducted in the absence of any commercial or financial relationships that could be construed as a potential conflict of interest.

frontiers in Physics

BRIEF RESEARCH REPORT
published: 07 December 2020
doi: 10.3389/fphy.2020.608894

Ghost Interaction of Breathers

Gang Xu[1], *Andrey Gelash*[2,3], *Amin Chabchoub*[4,5], *Vladimir Zakharov*[3,6,7] *and Bertrand Kibler*[1]*

[1]Laboratoire Interdisciplinaire Carnot de Bourgogne (ICB), UMR CNRS-Université Bourgogne Franche-Comté, Dijon, France, [2]Institute of Automation and Electrometry SB RAS, Novosibirsk, Russia, [3]Skolkovo Institute of Science and Technology, Moscow, Russia, [4]Centre for Wind, Waves and Water, School of Civil Engineering, The University of Sydney, Sydney, NSW, Australia, [5]Marine Studies Institute, The University of Sydney, Sydney, NSW, Australia, [6]Landau Institute for Theoretical Physics RAS, Chernogolovka, Russia, [7]Department of Mathematics, University of Arizona, Tucson, AZ, United States

Mutual interaction of localized nonlinear waves, e.g., solitons and modulation instability patterns, is a fascinating and intensively-studied topic of nonlinear science. Here we report the observation of a novel type of breather interaction in telecommunication optical fibers, in which two identical breathers propagate with opposite group velocities. Under controlled conditions, neither amplification nor annihilation occurs at the collision point and most interestingly, the respective envelope amplitude, resulting from the interaction, almost equals another envelope maximum of either oscillating and counterpropagating breather. This ghost-like breather interaction dynamics is fully described by an *N*-breather solution of the nonlinear Schrödinger equation.

Keywords: nonlinear waves, modulation instability, breathers, solitons, nonlinear fiber optics

OPEN ACCESS

Edited by:
Manuel Asorey,
University of Zaragoza, Spain

Reviewed by:
Haci Mehmet Baskonus,
Harran University, Turkey
Abdullahi Yusuf,
Federal University, Nigeria

***Correspondence:**
Bertrand Kibler
bertrand.kibler@u-bourgogne.fr

Specialty section:
This article was submitted to Mathematical and Statistical Physics, a section of the journal Frontiers in Physics

Received: *22 September 2020*
Accepted: *10 November 2020*
Published: *07 December 2020*

Citation:
Xu G, Gelash A, Chabchoub A, Zakharov V and Kibler B (2020) Ghost Interaction of Breathers. Front. Phys. 8:608894. doi: 10.3389/fphy.2020.608894

INTRODUCTION

The study of both, formation and interaction of localized waves has been a central task in nonlinear physics during the last decades, including plasma physics, fluid dynamics, Bose-Einstein condensates and photonics. Among different types of nonlinear localized waves, solitons are the most representative and ideal testbed to investigate nonlinear wave interactions due to their intrinsic particle-like properties during propagation [1–4]. A generic and relevant case of study for various fields of research is the elastic and nonlinear interaction of envelope solitons, which can be described by the focusing one-dimensional nonlinear Schrödinger equation (NLSE). In this conservative and integrable system, the possible collision of solitons with different velocities does not affect their shape or velocity after interaction, and their main physical properties keep unchanged. In general, the interaction-induced displacement in position and phase shift are independent on the relative phases of the envelope solitons. However, collision dynamics in the interaction region strongly depends on the relative phases. Consequently, in the simplest case of two-soliton collision with opposite velocities, as shown in **Figures 1A1–D1** the two solitons appear to attract with each other and cross (forming a transient peak) in the *in-phase* configuration, while they seem to repel each other and as such stay apart in the *out-of-phase* case. The wave magnitude at the central point of collision then evolves from the sum of the two solitons' amplitudes (i.e., amplification) to their difference (i.e., annihilation), respectively. A large range of theoretical descriptions, numerical simulations and experimental observations of such soliton interactions and their possible synchronization have been reported earlier [5–12].

Besides solitons, breather solutions of the NLSE are also exciting examples to investigate nonlinear wave interactions because of the salient complexities of breather synchronization in relation to their self-oscillating properties. From this point of view, phase-sensitive breather interactions are now widely studied [13–22]. More particularly, for co-propagative breathers,

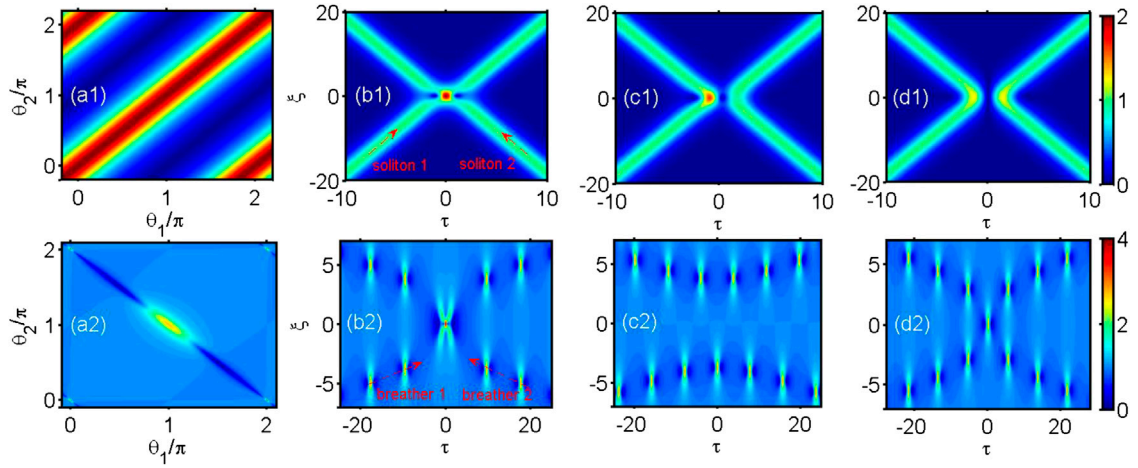

FIGURE 1 | Typical temporal evolution of soliton-pair interaction (first line) and breather-pair interaction (second line). **(A1)** Dependence of amplitude at the soliton collision point $|\psi_{2S}(0,0)|$ on the soliton phases θ_1 and θ_2. **(B1–D1)** Amplitude evolution of soliton collision with soliton phases: $\theta_1 = 0$, $\theta_2 = 0$ (b1); $\theta_1 = \pi/2$, $\theta_2 = 0$ (c1); $\theta_1 = \pi$, $\theta_2 = 0$ (d1). (b1-d1) are plotted based on the two-soliton solution of NLSE with the soliton parameters: angular frequencies $\Omega_1 = -\Omega_2 = 0.5$; soliton amplitudes $A_1 = A_2 = 1$. **(A2)** Dependence of amplitude at the breather collision point $|\psi_{2B}(0,0)|$ on temporal phases θ_1 and θ_2. Prototypes of interactions include Amplification **(B2)**, Annihilation **(C2)**, and "Ghost interaction" **(D2)**. **(A1–D2)** are plotted based on the one-pair breather solution of NLSE. In all these cases, key parameters of breathers are listed as follows $R_1 = R_2 = 1.05$, $\alpha_1 = -\alpha_2 = 0.4$, $\mu_1 = \mu_2 = 0$. while $\theta_1 = \theta_2 = 0$ for **(B2)**; $\theta_1 = \theta_2 = \pi/2$ for **(C2)** and $\theta_1 = \theta_2 = \pi$ for **(D2)**. Red arrows in **(B1)** and **(B2)** indicate the moving motions of solitons and breathers respectively.

breather molecules can be formed when group velocity and temporal phase of breathers are perfectly synchronized, while for counter-propagating breathers, the phase-sensitive collision process exhibits various dynamical behaviors. Two of them have been studied in detail in the context of rogue wave formation, namely amplification and annihilation cases that resemble soliton collisions. The above interactions are fully described by *N*-breather solutions of the NLSE [16, 18]. However, the two-breather collision has been recently found to provide a peculiar third configuration for particular phases, neither of the above-mentioned cases, the later leads to a peak amplitude at the central point of collision equivalent to the single breather amplitude before or after the collision. Phenomenologically, it seems that one breather *mysteriously* disappears in the nonlinear interaction region, but it then appears after that. That is why this intriguing breather interaction was vividly termed by "ghost interaction" [19]. Its generalization to the *N*-breather interaction is still under investigation. However, both, detailed analysis and experimental confirmation of this remarkable dynamics for the simplest two-breather collision are still to emerge into light.

To address this scientific gap, we present the observation of ghost interaction of two breathers in a single-pass telecommunication optical fiber experiment. By means of the Fourier-transform pulse shaping technique applied to an optical frequency comb, we generate the initial condition for two counter-propagating breathers with desired temporal phases. The experimental results are in excellent agreement with the exact two-breather solution of the NLSE. We confirm that this peculiar phase-sensitive breather interaction is strictly different to the well-known soliton interactions. Our study paves the way for novel directions of investigation in the rich landscape of complex nonlinear wave dynamics [23–26].

METHOD

Theoretical Model and Breather Solutions

Our theoretical framework and starting point is based on the dimensionless form of the self-focusing 1D-NLSE:

$$i\psi_\xi + \frac{1}{2}\psi_{\tau\tau} + |\psi|^2\psi = 0, \tag{1}$$

where subscripts stand for partial differentiations. Here, ψ is a wave envelope, which is a function of ξ (a scaled propagation distance or longitudinal variable) and τ (a co-moving time, or transverse variable, moving with the wave group-velocity). This conventional form of the NLSE is widely used to describe the nonlinear dynamics of one-dimensional optical and water waves [25]. This integrable equation can be solved using various techniques and admits a wide class of unstable pulsating solutions known as breathers [13]. The simplest cases (i.e., first-order breathers) are well-known localized structures emerging from the modulation instability process [26]. The general one-breather solution is a localized wave envelope which coat the plane wave in space-time and propagate with a particular group velocity and oscillating period in relation to carrier. This also includes limiting cases such as time-periodic Akhmediev breathers [13], space-periodic Kuznetsov-Ma breathers [27, 28] and the doubly-localized Peregrine breather [29], which have been observed in various experimental configurations [30–37]. Higher-order

breathers can be simply generated by considering the interaction of the above elementary breathers, thus, associated to the nonlinear superposition of multiple breathers [13, 38, 39]. More generally, the NLSE has an exact N-breather solution, which can be constructed by appropriate integration technique by studying the auxiliary linear Zakharov-Shabat system. More technical details to solve the NLSE, e.g., applications of the dressing method are reported in Refs. [16, 18]. In the following, we restrict our work to the general two-breather solution. It has four main parameters $R_{1,2}$, $\alpha_{1,2}$ (subscripts 1 and 2 correspond to the first and second breather) which control the main breather properties (localization, group velocity, and oscillation) and four additional parameters $\mu_{1,2} \in [-\infty, \infty]$ and $\theta_{1,2}$ varying between 0 et 2 π that define the location and phase of each breather. More details can be found in Ref. [40]. In particular, we study the simplest one-pair breather solution ψ_{2B} with breathers moving in opposite directions in the (ξ, τ) -plane that can be obtained by setting $R_1 = R_2 = 1 + \varepsilon = R$, $\alpha_1 = -\alpha_2 = \alpha$. The resulting solution can be written as follows:

$$\psi_{2B}(\xi, \tau) = \left[1 + \left(R^2 - \frac{1}{R^2}\right)\frac{N}{\Delta} sin2\alpha\right]e^{i\xi}, \tag{2}$$

where

$$N = \left(R - \frac{1}{R}\right)\sin\alpha\left(|q_1|^2 q_{21}^* q_{22} + |q_2|^2 q_{11}^* q_{12}\right) - i\left(R + \frac{1}{R}\right)\cos\alpha\left[\left(q_1^* q_2\right)q_{21}^* q_{12} - \left(q_1 q_2^*\right)q_{11}^* q_{22}\right]$$

and

$$\Delta = \left(R + \frac{1}{R}\right)^2 \cos^2\alpha\left|q_{11}q_{22} - q_{12}q_{21}\right|^2 + \left(R + \frac{1}{R}\right)^2 |q_1|^2 |q_2|^2 \sin^2\alpha$$

In these expressions, $q_i = (q_{i1}, q_{i2})$ with $i = 1, 2$ as a two-component vector function, which contains the following components:

$$q_{11} = e^{-\varphi_1} - \frac{e^{-\varphi_1 - i\alpha}}{R},$$

$$q_{12} = e^{\varphi_1} - \frac{e^{-\varphi_1 - i\alpha}}{R},$$

$$q_{21} = e^{-\varphi_2} - \frac{e^{\varphi_1 + i\alpha}}{R},$$

$$q_{22} = e^{\varphi_2} - \frac{e^{-\varphi_2 + i\alpha}}{R}$$

with $\varphi_1 = \eta\tau + \gamma\xi + \frac{\mu_1}{2} + i\left(k\tau + \omega\xi + \frac{\theta_1}{2}\right)$ and $\varphi_2 = \eta\tau - \gamma\xi + \frac{\mu_2}{2} - i\left(k\tau - \omega\xi + \frac{\theta_2}{2}\right)$.

The parameters η, k, γ and ω are defined as:

$$\eta = -\frac{1}{2}\left(R - \frac{1}{R}\right)\cos\alpha,$$

$$k = -\frac{1}{2}\left(R + \frac{1}{R}\right)\sin\alpha,$$

and

$$\gamma = -\frac{1}{2}\left(R^2 + \frac{1}{R^2}\right)\sin2\alpha$$

$$\omega = \frac{1}{2}\left(R^2 - \frac{1}{R^2}\right)\cos2\alpha$$

Figures 1A2–D2 presents the interaction of a pair of counter-propagating breathers when $R_1 = R_2 = 1.05$, $\alpha_1 = -\alpha_2 = 0.4$, thus corresponding to two identical and symmetric breathers propagating with the same oscillating frequency but opposite group velocities. Here, we fixed the temporal position $\mu_{1,2} = 0$, so the central point of collision locates at the origin $(\xi = 0, \tau = 0)$. According to the two-breather solution of the NLSE, we continuously vary the breather phase $\theta_{1,2}$ over the full range $[0, 2\pi]$ to analyze its impact on the resulting waveform and amplitude at the origin. As shown in **Figure 1A2**, the amplitude of the collision-induced wave $|\psi_{2B}(0,0)|$ strongly depends on $\theta_{1,2}$ values, the maximum is obtained for $\theta_{1,2} = 0$ or $\theta_{1,2} = 2\pi$, when synchronization of the maximal amplitude of pulsating breathers is perfectly reached. When $\theta_{1,2} \sim \pi/2$, the amplitude at the central point of collision decreases to a minimum value close to the constant background amplitude $|\psi_0| \sim 1$. Interestingly, there is another local peak of $|\psi_{2B}(0,0)|$ at $\theta_{1,2} = \pi$, whose amplitude is very close to that of a single breather before or after the collision $|\psi_1| \sim 2.7$. In order to improve the unveiling of the space-time dynamics of such breather interactions, we depict the full wave evolution in **Figure 1B2–D2** for the following cases: 1) $\theta_1 = \theta_2 = 0$, the synchronized collision of breathers that generates a rogue peak with extremely high amplitude (already reported experimentally in Ref. [15]); 2) $\theta_1 = \theta_2 = \pi/2$, the quasi-annihilation of breathers that gives rise to very small perturbations located on the plane wave (already reported experimentally in Ref. [19]). However, note that in this case, we observe a jump of wave field symmetry before and after the collision of these two breathers because of the noticeable π -phase shift (see **Figure 1C2**). This specific configuration of breather collision also known as superregular breathers can be regarded as a prototype of small localized perturbations of the plane wave for describing modulation instability [16]; 3) $\theta_1 = \theta_2 = \pi$, the two breathers are almost transformed into a single one in the main local interaction and interaction region, at the origin $|\psi_{2B}(0,0)| \sim |\psi_1|$, which raises the impression that one breather has vanished (see **Figure 1D2**).

We emphasize that such ghost interaction of breathers as illustrated in **Figure 1D2** cannot occur for the soliton counterpart (see **Figures 1A1–D1**). To clarify this point, we compare systematically the phase-dependent soliton collision and the phase-dependent breather collision. Similarly, we consider a pair of counter-propagating solitons with the amplitudes $A_1 = A_2 = A$ and the frequencies $\Omega_1 = -\Omega_2 = \Omega$. In this configuration, the two-soliton solution (on zero-background) can be written in the following form [18]:

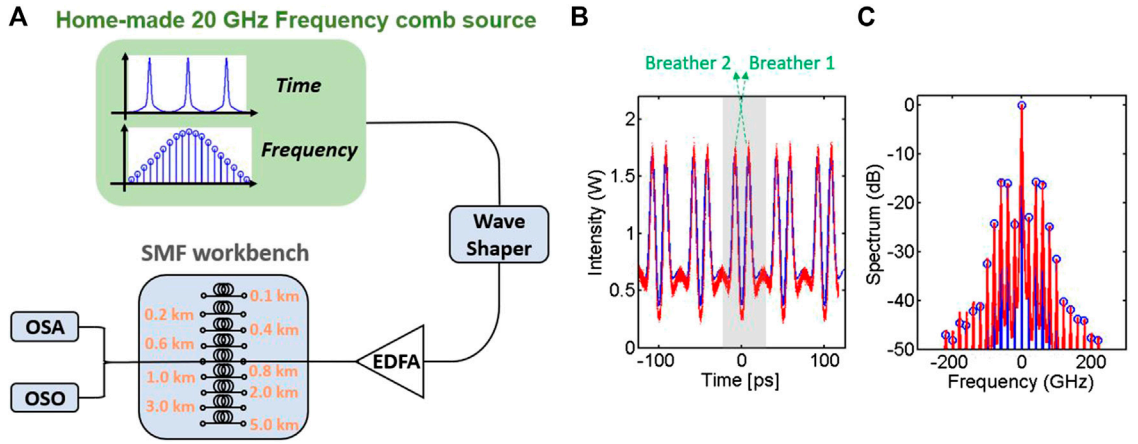

FIGURE 2 | Experimental setup and generation of initial conditions. **(A)** Schematic diagram of the experimental setup. EDFA: erbium-doped fiber amplification; SMF: single mode fiber; OSA: optical spectral analyzer; OSO: optical sampling oscilloscope. Shaded-green box represents the home-made frequency comb source with a repetition rate of 20 GHz. **(B–C)** Designed initial conditions at 20 GHz repetition rate for a pair of contra-propagative breathers in both temporal and spectral domains. Solid blue lines are theoretical curves; Solid red lines are experimental measurements. Here breather parameters are: $R_{1,2} = 1.5$, $\alpha_1 = -\alpha_2 = 0.5$, $\mu_{1,2} = 0$, $\theta_{1,2} = \pi$.

$$\psi_{2S}(\xi,\tau) = 2A\frac{\Omega^2\left(|q_1|^2 q_{21}^* q_{22} + |q_2|^2 q_{11}^* q_{12}\right) - i\mathbf{A}\Omega\left[(q_1^* q_2)q_{21}^* q_{12} - (q_2^* q_1)q_{11}^* q_{22}\right]}{A^2|q_{11}q_{22} - \boldsymbol{q}_{12}q_{21}|^2 + \Omega^2|q_1|^2|q_2|^2}e^{i\xi}, \tag{3}$$

In this expression, $q_i = (q_{i1}, q_{i2})$ with $i = 1, 2$ is a two-component vector function having the following components: $q_{11} = e^{-\varphi_1}$, $q_{12} = e^{\varphi_1}$, $q_{21} = e^{-\varphi_2}$, $q_{22} = e^{\varphi_2}$, with

$$\varphi_1 = \frac{A}{2}\tau + \frac{A\Omega}{2}\xi + \frac{\mu_1}{2} + i\left(\frac{\Omega}{2}\tau + \frac{\Omega^2 - A^2}{4}\xi + \frac{\theta_1}{2}\right) \text{ and}$$

$$\varphi_2 = \frac{A}{2}\tau - \frac{A\Omega}{2}\xi + \frac{\mu_2}{2} + i\left(-\frac{\Omega}{2}\tau + \frac{\Omega^2 - A^2}{4}\xi + \frac{\theta_2}{2}\right).$$

Again, the μ and θ are key parameter to control the soliton position and phase. We set $\mu_1 = \mu_2 = 0$ and **Figure 1A1** demonstrates the dependence of the amplitude at the collision point $|\psi_{2S}(0,0)|$ on θ_1 and θ_2. Compared to the breather collisions, here the key parameter for soliton collision is the relative soliton phase $\theta_1 - \theta_2$. In general, amplification interaction occurs for $\theta_1 - \theta_2 = 0$, and annihilation interaction happens for $\theta_1 - \theta_2 = \pi$. While for other values of relative soliton phase, $|\psi_{2S}(0,0)|$ keeps being low (~ 0), and a partial energy exchange occurs from one soliton to another in the collision area which leads to a remarkable significant time-parity symmetry transformation (examples shown in **Figures 1B1–D1**).

Experimental Setup

In order to validate these theoretical predictions with respect to ghost interaction of breathers, we have performed experiments with light waves propagating in high-speed telecommunication-grade components, as depicted in **Figure 2**. The main challenge here is the arbitrary wave shaping to establish the specific initial excitation of counter-propagating breathers with desired phases in the (ξ, τ) -plane (more details can be found in Ref. [41]).

To this end, a 20 GHz optical frequency comb passes through a programmable optical filter (wave-shaper) to precisely control both amplitude and phase characteristics of each comb line. As a result, we can synthesize any arbitrary perturbation of a continuous wave background in a time-periodic pattern whose frequency is equal to the comb spacing. This temporal pattern is then amplified by erbium-doped fiber amplifier (EDFA) to achieve the exact excitation of the two-breather solution in terms of average power for nonlinear propagation into our single-mode optical fiber (SMF). The corresponding temporal and spectral power profiles of the light-wave are presented in **Figures 2B–C**. Note that the initial condition for the breather pair is time-periodic with a period of 50 ps. Hereafter, we select the center time slot $(-25\,\text{ps} < t < 25\,\text{ps})$ to investigate the collision dynamics of the breather pair as shown in gray shaded area in **Figure 2B**. The nonlinear propagation is studied with different lengths of the same fiber and characterized by means of an optical sampling oscilloscope (OSO) with sub-picosecond resolution in the time domain and a high dynamics-range optical spectrum analyzer (OSA) in the Fourier domain. The maximum propagation distance fixed was chosen to limit the impact of linear propagation losses in our optical fiber as well as possible interaction occurring between neighboring elements of the periodic pattern. Our fiber properties are the following: group velocity dispersion $\beta_2 = -21.1\,\text{ps}^2\text{km}^{-1}$, linear losses $\alpha = 0.2\,\text{dB km}^{-1}$, and nonlinear coefficient $\gamma = 1.2\,\text{W}^{-1}\text{km}^{-1}$.

RESULTS

We present our experimental results on the nonlinear space-time evolution of the breather pair studied in the above theoretical section, for the specific temporal phases $\theta_1 = \theta_2 = \pi$. To this purpose, we fixed the average power to $P_0 = 0.74\,W$. Then, we

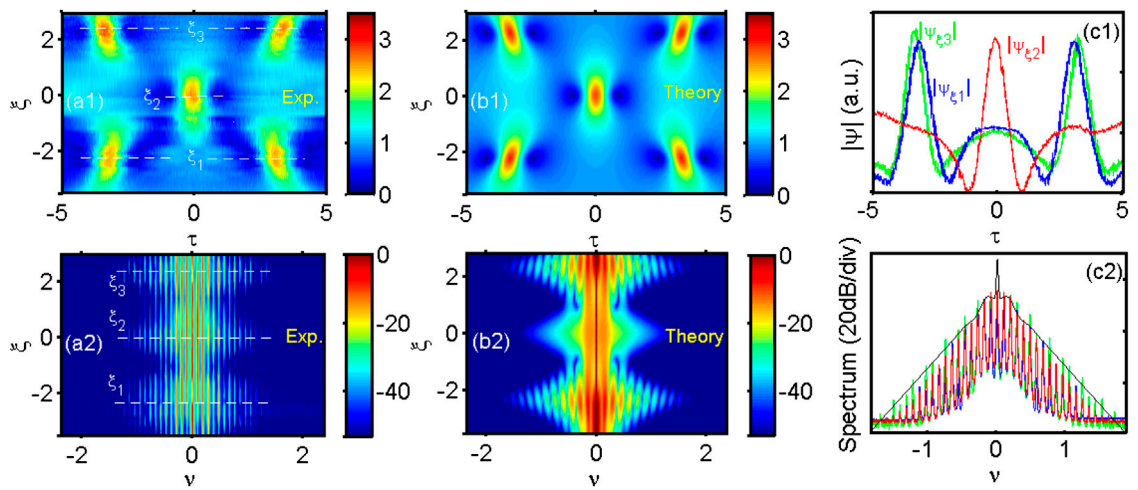

FIGURE 3 | Experimental observation of ghost interaction of two breathers. Color maps showing the evolution of temporal amplitude **(A1)** and power spectrum **(A2)** for the two breathers observed in experiment. Dashed white lines indicate the position of local maximum amplitudes, which are also the position of largest spectral broadenings, before collision ($\xi_1 \sim -2.2$), during collision ($\xi_2 \sim 0$) and after collision ($\xi_3 \sim 2.2$). **(B1–B2)** Corresponding theoretical predictions based on the two-breather solution of NLSE. **(C1)** Comparison of the amplitude profiles measured at $\xi = \xi_1$ (blue curve), $\xi = \xi_2$ (red curve) and $\xi = \xi_3$ (green curve). **(C2)** Comparison of power spectra recorded at $\xi = \xi_1$ (blue curve), $\xi = \xi_2$ (red curve) and $\xi = \xi_3$ (green curve). Thin dark curve is the theoretical spectrum at $\xi = 0$. Key parameters of the breather pair: $R_{1,2} = 1.5$, $\alpha_1 = -\alpha_2 = 0.5$, $\mu_{1,2} = 0$, $\theta_{1,2} = \pi$.

gradually increase the propagation distance (i.e., the fiber length) by a step of 100 m. The correspondence between normalized and physical units can be retrieved by making use of the following relations between dimensional distance z (m) and time t (s) with the previously mentioned normalized units: $z = \xi L_{NL}$ and $t = \tau t_0$. In these expressions, the characteristic (nonlinear) length and time scales are $L_{NL} = (\gamma P_0)^{-1} \sim 1216\,\mathrm{m}$ and $t_0 = \sqrt{|\beta_2| L_{NL}} \sim 4.74$ ps, respectively. The dimensional optical field $A(z,t)\,(\mathrm{W}^{1/2})$ is $A = \sqrt{P_0}\,\psi$.

Figures 3A1–A2 presents the concatenation of temporal (amplitude) profiles and power spectra which were recorded at the output of the distinct fiber segments with increasing length. The careful control of phases allows to observe the ghost interaction between the counter-propagating breathers. The full space-time dynamics is indeed in excellent agreement with theory shown in **Figures 3B1–B2**. We can notice the five mains peaks appearing during the whole evolution studied in **Figure 3A1**: two peaks at $\xi_1 \sim -2.2$ for the two breathers before collision; one peak at $\xi_2 \sim 0$ at the collision point; and two peaks at $\xi_3 \sim 2.2$ for the two breathers after the collision. Correspondingly, we observe the maxima of spectral broadening for respectively $\xi = \xi_1$, $\xi = \xi_2$ and $\xi = \xi_3$ (shown in **Figure 3A2**), thus, confirming the different nonlinear temporal focusing patterns. **Figure 3C1** presents the comparison of the recorded temporal waveforms for $|\psi(\xi = \xi_1, \tau)|$, $|\psi(\xi = \xi_2, \tau)|$ and $|\psi(\xi = \xi_3, \tau)|$. Strikingly, all these five peaks are found to nearly exhibit similar waveforms and maximum amplitudes, this is also corroborated by the spectral analysis reported in **Figure 3C2**. Only very minor discrepancies can be noticed mainly ascribed to the linear propagation losses in our optical fiber and some artifacts of the initial wave shaping.

DISCUSSION

As shown above, during the ghost interaction of two breathers, only a single breather peak remains occurrent at the collision point. The reason for this intriguing phenomenon is related to the fact that there is a continuous and varying power exchange between the background and each localized perturbation all along the propagation, which is an intrinsic property of breathers. Therefore, when these two breathers nonlinearly interact near the collision point, for a given particular phase-collision-interaction, one of the breather peaks appears to be almost hidden in the background and then emerges again after the collision by following the energy conservation. Moreover, the breather pair keeps the spatial and temporal symmetry during the whole evolution. It is also worth to mention that such peculiar ghost interaction does not occur in conventional soliton-soliton collision scenarios because of the lack of pulse-background energy exchange [see **Figures 1A1–D1**].

In summary, we performed a systematic theoretical comparison between the phase-sensitive soliton-soliton collisions and breather-breather collisions. All different configurations are fully described by the exact N-breather solution of the NLSE. More importantly, we provided the *first* experimental observation of the very fascinating type of ghost interaction of breathers, which confirms our theoretical predictions. We also point out that our study is here restricted to the interaction of two identic counter-propagating breathers, while much more complicated many-body interactions of breathers with asymmetric conditions, including different amplitudes and/or oscillating frequencies, still require

further investigations. Our current results concede a novel step toward the understanding of interactions between localized waves in nonlinear physics. These may naturally lead to encourage further relevant experimental studies and theoretical investigations in various fields of nonlinear wave physics.

DATA AVAILABILITY STATEMENT

The original contributions presented in the study are included in the article/Supplementary Material, further inquiries can be directed to the corresponding author.

AUTHOR CONTRIBUTIONS

All authors listed have made significant contributions to the theoretical and experimental developments, data acquisition, results interpretation and manuscript writing.

FUNDING

French National Research Agency (PIA2/ISITE-BFC, Grant No. ANR-15-IDEX-03, "Breathing Light" project). Theoretical part of the work was supported by Russian Science Foundation (Grant No. 19-72-30028).

REFERENCES

1. Dauxois T, Peyrard M. *Physics of solitons*. Cambridge: Cambridge University Press (2006).
2. Kivshar Y, Agrawal G. *Optical solitons: from fibers to photonic crystals*. London: Academic Press (2003).
3. Zabusky N, Kruskal M. Interaction of "solitons" in a collisionless plasmas and the recurrence of initial states. *Phys Rev Lett* (1965) 15:240. doi:10.1103/PhysRevLett.15.240
4. Stegeman G, Segev M. Optical spatial solitons and their interactions: universality and diversity. *Science* (1999) 286:1518. doi:10.1126/science.286.5444.1518
5. Zakharov V, Shabat A. Exact theory of two-dimensional self-focusing and one-dimensional self-modulation of wave in nonlinear media. *Sov Phys JETP* (1972) 34:62. Available from: http://www.jetp.ac.ru/cgi-bin/dn/e_034_01_0062.pdf (Accessed January 1972).
6. Yuen H, Lake B. Nonlinear dynamics of deep-water gravity waves. *Adv Appl Mech* (1982) 22:67. doi:10.1016/S0065-2156(08)70066-8
7. Gordon J. Interaction forces among solitons in optical fibers. *Opt Lett* (1983) 8:596. doi:10.1364/OL.8.000596
8. Mitschke F, Mollenaurer L. Experimental observation of interaction forces between solitons in optical fibers. *Opt Lett* (1987) 12:355. doi:10.1364/OL.12.000355
9. Islam M, Soccolich C, Gordon J. Ultrafast digital soliton logic gates. *Opt Quant Electron* (1992) 24:S1215. doi:10.1007/BF00624671
10. Antikainen A, Erkintalo M, Dudley J, Genty G. On the phase-dependent manifestation of optical rogue waves. *Nonlinearity* (2012) 25:R73. doi:10.1088/0951-7715/25/7/R73
11. Nguyen JHV, Dyke P, Luo D, Malomed BA, Hulet RG. Collisions of matter-wave solitons. *Nat Phys* (2014) 10:918. doi:10.1038/nphys3135
12. Sun Y-H. Soliton synchronization in the forcing nonlinear Schrodinger equation. *Phys Rev E* (2016) 93:052222. doi:10.1103/PhysRevE.93.052222
13. Akhmediev N, Ankiewicz A. *Nonlinear pulses and beams*. London: Chapman & Hall (1997).
14. Akhmediev N, Soto-Crespo J, Ankiewicz A. Extreme waves that appear from nowhere: on the nature of rogue waves. *Phys Lett* (2009) 373:2137. doi:10.1016/j.physleta.2009.04.023
15. Frisquet B, Kibler B, Millot G. Collision of Akhmediev breathers in nonlinear fiber optics. *Phys Rev X* (2013) 3:041032. doi:10.1103/PhysRevX.3.041032
16. Zakharov V, Gelash A. Nonlinear stage of modulation instability. *Phys Rev Lett* (2013) 111:054101. doi:10.1103/PhysRevLett.111.054101
17. Chabchoub A, Akhmediev N. Observation of rogue wave triplets in water waves. *Phys Lett* (2013) 377:2590. doi:10.1016/j.physleta.2013.07.027
18. Gelash A, Zakharov V. Superregular solitonic solutions: a novel scenario for the nonlinear stage of modulation instability. *Nonlinearity* (2014) 27:R1. doi:10.1088/0951-7715/27/4/R1
19. Kibler B, Chabchoub A, Gelash A, Akhmediev N, Zakharov V. Superregular breathers in optics and hydrodynamics: omnipresent modulation instability beyond simple periodicity. *Phys Rev X* (2015) 5:041026. doi:10.1103/PhysRevX.5.041026
20. Xu G, Gelash A, Chabchoub A, Zakharov V, Kibler B. Breather wave molecules. *Phys Rev Lett* (2019) 122:084101. doi:10.1103/PhysRevLett.122.084101
21. Wu Y, Liu C, Yang Z, Yang W. Breather interaction properties induced by self-steepening and space-time correction. *Chin Phys Lett* (2020) 37:040501. doi:10.1088/0256-307X/37/4/040501
22. Gelash A. Formation of rogue waves from a locally perturbed condensate. *Phys Rev E* (2018) 97:022208. doi:10.1103/PhysRevE.97.022208
23. Xu G, Chabchoub A, Pelinovsky DE, Kibler B. Observation of modulation instability and rogue breathers on stationary periodic waves. *Phys. Rev. Res.* (2020) 2:033528. doi:10.1103/PhysRevResearch.2.033528
24. Copie F, Randoux S, Suret P. The Physics of the one-dimensional nonlinear Schrödinger equation in fiber optics: rogue waves, modulation instability and self-focusing phenomena. *Rev. Phys.* (2020) 5:100037. doi:10.1016/j.revip.2019.100037
25. Dudley JM, Genty G, Mussot A, Chabchoub A, Dias F. Rogue waves and analogies in optics and oceanography. *Nat. Phys. Rev.* (2019) 1:675. doi:10.1038/s42254-019-0100-0
26. Dudley JM, Dias F, Erkintalo M, Genty G. Instability, breathers and rogue waves in optics. *Nat Photon* (2014) 8:755. doi:10.1038/nphoton.2014.220
27. Kuznetsov E. On solitons in parametrically unstable plasma. *Dokl Akad Nauk SSSR* (1977) 236:575, 1977 . Available from: http://mi.mathnet.ru/eng/dan41246 (Accessed May 2 1977).
28. Ma Y. The perturbed plan-wave solutions of the cubic Schrodinger equation. *Stud Appl Math* (1979) 60:43. doi:10.1002/sapm197960143
29. Peregrine D. Water waves, nonlinear Schrodinger equation and their solutions. *J. Aust. Soc. Series B, Appl. Math.* (1983) 25:16. doi:10.1017/S0334270000003891
30. Kibler B, Fatome J, Finot C, Millot G, Dias F, Genty G, et al. The Peregrine soliton in nonlinear fiber optics. *Nat Phys* (2010) 6:790. doi:10.1038/nphys1740
31. Kibler B, Fatome J, Finot C, Millot G, Genty G, Wetzel B, et al. Observation of Kuznetsov-Ma soliton dynamics in optical fiber. *Sci Rep* (2012) 2:463. doi:10.1038/srep00463
32. Chabchoub A, Hoffmann N, Akhmediev N. *Phys Rev Lett* (2011) 106:204502. doi:10.1103/PhysRevLett.106.204502
33. Bailung H, Sharma SK, Nakamura Y. Observation of Peregrine solitons in a multicomponent plasma with negative ions. *Phys Rev Lett* (2011) 107:255005. doi:10.1103/PhysRevLett.107.255005
34. Chabchoub A, Kibler B, Dudley JM, Akhmediev A. Hydrodynamics of periodic breathers. *Phil. Trans. R. Soc. A* (2014) 372:20140005. doi:10.1098/rsta.2014.0005
35. Närhi M, Wetzel B, Billet C, Toenger S, Sylvestre T, Merolla J-M, et al. Nat. Commun., Real-time measurements of spontaneous breathers and rogue wave events in optical fiber modulation instability. *Nat Commun* (2016) 7:13675. doi:10.1038/ncomms13675
36. Suret P, El Koussaifi R, Tikan A, Evain C, Randoux S, Szwaj C, et al. Bielawski S. Single-shot observation of optical rogue waves in integrable turbulence using time microscopy. *Nat Commun* (2016) 7:13136. doi:10.1038/ncomms13136
37. Xu G, Hammani K, Chabchoub A, Dudley JM, Kibler B, Finot C. Phase evolution of Peregrine-like breathers in optics and hydrodynamics. *Phys Rev E* (2019) 99:012207. doi:10.1103/PhysRevE.99.012207

38. Erkintalo M, Hammani K, Kibler B, Finot C, Akhmediev N, Dudley JM, et al.Genty G. Higher-order modulation instability in nonlinear fiber optics. *Phys Rev Lett* (2011) 107:253901. doi:10.1103/PhysRevLett.107.253901
39. Kedziora D, Ankiewicz A, Akhmediev N. Classifying the hierarchy of nonlinear-Schrodinger-equation rogue-wave solutions. *Phys Rev E* (2013) 88:013207. doi:10.1103/PhysRevE.88.013207
40. Kibler B, Chabchoub A, Gelash A, Akhmediev N, Zakharov V. Ubiquitous nature of modulation instability: from periodic to localized perturbations. In: Wabnitz S, editor. *Nonlinear guided wave optics*. Bristol: IOP Publishing (2017).
41. Frisquet B, Chabchoub A, Fatome J, Finot C, Kibler B, Millot G. Two-stage linear-nonlinear shaping of an optical frequency comb as rogue nonlinear-Schrödinger-equation-solution generator. *Phys. Rev. A* (2014) 89:023821. doi:10.1103/PhysRevA.89.023821

Conflict of Interest: The authors declare that the research was conducted in the absence of any commercial or financial relationships that could be construed as a potential conflict of interest.

frontiers in Physics

BRIEF RESEARCH REPORT
published: 14 January 2021
doi: 10.3389/fphy.2020.590415

A Peregrine Soliton-Like Structure That Has Nothing to Deal With a Peregrine Breather

*Christophe Finot**

Laboratoire Interdisciplinaire Carnot de Bourgogne, UMR 6303 CNRS-Université Bourgogne-Franche Comté, 21000 Dijon, France

We report on experimental results where a temporal intensity profile presenting some of the main signatures of the Peregrine soliton (PS) is observed. However, the emergence of a highly peaked structure over a continuous background in a normally dispersive fiber cannot be linked to any PS dynamics and is mainly ascribed to the impact of Brillouin backscattering.

Keywords: peregrine soliton, optical fiber, nonlinear propagation, brillouin scattering, ultrashort pulses

OPEN ACCESS

Edited by:
Heremba Bailung, Ministry of Science and Technology (India), India

Reviewed by:
Plerre Suret, Université de Lille, France
Supriyo Bandyopadhyay, Virginia Commonwealth University, United States

***Correspondence:**
Christophe Finot
christophe.finot@u-bourgogne.fr

Specialty section:
This article was submitted to Optics and Photonics, a section of the journal Frontiers in Physics

Received: *01 August 2020*
Accepted: *28 October 2020*
Published: *14 January 2021*

Citation:
Finot C (2021) A Peregrine Soliton-Like Structure That Has Nothing to Deal With a Peregrine Breather. Front. Phys. 8:590415. doi: 10.3389/fphy.2020.590415

INTRODUCTION

Peregrine soliton (PS) or breather that was initially analytically derived by H. Peregrine [1] has since its first experimental demonstration in a physical system in 2010 [2] generated a very large number of experimental and theoretical studies driven primarily by the search for extreme events [3]. Therefore this coherent structure presenting temporal and spatial localizations has been extensively investigated first in the field of fiber optics [2, 4] and then in the hydrodynamic domain [5] and multicomponent plasmas [6]. In optics, PS is a rational solution of the nonlinear Schrodinger equation (NLSE) that describes the evolution of light in a fiber with focusing nonlinearity: the combination of anomalous dispersion and self-phase modulation induced by Kerr nonlinearity leads to the emergence of a wave that appears from nowhere and disappears without leaving a trace [3]. The list of the fiber-based nonlinear processes that are linked to the PS evolution is a long one and includes the modulation instability [7], the propagation of turbulent fields [8-10], the initial stage of temporal compression of higher-order soliton pulses [11], the focusing of super-Gaussian structures [12], the generation of ultrashort structures [13]. . . Peregrine-like structures have also more recently been observed in other photonic systems that may deviate from the simple NLSE framework. Indeed, PS or breather features have been experimentally or theoretically reported in lasers [14], optical cavities [15], metamaterials [16], quadratic or photorefractive media [17, 18].

In this present brief report, we discuss a simple experimental fiber-based configuration where temporal intensity profiles presenting several signatures of the PS waveform are recorded. However, we demonstrate that even if intriguing similarities may exist, the observed coherent structure must be carefully analyzed and we conclude that our observations should not be straightforwardly associated with a PS dynamics.

METHOD

The experimental setup we implemented is sketched in **Figure 1A** and relies on devices from the telecommunication industry that are commercially available. A continuous wave at 1,550 nm is first intensity modulated thanks to a lithium niobate modulator operating at its point of maximum

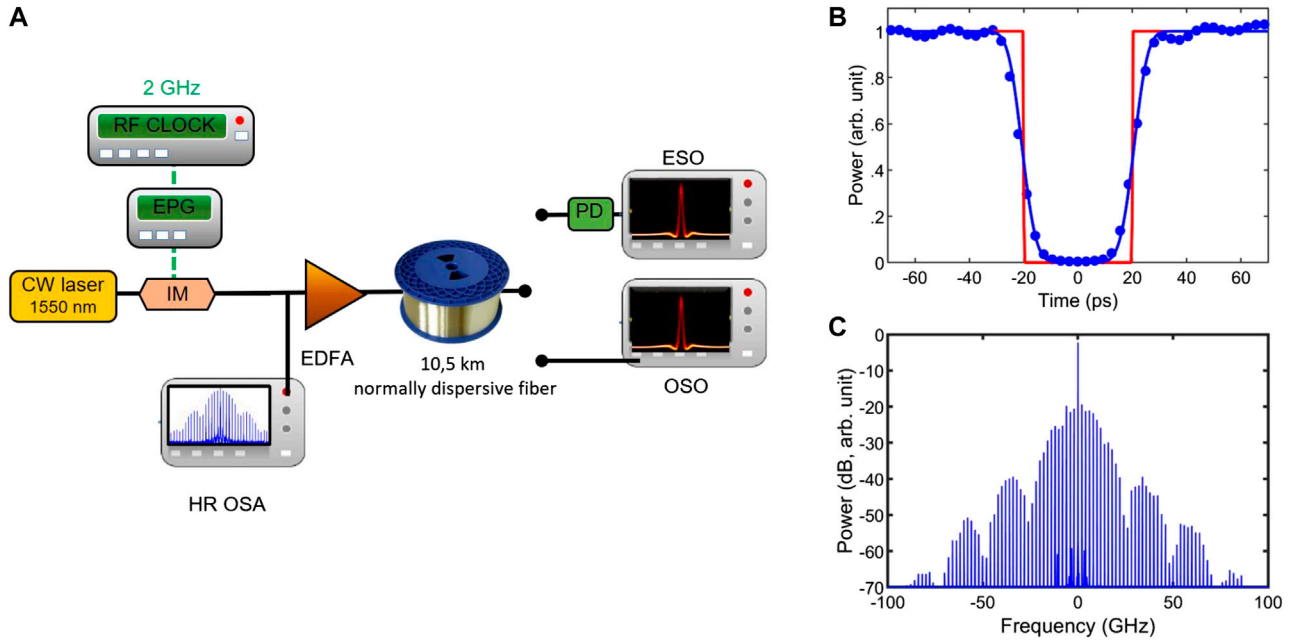

FIGURE 1 | (A) Experimental setup: CW: continuous wave; IM: intensity modulator; EDFA: erbium-doped fiber amplifier; OSO: optical sampling oscilloscope; PD: photodiode; ESO: electrical sampling oscilloscope; HR OSA: high-resolution optical spectrum analyzer. **(B)** Temporal intensity profile of the input pulse. Experimental results (circles) are fitted with an inverted super-Gaussian pulse (blue solid line) and compared with an ideal rectangular waveform (red). **(C)** Experimental optical spectrum of the input pulse.

transmission and driven by an electrical pulse generator that delivers super-Gaussian pulses at a repetition rate of 2 GHz. The resulting temporal intensity profile is plotted in **Figure 1B** and is a continuous wave where light has been switched off for a duration of 40 ps. Particular care has been devoted to the optimization of the extinction ratio in order to prevent parasitic interference between a residual unwanted background and the main structures [19]. The temporal profile can be well fitted by an inverted second-order super-Gaussian pulse. Its spectrum is recorded on a high-resolution optical spectrum analyzer (see **Figure 1C**) and exhibits a high signal-to-noise ratio as well as a high level of symmetry and coherence degree (the spectral linewidth of the components being below the resolution of the optical spectral analyzer, i.e., 5 MHz). The signal is then amplified thanks to a low-noise erbium-doped fiber amplifier that delivers an average power that can be continuously tuned from 10 dBm up to 23 dBm. Propagation occurs in a single spool of 10.5 km of dispersion-shifted fiber with normal dispersion (second-order dispersion β_2 of 19 ps^2/km and a nonlinear coefficient γ of 2/W/km). After propagation, the signal is analyzed with a photodiode and a high-speed sampling oscilloscope (electrical bandwidth of 50 GHz) as well as with an optical sampling oscilloscope.

Light propagation in a single-mode fiber can be described by the NLSE that also includes losses. The evolution of the complex scalar field $\psi(t, z)$ in the slowly varying approximation is therefore governed by Ref. 20:

$$i\frac{\partial\psi}{\partial z} = \frac{1}{2}\beta_2\frac{\partial^2\psi}{\partial t^2} - \gamma|\psi|^2\psi - \frac{\alpha}{2}\psi \quad (1)$$

with z and t being the longitudinal and temporal coordinates, respectively. α is a coefficient of optical losses. This equation can be numerically solved by the widely used split-step Fourier algorithm [20]. When light propagates in an anomalous dispersive fiber, one of the solutions of the loss-free NLSE is the PS which temporal profile $\psi_S(\tau)$ at the point of maximum focusing is described by the following typical rational solution:

$$\psi_S(\tau) = 1 - \frac{4}{1 + 4\ \tau^2} \quad (2)$$

where ψ_S is the field normalized with respect to the continuous background and τ a normalized time depending on the system parameters.

RESULTS

The temporal output profile recorded on a high-speed sampling oscilloscope for the highest input power available is plotted in **Figure 2A** (solid blue line). For this power, the initial 40 ps dip of light has significantly reshaped into a highly peaked structure having a temporal duration at half-maximum of 16.6 ps. The highly symmetric intensity profile goes down to a minimum value at $t = \pm 28$ ps and lies on a continuous background, that is, nine

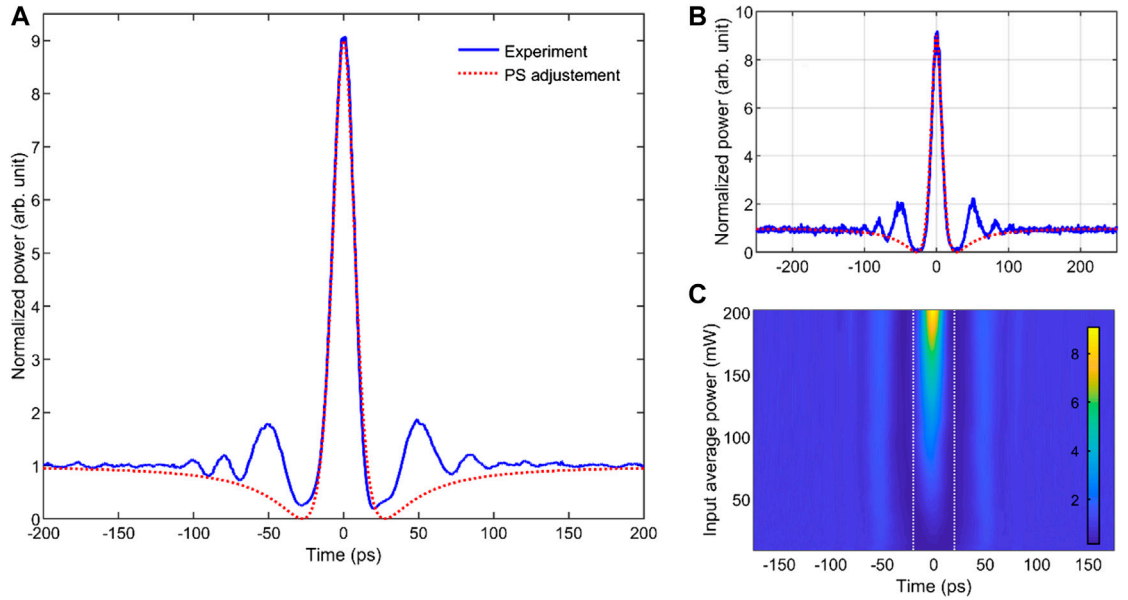

FIGURE 2 | (A) Experimental output temporal profile recorded on the ESO (blue line) compared with a fit by the PS waveform (**Eq. 2**, red dotted line). Input average power is 23 dBm. **(B)** Same as **(A)** but recorded on the OSO. **(C)** Evolution of the temporal intensity profile according to the input power. Intensity profiles are normalized by the intensity of the output continuous background. The white dashed line indicates the temporal location of the sharp edges of the input waveform.

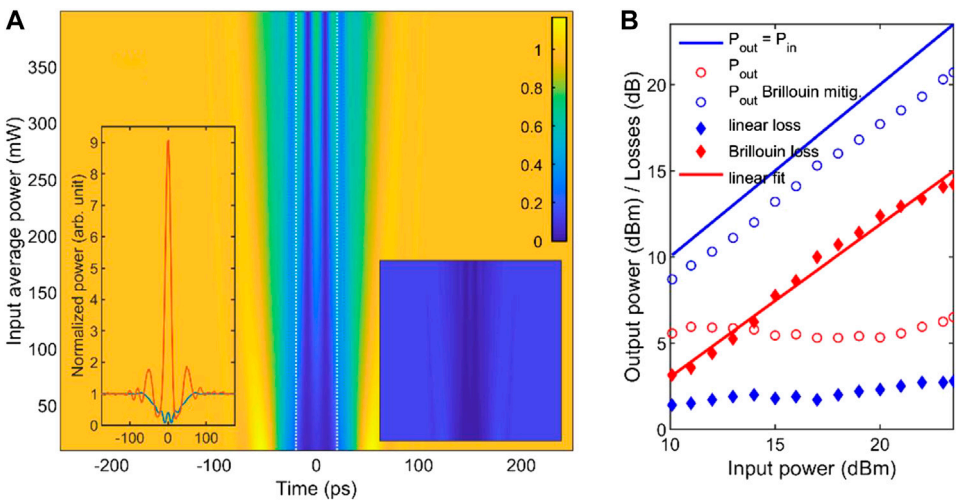

FIGURE 3 | (A) Numerical simulations of the power-dependent output temporal intensity profiles based on the NLSE including constant losses. Intensity profiles are normalized by the intensity of the output continuous background. Left inset: comparison of the experimental and numerical results (red and blue lines, respectively) obtained for an input average power of 200 mW. Right inset: numerical results plotted with the same temporal and power ranges as **Figure 2C** and with the same color scale. **(B)** Experimental measurement of the output average power (circles) according to the input average power. Results without any Brillouin mitigation (red circles) are compared with results when mitigation is applied (blue circles). Diamonds represent the level of losses, that is, experienced: linear losses (blue diamonds) and nonlinear losses (red diamonds). The evolution of the experimental nonlinear losses according to the input power is fitted by a linear trend (solid red line).

times weaker than the peak intensity. Results recorded independently on an optical sampling oscilloscope (**Figure 2B**) fully confirm these features of the intensity profile and stress that the minimum value of the wave is close to zero. The overall profile can be adjusted by the typical temporal intensity waveform of the PS at the point of maximum compression (**Eq. 2**, with τ adjusted to fit the experimental data, red dotted lines). Such a similarity is deeply intriguing as PS are supposed to exclusively exist in presence of focusing nonlinearity, i.e., in the anomalous regime of dispersion. The evolution of the output profile

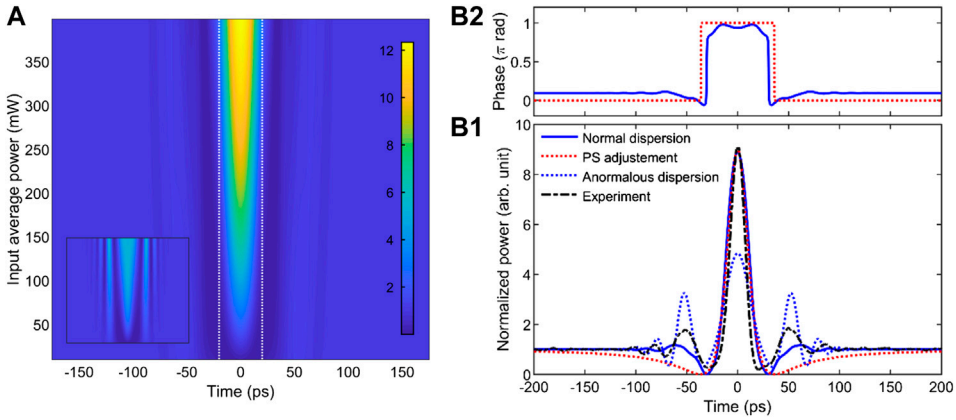

FIGURE 4 | (A) Numerical simulations of the output temporal intensity profiles based on the NLSE including power-dependent losses due to Brillouin backscattering. Intensity profiles are normalized by the intensity of the output continuous background. Inset shows the results obtained in a virtual fiber with opposite dispersion. **(B)**. Details of the temporal intensity and phase profiles (panel **(B1)** and **(B2)**, respectively) obtained for an input power of 23 dBm: numerical simulations of the propagation in the fiber with normal dispersion (blue line, nonlinear losses included) are compared with a fit with a PS waveform (dotted red line). The blue dotted line represents the results predicted with a virtual anomalously dispersive fiber (nonlinear losses included). The mixed black line recalls the experimental results.

according to the input power is summarized in **Figure 2C**. It confirms that the ratio R of the peak-power/continuous background continuously increases with the input power, similarly to what can be usually observed with breathers in the initial stage of the growth and decay cycle.

In order to confirm the experimentally recorded dynamics, we have run numerical simulations based on the NLSE (**Eq. 1**) including linear constant losses of 0.25 dB/km. The evolution of the output intensity profile according to the input power is summarized in **Figure 3A**. It is clear that the NLSE in its simplest form completely fails to reproduce the main experimental findings (see also the right and left insets for a direct comparison with the experimental results). The differences are so high that the NLSE cannot even be considered as a zero-order approximation giving a qualitative trend. A moderate bump is visible at the center of the waveform and can be interpreted as the temporal analog of the Arago spot as we have detailed in Ref. 21. However, its amplitude is well below the amplitude of the continuous wave. Even if its level increases with input power, numerical simulations ran for input powers up to 26 dBm do not predict any R above 1. This inability of the usual NLSE model to provide even qualitative insights on the pulse dynamics forces us to reconsider the validity of the various assumptions made and to rethink our model.

DISCUSSION

In order to better understand the physical origin of the major discrepancy between the numerical predictions and the experimental data, we recorded the output average power according to the input power. The results are reported in **Figure 3B** and outline that the assumption of a constant level of loss severely fails. Indeed, whereas the input power is increased by one order of magnitude, the output power remains more or less constant. This indicates that the losses grow continuously with power. Those extra-losses are ascribed to Brillouin backscattering [20, 22–24] induced by the constant background. Indeed, estimating the Brillouin threshold with the formula $P_{th} \simeq 21\ A_{eff}\ /(L_{eff}\ g_B)$ [20, 24] and standard values for single mode fiber ($g_B = 5 \times 10^{-11}$ m/W, $A_{eff} = 80\ \mu m^2$ and L_{eff} the effective length), we can expect impact of Brillouin scattering for a few mW of average power only. Note that in our previous experiments, we have conveniently mitigated this unwanted Brillouin signal by using a series of optical isolators [25] or an extra phase modulation [21]. Connections between Brillouin scattering and rogue events have already been highlighted in fiber lasers [26, 27], but to our knowledge never in the case of cavity-free passive propagation.

In order to take into account these extra losses in a very simple and empirical way, we have plotted in **Figure 3B** with red diamonds the difference between the output power when Brillouin mitigation is applied and when no mitigation is involved. The experimental evolution of these extra losses is found to follow as a first approximation a linear trend (see linear fit, red line, losses and power expressed in dB). The optical spectrum of our input condition (**Figure 1C**) reveals that the main central component has a spectral intensity, that is, more than 20 dB higher than the other components. Consequently, we may assume that Brillouin backscattering will very predominantly be induced by the CW component and will in return only deplete this component. In our experiment, we have not observed clear signatures of a double-Brillouin effect on the co-propagating wave so that we can also neglect as a first approximation double Brillouin backscattering and do not need to take into account the details of the Brillouin frequency gain.

In order to take into account the experimentally observed trends in a simple way, we also assume for the sake of simplicity that the losses accumulated over propagation can be considered as distributed losses. For the range of power we study (i.e., input powers above the Brillouin threshold), all these assumptions

result in the power and frequency dependent description of the losses as:

$$\alpha_{dB}\left(\omega, P_{in,dB}\right) = \alpha_{0,dB} + \delta\left(\omega\right)\left(AP_{in,dB} + B\right) \quad (3)$$

where α_0 is the level of linear losses, ω the angular frequency and A, B coefficients extracted from the experimental measurements that can be linked to the Brillouin gain and threshold.

Note that our goal in this brief report is not to perform a detailed and accurate modeling of the Brillouin gain properties of fiber under investigation, but rather to identify the key elements that qualitatively explain our dynamics. Therefore, we have not tried to develop complete and accurate simulations of the interactions of the signal with the Brillouin wave [24]. As such a modeling requires the simulation of at least two counter-propagating waves, it may become quickly a long dedicated work that does not correspond to the target of this brief report.

Results obtained with our experiment-inspired description of the losses plugged into the NLSE are reported in **Figure 4A** where we can make out the major differences compared to **Figure 3A**. A peak emerges from the central part and the ratio R between the peak power of the central structure and the continuous background is now clearly well above 1. The various trends recorded experimentally (**Figure 2C**) become well captured by the numerical simulations. The inset of **Figure 4A** shows results of the same simulations run with parameters of a virtual fiber having a dispersion coefficient opposite to the normally dispersive fiber under investigation (β_2 of -19 ps^2/km, all other parameters being kept identical). In this case, the central structure is much less pronounced, in agreement with the impact of the nonlinearity on the evolution of the temporal Arago spot [21].

Details of the temporal profile simulated in the normal regime of dispersion are provided in **Figure 4B** for an input average power of 23 dBm and confirm the ratio of nine between the peak intensity and the continuous background. Once again, the overall temporal intensity profile can be well fitted with the PS typical waveform and it is found that the intensity goes down to zero. However, some limits of our empirical and approximate description of the attenuation are also apparent such as its inability to retrieve quantitatively the pronounced oscillations surrounding the central peak. As a consequence, we cannot unambiguously identify the physical nature of the ripples observed on top of the continuous wave.

The numerical simulations also enable us to get access to the phase profile (**Figure 4B2**). Quite surprisingly, the observed phase profile also presents similarities with the phase profile of a PS, that is, characterized by a phase jump of π at the minimum of the intensity profile [28]. Profile simulated for propagation in the anomalous profile with nonlinear losses is also included and stresses that the combination of Kerr nonlinearity with dispersion affects the nonlinear dynamics even when Brillouin backscattering is a dominant effect. The focusing regime leads to a central peak with an amplitude, that is, underestimated whereas the two surrounding ripples are increased compared to the experiment.

From the numerical results based on our basic empirical description of the nonlinear losses, we can deduce that the physics involved in the emergence of the spiky structure is extremely different from the one involved in the PS dynamics. Contrary to the PS case where the wave emerges from the interaction of self-phase modulation and anomalous dispersion, the crucial component in our study is Brillouin scattering that depletes the continuous background and consequently increases the ratio R. In this context, normalization by the value of the continuous background may distort the interpretation as it gives the feeling that a strong peak emerges from an energy focusing process whereas the main effect is the drop of the value of the continuous background. One may also note that the coherent structure under investigation will not experience the growth-and-decay cycle typical of the PS and values of R above nine can be recorded as observed in **Figure 4A** with $R = 12$ for $P_0 = 400$ mW. We can finally notice that contrary to the usual PS which temporal width decreases in the stage of temporal compression, both in experiments as well as in the numerics, the temporal duration of the central peak is not severely influenced by the input power, confirming that the underlying dynamics is very different.

CONCLUSION

To conclude, we have described an experimental configuration where several features of the Peregrine soliton seem to be reproduced during the propagation of a temporal hole of light in a fiber with normal dispersion. However, we demonstrate that despite these observed signatures, the physics, that is, involved is radically different and is essentially ascribed to the Brillouin backscattering that depletes the continuous background. With this example as well as another work dealing with breathers' features [29], we stress that great care should always be devoted when trying to identify the nature of coherent structures in an experimental record. A deep understanding of the underlying physical dynamics is required before claiming that extreme structures such as Peregrine solitons are observed in a system. In this context, numerical simulations are of great help. For the problem under investigation, whereas the standard NLSE was unable to retrieve the experimental features, adding nonlinear losses that only affect the continuous component was sufficient to qualitatively reproduce the influence of the input power on the output field. Finally, note that in a recent contribution, we have numerically stressed that PS could be observed in a similar configuration when the intensity modulation is replaced by a phase modulation [30].

DATA AVAILABILITY STATEMENT

The raw data supporting the conclusions of this article will be made available by the authors, without undue reservation.

AUTHOR CONTRIBUTIONS

CF: Conceptualization, Methodology, Investigation, Validation, Writing, Project administration.

FUNDING

We acknowledge the financial support of the Institut Universitaire de France (IUF) and the Bourgogne-Franche Comté Region.

ACKNOWLEDGMENTS

The research work has benefited from the PICASSO experimental platform of the University of Burgundy.

REFERENCES

1. Peregrine H. Water waves, nonlinear Schrödinger equations and their solutions. *J Austral Math Soc Ser B* (1983) 25:16–43. doi:10.1017/S0334270000003891
2. Kibler B, Fatome J, Finot C, Millot G, Dias F, Genty G, et al. The Peregrine soliton in nonlinear fibre optics. *Nat Phys* (2010) 6:790–5. doi:10.1038/nphys1740
3. Akhmediev N, Ankiewicz A, Taki M. Waves that appear from nowhere and disappear without a trace. *Phys Lett* (2009) 373:675–8. doi:10.1016/j.physleta.2008.12.036
4. Hammani K, Kibler B, Finot C, Morin P, Fatome J, Dudley JM, et al. Peregrine soliton generation and breakup in standard telecommunications fiber. *Opt Lett* (2011) 36:112–4. doi:10.1364/OL.36.000112
5. Chabchoub A, Hoffmann NP, Akhmediev N. Rogue wave observation in a water wave tank. *Phys Rev Lett* (2011) 106:204502. doi:10.1103/PhysRevLett.106.204502
6. Bailung H, Sharma SK, Nakamura Y. Observation of Peregrine solitons in a multicomponent plasma with negative ions. *Phys Rev Lett* (2011) 107:255005. doi:10.1103/PhysRevLett.107.255005
7. Dudley JM, Genty G, Dias F, Kibler B, Akhmediev N. Modulation instability, Akhmediev Breathers and continuous wave supercontinuum generation. *Opt Express* (2009) 17:21497–508. doi:10.1364/OE.17.021497
8. Kibler B, Hammani K, Michel C, Finot C, Picozzi A. Rogue waves, rational solitons and wave turbulence theory. *Phys Lett A* (2011) 375:3149–55. doi:10.1016/j.physleta.2011.07.006
9. Tikan A, Bielawski S, Szwaj C, Randoux S, Suret P. Single-shot measurement of phase and amplitude by using a heterodyne time-lens system and ultrafast digital time-holography. *Nat Photon* (2018) 12:228–34. doi:10.1038/s41566-018-0113-8
10. Toenger S, Godin T, Billet C, Dias F, Erkintalo M, Genty G, et al. Emergent rogue wave structures and statistics in spontaneous modulation instability. *Sci Rep* (2015) 5:10380. doi:10.1038/srep10380
11. Tikan A, Billet C, El GA, Tovbis A, Bertola M, Sylvestre T, et al. Universality of the peregrine soliton in the focusing dynamics of the cubic nonlinear schrödinger equation. *Phys Rev Lett* (2017) 119:033901. doi:10.1103/PhysRevLett.119.033901
12. Audo F, Kibler B, Fatome J, Finot C. Experimental observation of the emergence of Peregrine-like events in focusing dam break flows. *Opt Lett.* (2018) 43:2864–7. doi:10.1364/OL.43.002864
13. Fatome J, Kibler B, Finot C. High-quality optical pulse train generator based on solitons on finite background. *Opt Lett* (2013) 38:1663–5. doi:10.1364/OL.38.001663
14. Hu X, Guo J, Song YF, Zhao LM, Li L, Tang DY. Dissipative pergrine solitons in fiber lasers. *J Phys Photonics* (2020) 2:034011. doi:10.1088/2515-7647/ab95f3
15. Bao C, Jaramillo-Villegas JA, Xuan Y, Leaird DE, Qi M, Weiner AM. Observation of fermi-pasta-ulam recurrence induced by breather solitons in an optical microresonator. *Phys Rev Lett* (2016) 117:163901. doi:10.1103/physrevlett.117.163901
16. Xu G, McNiff J, Boardman A, Kibler B. Space-time evolution of optical breathers and modulation instability patterns in metamaterial waveguides. *Wave Motion* (2020) 93:102448. doi:10.1016/j.wavemoti.2019.102448
17. Schiek R, Baronio F. Spatial Akhmediev breathers and modulation instability growth-decay cycles in a quadratic optical medium. *Phys Rev Res* (2019) 1:032036. doi:10.1103/physrevresearch.1.032036
18. Marcucci G, Pierangeli D, Agranat AJ, Lee RK, DelRe E, Conti C. Topological control of extreme waves. *Nat Commun* (2019) 10:5090. doi:10.1038/s41467-019–12815-0
19. Parriaux A, Conforti M, Bendahmane A, Fatome J, Finot C, Trillo S, et al. Spectral broadening of picosecond pulses forming dispersive shock waves in optical fibers. *Opt Lett* (2017) 42:3044–7. doi:10.1364/OL.42.003044
20. Agrawal GP. *Nonlinear fiber optics*. 4th ed. San Francisco, CA: Academic Press (2006)
21. Finot C, Rigneault H. Arago spot formation in the time domain. *J Opt* (2019) 21:105504. doi:10.1088/2040-8986/ab4105
22. Damzen MJ, Vlad V, Mocofanescu A, Babin V. *Stimulated Brillouin scattering: fundamentals and applications*. CRC Press (2003)
23. Ippen EP, Stolen RH. Stimulated Brillouin scattering in optical fibers. *Appl Phys Lett.* (1972) 21:539–41. doi:10.1063/1.1654249
24. Kobyakov A, Sauer M, Chowdhury D. Stimulated Brillouin scattering in optical fibers. *Adv Opt Photon.* (2010) 2:1–59. doi:10.1364/AOP.2.000001
25. Finot C. Optical pulse doublet resulting from the nonlinear splitting of a super-Gaussian pulse. Laser *Phys Lett.* (2020) 17:025103. doi:10.1088/1612-202X/ab66c3
26. Hanzard P-H, Talbi M, Mallek D, Kellou A, Leblond H, Sanchez F, et al. Brillouin scattering-induced rogue waves in self-pulsing fiber lasers. *Sci Rep.* (2017) 7:45868. doi:10.1038/srep45868
27. Boukhaoui D, Mallek D, Kellou A, Leblond H, Sanchez F, Godin T, et al. Influence of higher-order stimulated Brillouin scattering on the occurrence of extreme events in self-pulsing fiber lasers. *Phys Rev A.* (2019) 100:013809. doi:10.1103/PhysRevA.100.013809
28. Xu G, Hammani K, Chabchoub A, Dudley JM, Kibler B, Finot C. Phase evolution of Peregrine-like breathers in optics and hydrodynamics. *Phys Rev E.* (2019) 99:012207. doi:10.1103/PhysRevE.99.012207
29. Andral U, Kibler B, Dudley JM, Finot C. Akhmediev breather signatures from dispersive propagation of a periodically phase-modulated continuous wave. *Wave Motion.* (2020) 95:1025–45. doi:10.1016/j.wavemoti.2020.102545
30. Sheveleva A, Finot C. Temporal Fresnel diffraction induced by phase jumps in linear and nonlinear optical fibres. *Results Phys.* (2020) 19:103344. doi:10.1016/j.rinp.2020.103344

Conflict of Interest: The author declares that the research was conducted in the absence of any commercial or financial relationships that could be construed as a potential conflict of interest.

frontiers in Physics

REVIEW
published: 15 January 2021
doi: 10.3389/fphy.2020.612318

Waves that Appear From Nowhere: Complex Rogue Wave Structures and Their Elementary Particles

Nail Akhmediev *

Department of Theoretical Physics, Research School of Physics, The Australian National University, Canberra, NSW, Australia

The nonlinear Schrödinger equation has wide range of applications in physics with spatial scales that vary from microns to kilometres. Consequently, its solutions are also universal and can be applied to water waves, optics, plasma and Bose-Einstein condensate. The most remarkable solution presently known as the Peregrine solution describes waves that appear from nowhere. This solution describes unique events localized both in time and in space. Following the language of mariners they are called "rogue waves". As thorough mathematical analysis shows, these waves have properties that differ them from any other nonlinear waves known before. Peregrine waves can serve as 'elementary particles' in more complex structures that are also exact solutions of the nonlinear Schrödinger equation. These structures lead to specific patterns with various degrees of symmetry. Some of them resemble "atomic like structures". The number of particles in these structures is not arbitrary but satisfies strict rules. Similar structures may be observed in systems described by other equations of mathematical physics: Hirota equation, Davey-Stewartson equations, Sasa-Satsuma equation, generalized Landau-Lifshitz equation, complex KdV equation and even the coupled Higgs field equations describing nucleons interacting with neutral scalar mesons. This means that the ideas of rogue waves enter nearly all areas of physics including the field of elementary particles.

Keywords: nonlinear schrodinger equation, rogue waves, peregrine wave, water waves, optical fibers

OPEN ACCESS

Edited by:
Amin Chabchoub,
The University of Sydney, Australia

Reviewed by:
Fabio Baronio,
University of Brescia, Italy
Norbert Hoffmann,
Hamburg University of Technology, Germany

***Correspondence:**
Nail Akhmediev
nna124@rsphysse.anu.edu.au

Specialty section:
This article was submitted to Mathematical and Statistical Physics, a section of the journal Frontiers in Physics

Received: *30 September 2020*
Accepted: *01 December 2020*
Published: *15 January 2021*

Citation:
Akhmediev N (2021) Waves that Appear From Nowhere: Complex Rogue Wave Structures and Their Elementary Particles. Front. Phys. 8:612318. doi: 10.3389/fphy.2020.612318

1 INTRODUCTION

The nonlinear Schrödinger equation (NLSE) has wide range of applications in physics with spatial scales that vary from microns to kilometres and even light years. It describes nonlinear wave phenomena in optics [1, 2], oceanography [3, 4], plasmas [5, 6], atmosphere [7], Bose-Einstein condensate [8, 9] and cosmology [10]. Taking into account the lowest order nonlinearity and dispersion, this equation describes nonlinear wave phenomena at the fundamental level. NLSE serves as a basic tool for understanding modulation instability [11, 12], solitons [13], periodic waves [14] and extreme waves [15, 16]. The ideas born in the studies of NLSE solutions can be transferred to many other systems. Despite being studied for nearly 50 years, the NLSE solutions have a rich structure and provide surprises for researchers even today [17].

Being a practical introduction to a special issue, this article provides a basic review of mathematical results on NLSE that are important for understanding the nonlinear phenomena in general. It leaves aside the complexities of inverse scattering technique [13], Darboux transformation [18], theta functions [19] and other sophistications of modern mathematics [20].

Instead, it provides solutions in explicit form so that everyone can appreciate their clarity, simplicity of making useful plots and most importantly, the possibility of using them in applications.

The NLSE describes systems with an infinite number of degrees of freedom. Being integrable, it has an infinite number of solutions that can be presented in analytic form. Among them, there are fundamental ones such as soliton solutions [13], Akhmediev breathers [21–24], the Peregrine solution [26–28] and the general doubly-periodic solutions [17, 22]. These can be considered as fundamental modes of the nonlinear system each with a specific single eigenvalue of the inverse scattering transform [13]. More complicated solutions are nonlinear superpositions of these fundamental ones. Although mathematically, these superpositions may look highly complicated, conceptually, they can be understood as a combination of fundamental solutions. The corresponding spectrum of eigenvalues for complex solutions is a combined set of individual eigenvalues.

Presently, the most studied combinations are multi-soliton solutions [13, 29]. Next in complexity are multi-Akhmediev breathers [25, 31]. Rogue waves can also be superimposed resulting in multi-rogue wave solutions. In contrast to multi-solitons and multi-ABs, multi-rogue waves are degenerate solutions. The eigenvalues corresponding to the individual contributions are located at the same point of the complex plane. Despite this complication, multi-rogue waves are also well studied [32–34] but, perhaps, their physics is less understood [35–37] than the physics of any other solutions of the NLSE. The main reason is the unusual set of rules that control their superposition [35]. On the other hand, the superpositions of elementary doubly-periodic solutions studied in [17, 22] still need to be constructed. This task is mathematically challenging and has not been addressed so far. Existence of "explicit" solutions in terms of theta functions [19] does not provide any clue for solving this highly involved task.

Building higher-order superpositions consisting of the same type of fundamental solutions, say, multi-soliton solutions is relatively simple task [38]. This may be done using techniques such as Darboux transformation [30]. Mixing different types of fundamental solutions is more difficult. However, this has also been done in a few recent works. Mixing them is the way to address problems such as rogue waves on top of a periodic background [39, 40]. The number of possibilities is literally infinite.

After what is said above, it may seem strange that the NLSE model is the simplest one among the existing nonlinear evolution equations. However, this is indeed the case. The NLSE provides the conceptual background for further developments in the science of rogue waves. We should keep in mind that the first known integrable equation which is the real KdV equation [41] does not have rogue wave solutions. It cannot be used as a mathematical platform for rogue wave research. On the contrary, the ideas developed in the studies of NLSE solutions can be further extended to many other systems. These include Hirota equation [42], Sasa-Satsuma equation [43], Davey-Stewartson equations [44–46], Sine-Gordon equation [47], Landau-Lifschitz equation [48] and many others. The basic concepts are valid not only for integrable equations but can be expanded to non-integrable cases [49, 50] and, to some extent, to dissipative systems [51, 52].

The generality of the concept of rogue waves can be further expanded to extreme events in nature. Clearly, the equations that describe natural phenomena are more complex than the NLSE [53]. Nevertheless, these are also evolution equations that can be solved if not analytically, then numerically [54]. Rogue waves must be part of complex evolution of the system with either regular or chaotic initial conditions. These rogue waves may take more complicated forms than a simple Peregrine wave. They can take the form of tornadoes or hurricanes. These are also formations that "appear from nowhere". Thus, they do belong to the class of rogue waves or "extreme events".

Our task here is well defined by the subject of the special issue. Therefore, we will concentrate on the Peregrine wave, its analogs and its higher-order combinations. This is a very small subset of the whole set of multi-parameter families of solutions of the NLSE. Nevertheless, this subset plays an important role in explaining extreme events in many physical situations. Understanding variety of complex phenomena starts with the studies of simple examples. These simple examples are listed in the present rendition.

2 NLSE

The relative simplicity of the nonlinear Schrödinger equation, its integrability [13] and its applicability to many weakly nonlinear dispersive systems made it a universal model for wave propagation. The most common applications include deep ocean water waves [3, 4] and waves in an optical fiber [1, 2]. Universality means that this equation can be written in a standard form that is applicable to all major physical settings. Variables in this form are dimensionless and there are no free parameters. Namely,

$$i\frac{\partial\psi}{\partial x}+\frac{1}{2}\frac{\partial^2\psi}{\partial t^2}+\left|\psi\right|^2\psi=0 \tag{1}$$

Here, we consider x as the propagation distance and t as the retarded time in a reference frame moving with the group velocity. The function ψ means the envelope of the wave packet. Being a complex function, it defines both, the amplitude of the envelope and the phase shift of the carrier wave.

For a given central frequency of narrow banded waves, the group velocity of the waves is well defined by the dispersion relation. In this case, the propagation distance and time in the moving frame are linearly related. This means that the time and the distance can be easily exchanged in **Eq. 1** [4]. This replacement creates an alternative form of the equation that has been used in the earlier descriptions of water wave propagation [4]. Evolution in time is also convenient in problems related to Bose-Einstein condensate. For experiments in water tanks and in optical fibers, it is more convenient to stick to the notations taken in **Eq. 1**. Then waves are evolving along the

tank or along the fiber and the shape of the wave envelope can be observed moving along with the wave packet.

All solutions below will be given in dimensionless form that directly satisfy **Eq. 1**. For practical applications, solutions must be rescaled to dimensional variables, i.e. they must be expressed in meters (kilometres) along the tank or along the fiber, in seconds for the transverse variable and in the amplitude units for ψ. In the case of an optical fiber, this rescaling is given by:

$$X = L_{NL} \times x, \quad T = \sqrt{|\beta_2| L_{NL}} \times t, \quad \Psi = \sqrt{P_P} \times \psi, \tag{2}$$

where $L_{NL} = (\gamma P_P)^{-1}$ is the nonlinear length, γ is the nonlinear coefficient defined by the material of the fiber, β_2 is the group velocity dispersion defined by the fiber design, and P_P is the pump power. Coefficients in the rescaling can be transferred to the equation or used only with the transformation (2). The latter choice is more convenient as it allows us to keep the NLSE to be a universal model.

In the case of waves in deep water the rescaling takes the form:

$$X = \frac{x}{k\xi^2}, \quad T = \sqrt{2}\frac{t}{\omega\xi}, \quad \Psi = \frac{\psi\xi}{k}, \tag{3}$$

where X is dimensional distance along the tank, T is dimensional time in the frame moving with the group velocity $c_g = \frac{\omega}{2k}$, Ψ is the envelope of the water wave elevation, ω is the carrier frequency and k is carrier wavenumber that satisfies the dispersion relation $\omega = \sqrt{gk}$ with $g = 9.81$ m/s^2 being the gravitational acceleration. Dimensionless parameter ξ is the wave steepness defined as the product of the wave amplitude a and the wavenumber k.

Further adjustment of solutions can be done with the use of scaling transformation

$$\psi'(x,t) = \alpha\psi(\alpha x, \alpha^2 t) \tag{4}$$

Namely, if $\psi(x,t)$ is a solution of the NLSE (1), then ψ' is also a solution of the same equation. **Eq. 4** provides an additional tool for adjustment of initial conditions to the required levels in optical and hydrodynamic experiments.

3 PEREGRINE WAVE

One of the simplest non-singular rational solutions of the NLSE 1) is given by [15, 16, 26]:

$$\psi(x,t) = \left[4\,\frac{1+2ix}{1+4x^2+4t^2} - 1\right]e^{ix}, \tag{5}$$

It is known as the Peregrine solution or Peregrine soliton [27] or Peregrine breather [28]. The modulus of this complex solution is shown in **Figure 1**. The main feature of this solution is the localization of its central peak both in time and in space. The constant background represents a plane wave with an infinite source of energy. This solution has all features of rogue waves in the ocean [15, 16]. It represents an unexpected wave event on an otherwise flat background.

Peregrine solution has been observed in various experiments. The most notable ones are in water waves [55] and in optical fibers [27]. This solution appears in field evolution dynamics with variety of initial conditions [56]. Moreover, the Peregrine solution can be considered as a universal structure emerging in any type of intensity localization of high power pulses [57]. We can consider it as an "elementary particle" of more complicated patterns that can appear on a plane wave background. As the NLSE is the envelope equation, the Peregrine solution may describe both the wave of elevation or a depression. The latter is known as the rogue wave hole [58]. Solutions similar to the Peregrine one can also be found in other physical systems [59–62]. Thus, the phenomenon of rogue wave is even more universal than we can imagine.

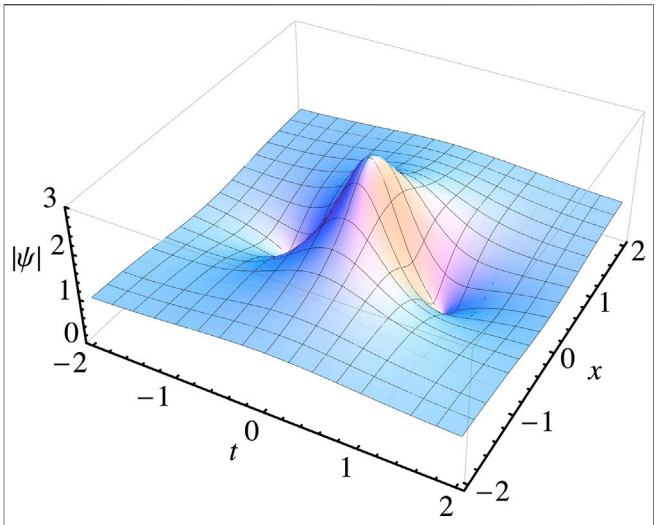

FIGURE 1 | A single Peregrine wave of the NLSE [15]. The maximum amplitude at the origin is three while the background amplitude is 1. The solution has two zeros along the t axis at each side of the maximum. This simple wave structure appears in more complicated rogue wave patterns.

4 HIGHER-ORDER ROGUE WAVE SOLUTIONS

There are higher-order rational solutions of the NLSE that we can call rogue waves. The second order solution has been first presented in [14]. Several methods are known for constructing higher-order solutions of integrable equations [18, 32–34]. A hierarchy of rogue wave solutions with progressively increasing central amplitudes are presently known as Akhmediev-Peregrine (AP) breathers [63–66]. Their general form can be written as:

$$\psi_N(x,t) = \left[(-1)^N + \frac{G_N(x,t) + ixH_N(x,t)}{D_N(x,t)}\right]e^{ix}, \tag{6}$$

where G, H and D are polynomials, and N is the order of the solution. In the case of the Peregrine solution **(5)**, $N = 1$ and we have: $G_1(x,t) = 4, H_1(x,t) = 8, D_1(x,t) = 1 + 4x^2 + 4t^2$.

For the second order solution, the polynomials are given by [14, 67]:

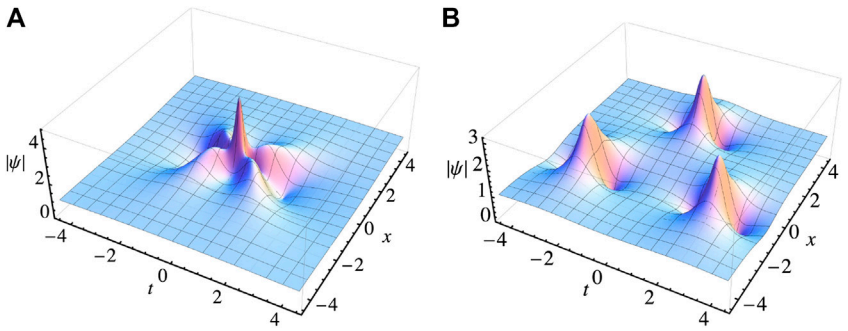

FIGURE 2 | (A) AP solution of the second order [15]. **(B)** Rogue wave triplet with parameters $\gamma = 200$ and $\beta = 0$ [73]. Here, the second order solution consists of three Peregrine waves.

$$G_2 = \frac{3}{8} - 3t^2 - 2t^4 - 9x^2 - 10x^4 - 12t^2x^2,$$

$$H_2 = \frac{15}{4} + 6t^2 - 4t^4 - 2t^4 - 2x^2 - 4x^4 - 8t^2x^2,$$

$$D_2 = \frac{1}{8}\left[\frac{3}{4} + 9t^2 + 4t^4 + \frac{16}{3}t^6 + 33x^2 + 36x^4 + \frac{16}{3}x^6 - 24t^2x^2 + 16t^4x^2 + 16t^2x^4\right].$$

This solutions is shown in **Figure 2A**. While for the first order solution shown in **Figure 1** the amplitude is 3 times the background, the maximum amplitude of the second order solution shown in **Figure 2A** is 5 times the background.

The second-order solution with free parameters has been given earlier in [32, 73]. The solution intensity $|\psi|^2$ is completely defined by the denominator $D_2(x,t)$. Namely, $|\psi_2(x,t)|^2 = 1 + [\log(D_2(x,t))]_{tt}$ [71]. The latter is now given by:

$$D_2(x,t) = \beta^2 + \gamma^2 + 64t^6 + 48t^4(4x^2+1) - 16\beta t^3 + 12t^2(16x^4 - 24x^2 + 4\gamma x + 9) + 12t\beta(1+4x^2) + 64x^6 + 432x^4 - 16\gamma x^3 + 396x^2 - 36\gamma x + 9$$

where β and γ are free real parameters of the solution. This solution is shown in **Figure 2B**. When $\beta = 0$ and $\gamma = 0$, the solution reduces to the second-order AP solution shown in 2(a). An interesting fact about the solution shown in **Figure 2B** is that despite being of the second order it contains three elementary rogue waves rather than two. This is a distinctive feature of multi-rogue wave solutions. They are different from multi-soliton solutions that have the number of solitons equal to the order of the solution [30].

The general form of the third-order rogue wave solution is cumbersome. It has several free parameters. Various forms of the third-order solution have been presented in [71, 73–75] and [76]. Instead of giving the general form, we restrict ourselves with a simpler one-parameter case. As the solution intensity $|\psi_3|^2$ is completely defined by the denominator $D_3(x,t)$, $|\psi_3(x,t)|^2 = 1 + [\log(D_3(x,t))]_{tt}$ [71], we only present the expression for $D_3(x,t)$ [37, 76]. It has a single free real parameter b:

$$D_3(x,t) = \sum_{j=0}^{12} d_j(T)(2x)^j, \tag{7}$$

where the polynomials $d_j(T = 2t)$ are:

$$d_0 = b^2(T^2+1) + T^{12} + 6T^{10} + 135T^8 + 2340T^6 + 3375T^4 + 12150T^2 + 2025,$$
$$d_1 = -10b(T^6 - 9T^4 - 45T^2 + 45),$$
$$d_2 = b^2 + 6(T^{10} - 15T^8 + 90T^6 + 2250T^4 - 6075T^2 + 15525),$$
$$d_3 = 10b(T^4 + 18T^2 + 9),$$
$$d_4 = 15(T^8 - 12T^6 - 90T^4 + 5220T^2 + 9585),$$
$$d_5 = 6b(3T^2 - 17),$$
$$d_6 = 20(T^6 + 3T^4 + 675T^2 + 765), d_7 = -2b,$$
$$d_8 = 15(T^4 + 18T^2 + 249),$$
$$d_9 = 0,$$
$$d_{10} = 6(T^2 + 21),$$
$$d_{11} = 0, d_{12} = 1.$$

The third-order solutions are shown in **Figure 3** for the cases $b = 0$ and $b = 2 \times 10^7$. The third-order solution consists of six Peregrine waves. When $b = 0$, all six are located at the origin leading to the central amplitude 7. For nonzero b, the solution splits into six components. Each of them is a Peregrine wave as can be seen from **Figure 3B**. One of them is located at the origin. Five others are at the corners of an equilateral pentagram. The total number of Peregrine waves is again higher than the order of the solution. Remarkably, the number of Peregrine waves in exact solutions cannot be equal to 2, 4, 5. We can consider the Peregrine wave as the elementary rogue wave solution. Equivalently, we can consider it as a rogue wave quantum or elementary particle of rogue wave patterns.

5 COMPLEX ROGUE WAVE PATTERNS

The N^{th} order rogue wave solution always contains $N(N+1)/2$ Peregrine waves. Namely, solution of the order $N = 1, 2, 3, 4, 5\cdots$ contains $1, 3, 6, 10, 15, \cdots$ Peregrine waves, respectively. These are known as 'triangular numbers' illustrated in **Figure 4**. They are defined as the total number of points in a regular pattern within a triangle with N points along its edges.

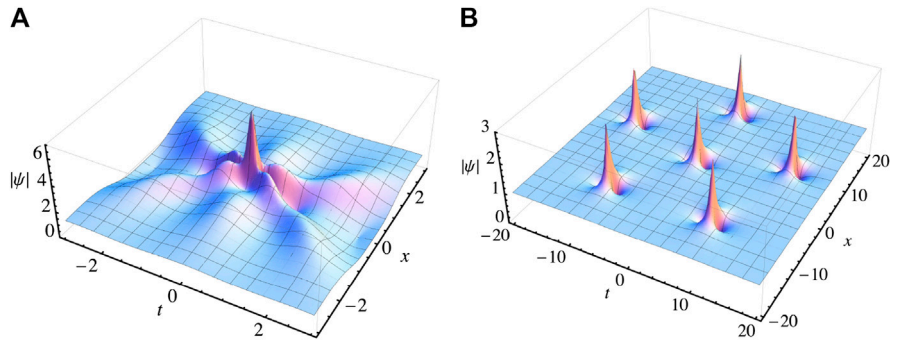

FIGURE 3 | (A) Third order rogue wave solution given by **Eq. (7)** with $b = 0$. **(B)** Third-order rogue wave solution with a circular pattern. It is given by **Eq. (7)** with $b = 2 \times 10^7$. Each 'elementary particle' in this structure is a single Peregrine wave.

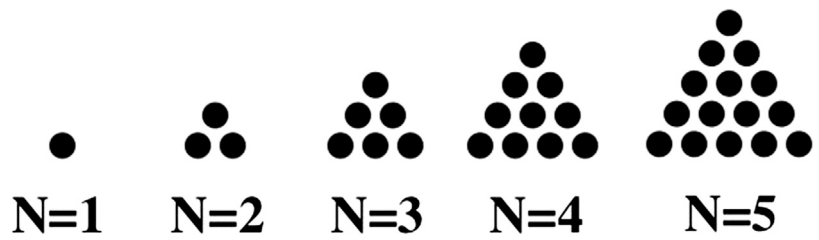

FIGURE 4 | The first five triangular numbers. They are represented by the number of solid dots within each triangle.

Rogue wave patterns are defined by the order of the solution, N, and may depend on additional free parameters. Two examples are given above. These free parameters split the solution into individual Peregrine waves. These parameters specify separations and relative positions of the individual components on the (x, t)-plane. Any solution of N^{th} order contains $N(N+1)/2$ individual components that, when well-separated, can be identified as Peregrine waves. This is a fundamental result [35]: the number of Peregrine waves in a multi-rogue wave solution of the NLSE is given by a triangular number. No other number of Peregrine waves can be present in a general multi-rogue wave solution. This number does not depend on whether the "elementary particles" in the higher-order rogue wave are well-separated or partially separated. In the latter case, when the free parameters are small, the number of Peregrine waves is not visually obvious.

The maximal amplitude of a rogue wave is one of its main characteristics. The maximal amplitude of the higher-order AP solutions when all Peregrine waves are located at the origin is $(2N+1)$ times the background, where N is the order of the solution [63, 68–70]. This is the highest possible amplitude for all imaginable rogue wave patterns.

A detailed classification of the rogue wave patterns has been given in [72]. The main results of this classification are shown in **Figure 5**. It shows the calculated rogue wave patterns that increase in order from top to bottom of table. A single Peregrine wave that is the solution of the first order is located in the top left cell. Higher-order AP solutions are located in the left column. The figure shows only solutions of up to 6-th order, although the list can be continued indefinitely. The second column represents regular triangular structures. The third column represents pentagram patterns. The fourth column provides examples of heptagram structures, i.e., patterns with seven Peregrine waves on one or several circles of different radii. Further columns have 9, 11, ... Peregrine waves in the outer and inner shells of the structure.

"Atomic-like" circular structures are located along the diagonal line. Starting from order 3, they consist of a central nucleus containing $N-2$ elementary rogue waves in the form of an AP solution and $2N-1$ Peregrine waves playing the role of the shell of "electrons". Patterns in inner cells of the table can be considered as "atomic structures" with several shells of "electrons". The larger variety of patterns for higher-order solutions is caused by the larger number of free parameters controlling the solution. The rogue wave patterns can also have a lower symmetry than in **Figure 5**. Some examples can be found in [36, 71].

There is no doubt that these patterns can be observed experimentally. Indeed, a single Peregrine wave has been observed in optics [27], in water waves [55] and in a multicomponent plasma [77]. It may soon be observed in Bose-Einstein condensate [78, 79]. The rogue wave triplet has

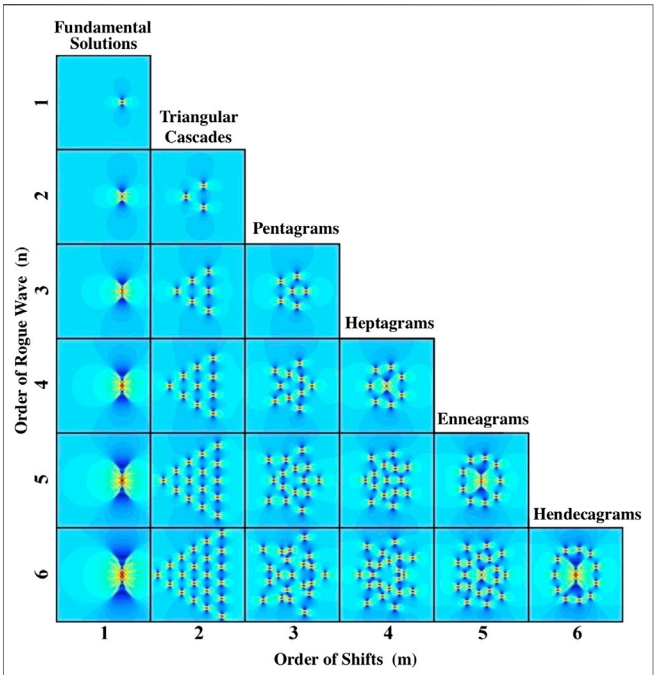

FIGURE 5 | Patterns of higher-order rogue wave solutions [72]. Only solutions of up to order six are shown. The Peregrine soliton is on the first row. Second-order solutions are of two types: the AP solution and the triplet. They are located in the second row. Variety of patterns increases with the order. For example, the third order solutions do exist in the AP, triangular and pentagram forms. This happens because of the larger number of free parameters in the solution. Patterns located along the diagonal line are circular. They have a ring of $(2N - 1)$ Peregrine solitons around a central rogue wave of order $N - 2$ (for $N > 2$). These are basically "atomic structures" with a nucleus and a shell of "electrons".

been observed in a water wave tank [80]. AP solutions up to fifth-order have also been observed in water waves [81]. As the NLSE has a wide range of applications, these solutions may appear in situations that we cannot even predict right now.

Can this approach be used for a description of elementary particles and atomic structures? Obviously, this will need more sophisticated equation than the NLSE. As mentioned, the phenomena described in this review are not unique to the NLSE although, perhaps, the NLSE case is the most studied of all. Rogue waves have been found in systems described by the Hirota and Maxwell-Bloch equations [42, 82], Sasa-Satsuma equation [83], Fokas-Lenells equation [84], in systems with self-steepening effect [85, 86] and even in the case of the complex KdV equation [87, 88]. Patterns of multi-rogue wave solutions similar to those in **Figure 5** have been found for the complex modified KdV equation [89], Kundu–Eckhaus equation [90], coupled nonlinear Schrödinger–Boussinesq equations [91], generalized derivative nonlinear Schrödinger equations [92, 93], generalized Landau-Lifshitz equation [48], Manakov equations [94], the three–wave resonant interaction equations [95, 96], discrete Ablowitz-Ladik equations [97] and even in the case of breather collisions [98, 99]. Most recent work [100] shows that the ideas of rogue waves now enter the field of elementary particles. Namely, patterns similar to those in **Figure 5** may appear in the case of coupled Higgs field equations describing nucleons interacting with neutral scalar mesons [100]. Further developments of the rogue wave theory along these lines may boost our vision of the complex world and how it is build out of simple fundamental particles.

AUTHOR CONTRIBUTIONS

The author confirms being the sole contributor of this work and has approved it for publication.

REFERENCES

1. Hasegawa A, Tappert F. Transmission of stationary nonlinear optical pulses in dispersive dielectric fibers. I. Anomalous dispersion. *Appl Phys Lett* (1973) 23: 142–4. doi:10.1063/1.1654836
2. Agrawal GP. *Nonlinear fiber optics* 4th Edn. NY: Academic Press (2007)
3. Zakharov VE. Stability of periodic waves of finite amplitude on a surface of deep fluid. *J Appl Mech Tech Phys* (1968) 9:190–4. doi:10.1007/BF00913182
4. Osborne A. *Nonlinear ocean waves and the inverse scattering transform* Academic Press (2010).
5. Moslem WM, Shukla PK, Eliasson B. Surface plasma rogue waves. *Europhys Lett* (2011) 96:25002. doi:10.1209/0295-5075/96/25002
6. El-Tantawy SA. Rogue waves in electronegative space plasmas: the link between the family of the KdV equations and the nonlinear Schrödinger equation. *Astrophys Space Sci* (2016) 361:164. doi:10.1007/s10509-016-2754-8
7. Stenflo L, Marklund M. Rogue waves in the atmosphere. *J Plasma Phys* (2010) 76:293. doi:10.1017/S0022377809990481
8. Gross EP. Structure of a quantized vortex in boson systems. *Nuovo Cimento* (1961) 20:454. doi:10.1007/BF02731494
9. Pitaevskii LP. Vortex lines in an imperfect Bose gas. *Zh Eksp Teor Fiz* (1961) 40:646.
10. Lidsey JE. Scalar field cosmologies hidden within the nonlinear Schrödinger equation (2013). Available at: https://arxiv.org/abs/1309.7181 (Accessed September 27 2013).
11. Bespalov VI, Talanov VI. Filamentary structure of light beams in nonlinear liquids. *Sov Phys JETP Lett* (1966) 3:307.
12. Benjamin TB, Feir J. The disintegration of wave trains on deep water: Part 1. *Theory J Fluid Mech* (1967) 27:417. doi:10.1017/S002211206700045X
13. Zakharov VE, Shabat AB. Exact theory of two-dimensional self-focusing and one-dimensional self-modulation of waves in nonlinear media. *J Exp Theor Phys* (1972) 34:62–9.
14. Akhmediev N, Eleonskii VM, Kulagin NE. Generation of periodic trains of picosecond pulses in an optical fiber: exact solutions. *Sov Phys JETP* (1985) 62(5):894–9.
15. Akhmediev N, Ankiewicz A, Taki M. Waves that appear from nowhere and disappear without a trace. *Phys Lett* (2009) 373:675–8. doi:10.1016/j.physleta.2008.12.036
16. Shrira VI, Geogjaev VV. What makes the Peregrine soliton so special as a prototype of freak waves? *J Eng Math* (2009) 67:11–22. doi:10.1007/s10665-009-9347-2
17. Conforti M, Mussot A, Kudlinski A, Trillo S, Akhmediev N. Doubly periodic solutions of the focusing nonlinear Schrödinger equation: recurrence, period doubling, and amplification outside the conventional modulation-instability band. *Phys Rev* (2020) 101:023843. doi:10.1103/PhysRevA.101.023843

18. Matveev VB, Salle MA. *Darboux transformations and solitons* Berlin-Heidelberg: Springer (1991).
19. Its OR, Kotlyarov V. Explicit formulas for solutions of the Schrödinger nonlinear equation. *Doklady Akad. Nauk Ukrainian SSR* (1976) 10:965–8.
20. Its AR, Rybin AV, Sall MA. Exact integration of nonlinear Schrodinger equation[original in Russian: teor. *Theor Math Phys* (1988) 69:29–32.
21. Akhmediev N, Korneev VI. Modulation instability and periodic solutions of nonlinear Schrödinger equation. *Theor Math Phys* (1986) 69:189–94.
22. Akhmediev N, Eleonskii VM, Kulagin NE. Exact first-order solutions of the nonlinear Schrödinger equation. *Theor Math Phys* (1987) 72:809.
23. Yang G, Wu FO, Lopez Aviles HE, Christodoulides D. Optical amplification and transmission of attenuated multi-soliton based on spectral characteristics of Akhmediev breather. *Optic Commun* (2020) 473:125899.
24. Andral U, Kibler B, Dudley JM, Finot C. Akhmediev breather signatures from dispersive propagation of a periodically phase-modulated continuous. *wave Motion* (2020) 95:102545.
25. Akhmediev N, Korneev VI, Mitskevich NV. N-modulation signals in a single-mode optical waveguide under nonlinear conditions. *Zh Exp Teor Fiz* (1988) 94:159–70.
26. Peregrine DH. Water waves, nonlinear Schrödinger equations and their solutions. *J Australian Math Soc Ser B* (1983) 25:16.
27. Kibler B, Fatome J, Finot C, Millot G, Dias F, Genty G, et al. The Peregrine soliton in nonlinear fibre optics. *Nat Phys* (2010) 6:790–5.
28. Gaillard P, Gastineau M. The Peregrine breather of order nine and its deformations with sixteen parameters solutions to the NLS equation. *Phys Lett* (2015) 379:1309–13.
29. Ablowitz MJ, Segur H. *Solitons and the inverse scattering transform* Philadelphia, Pa, USA: SIAM (1981).
30. Akhmediev N, Mitskevich NV. Extremely high degree of N-soliton pulse compression in an optical fiber. *IEEE J Quantum Electron QE* (1991) 27: 849–57.
31. Akhmediev N, Soto-Crespo JM, Ankiewicz A. Extreme waves that appear from nowhere: on the nature of rogue waves. *Phys Lett* (2009) 373:2137–45. doi:10.1016/j.physleta.2009.04.023
32. Dubard P, Gaillard P, Klein C, Matveev VB. On multi-rogue wave solutions of the NLS equation and positon solutions of the KdV equation. *Eur Phys J Spec Top* (2010) 185:247–58. doi:10.1140/epjst/e2010-01252-9
33. Ohta Y, Yang J. General high-order rogue waves and their dynamics in the nonlinear Schrödinger equation. *Proc R Soc A* (2012) 468:1716–40.
34. Gaillard P. Degenerate determinant representation of solutions of the nonlinear Schrödinger equation, higher order Peregrine breathers and multi-rogue waves. *J Math Phys* (2013) 54:013504. doi:10.1063/1.4773096
35. Ankiewicz A, Akhmediev N. Multi-rogue waves and triangular numbers. *Rom Rep Phys* (2017) 69:104.
36. Kedziora DJ, Ankiewicz A, Akhmediev N. Triangular rogue wave cascades. *Phys Rev E Stat Nonlinear Soft Matter Phys* (2012) 86:056602. doi:10.1103/PhysRevE.86.056602
37. Kedziora DJ, Ankiewicz A, Akhmediev N. Circular rogue wave clusters. *Phys Rev E Stat Nonlinear Soft Matter Phys* (2011) 84:056611. doi:10.1103/PhysRevE.84.056611
38. Satsuma J, Yajima N. Initial value problems of one-dimensional self-modulation of nonlinear waves in dispersive media. *Prog Theor Phys Suppl* (1974) 55:284.
39. Kedziora DJ, Ankiewicz A, Akhmediev N. Rogue waves and solitons on a cnoidal background. *Eur Phys J Spec Top* (2014) 223:43–62. 10.1140/epjst/e2014-02083-4.
40. Chen J, Pelinovsky DE, White RE. Rogue waves on the double-periodic background in the focusing nonlinear Schrödinger equation. *Phys Rev E* (2019) 100:052219. doi:10.1103/PhysRevE.100.052219
41. Zabusky NJ, Kruskal MD. Interaction of "solitons" in a collisionless plasma and the recurrence of initial states. *Phys Rev Lett* (1965) 15:240–3.
42. Ankiewicz A, Soto-Crespo JM, Akhmediev N. Rogue waves and rational solutions of the Hirota equation. *Phys Rev E Stat Nonlinear Soft Matter Phys* (2010) 81:046602. doi:10.1103/PhysRevE.81.046602
43. Bandelow U, Akhmediev N. Persistence of rogue waves in extended nonlinear Schrödinger equations: integrable Sasa-Satsuma case. *Phys Lett* (2012) 376: 1558–61. doi:10.1016/J.PHYSLETA.2012.03.032
44. Ohta Y, Yang J. Rogue waves in the Davey-Stewartson I equation. *Phys Rev E Stat Nonlinear Soft Matter Phys* (2012) 86:036604. doi:10.1103/PhysRevE.86.036604
45. Ohta Y, Yang JK. Dynamics of rogue waves in the Davey – stewartson II equation. *J Phys Math Theor* (2013) 46:105202. doi:10.1088/1751-8113/46/10/105202
46. Rao J, Cheng Y, He J. Rational and semirational solutions of the nonlocal Davey–Stewartson equations. *Stud Appl Math* (2017) 139:568–98. doi:10.1111/sapm.12178
47. Li R, Geng X. Rogue periodic waves of the sine—Gordon equation. *Appl Math Lett* (2020) 102:106147. doi:10.1016/j.aml.2019.106147
48. Li R, Geng X, Xue B. A generalization of the Landau-Lifschitz equation: breathers and rogue waves. *J Nonlinear Math Phys* (2020) 27:279–94. doi:10.1080/14029251.2020.1700636
49. Ankiewicz A, Devine N, Akhmediev N. Are rogue waves robust against perturbations? *Phys Lett* (2009) 373:3997–4000. doi:10.1016/j.physleta.2009.08.053
50. Ankiewicz A, Soto-Crespo JM, Chowdhury MA, Akhmediev N. Rogue waves in optical fibers in presence of third-order dispersion, self-steepening, and self-frequency shift. *J Opt Soc Am B* (2013) 30:87–94. doi:10.1364/JOSAB.30.000087
51. Zaviyalov A, Egorov O, Iliew R, Lederer F. Rogue waves in mode-locked fibre lasers. *Phys Rev* (2012) 85:013828. doi:10.1103/PhysRevA.85.013828
52. Soto-Crespo JM, Grelu P, Akhmediev N. Dissipative rogue waves: extreme pulses generated by passively mode-locked lasers. *Phys Rev E Stat Nonlinear Soft Matter Phys* (2011) 84:016604. doi:10.1103/PhysRevE.84.016604
53. Lynch P. The origins of computer weather prediction and climate modelling. *J Comput Phys* (2008) 227:3431–44. doi:10.1016/j.jcp.2007.02.034
54. Krishnamurti TN. Numerical weather prediction. *Annu Rev Fluid Mech* (1995) 27:195–225. doi:10.1146/annurev.fl.27.010195.001211
55. Chabchoub A, Hoffmann NP, Akhmediev N. Rogue wave observation in a water wave tank. *Phys Rev Lett* (2011) 106:204502. doi:10.1103/PhysRevLett.106.204502
56. Bertola M, Tovbis A. Universality for the focusing nonlinear Schrödinger equation at the gradient catastrophe point: rational breathers and poles of the tritronqué solution to Painlevé I, Commun. *Pure Appl Math* (2012) 66:678. doi:10.1002/cpa.21445
57. Tikan A, Billet C, El G, Tovbis A, Bertola M, Sylvestre T, et al. Universal Peregrine soliton structure in nonlinear pulse compression in optical fiber. *Phys Rev Lett* (2017) 119:033901. doi:10.1103/PhysRevLett.119.033901
58. Chabchoub A, Hoffmann NP, Akhmediev N. Observation of rogue wave holes in a water wave tank. *J Geophys Res* (2012) 117:C00J02. doi:10.1029/2011JC007636
59. Chen S, Grelu P, Soto-Crespo JM. Dark- and bright-rogue-wave solutions for media with long-wave-short-wave resonance. *Phys Rev E Stat Nonlinear Soft Matter Phys* (2014) 89:011201. doi:10.1103/PhysRevE.89.011201
60. Baronio F, Degasperis A, Conforti M, Wabnitz S. Solutions of the vector nonlinear Schrödinger equations: evidence for deterministic rogue waves. *Phys Rev Lett* (2012) 109:044102. doi:10.1103/PhysRevLett.109.044102
61. Baronio F. Akhmediev breathers and Peregrine solitary waves in a quadratic medium. *Opt Lett* (2017) 42:1756. doi:10.1364/OL.42.001756
62. Baronio F, Conforti M, Degasperis A, Lombardo S. Rogue waves emerging from the resonant interaction of three waves. *Phys Rev Lett* (2013) 111:114101. doi:10.1103/PhysRevLett.111.114101
63. Gaillard P. Other 2N-2 parameters solutions of the NLS equation and 2N+1 highest amplitude of the modulus of the N-th order Akhmediev-Peregrine breather. *J Phys Math Theor* (2015) 48:145203. doi:10.1088/1751-8113/48/14/145203
64. Dontsop PYG, Essama BGO, Doing JM, Dedzo MM, Atangana J, Yemele D, et al. Akhmediev-Peregrine rogue waves generation in a composite right/left-handed transmission line. *Opt Quant Electron* (2016) 48:59. doi:10.1007/s11082-015-0333-9
65. Chabchoub A, Fink M. Time-reversal generation of rogue waves. *Phys Rev Lett* (2014) 112:124101. doi:10.1103/PhysRevLett.112.124101
66. Vitanov NK, Chabchoub A, Hoffmann N. Deep-water waves: on the nonlinear Schrödinger equation and its solutions. *J Theor Appl Mech Sofia* (2013) 43: 43–54. doi:10.2478/jtam-2013-0013
67. Akhmediev N, Ankiewicz A. *Solitons, nonlinear pulses and beams* London: Chapman & Hall (1997).

68. Ankiewicz A, Clarkson P, Akhmediev N. Rogue waves, rational solutions, the patterns of their zeros and integral relations. *J Phys Math Theor* (2010) 43:122002.
69. Wang L, Yang C, Wang J, He J. The height of an n-th order fundamental rogue wave for the nonlinear Schrödinger equation. *Phys Lett* (2017) 381:1714–8. doi:10.1016/j.physleta.2017.03.023
70. Chin SA, Ashour OA, Nikolić SN, Belić MR. Maximal intensity higher-order Akhmediev breathers of the nonlinear Schrödinger equation and their systematic generation. *Phys Lett* (2016) 380:3625–9. doi:10.1016/j.physleta.2016.08.038
71. Ling L, Zhao LC. Simple determinant representation for rogue waves of the nonlinear Schrödinger equation. *Phys Rev E Stat Nonlinear Soft Matter Phys* (2013) 88:043201. doi:10.1103/PhysRevE.88.043201
72. Kedziora DJ, Ankiewicz A, Akhmediev N. Classifying the hierarchy of nonlinear-Schrödinger-equation rogue-wave solutions. *Phys Rev E - Stat Nonlinear Soft Matter Phys* (2013) 88:013207. doi:10.1103/PhysRevE.88.013207
73. Ankiewicz A, Kedziora DJ, Akhmediev N. Rogue wave triplets. *Phys Lett* (2011) 375:2782–5. doi:10.1016/j.physleta.2011.05.047
74. Gaillard P. Deformations of third-order Peregrine breather solutions of the nonlinear Schrödinger equation with four parameters. *Phys Rev E Stat Nonlinear Soft Matter Phys* (2013) 88:042903. doi:10.1103/PhysRevE.88.042903
75. Gaillard P. Degenerate determinant representation of solutions of the nonlinear Schrödinger equation, higher order Peregrine breathers and multi-rogue waves. *J Math Phys* (2013) 54:013504. doi:10.1063/1.4773096
76. Akhmediev N, Ankiewicz A, Soto-Crespo JM. Rogue waves and rational solutions of the nonlinear Schrödinger equation. *Phys Rev E - Stat Nonlinear Soft Matter Phys* (2009) 80:026601. doi:10.1103/PhysRevE.80.026601
77. Bailung H, Sharma SK, Nakamura Y. Observation of Peregrine solitons in a multicomponent plasma with negative ions. *Phys Rev Lett* (2011) 107:255005. doi:10.1103/PhysRevLett.107.255005
78. Bludov YV, Konotop VV, Akhmediev N. Matter rogue waves. *Phys Rev* (2009) 80:033610. doi:10.1103/PhysRevA.80.033610
79. Nguyen JHV, Luo D, Hulet RG. Formation of matter-wave soliton trains by modulational instability. *Science* (2017) 356:422–6. doi:10.1126/science.aal3220
80. Chabchoub A, Akhmediev N. Observation of rogue wave triplets in water waves. *Phys Lett* (2013) 377:2590–3. doi:10.1016/j.physleta.2013.07.027
81. Chabchoub A, Hoffmann N, Onorato M, Slunyaev A, Sergeeva A, Pelinovsky E, et al. Observation of a hierarchy of up to fifth-order rogue waves in a water tank. *Phys Rev E Stat Nonlinear Soft Matter Phys* (2012) 86:056601. doi:10.1103/PhysRevE.86.056601
82. Li C, He J, Porsezian K, Porseizan K. Rogue waves of the Hirota and the Maxwell-Bloch equations. *Phys Rev E Stat Nonlinear Soft Matter Phys* (2013) 87:012913. doi:10.1103/PhysRevE.87.012913
83. Gui M, Qin Z, Grimshaw R, Akhmediev N. Intricate dynamics of rogue waves governed by the Sasa-Satsuma equation. *Physica D* (2020) 402:132252. doi:10.1016/j.physd.2019.132252
84. He J, Xu S, Porsezian K. Rogue waves of the Fokas-Lenells equation. *J. Phys. Soc. Japan* (2012) 81:124007. doi:10.1143/JPSJ.81.124007
85. Liu C, Akhmediev N. Super-regular breathers in nonlinear systems with self-steepening effect. *Phys Rev E* (2019) 100:062201. doi:10.1103/PhysRevE.100.062201
86. Chen S, Pan C, Grelu P, Baronio F, Akhmediev N. Fundamental Peregrine solitons of ultrastrong amplitude enhancement through self-steepening in vector nonlinear systems. *Phys Rev Lett* (2020) 124:113901. doi:10.1103/PhysRevLett.124.113901
87. Ankiewicz A, Bokaeeyan M, Akhmediev N. Shallow-water rogue waves: an approach based on complex solutions of the Korteweg–de Vries equation. *Phys Rev E* (2019) 99:050201. doi:10.1103/PhysRevE.99.050201
88. Crabb M, Akhmediev N. Rogue wave multiplets in the complex KdV equation. *Rom Rep Phys* (2020) 72:118.
89. He J, Wang L, Li L, Porsezian K, Erdélyi R. Few-cycle optical rogue waves: complex modified Korteweg-de Vries equation. *Phys Rev E Stat Nonlinear Soft Matter Phys* (2014) 89:062917. doi:10.1103/PhysRevE.89.062917
90. Qiu D, He J, Zhang Y, Porsezian K. The Darboux transformation of the Kundu-Eckhaus equation. *Proc Royal Soc A Math Phys Eng Sci* (2015) 471:20150236. doi:10.1098/rspa.2015.0236
91. ZhangChen Y. General high-order rogue waves to nonlinear Schrödinger–Boussinesq equation with the dynamical analysis. *Nonlinear Dynam* (2018) 93:2169–84. doi:10.1007/s11071-018-4317-8
92. Yang B, Chen J, Yang J. Rogue waves in the generalised derivative nonlinear Schrödinger equations. *J. Nonlin. Science* (2020) 30:3027–56.
93. Yang B, Yang J. *Universal patterns of rogue waves* Available at: https://arxiv.org/abs/2009.06060 (Accessed September 13 2020).
94. Chen S, Mihalache D. Vector rogue waves in the Manakov system: diversity and compossibility. *J Phys Math Theor* (2015) 48:215202. doi:10.1088/1751-8113/48/21/215202
95. Chen S, Soto-Crespo JM, Grelu P. Watch-hand-like optical rogue waves in three-wave interactions. *Optic Express* (2015) 23:349–59. doi:10.1364/OE.23.000349
96. Wang X, Cao J, Chen Y. Higher-order rogue wave solutions of the three–wave resonant interaction equation via the generalized Darboux transformation. *Phys Scripta* (2015) 90:105201. doi:10.1088/0031-8949/90/10/105201
97. Ohta Y, Yang J. General rogue waves in the focusing and defocusing Ablowitz—Ladik equations. *J Phys Math Theor* (2014) 47:255201. doi:10.1088/1751-8113/47/25/255201
98. Kedziora DJ, Ankiewicz A, Akhmediev N. Second-order nonlinear Schrödinger equation breather solutions in the degenerate and rogue wave limits. *Phys Rev E Stat Nonlinear Soft Matter Phys* (2012) 85:066601. doi:10.1103/PhysRevE.85.066601
99. Wang L, He J, Xu H, Wang J, Porsezian K. Generation of higher-order rogue waves from multibreathers by double degeneracy in an optical fiber. *Phys Rev E* (2017) 95:042217. doi:10.1103/PhysRevE.95.042217
100. Zhaqilao. Dynamics of localized wave solutions for the coupled Higgs field equation. *Nonlinear Dynam* (2020) 101:1181–98.

Conflict of Interest: The author declares that the research was conducted in the absence of any commercial or financial relationships that could be construed as a potential conflict of interest.

frontiers in Physics

MINI REVIEW
published: 05 February 2021
doi: 10.3389/fphy.2020.599435

Local Emergence of Peregrine Solitons: Experiments and Theory

*Alexey Tikan[1], Stéphane Randoux[2], Gennady El[3], Alexander Tovbis[4], Francois Copie[2] and Pierre Suret[2]**

[1]Institute of Physics, Swiss Federal Institute of Technology Lausanne (EPFL), Lausanne, Switzerland, [2]University of Lille, CNRS, UMR 8523-PhLAM-Physique des Lasers Atomes et Molécules, Lille, France, [3]Department of Mathematics, Physics and Electrical Engineering, Northumbria University, Newcastle Upon Tyne, United Kingdom, [4]Department of Mathematics, University of Central Florida, Orlando, FL, United States

It has been shown analytically that Peregrine solitons emerge locally from a universal mechanism in the so-called semiclassical limit of the one-dimensional focusing nonlinear Schrödinger equation. Experimentally, this limit corresponds to the strongly nonlinear regime where the dispersion is much weaker than nonlinearity at initial time. We review here evidences of this phenomenon obtained on different experimental platforms. In particular, the spontaneous emergence of coherent structures exhibiting locally the Peregrine soliton behavior has been demonstrated in optical fiber experiments involving either single pulse or partially coherent waves. We also review theoretical and numerical results showing the link between this phenomenon and the emergence of heavy-tailed statistics (rogue waves).

Keywords: Peregrine soliton, optical fibers, semiclassical limit, one-dimensional nonlinear Schrödinger equation, self-compression of optical solitons

OPEN ACCESS

Edited by:
Bertrand Kibler, UMR6303 Laboratoire Interdisciplinaire Carnot de Bourgogne (ICB), France

Reviewed by:
Fabio Baronio, University of Brescia, Italy
Stefan Wabnitz, Sapienza University of Rome, Italy

****Correspondence:***
Pierre Suret
Pierre.Suret@univ-lille.fr

Specialty section:
This article was submitted to Mathematical and Statistical Physics, a section of the journal Frontiers in Physics

Received: *27 August 2020*
Accepted: *04 November 2020*
Published: *05 February 2021*

Citation:
Tikan A, Randoux S, El G, Tovbis A, Copie F and Suret P (2021) Local Emergence of Peregrine Solitons: Experiments and Theory. Front. Phys. 8:599435. doi: 10.3389/fphy.2020.599435

1 INTRODUCTION

Recent mathematical works have recently triggered new research by unifying two old concepts, namely, the Peregrine soliton (PS) and the pulse compression in focusing nonlinear media [1]. The latter has been in particular widely investigated in optical fiber experiments for obvious application purposes [2], while the former has been extensively studied as a remarkable localized solution of the one-dimensional focusing nonlinear Schrödinger equation (1-D NLSE) [3]

$$i\psi_z + \frac{1}{2}\psi_{tt} + |\psi|^2\psi = 0, \tag{1}$$

for a complex wave field $\psi(t, z)$.

The universal NLSE (**1**) describes at leading order nonlinear waves in various physical systems and is integrable [4]. Its exact solutions called solitons on finite background (SFBs) such as Akhmediev breathers, Kuznetsov–Ma, and Peregrine solitons have been derived several decades ago [3, 5–8]. First studied in the context of modulation instability, SFBs have been the subject of a renewed interest in the 2000s because these localized solutions are considered as possible prototypes of rogue waves [9–12]. The PS solution is given by

$$\psi_{PS}(t, z) = \left[1 - \frac{4(1 + 2iz)}{1 + 4t^2 + 4z^2}\right]e^{iz}, \tag{2}$$

and it exhibits the remarkable property to be localized both in space and in time [3]. It has been experimentally generated by using specifically designed initial conditions in optical fibers [13], plasmas [14], and water tank [15].

In a completely different context, pulse compression has been widely studied in the last 4 decades both experimentaly in optical fiber experiments and theoretically by using numerical simulations of the NLSE [2, 16–19]. The goal of these studies was to provide the shortest possible pulse with the highest peak power at the output of the fiber. It is very important to note that these studies have been focused on the so-called higher-order solitons, also named "N-solitons" which means that the initial pulse is "made" of several solitons in the framework of the inverse scattering transform (IST) [20]. As a consequence, it is often considered that the pulse compression arises from the propagation of bound-state multi-soliton solutions [17].

Mathematics has provided in the 2010s a different perspective on pulse compression in focusing regime of the NLSE [1]. It has been rigorously demonstrated that in the semiclassical (zero dispersion) limit of the NLSE, a sufficiently smooth pulse undergoes a gradient catastrophe, that is, the divergence of the derivatives of the field that is regularized by the generation of a coherent structure locally (asymptotically) described by the PS solution.

Very importantly, this theorem provides a local interpretation of the mechanism underlying the pulse compression and links this phenomenon with the famous PS. Note that the result is somehow surprising because the pulse compression is obviously achieved with zero boundary conditions, while the PS is a solution of the NLSE with nonzero boundary conditions. Moreover, this mechanism is universal because it is independent of the soliton content and of the exact shape of the initial pulse. As a consequence, while the exact PS is often seen as the interaction between a plane wave and a soliton [21], the local emergence of the PS arising in the pulse compression does not require the existence of the soliton.

This short review aims at presenting the main mathematical and experimental results related to the local emergence of the PS in the process of pulse compression. We also show the important consequences of this phenomenon on the statistical properties of nonlinear random waves in focusing NLSE systems [22–24].

2 MATHEMATICAL RESULTS: REGULARIZATION OF THE GRADIENT CATASTROPHE IN THE SEMICLASSICAL FOCUSING NLSE

Semiclassical limit is a powerful tool to study large space–time, z, t, behavior of the NLSE (**1**). It is achieved by introducing a small parameter $0 < \varepsilon \ll 1$ and rescaling $\xi = \varepsilon z, \tau = \varepsilon t, \psi(z,t) \to \psi(\xi, \tau; \varepsilon)$ so that focusing NLSE (**1**) assumes the form

$$i\varepsilon\psi_\xi + \frac{1}{2}\varepsilon^2\psi_{\tau\tau} + |\psi|^2\psi = 0. \tag{3}$$

In the following, we assume that the amplitude of ψ at $\xi = 0$ is $\mathcal{O}(1)$.

Physically, the nondimensional dispersion parameter ε is determined by the ratio of the nonlinear medium's internal coherence length (the soliton width/duration) and the typical scale of initial data. Therefore, the study of small-dispersion dynamics in (**3**) is equivalent to the study of the evolution of large-scale data in the original NLSE (**1**). Importantly, the limit as $\varepsilon \to 0$ in **Eq. 3** enables analysis of solutions to (**1**) for both large and $\mathcal{O}(1)$ t, z-scales using the same equation.

It is convenient to introduce a Wentzel–Kramers–Brillouin (WKB)-type representation for $\psi(\tau, \xi)$ (the Madelung transform):

$$\psi = \sqrt{\rho}\, e^{i\frac{\phi}{\varepsilon}}, \qquad \phi_\tau = u \tag{4}$$

to convert the semiclassical NLSE (**3**) into a system:

$$\begin{aligned} &\rho_\xi + (\rho u)_\tau = 0, \\ &u_\xi + u u_\tau - \rho_\tau - \varepsilon^2\left(\frac{\rho_{\tau\tau}}{4\rho} - \frac{\rho_\tau^2}{8\rho^2}\right)_\tau = 0, \end{aligned} \tag{5}$$

for the wave field intensity (power) $\rho(\tau, \xi) = |\psi|^2$ and the "chirp" $u(\tau, \xi)$. Note that the system (**5**) is strictly equivalent to the NLSE.

The *dispersionless limit* is obtained from (**5**) by setting $\varepsilon = 0$. In this limit, the system (**5**) is of elliptic type so that its solutions, when exist, have finite life span due to the development of infinite τ- and ξ-derivatives of ρ and u at some critical point $\tau = \tau_c, \xi = \xi_c$, which is often referred to as a point of gradient catastrophe [25]. In the vicinity of the gradient catastrophe point, the contribution of the dispersive term $\mathcal{O}(\varepsilon^2)$ in (**5**) becomes significant so that at $\xi > \xi_c$, the emerging regularized dynamics exhibit large-amplitude, ε-scaled oscillations of the intensity signifying the singular nature of the semiclassical $\varepsilon \to 0$ limit. The results reported in this review have been obtained mathematically and realized experimentally for small but nonzero values of ε [1]. Below, we summarize the history of the mathematical ideas underlying these results.

The semiclassical limit of the NLSE is most efficiently studied in the framework of the IST method [20]. At the heart of this theory is a linear differential [Zakharov–Shabat (ZS)] operator whose spectrum is determined by the NLSE wave field $\psi(\tau, \xi)$ playing the role of the scattering potential. Generally, the IST spectrum has two components: discrete and continuous. The discrete component is related to a soliton "content" of $\psi(\tau, \xi)$, while the continuous component corresponds to dispersive wave radiation as $\xi \to \infty$. The potentials $\psi(\tau, \xi)$ having pure continuous spectrum are called solitonless. The IST spectrum is invariant with respect to the NLSE evolution and so can be evaluated at $\xi = 0$.

The study of the semiclassical limit of integrable equations was initiated by Lax and Levermore [26] in the framework of the Korteweg–de Vries (KdV) equation for which the associated scattering operator is self-adjoint. The attempts to extend the Lax–Levermore theory to the focusing NLSE ran into complications due to non–self-adjoint nature of the ZS operator for (**3**). The first numerical studies [27–29] revealed an τ, ξ-region of the initial evolution of smooth modulated plane wave followed by the emergence of a region filled with rapid nonlinear oscillations exhibiting complex spatiotemporal behavior (see **Figure 1A**). The development of the steepest descent method of Deift–Zhou for matrix Riemann–Hilbert

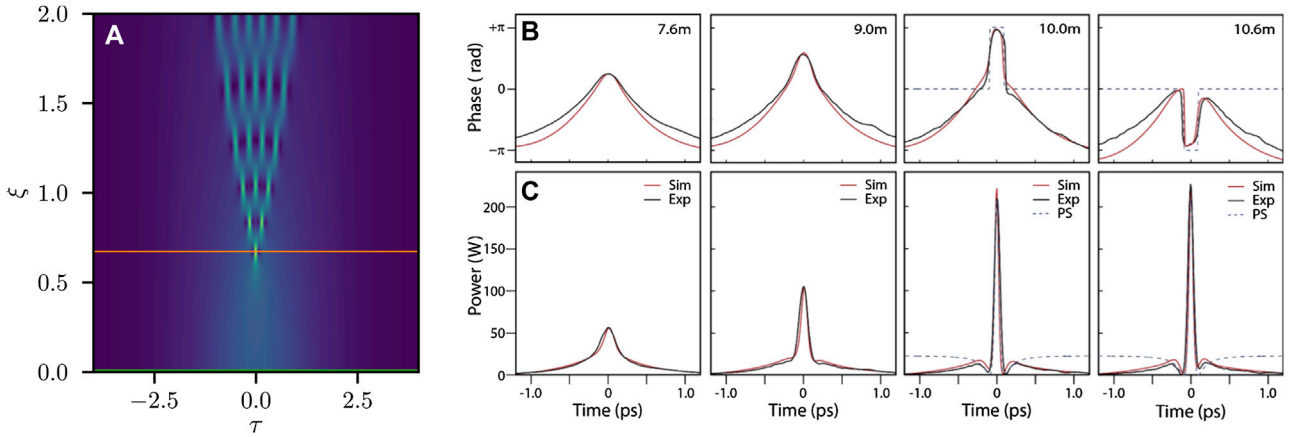

FIGURE 1 | Local emergence of the Peregrine soliton in the process of pulse compression. **(A)** Numerical simulations: space–time dynamics of a single hump, reproduced with permission from Ref. 24. **(B)** Intensity and **(C)** phase measurements of compressed pulse characteristics in optical fiber at the distances indicated, comparing experiment (black line) with simulations (red line). For the results at 10.0 and 10.6 m, there is a flip in the phase characteristics across the central intensity lobe. Dashed lines are the theoretical profiles of an ideal Peregrine soliton, reproduced with permission from Ref. 43.

problems (RHPs) (see, e.g., [30]) in 1990s led to rigorous mathematical studies of the semiclassical NLSE limit in Ref. 31 (pure discrete spectrum, i.e., solitons only) and in Ref. 32 (both purely radiative (solitonless) cases and radiation with solitons) revealed the detailed micro- and macroscopic structures of the emerging oscillations. In particular, in Ref. 32, the NLSE (**Eq. 3**) evolution of a one-parameter family of modulated plane wave potentials

$$\psi(\tau,0;\varepsilon)=\operatorname{sech}(\tau)e^{i\phi/\varepsilon},\quad \phi=-\mu\log(\cosh(\tau)),\qquad (6)$$

where $\mu\in\mathbb{R}$ is the chirp parameter controlling the phase, was studied. The advantage of this family of potentials is that the corresponding scattering data (the IST spectrum) can been calculated explicitly [33]; moreover, its soliton "content" is controlled by the chirp parameter μ; the discrete spectrum component (solitons) is only present when $|\mu|<2$; otherwise, the spectrum is purely continuous (radiation). The spectrum is purely discrete if and only if $\mu=0$ and $\varepsilon=\frac{1}{N}$, where $N=1,2,\ldots$. In this case, the potential (**6**) represents an exact N-soliton solution of the NLSE (**3**).

The RHP approach allowed establishing rigorous semiclassical asymptotics describing the complex nonlinear dynamics of the NLSE (**3**) with analytic initial data decaying as $|\tau|\to\infty$. In particular, it was shown in Ref. 32 that for the potential (**Eq. 6**), the initial evolution is approximated at leading order in ε by the solution of the dispersionless NLSE ($\varepsilon=0$ in **(Eq. 5)**) that undergoes gradient catastrophe at the point $(\tau_c,\xi_c)=\left(0,\frac{1}{\mu+2}\right)$ (see Ref. 34 for broader class of initial data $\psi(\tau,0;\varepsilon)$).

It was shown in Ref. 1 that if the gradient catastrophe occurs (for $\varepsilon=0$), it exhibits a regularization mechanism (for $\varepsilon\neq0$) *via* the emergence of a localized coherent structure, which is asymptotically close to PS (**2**). The mechanism is universal because it does not depend on the particular form of initial data $\psi(\tau,0;\varepsilon)$. Specifically, it was shown that the solution at the point of maximum localization $\tau_{\mathrm{m}}=\tau_c+\mathcal{O}(\varepsilon^{4/5})$, $\xi_{\mathrm{m}}=\xi_c+\mathcal{O}(\varepsilon^{4/5})$ assumes the form $|\psi(\tau,\xi_{\mathrm{m}})|=a_0[1-4/(1+4a_0^2((\tau-\tau_{\mathrm{m}})/\varepsilon)^2)](1+\mathcal{O}(\varepsilon^{1/5}))$, where $a_0=\sqrt{\rho(0,\xi_c)}+\mathcal{O}(\varepsilon^{1/5})$ is the background amplitude, that is, it is determined at the leading order by the value of instantaneous power at the gradient catastrophe point. In the case of potential (**6**), it was found that $\rho(0,\xi_c)=\mu+2$. The maximum value of $|\psi|$ in the local PS is then $3a_0$ and is determined up to $\mathcal{O}(\varepsilon^{1/5})$. We stress that the above approximate PS solution is valid locally, in the ε-vicinity of the point $(\tau_{\mathrm{m}},\xi_{\mathrm{m}})$.

Importantly, the effect of the local emergence of the PS right beyond the gradient catastrophe point is universal and does not depend on the composition of the (global) IST spectrum of the initial data. In other words, the initial condition for (**5**) can have high soliton content or be completely solitonless—in all cases, the PS appears as a nonlinear coherent structure locally regularizing the gradient catastrophe. The specific form of the initial condition affects only the time ξ_{m} of the PS development.

3 LOCAL EMERGENCE OF THE PEREGRINE SOLITON IN EXPERIMENTS WITH SINGLE PULSE

The self-compression of pulses has been a very widely investigated topic experimentally, especially since the first observation of solitonic behavior in optical fibers in 1980 [35]. Indeed, it has been observed that the propagation of solitonic pulses with sufficiently high initial peak power is always accompanied, at first, by a narrowing of the pulses and an increase in their peak power before eventually undergoing successive splittings. These observations have been successfully compared to the well-known dynamics of higher-order solitons or "N-solitons" such that the phenomenon of pulse self-compression was referred to as the "Soliton effect" [2, 36, 37]. This effect has been widely studied [16, 38], including the two-stage compression technique [39] and higher-order effects [40, 41].

In the context of 1-D hydrodynamics experiments, similar dynamics have been observed in the compression of the envelope of $N = 2$ and $N = 3$ solitons, which suggests that the underlying mechanism may be of the same origin [42].

The recent mathematical results described above provide a new interpretation of the mechanism underlying most of the past experiments on what was called "soliton self-compression." Two main ideas are important: (i) the mechanism actually does not depend on the soliton content of the pulse and (ii) the Peregrine soliton emerges locally as the regularization of gradient catrastrophe.

Point (ii) has been recently demonstrated in optical fiber experiments [43] using two different setups. In particular, picosecond pulses with a peak power $P_0 = 26.3$ W have been injected into a Ge-doped highly nonlinear optical fiber. The input pulses were well fitted by a sech profile corresponding to a soliton of an order $N \approx 6$, that is, $\varepsilon \approx 0.16$. These experiments were performed for different fiber lengths, and a complete characterization of the compressed pulse in both amplitude and phase was achieved using the FROG technique [44]. The retrieved intensity (bottom) and phase (top) at the fiber lengths indicated, comparing experiment (black line) with simulations (red line), are plotted in **Figures 1B,C**. In all cases, there is an excellent agreement between experiment and simulation. Importantly, the intensity and phase profiles of an ideal PS solution match very well the experiment and simulation across the pulse center while approaching the maximum compression point (for the lengths of the fiber around 10 m). The main difference is that the PS solution is characterized by the background that extends to $\tau \to \pm\infty$, whereas the pedestal observed in experiments is limited by the temporal width of the input pulse. As explained above, the emergence of the PS here is a local dynamical mechanism. As observed in **Figure 1B**, the π phase jump occurring at zero intensity between the central lobe and the background pedestal is a remarkable signature of the PS. Moreover, the change of the sign of the phase derivative across the maximum compression point, another characteristic of the exact PS solution, is also observed in the experiments between 10 and 10.6 m.

It is important to note that the experimental results of [43] show that the mechanism demonstrated in the semiclassical limit of NLSE [1] is very robust and can be observed over a very broad range of ε. The PS is observed at the maximum compression point of the pulse as long as $\varepsilon = \sqrt{L_D/L_{NL}} \leq 0.5$ $(N > 2)$.

4 STATISTICAL SIGNATURES IN NONLINEAR RANDOM WAVE EVOLUTION

Recent studies have shown that the dynamical mechanism leading to the local emergence of the PS (see **Sections 3** and **4**) plays a crucial role in the emergence of rogue waves (RWs) and in the statistics of integrable turbulence [22–24]. *Integrable turbulence* corresponds to complex dynamical phenomena arising along the nonlinear propagation of random waves in a system governed by an integrable equation such as the NLSE [22, 43, 45–49].

An important example of integrable turbulence in NLSE systems arises when the initial field corresponds to the linear superposition of numerous *independent* Fourier components:

$$\psi(\tau, \xi) = \sum_k a_k(\xi) e^{\frac{2\pi i}{T} k\tau} \text{ with } k \in \mathbb{Z}. \tag{7}$$

Here, periodic boundary conditions with a period T are used, and $a_k(0) = |a_{0k}| e^{i\phi_{0k}}$ is a kth Fourier component with a uniformly distributed random phase $\phi_{0k} \in [-\pi, \pi]$. This kind of partially coherent waves is fundamental because of the omnipresence, in natural environments, of stochastic waves with a finite Fourier spectrum having delta-correlated frequency components. The central limit theorem shows that the statistics of ψ given by **Eq. 7** is Gaussian and the statistics of $|\psi|^2$ is exponential [46].

First observed in the open sea, RWs have been studied in a large variety of nonlinear media and can be defined as extreme (high-amplitude) events that appear more frequently than predicted by the linear theory [11]. Experimental investigations of the evolution of the partially coherent wave first in a water tank [50] and later in controlled optical fiber experiments well described by the NLSE [46] demonstrated the emergence of non-Gaussian statistics. An example of corresponding numerical simulation is shown in **Figure 2**, where the nonlinear propagation of partially coherent initial condition characterized by the exponential distribution for $|\psi|^2$ (depicted by green in plots in **Figures 2A**,**D**) leads to the heavy-tailed probability density function (**Figure 2A** orange and red lines)—the main evidence of the rogue wave emergence.

It is important to note that at present, there is no theory describing these statistical properties in the focusing 1-D NLSE system [22, 23, 46, 49]. However, remarkably, the local PSs (see, e.g., inset in **Figure 2D**), previously considered as a prototype of RWs, were identified in numerical simulations of the NLSE, reported along with the pioneering experimental observations. By using temporal imaging techniques, it has been proved that the temporal *intensity* profile of some extreme events emerging during the evolution of partially coherent light in optical fibers resembles the localized PS [22]. Recent advances of heterodyne time microscopy have enabled the ultrafast single-shot measurement of both phase and amplitude of random waves [23]. By using this technique, the local emergence of the PS embedded in partially coherent waves propagating in optical fibers has been fully demonstrated [23]. Having access to the phase and intensity profiles, it becomes possible to reconstruct the complex amplitude and, therefore, numerically find the initial structure resulting in the RW simply by simulating the reversed NLSE. Such nonlinear temporal holography revealed that the typical structure that leads to the RW emergence is a large initial hump. This observation constitutes the first solid evidence of the gradient catastrophe regularization playing a role in the nonlinear dynamics of partially coherent waves. Note that similar observations have been made in deep water wave experiments [51, 52].

A systematic study of the local PS emergence in integrable turbulence behind the 1-D NLSE has been provided first numerically [24] and later verified experimentally in a 1-D water tank [52]. Employing the robust theoretical results

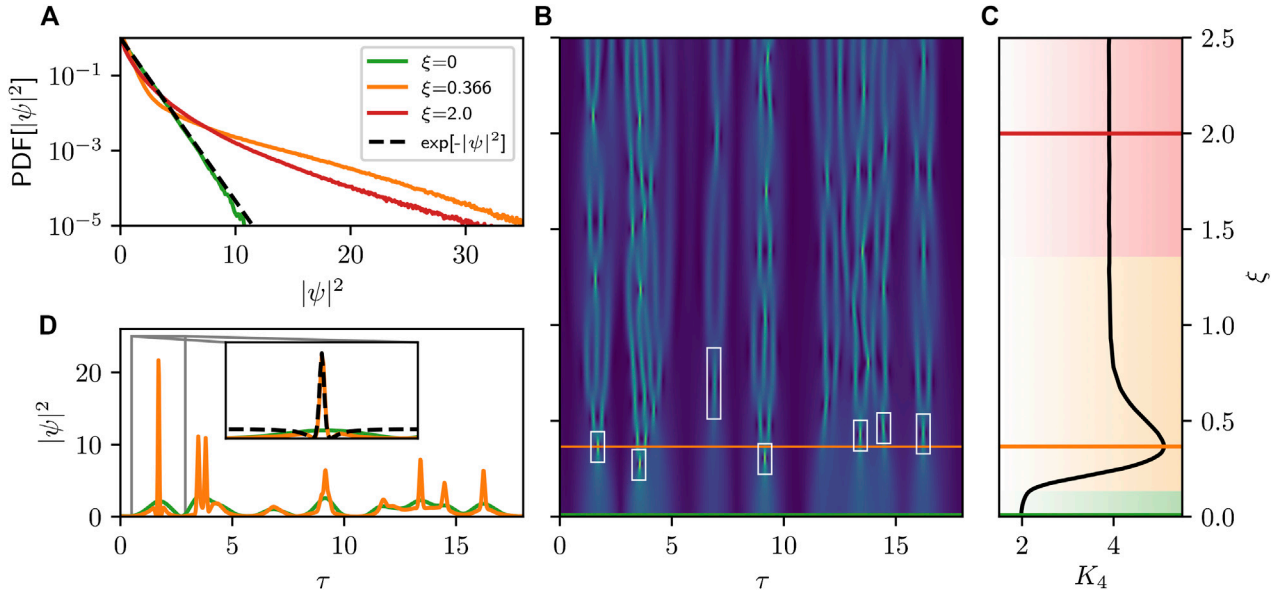

FIGURE 2 | Numerical simulations of partially coherent wave propagation in the focusing NLS system. **(A)** Probability density function of $|\psi|^2$ at three different propagation distances ξ = 0 (green), 0.366 (orange), and 2 (red). The dashed black line corresponds to $\exp(-|\psi|^2)$. **(B)** Spatiotemporal diagram of $|\psi|$. White boxes highlight the coherent structures that appear out of initial humps and can be locally fitted with the Peregrine soliton. The scale of ξ is identical in **(B)** and **(C)**. **(C)** Evolution of the kurtosis (black). Green, orange, and red lines correspond to ξ = 0, 0.366, and 2. The kurtosis and the probability density function are computed over 10'000 realizations of the partially coherent wave similar to one depicted in **(B)**. **(D)** $|\psi|^2$ profile at two values of ξ = 0, 0.366 (colors are preserved). Inset plot demonstrates a fit of the high-amplitude event with the exact formula of the Peregrine soliton. In all the simulations, the value of ε is 0.2, reproduced with permission from Ref. 24.

described in **Section 2**, a strong correlation between the distribution of lengths of local PS maximum compression and the most probable distances of the RW emergence has been found. Assuming that local humps present in the initial conditions evolve independently at least before the gradient catastrophe point, maximum compression points were estimated for each of them locally by renormalizing the NLSE according to the hump's amplitude and duration. The computed probability density of the local PS emergence position took a shape of an asymmetric overshoot having a distinct maximum. As a measure of deviation from the Gaussian distribution, and therefore, the increased probability of RW observation, a fourth moment of the distribution (kurtosis) was employed. The presence of the overshoot in the kurtosis evolution for partially coherent initial conditions (see **Figure 2C**) has been shown in Ref. 53. Numerical simulations reported in Ref. 24 demonstrate a remarkable correlation between these two overshoots, implying that the area of the highest probability of observation of the extreme events in the evolution of partially coherent waves in the focusing 1-D NLS model is directly related to the local emergence of PSs as a regularization of the gradient catastrophe. As well as for the deterministic initial conditions described in **Section 3**, this effect remains valid beyond the formal applicability of the results reported in Ref. 1.

5 DISCUSSION

The PS has been originally discovered as a breather solution of the focusing NLSE (with nonzero boundary conditions) that exhibits the remarkable property to be localized both in space and time [3]. It has been observed in experiments made in the 2000s with plasma waves [14], water waves [15], and optical waves [13]. In the 2010s, it has been shown mathematically that the PS also emerges locally as a universal mechanism of dispersive regularization of a gradient catastrophe arising in the self-focusing evolution of an initially broad pulse [1]. This mechanism of local emergence of the PS is universal in the sense that it depends neither on the exact shape of the initial pulse nor on its soliton content. The understanding that the PS emerges locally in the process of self-focusing of a broad wave packet [43] has shed new light on the self-compression of light pulses, which has been extensively studied in the fiber optics community in the 1980s.

The dynamical process of the emergence of the PS in the evolution of broad and smooth wave packets is highly relevant in the context of integrable turbulence where the nonlinear evolution of partially coherent waves is investigated at the statistical level. Partially coherent waves with an initial Gaussian statistics are indeed composed of a random collection of large humps (see **Figure 2**) which individually experience the self-focusing process leading to the gradient catastrophe regularized by the emergence of the PS [24]. As shown in Ref. [24], this feature explains well the behavior followed by statistical moments of the wave field such as the kurtosis. Remarkably, a similar conclusion draws from the large deviation theory with applications to the stochastic water wave dynamics [54].

The scenario of the local emergence of the PS in the regularization of a gradient catastrophe is expected to be robust against some perturbations such as dissipation and forcing [55, 56], and higher-order nonlinear effects [57].

However, the investigation of the role of higher-order effects now represents essentially an open question.

AUTHOR CONTRIBUTIONS

All the authors wrote this mini review. ATo is the author of the key mathematical results reported in **Section 2**. PS, GE, SR, and ATi are authors of experimental and numerical results reported in **Sections 3** and **4**.

FUNDING

The work of ATo supported in part by the NSF grant DMS-2009647. The work of PS, ATi, FC, and SR has been partially supported by the Agence Nationale de la Recherche through the LABEX CEMPI project (ANR- 11-LABX-0007) and by the Ministry of Higher Education and Research, Hauts-De-France Regional Council and European Regional Development Fund (ERDF) through the Contrat de Projets Etat-Region (CPER Photonics for Society P4S) and by ISITE-ULNE through the DYDICO project. The work of GE was partially supported by the Engineering and Physical Science Research Council (EPSRC), United Kingdom, grant no. EP/R00515X/2.

ACKNOWLEDGMENTS

ATo acknowledges the laboratory PhLAM and the University of Lille for the 2020 invitation.

REFERENCES

1. Bertola M, Tovbis A. Universality for the focusing nonlinear Schrödinger equation at the gradient catastrophe point: rational breathers and Poles of the Tritronquée Solution to Painlevé I. *Commun Pure Appl Math* (2013) 66: 678–752. doi:10.1002/cpa.21445
2. Mollenauer LF, Tomlinson WJ, Stolen RH, Gordon JP. Extreme picosecond pulse narrowing by means of soliton effect in single-mode optical fibers. *Opt Lett* (1983) 8:289–91. doi:10.1364/OL.8.000289
3. Peregrine DH. Water waves, nonlinear Schrödinger equations and their solutions. *J Aust Math Soc Ser B Appl Math* (1983) 25:16–43. doi:10.1017/S0334270000003891
4. Akhmediev NN, Ankiewicz A. *Solitons: nonlinear pulses and beams*. London: Chapman & Hall (1977).
5. Kuznetsov EA. Solitons in a parametrically unstable plasma. *DoSSR* (1977) 236: 575–7
6. Kawata T, Inoue H. Inverse scattering method for the nonlinear evolution equations under nonvanishing conditions. *J Phys Soc Jpn* (1978) 44:1722–9. doi:10.1143/jpsj.44.1722
7. Ma Y-C. The perturbed plane-wave Solutions of the cubic Schrödinger equation. *Stud Appl Math* (1979) 60:43–58. doi:10.1002/sapm197960143
8. Akhmediev NN, Eleonskii VM, Kulagin NE. Exact first-order solutions of the nonlinear Schrödinger equation. *Theor Math Phys* (1987) 72:809–18. doi:10.1007/bf01017105
9. Dysthe KB, Trulsen K. Note on breather type solutions of the nls as models for freak-waves. *Phys Scripta* (1999) T82:48. doi:10.1238/physica.topical.082a00048
10. Akhmediev N, Ankiewicz A, Taki M. Waves that appear from nowhere and disappear without a trace. *Phys Lett* (2009) 373:675–8. doi:10.1016/j.physleta.2008.12.036
11. Onorato M, Residori S, Bortolozzo U, Montina A, Arecchi FT. Rogue waves and their generating mechanisms in different physical contexts. *Phys Rep* (2013) 528:47–89. doi:10.1016/j.physrep.2013.03.001
12. Dudley JM, Dias F, Erkintalo M, Genty G. Instabilities, breathers and rogue waves in optics. *Nat Photon* (2014) 8:755–64. doi:10.1038/nphoton.2014.220
13. Kibler B, Fatome J, Finot C, Millot G, Dias F, Genty G, et al. The Peregrine soliton in nonlinear fibre optics. *Nat Phys* (2010) 6:790–5. doi:10.1038/nphys1740
14. Bailung H, Sharma SK, Nakamura Y. Observation of peregrine solitons in a multicomponent plasma with negative ions. *Phys Rev Lett* (2011) 107:255005: doi:10.1103/PhysRevLett.107.255005
15. Chabchoub A. Tracking breather dynamics in irregular sea state conditions. *Phys Rev Lett* (2016) 117:144103. doi:10.1103/PhysRevLett.117.144103
16. Dianov EM, Nikonova ZS, Prokhorov AM, Serkin VN. Optimal compression of multi-soliton pulses in optical fibers. *Sov Tech Phys Lett* (1986) 12:311–3
17. Akhmediev N, Betina L, Eleonskiĭ V, Kulagin N, Ostrovskaya NV, Poltoratskiĭ ÉA. Optimal self-compression of multisoliton pulses in an optical fiber. *Sov J Quant Electron* (1989) 19:1240. doi:10.1070/qe1989v019n09abeh009130
18. JR Taylor ed. *Optical solitons theory and experiment*. Cambridge: Cambridge University Press (1992).
19. Agrawal GP. *Nonlinear fiber optics*. London: Academic Press (2013).
20. Zakharov V, Shabat AB. Exact theory of two-dimensional self-focusing and one-dimensional self-modulation of waves in non linear media. *Sov Phys JETP* (1972) 34:62–9
21. Biondini G, Kovačič G. Inverse scattering transform for the focusing nonlinear schrödinger equation with nonzero boundary conditions. *J Math Phys* (2014) 55:031506. doi:10.1063/1.4868483
22. Suret P, El Koussaifi R, Tikan A, Evain C, Randoux S, Szwaj C, et al. Single-shot observation of optical rogue waves in integrable turbulence using time microscopy. *Nat Commun* (2016) 7:13136. doi:10.1038/ncomms13136
23. Tikan A, Bielawski S, Szwaj C, Randoux S, Suret P. Single-shot measurement of phase and amplitude by using a heterodyne time-lens system and ultrafast digital time-holography. *Nat Photon* (2018) 12:228–34. doi:10.1038/s41566-018-0113-8
24. Tikan A. Effect of local peregrine soliton emergence on statistics of random waves in the one-dimensional focusing nonlinear schrödinger equation. *Phys Rev E* (2020) 101:012209. doi:10.1103/physreve.101.012209
25. Dubrovin B, Grava T, Klein C. On Universality of critical behavior in the focusing nonlinear Schrödinger equation, elliptic Umbilic catastrophe and the Tritronquée Solution to the Painlevé-I equation. *J Nonlinear Sci* (2009) 19: 57–94. doi:10.1007/s00332-008-9025-y
26. Lax PD, David Levermore C. The small dispersion limit of the Korteweg–de Vries equation. I. *Commun Pure Appl Math* (1983) 36, 253–90. doi:10.1002/cpa.3160360302
27. Bronski JC. Semiclassical eigenvalue distribution of the Zakharov–Shabat eigenvalue problem. *Phys Nonlinear Phenom* (1996) 97, 376–97. doi:10.1016/0167-2789(95)00311-8
28. Bronski JC, Nathan Kutz J. Numerical simulation of the semi-classical limit of the focusing nonlinear Schrödinger equation. *Phys Lett* (1999) 254:325–36. doi:10.1016/s0375-9601(99)00133-4
29. Cai D, McLaughlin DW, McLaughlin KT. The nonlinear schrödinger equation as both a pde and a dynamical system. In *Handbook of dynamical systems. vol. 2* Amsterdam: Elsevier (2002). p. 599–675.
30. Deift P, Venakides S, Zhou X. New results in small dispersion KdV by an extension of the steepest descent method for Riemann-Hilbert problems. *Int Math Res Not* (1997) 1997:286–99. doi:10.1155/S1073792897000214
31. Kamvissis S, McLaughlin KDT-R, Miller PD. Semiclassical soliton ensembles for the focusing nonlinear Schrödinger equation. Princeton: Princeton University Press (2003).
32. Tovbis A, Venakides S, Zhou X. On semiclassical (zero dispersion limit) solutions of the focusing nonlinear Schrödinger equation. *Commun Pure Appl Math* (2004) 57:877–985. doi:10.1002/cpa.20024
33. Tovbis A, Venakides S. The eigenvalue problem for the focusing nonlinear Schrödinger equation: new solvable cases. *Physica D: Nonlinear Phenomena* (2000) 146:150–64. doi:10.1016/S0167-2789(00)00126-3

34. Tovbis A, Venakides S, Zhou X. Semiclassical focusing nonlinear Schrodinger Equation I: inverse scattering map and its evolution for radiative initial data. *Int Math Res Not* (2007) 20:12–9. doi:10.1093/imrn/rnm094
35. Mollenauer LF, Stolen RH, Gordon JP. Experimental observation of picosecond pulse narrowing and Solitons in optical fibers. *Phys Rev Lett* (1980) 45:1095–8. doi:10.1103/PhysRevLett.45.1095
36. Mitschke FM Mollenauer LF. Ultrashort pulses from the soliton laser. *Opt Lett* (1987) 12:407. doi:10.1364/OL.12.000407
37. Potasek MJ. Experimental and numerical results of optical subpulse formation of long optical pulses in monomode fibers. *Opt Lett* (1987) 12:717. doi:10.1364/OL.12.000717
38. Agrawal GP. *Applications of nonlinear fiber optics*. London: Academic Press (2001).
39. Tai K, Tomita A. 1100× optical fiber pulse compression using grating pair and soliton effect at 1.319 μm. *Appl Phys Lett* (1986) 48:1033–5. doi:10.1063/1.96639
40. Beaud P, Hodel W, Zysset B, Weber H. Ultrashort pulse propagation, pulse breakup, and fundamental soliton formation in a single-mode optical fiber. *IEEE J Quant Electron* (1987) 23:1938–46. doi:10.1109/JQE.1987.1073262
41. Gouveia-Neto AS, Gomes ASL, Taylor JR. Generation of 33-fsec pulses at 132 μm through a high-order soliton effect in a single-mode optical fiber. *Opt Lett* (1987) 12:395. doi:10.1364/OL.12.000395
42. Chabchoub A, Hoffmann N, Onorato M, Genty G, Dudley JM, Akhmediev N. Hydrodynamic supercontinuum. *Phys Rev Lett* (2013b) 111:054104. doi:10.1103/PhysRevLett.111.054104
43. Tikan A, Billet C, El G, Tovbis A, Bertola M, Sylvestre T, et al. Universality of the peregrine soliton in the focusing dynamics of the cubic nonlinear schrödinger equation. *Phys Rev Lett* (2017) 119:033901. doi:10.1103/physrevlett.119.033901
44. Trebino R. *Frequency-resolved optical Gating: the measurement of ultrashort laser pulses*. Berlin: Springer (2002).
45. Zakharov VE (2009). Turbulence in integrable systems. *Stud Appl* 122:219–34. doi:10.1111/j.1467-9590.2009.00430.x
46. Walczak P, Randoux S, Suret P. Optical rogue waves in integrable turbulence. *Phys Rev Lett* (2015) 114:143903. doi:10.1103/PhysRevLett.114.143903
47. Agafontsev DS, Zakharov VE. Integrable turbulence and formation of rogue waves. *Nonlinearity* (2015) 28:2791. doi:10.1088/0951-7715/28/8/2791
48. Soto-Crespo JM, Devine N, Akhmediev N. Integrable turbulence and rogue waves: breathers or solitons? *Phys Rev Lett* (2016) 116:103901. doi:10.1103/PhysRevLett.116.103901
49. Copie F, Randoux S, Suret P. The physics of the one-dimensional nonlinear schrödinger equation in fiber optics: rogue waves, modulation instability and self-focusing phenomena. *Rev Phys* (2020) 14:10–37. doi:10.1016/j.revip.2019.100037
50. Onorato M, Osborne AR, Serio M, Cavaleri L, Brandini C, Stansberg CT. Observation of strongly non-Gaussian statistics for random sea surface gravity waves in wave flume experiments. *Phys Rev E* (2004) 70:067302. doi:10.1103/PhysRevE.70.067302
51. Cazaubiel A, Michel G, Lepot S, Semin B, Aumaître S, Berhanu M, et al. Coexistence of solitons and extreme events in deep water surface waves. *Phys Rev Fluids* (2018) 3:114802. doi:10.1103/PhysRevFluids.3.114802
52. Michel G, Bonnefoy F, Ducrozet G, Prabhudesai G, Cazaubiel A, Copie F, et al. Emergence of peregrine solitons in integrable turbulence of deep water gravity waves. *Phys Rev Fluids* (2020) 5:082801. doi:10.1103/PhysRevFluids.5.082801
53. Onorato M, Proment D, El, G, Randoux S, Suret P. On the origin of heavy-tail statistics in equations of the Nonlinear Schrödinger type. *Phys Lett* (2016) 380:3173–7. doi:10.1016/j.physleta.2016.07.048
54. Dematteis G, Grafke T, Onorato M, Vanden-Eijnden E. Experimental evidence of hydrodynamic instantons: the universal route to rogue waves. *Phys Rev X* (2019) 9:041057. doi:10.1103/PhysRevX.9.041057
55. Fotopoulos G, Frantzeskakis DJ, Karachalios NI, Kevrekidis PG, Koukouloyannis V, Vetas K. Extreme wave events for a nonlinear Schrödinger equation with linear damping and Gaussian driving. *Commun Nonlinear Sci Numer Simulat* (2020) 82:105058. doi:10.1016/j.cnsns.2019.105058
56. Chabchoub A, Hoffmann N, Branger H, Kharif C, Akhmediev N. Experiments on wind-perturbed rogue wave hydrodynamics using the peregrine breather model. *Phys Fluids* (2013a) 25:101704. doi:10.1063/1.4824706
57. Dudley JM, Genty G, Coen S. Supercontinuum generation in photonic crystal fiber. *Rev Mod Phys* (2006) 78:1135–84. doi:10.1103/RevModPhys.78.1135

Conflict of Interest: The authors declare that the research was conducted in the absence of any commercial or financial relationships that could be construed as a potential conflict of interest.

frontiers in Physics

ORIGINAL RESEARCH
published: 18 February 2021
doi: 10.3389/fphy.2021.580224

On the Analytical and Numerical Solutions of the Linear Damped NLSE for Modeling Dissipative Freak Waves and Breathers in Nonlinear and Dispersive Mediums: An Application to a Pair-Ion Plasma

S. A. El-Tantawy[1,2]*, *Alvaro H. Salas*[3] *and M. R. Alharthi*[4]

[1]Department of Physics, Faculty of Science, Port Said University, Port Said, Egypt, [2]Research Center for Physics (RCP), Department of Physics, Faculty of Science and Arts, Al-Mikhwah, Al-Baha University, Al-Baha, Saudi Arabia, [3]Universidad Nacional de Colombia – Sede Manizales Department of Mathematics and Statistics, FIZMAKO Research Group, Bogotá, Colombia, [4]Department of Mathematics and Statistics, College of Science, Taif University, Taif, Saudi Arabia

OPEN ACCESS

Edited by:
Bertrand Kibler,
UMR6303 Laboratoire Interdisciplinaire Carnot de Bourgogne (ICB), France

Reviewed by:
Chao-Qing Dai,
Zhejiang Agriculture and Forestry University, China
Samiran Ghosh,
University of Calcutta, India

***Correspondence:**
S. A. El-Tantawy
samireltantawy@yahoo.com

Specialty section:
This article was submitted to Plasma Physics, a section of the journal Frontiers in Physics

Received: 05 July 2020
Accepted: 07 January 2021
Published: 18 February 2021

Citation:
El-Tantawy SA, Salas AH and Alharthi MR (2021) On the Analytical and Numerical Solutions of the Linear Damped NLSE for Modeling Dissipative Freak Waves and Breathers in Nonlinear and Dispersive Mediums: An Application to a Pair-Ion Plasma. Front. Phys. 9:580224. doi: 10.3389/fphy.2021.580224

In this work, two approaches are introduced to solve a linear damped nonlinear Schrödinger equation (NLSE) for modeling the dissipative rogue waves (DRWs) and dissipative breathers (DBs). The linear damped NLSE is considered a non-integrable differential equation. Thus, it does not support an explicit analytic solution until now, due to the presence of the linear damping term. Consequently, two accurate solutions will be derived and obtained in detail. The first solution is called a semi-analytical solution while the second is an approximate numerical solution. In the two solutions, the analytical solution of the standard NLSE (i.e., in the absence of the damping term) will be used as the initial solution to solve the linear damped NLSE. With respect to the approximate numerical solution, the moving boundary method (MBM) with the help of the finite differences method (FDM) will be devoted to achieve this purpose. The maximum residual (local and global) errors formula for the semi-analytical solution will be derived and obtained. The numerical values of both maximum residual local and global errors of the semi-analytical solution will be estimated using some physical data. Moreover, the error functions related to the local and global errors of the semi-analytical solution will be evaluated using the nonlinear polynomial based on the Chebyshev approximation technique. Furthermore, a comparison between the approximate analytical and numerical solutions will be carried out to check the accuracy of the two solutions. As a realistic application to some physical results; the obtained solutions will be used to investigate the characteristics of the dissipative rogue waves (DRWs) and dissipative breathers (DBs) in a collisional unmagnetized pair-ion plasma. Finally, this study helps us to interpret and understand the dynamic behavior of modulated structures in various plasma models, fluid mechanics, optical fiber, Bose-Einstein condensate, etc.

Keywords: semi-analytical solution, finite difference method, dissipative rogue waves and breathers, moving boundary method, collisional pair-ion plasmas

1 INTRODUCTION

In the past few years, interest has increased in the treatment required to solve differential equations analytically and numerically which led to the interpretation of ambiguous nonlinear phenomena that exist and propagate in various fields of science such as the field of optical fiber, Bose-Einstein condensate, biophysics, Ocean, physics of plasmas, etc. [1–19]. For instance, the Schrödinger-type equation and its family are devoted to interpreting and investigating the behavior of waves accompanied by the movement of particles in multimedia [4–20]. Additionally, the family of the nonlinear Schrödinger-type equation is used to investigate modulated envelope structures such as dark solitons, bright solitons, gray solitons, rogue waves, breathers structures etc. which can propagate with group wave velocity [11–20]. This family has been solved analytically and numerically using several analytical and numerical methods [1]. The following standard/cubic NLSE

$$i\partial_t \Psi + \frac{1}{2} P \partial_x^2 \Psi + Q|\Psi|^2 \Psi = 0, \tag{1}$$

is considered one of the most universal models used to describe and interpret various physical nonlinear phenomena that can exist and propagate in nonlinear and dispersive media. Numerous monographs and published papers are devoted to studying the NLSE which possesses a special solution in the form of pulses, which retain their shapes and velocities after interacting among themselves. Such a solution is called modulated envelope dark soliton. Other nonlinear modulated structures such as bright and gray solitons, cnoidal waves, etc. could be modeled using **Eq. 1** and its family. Furthermore, the importance of **Eq. 1** extends to the explanation of some mysterious modulated unstable phenomena such as rogue waves (RWs)/freak waves (FWs)/killer waves/huge waves/rogons, all names are synonymous. These waves were observed for the first time in ocean and marine engineering [21] and then extended to appear in many branches of science such as in water tanks [18, 22], finance [23], optical fibers [24–26], in atmosphere and astrophysics [27, 28], and in electronegative plasmas [29–32], etc. In recent decades, explaining the mechanisms of rogue wave (RW) propagation in different systems have been one of the main topics that occupy the minds of many researchers.

RWs have been described by many researchers as temporary/instantaneous waves "that appear suddenly and abruptly disappear without a trace" [33]. RWs possess some characteristics that distinguish them from other modulated waves such as, 1) it is a space-time localized wave i.e., not periodic in both space and time 2) it is a single wave which propagates with the largest amplitude compared to the surrounding waves (almost three times [29] (for first-order RWs) or five times [31] (for second-order RWs), and 3) the statistical distribution of the RW amplitude has a tail that does not follow the Gaussian distribution [34]. Furthermore, there is another type of unstable modulated structure that can be described and investigated by **Eq. 1** and its family, which are called the solitons on finite backgrounds (SFB) or are known as breathers waves including the Akhmediev breathers (ABs) and the Kuznetsov–Ma breathers (KMBs) [35]. Both the ABs and the KMBs are exact periodic solutions to **Eq. 1**. With respect to the ABs and according to **Eq. 1**, it is a space-periodic solution but is localized in the time domain. On the contrary, with respect to the KMBs, it is a time-periodic solution but is localized in the space domain. Both the ABs and KMBs have a plane wave solution when $|t| \to \infty$ and $|x| \to \infty$, respectively. Furthermore, for a limiting case of the periodic breathers, both the ABs and KMBs become localized (i.e., the ABs and KMBs become RWs) in the temporary and spatial domain, [36, 37].

To understand and interpret the puzzle of generating and propagating these types of huge waves in various fields of sciences, many researchers focused their efforts to solve the integrable NLSE and its higher-orders, which describe the analytical RWs and breathers solutions. Most published papers about these waves have been confined to investigating the undamped RWs and breathers in the absence of the damping forces (the friction force or collisions between the media particles) [19, 38–40]. In fact, we can only neglect the force of friction in very few cases of superfluids (no viscosity). So consequently, this force must be taken into consideration when studying the propagation of these waves in optical fiber, laser, physics of plasmas, etc. to ensure the phenomenon under consideration is described accurately and comprehensively. Recently, different experimental approaches have been used to generate the dissipative RWs (DRWs) in Mode-Locked Laser [41], multiple-pulsing mode-locked fiber laser [42], fiber laser [43], and in an ultrafast fiber laser [44]. Theoretically, few attempts have been made to understand the physical mechanism of generating and propagating DRWs and DBs (dissipative Akhmediev breathers (DABs) and dissipative Kuznetsov-Ma breathers (DKMBs) in the fluid mechanics and in plasma physics when considering the friction forces [45–50]. In these papers, authors tried to find an approximate analytical solution to the following non-integrable linear damped NLSE.

$$i\partial_t \Psi + P\partial_x^2 \Psi + Q|\Psi|^2 \Psi + iR\Psi = 0 \tag{2}$$

These studies relied on the use of an appropriate transformation [45] to convert **Eq. 2** into the integrable NLSE (1) which has a hierarchy of exact analytical solutions such as envelope solitons, RWs, breathers, cnoidal waves, etc. Motivated by the observations of RWs in the laboratory in the case of electronegative plasmas and a fiber laser, we have made some subtle and distinguishable attempts to obtain some approximate analytical and numerical solutions for **Eq. 2** without converting this equation to the standard cubic NLSE (1). In the first attempt (our first objective), the DRWs and DBs solutions will be obtained in the form of semi-analytical solutions based on the exact analytical solution to **Eq. 1**. To our knowledge, this is the first attempt to derive an approximate analytical solution with high accuracy for the DRWs and DBs of **Eq. 2** without transforming it to **Eq. 1**. The second objective of our study, is to use some hybrid numerical methods, such as the moving boundary method (MBM) with the finite difference method (FDM), to solve the non-integrable **Eq. 2** numerically and to make a comparison between the numerical

approximate solution and the semi-analytical solution to check the accuracy and the effectiveness of both of them. Moreover, the maximum local (at a certain value of time, say, at final time) and global (taken over all space-time domain) errors of the semi-analytical solution are estimated. Furthermore, the error functions related to the whole space-time domain and final time for the semi-analytical solution is evaluated using the polynomial based on the Chebyshev approximation technique. The most important characteristic of our techniques is their ability to give an excellent, accurate, and comprehensive description for the phenomena under study.

The remainder of this paper is structured as follows: in **Section 2**, we briefly review the results obtained by Sikdar et al. [49] studying both collisionless and collisional envelope solitons in collisional pair-ion unmagnetized plasmas with completely depleted electrons. The profile of modulational instability (MI) of the (un)damped electrostatic potential is also analyzed and investigated in **Section 2**. Moreover, the (un)stable regions of ion-acoustic (IA) modulated structures are determined precisely, depending on the criteria of the MI of non-dissipative and dissipative modulated structures. In **Section 3**, the exact analytical RW and breathers solutions to **Eq. 1** are discussed briefly. Thereafter, we devote great effort to solve and analyze **Eq. 2** analytically to obtain a semi-analytical solution to the DRWs and DBs. In **Section 4**, the hybrid MBM-FDM is introduced to analyze **Eq. 2** to investigate the characteristics behavior of both the DRWs and DBs. The results are summarized in **Section 5**.

2 THE PHYSICAL MODEL AND A LINEAR DAMPED NLSE

Sikdar et al. [49] reduced the fluid governing equations of the collisional pair-ion unmagnetized plasmas to the linear damped NLSE using a reductive perturbation technique (the derivative expansion method) to study both collisionless and collisional envelope solitons (bright and dark solitons). In this model, the plasma system consists of warm positive and negative fullerene ions (C_{60}^{+} and C_{60}^{-}) in addition to considering the ion-neutral collision [49, 51]. The linear damped NLSE obtained by Sikdar et al. [49] is similar to **Eq. 2**. In Sikdar et al. [49] model, the linear damping term ($iR\Psi$) appeared as a result of considering the ion-neutral collision. The coefficients P, Q, and R represent the coefficients of the dispersion, nonlinear, and linear damping terms, respectively. These coefficients are functions of various plasma parameters such as, the temperature $T_{\pm}$ and the ion-neutral collision frequency $\nu_{\pm}$ of both the positive and negative ions. The derivation details of the linear damped NLSE for the present model and the values of P, Q, and Γ_c can be found in Ref. 49. Sikdar et al. [49] observed that in the dimensional form, the system supports two modes, namely, high frequency ion plasma wave (IPW) and low frequency ion-acoustic wave (IAW). They also observed that for the IPW both P and Q are always positive against the modulated wavenumber (k) and for different values of $(T_+, T_-) = (0.9, 0.6)$ and $(T_+, T_-) = (0.0.54, 0.9)$. On the other hand, for the IAW, the coefficient P is always negative while the coefficient Q may be positive or negative depending on the value of the modulated wavenumber. Moreover, it was found that the coefficient of the dissipative term Γ_c is always positive for all cases. It is known that in the absence of the dissipative/damping term ($\Gamma_c = 0$), the standard NLSE supports a series of exact analytical solutions like the dark solitons, bight solitons, gray solitons, RWs, breathers (Akhmediev breathers (ABs), and Kuznetsov–Ma breathers (KMBs)), etc. On the contrary, in the presence of the dissipative term ($\Gamma_c \neq 0$), the linear damped NLSE becomes completely non-integrable, i.e., it does not have an exact analytical solution in its present form. As a result, this equation could be solved numerically or semi-analytically by one of the known methods describing many nonlinear modulated structures that can exist and propagate in different branches of science [49].

Without loss of generality, we can rewrite the linear damped NLSE in the following form Refs. 49 and 52.

$$i\partial_t \Psi + \frac{1}{2} P \partial_x^2 \Psi + Q\left|\Psi\right|^2 \Psi + iR\Psi = 0, \tag{3}$$

where $P \equiv P/2$ and $\Gamma_c \equiv R$.

According to the linear stability analysis and for undamped modulated structures ($R = 0$), the nonlinear modulated envelope excitations (IWA and IPW) become stable (unstable) if $Q > 0\,(Q < 0)$ is fulfilled [53]. In this case, the sign of the product PQ is a necessary and sufficient condition to determine the regions of different types of modulated excitations in the present model. However, for damped modulated structures ($R \neq 0$), the criteria for MI of envelope excitations become a function of time in addition to the physical parameters related to the model under consideration and in this case, there are other restrictions on the propagation of the dissipative IAW and IPW envelope structures [46–50, 54, 55]. In this case and according to the linear stability analysis, the value of nonlinear dispersion relation is obtained as: $\Omega^2 = (PK^2)^2\,(1 - K_c^2\,(\tau)/K^2)$, with the critical modulated wavenumber $K_c^2\,(\tau) = (2Q/P)\left|\psi_0\right|^2 \exp\left(-2R\tau\right)$ where $\Omega\,(\ll \omega)$ and $K\,(\ll k)$ refer to the perturbation frequency and wavenumber in the slowly coordinates (x, t), ψ_0 donates the amplitude of the pumping carrier wave (which is a constant value and larger than the perturbation value). At first glance, we can see that the modulated structures become unstable if $PQ > 0$ & $\Omega^2 < 0$ & $t < t_{\max}$ are fulfilled. Here, t donates the time (or period) of the wave propagation and $t_{\max} = [1/(2R)]\ln[2Q\left|\psi_0\right|^2/(PK^2)]$ gives the MI period [46–50]. On the contrary, for $t > t_{\max}$ even if $PQ > 0$, the modulated envelope structures become stable and in this case both dissipative RWs and dissipative breathers cannot exist in this model. It can be seen that for $R = 0$, the critical wavenumber of modulated structures $K_c^2 = (2Q/P)\left|\psi_0\right|^2$ does not depend on t.

In the present study, we take the IAW mode as an example for applying our numerical and semi-analytical solutions for investigating the behavior of the dissipative RWs and dissipative breathers. Knowing that the analytical and numerical solutions that we obtain can be applied to any system and mode, we only take the IAW mode as an example. The (in)stability regions electrostatic modulated structures must

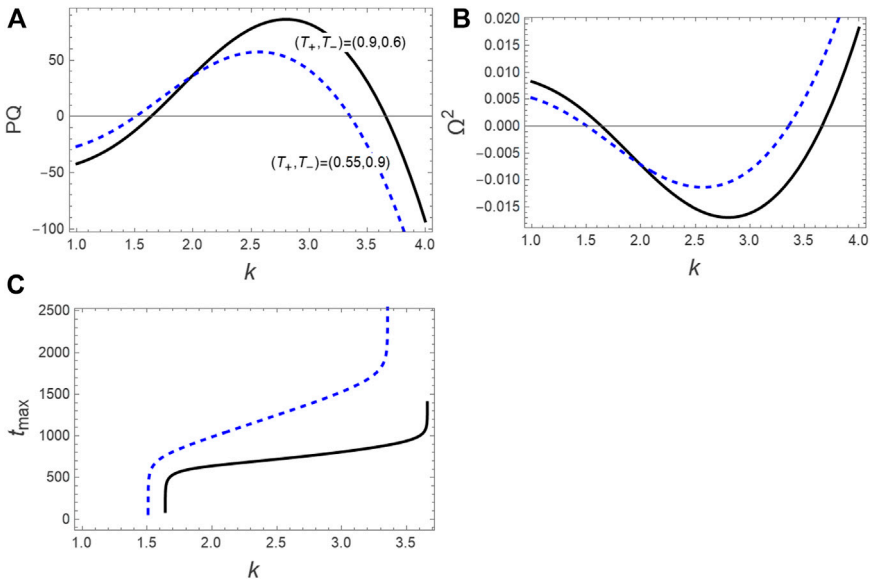

FIGURE 1 | The regions of (un)stable electrostatic ion-acoustic modulated structures according to **(A)** the sign of the product PQ and **(B)** the sign of both Ω^2 are plotted against the wavenumber k for different values of (T_+, T_-). Also, **(C)** the maximum value of modulational instability period t_{max} is plotted against the wavenumber k for different values of (T_+, T_-). Note that the DRWs and DBs only exist in the regions that meet the instability conditions $(PQ > 0 \,\&\, \Omega^2 < 0 \,\&\, t < t_{max})$.

be determined precisely before embarking on solving this equation. **Figure 1** demonstrates the (un)stable regions of the (un)damped modulated structures according to the above mentioned criteria. In **Figures 1A–C** the product of PQ, the square perturbation frequency of modulated structures Ω^2, and t_{max} are, respectively, plotted against the wavenumber k for $(T_+, T_-) = (0.9, 0.6)$ and $(T_+, T_-) = (0.0.54, 0.9)$. As mentioned above, the necessary and sufficient condition to define the (in)stability regions of modulated structures is the sign of the product of PQ which for $PQ < 0$ $(PQ > 0)$, the wave becomes stable (unstable) as shown in **Figure 1A**. With respect to the damped modulated structures $(R \neq 0)$ when propagating the unstable wave, the conditions $PQ > 0$ & $\Omega^2 < 0$ & $t < t_{max}$ must be fulfilled, otherwise the stable wave can be existed and propagated. Form **Figure 1C**, we can determine the time of propagation for the unstable wave by taking any time value which satisfies the unstable conditions: $PQ > 0$ & $\Omega^2 < 0$ & $t < t_{max}$. It should be mentioned here that the RWs and breathers could propagate only in the unstable regions.

In the following sections, we devote our effort to solving **Eq. 3** using two approximate methods to investigate the characteristic behavior of some modulated structures that propagate within such a model of DRWs and DBs (DABs and DKMBs), etc.

3 ROGUE WAVES AND BREATHERS SOLUTIONS OF LINEAR DAMPED NLSE

The two approximate methods used to find some approximate solutions for **Eq. 3** are:

(1) The first method is the semi-analytical method where the exact solution to the standard NLSE $(R = 0)$ is used to construct an approximate analytical solution to **Eq. 3** without any iterations or use of computer code. In addition, the speed obtaining the result does not depend on the efficiency of the device.

(2) The second method is a hybrid method between two numerical methods; the moving boundary method (MBM) and the finite difference method (FDM). Furthermore, in these methods, the exact solution to the standard NLSE $(R = 0)$ is used as the initial solution to finding the approximate numerical solutions to **Eq. 3**. In this case, the numerical solutions depend on a computer code and the accuracy depends on the number of iterations. The speed of running a code also depends on the efficiency of the device.

3.1 Analytical RWs and Breathers Solutions to the NLSE

It is obvious that the dissipation effect can be neglected $(R = 0)$ as compared to the dispersion effect, if the dispersion effect becomes more dominant than the dissipation effect. In this case, the linear damped NLSE (3) can be reduced to the following standard NLSE

$$i\partial_t \Phi + \frac{1}{2} P \partial_x^2 \Phi + Q|\Phi|^2 \Phi = 0 \;\&\; \forall (x,t) \in \mathcal{O} \tag{4}$$

where $\mathcal{O} \in [L_i, L_f] \times [T_i, T_f]$ represents the physical domain of x and t, $L_i + L_f$ gives the length of the plasma system, and $T_f < t_{max}$, and for simplicity $\Phi_\delta \equiv \Phi_\delta(x,t) \equiv \Psi|_{R=0}$ is used.

The exact breathers and RWs solutions of **Eq. 4** is Refs. 20 and 38.

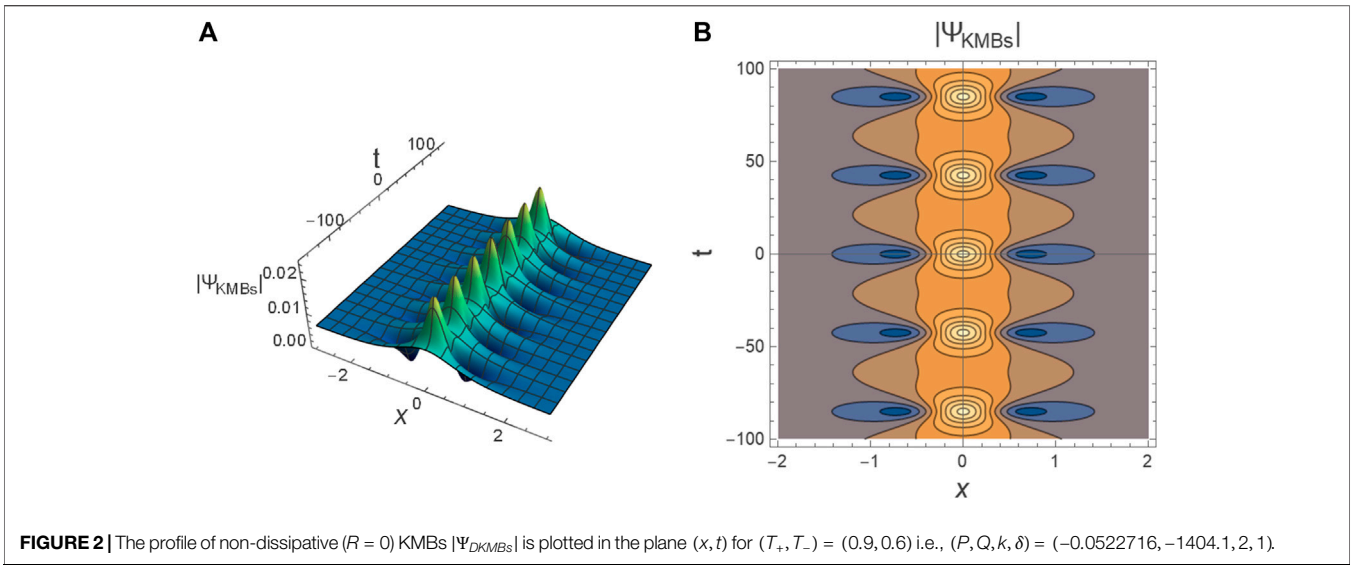

FIGURE 2 | The profile of non-dissipative ($R = 0$) KMBs $|\Psi_{DKMBs}|$ is plotted in the plane (x,t) for $(T_+, T_-) = (0.9, 0.6)$ i.e., $(P, Q, k, \delta) = (-0.0522716, -1404.1, 2, 1)$.

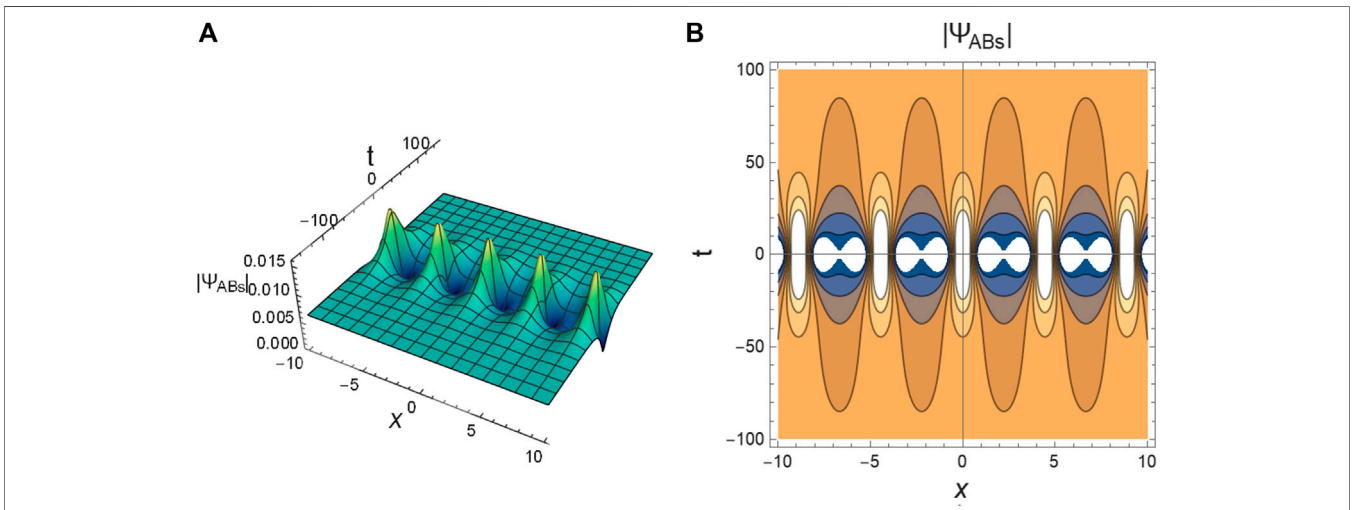

FIGURE 3 | The profile of non-dissipative ($R = 0$) ABs $|\Psi_{DABs}|$ is plotted in the plane (x,t) for $(T_+, T_-) = (0.9, 0.6)$ i.e., $(P, Q, k, \delta) = (-0.0522716, -1404.1, 2, 0.25)$.

$$\Phi_\delta = \sqrt{\frac{P}{Q}}\left[1 + \frac{2(1-2\delta)\cosh(l_1 Pt) + il_1 \sinh(l_1 Pt)}{\sqrt{2\delta}\cos(l_2 x) - \cosh(l_1 Pt)}\right] e^{iPt}, \quad (5)$$

where the growth factor $l_1 = \sqrt{8\delta(1-2\delta)}$ and the instability wavenumber of the breathers is $l_2 = \sqrt{4(1-2\delta)}$, and δ is a real and positive parameter ($\delta > 0$) responsible for determining the type of breathers structures as follows: for $\delta > 1/2$, the time-periodic KMBs solution is covered as shown in **Figure 2**, for $0 < \delta < 1/2$, the space-periodic ABs solution is obtained (see **Figure 3**), and the RW solution is covered for $\delta \to 1/2$ as illustrated in **Figure 4**. At $(x, t = 0)$ and $(x = 0, t = 0)$, both the peaks $\Phi_\delta(x, 0)$ and the maximum amplitudes (the amplification) $\Phi_{\delta-\mathrm{Max}}$ of RWs and breathers (ABs and KMBs) are

$$\Phi_\delta(x, 0) = \sqrt{\frac{P}{Q}}\left(1 + \frac{2(1-2\delta)}{\sqrt{2\delta}\cos(b_2 x) - 1}\right), \quad (6)$$

and

$$\Phi_{\delta-\mathrm{Max}} = \sqrt{\frac{P}{Q}}\left(1 + 2\sqrt{2\delta}\right) \quad (7)$$

It is also known that parameter δ is responsible for the periodicity of both KMBs and ABs, as depicted in **Figure 3**. An increase in δ leads to an increase in the number of periodicity for both KMBs (see **Figure 5A**) and ABs (see **Figure 5B**). Moreover, as seen from **Figures 2–4** and **Eq. 7** the maximum amplitude of RWs $\Phi_{\delta \to \frac{1}{2}-\mathrm{Max}}$ is larger than the ABs $\Phi_{0<\delta<\frac{1}{2}-\mathrm{Max}}$ but smaller than the KMBs $\Phi_{\delta>\frac{1}{2}-\mathrm{Max}}$ i.e., $\Phi_{\delta>\frac{1}{2}-\mathrm{Max}} > \Phi_{\delta\to\frac{1}{2}-\mathrm{Max}} > \Phi_{0<\delta<\frac{1}{2}-\mathrm{Max}}$.

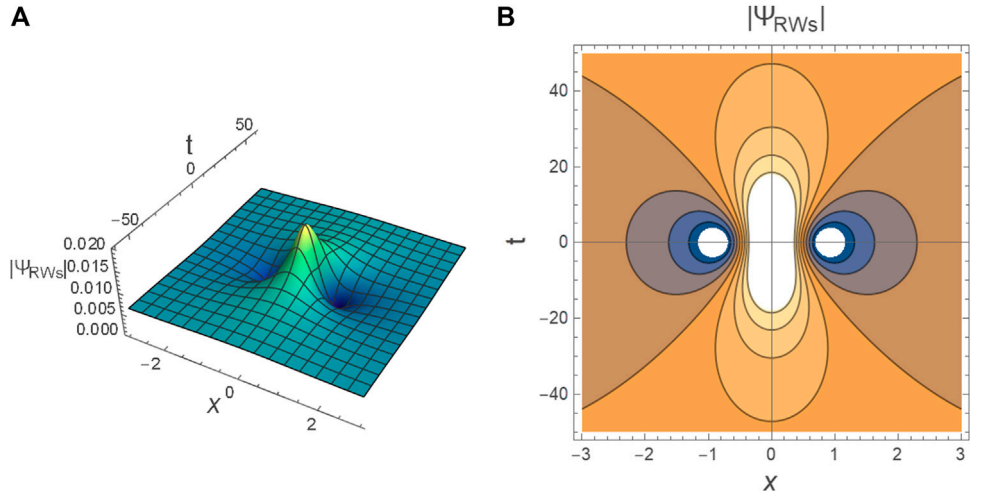

FIGURE 4 | The profile of non-dissipative ($R = 0$) RWs $|\Psi_{DRWs}|$ is plotted in the plane (x, t) for $(T_+, T_-) = (0.9, 0.6)$ i.e., $(P, Q, k, \delta) = (-0.0522716, -1404.1, 2, \rightarrow 0.5)$.

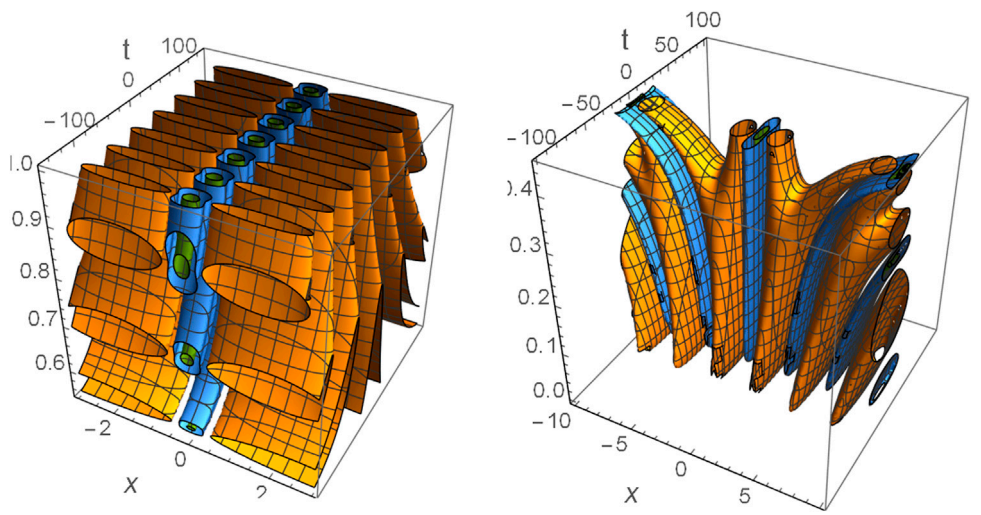

FIGURE 5 | The non-dissipative ($R = 0$) KMBs and ABs solutions are plotted against (x, t, δ) for $(T_+, T_-) = (0.9, 0.6)$ i.e., $(P, Q, k) = (-0.0522716, -1404.1, 2)$.

3.2 Semi-Analytical Solution of Dissipative RWs and Breathers

It is known that **Eq. 3** is a non-integrable equation i.e., it has no analytical solution in its current form without using any transformation. So, in this section, we devote our efforts to obtain an approximate analytical solution for this equation. To do that let us suppose that $Q = 0$, then **Eq. 3** becomes

$$i\partial_t \Psi + \frac{1}{2} P \partial_x^2 \Psi + iR\Psi = 0. \tag{8}$$

Also, suppose that $\phi \equiv \phi(x, t)$ is an exact analytical solution to

$$i\partial_t \phi + \frac{1}{2} P \partial_x^2 \phi = 0. \tag{9}$$

According to **Eqs. 8, 9**, the definition of Ψ reads

$$\Psi = f\phi. \tag{10}$$

where $f \equiv f(t)$ is a time-dependent function which will be determined later.

Inserting **Eq. 10** into **Eq. 8**, we get

$$\begin{aligned} &i\partial_t \Psi + \frac{1}{2} P \partial_x^2 \Psi + iR\Psi \\ &= i\phi\left(f' + Rf\right) \\ &= 0. \end{aligned} \tag{11}$$

here, the prime "′" represents the derivative with respect to t.

It is clear that for $f' + Rf = 0$, we have

$$f = e^{-Rt}. \tag{12}$$

Then $\Psi = f(t)\phi(x,t)$ becomes a solution to **Eq. 8**. This motivates us to seek an approximate analytical solution to **Eq. 3** in the ansatz form

$$\Psi = f\Phi, \tag{13}$$

where $\Phi \equiv \Phi(x,t)$ represents any exact analytical solution to **Eq. 4**.

Inserting ansatz **Eq. 13** into **Eq. 3** and taking the following definition into account

$$Q|\Phi|^2\Phi = -\frac{1}{2}P\partial_x^2\Phi - i\partial_t\Phi, \tag{14}$$

we obtain

$$\left\{ i\partial_t\Psi + \frac{1}{2}P\partial_x^2\Psi + Q|\Psi|^2\Psi + iR\Psi = i\Phi(f' + Rf) + \frac{1}{2}Pf(1-f^2)\partial_x^2\Phi + if(1-f^2)\partial_t\Phi. \right. \tag{15}$$

Equation 15 suggests the choice

$$f' + Rf = 0 \text{ for all } t, \tag{16}$$

by integrating **Eq. 16** once over t, yields

$$f = e^{-Rt}. \tag{17}$$

Finally, the semi-analytical solution to **Eq. 3** for DRWs ($\delta \to 1/2$), DKMBs ($\delta > 1/2$), and DABs ($0 < \delta < 1/2$) can be expressed by

$$\Psi = \Phi_\delta e^{-Rt}, \tag{18}$$

where Φ_δ is given by **Eq. 5**.

The residual associated to **Eq. 3** reads

$$H(x,t) = i\partial_t\Psi + \frac{1}{2}P\partial_x^2\Psi + Q|\Psi|^2\Psi + iR\Psi. \tag{19}$$

In view of **Eq. 15**, we get

$$H(x,t) = \frac{1}{2}Pf(1-f^2)\partial_x^2\Phi + if(1-f^2)\partial_t\Phi. \tag{20}$$

From **Eq. 20**, we obtain

$$L_R \equiv |H(x,t)| \le \max_{\Omega}\left[\left|\frac{1}{2}f(1-f^2)\left(2\partial_t\Phi + iP\partial_x^2\Phi\right)\right|\right] \tag{21}$$

For example, the expression of the square residual error for the DRWs ($\delta = 1/2$) can be estimated from **Eqs. 5, 21** as follows

$$|H(x,t)|^2 = \frac{4P^3\left[16P^4t^4 + 8P^2t^2\left(4x^2+5\right) + \left(3-4x^2\right)^2\right]^3}{Q\left(4P^2t^2 + 4x^2 + 1\right)^6} f^2(1-f^2)^2. \tag{22}$$

By simplifying the square root of **Eq. 22**, we get

$$|H(x,t)| \le 54\left|\sqrt{\frac{P^3}{Q}}\sinh(Rt)e^{-2Rt}\right|. \tag{23}$$

Similarly, the expression of the residual error for $\delta \neq 1/2$ can be estimated after some algebraic manipulations using **Eqs. 5, 21** but the details are not inserted here because they are too large.

Let us introduce some numerical examples (or sometimes it is called experimental examples) to investigate the characteristic behavior of DRWs and DBs (DABs and DKMBs) to be able to evaluate the residual errors of solution **Eq. 18**. In the unstable region for the damped wave ($PQ > 0$ & $\Omega^2 < 0$ & $t < t_{\max}$), the values of the physical plasma parameters $(T_+, T_-, k) = (0.9, 0.6, 2)$ give $(P, Q) \approx (-0.0522716, -1404.1)$. Also, for the same values of the last plasma parameters $(T_+, T_-) = (0.9, 0.6)$ and different values of wavenumber k, the values of both R and $t_{\max}$ could be obtained as given in the table below.$|\Psi_{DKMBs}|$, DABs $|\Psi_{DABs}|$, and DRWs $|\Psi_{DRWs}|$ are, respectively, illustrated in **Figures 6–8** corresponding to the semi-analytical solution **Eq. 18**. Also, the impact of normalized ion-neutral collision frequencies $\nu_\pm$ on the profile of DKMBs $|\Psi_{DKMBs}|$ (similarly DABs $|\Psi_{DABs}|$ and DRWs $|\Psi_{DRWs}|$ but we have not included their illustrations here) is investigated as elucidated in **Figure 9**, for different values of $\nu_\pm$. It is observed that the KMBs create low intensity pulses with increasing R which has been confirmed in some laboratory experiments [41–44]. Moreover, for $(T_+, T_-, k) = (0.9, 0.6, 1.8)$ which means $(P, Q) \approx (-0.0608182, -525.935)$ and for different values of R, both the maximum local (at final time T_f) and maximum global (on the whole domain space-time domain $x_i(-10) \le x \le x_f$ (10) & $0 \le |t| \le T_f$ (10)) residual errors (L_R) of the approximate analytical solution **Eq. 18** are evaluated as shown in **Figures 10**, **11**, respectively. These errors are estimated according to formula **Eq. 21** for the solution **Eq. 18**. Furthermore, the functions of the maximum local and maximum global errors of solution **Eq. 18** could be evaluated using the polynomials based on the Chebyshev approximation technique [18, 19]. The comparison between the maximum residual (local and global) errors (L_R) using relation **Eq. 22** and the errors functions evaluated by the Chebyshev approximation technique is illustrated in **Figure 10** for the maximum local error and in **Figure 11** for the maximum global error. It is observed that the results produced by relation **Eq. 22** are in good agreement with the results obtained by Chebyshev polynomials. This enhances the high accuracy of the obtained semi-analytical solution **Eq. 18**. It should be noted here that the solution **Eq. 18** could be used to explain and interpret the dissipative RWs and breathers that can occur and propagate in many branches of science such as optical fibers. Thus, any values for the coefficients P, Q, and R could be used for any application and not only in plasma physics which in our solution is considered to be stable with any values for P, Q, and R.

4 NUMERICAL APPROXIMATE SOLUTIONS

Let us define the following initial value problem (i.v.p.)

$$i\partial_t\Psi + \frac{1}{2}P\partial_x^2\Psi + Q|\Psi|^2\Psi + iR\Psi = 0, \tag{24}$$

which is subjected to the initial condition

$$\Psi(x, t = T_i) \equiv \Psi_0(x, T_i) = \Phi(x), \ \forall\ (x,t) \in \mathcal{O}, \tag{25}$$

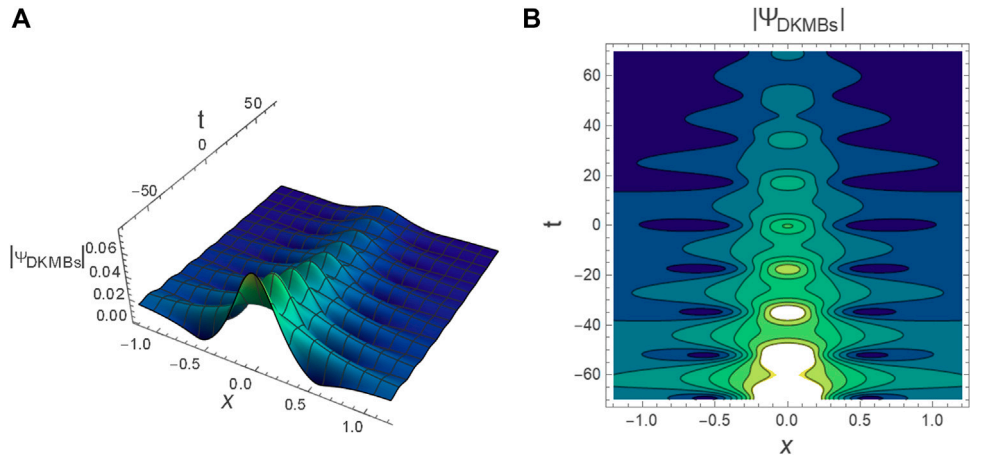

FIGURE 6 | The profile of DKMBs $|\Psi_{DKMBs}|$ is plotted in the plane (x,t) for $(P,Q,k,\delta,R) = (-0.0522716, -1404.1, 2, 2, 0.0136)$. **(A)** Plot3D for DKMBs $|\Psi_{DKMBs}|$ and **(B)** Contourplot for DKMBs $|\Psi_{DKMBs}|$.

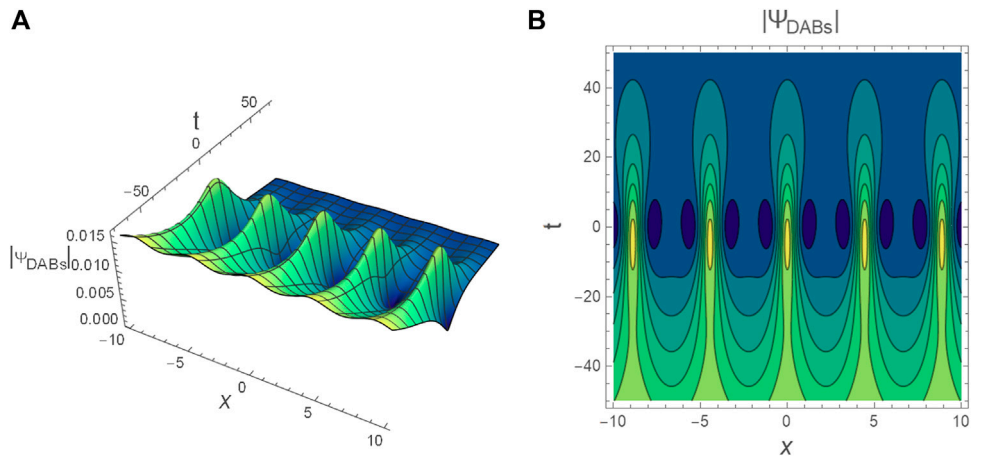

FIGURE 7 | The profile of DABs $|\Psi_{DABs}|$ is plotted in the plane (x,t) for $(P,Q,k,\delta,R) = (-0.0522716, -1404.1, 2, 0.25, 0.0136)$. **(A)** Plot3D for DABs $|\Psi_{DABs}|$ and **(B)** Contourplot for DABs $|\Psi_{DABs}|$.

and the Dirichlet boundary conditions

$$\begin{cases} \Psi(L_i,t) = \mathcal{F}_L(t), \\ \Psi\big(L_f,t\big) = \mathcal{F}_R(t), \end{cases} \tag{26}$$

where $0 < |t| < t_{\max}$, $\mathcal{O} = [L_i, L_f] \times [T_i, T_f]$ represents the space-time domain, $L_i + L_f$ denotes the plasma system length, and $\Phi(x)$ indicates any exact analytical solution to the undamped NLSE i.e., **Eq. 24** for $R = 0$. As a special case, the RW and breathers solutions given in **Eq. 5** could be used as the initial solution for **Eq. 24** at a certain time (say $t = T_i$).

4.1 Finite Differences Method

To solve the i. v.p. **Eqs. 24–26** numerically using the FDM. [40, 56], we first divide the complex function $\Psi \equiv \Psi(x,t)$ into real and imaginary parts

$$\Psi = U + iV, \tag{27}$$

where $U \equiv U(x,t) = \mathrm{Re}(\Phi)$ and $V \equiv V(x,t) = \mathrm{Im}(\Phi)$. As a special case, the values of U and V could be obtained from solution **Eq. 5** as

$$U = \sqrt{\frac{P}{Q}}\Bigg[\cos(Pt) + \frac{2(1-2\delta)\cosh(l_1 Pt)\cos(Pt) - l_1\sinh(l_1 Pt)\sin(Pt)}{\sqrt{2\delta}\cos(l_2 x) - \cosh(l_1 pt)}\Bigg], \tag{28}$$

and

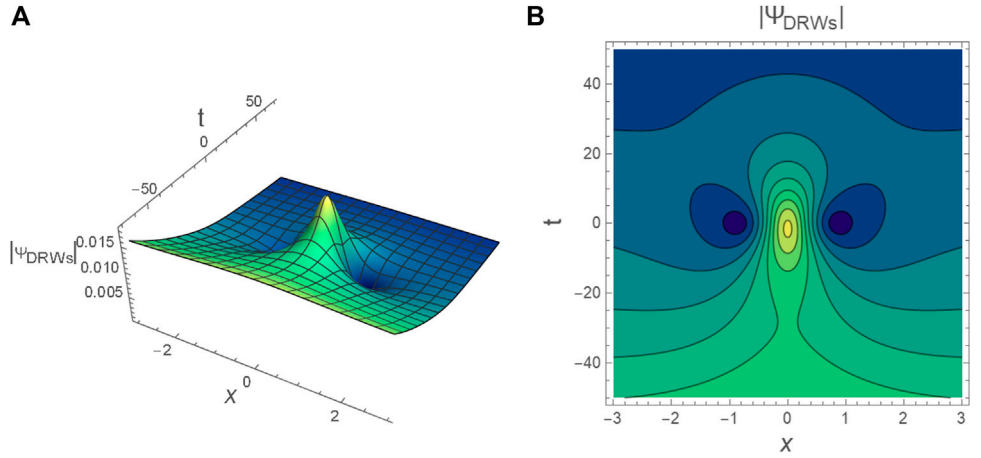

FIGURE 8 | The profile of DRWs $|\Psi_{DRWs}|$ is plotted in the plane (x,t) for $(P,Q,k,\delta,R) = (-0.0522716, -1404.1, 2, \rightarrow 0.5, 0.0136)$. **(A)** Plot3D for DRWs $|\Psi_{DRWs}|$ and **(B)** Contourplot for DRWs $|\Psi_{DRWs}|$.

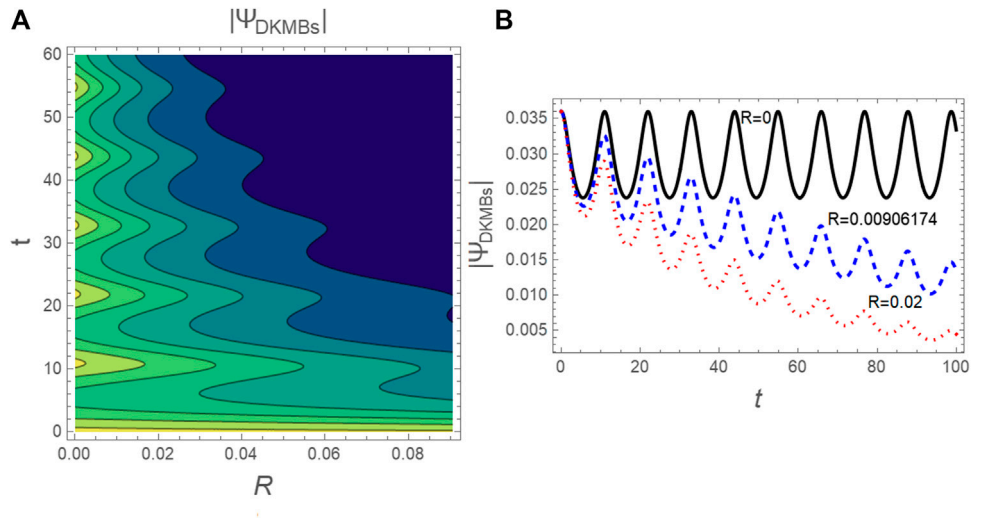

FIGURE 9 | (A) The contourplot of DKMBs profile $|\Psi_{DKMBs}|$ according to the semi-analytical solution **Eq. 18** is plotted in the plane (t,R) and **(B)** The DKMBs profile $|\Psi_{DKMBs}|$ according to the semi-analytical solution **Eq. 18** is plotted against t for different values of R. Here, $(P,Q,k,\delta) = (-0.0522716, -1404.1, 2, 3)$.

$$V = \sqrt{\frac{P}{Q}}\left[\sin(Pt) + \frac{2(1-2\delta)\cosh(l_1 Pt)\sin(Pt) + l_1 \sinh(l_1 Pt)\cos(Pt)}{\sqrt{2\delta}\cos(l_2 x) - \cosh(l_1 Pt)}\right] \tag{29}$$

By substituting **Eq. 27** into **Eq. 24** and separating the obtained equation into real and imaginary parts, we get

$$\begin{cases} \frac{1}{2}P\partial_x^2 U + QU(U^2+V^2) - \partial_t V - RV = 0, \\ \frac{1}{2}P\partial_x^2 V + QV(U^2+V^2) + \partial_t U + RU = 0. \end{cases} \tag{30}$$

To apply the FDM, the following discretization for the space-time domain Ω are introduced

$$\begin{cases} x_k = L_i + k\Delta x \& \Delta x = \frac{L_f - L_i}{m}, \ k = 0, 1, 2, \cdots, m, \\ t_j = T_i + j\Delta t \& \Delta t = \frac{T_f - T_i}{n}, \ j = 0, 1, 2, 3, \cdots, n, \end{cases} \tag{31}$$

where m and n indicate the number of iterations. According to the FDM, the values of the space and time derivatives can be found in detail in Ref. 57.

It should be mentioned here that the FDM gives good results for small time intervals, and this is consistent with the values of observed time for the existing acoustic-waves in the plasma model. In general, the large time intervals give ill conditioned systems of nonlinear equations and they are associated to stiffness, causing numerical instability. On the other hand, for large time intervals, the hybrid MBM-FDM works significantly better than FDM.

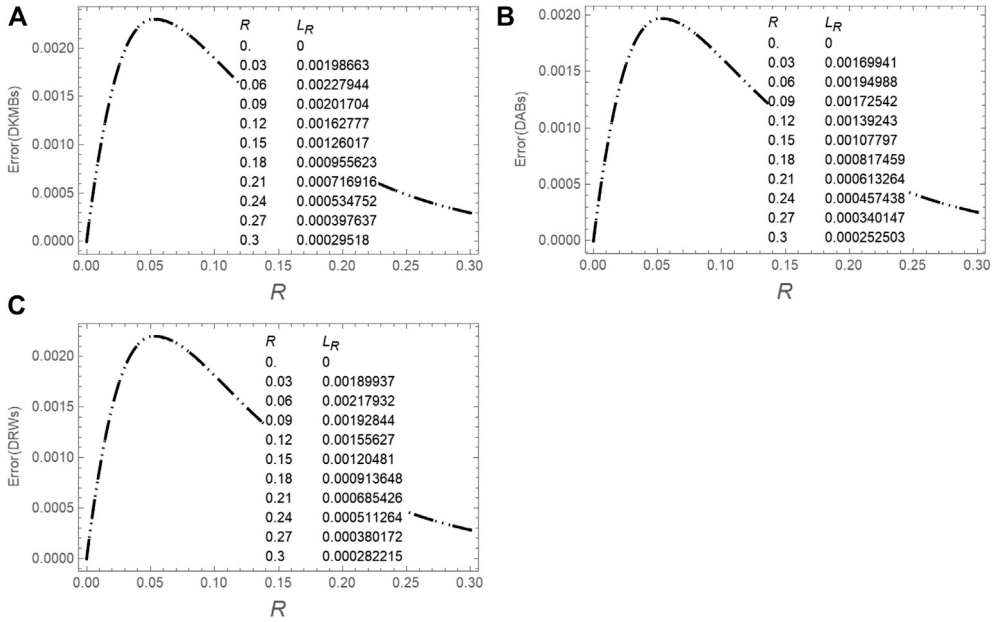

FIGURE 10 | A comparison between the maximum local error (at final time $T_f = 10$) of the semi-analytical solution **Eq. 18** according to the relation **Eq. 22** and the function of the local error related to the final time $T_f = 10$ based on Chebyshev approximation technique is plotted against R for **(A)** DKMBs $\delta = 0.75$, **(B)** DABs $\delta = 0.25$, and **(C)** DRWs $\delta \to 0.5$. Here, $(T_+, T_-) = (0.9, 0.6)$ i.e., $(P, Q, k) = (-0.0608182, -525.935, 1.8)$.

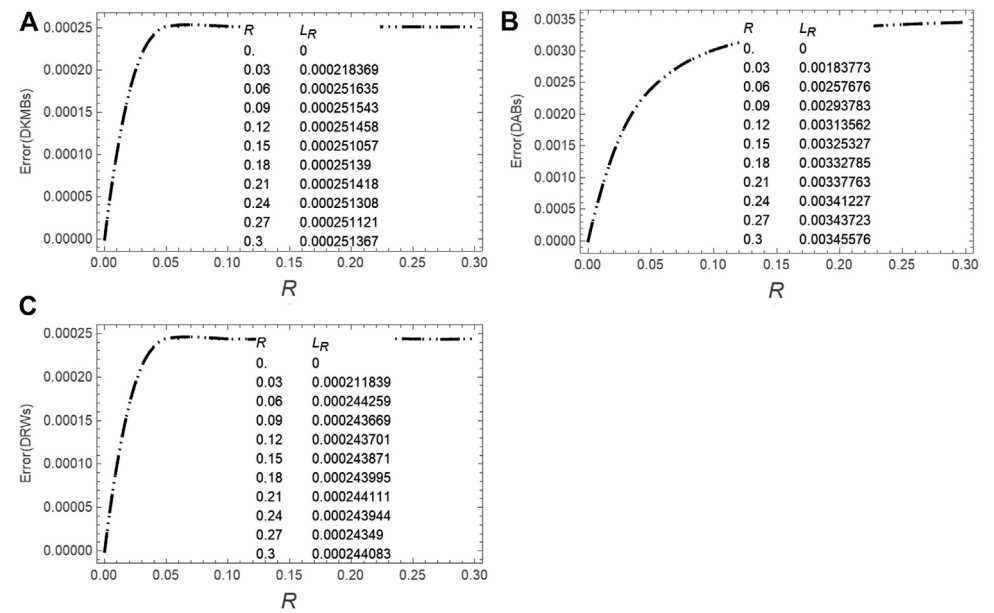

FIGURE 11 | A comparison between the maximum global error (on the whole domain space-time domain $-10 \le x \le 10$ & $0 \le |t| \le 10$) of the semi-analytical solution **Eq. 18** according to the relation **Eq. 22** and the function of the global error related to the whole domain space-time domain based on Chebyshev approximation technique is plotted against R for **(A)** DKMBs $\delta = 0.75$, **(B)** DABs $\delta = 0.25$, and **(C)** DRWs $\delta \to 0.5$. Here, $(T_+, T_-) = (0.9, 0.6)$ i.e., $(P, Q, k) = (-0.0608182, -525.935, 1.8)$.

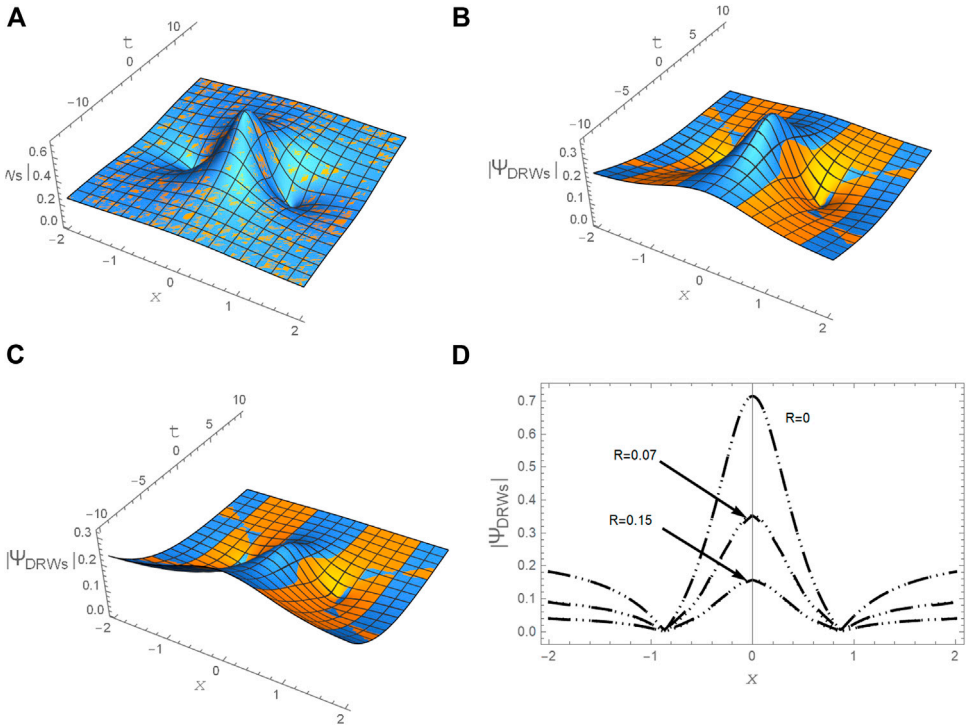

FIGURE 12 | A comparison between the semi-analytical solution **Eq. 18** and the approximate numerical solution **Eq. 32** for DRWs is plotted in the plane (x, t) for **(A)** $R = 0$, **(B)** $R = 0.07$, and **(C)** $R = 0.15$. In **Figure 12D** the comparison between the two approximate solutions (dashed curve for solution **Eq. 18** and dotted curve for solution **Eq. 32**) is plotted against x for different values of R. Here, $(P, Q) \approx (-0.148, -2.6)$.

4.2 The Mechanism of the Moving Boundary Method to Analyze the Linear Damped NLSE

To improve the approximate numerical solution that has been obtained by the FDM, the MBM is introduced to achieve this purpose. In this method we divide the whole-time interval $T_i \le t \le T_f$ into subintervals of length $d\tau = (T_f - T_i)/n$; say $T_i = t_0 < t_1 < t_2 < \cdots < t_j < \cdots < t_n = T_f$, where $t_j = T_i + jd\tau$ $(j = 0, 1, \ldots, n)$. Thereafter, we try to find the solution through the subintervals say: $\Psi_0(x, T_i) = \Phi_0(x, T_i)$ in the subinterval $[T_i, t_1] \times [L_i, L_f]$, $\Psi_1(x, t_1) = \Phi_1(x)$ in the next subinterval $[t_1, t_2] \times [L_i, L_f]$, $\cdots$ until arrive to the final solution $\Psi_j(x, t_j) = \Phi_j(x)$ in the final subinterval $[t_j, t_{j+1}] \times [L_i, L_f]$ with $T_f = T_i + nd\tau \equiv t_n$ where $j = 0, 1, 2, 3, n-1$. Thus, the solution on the whole domain $\Pi = [X_i, X_f] \times [T_i, T_f]$ could be written in the form of a linear combination of characteristic functions such as

$$\Psi(x, t) = \sum_{j=0}^{n-1} \chi_{[t_j, t_{j+1}]}(t) \Psi_j\big(x, t_j\big), \tag{32}$$

with

$$\chi_{[t_j, t_{j+1}]}(t) = \begin{cases} 1 & \text{if } t_r \le t < t_{j+1}, \\ 0 & \text{otherwise.} \end{cases} \tag{33}$$

To illustrate the high accuracy and effectiveness of the hybrid MBM-FDM, we present some numerical examples. For instance, let us analyze the i. v.p. **Eqs. 24–26** using the hybrid MBM-FDM and make a comparison between the semi-analytical solution **Eq. 18** and the numerical approximate solution **Eq. 32** for modeling the DRWs and DBs. The profiles of the DRWs, DABs, and DKMBs are plotted in **Figures 12–14**, respectively, according to the semi-analytical solution **Eq. 18** and approximate numerical solution **Eq. 32** for any random values to the coefficients (P, Q, R) that meet the MI criteria $(PQ > 0 \,\&\, \Omega^2 < 0 \,\&\, t < t_{\max})$. It is observed that both the amplitude and the width of DRWs, DABs, and DKMBs decrease gradually with the increase of the collisional frequency. Generally, the waves decay with an increasing damping coefficient R. Physically, increasing R leads to dissipating wave energy, and consequently it leads to a decrease in the nonlinearity, which leads to the decay of these waves. The local errors (at a certain value of time (say T_f)) of both semi-analytical and numerical solutions are also estimated according to **Eq. 19** as shown in **Table 1**.

The numerical values of the maximum local and global errors of both approximate analytical and numerical solutions for DRWs $(\delta \to 1/2)$ are presented in **Table 1**. It is noted that both approximate analytical and numerical solutions give excellent results as illustrated in **Table 1**. In general, our numerical method does not require a highly efficient device whereas the calculations of this method could be performed by simply using a personal computer. Moreover, the semi-analytical solution provides excellent results, and it is more stable.

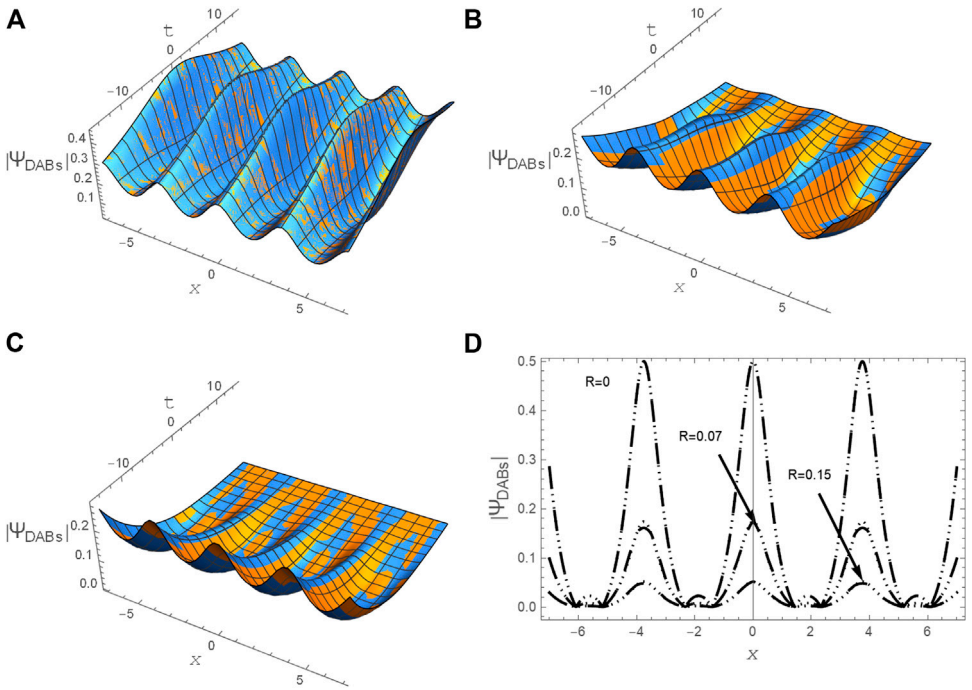

FIGURE 13 | A comparison between the semi-analytical solution **Eq. 18** and the numerical approximate solution **Eq. 32** for DABs ($\delta = 0.15$) is plotted in the plane (x, t) for **(A)** $R = 0$, **(B)** $R = 0.07$, and **(C)** $R = 0.15$. In **Figure 13D** the comparison between the two approximate solutions (dashed curve for solution **Eq. 18** and dotted curve for solution **Eq. 32**) is plotted against x for different values of R. Here, $(P, Q) \approx (-0.148, -2.6)$.

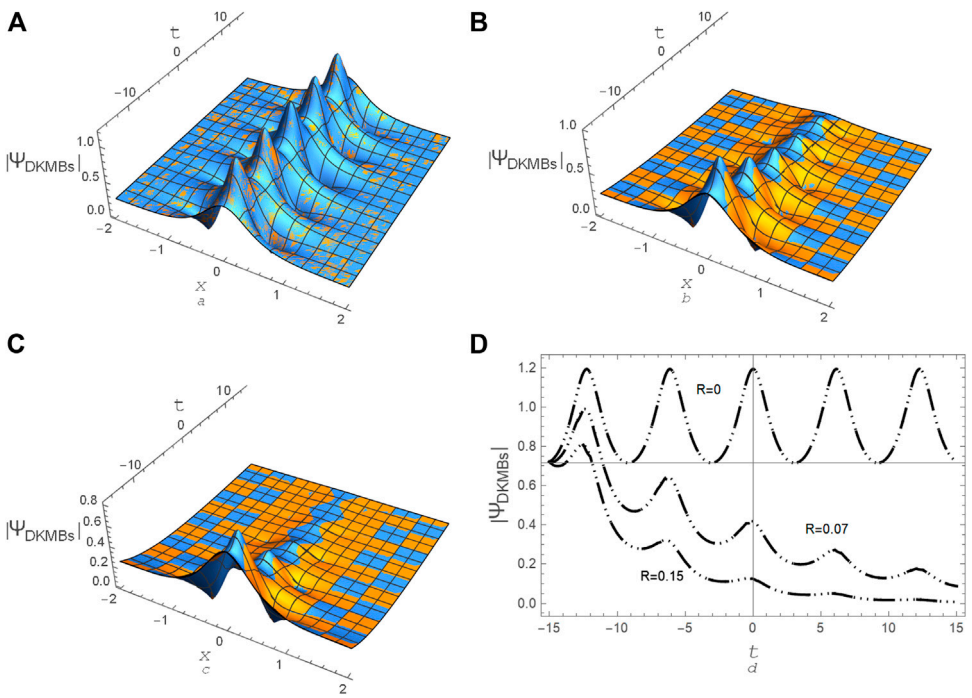

FIGURE 14 | A comparison between the semi-analytical solution **Eq. 18** and the numerical approximate solution **Eq. 32** (Dotted curve) for DKMBs ($\delta = 2$) is plotted in the plane (x, t) for **(A)** $R = 0$, **(B)** $R = 0.07$, and **(C)** $R = 0.15$. In **Figure 14D** the comparison between the two approximate solutions (dashed curve for solution **Eq. 18** and dotted curve for solution **Eq. 32**) is plotted against x for different values of R. Here, $(P, Q) \approx (-0.148, -2.6)$.

TABLE 1 | The maximum local and global residual errors of both approximate analytical and numerical solutions for DRWs have been estimated for $(P, Q) \approx (-0.148, -2.6)$ and with different values to R.

The error type	The maximum residual errors for DRWs			
	For semi-analytical solution		For numerical solution	
	R = 0.07	R = 0.15	R = 0.07	R = 0.15
Local error	0.011573	0.00248082	0.0121557	0.00258409
Global error	0.235132	0.12671	0.178908	0.116047

5 SUMMARY

The propagation of electrostatic nonlinear dissipative envelope structures including dissipative rogue waves (DRWs) and dissipative breathers (DBs) in nonlinear and dispersive mediums, such as unmagnetized collisional pair-ion plasmas composed of warm positive and negative ions, has been investigated analytically and numerally. Sikdar et al. [49] reduced the fluid governing equations of this model to the linear damped nonlinear Schrödinger equation (NLSE) using a reductive perturbation technique (the derivative expansion method) to study both collisionless and collisional envelope solitons (bright and dark solitons). In our study, we used the linear damped NLSE to study both DRWs and DBs in any nonlinear and dispersive medium. The exact analytical solution of the linear damped NLSE has not been possible until now, due to the presence of the damping term. Consequently, two effective methods were devoted to model and solve this problem. The first one is called the semi-analytical method which was built depending on the exact analytical solution of the standard NLSE (without linear damping term). The semi-analytical solution of the linear damped NLSE is considered to be the first attempt at modeling the DRWs and DBs in plasmas or in any other physical medium like optical fiber and so on. In the second method, the numerical simulation solution to the linear damped NLSE using the hybrid new method namely, the moving boundary method (MBM) with the finite difference method (FDM), has been carried out. In this method, the exact solution of the standard NLSE is used as the initial condition to solve the linear damped NLSE using the hybrid MBM-FDM. Moreover, both the local (at final time) and global (on the whole domain space-time domain) maximum residual errors of the approximate solutions have been estimated precisely depending on the physical parameters of the model under consideration. Furthermore, the functions of both the local and global residual errors for solution **Eq. 18** have been evaluated using the polynomials based on the Chebyshev approximation technique. The comparison between the error of both the semi-analytical and numerical solutions have also been examined and it was found that the error is very small, which enhances the high accuracy of the two solutions. This investigation helped us to understand the dynamic mechanism of modulated envelope structures in a strongly coupled complex plasma and many other branches of science such as optical fiber or mechanical fluid, etc.

DATA AVAILABILITY STATEMENT

The original contributions presented in the study are included in the article/Supplementary Material, further inquiries can be directed to the corresponding author.

AUTHOR CONTRIBUTIONS

All authors listed have made a substantial, direct, and intellectual contribution to the work and approved it for publication.

FUNDING

Taif University Researchers Supporting Project number (TURSP-2020/275), Taif University, Taif, Saudi Arabia.

REFERENCES

1. Wazwaz AM. *Partial differential equations and solitary waves theory*. Beijing, USA: Higher Education Press (2009).
2. Wazwaz A-M. A variety of optical solitons for nonlinear Schrödinger equation with detuning term by the variational iteration method. *Optik* (2019) 196:163–9. doi:10.1016/j.ijleo.2019.163169
3. Dai C-Q, Fan Y, Zhang N. Re-observation on localized waves constructed by variable separation solutions of (1+1)-dimensional coupled integrable dispersionless equations via the projective Riccati equation method. *Appl Math Lett* (2019) 96:20–6. doi:10.1016/j.aml.2019.04.009
4. Chen Y-X, Xu F-Q, Hu Y-L. Excitation control for three-dimensional Peregrine solution and combined breather of a partially nonlocal variable-coefficient nonlinear Schrödinger equation. *Nonlinear Dynam* (2019) 95:1957. doi:10.1007/s11071-018-4670-7
5. Dai C-Q, Fan Y, Wang Y-Y. Three-dimensional optical solitons formed by the balance between different-order nonlinearities and high-order dispersion/diffraction in parity-time symmetric potentials. *Nonlinear Dynam* (2019) 98:489–99. doi:10.1007/s11071-019-05206-z
6. Dai C-Q, Liu J, Fan Y, Yu D-G. Two-dimensional localized Peregrine solution and breather excited in a variable-coefficient nonlinear Schrödinger equation with partial nonlocality. *Nonlinear Dynam* (2017) 88:1373–83. doi:10.1007/s11071-016-3316-x
7. Dai C-Q, Wang Y-Y, Fan Y, Yu D-G. Reconstruction of stability for Gaussian spatial solitons in quintic-septimal nonlinear materials under $${{\varvec{\mathcal {P}}}}{\varvec{\mathcal {T}}}$$ P T -symmetric potentials. *Nonlinear Dynam* (2018) 92:1351–8. doi:10.1007/s11071-018-4130-4
8. Dai C-Q, Zhang J-F. Controlling effect of vector and scalar crossed double-Ma breathers in a partially nonlocal nonlinear medium with a linear potential. *Nonlinear Dynam* (2020) 100:1621–8. doi:10.1007/s11071-020-05603-9
9. Yu L-J, Wu G-Z, Wang Y-Y, Chen Y-X. Traveling wave solutions constructed by Mittag-Leffler function of a (2 + 1)-dimensional space-time fractional NLS equation. *Results Phys* (2020) 17:103156. doi:10.1016/j.rinp.2020.103156

10. Wu G-Z, Dai C-Q. Nonautonomous soliton solutions of variable-coefficient fractional nonlinear Schrödinger equation. *Appl Math Lett* (2020) 106:106365. doi:10.1016/j.aml.2020.106365
11. Ruderman MS, Talipova T, Pelinovsky E. Dynamics of modulationally unstable ion-acoustic wavepackets in plasmas with negative ions. *J Plasma Phys* (2008) 74:639–56. doi:10.1017/s0022377808007150
12. Ruderman MS. Freak waves in laboratory and space plasmas. *Eur Phys J Spec Top* (2010) 185:57–66. doi:10.1140/epjst/e2010-01238-7
13. Lü X, Tian B, Xu T, Cai K-J, Liu W-J. Analytical study of the nonlinear Schrödinger equation with an arbitrary linear time-dependent potential in quasi-one-dimensional Bose-Einstein condensates. *Ann Phys* (2008) 323: 2554–65. doi:10.1016/j.aop.2008.04.008
14. Onorato M, Residori S, Bortolozzo U, Montina A, Arecchi FT. Rogue waves and their generating mechanisms in different physical contexts. *Phys Rep* (2013) 528:47–89. doi:10.1016/j.physrep.2013.03.001
15. Chabchoub A, Hoffmann N, Onorato M, Slunyaev A, Sergeeva A, Pelinovsky E, et al. Observation of a hierarchy of up to fifth-order rogue waves in a water tank. *Phys Rev E – Stat Nonlinear Soft Matter Phys* (2012) 86, 056601. doi:10.1103/PhysRevE.86.056601
16. Xu G, Chabchoub A, Pelinovsky DE, Kibler B. Observation of modulation instability and rogue breathers on stationary periodic waves. *Phys Rev Res* (2020) 2:033528. doi:10.1103/physrevresearch.2.033528
17. Biswas A. Chirp-free bright optical soliton perturbation with Chen-Lee-Liu equation by traveling wave hypothesis and semi-inverse variational principle. *Optik* (2018) 172:772–6. doi:10.1016/j.ijleo.2018.07.110
18. Fox L, Parker IB (1968). *Chebyshev polynomials in numerical analysis*. London: Oxford University Press.
19. Clement PR. The Chebyshev approximation method. *Q Appl Math* (1953) 11: 167. doi:10.1090/qam/58024
20. Kibler B, Fatome J, Finot C, Millot G, Genty G, Wetzel B, et al. Observation of Kuznetsov-Ma soliton dynamics in optical fibre. *Sci Rep* (2012) 2:463. doi:10.1038/srep00463
21. Osborne AR. *Nonlinear ocean wave*. New York: Academic Press (2009).
22. Chabchoub A, Hoffmann NP, Akhmediev N. Rogue wave observation in a water wave tank. *Phys Rev Lett* (2011) 106(20):204502. doi:10.1103/PhysRevLett.106.204502
23. Yan Z. Vector financial rogue waves. *Phys Lett* (2011) 375:4274–9. doi:10.1016/j.physleta.2011.09.026
24. Kibler B, Fatome J, Finot C, Millot G, Dias F, Genty G, et al. The Peregrine soliton in nonlinear fibre optics. *Nat Phys* (2010) 6:790–5. doi:10.1038/nphys1740
25. Lecaplain C, Grelu P, Soto-Crespo JM, Akhmediev N. Dissipative rogue waves generated by chaotic pulse bunching in a mode-locked laser. *Phys Rev Lett* (2012) 108:233901. doi:10.1103/PhysRevLett.108.233901
26. Solli DR, Ropers C, Koonath P, Jalali B. Optical rogue waves. *Nature* (2018) 450:1054–7. doi:10.1038/nature06402
27. Marklund M, Stenflo L. Exciting rogue waves. *Physics* (2009) 2:86. doi:10.1103/physics.2.86
28. Stenflo L, Marklund M. Rogue waves in the atmosphere. *J Plasma Phys* (2010) 76:293–5. doi:10.1017/s0022377809990481
29. Bailung H, Sharma SK, Nakamura Y. Observation of peregrine solitons in a multicomponent plasma with negative ions. *Phys Rev Lett* (2011) 107:255005. doi:10.1103/PhysRevLett.107.255005
30. Sharma SK, Bailung H. Observation of hole Peregrine soliton in a multicomponent plasma with critical density of negative ions. *J Geophys Res Space Phys* (2013) 118(2):919–24. doi:10.1002/jgra.50111
31. Pathak P, Sharma SK, Nakamura Y, Bailung H. Observation of second order ion acoustic Peregrine breather in multicomponent plasma with negative ions. *Phys Plasmas* (2016) 23:022107. doi:10.1063/1.4941968
32. Pathak P, Sharma SK, Nakamura Y, Bailung H. Observation of ion acoustic multi-Peregrine solitons in multicomponent plasma with negative ions. *Phys Lett* (2017) 381:4011–18. doi:10.1016/j.physleta.2017.10.046
33. Akhmediev N, Soto-Crespo JM, Ankiewicz A. Extreme waves that appear from nowhere: on the nature of rogue waves. *Phys Lett* (2009) 373.(25):2137–45. doi:10.1016/j.physleta.2009.04.023
34. Demircan A, Amiranashvili S, Brée C, Mahnke C, Mitschke F, Steinmeyer G. Rogue events in the group velocity horizon. *Sci Rep* (2012) 2:850. doi:10.1038/srep00850
35. Dysthe KB, Trulsen K. Note on breather type solutions of the NLS as models for freak-waves. *Phys Scripta* (1999) T82:48. doi:10.1238/physica.topical.082a00048
36. Li M, Shui J-J, Xu T. Generation mechanism of rogue waves for the discrete nonlinear Schrödinger equation. *Appl Math Lett* (2018) 83:110–5. doi:10.1016/j.aml.2018.03.018
37. Li M, Shui J-J, Huang Y-H, Wang L, Li H-J. Localized-wave interactions for the discrete nonlinear Schrödinger equation under the nonvanishing background. *Phys Scripta* (2018) 93(11):115203. doi:10.1088/1402-4896/aae213
38. Akhmediev N, Ankiewicz A, Soto-Crespo JM. Rogue waves and rational solutions of the nonlinear Schrödinger equation. *Phys Rev E – Stat Nonlinear Soft Matter Phys* (2009) 80, 026601. doi:10.1103/PhysRevE.80.026601
39. Guob S, Mei L. Three-dimensional dust-ion-acoustic rogue waves in a magnetized dusty pair-ion plasma with nonthermal nonextensive electrons and opposite polarity dust grains. *Phys Plasmas* (2014) 21:082303. doi:10.1063/1.4891879
40. Delfour M, Fortin M, Payr G. Finite-difference solutions of a non-linear Schrödinger equation. *J Comput Phys* (1981) 44:277–88. doi:10.1016/0021-9991(81)90052-8
41. Lecaplain C, Grelu P, Soto-Crespo JM, Akhmediev N. Dissipative rogue waves generated by chaotic pulse bunching in a mode-locked laser. *Phys Rev Lett* (2012) 108:233901. doi:10.1103/PhysRevLett.108.233901
42. Lecaplain C, Grelu Ph, Soto-Crespo JM, Akhmediev N. Dissipative rogue wave generation in multiple-pulsing mode-locked fiber laser. *J Optic* (2013) 15: 064005. doi:10.1088/2040-8978/15/6/064005
43. Liu M, Cai ZR, Hu S, Luo AP, Zhao CJ, Zhang H, et al. Dissipative rogue waves induced by long-range chaotic multi-pulse interactions in a fiber laser with a topological insulator-deposited microfiber photonic device. *Opt Lett* (2015) 40: 4767–70. doi:10.1364/OL.40.004767
44. Liu M, Luo AP, Xu WC, Luo ZC. Dissipative rogue waves induced by soliton explosions in an ultrafast fiber laser. *Opt Lett* (2016) 41:3912–15. doi:10.1364/OL.41.003912
45. Onorato M, Proment D. Approximate rogue wave solutions of the forced and damped nonlinear Schrödinger equation for water waves. *Phys Lett* (2012) 376: 3057. doi:10.1016/j.physleta.2012.05.063
46. Guo S, Mei L. Modulation instability and dissipative rogue waves in ion-beam plasma: roles of ionization, recombination, and electron attachment. *Phys Plasmas* (2014) 21:112303. doi:10.1063/1.4901037
47. Amin MR. Modulation of a compressional electromagnetic wave in a magnetized electron-positron quantum plasma. *Phys Rev E – Stat Nonlinear Soft Matter Phys* (2015) 92, 033106. doi:10.1103/PhysRevE.92.033106
48. El-Tantawy SA. Ion-acoustic waves in ultracold neutral plasmas: modulational instability and dissipative rogue waves. *Phys Lett* (2017) 381:787. doi:10.1016/j.physleta.2016.12.052
49. Sikdar A, Adak A, Ghosh S, Khan M. Electrostatic wave modulation in collisional pair-ion plasmas. *Phys Plasmas* (2018) 25:052303. doi:10.1063/1.4997224
50. El-Tantawy SA, Salas AH, Hammad Mm. A, Ismaeel SME, Moustafa DM, El-Awady EI. Impact of dust kinematic viscosity on the breathers and rogue waves in a complex plasma having kappa distributed particles. *Waves Random Complex Media* (2019) 1–21. doi:10.1080/17455030.2019.1698790
51. Adak A, Ghosh S, Chakrabarti N. Ion acoustic shock wave in collisional equal mass plasma. *Phys Plasmas* (2015) 22:102307. doi:10.1063/1.4933356
52. Sarkar S, Adak A, Ghosh S, Khan M. Ion acoustic wave modulation in a dusty plasma in presence of ion loss, collision and ionization. *J Plasma Phys* (2016) 82:905820504. doi:10.1017/s0022377816000799
53. Saini NS, Kourakis I. Dust-acoustic wave modulation in the presence of superthermal ions. *Phys Plasmas* (2008) 15:123701. doi:10.1063/1.3033748
54. Xue J-K. Modulation of dust acoustic waves with non-adiabatic dust charge fluctuations. *Phys Lett* (2003) 320:226–33. doi:10.1016/j.physleta.2003.11.018

55. Kui XJ. Modulational instability of dust ion acoustic waves in a collisional dusty plasma. *Commun Theor Phys* (2003) 40:717–20. doi:10.1088/0253-6102/40/6/717
56. Griffiths DF, Mitchell AR, Morris JL. A numerical study of the nonlinear Schrödinger equation. *Comput Methods Appl Mech Eng* (1984) 45:177–215. doi:10.1016/0045-7825(84)90156-7
57. Salas AH, El-Tantawy SA, Castillo HJE. The hybrid finite difference and moving boundary methods for solving a linear damped nonlinear Schrödinger equation to model rogue waves and breathers in plasma physics. *Math Probl Eng* (2020) 1.11. doi:10.1155/2020/6874870

Conflict of Interest: The authors declare that the research was conducted in the absence of any commercial or financial relationships that could be construed as a potential conflict of interest.

frontiers in Physics

ORIGINAL RESEARCH
published: 19 February 2021
doi: 10.3389/fphy.2020.603112

Ion Acoustic Peregrine Soliton Under Enhanced Dissipation

Pallabi Pathak *

Institute of Advanced Study in Science and Technology, Ministry of Science and technology, Guwahati, India

The effect of enhanced Landau damping on the evolution of ion acoustic Peregrine soliton in multicomponent plasma with negative ions has been investigated. The experiment is performed in a multidipole double plasma device. To enhance the ion Landau damping, the temperature of the ions is increased by applying a continuous sinusoidal signal of frequency close to the ion plasma frequency ~1 MHz to the separation grid. The spatial damping rate of the ion acoustic wave is measured by interferometry. The damping rate of ion acoustic wave increases with the increase in voltage of the applied signal. At a higher damping rate, the Peregrine soliton ceases to show its characteristics leaving behind a continuous envelope.

Keywords: peregrine soliton, landau damping, ion acoustic wave, multicomponent plasma, modulational instability

OPEN ACCESS

Edited by:
Amin Chabchoub,
The University of Sydney, Australia

Reviewed by:
Nareshpal Singh Saini,
Guru Nanak Dev University, India
Ata ur Rahman,
Islamia College University, Peshawar, Pakistan

***Correspondence:**
Pallabi Pathak
pallabipathak276@gmail.com

Specialty section:
This article was submitted to Plasma Physics, a section of the journal Frontiers in Physics

Received: *05 September 2020*
Accepted: *07 December 2020*
Published: *19 February 2021*

Citation:
Pathak P (2021) Ion Acoustic Peregrine Soliton Under Enhanced Dissipation. Front. Phys. 8:603112. doi: 10.3389/fphy.2020.603112

INTRODUCTION

The Peregrine soliton is an isolated large-amplitude wave commonly known as rogue waves. These are extreme and rare wave events that usually appear on the ocean surfaces. It has two unique properties that distinguish the Peregrine soliton from ordinary solitons. Firstly, this large-amplitude wave is localized in both time and space axis; secondly, it has amplitude amplification of more than ~3 times that of the background wave height. One generic mechanism considered responsible for the evolution of rogue waves is modulational instability. In this process, phase and amplitude modulation grow due to a delicate balance between nonlinearity and group velocity dispersion. Different solutions of nonlinear Schrodinger equation (NLSE) deal with such type of instability. In 1983, Peregrine derived a rational solution of NLSE in the context of water waves as a limit of a wide class of solutions to the NLSE [1]. This solution was later known as Peregrine soliton, which has been considered as a prototype of a rogue wave. Almost 3 decades later, the Peregrine soliton has been experimentally observed in various nonlinear mediums such as fiber optics, water, and plasma [2–4]. The NLSE, in its many forms, provides the solutions of extreme wave events (rogue waves, breathers, and envelope solitons) [5–7, 9]. Using the NLSE framework, the vigours properties of rogue waves have been theoretically studied in different plasma systems, such as electron-positron plasma [8], magnetized plasma [9], plasma with nonextensive electron velocity distribution [10], nonthermal plasma [11], and dusty plasma [12–16]. Recently, Tsai et al. [17] confirmed the presence of dust acoustic rogue waves in a self-excited laboratory dusty plasma medium. The existence of rogue waves has also been studied in a degenerate Thomas-Fermi plasma system [18]. The NLSE was derived for this purpose by considering cold inertial ions and Thomas-Fermi distributed electrons and positrons. Similar studies in electron-positron-ion plasma using a semirelativistic fluid model predicted the evolution of both bright and dark type envelope solitons [19, 20].

In multicomponent plasma with a critical concentration of negative ions, an initial amplitude-modulated ion wave packet undergoes self-modulation due to modulational instability and gives rise to the formation of bright and dark (hole) ion acoustic Peregrine soliton [4, 21]. The criteria for the generation of bright and hole Peregrine soliton out of an initial amplitude-modulated perturbation

depend on the relative phase between the carrier and the envelope. The evolution of envelope-like solitons in such plasma is too described by the NLSE [22, 23]. The NLSE also supports the existence of higher-order and multiple Peregrine solitons [7, 24–26]. In our previous works, we have experimentally observed both second-order Peregrine soliton and multi-Peregrine soliton in multicomponent plasma containing negative ions [27, 28]. It was found that the characteristics of initial perturbations such as the amplitude (steepness) and modulation length (and depth) play a crucial role in the generation of both kinds of solitons.

Landau damping is a collisionless process because of which a longitudinal space charge wave (e.g., ion acoustic wave) in plasma decays exponentially with time. It occurs due to energy exchange between the waves and particles in plasma when their velocities are comparable. Eventually, Landau damping prevents the growth of instability and creates a region of stability in the parameter space. In laboratory discharge plasma with Maxwellian electrons, ion waves suffer Landau damping which become dominant when ion temperature is comparable to electron temperature ($T_i \sim T_e$). Various research works have been performed to study the solitary waves in plasmas containing additional components like multispecies ions, negative ions, and dust particles [29–34]. Landau damping modifies the nature of solitary waves in such plasmas, and it has been extensively studied both experimentally and theoretically [35–39]. The first experiment to detect the Landau damping of ion acoustic wave was performed in a highly ionized cesium and potassium plasma [40]. In a Q machine plasma experiment, Landau damping was found to prevent the formation of solitary waves by dominating over the steepening effect of nonlinearity [41]. However, the strength of Landau damping reduces in the presence of negatively charged dust particles in a Q machine plasma [42, 43]. In the double plasma (DP) device, experiments on shock and solitary waves under enhanced Landau damping have been performed [44, 45]. The study showed that the presence of lighter ions enhances the damping, which prevents the formation of solitons in a DP device [46].

The purpose of this paper is to report the experimental investigation of the Landau damping effect on Peregrine soliton in multicomponent plasma with a critical concentration of negative ions. The experimental setup and procedure to enhance the strength of Landau damping are discussed in *Experimental Setup*. The experimental measurement of Landau damping rate using interferometry and the observation of Peregrine soliton under enhanced damping are conferred in *Results and Discussion*. Finally, we present the concluding remarks in *Conclusion*.

EXPERIMENTAL SETUP

Production of Multicomponent Plasma

The experiment is carried out in a DP device of a length of 120 cm and a diameter of 30 cm with a surface plasma confinement facility [21, 27]. The device consists of two magnetic cages separated by a floating mesh grid in between. Argon plasma is produced in both chambers at an operating pressure of 3.8×10^{-4} Torr by the independent dc discharge process. The discharge voltages and currents are maintained at 60 V and 10–50 mA, respectively. The plasma parameters are measured with the help of an axially movable planar Langmuir probe. The measured electron temperature and density are in the range of 1–2 eV and 10^8–10^9 cm^{-3}, respectively. Next, to produce the multicomponent plasma, SF_6 gas is inserted into the chamber through a fine control needle valve at a partial pressure of $(1 - 4) \times 10^{-5}$ Torr and as a result, the F^- ions are produced mainly through a dissociative attachment process. For the present experiment, the multicomponent plasma is thus created, which contains electrons and Ar^+ and F^- ions. The density of F^- ions is finely controlled to maintain the critical density ratio of negative to positive ion, i.e., $n_-/n_+ = 0.1$, where n_- is the negative ion (F^-) density and n_+ is the positive ion (Ar^+) density. The I–V characteristics curves are obtained for Ar and Ar + SF_6 plasma separately, and the electron and ion saturation currents are measured from it. From these saturation currents, the critical density ratio is calculated by the formula $r = 1 - I_{es}/I_{es0}$, where I_{es} and I_{es0} are the Langmuir probe saturation current with and without SF_6, respectively. After attaining the desired conditions, a slowly amplitude-modulated sinusoidal wave packet is applied to the source anode as the initial perturbation to excite the Peregrine soliton. The mean free path of the ion-neutral collision is estimated to be in the order of meters; hence, the generated plasma can be considered as collisionless [47, 48].

Method to Enhance the Strength of Landau Damping

In a DP device, the electron to ion temperature ratio is usually high (≥ 10), and hence the propagating wave suffers negligible Landau damping. For this reason, the DP device is used for wave experiments in plasma from the early days [49, 50]. Two methods are widely used to enhance Landau damping in a DP device. The first one is to mix lighter mass ions to increase the number of resonant particles. In a pioneering experiment, the addition of a trace of light helium ions to a xenon plasma has led to Landau damping of ion acoustic wave [41]. In the presence of lighter helium ions, the wave phase velocity and temperature ratio changes only up to 10%, which induces the Landau damping, providing all other plasma parameters unaltered. This technique was applied to examine the enhanced Landau damping effect on shock propagation in a DP device [44]. The damping rate was found to be proportional to the wave number in the linear regime. The second method is to apply a radio frequency (rf) signal (frequency $\sim \omega_{pi}$) to the separation grid of a DP device to heat the ions [45]. The ions near the grid oscillate at this frequency and gain energy. Hence, by adjusting the amplitude of the rf signal, plasma ion temperature enhancement can be obtained. The experimental investigation of collisionless damping effect on the propagation of ion acoustic solitary waves has already been performed by using this method [45], where an rf signal of frequency 1.78 MHz with a peak to peak voltage (V_{HF}) ranging from 0 to 400 mV was applied to the separation grid. This value of V_{HF} is too small to affect the plasma parameters other than the ion temperature. In the present experiment,

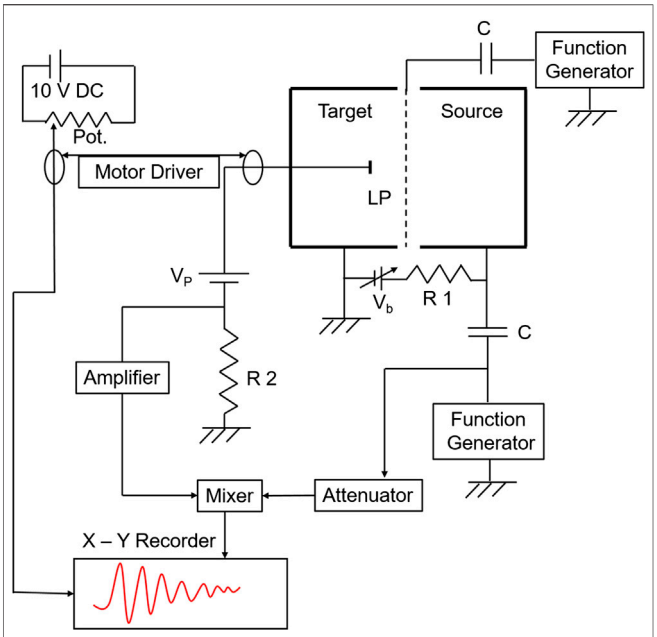

FIGURE 1 | Block diagram of the experimental arrangement to enhance the Landau damping as well as measure the dispersion relation of ion acoustic waves.

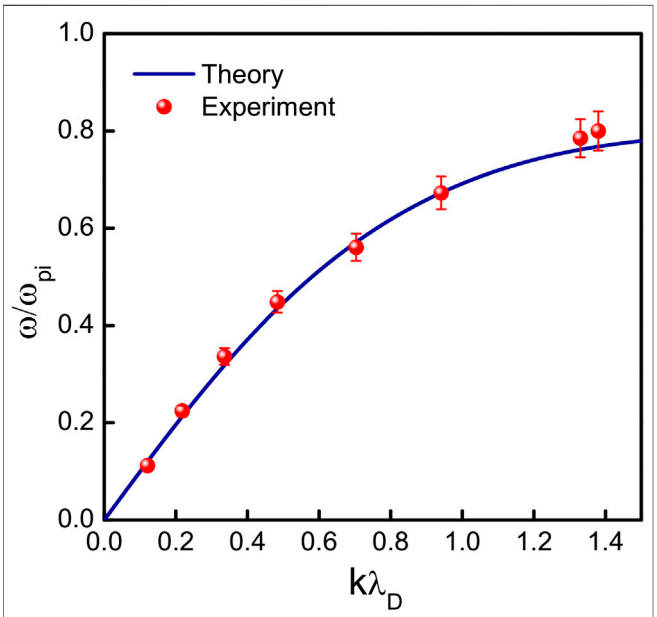

FIGURE 2 | Dispersion relation of ion acoustic wave. The solid line is the theoretical curve calculated from **Eq. 1**.

an rf signal of frequency f_{HF} = 900 kHz is applied to the separation grid to heat the ions from a function generator. The desired Landau damping rate is obtained by varying the peak to peak voltage (V_{HF}) in the range 0–100 mV. In **Figure 1**, the schematic of the experimental arrangement to control the Landau damping strength is presented.

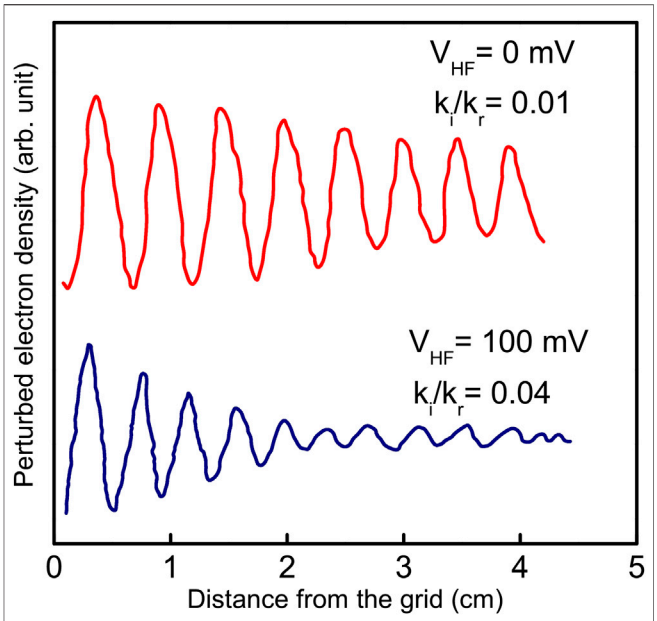

FIGURE 3 | Typical interferometer pattern for a 500 kHz signal at V_{HF} = 0 and 100 mV. The measured damping rates are also shown.

RESULTS AND DISCUSSION

Measurement of Landau Damping Rate of Ion Acoustic Wave

Experimentally, we first examine the linear dispersion relation of ion acoustic wave in the present argon plasma condition using interferometry. For this, continuous sinusoidal waves of frequency 100–800 kHz (100 kHz in step) with amplitude ≤200 mV are applied to the source anode from a function generator through a 1 μF capacitor. A reference signal from the function generator is applied to the balanced mixer's right input through an attenuator. The plane Langmuir probe collects the signal continuously against the axial position with a motorized probe driving system. The probe is biased above the plasma potential in order to detect perturbations in electron saturation current. The signal is detected by the probe that is coupled to the left input of the mixer. The output of the mixer is fed to the *Y* axis of the X–Y recorder. The probe distance from the grid is calibrated using a separate voltage source with a potentiometer attached to the motor driving system and is connected to the *X* axis of the X–Y recorder. **Figure 2** shows a typical linear dispersion relation for ion acoustic waves in a normal argon plasma. The solid line represents the theoretical dispersion relation, which is obtained by putting the experimental plasma parameters in **Eq. 1**. The theoretical relation (**Eq. 1**) is derived by considering the Maxwellian distribution having $T_e >> T_i$ [51].

$$\frac{\omega^2}{k_r^2} = \frac{K_B T_e}{m_i}\left(\frac{1+\frac{3T_i}{T_e}}{1+k_r^2\lambda_D^2}\right). \quad (1)$$

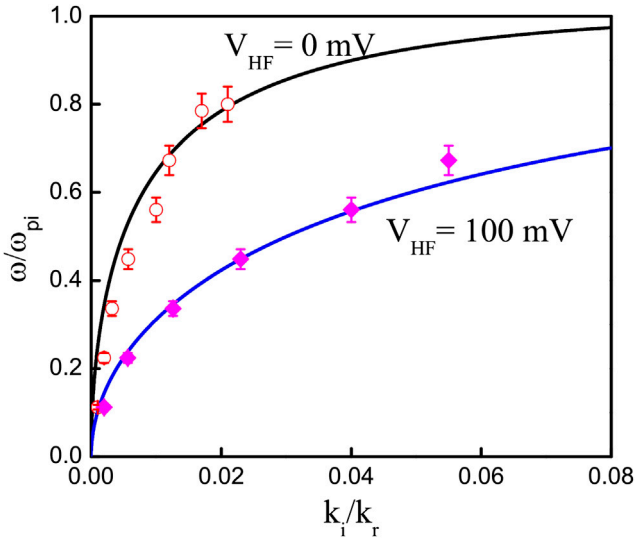

FIGURE 4 | Normalized wavenumber ω/ω_{pi} as a function of the spatial damping rate k_i/k_r. The solid curves are theoretically obtained from **Eq. 2**. The open and closed symbols are experimentally measured values at V_{HF} = 0 and V_{HF} = 100 mv, respectively.

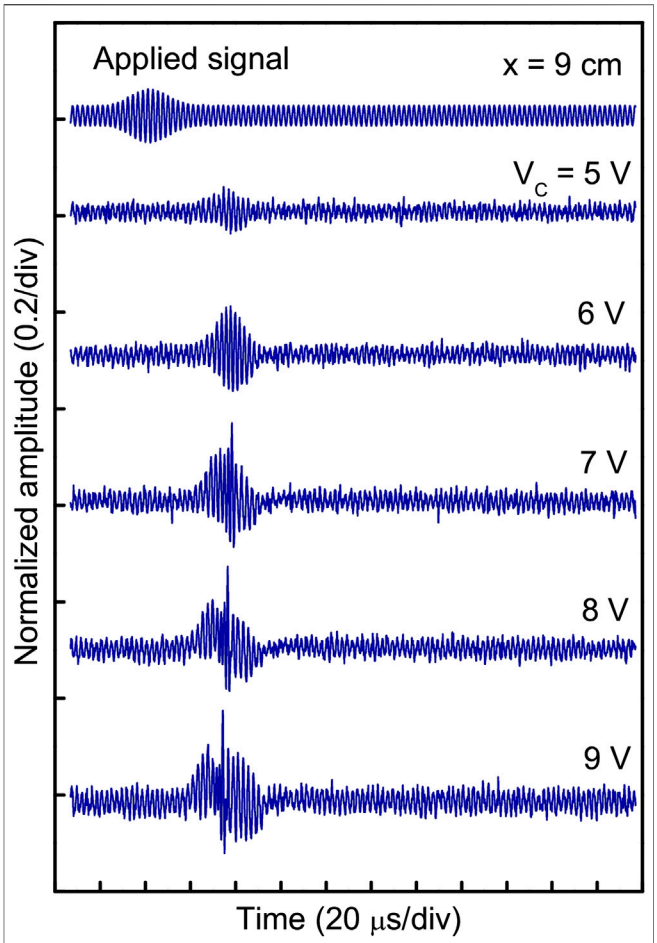

FIGURE 5 | Typical examples experimentally observed Peregrine soliton at x = 9 cm from the grid. The top trace is the applied signal with carrier and modulation frequencies 380 and 30 kHz, respectively.

Here ω is the frequency component, k_r is the real wavenumber, T_i and T_e are the ion and electron temperatures, respectively, and m_i is the ion mass. The Debye length, λ_D = 0.02 cm, and ion plasma frequency, ω_{pi} = 892 kHz, are measured from the plasma parameters. In **Figure 2**, it is observed that the measured $\omega - k$ relation fits well with the theoretical one. The phase velocity of the ion acoustic wave measured from the lower $k\lambda_D$ region is $\sim 1.04 \times 10^5 \mathrm{cms}^{-1}$.

Usually, the Landau damping rate is calculated from the real (k_r) and imaginary (k_i) parts of the wavenumber. As the wave varies in space as $exp\,(ikx)$, the imaginary part of the wavenumber will produce spatial exponential damping. Here, the spatial damping rate (k_i/k_r) of the wave is calculated from the phase plots for a fixed value of V_{HF}. The phase plots for V_{HF} = 0 and 100 mV at applied frequency 500 kHz are shown in **Figure 3**. The fast reduction of amplitude at V_{HF} = 100 mV signifies the increment in Landau damping rate. Generally, in basic plasma wave experiments, the effect of Landau damping is often observed as damping of an exciting wave during propagation. We observe the impact of damping through resonant particles traveling at wave phase velocity. The graphs of the measured damping rate (k_i/k_r) with normalized frequency are shown in **Figure 4**. The theoretical plot is obtained from the following relation [51]:

$$\frac{1}{2\pi}\frac{k_i}{k_r} = \frac{\left(\frac{T_e}{T_i}\right)^{3/2} exp\left\{\left(\frac{T_e}{3T_i}\right)\left(1-\frac{\omega^2}{\omega_{pi}^2}\right)\left(1+\frac{3T_i}{T_e}\right)\right\}.}{2\pi^{3/2}\left(1-\frac{\omega^2}{\omega_{pi}^2}\right)^{1/2}} \qquad (2)$$

The damping rate of the ion acoustic wave increases as the amplitude of the rf signal is increased. In **Figure 4**, the solid lines are calculated for V_{HF} = 0 and V_{HF} = 100 mV from **Eq. 2**, whereas the open and closed symbols are calculated values of k_i/k_r for V_{HF} = 0 and V_{HF} = 100 mV, respectively. The experimental points are found to coincide with the theory nicely.

Peregrine Soliton Under Enhanced Landau Damping

Initially, to excite the Peregrine soliton, an amplitude-modulated continuous sinusoidal wave of carrier frequency 380 kHz and modulation frequency 30 Hz is synthesized using a pair of function generators. The carrier frequency is typically selected at nearly half of the ion plasma frequency ($f_{pi} \sim$ 892 kHz). The excitation amplitude of the carrier wave is varied from 2 to 9 V. Example of the evolution of Peregrine soliton at different initial amplitude is shown in **Figure 5** at a fixed distance from the grid x = 9 cm. The initially applied signal is shown at the top. For carrier amplitude V_c = 5 V, the perturbation resembles the applied perturbation, which indicates linear wave propagation. The carrier amplitude is small, and the effective nonlinearity is just below the threshold, due to which the perturbation is linear. Gradually, with the increase in excitation amplitude, the wave packet suffers steepening due to nonlinearity. When the self-modulation of

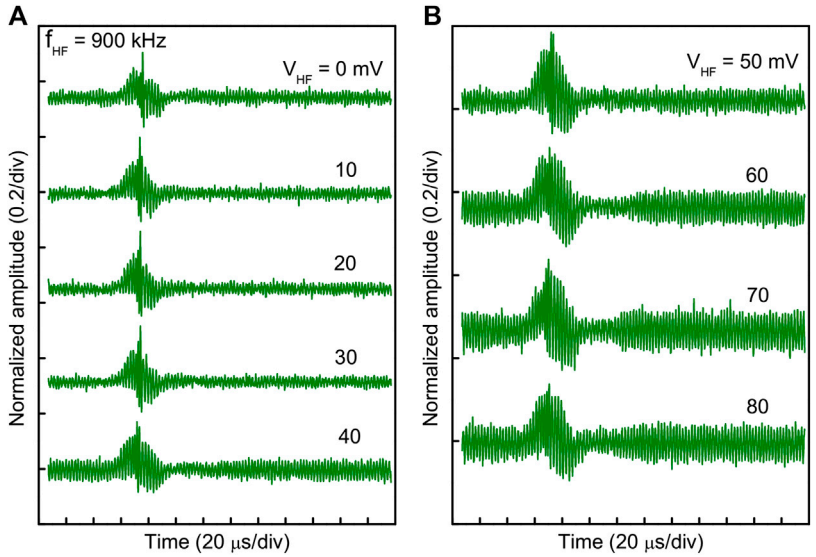

FIGURE 6 | Observed oscilloscope trace at a fixed probe position 9 cm from the separation grid showing the transition of ion acoustic Peregrine soliton to an envelope with an increase in V_{HF}. **(A)** For V_{HF} = 0–40 mV. **(B)** For V_{HF} = 50–80 mV.

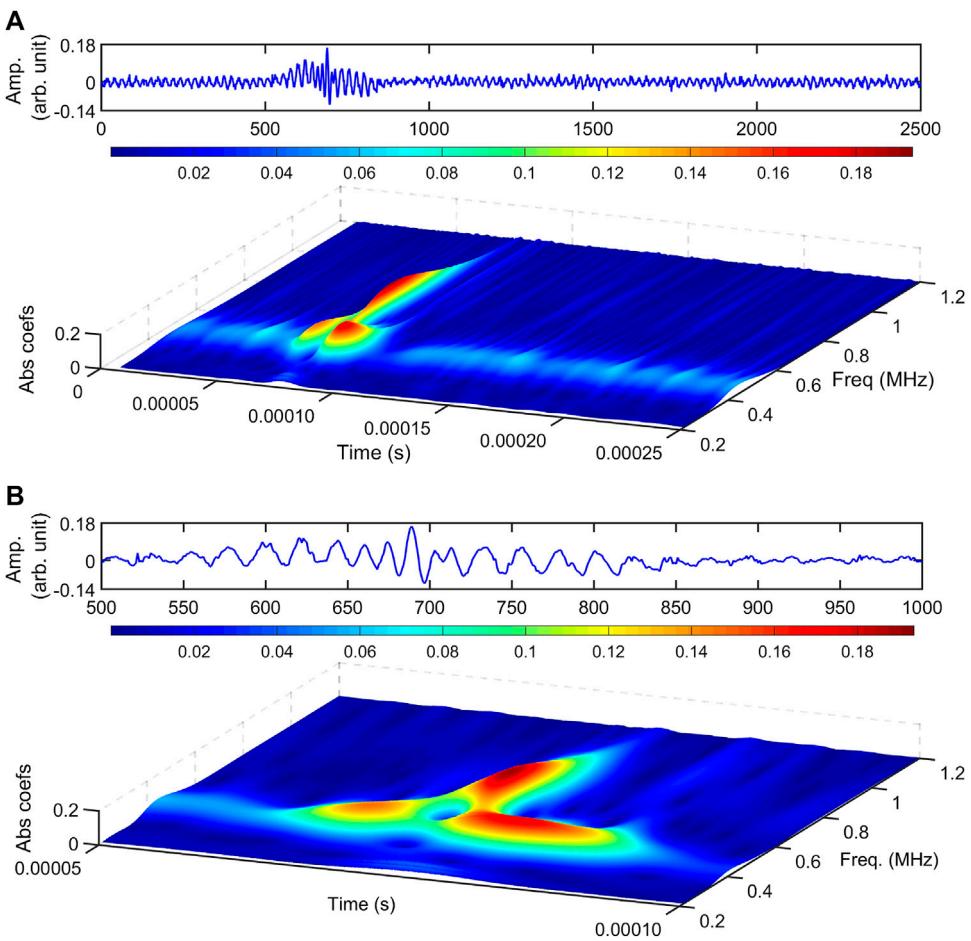

FIGURE 7 | Typical CWT scalogram of fundamental Peregrine soliton without application of V_{HF}. The probe position is at 9 cm. **(A)** Time series (top) and CWT scalogram (bottom) for Peregrine soliton **f**or data length 0–250 μs. **(B)** Enlarged view of **(A)** for data length 50–100 μs.

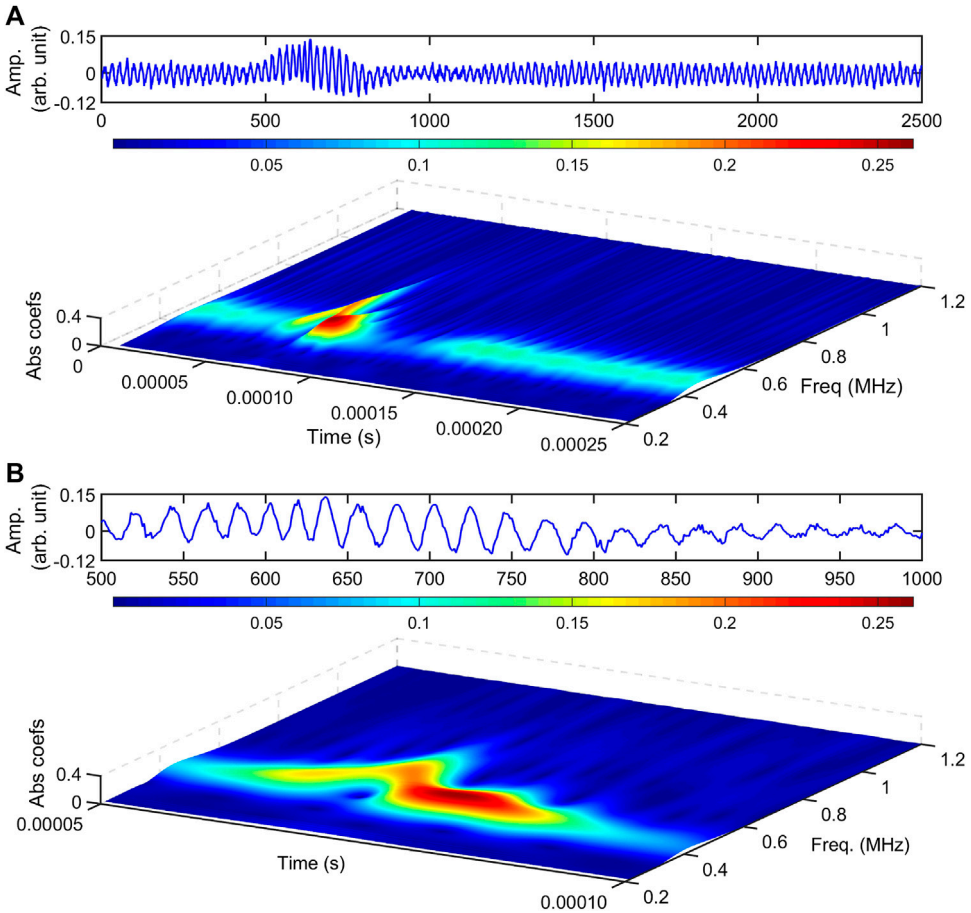

FIGURE 8 | Typical CWT scalogram of fundamental Peregrine soliton with the application of V_{HF} = 80 mV. The probe position is at 9 cm. **(A)** Time series (top) and CWT scalogram for data length 0–250 μs (bottom). **(B)** Enlarged view of **(A)** for data length 50–100 μs.

the wave packet reaches 100% at $V_c = 8$ V, the nonlinearity is entirely balanced by the group velocity dispersion, leading to the formation of Peregrine soliton. The amplitude amplification factor of the Peregrine soliton is found to be ~3 (ratio of the peak amplitude of the wave packet to the background carrier wave amplitude). The group velocity of the perturbation is $\sim 2 \times 10^5$ cms^{-1}.

Next, a high-frequency rf signal is applied to the grid to enforce Landau damping on the evolution of Peregrine soliton while keeping the probe distance fixed at 9 cm (with $V_c = 8$ V). The frequency of the applied continuous signal is kept fixed at 900 kHz, which is in the range of ion plasma frequency. Modification of the Peregrine soliton due to the dissipative effect is shown in **Figures 6A,B**. At V_{HF} = 0 mV, i.e., without the rf voltage, the Peregrine soliton is undisturbed. As V_{HF} increases, the Peregrine soliton amplitude decreases, which signifies the enhancement of the strength of Landau damping. At V_{HF} = 60 mV, the peak of the Peregrine soliton completely disappears. As indicated by the damping rate calculation, an increase in V_{HF} provides strong Landau damping. As shown in **Figures 6A,B**, the amplitude of the Peregrine soliton decreases with an increase in V_{HF}. Although the amplitude of the background carrier wave is increased at high $V_{HF,}$ which indicates the increase in ion temperature.

A close observation of the evolution indicates that the solitary peak amplitude gradually decreases with the reduction of compression in the middle of the wave packet (due to which wave energy focuses on forming a soliton). An increase in ion temperature raises the number of resonant ions near the phase velocity of the wave, due to which Landau damping is enhanced, and the wave becomes less dispersive. As nonlinearity remains the same, now both dissipation (due to enhanced Landau damping) and dispersion compete to balance the nonlinearity.

Continuous Wavelet Transformation Analysis

The continuous wavelet transformation (CWT) analysis is performed for time-series data (presented in **Figures 6A,B**) and shown in **Figures 7**, **8**. The time-series data are presented along with the CWT scalogram (3-dimensional surface plot of the absolute coefficient matrix) to clarify the temporal locations of the envelope. In **Figure 7A**, the CWT analysis of the Peregrine

soliton for a temporal data length of 250 μs is shown (which corresponds to the top trace of **Figure 6A**). The CWT scalogram shows the broadening of the frequency spectrum at 75 μs, i.e., at the isolated peak location. For better resolution, CWT analysis is performed for a temporal length of 50–100 μs and shown in **Figure 7B**. A deep hole (dark blue) in front of the soliton peak is observed here. This hole represents the complete self-modulation of the initially applied wave packet due to modulational instability.

The CWT scalogram, along with the time-series data of envelope with enhanced Landau damping (with V_{HF} = 80 mV), is shown in **Figures 8A,B**. Here, the reduction in the broadening of the frequency spectrum is clearly observed. Also, in **Figure 8B**, it is noticed that the deep hole in front of the largest wave crest almost disappears. **Figure 7B** shows the focusing of energy on the narrow wave group in the middle of the wave packet, whereas in **Figure 8B**, a continuous wave envelope is noticed. This signifies that wave energy focusing due to modulational instability vanishes because of the strong Landau damping (at V_{HF} = 80 mV).

CONCLUSION

The evolution of ion acoustic Peregrine soliton under dissipation is observed in multicomponent plasma with negative ions. The strength of the Landau damping is increased by heating of ions via rf signal (close to the ion plasma frequency) application to the separation grid. The spatial damping rate of the ion acoustic wave is measured from the interferometer phase plot. The experimentally measured damping rate shows good agreement with the theory. The results show the modification of the evolution characteristics of Peregrine soliton. With high rf amplitude ($V_{HF} \geq 60$ mV), the soliton peak disappears, leaving behind an envelope only. At high V_{HF}, the damping rate increases due to the rise in the thermal velocity of ions and thereby increasing resonant ions numbers close to the phase velocity of the wave. Once the dissipative effect becomes more substantial, the delicate balance between nonlinearity and group velocity dispersion gets affected, and the soliton disappears. However, a theoretical model considering the enhanced Landau damping effect is yet to be established and will be considered as a future study.

DATA AVAILABILITY STATEMENT

The raw data supporting the conclusions of this article will be made available by the authors, without undue reservation.

AUTHOR CONTRIBUTIONS

PP has done the experiment and data analysis as well as writing the manuscript.

ACKNOWLEDGMENTS

The author would like to thank H. Bailung for his guidance throughout the experiment.

REFERENCES

1. Peregrine D. Water waves, nonlinear Schrödinger equations and their solutions. *J Aust Math Soc Ser B Appl Math* (1983) 25:16–43. doi:10.1017/S0334270000003891
2. Kibler B, Fatome J, Finot C, Millot G, Dias F, Genty G, et al. The Peregrine soliton in nonlinear fibre optics. *Nat Phys* (2010) 6:790. doi:10.1038/nphys1740
3. Chabchoub A, Hoffmann NP, Akhmediev N. Rogue wave observation in a water wave tank. *Phys Rev Lett* (2011) 106:204502. doi:10.1103/PhysRevLett.106.204502
4. Bailung H, Sharma SK, Nakamura Y. Observation of Peregrine solitons in a multicomponent plasma with negative ions. *Phys Rev Lett* (2011) 107:255005. doi:10.1103/PhysRevLett.107.255005
5. Moslem WM, Shukla PK, Eliasson B. Surface plasma rogue waves. *EPL (Europhysics Lett)* (2011) 96:25002. doi:10.1209/0295-5075/96/25002
6. El-Tantawy SA, Wazwaz AM, Ali Shan S. On the nonlinear dynamics of breathers waves in electronegative plasmas with Maxwellian negative ions. *Phys Plasmas* (2017) 24:022105. doi:10.1063/1.4975090
7. Akbari-Moghanjoughi M. Electrostatic rogue-waves in relativistically degenerate plasmas. *Phys Plasmas* (2014) 21:102111. doi:10.1063/1.4897928
8. Moslem WM. Langmuir rogue waves in electron-positron plasmas. *Phys Plasmas* (2011) 18:10–4. doi:10.1063/1.3559486
9. Veldes GP, Borhanian J, McKerr M, Saxena V, Frantzeskakis DJ, Kourakis I. Electromagnetic rogue waves in beam–plasma interactions. *J Optic* (2013) 15:064003. doi:10.1088/2040-8978/15/6/064003
10. Moslem WM, Sabry R, El-Labany SK, Shukla PK. Dust-acoustic rogue waves in a nonextensive plasma. *Phys Rev E - Stat Nonlinear Soft Matter Phys* (2011) 84:066402. doi:10.1103/PhysRevE.84.066402
11. Wang Y, Li J, Dai C, Chen X, Zhang J. Solitary waves and rogue waves in a plasma with nonthermal electrons featuring Tsallis distribution. *Phys Lett* (2013) 377:2097–104. doi:10.1016/j.physleta.2013.06.008
12. Abdelsalam UM, Moslem WM, Khater AH, Shukla PK. Solitary and freak waves in a dusty plasma with negative ions. *Phys Plasmas* (2011) 18:092305. doi:10.1063/1.3633910
13. Chahal BS, Singh M, Shalini, Saini NS. Dust ion acoustic freak waves in a plasa with two temperature electrons featuring Tsallis distributio. *Physica A* (2018) 491:935–45. doi:10.1016/j.physa.2017.10.004
14. Shalini, Saini NS. Dust ion acoustic rogue waves in superthermal warm ion plasma. *J Plasma Phys* (2015) 81:905810316. doi:10.1017/S0022377815000082
15. Singh K, Kaur N, Saini NS. Head-on collision between two dust acoustic solitary waves and study of rogue waves in multicomponent dusty plasma. *Phys Plasmas* (2017) 24:063703. doi:10.1063/1.4984996
16., Saini NS, Kaur B, Singh M, Bains AS. Dust kinetic Alfvén solitary and rogue waves in a dusty plasma with two temperature n solitary and rogue waves in a dusty plasma with two Dust kinetic Alfv e temperature nonextensive ions. *Phys Plasmas* (2017) 24:073701. doi:10.1063/1.4989712
17. Tsai Y, Tsai J, Lin I. Generation of acoustic rogue waves in dusty plasmas through three-dimensional particle focusing by distorted waveforms. *Nat Phys Lett* (2016) 12:537–77. doi:10.1038/NPHYS3669
18. Ata-ur-Rahman. Electrostatic rogue waves in a degenerate Thomas-Fermi plasma. *Braz J Phys* (2019) 49:517–25. doi:10.1007/s13538-019-00676-3
19. Rahman A, Kerr MM, El-taibany WF, Kourakis I, Qamar A. Amplitude modulation of quantum-ion-acoustic wavepackets in electron-positron-ion plasmas : modulational instability, envelope modes, extreme waves. *Phys Plasmas* (2015) 22:022305. doi:10.1063/1.4907247
20. Kourakis I, Mc Kerr M, Ur-Rahman A. Semiclassical relativistic fluid theory for electrostatic envelope modes in dense electron-positron-ion plasmas:

modulational instability and rogue waves. *J Plasma Phys* (2013) 79:1089–94. doi:10.1017/S0022377813001323
21. Sharma SK, Bailung H. Observation of hole Peregrine soliton in a multicomponent plasma with critical density of negative ions. *J Geophys Res Sp Phys* (2013) 118:919–24. doi:10.1002/jgra.50111
22. Bailung H, Nakamura Y. Observation of modulational instability in a multi-component plasma with negative ions. *J Plasma Phys* (1993) 50:231–42. doi:10.1017/S0022377800027033
23. Saito M, Watanabe S, Tanaca H. Modulational instability of ion wave in plasma with negative ion. *J Phys Soc Japan* (1984) 53:2304–10.
24. El-Tantawy SA, El-bedwehy NA, El-Labany SK. Ion-acoustic super rogue waves in ultracold neutral plasmas with nonthermal electrons Ion-acoustic super rogue waves in ultracold neutral plasmas with nonthermal electrons. *Phys Plasmas* (2013) 20:072102. doi:10.1063/1.4812630
25. El-Tantawy SA, Ali S, Maroof R, Wazwaz AM, El-Labany SK. On the super freak waves in multicomponent plasmas having two-negative ions: Xe+ – F– – SF6–and Ar+ – F– –SF6–plasmas. *Indian J Phys* (2017) 91:939–46. doi:10.1007/s12648-017-0982-6
26. El-Tantawy SA, El-Bedwehy NA, El-Labany SK. Ion-acoustic super rogue waves in ultracold neutral plasmas with nonthermal electrons. *Phys Plasmas* (2013) 20:072102. doi:10.1063/1.4812630
27. Pathak P, Sharma SK, Nakamura Y, Bailung H. Observation of second order ion acoustic Peregrine breather in multicomponent plasma with negative ions. *Phys Plasmas* (2016) 23:022107. doi:10.1063/1.4941968
28. Pathak P, Sharma SK, Nakamura Y, Bailung H. Observation of ion acoustic multi-Peregrine solitons in multicomponent plasma with negative ions. *Phys Lett* (2017) 381:4011–8. doi:10.1016/j.physleta.2017.10.046
29. McKenzie JF, Verheest F, Doyle TB, Hellberg MA. Compressive and rarefactive ion-acoustic solitons in bi-ion plasmas. *Phys Plasmas* (2017) 11:1762. doi:10.1063/1.1688332
30. Gill TS, Kaur H, Saini NS. Ion-acoustic solitons in a plasma consisting of positive and negative ions with nonisothermal electrons. *Phys Plasmas* (2003) 10:3927. doi:10.1063/1.1611486
31. Xue J. Head-on collision of dust-acoustic solitary waves. *Phys Rev E - Stat Nonlinear Soft Matter Phys* (2004) 69:016403. doi:10.1103/PhysRevE.69.016403
32. Sharma SK, Boruah A, Bailung H. Head-on collision of dust-acoustic solitons in a strongly coupled dusty plasma. *Phys Rev E - Stat Nonlinear Soft Matter Phys* (2014) 89:013110. doi:10.1103/PhysRevE.89.013110
33. Boruah A, Sharma SK, Nakamura Y, Bailung H. Observation of dust acoustic multi-solitons in a strongly coupled dusty plasma. *Phys Plasmas* (2016) 23:93704. doi:10.1063/1.4962566
34. Boruah A, Sharma SK, Bailung H, Nakamura Y. Oblique collision of dust acoustic solitons in a strongly coupled dusty plasma. *Phys Plasmas* (2015) 22:781035. doi:10.1063/1.4931735
35. Karpman VI, Shklyar DR. Nonlinear Landau damping in an inhomogeneous plasma. *Sov Phys - JETP* (1975) 40:53–6.
36. Ott E, Sudan RN. Nonlinear theory of ion acoustic waves with Landau damping. *Phys Fluids* (1969) 12:2388. doi:10.1063/1.1692358
37. VanDam JW, Taniuti T. Nonlinear ion acoustic waves with Landau Damping.pdf. *J Phys Soc Japan* (1973) 35:1973.
38. Mendonca JT, Bingham R. Plasmon beam instability and plasmon Landau damping of ion acoustic waves. *Phys Plasmas* (2002) 9:2604. doi:10.1063/1.1479142
39. Amendt P. Pseudomoment fluid modeling : electron Landau damping of ion-acoustic waves. *Phys Plasmas* (2001) 8:1437. doi:10.1063/1.1355681
40. Wong AY, Motley RW, D'Angelo N. Landau damping of ion acoustic waves in highly ionized plasmas. *Phys Rev* (1964) 133:A436. doi:10.1103/PhysRev.133.A436
41. Alexeff I, Jones WD, Montgomeryt D. Controlled Landau damping of ion acoustic waves. *Phys Rev Lett* (1967) 19:422–5.
42. Luo QZ, D'Angelo N, Merlino RL. Experimental study of shock formation in a dusty plasma. *Phys Plasmas* (1999) 6:3455. doi:10.1063/1.873605
43. Luo QZ, D'Angelo N, Merlino RL. Shock formation in a negative ion plasma. *Phys Plasmas* (1998) 5:2868–70. doi:10.1063/1.873007
44. Nakamura Y, Bailung H, Saitou Y. Observation of ion-acoustic shock waves undergoing Landau damping. *Phys Plasmas* (2004) 11:3925. doi:10.1063/1.1771654
45. Saitou Y, Nakamura Y. Ion-acoustic soliton-like waves undergoing Landau damping. *Phys Lett* (2005) 343:397–02. doi:10.1016/j.physleta.2005.06.035
46. Kozima H, Yamagiwa K, Tanaka T, Matsubara H, Yoshino H. Experimental study of an ion acoustic soliton with dissipation. *J Phys Soc Japan* (1989) 58:504–510.
47. Brown SC. *Basic data of plasma physics*. New York, NY: Wiley (1969).
48. Mizuno Y. *Plasma Physics*. Tokyo, Japan: Kyoritu (1984). (in Japanese).
49. Taylor RJ, Ikezi H, Mackenzie KR. A large double plasma device for plasma beam and wave studies A large double plasma device for plasma beam and wave studies. *Rev Sci Instrum* (1972) 43:1675. doi:10.1063/1.1685522
50. Nakamura Y, Ooyama M, Ogino T. Observation of spherical ion acoustic solitons. *Phys Rev Lett* (1980) 45:1565–69.
51. Wong AY ed. *Introduction to experimental plasma physics*. Los Angeles, CA: University of California at Los Angeles (1977).

Conflict of Interest: The author declares that the research was conducted in the absence of any commercial or financial relationships that could be construed as a potential conflict of interest.

frontiers in Physics

MINI REVIEW
published: 22 February 2021
doi: 10.3389/fphy.2021.599146

Instability of Double-Periodic Waves in the Nonlinear Schrödinger Equation

Dmitry E. Pelinovsky *

Department of Mathematics, McMaster University, Hamilton, ON, Canada

It is shown how to compute the instability rates for the double-periodic solutions to the cubic NLS (nonlinear Schrödinger) equation by using the Lax linear equations. The wave function modulus of the double-periodic solutions is periodic both in space and time coordinates; such solutions generalize the standing waves which have the time-independent and space-periodic wave function modulus. Similar to other waves in the NLS equation, the double-periodic solutions are spectrally unstable and this instability is related to the bands of the Lax spectrum outside the imaginary axis. A simple numerical method is used to compute the unstable spectrum and to compare the instability rates of the double-periodic solutions with those of the standing periodic waves.

Keywords: modulational instability, double-periodic solutions, Floquet spectrum, nonlinear Schrödinger equation, standing waves

OPEN ACCESS

Edited by:
Heremba Bailung, Ministry of Science and Technology, India

Reviewed by:
Maximo Aguero, Universidad Autónoma del Estado de México, Mexico
Constance Schober, University of Central Florida, United States

***Correspondence:**
Dmitry E. Pelinovsky
dmpeli@math.mcmaster.ca

Specialty section:
This article was submitted to Mathematical and Statistical Physics, a section of the journal Frontiers in Physics

Received: *26 August 2020*
Accepted: *04 January 2021*
Published: *22 February 2021*

Citation:
Pelinovsky DE (2021) Instability of Double-Periodic Waves in the Nonlinear Schrödinger Equation. Front. Phys. 9:599146. doi: 10.3389/fphy.2021.599146

1 INTRODUCTION

Peregrine breather is a rogue wave arising on the background of the constant-amplitude wave due to its modulational instability [1, 2]. The focusing cubic NLS (nonlinear Schrödinger) equation is the canonical model which describes both the modulational instability and the formation of rogue waves. Formation of rogue waves on the constant-amplitude background have been modeled from different initial data such as local condensates [3], multi-soliton gases [4–6], and periodic perturbations [7, 8]. Rogue waves have been experimentally observed both in hydrodynamical and optical laboratories [9] (see recent reviews in [10, 11]).

Mathematical theory of rogue waves on the constant-amplitude background has seen many recent developments. universal behavior of the modulationally unstable constant-amplitude background was studied asymptotically in [12, 13]. The finite-gap method was employed to relate the unstable modes on the constant-amplitude background with the occurrence of rogue waves [14, 15]. Rogue waves of infinite order were constructed in [16] based on recent developments in the inverse scattering method [17]. Rogue waves of the soliton superposition were studied asymptotically in the limit of many solitons [18, 19].

At the same time, rogue waves were also investigated on the background of standing periodic waves expressed by the Jacobian elliptic functions. Such exact solutions to the NLS equation were constructed first in [20] (see also early numerical work in [21] and the recent generalization in [22]). It was confirmed in [23] that these rogue waves arise due to the modulational instability of the standing periodic waves [24] (see also [25, 26]). Instability of the periodic standing waves can be characterized by the separation of variables in the Lax system of linear equations [27] (see also [28, 29]), compatibility of which gives the NLS equation. Instability and rogue waves on the background of standing periodic waves have been experimentally observed in [30].

The main goal of this paper is to compute the instability rates for the double-periodic solutions to the NLS equation, for which the wave function modulus is periodic with respect to both space and time coordinates. In particular, we consider two families of double-periodic solutions expressed as rational functions of the Jacobian elliptic functions which were constructed in the pioneering work [31]. These solutions

represent perturbations of the Akhmediev breathers and describe generation of either phase-repeated or phase-alternating wave patterns [32, 33]. Rogue waves on the background of the double-periodic solutions were studied in [34] (see also numerical work in [35, 36]). Experimental observation of the double-periodic solutions in optical fibers was reported in [37].

The double-periodic solutions constructed in [31] are particular cases of the quasi-periodic solutions of the NLS equation given by the Riemann Theta functions of genus two [38–40]. Rogue waves for general quasi-periodic solutions of any genus were considered in [41–43].

Instability of the double-periodic solutions is studied using the Floquet theory for the Lax system of linear equations both in space and time coordinates. We compute the instability rates of the double-periodic solutions and compare them with those for the standing periodic waves. In order to provide a fair comparison, we normalize the amplitude of all solutions to unity. *As a main outcome of this work, we show that the instability rates are larger for the constant-amplitude waves and smaller for the double-periodic waves.*

The article is organized as follows. The explicit solutions to the NLS equation are reviewed in **Section 2**. Instability rates for the standing periodic waves and the double-periodic solutions are computed in **Sections 3 and 4** respectively. Further directions are discussed in **Section 5**.

2 EXPLICIT SOLUTIONS TO THE NLS EQUATION

The nonlinear Schrödinger (NLS) equation is a fundamental model for nonlinear wave dynamics [44, 45]. We take the NLS equation in the standard form:

$$i\psi_t + \frac{1}{2}\psi_{xx} + |\psi|^2\psi = 0. \tag{2.1}$$

This model has several physical symmetries which are checked directly:

- translation:

$$\text{if } \psi(x,t) \text{ is a solution, so is } \psi(x+x_0, t+t_0), \text{ for every } (x_0,t_0) \in \mathbb{R}\times\mathbb{R}, \tag{2.2}$$

- scaling:

$$\text{if } \psi(x,t) \text{ is a solution, so is } \alpha\psi(\alpha x, \alpha^2 t), \text{ for every } \alpha \in \mathbb{R}, \tag{2.3}$$

- Lorentz transformation:

$$\text{if } \psi(x,t) \text{ is a solution, so is } \psi(x+\beta t, t)e^{-i\beta x - \frac{i}{2}\beta^2 t}, \text{ for every } \beta \in \mathbb{R}. \tag{2.4}$$

In what follows, we use the scaling symmetry **Eq. 2.3** to normalize the amplitude of periodic and double-periodic solutions to unity and the Lorentz symmetry **Eq. 2.4** to set the wave speed to zero. We also neglect the translational parameters (x_0, t_0) due to the symmetry **Eq. 2.2**.

A solution $\psi(x,t) : \mathbb{R}\times\mathbb{R} \to \mathbb{C}$ to the NLS **Eq. 2.1** is a compatibility condition of the Lax system of linear equations on $\varphi(x,t) : \mathbb{R}\times\mathbb{R} \to \mathbb{C}^2$:

$$\varphi_x = U(\lambda,\psi)\varphi, \; U(\lambda,\psi) = \begin{pmatrix} \lambda & \psi \\ -\overline{\psi} & -\lambda \end{pmatrix} \tag{2.5}$$

and

$$\varphi_t = V(\lambda,\psi)\varphi, V(\lambda,\psi) = i\begin{pmatrix} \lambda^2 + \frac{1}{2}|\psi|^2 & \frac{1}{2}\psi_x + \lambda\psi \\ \frac{1}{2}\overline{\psi}_x - \lambda\overline{\psi} & -\lambda^2 - \frac{1}{2}|\psi|^2 \end{pmatrix}, \tag{2.6}$$

where $\overline{\psi}$ is the conjugate of ψ and $\lambda \in \mathbb{C}$ is a spectral parameter.

The algebraic method developed in [34] allows us to construct the stationary (Lax–Novikov) equations which admit a large class of bounded periodic and quasi-periodic solutions to the NLS **Eq. 2.1**. The simplest first-order Lax–Novikov equation is given by

$$\frac{du}{dx} + 2icu = 0, \tag{2.7}$$

where c is arbitrary real parameter. A general solution of this equation is given by $u(x) = Ae^{-2icx}$, where A is the integration constant. This solution determines the constant-amplitude waves of the NLS **Eq. 2.1** in the form:

$$\psi(x,t) = Ae^{-2ic(x+ct)+iA^2t}, \tag{2.8}$$

where $A > 0$ is the constant amplitude and translations in (x,t) are neglected due to the translational symmetry **Eq. 2.2**. Without loss of generality, c can be set to 0 due to the Lorentz transformation. Indeed, transformation **Eq. 2.4** with $\beta = -c$ transforms **Eq. 2.8** to the equivalent form $\psi(x,t) = Ae^{-icx-\frac{i}{2}c^2t+iA^2t}$, which is obtained from $\psi(x,t) = Ae^{-iA^2t}$ due to transformation **Eq. 2.4** with $\beta = c$. By the scaling transformation **Eq. 2.3** with $\alpha = A^{-1}$, the amplitude A can be set to unity, which yields the normalized solution $\psi(x,t) = e^{it}$.

The second-order Lax–Novikov equation is given by

$$\frac{d^2u}{dx^2} + 2|u|^2u + 2ic\frac{du}{dx} - 4bu = 0, \tag{2.9}$$

where (c,b) are arbitrary real parameters. Solutions u to the second-order **Eq. 2.9** determines the standing traveling waves of the NLS **Eq. 2.1** in the form:

$$\psi(x,t) = u(x+ct)e^{2ibt}. \tag{2.10}$$

Without loss of generality, we set $c = 0$ due to the Lorentz transformation **Eq. 2.4** with $\beta = -c$. Waves with the trivial phase are of particular interest [20, 27]. There are two families of such standing periodic waves given by the Jacobian elliptic functions in the form:

$$\psi(x,t) = \mathrm{dn}(x;k)e^{i\left(1-k^2/2\right)t} \tag{2.11}$$

and

$$\psi(x,t) = k\mathrm{cn}(x;k)e^{i\left(k^2-1/2\right)t}, \tag{2.12}$$

where the parameter $k \in (0,1)$ is the elliptic modulus. The solutions **Eqs. 2.11, 2.12** are defined up to the scaling transformation **Eq. 2.3** and translations **Eq. 2.2**. The amplitude (maximal value of $|\psi|$) is set to unity for **Eq. 2.11** and to k for **Eq. 2.12**. In order to normalize the amplitude to unity for the cnoidal wave **Eq. 2.12**, we can use the scaling transformation **Eq. 2.3** with $\alpha = k^{-1}$.

Due to the well-known expansion formulas

$$\begin{aligned}\mathrm{dn}(x;k) &= \mathrm{sech}(x) + \frac{1}{4}\left(1-k^2\right)[\sinh(x)\cosh(x)+x]\\ &\quad\times\tanh(x)\mathrm{sech}(x) + \mathcal{O}\left(\left(1-k^2\right)^2\right),\\ \mathrm{cn}(x;k) &= \mathrm{sech}(x) - \frac{1}{4}\left(1-k^2\right)[\sinh(x)\cosh(x)-x]\\ &\quad\times\tanh(x)\mathrm{sech}(x) + \mathcal{O}\left(\left(1-k^2\right)^2\right),\end{aligned}$$

both the periodic waves **Eqs. 2.11, 2.12** approaches the NLS soliton $\psi(x,t) = \mathrm{sech}(x)e^{it/2}$ as $k \to 1$. In the other limit, the dnoidal periodic wave **Eq. 2.11** approaches the constant-amplitude wave $\psi(x,t) = e^{it}$ as $k \to 0$, whereas the normalized cnoidal periodic wave **Eq. 2.12** approaches the harmonic wave $\psi(x,t) \sim \cos(x/k)e^{-it/(2k^2)}$ as $k \to 0$.

The third-order Lax–Novikov equation is given by

$$\frac{d^3u}{dx^3} + 6|u|^2\frac{du}{dx} + 2ic\left(\frac{d^2u}{dx^2} + 2|u|^2u\right) - 4b\frac{du}{dx} + 8iau = 0, \tag{2.13}$$

where (a,b,c) are arbitrary real parameters. Waves with $a = c = 0$ are again of particular interest [31]. After a transformation of variables [34], such solutions can be written in the form:

$$\psi(x,t) = [Q(x,t) + i\delta(t)]e^{i\theta(t)}, \tag{2.14}$$

where $Q(x,t) : \mathbb{R}\times\mathbb{R} \to \mathbb{R}$ is periodic both in the space and time coordinates and $\delta(t) : \mathbb{R} \to \mathbb{R}$ has a double period in t compared to $Q(x,t)$. There are two particular families of the double-periodic solutions **Eq. 2.14**, which can be written by using the Jacobian elliptic functions (see Appendices A and B in [34]):

$$\begin{aligned}\psi(x,t) &= k\frac{\mathrm{cn}(t;k)\mathrm{cn}\left(\sqrt{1+k}\,x;\kappa\right) + i\sqrt{1+k}\,\mathrm{sn}(t;k)\mathrm{dn}\left(\sqrt{1+k}\,x;\kappa\right)}{\sqrt{1+k}\,\mathrm{dn}\left(\sqrt{1+k}\,x;\kappa\right) - \mathrm{dn}(t;k)\mathrm{cn}\left(\sqrt{1+k}\,x;\kappa\right)}e^{it},\\ \kappa &= \frac{\sqrt{1-k}}{\sqrt{1+k}}\end{aligned} \tag{2.15}$$

and

$$\begin{aligned}\psi(x,t) &= \frac{\mathrm{dn}(t;k)\mathrm{cn}\left(\sqrt{2}\,x;\kappa\right) + i\sqrt{k(1+k)}\,\mathrm{sn}(t;k)}{\sqrt{1+k} - \sqrt{k}\mathrm{cn}(t;k)\mathrm{cn}\left(\sqrt{2}\,x;\kappa\right)}e^{ikt},\\ \kappa &= \frac{\sqrt{1-k}}{\sqrt{2}},\end{aligned} \tag{2.16}$$

where $k \in (0,1)$ is the elliptic modulus. The solutions **Eqs. 2.15, 2.16** are defined up to the scaling transformation **Eq. 2.3** and the translations **Eq. 2.2**. The amplitude (maximal value of $|u|$) is $\sqrt{1+k}+1$ for **Eq. 2.15** and $\sqrt{1+k}+\sqrt{k}$ for **Eq. 2.16**. In order to normalize the amplitudes of the double-periodic waves to unity, we can use the scaling transformation **Eq. 2.3** with $\alpha = \left(\sqrt{1+k}+1\right)^{-1}$ and $\alpha = \left(\sqrt{1+k}+\sqrt{k}\right)^{-1}$ respectively.

The double-periodic solutions **Eqs. 2.15, 2.16** can be written in the form:

$$\psi(x,t) = \phi(x,t)e^{2ibt}, \quad \phi(x+L,t) = \phi(x,t+T) = \phi(x,t), \tag{2.17}$$

where $L > 0$ and $T > 0$ are fundamental periods in space and time coordinates, respectively, whereas $2b = 1$ for **Eq. 2.15** and $2b = k$ for **Eq. 2.16**.

Figure 1 shows surface plots of $|\psi|$ on the (x,t) plane within the fundamental periods. The amplitudes of the double-periodic waves on **Figure 1** have been normalized to unity by the scaling transformation **Eq. 2.3**. The solution **Eq. 2.15** generates the phase-repeated wave patterns, whereas the solution **Eq. 2.16** generates the phase-alternating patterns [32–34, 36].

As $k \to 1$, both the double-periodic solutions **Eqs. 2.15** and **2.16** approach to the same Akhmediev breather given by

$$\psi(x,t) = \frac{\cos\left(\sqrt{2}\,x\right) + i\sqrt{2}\sinh(t)}{\sqrt{2}\cosh(t) - \cos\left(\sqrt{2}\,t\right)}e^{it}. \tag{2.18}$$

As $k \to 0$, the solution **Eq. 2.15** approaches the scaled NLS soliton

$$\psi(x,t) = 2\mathrm{sech}(2x)e^{2it}, \tag{2.19}$$

whereas the solution **Eq. 2.16** approaches the scaled cnoidal wave

$$\psi(x,t) = \mathrm{cn}\left(\sqrt{2}\,x;\frac{1}{\sqrt{2}}\right). \tag{2.20}$$

These limits are useful to control accuracy of numerical computations of the modulational instability rate for the double-periodic solutions in comparison with the similar numerical computations for the standing waves.

3 INSTABILITY OF STANDING WAVES

Here we review how to use the linear **Eq. 2.5, 2.6** in order to compute the instability rates for the standing periodic waves (**Eq. 2.10**) (see [23, 27]). Due to the separation of variables in **Eq. 2.10**, one can write

$$\varphi_1(x,t) = \chi_1(x+ct)e^{ibt+t\Omega}, \quad \varphi_2(x,t) = \chi_2(x+ct)e^{-ibt+t\Omega}, \tag{3.1}$$

where $\Omega \in \mathbb{C}$ is another spectral parameter and $\chi = (\chi_1,\chi_2)^T$ satisfies the following spectral problems:

$$\chi_x = \begin{pmatrix}\lambda & u\\ -\overline{u} & -\lambda\end{pmatrix}\chi, \tag{3.2}$$

and

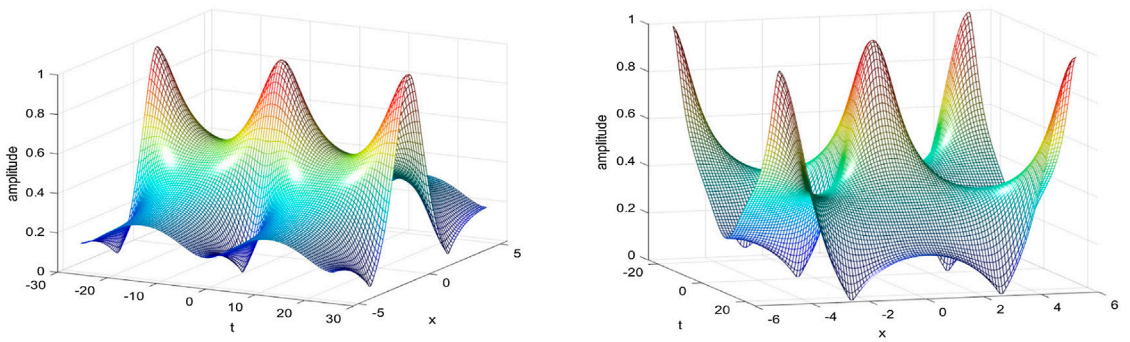

FIGURE 1 | Amplitude-normalized double-periodic waves **Eq. 2.15 (left)** and **Eq. 2.16 (right)** with $k = 0.9$.

$$\Omega\chi + c\begin{pmatrix} \lambda & u \\ -\overline{u} & -\lambda \end{pmatrix}\chi = i\begin{pmatrix} \lambda^2 + \frac{1}{2}|u|^2 - b & \frac{1}{2}\frac{du}{dx} + \lambda u \\ \frac{1}{2}\frac{d\overline{u}}{dx} - \lambda\overline{u} & -\lambda^2 - \frac{1}{2}|u|^2 + b \end{pmatrix}\chi. \tag{3.3}$$

We say that λ belongs to *the Lax spectrum* of the spectral problem **Eq. 3.2** if $\chi \in L^\infty(\mathbb{R})$. Since $u(x+L) = u(x)$ is periodic with the fundamental period $L > 0$, Floquet's Theorem guarantees that bounded solutions of the linear **Eq. 3.2** can be represented in the form:

$$\chi(x) = \widehat{\chi}(x)e^{i\theta x}, \tag{3.4}$$

where $\widehat{\chi}(x+L) = \widehat{\chi}(x)$ and $\theta \in \left[-\frac{\pi}{L}, \frac{\pi}{L}\right]$. When $\theta = 0$ and $\theta = \pm\frac{\pi}{L}$, the bounded solutions **Eq. 3.4** are periodic and anti-periodic, respectively.

Since the spectral problem **Eq. (3.3)** is a linear algebraic system, it admits a nonzero solution if and only if the determinant of the coefficient matrix is zero. The latter condition yields the x-independent relation between Ω and λ in the form $\Omega^2 + P(\lambda) = 0$, where $P(\lambda)$ is given by

$$P(\lambda) = \lambda^4 + 2ic\lambda^3 - (c^2 + 2b)\lambda^2 + 2i(a - bc)\lambda + b^2 - 2ac + 2d, \tag{3.5}$$

with parameters a and d being the conserved quantities of the second-order **Eq. 2.9**:

$$\left|\frac{du}{dx}\right|^2 + |u|^4 - 4b|u|^2 = 8d, \tag{3.6}$$

and

$$i\left(\frac{du}{dx}\overline{u} - u\frac{d\overline{u}}{dx}\right) - 2c|u|^2 = 4a. \tag{3.7}$$

Polynomial $P(\lambda)$ naturally occurs in the algebraic method [34]. For the standing waves of the trivial phase with $a = c = 0$, the polynomial $P(\lambda)$ can be written explicitly in the form:

$$P(\lambda) = \lambda^4 - \frac{1}{2}(u_1^2 + u_2^2)\lambda^2 + \frac{1}{16}(u_1^2 - u_2^2)^2, \tag{3.8}$$

where the turning points u_1 and u_2 parameterize b and d in the form:

$$\begin{cases} 4b = u_1^2 + u_2^2, \\ 8d = -u_1^2 u_2^2. \end{cases} \tag{3.9}$$

Roots of $P(\lambda)$ are located at $\{\pm\lambda_1, \pm\lambda_2\}$ given by

$$\lambda_1 = \frac{u_1 + u_2}{2}, \quad \lambda_2 = \frac{u_1 - u_2}{2}, \tag{3.10}$$

so that the polynomial $P(\lambda)$ can be written in the factorized form:

$$P(\lambda) = (\lambda^2 - \lambda_1^2)(\lambda^2 - \lambda_2^2). \tag{3.11}$$

By adding a perturbation v to the standing wave u in the form

$$\psi(x,t) = e^{2ibt}[u(x+ct) + v(x+ct,t)] \tag{3.12}$$

and dropping the quadratic terms in v, we obtain the linearized system of equations which describe linear stability of the standing waves (**Eq. 2.10**):

$$\begin{cases} iv_t - 2bv + icv_x + \frac{1}{2}v_{xx} + 2|u|^2 v + u^2\overline{v} = 0, \\ -i\overline{v}_t - 2b\overline{v} - ic\overline{v}_x + \frac{1}{2}\overline{v}_{xx} + 2|u|^2\overline{v} + \overline{u}^2 v = 0. \end{cases} \tag{3.13}$$

The variables can be separated in the form:

$$v(x,t) = w_1(x)e^{t\Lambda}, \quad \overline{v}(x,t) = w_2(x)e^{t\Lambda}, \tag{3.14}$$

where Λ is a spectral parameter and $w = (w_1, w_2)^T$ satisfies the spectral stability problem

$$i\Lambda\sigma_3 w + \begin{pmatrix} \frac{1}{2}\partial_x^2 + 2|u|^2 - 2b + ic\partial_x & u^2 \\ \overline{u}^2 & \frac{1}{2}\partial_x^2 + 2|u|^2 - 2b - ic\partial_x \end{pmatrix} w = 0, \tag{3.15}$$

where $\sigma_3 = \mathrm{diag}(1, -1)$. Note that w_1 and w_2 are no longer complex conjugate if $\Lambda \notin \mathbb{R}$.

We say that Λ belongs to *the stability spectrum* of the spectral problem **Eq. 3.15** if $w \in L^\infty(\mathbb{R})$. If λ is in the Lax spectrum of the spectral problem **Eq. 3.2**, then the bounded squared eigenfunctions χ_1^2 and χ_2^2 determine the bounded eigen

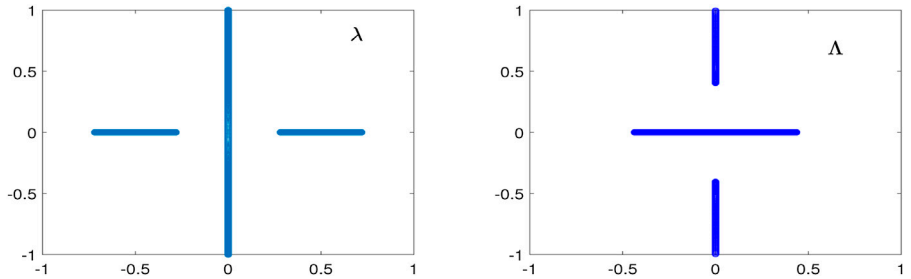

FIGURE 2 | Lax spectrum on the λ-plane **(left)** and stability spectrum on the Λ-plane **(right)** for the dn-periodic wave **Eq. 2.11** with $k = 0.9$.

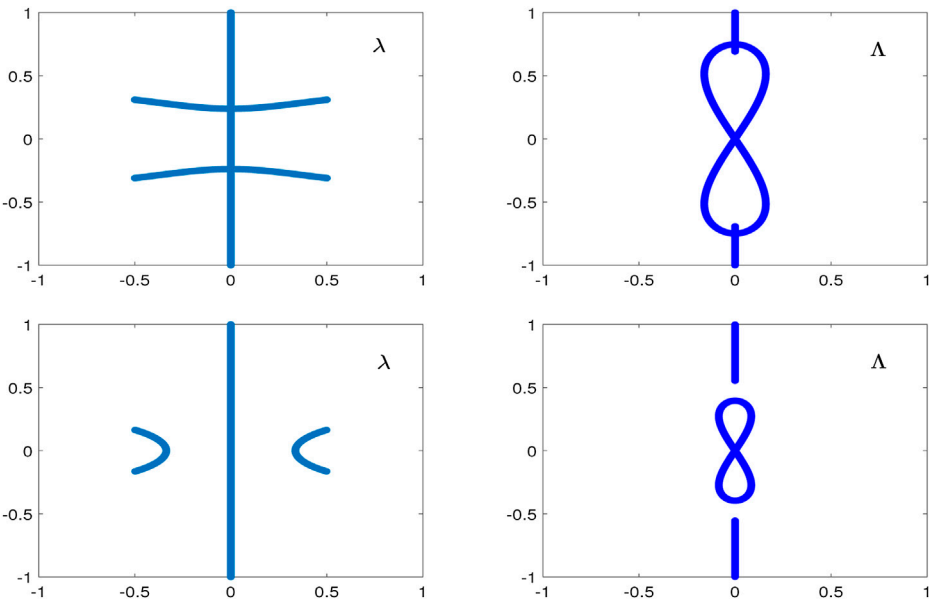

FIGURE 3 | The same as **Figure 2** but for the amplitude-normalized cn-periodic wave with $k = 0.85$ **(top)** and $k = 0.95$ **(bottom)**.

functions w_1 and w_2 of the spectral stability problem **Eq. 3.15** and Ω determines eigenvalues Λ as follows:

$$w_1 = \chi_1^2, \quad w_2 = -\chi_2^2, \quad \Lambda = 2\Omega. \tag{3.16}$$

Validity of **Eq. 3.16** can be checked directly from **Eqs. 3.2**, **3.3**, **3.14**, and **3.15**. If $\mathrm{Re}(\Lambda) > 0$ for λ in the Lax spectrum, the periodic standing wave **Eq. 2.10** is called *spectrally unstable*. It is called *modulationally unstable* if the unstable spectrum with $\mathrm{Re}(\Lambda) > 0$ intersects the origin in the Λ-plane transversely to the imaginary axis.

The importance of distinguishing between spectral and modulational instability of the periodic standing waves appears in the existence of rogue waves on their background. It was shown in [46] that if the periodic standing waves are spectrally unstable but modulationally stable, the rogue waves are not fully localized and degenerate into propagating algebraic solitons. Similarly, it was shown in [23] that if the unstable spectrum with $\mathrm{Re}(\Lambda) > 0$ intersects the origin in the Λ-plane tangentially to the imaginary axis, the corresponding rogue wave degenerates into a propagating algebraic soliton.

Next, we compute the instability rates for the standing periodic waves (2.10) of the trivial phase with $a = c = 0$. It follows from **Eq. 3.11** with either real λ_1, λ_2 or complex-conjugate $\lambda_1 = \overline{\lambda_2}$ that if $\lambda \in i\mathbb{R}$ belongs to the Lax spectrum, then $\Lambda \in i\mathbb{R}$ belongs to the stable spectrum. Thus, the spectral instability of the standing periodic waves of the trivial phase is only related to the Lax spectrum with $\lambda \notin i\mathbb{R}$.

For the dn-periodic wave **Eq. 2.11** with $u_1 = 1$ and $u_2 = \sqrt{1-k^2}$, the amplitude is already normalized to unity and no scaling transformation is needed. Lax spectrum of the spectral problem **Eq. 3.2** is shown on **Figure 2** (left) for $k = 0.9$. It follows from **Eq. 3.11** that $P(\lambda) < 0$ for $\lambda \in (\lambda_2, \lambda_1)$ with $P(\lambda_{1,2}) = 0$, where $\lambda_{1,2}$ are given by **Eq. 3.10**. The unstable spectrum on the Λ-plane belongs to the finite segment on the real line which touches the origin as is shown on **Figure 2** (right), hence the dn-periodic wave Eq. (2.11) is both spectrally and modulationally unstable. It follows from **Eq. 3.16** that

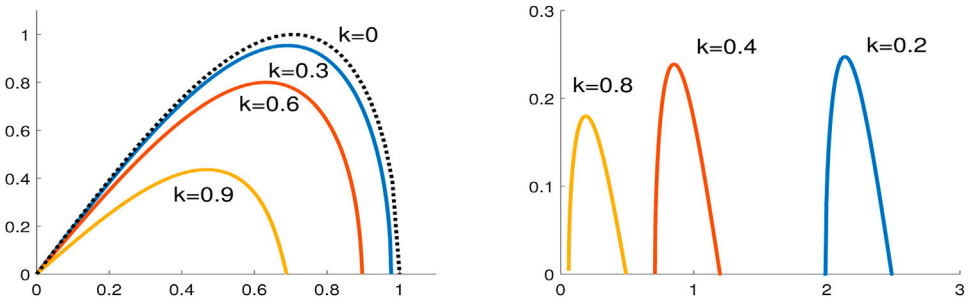

FIGURE 4 | Instability rate Re(Λ) versus the Floquet parameter θ for the amplitude-normalized dn-periodic **(left)** and cn-periodic **(right)** waves. The values of *k* in the elliptic functions are given in the plots.

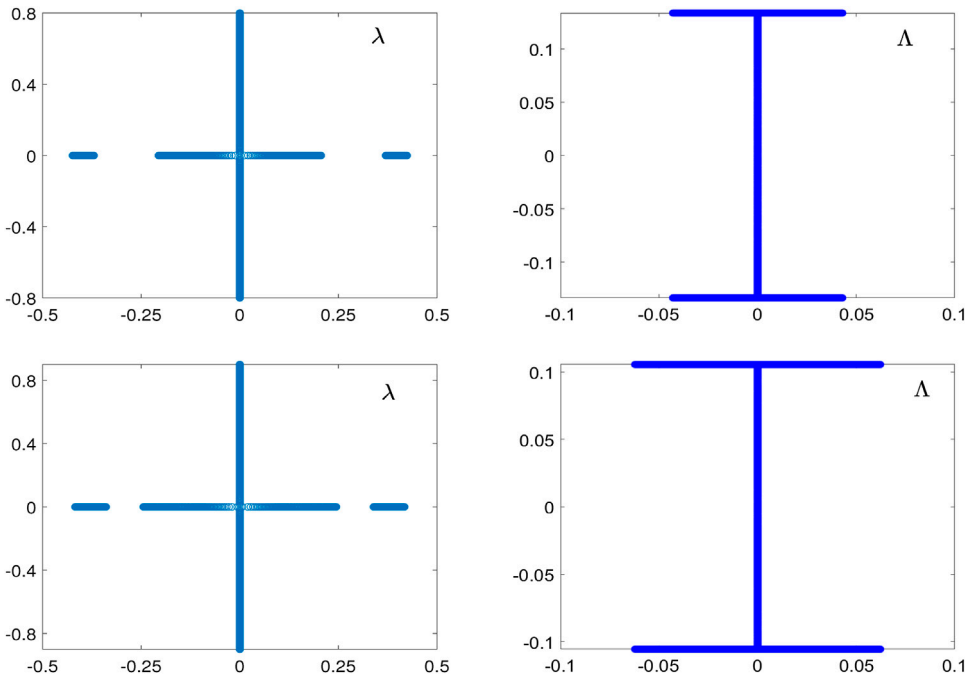

FIGURE 5 | Lax spectrum on the λ-plane **(left)** and stability spectrum on the Λ-plane **(right)** for the amplitude-normalized double-periodic wave **Eq. 2.15** with $k = 0.85$ **(top)** and $k = 0.95$ **(bottom)**.

$$\max_{\lambda \in [\lambda_2,\lambda_1]} \Lambda = \max_{\lambda \in [\lambda_2,\lambda_1]} 2\sqrt{(\lambda_1^2 - \lambda^2)(\lambda^2 - \lambda_2^2)} = (\lambda_1^2 - \lambda_2^2) = \sqrt{1-k^2}.$$

Since the dn-periodic wave becomes the constant-amplitude wave of unit amplitude if $k = 0$, it is clear that the maximal instability rate is largest for the constant-amplitude wave with $k = 0$, monotonically decreasing in k, and vanishes for the soliton limit $k = 1$. As $k \to 1$, the horizontal band on **Figure 2** (right) shrinks to an eigenvalue at the origin.

For the cn-periodic wave **Eq. 2.12** with $u_1 = k$ and $u_2 = i\sqrt{1-k^2}$, the amplitude is k. Hence, we use the scaling transformation (2.3) with $\alpha = k^{-1}$ in order to normalize the amplitude to unity. Lax spectrum of the spectral problem **Eq. 3.2** for such an amplitude-normalized cn-periodic wave is shown on left panels of **Figure 3** for $k = 0.85$ (top) and $k = 0.95$ (bottom). The unstable spectrum on the Λ-plane is obtained from the same expressions $\Lambda = \pm 2i\sqrt{P(\lambda)}$ when λ traverses along the bands of the Lax spectrum outside $i\mathbb{R}$. The unstable spectrum resembles the figure-eight band as is shown on the right panels of **Figure 3**. The figure-eight band starts and ends at $\Omega = 0$ for $\lambda = \lambda_1$ and $\lambda = \lambda_2$. Stability spectrum for both examples is similar in spite of the differences in the Lax spectrum. The only difference is that the figure-eight band and the purely imaginary bands intersect for $k = 0.85$ (top) and do not intersect for $k = 0.95$ (bottom). Thus, the cn-periodic wave **Eq. 2.12** is spectrally and modulationally unstable. As $k \to 1$, the figure-eight band shrinks to an eigenvalue at the origin.

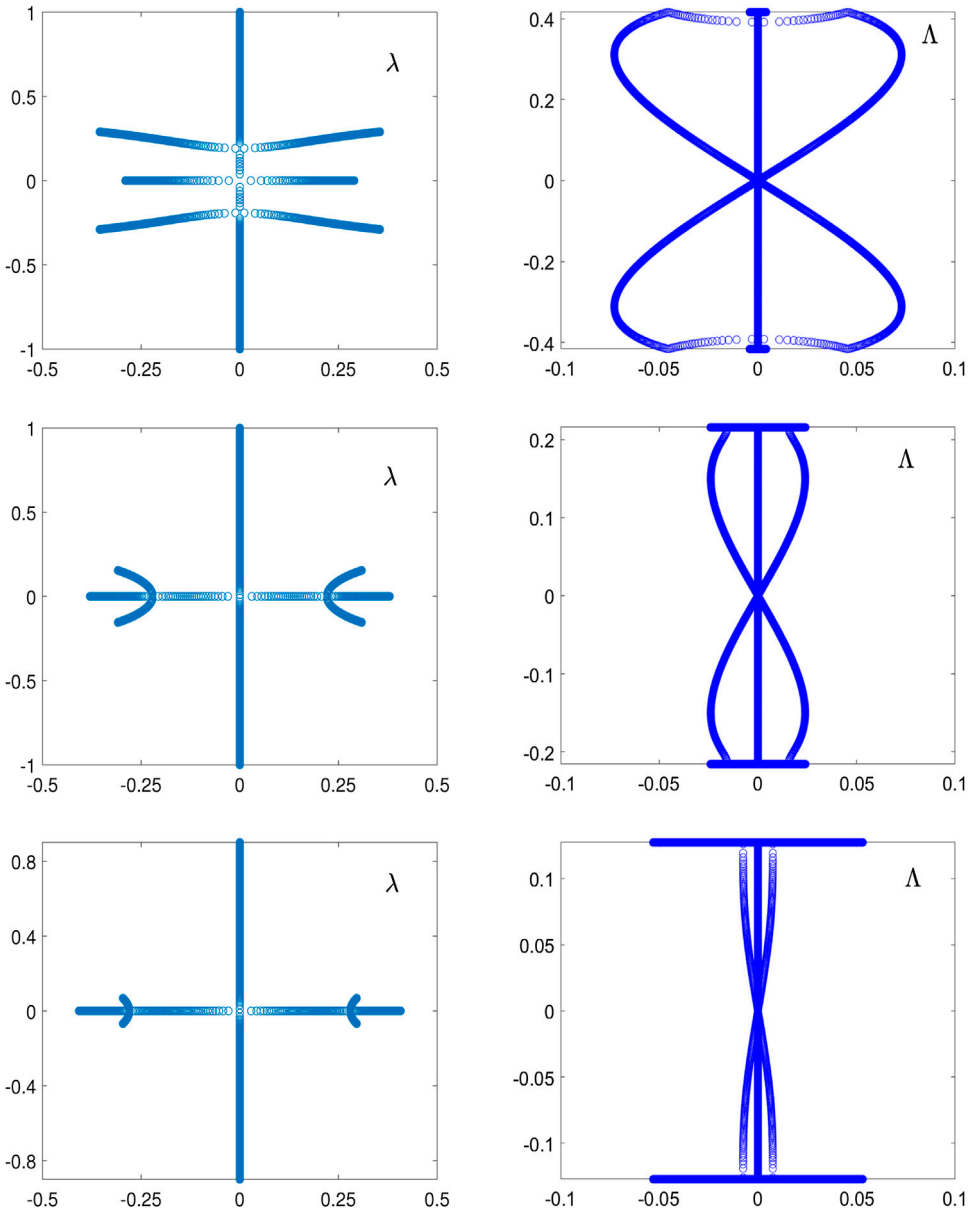

FIGURE 6 | The same as **Figure 5** but for the amplitude-normalized double-periodic wave (2.16) with $k = 0.3$ **(top)**, $k = 0.6$ **(middle)**, and $k = 0.9$ **(bottom)**.

Figure 4 compares the instability rates for different standing waves of the same unit amplitude. $\mathrm{Re}(\Lambda)$ is plotted versus the Floquet parameter θ in $\left[0, \frac{\pi}{L}\right]$ in **Eq. 3.4**. For the dn-periodic wave (left), we confirm that the growth rate is maximal for the constant-amplitude wave $(k = 0)$ and is monotonically decreasing as k is increased in $(0, 1)$. For the cn-periodic wave (right), the growth rate is also maximal in the limit $k \to 0$, for which the amplitude-normalized cn-periodic wave is expanded as

$$u(x) = \mathrm{cn}\left(k^{-1}x; k\right) \sim 0.5e^{ik^{-1}x} + 0.5e^{-ik^{-1}x} \quad \text{as} \quad k \to 0. \qquad (3.17)$$

Due to the scaling transformation **Eq. 2.3** and the expansion **Eq. 3.17**, the maximal growth rate in the limit $k \to 0$ is 0.25 instead of 1 and the Floquet parameter θ, for which it is attained, diverges to infinity as $k \to 0$. As k increases in $(0, 1)$, the growth rate becomes smaller and the Floquet parameter θ for which $\mathrm{Re}(\Lambda) > 0$ moves toward the origin. The end point of the unstable band reaches $\theta = 0$, when the bands of the Lax spectrum outside $i\mathbb{R}$ do not intersect $i\mathbb{R}$ like on **Figure 3** (bottom).

4 INSTABILITY OF DOUBLE-PERIODIC WAVES

Here we describe the main result on how to compute the instability rates for the double-periodic waves by using the linear **Eqs. 2.5, 2.6**. We write the solutions **Eqs. 2.15, 2.16** in

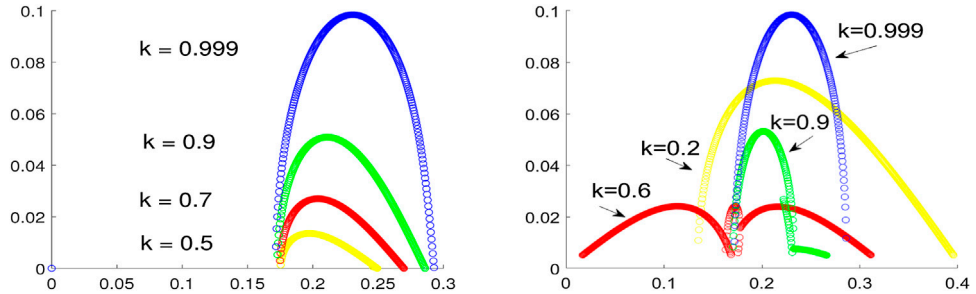

FIGURE 7 | Instability rate $\mathrm{Re}(\Lambda)$ versus the Floquet parameter θ for the amplitude-normalized double-periodic wave **Eq. 2.15 (left)** and the double-periodic wave **Eq. 2.16 (right)**. The values of k are given in the plots.

the form **Eq. 2.17**. We represent solution φ to the linear **Eqs. 2.5, 2.6** in the form:

$$\varphi_1(x,t) = \chi_1(x,t)e^{ibt+x\mu+t\Omega}, \quad \varphi_2(x,t) = \chi_2(x,t)e^{-ibt+x\mu+t\Omega}, \quad (4.1)$$

where $\mu, \Omega \in \mathbb{C}$ are spectral parameters and $\chi = (\chi_1, \chi_2)^T$ satisfies the following spectral problems:

$$\chi_x + \mu\chi = \begin{pmatrix} \lambda & \phi \\ -\overline{\phi} & -\lambda \end{pmatrix}\chi, \quad (4.2)$$

and

$$\chi_t + \Omega\chi = i\begin{pmatrix} \lambda^2 + \frac{1}{2}|\phi|^2 - b & \frac{1}{2}\frac{d\phi}{dx} + \lambda\phi \\ \frac{1}{2}\frac{d\overline{\phi}}{dx} - \lambda\overline{\phi} & -\lambda^2 - \frac{1}{2}|\phi|^2 + b \end{pmatrix}\chi. \quad (4.3)$$

Parameters $\mu, \Omega \in \mathbb{C}$ are independent of (x,t). This follows from the same compatibility of the linear Lax **Eqs. 2.5, 2.6** if $\psi(x,t)$ in **Eq. 2.17** satisfies the NLS **Eq. 2.1**.

By Floquet theorem, spectral parameters $\mu, \Omega \in \mathbb{C}$ are determined from the periodicity conditions $\chi(x+L,t) = \chi(x,t+T) = \chi(x,t)$ in terms of the spectral parameter λ. We distinguish between the space coordinate x and the time coordinate t in order to consider stability of the double-periodic waves **Eq. 2.17** in the time evolution of the NLS **Eq. 2.1**.

The Lax spectrum is defined by the condition that λ belongs to an admissible set for which the solution **Eq. 4.1** is bounded in x. Hence $\mu = i\theta$ with real θ in $\left[-\frac{\pi}{L}, \frac{\pi}{L}\right]$ and λ is computed from the spectral problem **Eq. 4.2** with $\chi(x+L,t) = \chi(x,t)$ for every $t \in \mathbb{R}$

With λ defined in the Lax spectrum, the spectral problem **Eq. 4.3** can be solved for the spectral parameter Ω under the condition that $\chi(x,t+T) = \chi(x,t)$ for every $x \in \mathbb{R}$. The corresponding solution to the linear system **Eqs. 4.2, 4.3** generates the solution $v(x,t)$ of the linearized system **Eq. 3.13** with $u \equiv \phi$ and $c = 0$ by means of the transformation formulas **Eqs. 3.14, 3.16**. Spectral parameter Ω is uniquely defined in the fundamental strip $\mathrm{Im}(\Omega) \in \left[-\frac{\pi}{T}, \frac{\pi}{T}\right]$, while $\mathrm{Re}(\Omega)$ determines the instability rate $\mathrm{Re}(\Lambda)$ by $\Lambda = 2\Omega$.

If $\mathrm{Re}(\Lambda) > 0$ for λ in the Lax spectrum, the double-periodic wave (2.17) is called *spectrally unstable*. The amplitude-normalized double-periodic waves are taken by using the scaling transformation (2.3). We observe again that the unstable spectrum with $\mathrm{Re}(\Lambda) > 0$ is related with λ in the Lax spectrum outside the imaginary axis.

For the amplitude-normalized double-periodic wave **Eq. 2.15** with $k = 0.85$ (top) and $k = 0.95$ (bottom), **Figure 5** shows the Lax spectrum of the spectral problem **Eq. 4.2** with $\mu = i\theta$ and $\theta \in \left[-\frac{\pi}{L}, \frac{\pi}{L}\right]$ on the λ-plane (left) and the stability spectrum on the Λ-plane (right). The unstable spectrum is located at the boundary $\mathrm{Im}(\Lambda) = \pm\frac{2\pi}{T}$ of the strip for every $k \in (0,1)$. The double-periodic wave **Eq. 2.15** is spectrally unstable.

Figure 6 shows the same as **Figure 5** but for the amplitude-normalized double-periodic wave **Eq. 2.16** with $k = 0.3$ (top), $k = 0.6$ (middle), and $k = 0.9$ (bottom). The Lax spectrum on the λ-plane has three bands, two of which are connected either across the imaginary axis (top) or across the real axis (middle and bottom), the third band is located on the real axis. The unstable spectrum on the Λ-plane includes the figure-eight band and bands located near the boundary $\mathrm{Im}(\Lambda) = \pm\frac{2\pi}{T}$. As $k \to 1$, the figure-eight band becomes very thin and the stability spectrum looks similar to the one on **Figure 5** because both the double-periodic solutions approach the Akhmediev breather **Eq. 2.18**.

Figure 7 compares the instability rates for different double-periodic waves of the same unit amplitude. $\mathrm{Re}(\Lambda)$ is plotted versus the Floquet parameter θ in $\left[0, \frac{\pi}{L}\right]$, where $\mu = i\theta$ is defined in **Eq. 4.2**.

For the amplitude-normalized double-periodic wave **Eq. 2.15** (left), the instability rate is maximal as $k \to 1$, that is, at the Akhmediev breather **Eq. 2.18**. The unstable band starts with the same cut-off value of θ and extends all the way to $\theta = \frac{\pi}{L}$. When $k \to 0$, the instability rates quickly decrease as the double-periodic wave approaches the NLS soliton **Eq. 2.19**.

For the amplitude-normalized double-periodic wave **Eq. 2.16** (right), the instability rate is large in the limit $k \to 0$, when the double-periodic wave is close to the particular cn-periodic wave **Eq. 2.20**. Then, the rates decrease when k is increased, however, the rates increase again and reach the maximal values as $k \to 1$ when the double-periodic wave approaches the Akhmediev breather **Eq. 2.18**.

5 CONCLUSION

We have computed the instability rates for the double-periodic waves of the NLS equation. By using the Lax pair of linear equations, we obtain the Lax spectrum with the Floquet theory in the spatial coordinate at fixed t and the stability spectrum with the Floquet theory in the temporal coordinate at fixed x. This separation of variables is computationally simpler than solving the full two-dimensional system of linearized NLS equations on the double-periodic solutions.

As the main outcome of the method, we have shown instability of the double-periodic solutions and have computed their instability rates, which are generally smaller compared to those for the standing periodic waves.

The concept can be extended to other double-periodic solutions of the NLS equation which satisfy the higher-order Lax–Novikov equations. Unfortunately, the other double-periodic solutions are only available in Riemann theta functions of genus $d \geq 2$, and for practical computations, one needs to construct such double-periodic solutions numerically, similarly to what was done in [41]. This task is opened for further work.

AUTHOR CONTRIBUTIONS

The author confirms being the sole contributor of this work and has approved it for publication.

ACKNOWLEDGMENTS

This work was supported in part by the National Natural Science Foundation of China (No. 11971103).

REFERENCES

1. Peregrine DH. Water waves, nonlinear Schrödinger equations and their solutions. *J Aust Math Soc Series B Appl Math* (1983) 25:16–43. doi:10.1017/s0334270000003891
2. Akhmediev NN, Eleonsky VM, Kulagin NE. Generation of periodic trains of picosecond pulses in an optical fiber: exact solutions. *Sov Phys JETP* (1985) 62: 894–899.
3. Gelash AA, "Formation of rogue waves from a locally perturbed condensate", *Phys Rev E* (2018) 97:022208. doi:10.1103/PhysRevE.97.022208
4. Zakharov VE, Gelash AA, "Nonlinear stage of modulation instability", *Phys Rev Lett* (2013) 111:054101. doi:10.1103/PhysRevLett.111.054101
5. Gelash AA, Agafontsev DS, "Strongly interacting soliton gas and formation of rogue waves", *Phys Rev E* (2018) 98:042210. doi:10.1103/physreve.98.042210
6. Gelash AA, Agafontsev D, Zakharov V, El G, Randoux S, Suret P, "Bound state soliton gas dynamics underling the spontaneous modulational instability", *Phys Rev Lett* (2019) 123:234102. doi:10.1103/physrevlett.123.234102
7. Agafontsev DS, Zakharov VE. Integrable turbulence and formation of rogue waves. *Nonlinearity* (2015) 28:2791–2821. doi:10.1088/0951-7715/28/8/2791
8. Agafontsev DS, Zakharov VE. Integrable turbulence generated from modulational instability of conoidal waves. *Nonlinearity* (2016) 29: 3551–3578. doi:10.1088/0951-7715/29/11/3551
9. Randoux S, Suret P, Chabchoub A, Kibler B, El G, "Nonlinear spectral analysis of Peregrine solitons observed in optics and in hydrodynamic experiments", *Phys Rev E* (2018) 98:022219. doi:10.1103/PhysRevE.98.022219
10. Dudley JM, Genty G, Mussot A, Chabchoub A, Dias F. Rogue waves and analogies in optics and oceanography. *Nat Rev Phys* (2019) 1:675. doi:10.1038/s42254-019-0100-0
11. Copie F, Randoux S, Suret P, "The Physics of the one-dimensional nonlinear Schrödinger equation in fiber optics: rogue waves, modulation instability and self-focusing phenomena", *Reviews in Physics* (2020) 5:100037. doi:10.1016/j.revip.2019.100037
12. Biondini G, Mantzavinos D, "Universal nature of the nonlinear stage of modulational instability", *Phys Rev Lett* (2016) 116:043902. doi:10.1103/PhysRevLett.116.043902
13. Biondini G, Li S, Mantzavinos D, Trillo S. Universal behavior of modulationally unstable media. *SIAM Rev* (2018) 60:888–908. doi:10.1137/17m1112765
14. Grinevich PG, Santini PM. The finite gap method and the analytic description of the exact rogue wave recurrence in the periodic NLS Cauchy problem. 1. *Nonlinearity* (2018) 31:5258–5308. doi:10.1088/1361-6544/aaddcf
15. Grinevich PG, Santini PM. The finite-gap method and the periodic NLS Cauchy problem of anomalous waves for a finite number of unstable modes. *Russ Math Surv* (2019) 74:211–263. doi:10.1070/rm9863
16. Bilman D, Ling L, Miller PD. Extreme superposition: rogue waves of infinite order and the Painlevé-III hierarchy. *Duke Math J* (2020) 169:671–760. doi:10.1215/00127094-2019-0066
17. Bilman D, Miller PD. A robust inverse scattering transform for the focusing nonlinear schrödinger equation. *Commun Pure Appl Math* (2019) 72: 1722–1805. doi:10.1002/cpa.21819
18. Slunyaev AV, Pelinovsky EN, "Role of multiple soliton Interactions in the generation of rogue waves: the modified Korteweg-de Vries framework", *Phys Rev Lett* (2016) 117:214501. doi:10.1103/PhysRevLett.117.214501
19. Bilman D, Buckingham R. Large-order asymptotics for multiple-Pole solitons of the focusing nonlinear schrödinger equation. *J Nonlinear Sci* (2019) 29: 2185–2229. doi:10.1007/s00332-019-09542-7
20. Chen J, Pelinovsky DE, "Rogue periodic waves of the focusing nonlinear Schrödinger equation", *Proc R Soc A* (2018) 474:20170814. doi:10.1098/rspa.2017.0814
21. Kedziora DJ, Ankiewicz A, Akhmediev N. Rogue waves and solitons on a conoidal background. *Eur Phys J Spec Top* (2014) 223:43–62. doi:10.1140/epjst/e2014-02083-4
22. Feng BF, Ling L, Takahashi DA. Multi-breather and high-order rogue waves for the nonlinear Schrödinger equation on the elliptic function background. *Stud Appl Math* (2020) 144:46–101. doi:10.1111/sapm.12287
23. Chen J, Pelinovsky DE, White RE, "Periodic standing waves in the focusing nonlinear Schrödinger equation: rogue waves and modulation instability", *Physica D* (2020) 405:132378. doi:10.1016/j.physd.2020.132378
24. Bronski JC, Hur VM, Johnson MA. "Instability in equations of KdV type", In: *New approaches to nonlinear waves, lecture notes in phys*. Cham: Springer (2016) 908:83–133.
25. Kamchatnov AM. On improving the effectiveness of periodic solutions of the NLS and DNLS equations. *J Phys Math Gen* (1990) 23:2945–2960. doi:10.1088/0305-4470/23/13/031
26. Kamchatnov A. New approach to periodic solutions of integrable equations and nonlinear theory of modulational instability. *Phys Rep* (1997) 286: 199–270. doi:10.1016/s0370-1573(96)00049-x
27. Deconinck B, Segal BL. The stability spectrum for elliptic solutions to the focusing NLS equation. *Physica D* (2017) 346:1–19. doi:10.1016/j.physd.2017.01.004
28. Deconinck B, Upsal J. The orbital stability of elliptic solutions of the focusing nonlinear schrödinger equation. *SIAM J Math Anal* (2020) 52:1–41. doi:10.1137/19m1240757
29. Upsal J, Deconinck B. Real Lax spectrum implies spectral stability. *Stud Appl Math* (2020) 145:765–790. doi:10.1111/sapm.12335
30. Xu G, Chabchoub A, Pelinovsky DE, Kibler B, "Observation of modulation instability and rogue breathers on stationary periodic waves", *Phys Rev Res* (2020) 2:033528. doi:10.1103/physrevresearch.2.033528
31. Akhmediev NN, Eleonskii VM, Kulagin NE. Exact first-order solutions of the nonlinear Schrödinger equation. *Theor Math Phys* (1987) 72:809–818. doi:10.1007/bf01017105

32. Akhmediev N, Ankiewicz A, Soto-Crespo JM, "Rogue waves and rational solutions of the nonlinear Schrödinger equation", *Phys Rev E Stat Nonlinear Soft Matter Phys* (2009) 80:026601. doi:10.1103/PhysRevE.80.026601
33. Kimmoun O, Hsu HC, Branger H, Li MS, Chen YY, Kharif C, et al. Modulation instability and phase-shifted Fermi-pasta-ulam recurrence, *Sci Rep* (2016) 6: 28516. doi:10.1038/srep28516
34. Chen J, Pelinovsky DE, White RE, "Rogue waves on the double-periodic background in the focusing nonlinear Schrödinger equation", *Phys Rev E* (2019) 100:052219. doi:10.1103/PhysRevE.100.052219
35. Calini A, Schober CM. Characterizing JONSWAP rogue waves and their statistics via inverse spectral data. *Wave Motion* (2017) 71:5–17. doi:10.1016/j.wavemoti.2016.06.007
36. Conforti M, Mussot A, Kudlinski A, Trillo S, Akhmediev N, "Doubly periodic solutions of the focusing nonlinear Schrödinger equation: recurrence, period doubling, and amplification outside the conventional modulation-instability band", *Phys Rev A* (2020) 101:023843. doi:10.1103/physreva.101.023843
37. Vanderhaegen G, Szriftgiser P, Naveau C, Kudlinski A, Conforti M, Trillo S, et al. Observation of doubly periodic solutions of the nonlinear Schrödinger equation in optical fibers. *Opt Lett* (2020) 45:3757–3760. doi:10.1364/OL.394604
38. Smirnov AO. Solution of a nonlinear Schrödinger equation in the form of two-phase freak waves. *Theor Math Phys* (2012) 173:1403–1416. doi:10.1007/s11232-012-0122-6
39. Smirnov AO. Periodic two-phase "Rogue waves". *Math Notes* (2013) 94: 897–907. doi:10.1134/s0001434613110266
40. Wright OC. Effective integration of ultra-elliptic solutions of the focusing nonlinear Schrödinger equation. *Phys Nonlinear Phenom* (2016) 321-322: 16–38. doi:10.1016/j.physd.2016.03.002
41. Bertola M, El GA, Tovbis A, "Rogue waves in multiphase solutions of the focusing nonlinear Schrödinger equation", *Proc R Soc A* (2016) 472:20160340. doi:10.1098/rspa.2016.0340
42. Bertola M, Tovbis A. Maximal amplitudes of finite-gap solutions for the focusing Nonlinear Schrödinger equation. *Commun Math Phys* (2017) 354: 525–47. doi:10.1007/s00220-017-2895-9
43. Wright OC. Sharp upper bound for amplitudes of hyperelliptic solutions of the focusing nonlinear Schrödinger equation. *Nonlinearity* (2019) 32:1929–1966. doi:10.1088/1361-6544/aafbd2
44. Sulem C, Sulem PL, The nonlinear Schrödinger equation: self-focusing and wave collapse. In: *Applied mathematical sciences*. New York: Springer-Verlag (1999) 139.
45. Fibich G, The nonlinear Schrödinger equation: singular solutions and optical collapse. In: *Applied mathematical sciences*. New York: Springer-Verlag (2015) 192.
46. Pelinovsky DE, White RE, "Localized structures on librational and rotational travelling waves in the sine-Gordon equation", *Proc R Soc A* (2020) 476: 20200490. doi:10.1098/rspa.2020.0490

Conflict of Interest: The author declares that the research was conducted in the absence of any commercial or financial relationships that could be construed as a potential conflict of interest.

frontiers in Physics

BRIEF RESEARCH REPORT
published: 17 March 2021
doi: 10.3389/fphy.2021.631993

Transformation of the Peregrine Breather Into Gray Solitons on a Vertically Sheared Current

H. C. Hsu[1], *M. Abid*[2], *Y. Y. Chen*[1] *and C. Kharif*[2]*

[1]Department of Marine Environment and Engineering, National Sun Yat-sen University, Kaohsiung, Taiwan, [2]Aix Marseille Université, CNRS, Centrale Marseille, IRPHE UMR 7342, F-13384, Marseille, France

In this Brief Research Report, we show, within the framework of the nonlinear Schrödinger equation in deep water and in the presence of vorticity (vor-NLS), that the Peregrine breather traveling at the free surface of a shear current of slowly varying vorticity may transform into gray solitons.

Keywords: nonlinear schrödinger equation, water waves, Solitons, breather, vorticity

1 INTRODUCTION

Within the framework of a fully nonlinear two-dimensional potential solver [4], computed the temporal evolution of a Stokes wavetrain with a small modulation. They found that the energy becomes focused, at the maximum of modulation, into a short wave packet of large amplitude they called a steep wave event (SWE). They showed that the Peregrine breather, which is an exact solution of the self-focusing nonlinear Schrödinger equation, was the most convenient approximation of the envelope of the SWE. Note that the Peregrine breather can be derived from the Kuznetsov-Ma breather and the Akhmediev breather in the limit of infinite temporal and spatial period (see [7]) [3]. suggested that the Peregrine breather may provide a useful and simple model for rogue wave events [1]. presented the first experimental observation of the Peregrine breather in a water wave tank. More recently [2], presented the first ever observation in a wave tank of dark solitons on the surface of water, so demonstrating the probable existence at the sea surface of dark solitons in finite depth for $kh < 1.363$ where k is the carrier wavenumber and h the water depth. They found a good agreement between the experimental soliton and the dark soliton solution of the defocusing nonlinear Schrödinger equation. Dark solitons occur as envelope holes. Rogue waves are large-amplitude waves which occurs at the sea surface suddenly without warning. Such waves are accompanied by deep holes before and/or after the largest crest. Another possible mechanism of these holes in the ocean could be dark or gray soliton generation. There is an abundant literature on the interaction between surface water waves and spatially uniform currents. In the real ocean, currents are never uniform. Spatially varying currents may affect strongly the water wave behavior. Herein, we paid attention to the evolution of a Peregrine breather propagating at the surface of a vertically sheared current. In this Brief Research Report we propose, based on the NLS equation in infinite depth, a physical mechanism of gray soliton generation from a Peregrine breather evolving on slowly varying underlying water vorticity. **Section 2** is devoted to the presentation of the vor-NLS equation in the presence of constant vorticity derived by [8]. The vor-NLS equation is self-focusing or defocusing according to the magnitude of the vorticity. Vorticity effect on the soliton solutions of the vor-NLS of self-focusing and defocusing types is displayed. A numerical simulation of the transformation of the Peregrine breather propagating at the free surface of a water flow of slowly varying vorticity is presented in **section 3**. A conclusion is given in **section 4**.

OPEN ACCESS

Edited by:
Amin Chabchoub,
The University of Sydney, Australia

Reviewed by:
Miguel Onorato,
University of Turin, Italy
Ton Van Den Bremer,
University of Oxford, United Kingdom

****Correspondence:***
C. Kharif
kharif@irphe.univ-mrs.fr

Specialty section:
This article was submitted to Interdisciplinary Physics, a section of the journal Frontiers in Physics

Received: *23 November 2020*
Accepted: *26 January 2021*
Published: *17 March 2021*

Citation:
Hsu HC, Abid M, Chen YY and Kharif C (2021) Transformation of the Peregrine Breather Into Gray Solitons on a Vertically Sheared Current. Front. Phys. 9:631993. doi: 10.3389/fphy.2021.631993

2 THE VOR-NLS

We choose an Eulerian frame $(Oxyz)$ with unit vectors (e_x, e_y, e_z). The vector e_z is oriented upwards so that the acceleration due to gravity is $g = -ge_z$ with $g > 0$. The equation of the undisturbed free surface is $z = 0$. The water waves are traveling at the surface of an underlying vertically sheared current of constant vorticity given by $U(z) = \Omega z$. The study is restricted to modulated wave trains propagating with positive phase velocities so long as both negative and positive values of Ω are considered. [8], have shown that the spatio-temporal evolution of the complex envelope $a(\xi, \tau)$ of the surface elevation of a two-dimensional weakly nonlinear modulated wave train propagating in the presence of constant water vorticity is governed by the nonlinear Schrödinger equation (NLS equation)

$$ia_\tau + \alpha a_{\xi\xi} + \gamma |a|^2 a = 0 \tag{1}$$

In the case of a wave train propagating at the surface of a deep water flow of constant vorticity $\zeta = -\Omega$, the dispersive and nonlinear coefficients of the vor-NLS **Eq.1** are

$$\alpha = -\frac{\omega\left(1+\overline{\Omega}\right)^2}{k^2\left(2+\overline{\Omega}\right)^3}, \qquad \gamma = -\frac{\omega k^2}{8}\frac{\left(\overline{\Omega}+2/3\right)\left(3\overline{\Omega}^2+6\overline{\Omega}+6\right)}{1+\overline{\Omega}},$$

with $\overline{\Omega} = \Omega/\omega$. We consider a carrier wave traveling from left to right in deep water whose intrinsic frequency, intrinsic phase velocity and intrinsic group velocity are

$$\omega = -\frac{\Omega}{2} + \sqrt{\frac{\Omega^2}{4} + gk},$$

$$c_p = -\frac{\Omega}{2k} + \sqrt{\frac{\Omega^2}{4k^2} + \frac{g}{k}},$$

$$c_g = \frac{\Omega + \sqrt{\Omega^2 + 4gk}}{2\sqrt{\Omega^2 + 4gk}} c_p,$$

with k the carrier wavenumber and g the gravitational acceleration.

[5] have compared both the linear intrinsic phase velocities and total energies of gravity waves in the presence of constant vorticity in finite depth and deep water and came to the conclusion that linear gravity waves in finite depth propagating at the surface of a water flow of constant vorticity behave like waves in infinite depth if $kh > \pi$. We can conclude that the unbounded water flow at $z = -\infty$ does not influence the kinematics and dynamics of the surface waves. In addition to the results of [5], **Figure 1** shows the dimensionless intrinsic group velocity deviation between finite and infinite depths for different values of the vorticity. As we can see the difference between the group velocities in finite and infinite depth becomes very weak as kh increases beyond the value π. **Equation 1** is focusing for $\overline{\Omega} > -2/3$ and defocusing for $\overline{\Omega} < -2/3$. Note that $\overline{\Omega} > -1$, $\forall\Omega$.

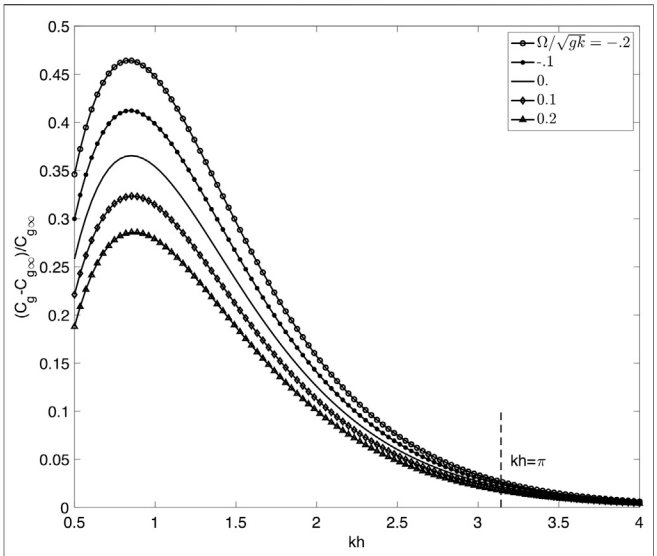

FIGURE 1 | Dimensionless group velocity deviation between finite and infinite depths as a function of the dispersive parameter for several values of the dimensionless vorticity. In dimensionless terms, the units of acceleration and length are the acceleration of gravity g and 2π ($g = 1$ and $k = 1$).

2.1 Effect of Vorticity on the Peregrine Breather and Gray Soliton

The focusing vor-NLS equation admits the Peregrine breather as solution

$$a_P(\xi,\tau) = a_0 k\sqrt{-\frac{\omega}{2\gamma}}\left(1 - \frac{4\left(1 - ia_0^2k^2\omega\tau\right)}{1 - \omega a_0^2k^2\xi^2\Big/\alpha + a_0^4k^4\omega^2\tau^2}\right) \exp\left(-ia_0^2k^2\omega\tau/2\right). \tag{2}$$

Note that $\alpha < 0$ and $\gamma < 0$, $\forall\overline{\Omega} > -2/3$. The defocusing vor-NLS equation admits the dark, a_D, and the gray, a_G, solitons as solutions.

$$a_D = a_0 \tanh\left(\sqrt{-\frac{\gamma}{2\alpha}}a_0\xi\right)\exp\left(i\gamma a_0^2\tau\right) \tag{3}$$

$$a_G = a_0\frac{\exp(2im) + \exp\left(2a_0\sin(m)\left(\sqrt{-\frac{\gamma}{2\alpha}}\xi + a_0\gamma\tau\cos(m)\right)\right)}{1 + \exp\left(2a_0\sin(m)\left(\sqrt{-\frac{\gamma}{2\alpha}}\xi + a_0\gamma\tau\cos(m)\right)\right)}e^{ia_0^2\gamma\tau} \tag{4}$$

where a_0 is the envelope amplitude of the background carrier wave. The parameter m fixes the minimum of amplitude at the center of the soliton. For $m = \pi/2$ this minimum is zero, with a phase shift, that corresponds to the dark soliton. Note that $\alpha < 0$ and $\gamma > 0$, $\forall -1 < \overline{\Omega} < -2/3$ ($\overline{\Omega} > -1$ whatever the value of Ω). **Equation 3** can be derived from **Eq. 4** when $m = \pi/2$. In **Figure 2** are plotted several dimensionless profiles of the Peregrine breather and the gray soliton for different values of the vorticity $\zeta = -\Omega$. The vorticity does not modify the amplification factor $|a_P|/|a_{P\infty}|$. The envelope amplitude of the background carrier wave is $|a_{P\infty}| = a_0 k\sqrt{-\omega/(2\gamma)}$ whereas the

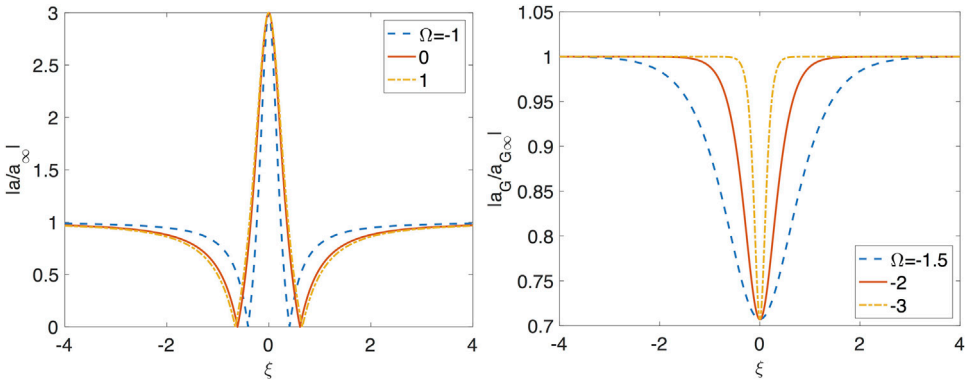

FIGURE 2 | Dimensionless profiles of the Peregrine breather **(left)** and the gray soliton **(right)** for several values of the vorticity with $g = 1$ and $k = 1$.

maximum amplitude of the envelope is $3a_0k\sqrt{-\omega/(2\gamma)}$. Consequently, the normalized maximum of the modulation envelope does not depend on the vorticity. The Peregrine breather is narrower (wider) for positive (negative) vorticity. The width of the breather decreases as the vorticity increases. The minimal amplitude at the center of the gray soliton is not modified by the presence of the vortical flow. The gray solitons becomes narrower as the positive vorticity increases.

3 EVOLUTION OF THE PEREGRINE BREATHER ON SLOWLY VARYING VORTICAL FLOW

Within the framework of **Eq. 1**, we have performed a numerical simulation of the transformation of a Peregrine breather traveling at the free surface of a vortical water flow whose vorticity varies very slowly. $\overline{\Omega}$ varies from zero to a value less than −2/3. For $\overline{\Omega} = 0$ **Eq. 1** is focusing whereas for $\overline{\Omega} < -2/3$ this equation is defocusing. Consequently, the slow variation of the vorticity transforms the focusing vor-NLS equation into defocusing. We consider a Peregrine breather that meets progressively a vortical water flow whose temporal variation is

$$\Omega(\tau) = \sin(\sigma\tau + \pi/2) - 1, \qquad 0 \le \sigma\tau \le \pi$$
$$\Omega(\tau) = -2, \qquad \sigma\tau > \pi.$$

The parameter σ is chosen such that the average temporal variation of the vorticity along the ramp is of $\mathcal{O}(a_0^2k^2)$. The vorticity remains constant when $\sigma\tau > \pi$. Note that $\overline{\Omega}(0) = 0$ and $\overline{\Omega}(\sigma\tau = \pi) \approx -0.828$. The vor-NLS equation is solved numerically using a pseudo-spectral Fourier method. The periodicity length of the spatial domain is $L = 160\pi$. The number of grid points is $N = 6000$. Dealiasing is used. Time integration is carried out with a second order time-splitting method and a fourth order Runge Kutta scheme as well. The numerical code is checked using comparisons with the exact breather solutions and by the self consistency of the results of the two time integration schemes also. We have used a spatial filter similar to that of [6] to avoid numerical instabilities. The filter does not modify the envelope evolution because it cancels the highest modes that do not participate in the global dynamic of the envelope. The transfer function of the filter is $\exp(-\nu\kappa^2)$, where κ is a wavenumber in the Fourier space and $\nu = 10^{-5}$ is used. With this value of ν the loss of the energy of the carrier wave is of the order of 1% over approximately 1,000 periods of time evolution of the carrier. The numerical simulation has been run in dimensionless units with $k = 1$ and $g = 1$. The initial condition at $\tau = 0$ is the Peregrine breather with $a_0 = 0.10$ and $\Omega = 0$. **Figure 3** shows the evolution of the envelope at several times. The vorticity $\zeta = -\Omega$ varies slowly along the ramp from $\zeta(\tau = 0) = 0$ to $\zeta(\tau \approx 10T) = 2$. At $\tau \approx 6\,T$ the vor-NLS equation becomes defocusing. T is the period of the background of the Peregrine breather. During its propagation along the ramp the width of the breather increases whereas its amplitude decreases. At $\tau \approx 20\,T$, on both sides of the crest of the envelope two small local troughs occur that then deepen during the propagation of the envelope to give rise to the formation of two gray solitons whose profiles are close to that of a dark soliton. **Figure 4** shows the profiles of the two gray solitons at two different times. An excellent agreement is obtained between the numerical and analytical profiles.

4 CONCLUSION

Within the framework of the vor-NLS equation in infinite depth we have shown numerically that a Peregrine breather propagating at the free surface of a slowly varying vortical flow may generate gray solitons. The present simulation confirms in a different context the result of [2] on the existence of dark solitons on the surface of shallow water ($kh < 1.363$) in the absence of vorticity. Our approach presents two limitations. The vor-NLS equation which was derived for constant vorticity has been used with a slowly varying vorticity to transform the focusing NLS equation into defocusing during a limited time. Nevertheless, the very slow variation of the vorticity on a small number of periods lead us to believe that our results are physically relevant. The time to obtain the formation of the gray solitons is beyond the time range of

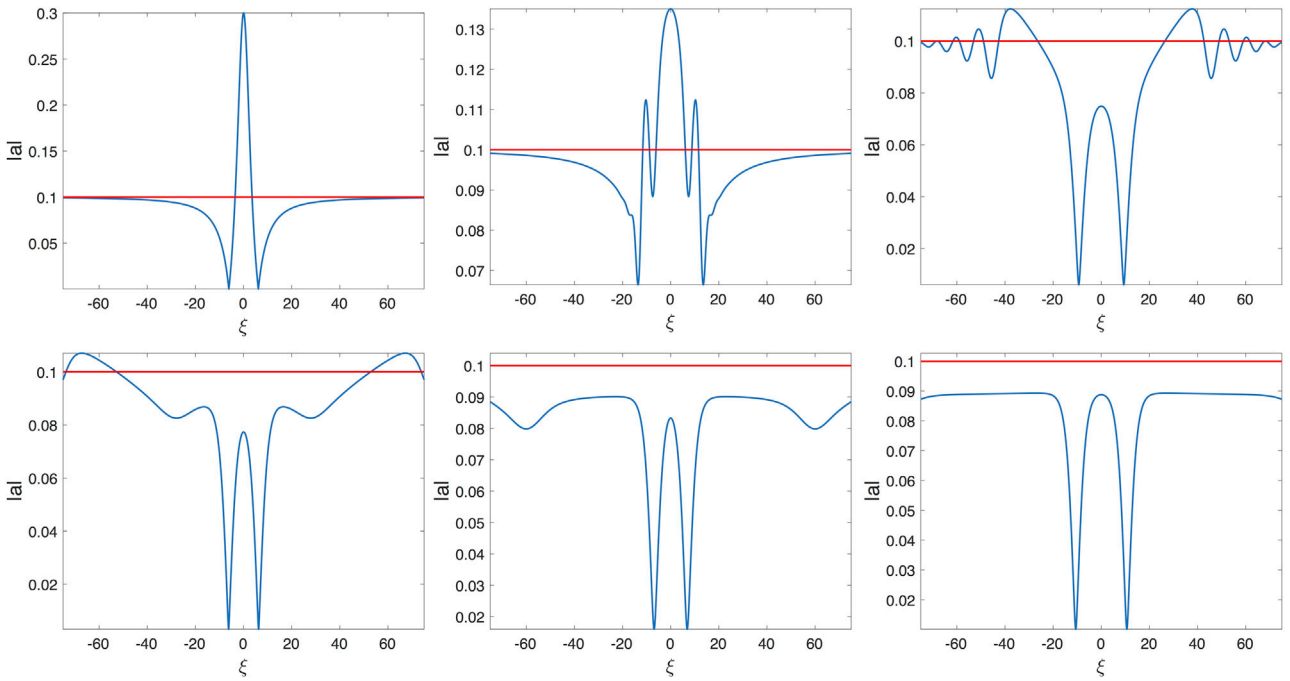

FIGURE 3 | Time evolution of the tranformation of the Peregrine breather into a two-grey soliton with $g = 1$ and $k = 1$. Top panels from left to right: $\tau = 0, 23\,T, 145\,T$. Bottom panels from left to right: $\tau = 298\,T, 596\,T, 901\,T$. T is the period of the Peregrine breather background.

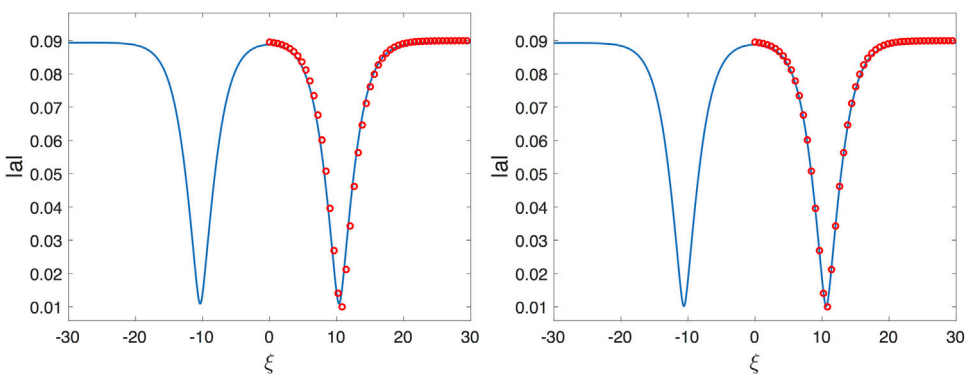

FIGURE 4 | Gray soliton profiles at $t = 867\,T$ **(left)** and $t = 900\,T$ **(right)**. The solid lines correspond to the numerical simulation whereas the circles correspond the analytical solution of **Eq. 4** for $a_0 = 0.09$ and $m = \pi/2 - 1/10$.

validity of the NLS equation. However, it is well known that approximate models can be valid beyond their validity domain [4]. found, from their numerical simulations of the NLS equation over several thousands of periods, that their computations were in qualitative good agreement over a much longer time scale than expected, namely when the wave steepness of the carrier wave is not too steep. Despite these limitations we conjecture the existence of gray solitons on deep water in the presence of varying water shear flows. Our numerical simulation provides only preliminary results on this transition which has to be confirmed by using models free of these two limitations.

DATA AVAILABILITY STATEMENT

The original contributions presented in the study are included in the article/Supplementary Material, further inquiries can be directed to the corresponding author.

AUTHOR CONTRIBUTIONS

HH, Conceptualization of the project, Methodology, and formal analysis checking. MA, Formal analysis checking; Software

design; Numerical simulations; Validation; Investigation; Visualization. YC, Conceptualization of the project and formal analysis checking. CK, Conceptualization; Methodology; Formal analysis; Investigation; Writing.

REFERENCES

1. Chabchoub A, Hoffmann N, Akhmediev N. Rogue wave observation in a water wave tank. *Phys Rev Lett* (2011) 106:204502. doi:10.1103/PhysRevLett.106.204502
2. Chabchoub A, Kimmoun O, Branger H, Hoffmann N, Proment D, Onorato M, et al. Experimental observation of dark solitons on the surface of water. *Phys Rev Lett* (2013) 110:124101. doi:10.1103/PhysRevLett.110.124101
3. Dysthe KB, Trulsen K. Note on breather type solutions of the NLS as models for freak-waves. *Physica Scripta* (1999) T82:48–52. doi:10.1238/physica.topical.082a00048
4. Henderson KL, Peregrine DH, Dold JW. Unsteady water wave modulations: fully nonlinear solutions and comparison with the nonlinear schrödinger equation. *Wave Motion* (1999) 29:341–61. doi:10.1016/s0165-2125(98)00045-6
5. Kharif C, Abid M. Miles theory revisited with constant vorticity in water of infinite depth. *Jmse* (2020) 8(8):623. doi:10.3390/jmse8080623
6. Lo E, Mei CC. A numerical study of water-wave modulation based on a higher-order nonlinear schrödinger equation. *J Fluid Mech* (1985) 150:395–416. doi:10.1017/s0022112085000180
7. Peregrine DH. Water waves, nonlinear schrödinger equations and their solutions. *J Aust Math Soc Ser B, Appl. Math* (1983) 25:16–43. doi:10.1017/s0334270000003891
8. Thomas R, Kharif C, Manna M. A nonlinear schrödinger equation for water waves on finite depth with constant vorticity. *Phys Fluids* (2012) 24:127102. doi:10.1063/1.4768530

Conflict of Interest: The authors declare that the research was conducted in the absence of any commercial or financial relationships that could be construed as a potential conflict of interest.

frontiers in Physics

ORIGINAL RESEARCH
published: 19 March 2021
doi: 10.3389/fphy.2021.640025

Boosting and Taming Wave Breakup in Second Harmonic Generation

Raphaël Jauberteau[1,2], *Sahar Wehbi*[1,3], *Tigran Mansuryan*[1], *Katarzyna Krupa*[4], *Fabio Baronio*[2], *Benjamin Wetzel*[1], *Alessandro Tonello*[1], *Stefan Wabnitz*[5]* and *Vincent Couderc*[1]

[1]XLIM, UMR CNRS 7252, Université de Limoges, Limoges, France, [2]Dipartimento di Ingegneria dell'Informazione, Università di Brescia, Brescia, Italy, [3]ALPhANOV, Optics & Lasers Technology Center, Institut d'optique d'Aquitaine, Talence, France, [4]Institute of Physical Chemistry, Polish Academy of Sciences, Warsaw, Poland, [5]Dipartimento di Ingegneria dell'Informazione, Elettronica e Telecomunicazioni, Sapienza University of Rome, Rome, Italy

Modulation instability is a universal phenomenon that can be found in a wide variety of nonlinear systems where, in the presence of a noise seed, peaks of random intensities can be generated. Several dynamical systems admit exact solutions in the form of breathers or solitons on a finite background. The vast majority of soliton studies has been restricted so far to one-dimensional systems. In contrast, the occurrences of localized structures in fully spatiotemporal systems has been only sporadically explored. In this work, we experimentally study the conditions for the wave-breaking of spatially extended optical beams in the process of second harmonic generation. Whenever the pump energy of the picosecond-long fundamental beam reaches a critical level, the beam shape at the second harmonic in a KTP crystal breaks into small filaments. These filaments exhibit extreme local intensity peaks, and their statistical distribution can be modified by the input energy of the fundamental beam. Moreover, by analyzing similar wave-breaking dynamics in a PPLN crystal in the presence of a higher nonlinear quadratic response, we observe that the spatial beam breaking may even gradually vanish as the laser intensity grows larger, leading to a spatial reshaping into a smooth and wider beam, accompanied by a substantial broadening of its temporal spectrum.

Keywords: second-harmonic (SH) generation (SHG), statistical optics, optical instabilities, optical chaos and complexity, optical spatio-temporal dynamics, optical soliton, rogue wave

OPEN ACCESS

Edited by:
Bertrand Kibler, UMR6303 Laboratoire Interdisciplinaire Carnot de Bourgogne (ICB), France

Reviewed by:
Venugopal Rao Soma, University of Hyderabad, India
Shihua Chen, Southeast University, China
Giorgos P. Tsironis, University of Crete, Greece

***Correspondence:**
Stefan Wabnitz
stefan.wabnitz@uniroma1.it

Specialty section:
This article was submitted to Optics and Photonics, a section of the journal Frontiers in Physics

Received: *11 December 2020*
Accepted: *10 February 2021*
Published: *19 March 2021*

Citation:
Jauberteau R, Wehbi S, Mansuryan T, Krupa K, Baronio F, Wetzel B, Tonello A, Wabnitz S and Couderc V (2021) Boosting and Taming Wave Breakup in Second Harmonic Generation. Front. Phys. 9:640025. doi: 10.3389/fphy.2021.640025

INTRODUCTION

A wide class of nonlinear systems exhibits Modulation Instability (MI): the onset stage of the nonlinear dynamics of MI leads to an exponential growth of periodic perturbations [1]. Although in presence of a noise seed, MI can give rise to peaks of random intensities, exact solutions are known, including first-order ones such as Akhmediev breathers or Peregrine solitons. Interestingly, MI has been largely studied in single mode optical fibers in the presence of dispersion and Kerr nonlinearity, and solitons on a finite background take the form of pulses (in the time domain) evolving along the fiber [2, 3]. In this work we focus our attention on a wider class of higher-dimensional nonlinear systems that involve spatially extended optical beams, whose combined spatial and temporal instabilities are expected to stimulate a host of further studies on nonlinear waves.

Wave-breaking, a mechanism of disintegration of optical beams or temporal pulses, has been extensively studied in nonlinear optics. In materials with cubic (Kerr) nonlinearity, there are two principal mechanisms of wave breaking, namely, MI and gradient catastrophe (GC): they appear in

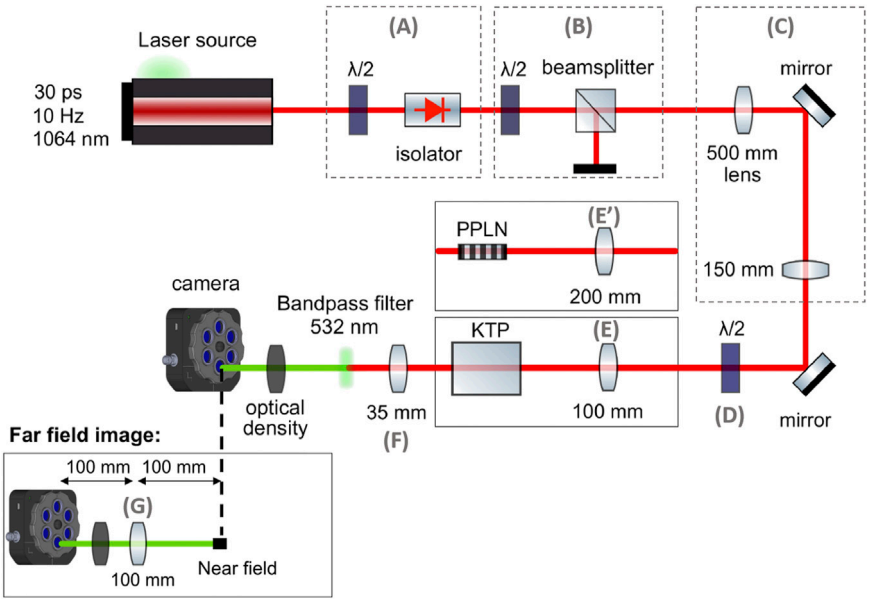

FIGURE 1 | Schematic of the experimental setup.

either the focusing or the defocusing regime, respectively. Conversely, in materials with quadratic nonlinearities the MI and GC processes may even coexist [4].

It is well known that beam instabilities may arise in three-wave mixing interactions in the presence of dispersion and diffraction [5, 6]. When limiting the analysis to pure spatial waves having a dominant transverse dimension, such as it occurs in the case of elliptical beams, it is possible to reduce the description of the transverse beam evolution into a single spatial coordinate. In this limit, MI based on quadratic interactions in type-II second harmonic generation (SHG) may occur, see for instance Ref. [7]. Moreover, in the limit known as cascading, it is possible to reduce the three-wave mixing interaction to a single nonlinear Schrödinger equation; some direct analogies can be established with temporal effects in nonlinear fibers.

When considering the full two-dimensional (2D) nature of the spatial transverse domain, an extended version of MI is still possible. In particular, purely 2D MI was numerically and experimentally discussed in Ref. [8] for type-II SHG. In Ref. [8] the authors observed the dramatic breakup of the beam shape at the SH, leading to spatial pattern formation: by increasing the input power of the fundamental wave, they were able to move from the pump depletion regime (characterized by a localized energy exchange between the fundamental and SH) into the MI regime, leading to a complete breakup of the SH beam. Among other types of beam instabilities in quadratic nonlinear media, transverse MI in three-wave mixing was reported, by considering the vector nature of the nonlinear interaction [9]. Correspondingly, azimuthal MI was theoretically and experimentally studied in Ref. [10], again in a type-II SHG in potassium titanyl phosphate (KTP) crystal.

It is important to stress that, in the realm of beam instabilities in quadratic crystals, the spatial dimensions cannot be easily disjoined from the temporal/spectral dimensions. This is particularly true in the high-energy regime: the ultimate nature of MI in quadratic nonlinear media involves a coupling between spatial and temporal dimensions [11]. This means that MI in quadratic crystals cannot be described as a simple product of spatial filamentation and temporal breakup; consider for example the mechanism of colored conical emission [12].

The presence of spatiotemporal beam instabilities can be associated, in a phase space representation of the dynamic evolution of a wave system, with the exponential amplification of small initial perturbations. This means that it is also interesting to study the beam evolution in the nonlinear stage of the instabilities, that is beyond the initial wave breakup or in the depleted pump regime. For instance, it may occur that, once the multiple filaments are formed, they may subsequently self-organize or combine (e.g., in the case of multiple filaments in air [13]). It is also possible to observe clustering phenomena, involving the aggregation at large scales of fine-scale structures. In astrophysics, these phenomena are at the basis of the formation of galaxies. In this perspective, a detailed study for the case of saturable nonlinear media was reported in Ref. [14].

Beam instabilities often provide the mechanism for the generation of rogue waves in 2D nonlinear wave systems. This perspective is particularly interesting, for example, in the recently reported cases of caustics [15], and of rogue waves in ferroelectrics boosted by nonlinearity [16]. In the process of rogue wave generation, the role played by nonlinearity may be twofold. For instance, Ref. [17] describes a system in which the presence of a weak nonlinearity was responsible for enhancing rogue waves. Whereas the rogue wave statistics was quenched in the strongly nonlinear regime [17]. The generation of spatial extreme waves with non-Gaussian statistics in a nonlinear cavity

with a liquid crystal light valve was studied for instance in Ref. [18].

In a recent related work [19], we studied the generation of 2D transverse rogue waves in the fundamental beam, as a result of type II SHG in a KTP quadratic nonlinear crystal. These represent a new class of transient, Peregrine-like 2D self-guided beams, which spontaneously appear from nowhere and then disappear, as the beam intensity grows larger. In the strong conversion regime, temporal reshaping followed by spatiotemporal wave breaking, acting against spatial focusing, was observed to destabilize beam trapping.

In this work we explore, by a series of experimental studies, the spatiotemporal beam breakup which occurs in the SH beam. Specifically, we observed that, in a regime close to phase matching of SHG, the SH spatial beam breaks up, leading to the formation of a multitude of filaments. Hereafter, we simply call filaments the nonlinear self-trapped and self-sustained solitary waves, or quasi-solitons, that spontaneously form (and disappear) in a non-integrable wave system. Unveiling a new mechanism for the generation of nonlinear extreme waves with peculiar statistical properties is of fundamental scientific interest. In addition, we envisage that these sources of structured light may also find interesting technological applications. Some applications of similar structured light sources are discussed for instance in Ref. [20], which points to the interest in generating speckled beams with statistics that differ from a classical Rayleigh distribution [21]. Nonlinear waves, including rogue waves have been also recently proposed as computing reservoirs [22].

Remarkably, in our experiments we observed an unexpected behavior in SH beam filamentation. Specifically, as the power of the fundamental wave grows larger, instead of clustering, the multitude of filaments composing the SH gradually sinks into a spatially wide, and nearly uniform beam. At that point, the SH beam partially recovers its brightness, both in the near and in the far-field. This effect was accompanied by a significant broadening of the temporal spectrum, ultimately evolving into a supercontinuum, similarly to what previously observed in the formation of a single, stable polychromatic filament [23]. The efficiency of SHG, which can be attained in similar crystals in the absence of nonlinear wave breaking, was recently discussed in Ref. [24].

MATERIALS AND METHODS

The experimental setup is illustrated in **Figure 1**. In all of our experiments, we used a Q-switched, mode-locked Nd:YAG laser (EKSPLA PL2250 series), delivering 30 ps duration high-energy pulses, at the central wavelength of 1064 nm, with a repetition rate of 10 Hz. The laser output was protected from back-reflections by means of a half-wave plate and a polarization sensitive isolator (A). The laser output beam was controlled by a second half-wave plate and a polarization beam splitter (B). An afocal system (C), composed by two lenses of 500 mm and 150 mm, respectively, reduced the Gaussian beam diameter by almost three times with respect to the original diameter of the laser beam.

Two different crystals were used in our experiments. In a first series of measurements, we used a KTP crystal, manufactured by CASTECH. The KTP crystal was 30 mm long, 8 mm thick, and 8 mm wide. The SHG phase mismatch was controlled by means of two rotational axes (Newport gimbal optic mount). A half-wave plate (D) controlled the orientation of the input linear state of polarization (SOP). The crystal cut permitted phase-matching of type-II SHG for an input SOP at 45° between ordinary and extraordinary axes, for a light beam at normal input incidence (polar angles $\theta = 90°$, $\Phi = 23.5°$, with reference to the crystallographic axes).

In a second series of measurements, we replaced the KTP crystal by a PPLN crystal (manufactured by HCP Photonics Corporation), being 15 mm long, 1 mm thick, and 2 mm wide. The period of inversion of the ferroelectric domain was Λ_{PPLN} = 7.97 μm. For the PPLN crystal, SHG was obtained through the quasi-phase-matching (QPM) technique, and the phase mismatch was adjusted by changing the temperature of the oven in which the crystal was placed. The phase-matching of SHG was obtained at the temperature of 60°C, the linear SOP of the input laser light at the fundamental frequency was kept fixed, and aligned with the extraordinary axis of the PPLN crystal (type-0 QPM) by means of the half-wave plate (D).

The input laser beam was adapted to the crystal type. For the PPLN crystal, the pump beam was injected with an input diameter of 200 μm, measured at $1/e^2$, by means of a 200 mm converging lens E'. For the KTP crystal, the input beam diameter was of 400 μm ($1/e^2$), obtained with the help of a converging lens E with a 100 mm focal length. In both cases, the point of beam injection was located after the focal point of the lenses E or E' for the KTP or the PPLN crystal, respectively. In both cases, the beam diffraction length at 1064 nm was much longer than the physical length of the crystal itself, so that, at low energy levels, i.e., in the absence of nonlinear effects, the laser beam could be considered as non-diverging along its propagation in the crystal.

At the output face of the crystals, the SHG beam at 532 nm at the output of the KTP crystal was filtered by means of a bandpass filter at 532 nm ± 3 nm. We also used a larger passband filter at 532 nm ± 10 nm for the experiments with the PPLN. The near-field at the crystal output was magnified by a 35 mm converging lens (F), and analyzed by a BC106N-VIS CCD Thorlabs camera, with a magnification of 4.56. The same setup was also used to analyze the near-field at the output of the PPLN crystal: in that case, the corresponding magnification was 8.375. To measure the far-field, we displaced the camera. A new converging lens G was interposed at equal distances between the camera and the near-field: such a distance was matched to the focal length of lens G (100 mm).

RESULTS

We analyzed the output SH beam shape for different input intensities of the fundamental pump (we refer here to the peak intensities of the input beam at the fundamental wave I_{FF}). Specifically, by increasing the pump beam intensity, we observed a gradual spatial reshaping of the SH beam, which is induced by nonlinear beam propagation in the crystal. **Figure 2** summarizes the results when using the KTP crystal, for six different

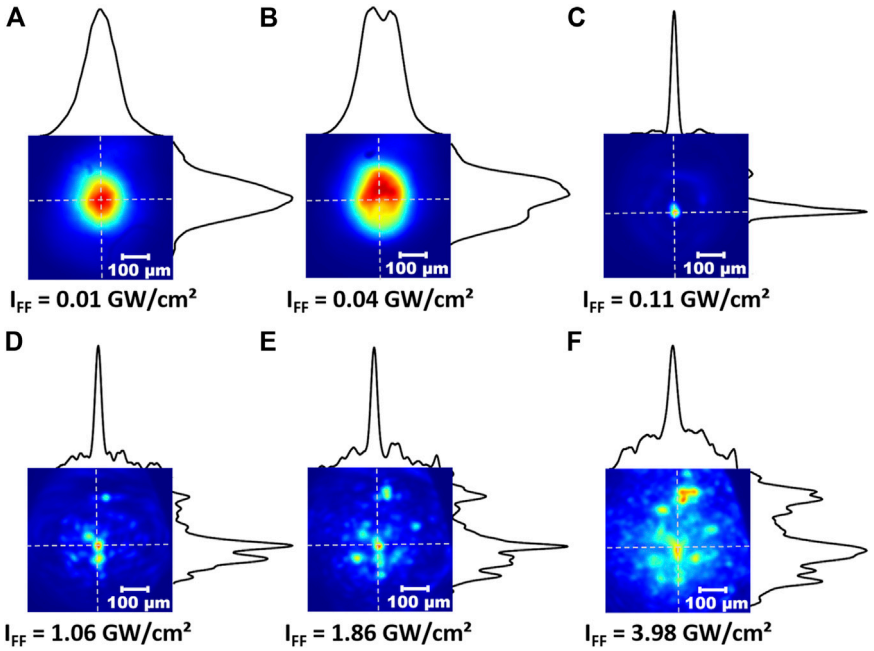

FIGURE 2 | Near-field images of the SH beam at the output face of the KTP crystal. The SH beam shape is nearly Gaussian for an input intensity of 0.01 GW/cm^2 **(A)**. The beam is depleted near the center of the Gaussian at 0.04 GW/cm^2 of input intensity **(B)** then, for a pump intensity of 0.11 GW/cm^2 **(C)**, strong spatial compression of the SH beam is observed. Whereas for pump intensities above 1 GW/cm^2 **(D)–(F)** the output SH beam breaks in an irregular pattern of localized spots. These results refer to crystal orientations of $\theta = 90^\circ$, $\Phi = 23.5^\circ + 0.33^\circ$ (focusing case) and input SOP orientation of 47°. Colormaps are normalized to the local maximum intensity detected.

levels of I_{FF}. The crystal orientation was kept fixed with an angular shift of $\Delta\Phi = +0.33^\circ$ from the phase-matching angles ($\theta = 90^\circ$, $\Phi = 23.5^\circ$). As can be seen in panels (a–c) of **Figure 2**, for input intensities close to 0.11 GW/cm^2, we observed a spatial focusing of the SH beam: its diameter at 1/e^2 dropped from 320 µm down to 50 µm (here the pump pulse energy was 2 µJ). Panels (d–f) of **Figure 2** show that, when increasing the pump intensity I_{FF} above 1 GW/cm^2, we observed a breakup of the SH beam into a seemingly random pattern of tightly focalized light filaments. The resulting light intensity distribution is reminiscent of the speckled beams which result from beam propagation through random media. Such a nonlinear SH beam breakup was observed for both negative and positive values of the phase mismatch (we analyzed the range from $\Delta\Phi = -1.67^\circ$ to $\Delta\Phi = +1.67^\circ$), and for nearly all orientations of the linear SOP of the input pump. SH beam breakup only vanished when the input SOP was aligned with the direction of either the ordinary or the extraordinary KTP axes, so that type-II three-wave mixing is not permitted.

We characterized the random nature of the multiple filaments resulting from SH breakup by estimating the statistical distribution of the patterns of light spots in each image. For that purpose, we calculated the scintillation index of the SH as

$$S_{SHG} = \frac{\langle I_{SHG}^2 \rangle - \langle I_{SHG} \rangle^2}{\langle I_{SHG} \rangle^2} \quad (1)$$

where <> denotes the average over the different pixel samples of a given image. For classical speckle patterns that obey Gaussian statistics, the scintillation index is equal to one. For the SH output intensity patterns in **Figure 2**, the SH scintillation index S_{SHG} is equal to 1.11 for I_{FF} = 1.1 GW/cm^2 pump intensity (**Figure 2D**). The SH scintillation index drops to S_{SHG} = 0.74 when the input beam intensity is increased up to I_{FF} = 1.9 GW/cm^2 (**Figure 2E**).

Figure 3 illustrates the statistics of pixel intensities upon different input beam powers. These statistics refer to the images reported in panels (c), (d), (e) and (f) of **Figure 2**. For each pump intensity level, we report the histogram of the SH intensity in linear and in log scale (square inset). For ease of comparison, the round insets reproduce the corresponding image over which the histogram is calculated. In **Figures 3B,C**, the dashed curves trace the negative-exponential probability density function (PDF) $p(I)$ [21]:

$$p(I) = \frac{1}{\langle I \rangle} e^{-\frac{I}{\langle I \rangle}} \quad (2)$$

In order to measure the mean value of the speckle spots size, we also calculated the deterministic intensity correlations of the images shown in **Figure 2** for three values of I_{FF}. From the image distribution $I_{SHG}(x,y)$ of the SH, being x,y the coordinates of the pixel images, we calculated first the intensity deviation from its mean value $\delta I_{SHG} = I_{SHG} - \langle I_{SHG} \rangle$. Next, we calculated the corresponding deterministic intensity correlation CI (Δx, Δy).

$$C_I(\Delta x, \Delta y) = \iint_{-\infty}^{+\infty} \delta I_{SHG}(x,y) \delta I_{SHG}(x + \Delta x, y + \Delta y) \mathrm{d}x\mathrm{d}y \quad (3)$$

The results, for three selected intensity levels I_{FF} are illustrated in **Figure 4**.

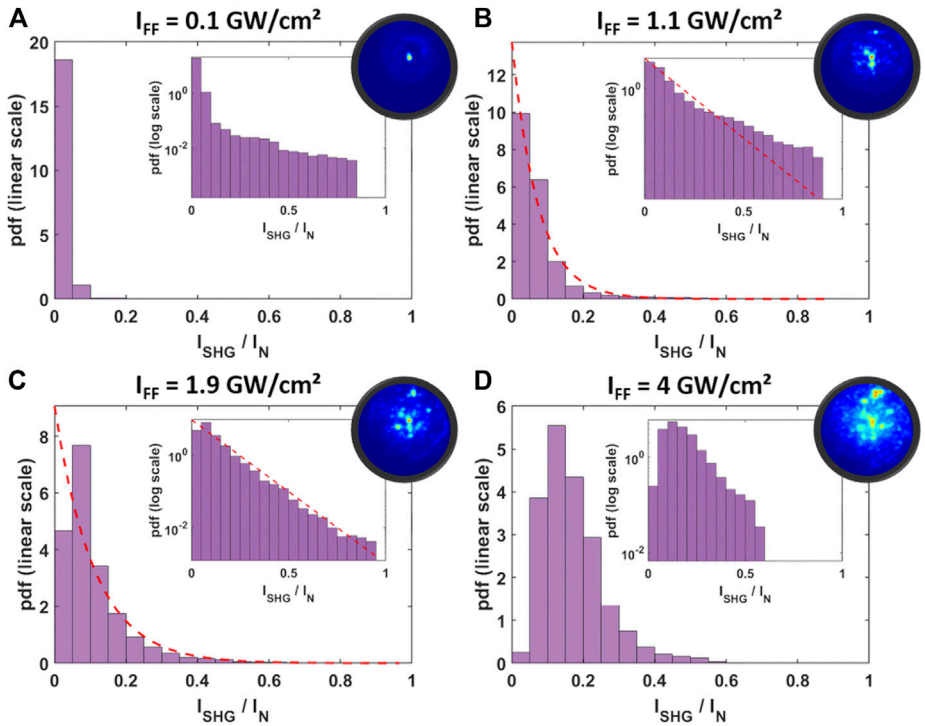

FIGURE 3 | Statistics of the SH intensity levels, obtained in KTP for different input pump intensities I_{FF}. In the histograms the intensity axis of the SH is normalized to the maximum level permitted by the 8-bit camera. Note that the SH beam intensity was reduced by a variable attenuation to avoid saturation of the camera. The attenuation was modified for each value of I_{FF} **(A**, **B)**. The circular insets are extracted from the corresponding cases of **Figure 2**. The red dashed curves represent the applications of **Eq.2** for the different cases.

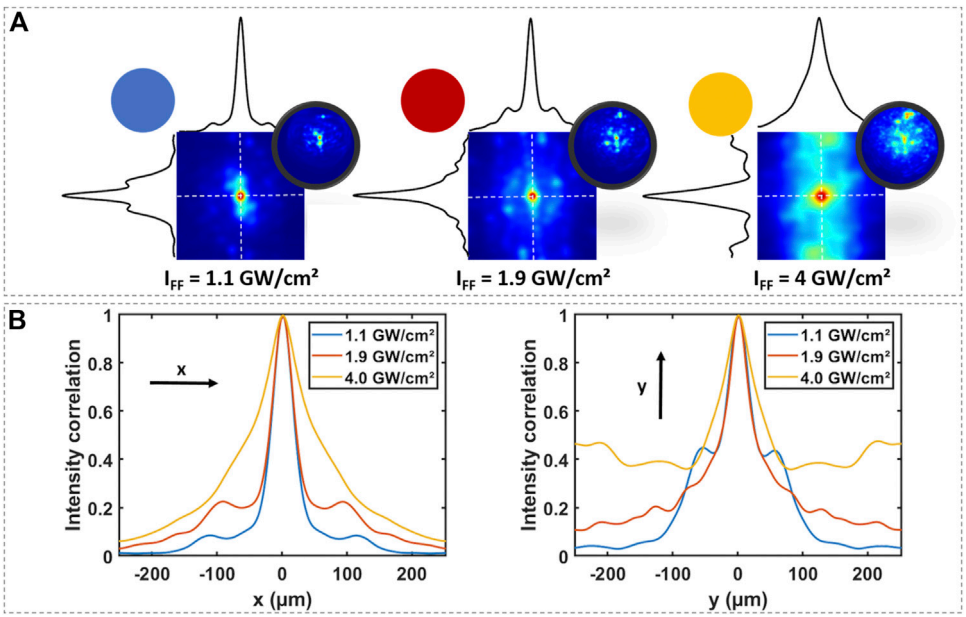

FIGURE 4 | (A)—intensity correlations C_I of the near-field images of the SH beam at the output of the KTP crystal, **(B)**—comparison of the spatial profile of intensity correlations along the *x* and *y* directions, respectively. Data refer to a crystal orientation of $\theta = 90^\circ$, $\Phi = 23.5^\circ + 0.33^\circ$ and input polarization orientation of 47°. The circular insets are extracted from the corresponding cases of **Figure 2**.

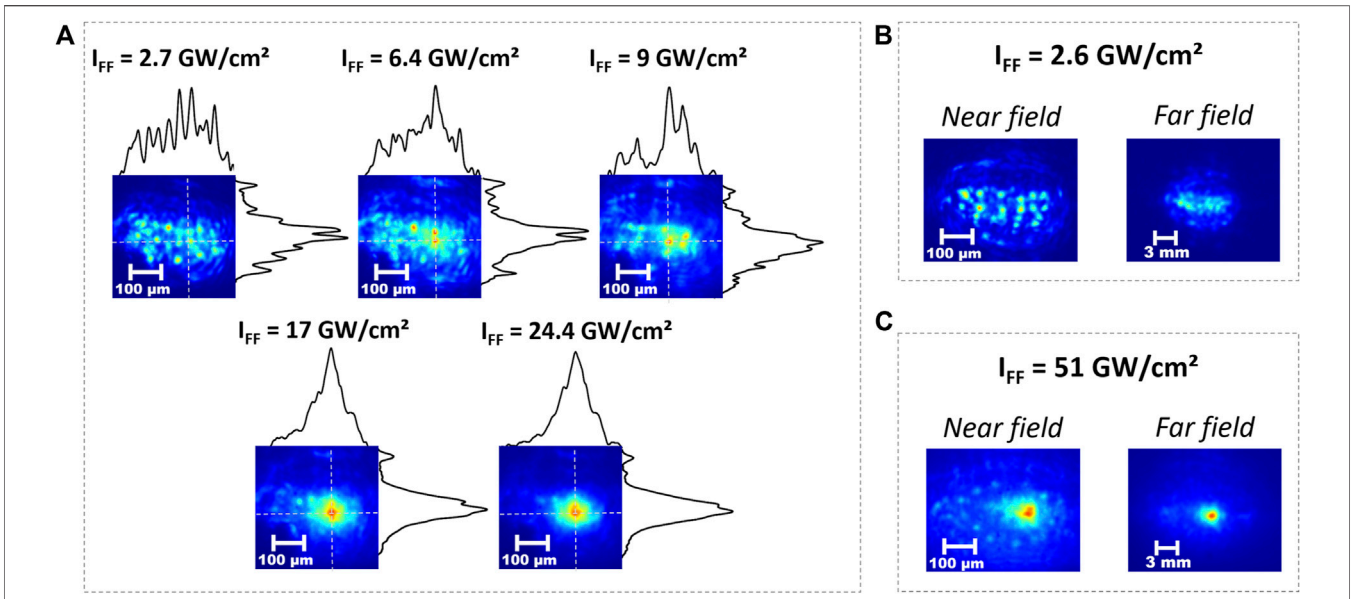

FIGURE 5 | (A)—near field-images of the SH beam at the output face of the PPLN crystal for different pump intensities. Near and far-fields of SH beams for **(B)** I_{FF} = 2.6 GW/cm^2, **(C)** I_{FF} = 51 GW/cm^2. The scale in the far-field image is proportional to the spatial spectrum and it refers to the experimental setup described in Methods. These experimental results refer to a crystal temperature T = 60°C.

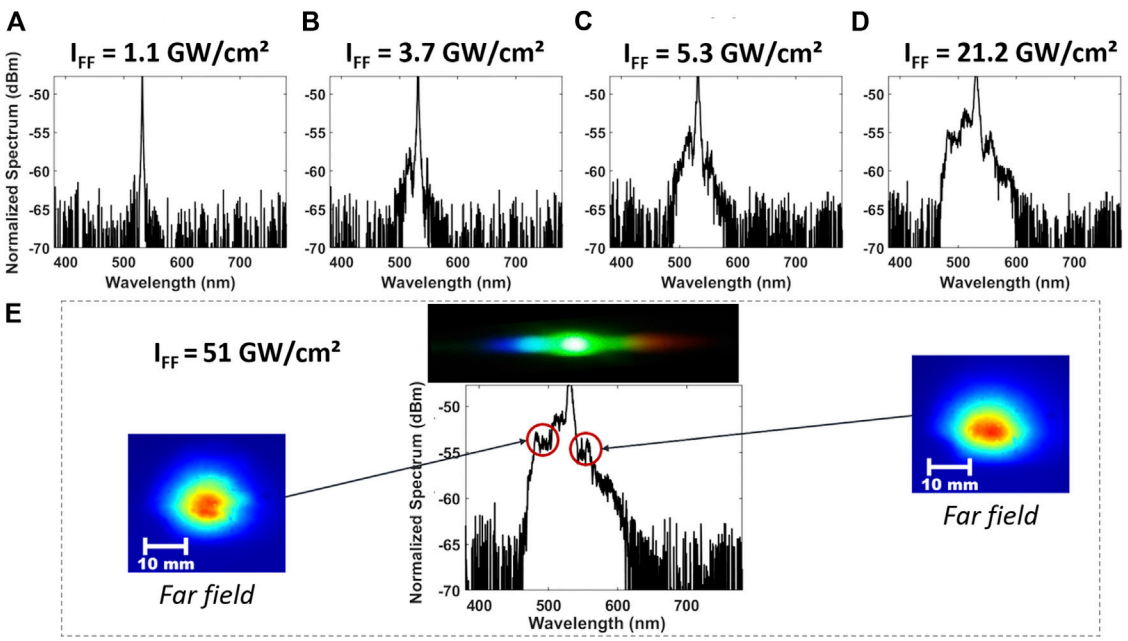

FIGURE 6 | (A)–(D)—spectral evolution of the SH beam for different input pump intensities. **(E)**—spectrum of the SH beam at I_{FF} = 51 GW/cm^2 with corresponding photographic image. The two insets show the far-field beam shape of the two selected spectral components at 500 nm (left) and 550 nm (right), respectively.

In a second series of experiments, we analyzed nonlinear SH beam reshaping when replacing the KTP crystal by PPLN crystal, which results in a stronger nonlinear optical response. The experimental results illustrating the evolution of the output SH beam shape are reported in **Figure 5**. In particular, as shown in panel 5(a), we observed that the SH is fully broken in multiple filaments for a pump intensity I_{FF} = 2.7 GW/cm^2. We observed that the distribution of filaments evolves as the pump intensity is further increased. For pump intensities I_{FF} = 16 GW/cm^2 and higher, output SH filaments disappear: the spatial breakup is

mitigated, and the SH beam increases its brightness both in the near and in the far-field (see **Figure 5C** for 51 GW/cm^2). This type of SH spatial beam reshaping, which is not observed when using a KTP crystal, is accompanied by large spectral broadening of the SH, as illustrated by the series of spectra measurement which are reported in **Figure 6**.

DISCUSSION

Our first series of experiments (carried out by using a KTP crystal, and illustrated in **Figure 2**) demonstrates an unexpected complex and strong spatial reshaping of SH beams in the process of type-II SHG. For relatively weak pump intensity levels (e.g., 0.04 GW/cm^2), the output SH beam remains wide and nearly flat. Whenever the pump intensity reaches I_{FF} = 0.11 GW/cm^2 level, we observed a strong self-focusing of the SH beam, involving a significant compression of its diameter. When further increasing the input pump intensity I_{FF} by one order of magnitude, we observed the spatial breakup of the SH beam, and the formation of randomly distributed filaments. The presence of multiple filaments was confirmed till we reached the maximum available intensity I_{FF} = 4 GW/cm^2. The corresponding statistical analysis of the pixel intensities, corresponding to the four images of **Figure 3**, shows that the level of pump intensity has direct consequences on the PDF of the spatial intensity distribution of the SH beam. We underline that one could modify the speckles statistics by exploiting the mechanism of spatial nonlinear beam breaking, while otherwise keeping the KTP crystal unchanged.

As a possible perspective application of these results, we envisage the possibility to customize the statistics of filaments by exploiting nonlinear wave breaking, in alternative to other methods for modifying the speckle intensity statistics, e.g., by using a spatial light modulator [19]. Specifically, for an input pump intensity of 1.1 GW/cm^2, the speckles PDF in **Figure 3B**. agrees fairly well with the classical distribution of a Rayleigh speckle pattern. This is confirmed by the scintillation index, which is close to unity in that case. However, **Figure 3D** shows that, for input pump intensities I_{FF} as high as 4 GW/cm^2, the PDF of speckles strongly diverges from a Rayleigh PDF, and it even becomes not monotonic upon intensity. These changes in the intensity statistics reflect the different topologies of the pattern of filaments. A careful analysis of the PDF tails and their connection with extreme spatial waves (like the brightest filaments shown in **Figures 2** and **5**) will be the subject of future analysis.

In order to compare the typical size of the generated SH, we calculated for some of the images in **Figure 2** the corresponding deterministic correlations for the beam pattern at SH, as shown in **Figure 4**. We considered three different intensities levels of I_{FF}. **Figure 4** reveals that the short-range correlation, which is related to the typical size of speckles, remains very similar as the pump intensity increases from 1.1 GW/cm^2 up to 1.9 GW/cm^2, in spite of some differences in the PDFs of the SH beam intensity for these two cases. When further increasing the pump intensity up to 4 GW/cm^2, the deterministic spatial intensity correlation applied to the image shows that the filaments tend to increase their size. The long-range correlation is also gradually enhanced and the pump intensity grows larger. As a matter of fact, for I_{FF} = 4 GW/cm^2 we can see that the SH beam breakup is boosted by the large intensity of the fundamental beam. One may thus extrapolate that, by further increasing the pump intensity, one could gradually fill the gaps among different filaments, which would reduce the speckle contrast.

As illustrated in **Figure 5**, we repeated the study of the dependence of the SH beam breakup and its statistics by considering SHG in a PPLN crystal. In this case, the larger effective quadratic nonlinear response (about 15 pm/V to compare with 3 pm/V for KTP) and the absence of walk-off allow for a stronger nonlinear interaction. Again, we observed the presence of SH beam breakup, leading to the generation of filaments (see **Figure 5**, for pump intensities from 2.7 GW/cm^2 till 9 GW/cm^2). Moreover, we revealed that the initial sea of filaments (some of them possessing extreme intensity values) becomes gradually interconnected via the generation of a broad intensity background. Eventually, SH filaments nearly disappear, and a spatially wide SH beam is observed for the largest values of the pump power (see **Figure 5**, for pump intensities from 17 GW/cm^2 up to 51 GW/cm^2). In particular, it is important to notice in **Figure 5** that both the near and the far-field patterns observed for a 51 GW/cm^2 pump intensity are strongly spatially localized, although the central spot is surrounded by a broad background. In this case, we can somehow see that the consequences of the spatial instability which leads to SH breaking into multiple filaments are eventually tamed by nonlinearity. It is important to notice that this nonlinear taming process takes place in *the presence* of a substantial broadening of the temporal spectrum around the SH wavelength. The mechanism of spectral broadening and supercontinuum generation in PPLN for a single smooth beam in PPLN was discussed, both experimentally and numerically, in Ref. [23]. In the present case, the spectral broadening is taking place out of a plurality of randomly distributed filaments, and it may possibly involve self-phase modulation, spatial and temporal MI. The detailed dynamics and the relative impact of these phenomena deserve to be further investigated with numerical and analytical studies. **Figure 6** clearly illustrates the process of spectral broadening that accompanies spatial reshaping, which occurs in the present specific case, both in the near- and in the far-field. The photographic images in **Figure 6E** show that, for such pump intensity levels, spectral broadening emanated from the SH beam may cover both the blue and the red regions of the visible spectrum. These two insets show how the newly generated colors inherit the nearly bell-shape of the SH beam.

In conclusion, in this work we have experimentally shown how the beam shape obtained at the SH of a non-diverging pump beam can break into multiple filaments. Moreover, we carried out a statistical study of the intensity distribution of such filaments. We revealed that the statistical properties of SH filaments can be partially controlled by the level of intensity of the fundamental beam, while keeping fixed both the crystal and polarization beam orientations with respect to the crystallographic axes. The generation of multiple filaments with customized statistics may be of interest in all advanced applications requiring a structured light illumination, for example, in the fields of microscopy or reservoir computing. Moreover, we surprisingly observed that the aftermath of beam breakup can lead to a taming of spatiotemporal instabilities when the intensity of the fundamental beam is increased well above the instability threshold. Specifically, a re-

localization of the SH beam is accompanied by a corresponding spectral broadening, leading to the generation of new colors in the visible. Such spatial beam reshaping accompanied by spectral broadening can be used to develop novel and versatile light sources in a variety of applications ranging from nonlinear fluorescence imaging to multispectral LIDAR measurements.

DATA AVAILABILITY STATEMENT

The raw data supporting the conclusion of this article will be made available by the authors, without undue reservation.

AUTHOR CONTRIBUTIONS

RJ and VC conceived, planned and carried out the experiments, and interpreted the experimental results. SWe and TM carried out a complementary series of experiments to complete the interpretation of the results. AT, FB, BW, and SWa worked on the theoretical and bibliographic part and wrote part of the text. KK worked on a previous version of the setup and initial experimental results in PPLN crystal. All authors contributed to the preparation of the manuscript by providing critical feedback.

FUNDING

H2020 European Research Council (740355, 874596, 950618); CILAS (ArianeGroup) through the shared X-LAS laboratory; the French ANR through the "TRAFIC project: ANR-18-CE080016-01; the *Investissements d'Avenir* with the reference *ANR-10-LABX-0074-01 Sigma-LIM*; "Region Nouvelle Aquitaine" through projects F2MH, SCIR, SIP2 and Nematum.

REFERENCES

1. Randoux S, Suret P, Chabchoub A, Kibler B, El G. Nonlinear spectral analysis of Peregrine solitons observed in optics and in hydrodynamic experiments. *Phys Rev E* (2018) 98:022219. doi:10.1103/PhysRevE.98.022219
2. Dudley JM, Dias F, Erkintalo M, Genty G. Instabilities, breathers and rogue waves in optics. *Nat Photon* (2014) 8:755–64. doi:10.1038/nphoton.2014.220
3. Dudley JM, Genty G, Dias F, Kibler B, Akhmediev N. Modulation instability, Akhmediev Breathers and continuous wave supercontinuum generation. *Opt Express* (2009) 17:21497–508. doi:10.1364/OE.17.021497
4. Conforti M, Baronio F, Trillo S. Competing wave-breaking mechanisms in quadratic media. *Opt Lett* (2013) 38(10):1648–50. doi:10.1364/OL.38.001648
5. Kanashov AA, Rubenchik AM. On diffraction and dispersion effect on three wave interaction. *Physica D: Nonlinear Phenomena* (1981) 4(1):122–34. doi:10.1016/0167-2789(81)90009-9
6. Bespalov VI, Talanov VI. Filamentary structure of light beams in nonlinear liquids. *J Exp Theor Phys Lett* (1966) 3(12):307–10.
7. Fuerst RA, Baboiu D-M, Lawrence B, Torruellas WE, Stegeman GI, Trillo S, et al. Spatial modulational instability and multisolitonlike generation in a quadratically nonlinear optical medium. *Phys Rev Lett* (1997) 78(14):2756–9. doi:10.1103/PhysRevLett.78.2756
8. Delqué M, Fanjoux G, Gorza SP, Haelterman M. Spontaneous 2D modulation instability in second harmonic generation process. *Opt Commun* (2011) 284(5):1401–4. doi:10.1016/j.optcom.2010.10.098
9. Boardman AD, Bontemps P, Xie K. Transverse modulation instability of vector optical beams in quadratic nonlinear media. *J Opt Soc Am B* (1997) 14(11):3119–26. doi:10.1364/JOSAB.14.003119
10. Petrov DV, Torner L, Martorell J, Vilaseca R, Torres JP, Cojocaru C. Observation of azimuthal modulational instability and formation of patterns of optical solitons in a quadratic nonlinear crystal. *Opt Lett* (1998) 23(18):1444–6. doi:10.1364/OL.23.001787
11. Salerno D, Jedrkiewicz O, Trull J, Valiulis G, Picozzi A, Di Trapani P. Noise-seeded spatiotemporal modulation instability in normal dispersion. *Phys Rev E Stat Nonlin Soft Matter Phys* (2004) 70:065603. doi:10.1103/PhysRevE.70.065603
12. Trillo S, Conti C, Di Trapani P, Jedrkiewicz O, Trull J, Valiulis G, et al. Colored conical emission by means of second-harmonic generation. *Opt Lett* (2002) 27(16):1451–3. doi:10.1364/OL.27.001451
13. Méchain G, Couairon A, Franco M, Prade B, Mysyrowicz A. Organizing multiple femtosecond filaments in air. *Phys Rev Lett* (2004) 93(3):035003. doi:10.1103/PhysRevLett.93.035003
14. Chen Z, Sears SM, Martin H, Christodoulides DN, Segev M. Clustering of solitons in weakly correlated wavefronts. *Proc Natl Acad Sci USA* (2002) 99(8):5223–7. doi:10.1073/pnas.072287299
15. Safari A, Fickler R, Padgett MJ, Boyd RW. Generation of caustics and rogue waves from nonlinear instability. *Phys Rev Lett* (2017) 119(20):203901. doi:10.1103/PhysRevLett.119.203901
16. Pierangeli D, Di Mei F, Conti C, Agranat AJ, DelRe E. Spatial rogue waves in photorefractive ferroelectrics. *Phys Rev Lett* (2015) 115(9):093901. doi:10.1103/PhysRevLett.115.093901
17. Mattheakis M, Pitsios IJ, Tsironis GP, Tzortzakis S. Extreme events in complex linear and nonlinear photonic media. *Chaos, Solitons & Fractals* (2016) 84:73–80. doi:10.1016/j.chaos.2016.01.008
18. Montina A, Bortolozzo U, Residori S, Arecchi FT. Non-Gaussian statistics and extreme waves in a nonlinear optical cavity. *Phys Rev Lett* (2009) 103(17):173901–4. doi:10.1103/PhysRevLett.103.173901
19. Jauberteau R, Tonello A, Baronio F, Krupa K, Millot G, Wetzel B, et al. Observation of 2D spatiotemporal rogue events in a quadratic nonlinear medium. In: Conference on lasers and electro-optics, OSA technical digest; 2020 May 10-15; Washington, DC United States: Optical Society of America (2020) [paper JTu2F.18].
20. Bender N, Yılmaz H, Bromberg Y, Cao H. Customizing speckle intensity statistics. *Optica* (2018) 5(5):595–600. doi:10.1364/OPTICA.5.000595
21. Goodman JW. Some fundamental properties of speckle*. *J Opt Soc Am* (1976) 66(11):1145–50. doi:10.1364/JOSA.66.001145
22. Marcucci G, Pierangeli D, Conti C. Theory of neuromorphic computing by waves: machine learning by rogue waves, dispersive shocks, and solitons. *Phys Rev Lett* (2020) 125(9):093901. doi:10.1103/PhysRevLett.125.093901
23. Krupa K, Labruyère A, Tonello A, Shalaby BM, Couderc V, Baronio F, et al. Polychromatic filament in quadratic media: spatial and spectral shaping of light in crystals. *Optica* (2015) 2(12):1058–64. doi:10.1364/OPTICA.2.001058
24. Krupa K, Fona R, Tonello A, Labruyère A, Shalaby BM, Wabnitz S, et al. Spatial beam self-cleaning in second-harmonic generation. *Sci Rep* (2020) 10:7204. doi:10.1038/s41598-020-64080-7

Conflict of Interest: The authors declare that the research was conducted in the absence of any commercial or financial relationships that could be construed as a potential conflict of interest.

frontiers in Physics

ORIGINAL RESEARCH
published: 22 March 2021
doi: 10.3389/fphy.2021.644584

Spatiotemporal Complexity Mediated by Higher-Order Peregrine-Like Extreme Events

Saliya Coulibaly[1]*, *Camus G. L. Tiofack*[2] *and Marcel G. Clerc*[3]

[1] *Université de Lille, CNRS, UMR 8523–PhLAM–Physique des Lasers Atomes et Molécules, Lille, France,* [2] *Faculty of Sciences, University of Maroua, Maroua, Cameroon,* [3] *Departamento de Física and Millennium Institute for Research in Optics, FCFM, Universidad de Chile, Santiago, Chile*

The Peregrine soliton is the famous coherent solution of the non-linear Schrödinger equation, which presents many of the characteristics of rogue waves. Usually studied in conservative systems, when dissipative effects of injection and loss of energy are included, these intrigued waves can disappear. If they are preserved, their role in the dynamics is unknown. Here, we consider this solution in the framework of dissipative systems. Using the paradigmatic model of the driven and damped non-linear Schrödinger equation, the profile of a stationary Peregrine-type solution has been found. Hence, the Peregrine soliton waves are persistent in systems outside of the equilibrium. In the weak dissipative limit, analytical description has a good agreement with the numerical simulations. The stability has been studied numerically. The large bursts that emerge from the instability are analyzed by means of the local largest Lyapunov exponent. The observed spatiotemporal complexity is ruled by the unstable second-order Peregrine-type soliton.

Keywords: Peregrine soliton, spatiotemporal chaos, fiber ring cavity, Lugiato-Lefever equation, Kerr frequency comb

OPEN ACCESS

Edited by:
Bertrand Kibler, UMR6303 Laboratoire Interdisciplinaire Carnot de Bourgogne (ICB), France

Reviewed by:
Haci Mehmet Baskonus, Harran University, Turkey
Sakkaravarthi K., Bishop Heber College, India
Andrey A. Gelash, Skolkovo Institute of Science and Technology, Russia

***Correspondence:**
Saliya Coulibaly
saliya.coulibaly@univ-lille.fr

Specialty section:
This article was submitted to Mathematical and Statistical Physics, a section of the journal Frontiers in Physics

Received: *21 December 2020*
Accepted: *23 February 2021*
Published: *22 March 2021*

Citation:
Coulibaly S, Tiofack CGL and Clerc MG (2021) Spatiotemporal Complexity Mediated by Higher-Order Peregrine-Like Extreme Events. Front. Phys. 9:644584. doi: 10.3389/fphy.2021.644584

1. INTRODUCTION

Among a large number of the exact solutions of the Non-linear Schrödinger equation, Over the past decade, the Peregine soliton (PS) [1] has become one of the most attractive ones within the non-linear science community. So far, PS is the best-known coherent structure that has been successfully proposed as a prototype solution for rogues waves in conservative systems, and it aims its localization in both temporal and spatial directions. The interest in PS has also been reinforced by the experimental observation in an optical fiber [2], with a suitable pulse sent through the fiber. The Peregrine soliton has been reported to spontaneously emerge from a saturated state of modulational instability displayed by any continuous-wave solution of the non-linear Schrödinger equation [3, 4]. The common feature of all the aforementioned works is that they are considered in the conservative limit. An open question is the persistence and role of Peregrine waves in the complex spatiotemporal dynamic observed in the dissipative system. Indeed, when losses are added into the equation of a conservative dynamical system, solutions of a family generally reduce to a single one [5]. A classic example is how the solitons form a family in the non-linear Schrödinger equations (NLS) equation due to infinite conserved quantities for the same set of parameters.

From these families, only one persists in the dissipative regime due to the additional balance between losses and energy injection. Many dissipative systems are described by the NLS equation alongside driving and energy loss. Examples include the driven-damped [6–8] and, parametrically, the driven-damped [9] non-linear Schrödinger equations. In the case of the driven and damped [7] non-linear Schrödinger equation, the equation becomes non-integrable. Hence, emerges the question of the persistence of the NLS Peregrine soliton. Another open question is the following: if the PSs persist, do they play the same role here also as some coherent rogue wave-like solutions? Indeed, rogue wave and extremes events were also reported in dissipative systems. In those systems, a new mechanism has been found to induce extreme events or rogue waves: the chaos in purely temporal systems and the spatiotemporal chaos in large degree of freedom systems [10–13]. To infer the existence of chaos, it is mandatory to prove the largest Lyapunov exponent is positive [14]. For large degree of freedom, such as systems with a transport or coupling mechanism (diffraction, diffusion, dispersion, etc.), there exists a continuous set of exponents: the Lyapunov spectrum [15]. Spatiotemporal chaos is characterized by that must have a positive range. In this work, we address the problem of the persistence of the NLS Peregrine Soliton and study the link with some of the rogue waves reported in the dissipative regime.

For this purpose, we consider the paradigmatic optical dissipative system, which consists of the synchronous injection of a light wave in ring-type Kerr medium waveguides such as optical fiber or microresonators. The envelope of the temporal profile of the light inside the waveguide is well-described by the driven and damped non-linear Schrödinger equation [6–8]. This model was derived initially from the context of forced plasmas with oscillatory fields [6, 7] and dipole excitations in condensed matter. In the optics, this envelope equation is also known as the Lugiato-Lefever equation (LLE) [16–18]. The LLE is a non-integrable equation and, to our knowledge, no closed-form solution has been reported, yet. However, neglecting only the dissipation may allow us to find some solutions [9, 19] in the form of rational periodic or localized solutions. Even in this limit, intriguingly, no rational solution of Peregrine-type was reported. Likewise to the conservative systems, rogue waves have been reported in the LLE [18, 20, 21]. For one of the operating modes, the bistable regime–three possible outputs for a same value of the driving–the rogue waves emerge in the dynamics where the spatiotemporal chaos is seeded by a breathing cavity solitons [18, 20]. However, the analytical profile itself and the features of these spatiotemporal chaotic rogue waves are not well-known. The purpose of this report is an attempt to open up a discussion about this point. Therefore, we use the dissipationless limit to write a closed-form rational polynomial solution of the LLE. This analytical result is then compared to the numerically integrated solution. Next, we consider the persistence of this ideal case solution in the full LLE, and it can be linked to the dissipative rogue wave previously reported. In particular, we will show that the complexity in the LLE is mediated by rogue waves approximated by second-order Peregrine-like solitons.

2. THE PEREGRINE-TYPE SOLUTION

As mention in the introduction, the propagation of light in the optical fiber loop is modeled without loss of generality by the non-linear Schrödinger equation augmented with boundary conditions or an Ikeda map [17, 22, 23]:

$$\partial_z A\left(z,T\right) = -i\frac{\beta_2}{2}\partial_T^2 A\left(z,T\right) + i\gamma A\left(z,T\right)\left|A\left(z,T\right)\right|^2, \quad (1)$$

$$A\left(0,T+T_R\right) = \sqrt{\theta}E_i\left(T\right) + \sqrt{\rho}A\left(L,T\right)e^{-i\Phi_0}, \quad (2)$$

where T_R stands for the round-trip time, which is the time taken by the pulse to propagate along the cavity with the group velocity, Φ_0 is the linear phase shift, θ (ρ) is the mirror transmission (reflection) coefficient, and L is the geometrical cavity length. The complex amplitude of the electric field inside the cavity is A. Each of the coefficients β_2 is responsible for the second order dispersion, and γ is the non-linear coefficient of the fiber. The independent variable z refers to the longitudinal coordinate while T is the time in a reference frame moving with the group velocity of the light and $E_i(T)$ is the amplitude of the pump field. For large enough cavity finesse $\mathcal{F} = \pi/\alpha$, with α the effective losses of the cavity, the evolution of the electric field inside the loop is well-described by the Lugiato-Lefever equation [16, 17]:

$$\frac{\partial\psi}{\partial t} = S - (\alpha + i\delta)\psi - i\eta\frac{\partial^2\psi}{\partial\tau^2} + i|\psi|^2\psi, \quad (3)$$

where $\alpha = \theta/2$, $S = 2E_i\sqrt{\gamma L}$, $\psi = A\sqrt{\gamma L}$, $t = \alpha T/T_R$ $t = \alpha m$, and $\tau = T/T_n$ with $T_n = \sqrt{|\beta_2 L|/2}$. $\delta = (2k\pi - \Phi_0)$ is the detuning with respect to the nearest cavity resonance k. The integer m gives the roundtrip number and the coefficient $\eta = \pm 1$ is the sign of the group velocity dispersion term (β_2). In the following, we will consider $\eta = -1$ as corresponding to an anomalous group velocity dispersion. Despite its apparent simplicity this equation is non-integrable and closed form solution have been found only for $\alpha = 0$ [9, 19], which corresponds to a Hamiltonian equation. Numerically and experimentally, almost all the solutions obtained in this limit of $\alpha = 0$ have been observed [24]. Among these solutions, the localized structure and cavity solution have been the most studied but have never been described by a Peregrine-like profile. This is the purpose of the following. Considering $\alpha = 0$, assuming a constant phase, and introducing $u(t,\tau) = \psi(\tau)\exp(i\pi/2)$, the equation for the steady solution of the LLE reads as follows:

$$u_{\tau\tau} - \delta u + u^3 = -S. \quad (4)$$

Multiplying Equation (4) by u_τ, integrating over τ and introducing $f = u + a$, its follows

$$f_\tau = f\sqrt{f^2/2 + 2af + (\delta - 3a^2)}, \quad (5)$$

where a is solution of the cubic equation

$$a^3 - \delta\, a - S = 0. \quad (6)$$

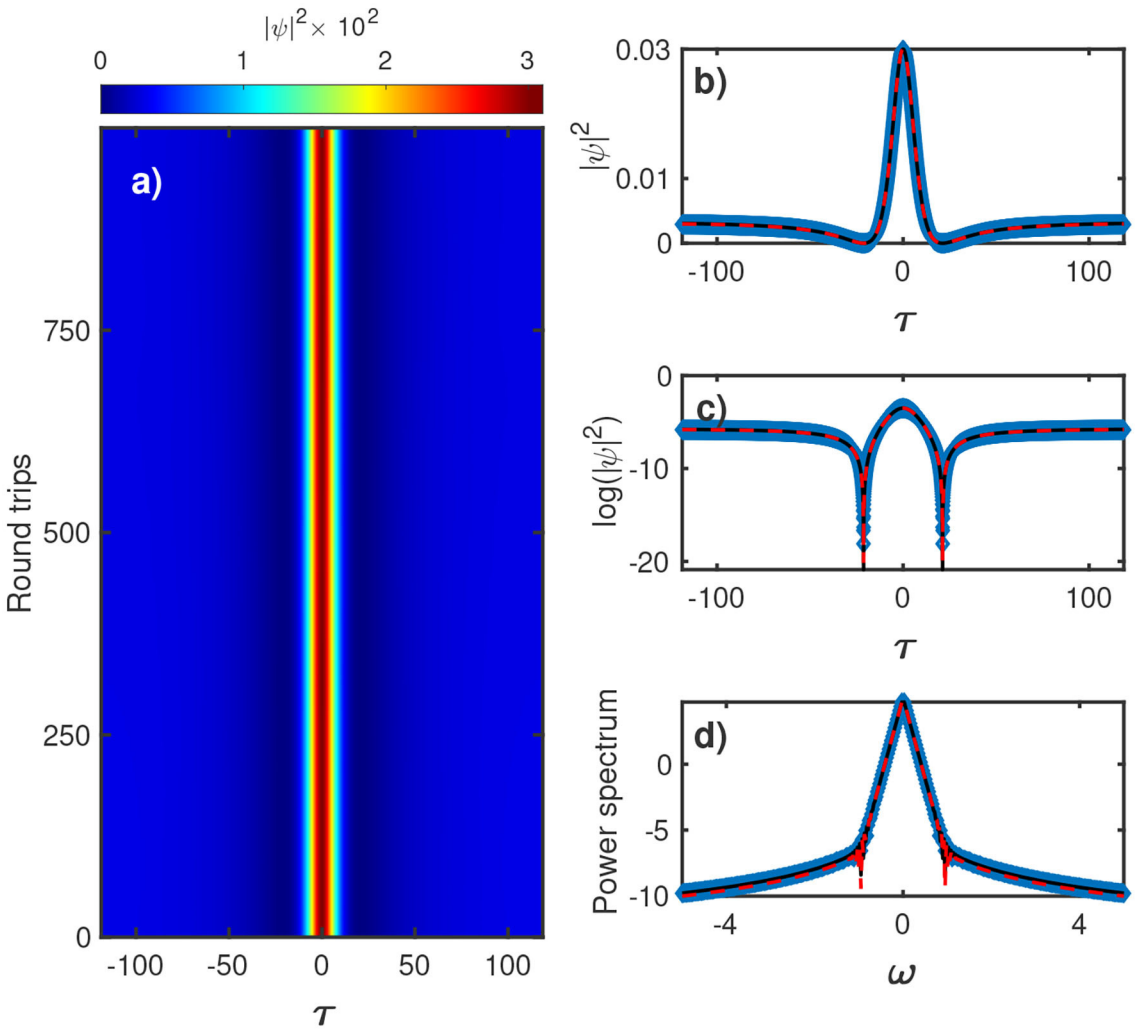

FIGURE 1 | Localized structure of the driven dissipative non-linear Schrödinger Equation (3). **(a)** Evolution of the driven dissipative non-linear Schrödinger obtained by integration of Equation (3) with $\alpha = 10^{-5}$, $\delta = 10^{-2}$, and $S = 4 \times 10^{-4}$. In the right panel, **(b–d)**, the black dashed lines correspond to the initial condition given by the stationary Peregine profile (7), blue diamonds correspond to the numerical profile at $T = 1,000$ and the red dash line to the solution from [19], respectively.

Namely, a accounts for a uniform solution of the driven dissipative non-linear Schrödinger Equation (3). Hence, for $\delta - a^2 > 0$ we can recover the solution founded in [9, 25]. Then, for the special case of $a^2 = \delta/3$ the solution is as follows:

$$u_P(\tau) = \frac{\delta}{\sqrt{3}}\left[-1 + \frac{12}{(\tau/\tau_0)^2 + 3}\right], \tag{7}$$

where $\tau_0 = 2\delta$. Note that this function corresponds to a decent Lorentzian, that is, a Lorentzian supported on a negative value. Then $u_P^2(\tau)$ has the shape of a Mexican hat as illustrated in **Figure 1**. $u_P(\tau)$ has the same profile as the maximally compressed Peregrine soliton.

The result of the numerical integration of the LLE (3) for $\alpha = 10^{-5}$, $\delta = 10^{-2}$, and $S = 4 \times 10^{-3}$ starting with $u_P(\tau)$ (Equation 7) is shown in **Figure 1**. These parameters are chooses for the purpose to numerically test the stability of the solution of Equation (7). As can be seen from the left panel this figure, the solution remains stable. The right panel of **Figure 1** gives the instantaneous profiles in linear (b) and logarithmic (c) scales, respectively. This chart reveals that $u_P(\tau)$ (black dashed line) is a good approximation of the numerical solution (blue diamonds). The red dashed line corresponding to the solution provided by [25] is plotted for comparison. The spectra profiles **Figure 1c** are also in a good agreement.

Increasing, the detuning parameter, the solution $u_P(\tau)$ develops an instability and shows a breathing dynamical behaviors [26]. By increasing the detuning or forcing strength further, the localized structure gives rise to a complex spatiotemporal dynamic, as illustrated in **Figure 2**, characterized by two counter-propagating fronts between the homogeneous and the complex spatiotemporal states [20, 24]. The inserts of **Figure 2** account for the profile of the highest peak in the spatiotemporal map. Hence, the destabilization of the localized

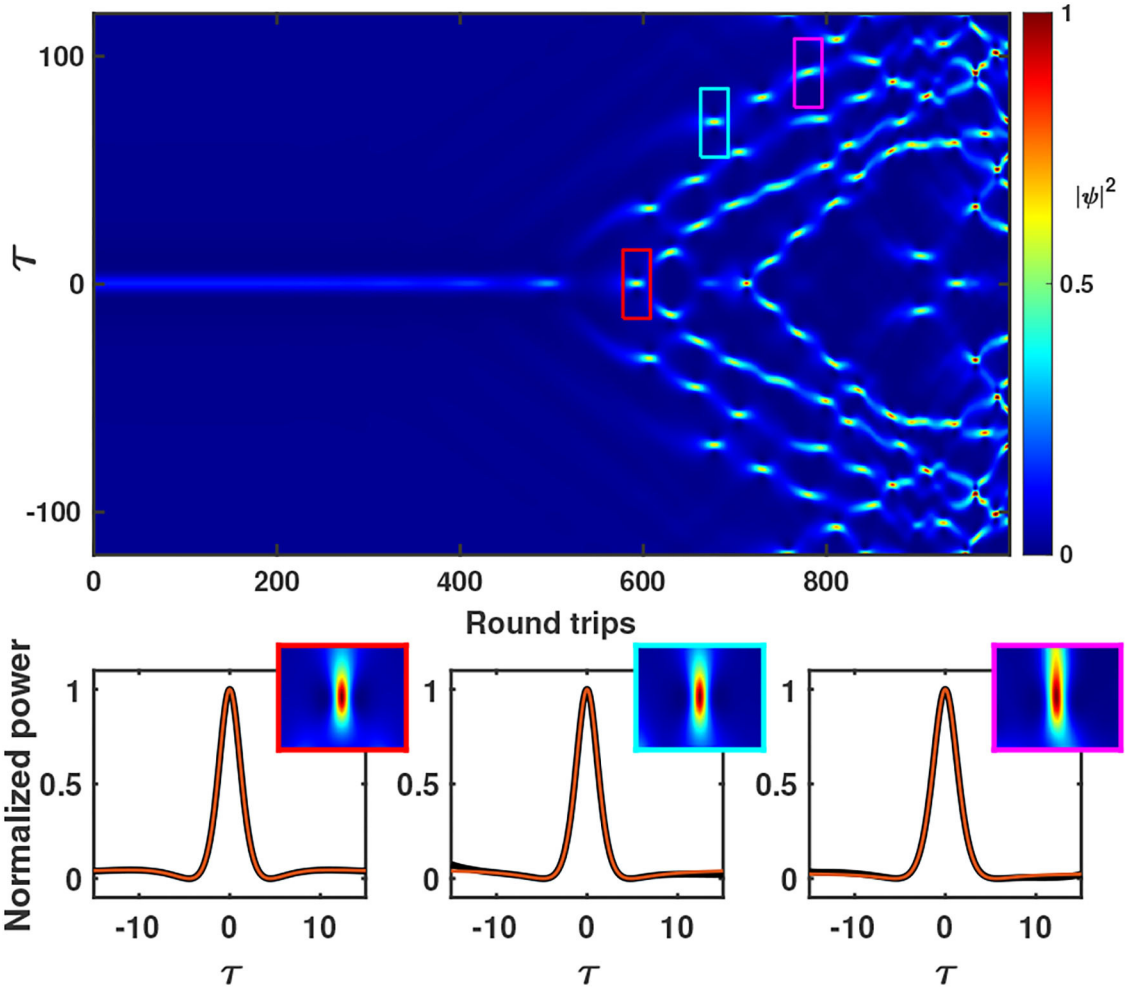

FIGURE 2 | Evolution of the LLE obtained by integration of Equation (3) with $\alpha = 10^{-5}$, $\delta = 5 \times 10^{-2}$, and $S = 4.3 \times 10^{-3}$. The bottom panels show the instantaneous profile of the highest peak obtained in the red, cyan, and magenta box and the red line correspond to the best fit using the maximally compressed second order Peregrine soliton (8), respectively.

solution corresponds to a process of self-replication [27]. In turn, the complex spatiotemporal dynamical behavior observed is a consequence of the interaction of these localized structures that self-replicate. For comparison, we have also plotted in the same figure the profile of $u_P(\tau)$ (dash line). It clear that u_P fails to describe this local profile. However, using the expression of the maximally compressed second-order Peregrine soliton given by

$$u_{SP}(\tau) = \left[a_0 + \frac{\tau^4 + a_1\tau^2 + a_2}{\tau^6 + a_3\tau^4 + a_4\tau^2 + a_5}\right]^2. \quad (8)$$

the best fit profile corresponds to the red solid lines in the bottom panel of **Figure 2**. This suggests that the complex behavior observed may be mediated by a higher-order Peregrine soliton. The current instability scenario of the stationary non-dissipative solution $u_P(\tau)$ qualitatively preserve in the dissipative regime [18, 20, 24]. In this limit, the dynamics have been demonstrated to be of spatiotemporal chaos [20], and statistics on the bursts emitted have revealed rogue waves [18]. In the following, we investigate the local dynamics in the dissipative case to see how the emerging rogues waves relate to the undamped solutions.

3. PEREGRINE-TYPE SOLITONS IN THE SPATIOTEMPORAL CHAOS OF THE LLE

Strictly speaking, to prove a spatiotemporal chaotic dynamic one may have to compute several quantities. In particular, it is mandatory to compute the Lyapunov spectrum. Next, this spectrum must have a positive part and a continuous region that has an area to linearly increase along with the size of the system. The computation of the Lyapunov spectrum itself is very well-documented [28] and is not the purpose here. Let us recall the main steps.

From the state of the system at a given time, the linear evolution of any small perturbation $\delta\mathbf{X}$ can be described by

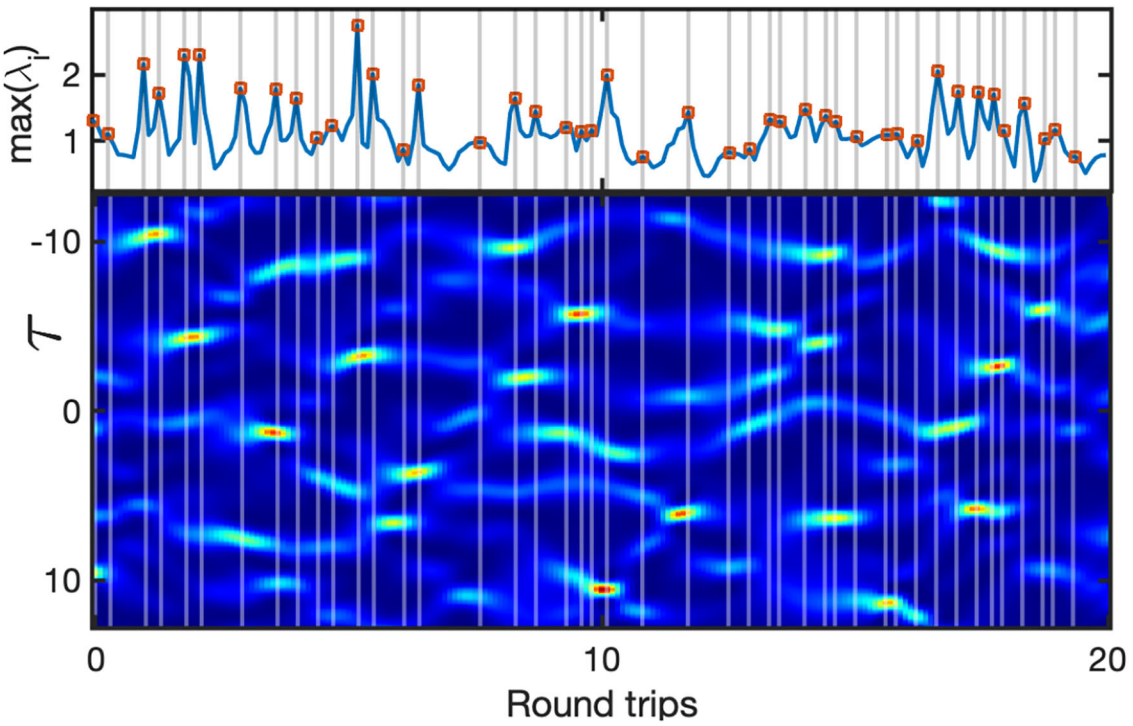

FIGURE 3 | Evolution of the driven dissipative non-linear Schrödinger obtained by integration of Equation (3) for $\alpha = 0.2$, $\delta = 1$, and $S = 0.43$. The blue line correspond to the local largest Lyapunov exponent, while the red circles are the local maxima detected. The gray bars mark the location of these local maxima.

$\partial_t \delta\mathbf{X} = \mathbf{J}\delta\mathbf{X}$, where $\mathbf{J}$ is the respective Jacobian. In the present case, we introduce $\psi = \psi_r + i\psi_i$, with ψ_r and ψ_i being the real and imaginary part of ψ respectively. At a time $t = t_0$, introducing $\psi = \psi_0 + \delta\psi$, with $\delta\psi \ll \psi(t = t_0) = \psi_0$ the matrix $\mathbf{J}$ reads as follows:

$$\mathbf{J} = \begin{bmatrix} -(\alpha + 2\psi_{0_r}\psi_{0_i}) & \delta - \psi_{0_r}^2 - 3\psi_{0_i}^2 - \partial_\tau^2 \\ -\delta + \psi_{0_i}^2 + 3\psi_{0_r}^2) + \partial_\tau^2 & -(\alpha - 2\psi_{0_r}\psi_{0_i}) \end{bmatrix}, \quad (9)$$

and $\delta\mathbf{X} = (\delta\psi_r, \delta\psi_r)^t$. Suppose that we want to compute the n-th first dominant exponents of the spectrum, we introduce the matrix $\mathbf{L}$, which contains n orthonormal vectors $\mathbf{v}_i$ to be used as initial conditions when solving $\partial_t \delta\mathbf{X} = \mathbf{J}\delta\mathbf{X}$:

$$\mathbf{L}(t = t_0) \equiv [\mathbf{v}_1 \quad \mathbf{v}_2 \quad \dots \quad \mathbf{v}_n] = \begin{bmatrix} x_{11} & x_{12} & x_{13} & \dots & x_{1n} \\ x_{21} & x_{22} & x_{23} & \dots & x_{2n} \\ & & \dots\dots\dots & & \\ x_{d1} & x_{d2} & x_{d3} & \dots & x_{dn} \end{bmatrix}, \quad (10)$$

where d is the dimension of the system. After a time increment dt, the matrix $\mathbf{L}$ evolves to $\mathbf{L}(t_0 + dt) = \hat{\mathbf{U}}\mathbf{L}(t_0)$ where $\hat{\mathbf{U}} = e^{\mathbf{J}*dt}$. Using the modified Gram-Schmidt **QR** decomposition on $\mathbf{L}(t_0 + dt)$, the diagonal elements of $\mathbf{R}$ account for the Lyapunov exponents $\tilde{\lambda}_i$ $(i = 1, \dots, n)$ at time $t_0 + dt$, that is

$$\tilde{\lambda}_i(t_0 + dt) = \frac{1}{dt} \ln\left(\mathbf{R}_{ii}(t_0 + dt)\right). \quad (11)$$

Repeating this procedure several time, after a large number of iterations N, the Lyapunov exponents can be approximated by

$$\lambda_i \equiv \langle\tilde{\lambda}_i\rangle = \frac{1}{Ndt} \sum_{k=1}^{N} \ln\left(\mathbf{R}_{ii}(t_0 + kdt)\right). \quad (12)$$

From the spectrum $\{\lambda_i\}$ an estimator of the dimension of the chaotic attractor is given by the York-Kaplan dimension $D_{kY} = p + \sum_{i=1}^{p} \lambda_i / |\lambda_{p+1}|$ where p is such that $\sum_{i=1}^{p} \lambda_i > 0$ and $\sum_{i=1}^{p+1} \lambda_i < 0$ [29]. For a one-dimensional system of size L, a spatiotemporal chaos implies that D_{KY} increase linearly with L. The spatiotemporal chaotic nature of the current dynamic has already been proven [20] and is not the purpose here. Our purpose now is to go inside the local dynamics. Indeed, from the whole process of computing the Lyapunov spectrum, only average quantities are used to make conclusion. However, looking at the spatiotemporal evolution such as that shown in **Figure 3** (bottom panel) it is obvious that local bursts may impact the average value. To verify this point, we have also plotted the evolution of the largest Lyapunov exponent. The local maxima of this exponent, marked by gray lines, always correspond to a spatiotemporal local maximum. This shows that local bursts are those with the largest contribution to the average of the first Lyapunov exponent. After all, this also means that the spatiotemporal local maxima are the highest unstable structures that can appear in the dynamics. We can now extract from the temporal local maxima the profile of the local maximally

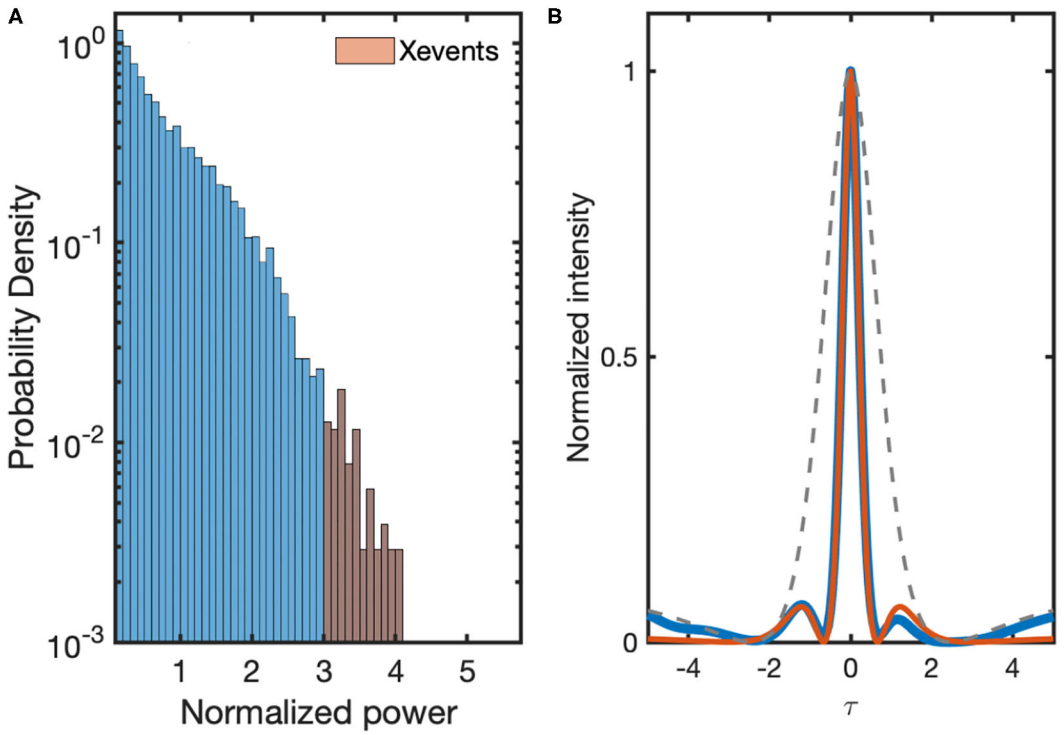

FIGURE 4 | Probability density function **(A)** of intensity bursts observed in the spatiotemporal chaos of Equation (3) for $\alpha = 0.2$, $\delta = 1$, and $S = 0.43$. Light red bars correspond to the values above the characteristic wave height. **(B)** Mean intensity profile from the five larger pulses and the result of the best fit of this profile with Equation (8). Xevents in **(A)** correspond to the bursts with peak values above twice the significant wave height. This height is defined as the average value of the largest 1/3 burst.

compressed spatiotemporal bursts. As expected in the parameters used [18], a fraction of the peak values represent extreme events, as can be seen from **Figure 4A**. The mean profiles of the five highest peaks have been used with the Equation (8) to find the best-fit parameters. The result is given in **Figure 4B** and shows a good agreement between the two profiles. This confirms that the persistent of the behavior observed in the non-dissipative limit comes also with the fact that the spatiotemporal chaos observed in the dissipative limit is mediated by second-order Peregrine-type solitons.

4. DISCUSSION

The Peregrine soliton is the famous coherent solution of the nonlinear Schrödinger equation that presents many of the characteristics of rogue waves. As a result, it became one of the most studied localized solution of the Non-linear Schrödinger equation. Despite the great interest around this solution, the studies in dissipative systems are few relatively compared to those in conservative systems. In this work, we have considered the emergence of the Peregrine solitons in the paradigmatic dissipative system and the driven and damped Non-linear Schrödinger equation. Using the dissipationless limit, we were able to obtain a Peregrine-like solution of this system. Even in this limit, such a rational polynomial solution was not reported up to now. The comparison of our solution to the result of the numerical simulation is in quite good agreement (cf. **Figure 1**). With the dissipation as no closed-form solution can be found, we have performed numerical integration. The stationary Peregrine soliton bifurcates to a breathing state. The local maximally compressed state was successfully interpolated by the profile of a second-order Peregrine soliton (see **Figure 2**). Unfortunately, as a result of a bifurcation, the derivation of the corresponding closed-form solution can not be done from the dissipationless limit. The instability that can develop this intrigued solution leads to the emergence of the second-order type Peregrine soliton. In the dissipative limit, the complex behavior observed in the conservative case persevere. Indeed, using the tools of the theory of chaos, we were able to follow the local dynamics (see **Figure 3**). In this spatiotemporal complexity shown to be extensive chaos, we have shown that the dynamics are ruled by the same profile of the second-order Peregrine-type soliton. Indeed, we show that burst in local metric entropy occurs at the same time as the emergence of a maximally compressed second-order Peregrine soliton. Despite the effort made to find configurations of the Non-linear Schrödinger equation, such as variable parameters, the fact is that losses and dissipation are the rules instead of the exceptions in real-world systems. Hence, we believe that as with dissipative solitons, dissipative systems are the opportunity to investigate new dynamics for the Peregrine soliton. This work attempts to that this is possible, and we are convinced that many other works will follow this one.

DATA AVAILABILITY STATEMENT

The raw data supporting the conclusions of this article will be made available by the authors, without undue reservation.

AUTHOR CONTRIBUTIONS

All authors equally contributed to the theoretical work and the preparation to the manuscript.

FUNDING

MC was thankful for financial support from the ANID–Millennium Science Initiative Program–ICN17_012 and Fondecyt 1180903 project. SC acknowledges the LABEX CEMPI (ANR-11-LABX-0007) as well as the Ministry of Higher Education and Research, Hauts de France council, and the European Regional Development Fund (ERDF) through the Contract de Projets Etat-Region (CPER Photonics for Society P4S).

REFERENCES

1. Peregrine DH. Water waves, nonlinear Schrödinger equations and their solutions. *ANZIAM J*. (1983) 25:16–43. doi: 10.1017/S0334270000003891
2. Kibler B, Fatome J, Finot C, Millot G, Dias F, Genty G, et al. The Peregrine soliton in nonlinear fibre optics. *Nat Phys*. (2010) 6:790–5. doi: 10.1038/nphys1740
3. Toenger S, Godin T, Billet C, Dias F, Erkintalo M, Genty G, et al. Emergent rogue wave structures and statistics in spontaneous modulation instability. *Sci Rep*. (2015) 5:10380. doi: 10.1038/srep10380
4. Agafontsev DS, Zakharov VE. Integrable turbulence and formation of rogue waves. *Nonlinearity*. (2015) 28:2791–821. doi: 10.1088/0951-7715/28/8/2791
5. Akhmediev N, Ankiewicz A. *Dissipative Solitons: From Optics to Biology and Medicine*. Vol. 751. Verlag Berlin; Heidelberg: Springer Science & Business Media; 2008.
6. Morales G, Lee Y. Ponderomotive-force effects in a nonuniform plasma. *Phys Rev Lett*. (1974) 33:1016. doi: 10.1103/PhysRevLett.33.1016
7. Kaup DJ, Newell AC. Theory of nonlinear oscillating dipolar excitations in one-dimensional condensates. *Phys Rev B*. (1978) 18:5162. doi: 10.1103/PhysRevB.18.5162
8. Nozaki K, Bekki N. Solitons as attractors of a forced dissipative nonlinear Schrödinger equation. *Phys Lett A*. (1984) 102:383–6. doi: 10.1016/0375-9601(84)91060-0
9. Barashenkov I, Smirnov YS. Existence and stability chart for the ac-driven, damped nonlinear Schrödinger solitons. *Phys Rev E*. (1996) 54:5707. doi: 10.1103/PhysRevE.54.5707
10. Bonatto C, Feyereisen M, Barland S, Giudici M, Masoller C, Leite JRR, et al. Deterministic optical rogue waves. *Phys Rev Lett*. (2011) 107:053901. doi: 10.1103/PhysRevLett.107.053901
11. Pisarchik AN, Jaimes-Reátegui R, Sevilla-Escoboza R, Huerta-Cuellar G, Taki M. Rogue waves in a multistable system. *Phys Rev Lett*. (2011) 107:274101. doi: 10.1103/PhysRevLett.107.274101
12. Selmi F, Coulibaly S, Loghmari Z, Sagnes I, Beaudoin G, Clerc MG, et al. Spatiotemporal chaos induces extreme events in an extended microcavity laser. *Phys Rev Lett*. (2016) 116:013901. doi: 10.1103/PhysRevLett.116.013901
13. Coulibaly S, Clerc M, Selmi F, Barbay S. Extreme events following bifurcation to spatiotemporal chaos in a spatially extended microcavity laser. *Physi Rev A*. (2017) 95:023816. doi: 10.1103/PhysRevA.95.023816
14. Pikovsky A, Politi A. *Lyapunov Exponents: A Tool to Explore Complex Dynamics*. Cambridge: Cambridge University Press (2016).
15. Ruelle D. Large volume limit of the distribution of characteristic exponents in turbulence. *Commun Math Phys*. (1982) 87:287–302. doi: 10.1007/BF01218566
16. Lugiato LA, Lefever R. Spatial dissipative structures in passive optical systems. *Phys Rev Lett*. (1987) 58:2209. doi: 10.1103/PhysRevLett.58.2209
17. Haelterman M, Trillo S, Wabnitz S. Dissipative modulation instability in a nonlinear dispersive ring cavity. *Optics Commun*. (1992) 91:401–7. doi: 10.1016/0030-4018(92)90367-Z
18. Coillet A, Dudley J, Genty G, Larger L, Chembo YK. Optical rogue waves in whispering-gallery-mode resonators. *Phys Rev A*. (2014) 89:13835. doi: 10.1103/PhysRevA.89.013835
19. Renninger WH, Rakich PT. Closed-form solutions and scaling laws for Kerr frequency combs. *Sci Rep*. (2016) 6:24742. doi: 10.1038/srep24742
20. Liu Z, Ouali M, Coulibaly S, Clerc M, Taki M, Tlidi M. Characterization of spatiotemporal chaos in a Kerr optical frequency comb and in all fiber cavities. *Optics Lett*. (2017) 42:1063–6. doi: 10.1364/OL.42.001063
21. Coulibaly S, Taki M, Bendahmane A, Millot G, Kibler B, Clerc MG. Turbulence-induced rogue waves in Kerr resonators. *Phys Rev X*. (2019) 9:11054. doi: 10.1103/PhysRevX.9.011054
22. Ikeda K. Multiple-valued stationary state and its instability of the transmitted light by a ring cavity system. *Optics Commun*. (1979) 30:257–61. doi: 10.1016/0030-4018(79)90090-7
23. Coen S, Haelterman M. Modulational instability induced by cavity boundary conditions in a normally dispersive optical fiber. *Phys Rev Lett*. (1997) 79:4139. doi: 10.1103/PhysRevLett.79.4139
24. Leo F, Gelens L, Emplit P, Haelterman M, Coen S. Dynamics of one-dimensional Kerr cavity solitons. *Optics Express*. (2013) 21:9180–91. doi: 10.1364/OE.21.009180
25. Gradshteyn IS, Ryzhik IM. *Table of Integrals, Series, and Products, (see 2.266, pp. 97)*. Amsterdam: Academic Press (2014).
26. Taki M, Spatschek K, Fernandez J, Grauer R, Reinisch G. Breather dynamics in the nonlinear Schrödinger regime of perturbed sine-Gordon systems. *Physica D*. (1989) 40:65–82. doi: 10.1016/0167-2789(89)90027-4
27. Bordeu I, Clerc MG, Couteron P, Lefever R, Tlidi M. Self-replication of localized vegetation patches in scarce environments. *Sci Rep*. (2016) 6:33703. doi: 10.1038/srep33703
28. Skokos C. *The Lyapunov Characteristic Exponents and Their Computation*. Berlin; Heidelberg: Springer (2010). p. 63–135.
29. Ott E. *Chaos in Dynamical Systems*. Cambridge: Cambridge University Press (2002).

Conflict of Interest: The authors declare that the research was conducted in the absence of any commercial or financial relationships that could be construed as a potential conflict of interest.

frontiers in Physics

ORIGINAL RESEARCH
published: 24 March 2021
doi: 10.3389/fphy.2021.594680

Storage, Splitting, and Routing of Optical Peregrine Solitons in a Coherent Atomic System

Chong Shou[1] *and Guoxiang Huang*[1,2]*

[1]State Key Laboratory of Precision Spectroscopy, East China Normal University, Shanghai, China, [2]NYU-ECNU Joint Institute of Physics, New York University at Shanghai, Shanghai, China

We propose a scheme to realize the storage and retrieval of optical Peregrine solitons in a coherent atomic gas via electromagnetically induced transparency (EIT). We show that optical Peregrine solitons with very small propagation loss, ultraslow motional velocity, and extremely low generation power can be created in the system via EIT. We also show that such solitons can be stored, retrieved, split, and routed with high efficiency and fidelity through the manipulation of control laser fields. The results reported here are useful for the active control of optical Peregrine solitons and promising for applications in optical information processing and transmission.

Keywords: electromagnetically induced transparency, rogue waves, Peregrine solitons, optical memory, optical routing

OPEN ACCESS

Edited by:
Amin Chabchoub,
The University of Sydney, Australia

Reviewed by:
Saeid Asgarnezhad Zorgabad,
Sharif University of Technology, Iran
Stefano Trillo,
University of Ferrara, Italy

***Correspondence:**
Guoxiang Huang
gxhuang@phy.ecnu.edu.cn

Specialty section:
This article was submitted to Optics and Photonics, a section of the journal Frontiers in Physics

Received: *14 August 2020*
Accepted: *18 January 2021*
Published: *24 March 2021*

Citation:
Shou C and Huang G (2021) Storage, Splitting, and Routing of Optical Peregrine Solitons in a Coherent Atomic System. Front. Phys. 9:594680. doi: 10.3389/fphy.2021.594680

1 INTRODUCTION

Rogue waves, first observed in ocean surfaces, are highly isolated spatial-temporal wave packets with very large amplitudes when some special conditions are attained [1]. Such waves are ubiquitous in nature and quite intriguing, since they "appear from nowhere and disappear without a trace" and have extremely destructive power [2]. Except for ocean waves, the study on rogue waves has been extended to many other different physical contexts, including atmosphere [3], superfluid helium [4], capillary waves [5], water waves [6], photorefractive ferroelectrics [7], plasmas [8], ferromagnetic materials [9], and so on [10, 11].

Peregrine soliton, firstly suggested by D. H. Peregrine in the early 1980s for nonlinear dynamics of deep waters [12], is commonly taken as a prototype of rogue waves [13, 14]. Such soliton, i.e., localized rational solution of nonlinear Schrödinger equation, can be taken as a limiting case of the one-parameter family of Kuznetsov–Ma breathers [15] or Akhmediev breathers [16]. There have been considerable interests on Peregrine solitons occurring in a variety of physical systems [17–39]. Many efforts have also been devoted to the new understanding of Peregrine solitons through the analysis of other types of nonlinear partial differential equations [40–51].

Among various rogue waves, optical rogue waves have received much attention due to their interesting properties and promising applications [10, 11, 25–39, 52–54]. However, the creation of the optical rogue waves is not an easy task in conventional optical media (such as optical fibers and waveguides). The reason is that the nonlinear optical effect in such media is very weak, and hence a large input optical power is needed to obtain a significant optical nonlinearity required for the formation of rogue waves. Although some resonance mechanisms may be exploited to enhance nonlinear effects, near resonances significant optical absorptions occur, which result in serious attenuation and distortion of optical pulses during propagation.

In recent years, many efforts have been focused on the investigation of electromagnetically induced transparency (EIT), a typical quantum interference effect occurring in three-level atomic systems, by which the light absorption due to resonance may be largely suppressed and giant Kerr nonlinearity may be obtained simultaneously [55]. By means of EIT, it has been shown that weak-light solitons and their storage and retrieval can be realized [56–58]. Recent works [59, 60] have demonstrated that it is possible to generate optical Peregrine solitons with low generation power in EIT-base atomic systems.

In this work, we suggest a scheme to realize the memory of optical Peregrine solitons in a Λ-shaped three-level atomic gas via EIT. We show that such solitons may have very small propagation loss, ultraslow motional velocity, and extremely low generation power; they can be stored, retrieved, split, and routed with high efficiency and fidelity through the manipulation of control laser fields. The results reported here are helpful for the active control of optical Peregrine solitons and promising for practical applications in optical information processing and transmission.

The article is arranged as follows. In **Section 2**, the physical model and ultraslow weak-light Peregrine solitons and their propagation are described. In **Section 3**, the storage, retrieval, splitting, and routing of such solitons are presented. Finally, **Section 4** gives a summary of the main results obtained in this work.

2 MODEL AND ULTRASLOW WEAK-LIGHT PEREGRINE SOLITONS

2.1 Model

We start to consider a cold three-state atomic gas with Λ-shaped level configuration, interacting with a weak, pulsed probe laser field (center wavenumber $\mathbf{k}_p$ and center angular frequency ω_p) and a strong, continuous-wave (CW) control laser field (wavenumber $\mathbf{k}_c$ and angular frequency ω_c). The probe (control) field drives the transition $|1\rangle \leftrightarrow |3\rangle$ ($|2\rangle \leftrightarrow |3\rangle$); see **Figure 1A**.

The total electric field in the system reads $\mathbf{E} = \mathbf{E}_p + \mathbf{E}_c = \sum_{l=p,c} \mathbf{e}_l \mathcal{E}_l \exp[i(k_l z - \omega_l t)] + \text{c.c.}$, where $\mathbf{e}_l$ ($\mathcal{E}_l$) is the unit polarization vector (envelope) of the electric field $\mathbf{E}_l$. To suppress Doppler effect, both the probe and control fields are assumed to propagate along z direction.

The Hamiltonian of the system in the interaction picture reads $\hat{H}_{\text{int}} = -\hbar(\sum_{j=2}^{3} \Delta_j |j\rangle\langle j| + \Omega_p |3\rangle\langle 1| + \Omega_c |3\rangle\langle 2| + \text{H.c.})$, where $\Delta_3 = \omega_p - (E_3 - E_1)/\hbar$ ($\Delta_2 = \omega_p - \omega_c - (E_2 - E_1)/\hbar$) is one-(two-) photon detuning; E_j is the eigenvalue of the atomic state $|j\rangle$; $\Omega_p = (\mathbf{e}_p \cdot \mathbf{p}_{13})\mathcal{E}_p/\hbar$ ($\Omega_c = (\mathbf{e}_c \cdot \mathbf{p}_{23})\mathcal{E}_{c1}/\hbar$) is the half Rabi frequency of the probe (control) field; $\mathbf{p}_{ij}$ is the electric-dipole matrix element associated with levels $|i\rangle$ and $|j\rangle$. The atomic dynamics is described by a 3 × 3 density matrix σ, obeying the optical Bloch equation

$$\frac{\partial \sigma}{\partial t} = -\frac{i}{\hbar}\left[\hat{H}_{\text{int}}, \sigma\right] - \Gamma[\sigma], \tag{1}$$

where Γ is a relaxation matrix characterizing the spontaneous emission and dephasing [61]. The explicit form of **Eq. 1** is presented in **Section 1 of the Supplementary Material**.

The evolution of the probe field $\mathbf{E}_p$ is governed by the Maxwell equation $\nabla^2 \mathbf{E}_p - (1/c^2)\partial^2 \mathbf{E}_p/\partial t^2 = (1/\varepsilon_0 c^2)\partial^2 \mathbf{P}_p/\partial t^2$, where $\mathbf{P}_p = N_a\{\mathbf{p}_{13}\sigma_{31}\exp[i(k_p z - \omega_p t)] + \text{c.c.}\}$ is the electric polarization intensity, with N_a the atomic density. Under slowly varying envelope and paraxial approximations, the Maxwell equation is reduced into the form

$$i\left(\frac{\partial}{\partial z} + \frac{1}{c}\frac{\partial}{\partial t}\right)\Omega_p + \kappa_{13}\sigma_{31} = 0, \tag{2}$$

with $\kappa_{13} = N_a \omega_p |\mathbf{p}_{13}|^2/(2\varepsilon_0 c\hbar)$. Note that we have assumed that the probe field has a large transverse size so that its diffraction effect is negligible. The model described here may be realized, e.g., by a cold ^{87}Rb atomic gas [62], with the levels selected by $|1\rangle = |5^2S_{1/2}, F = 1, m_F = 0\rangle$, $|2\rangle = |5^2S_{1/2}, F = 2, m_F = 0\rangle$, and $|3\rangle = |5^2P_{1/2}, F = 1, m_F = 0\rangle$. Thus we have $\omega_p = 2.37 \times 10^{15}$ Hz, $|\mathbf{p}_{13}| = 2.54 \times 10^{-27}$ C cm. If the atomic density $N_a = 8.8 \times 10^{11}\text{cm}^{-3}$, κ_{13} takes the value of $2.4 \times 10^{10}\text{cm}^{-1}\text{s}^{-1}$. This set of parameters will be used in the following analysis and calculation.

2.2 Ultraslow Weak-Light Peregrine Solitons and Their Propagation

We first investigate the linear propagation of the probe field. When a very weak probe pulse is applied, the system undergoes a linear evolution. In this case, the Maxwell–Bloch (MB) (Eqs. **1** and **2**) admit the solution $\Omega_p = F\exp[i(Kz - \omega t)]$, where F is a constant,

$$K(\omega) = \frac{\omega}{c} - \kappa_{13}\frac{\omega + d_{21}}{(\omega + d_{21})(\omega + d_{31}) - |\Omega_c|^2} \tag{3}$$

is linear dispersion relation, and $d_{\alpha\beta} = \Delta_\alpha - \Delta_\beta + i\gamma_{\alpha\beta}$ (with $\gamma_{\alpha\beta} \equiv (\Gamma_\alpha + \Gamma_\beta)/2 + \gamma_{\alpha\beta}^{\text{dep}}$, $\Gamma_\beta \equiv \sum_{\omega_\alpha < \omega_\beta} \Gamma_{\alpha\beta}$, and $\gamma_{\alpha\beta}^{\text{dep}}$ is the dephasing rate associated with the states $|\alpha\rangle$ and $|\beta\rangle$).

Shown in **Figure 1B** is the imaginary part Im(K) and the real part Re(K) of K as functions of ω. Due to the quantum interference effect induced by the control field, an EIT transparency window is opened in Im(K) (dashed line), which implies that the probe field can propagate in this resonant atomic gas with a very small absorption. Parameters used for plotting the figure are $\Delta_2 = -2\pi \times 0.64$ MHz, $\Delta_3 = -2\pi \times 9.6$ MHz, $\gamma_{21} = 2\pi \times 1.09$ kHz, $\gamma_{31} = 2\pi \times 2.5$ MHz, and $\Omega_c = 2\pi \times 31.8$ MHz.

From the MB **Eqs. 1** and **2** and using the method of multiple-scales [63], we can derive the controlling equation governing the nonlinear evolution of the probe-field envelope F (see **Section 2 of the Supplementary Material**), which reads

$$i\frac{\partial}{\partial z}F - \frac{1}{2}K_2\frac{\partial^2}{\partial \tau^2}F + W|F|^2F = 0, \tag{4}$$

where $\tau = t - z/\tilde{V}_g$ [$\tilde{V}_g \equiv (\partial \tilde{K}/\partial\omega)^{-1}$ is the group velocity of the envelope; here and in the following, the quantity with a tilde represents the corresponding real part]; $K_2 = \partial^2 K/\partial\omega^2$ is the

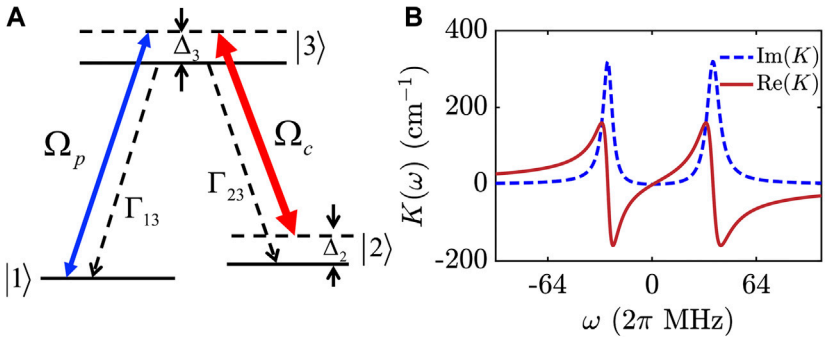

FIGURE 1 | (A) Energy-level diagram and excitation scheme of the Λ-shaped three-level atomic system for realizing EIT. The probe field (with center angular frequency ω_p and half Rabi frequency Ω_p) couples the atomic levels $|1\rangle$ and $|3\rangle$; the CW control field (with angular frequency ω_c and half Rabi frequency Ω_c) couples the atomic levels $|2\rangle$ and $|3\rangle$; Γ_{13} (Γ_{23}) is the decay rate from $|3\rangle$ to $|1\rangle$ ($|3\rangle$ to $|2\rangle$); Δ_3 (Δ_2) is one-photon (two-photon) detuning. **(B)** The imaginary part Im(K) and real part Re(K) of the linear dispersion relation K as a function of ω ($\omega = 0$ corresponds to the central frequency of the probe pulse).

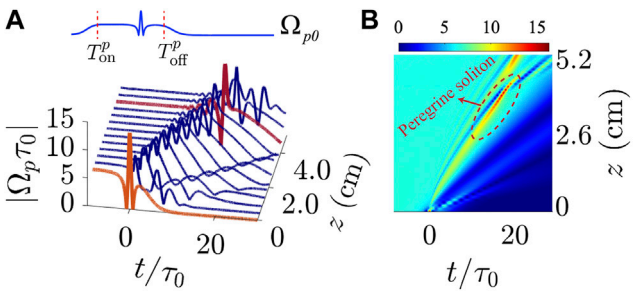

FIGURE 2 | Propagation of ultraslow weak-light Peregrine solitons. **(A)** $|\Omega_p\tau_0|$ as a function of t/τ_0 and z. The solid blue line in the upper part is the input temporal shape of the probe field with the dashed vertical lines representing the temporal boundaries. The orange line in the lower part is the input Peregrine soliton at $z = 0$. The red line represents the Peregrine soliton propagating to $z = 4.3$ cm with the maximum intensity $|\Omega_p\tau_0|_{max} \simeq 15.2$ at $t = 16.9\tau_0$ **(B)** The contour map for the propagation of the Peregrine soliton (the red dashed circle) on the t-z plane. The upper color bar shows the intensity of the probe field.

coefficient describing group-velocity dispersion; W is the coefficient (describing self-phase modulation) proportional to Kerr nonlinearity. The explicit expression of W is given in **Section 2 of the Supplementary Material**.

If the imaginary parts of K and W are much smaller than their corresponding real parts, **Eq. 4** admits the Peregrine soliton solution, which can be expressed by the half Rabi frequency

$$\Omega_p(z,t) = U_0\left[1 - 4\frac{1 + 2iz/L_{\rm Non}}{1 + 4z^2\Big/L_{\rm Non}^2 + 4\left(t - z/\tilde{V}_g\right)^2\Big/\tau_0^2}\right]e^{iK_0 z + iz/L_{\rm Non}}, \tag{5}$$

where $K_0 \equiv K|_{\omega=0}$, U_0 and τ_0 are respectively the characteristic half Rabi frequency and time duration of the probe field, and $L_{\rm Non} \equiv 1/(U_0^2|\tilde{W}|)$ is the characteristic nonlinearity length (which has been assumed to equal the dispersion length defined by $L_{\rm Dis} \equiv \tau_0^2/|\tilde{K}_2|$ for simplicity). One sees that the Peregrine soliton consists of a CW background and a bump in its envelope that first grows and then decay rapidly on the background. The physical reason for the formation of such optical Peregrine soliton can be understood as follows. When a plane-wave probe field with a finite amplitude is applied to and propagates in the atomic gas, the Kerr nonlinearity brings a modulational instability and a phase modulation to the probe field; due to the role played by the group-velocity dispersion, the phase modulation is converted into amplitude modulation and peak amplification. Because of the joint phase and amplitude modulations, the probe field reorganizes its spatial distribution and hence the Peregrine soliton is generated in the system.

As an example, we take $\tau_0 = 2.36 \times 10^{-7}$ s, $U_0 = 2\pi \times 8.0$ MHz, and other system parameters which are the same as those used in **Figure 1B**. Then we obtain $K_0 = -1.70 + i0.02$ cm^{-1}, $K_1 = \partial K/\partial\omega \approx (4.5 - i0.05) \times 10^{-7}$ cm^{-1} s, $K_2 \approx (-1.5 - i0.1) \times 10^{-14}$ cm^{-1} s^2, and $W \approx (1.05 - 0.004) \times 10^{-16}$ cm^{-1} s^2 (estimated at $\omega = 0$). We see that the imaginary parts of K_j ($j = 0, 1, 2$) and W are much smaller than their corresponding real parts, which is due to the EIT effect that results in the suppression of the optical absorption in the system. Based on these results, we obtain $L_{\rm Non} \simeq L_{\rm Dis} \simeq 3.8$ cm and

$$\tilde{V}_g \simeq 7.34 \times 10^{-5} c. \tag{6}$$

Thus, the propagation velocity of the optical Peregrine soliton is much slower than the light speed c in vacuum. If the transverse cross-section area of the probe pulse takes the value $S = 8.0 \times 10^{-3}$ cm^2, the generation power of the soliton (which can be estimated by using the Poynting vector [56]) reads

$$P_{\rm max} \simeq 1.8\ \mu{\rm W}, \tag{7}$$

i.e., very small power needed for creating such soliton. Consequently, the Peregrine solitons given here are different from those obtained in conventional optical systems [25, 27, 28, 31].

We now investigate the propagation of the ultraslow Peregrine soliton by exploiting Runge–Kutta method based on solving the MB **Eqs. 1** and **2** numerically. Since solution (**5**) has an infinite

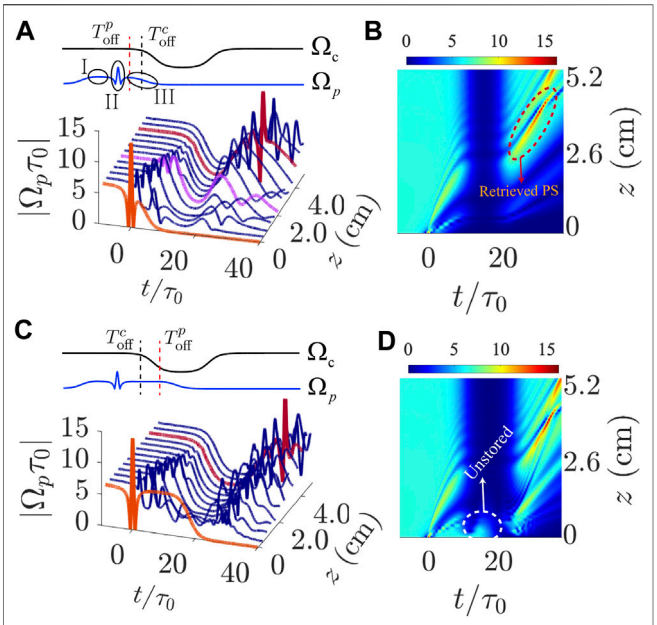

FIGURE 3 | Storage and retrieval of optical Peregrine solitons. **(A)** Upper part: the black line (blue line) is the time sequence of the control (probe) field, the red dashed vertical line is T^p_{off}, and the black dashed vertical line is T^c_{off}. Symbols I, II, and III denote the CW background, the Peregrine soliton, and the low-intensity component of the probe field, respectively. Lower part: $|\Omega_p\tau_0|$ vs. t/τ_0 and z with $T^p_{\text{off}} < T^c_{\text{off}}$; i.e., the switching-off time of the input probe field is before the time when the control field is switched off. The orange line represents the input Peregrine soliton at $z = 0$; the purple line represents the probe field at the storage period; the red line represents the retrieved Peregrine soliton propagating to $z = 4.1$ cm with the maximum intensity $|\Omega_p\tau_0|_{\max} \simeq 15.4$ at $t \simeq 30.3\tau_0$. **(B)** The contour map of the storage and retrieval of the Peregrine soliton in the t-z plane with $T^p_{\text{off}} < T^c_{\text{off}}$. The red dashed circle denotes the retrieved Peregrine soliton (i.e., "Retrieved PS"). The upper color bar shows the intensity of the probe field. **(C)** The same as panel **(A)** but with $T^p_{\text{off}} > T^c_{\text{off}}$. **(D)** The contour map of the Peregrine soliton in the t-z plane with $T^p_{\text{off}} > T^c_{\text{off}}$. The unstored component of the probe field is marked by the white circle.

energy due to the existence of the CW background, it cannot be generated in a real experiment. To avoid this, we assume the probe field at $z = 0$ has the form

$$\Omega_p(0,t) = \Omega_{p0}(t)\left[\frac{1}{2}\tanh\left(\frac{t-T^p_{\text{on}}}{T^p_s}\right) - \frac{1}{2}\tanh\left(\frac{t-T^p_{\text{off}}}{T^p_s}\right)\right]. \quad (8)$$

Here $\Omega_{p0}(t) = 6.67[1 - 3.2/(1 + 4t^2/\tau_0^2)]$ is chosen to match the analytical solution (**5**); the hyperbolic tangent function is used to impose temporal boundaries on both sides of CW background (far from the pump part), which can make the soliton have finite energy and also have a clear illustration on its waveshape (similar to the case for generating dark solitons [64, 65]); $T^p_s = 3.0\tau_0$ is the switching time when switching on and off the probe field; $T^p_{\text{on}} = -80\tau_0$ and $T^p_{\text{off}} = 4\tau_0$ are parameters characterizing the two temporal boundaries, respectively. The waveshape of the input probe field at $z = 0$ is shown by a solid blue line in the upper part of **Figure 2A**, where the dashed vertical lines represent temporal boundaries.

The lower part of **Figure 2A** illustrates the result of a numerical simulation on the propagation of the Peregrine soliton (with $\Delta_3 = -2\pi \times 95.5$ MHz, $\tau_0 = 1.5 \times 10^{-7}$ s, and other parameters the same as those used in **Figure 1B**), by taking $|\Omega_p\tau_0|$ as a function of t/τ_0 and z. The orange line is the input Peregrine soliton at $z = 0$; the red line denotes the Peregrine soliton propagating to $z = 4.3$ cm; the maximum value ($|\Omega_p\tau_0|_{\max} \simeq 15.2$) of the soliton along the trajectory appears sharply around $z = 4.3$ cm at $t = 16.9\tau_0$. **Figure 2B** shows the contour map for the propagation of the Peregrine soliton, which can be taken as a projection of **Figure 2A** onto the t-z plane. One sees that the Peregrine soliton (indicated by the red dashed circle in **Figure 2B**) appears sharply and disappears suddenly; a secondary peak (soliton) emerges at longer distance, as a result of phase modulation when the first soliton is excited.

3 STORAGE, RETRIEVAL, SPLITTING, AND ROUTING OF THE OPTICAL PEREGRINE SOLITONS

We now turn to consider the memory of the optical Peregrine solitons and related applications in optical splitting and routing through the manipulation of the control fields.

3.1 Storage and Retrieval of the Optical Peregrine Solitons

We first consider the storage and retrieval of optical Peregrine solitons obtained above, which can be implemented by switching off and on the control field described by the following switching function:

$$\Omega_c = \Omega_{c0}\left[1 - \frac{1}{2}\tanh\left(\frac{t-T^c_{\text{off}}}{T^c_s}\right) + \frac{1}{2}\tanh\left(\frac{t-T^c_{\text{on}}}{T^c_s}\right)\right], \quad (9)$$

where Ω_{c0} is a constant, T^c_s is the time interval for switching off and switching on the control field (switching time), and T^c_{off} (T^c_{on}) is the time when the control field is switched off (on).

As an example, we take $\Omega_{c0} = 2\pi \times 31.8$ MHz, $T^c_{\text{off}} = 10.0\tau_0$, $T^c_{\text{on}} = 20.0\tau_0$, $T^c_s = 3.0\tau_0$ ($\tau_0 = 1.5 \times 10^{-7}$s), and other system parameters are the same as those used in **Figure 2**. The upper part of **Figure 3A** shows the time sequences of the control field (black line) and the probe field (blue line); the red dashed vertical line (black dashed vertical line) represents the time T^p_{off} (T^c_{off}). Symbols I, II, and III denote the CW background, the Peregrine soliton, and the low-intensity component of the probe field, respectively. The lower part of the figure shows the result of a numerical simulation on the storage and retrieval of the Peregrine soliton by taking $|\Omega_p\tau_0|$ as a function of t/τ_0 and z. Here the orange line is the input Peregrine soliton at $z = 0$; the purple line represents the Peregrine soliton at the storage period; the red line represents the retrieved Peregrine soliton propagating to $z = 4.1$ cm with the maximum intensity $|\Omega_p\tau_0|_{\max} \simeq 15.4$ at $t = 30.3\tau_0$. Shown in **Figure 3B** is the contour map of the storage and retrieval of the Peregrine soliton in the t-z plane

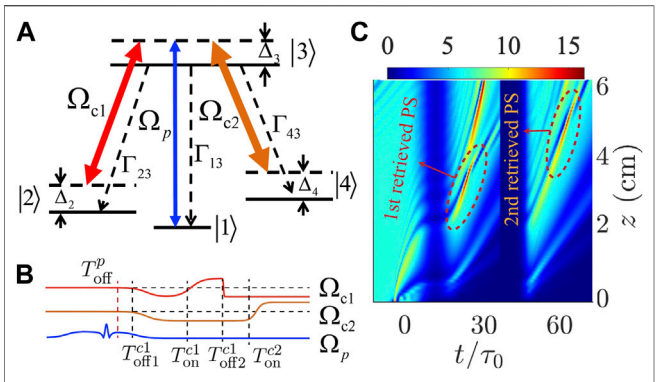

FIGURE 4 | Splitting of optical Peregrine solitons. **(A)** Energy-level diagram and excitation scheme of the tripod-type four-level atomic system. Here, a probe laser field Ω_p drives the transition $|1\rangle \leftrightarrow |3\rangle$; the two CW control fields Ω_{c1} and Ω_{c2} drive the transitions $|2\rangle \leftrightarrow |3\rangle$ and $|4\rangle \leftrightarrow |3\rangle$, respectively; Γ_{j3} is the decay rate from $|3\rangle$ to $|j\rangle$ ($j = 1, 2, 4$); Δ_3 and Δ_l ($l = 2, 4$) are respectively one-photon and two-photon detunings. **(B)** Time sequences of the control and the probe fields for realizing the optical splitting. The vertical red dashed line is for $t = T^p_{\rm off}$; the vertical black dashed lines represent the times when switching off and on the two control fields. For detailed meanings of the symbols $T^{c1}_{\rm off1}$, etc., see text. **(C)** The contour map of the splitting process of the Peregrine soliton in the t-z plane. The intensities of two split Peregrine solitons are $|\Omega_p\tau_0|_{\rm max} = 15.4$ when $t = 23.0\tau_0$ at the position $z = 3.7$ cm (first retrieved Peregrine soliton, i.e., "1st retrieved PS" indicated in the figure) and $|\Omega_p\tau_0|_{\rm max} = 14.0$ when $t = 61.5\tau_0$ at the position $z = 5.5$ cm (second retrieved Peregrine soliton, i.e., "2nd retrieved PS" indicated in the figure), respectively.

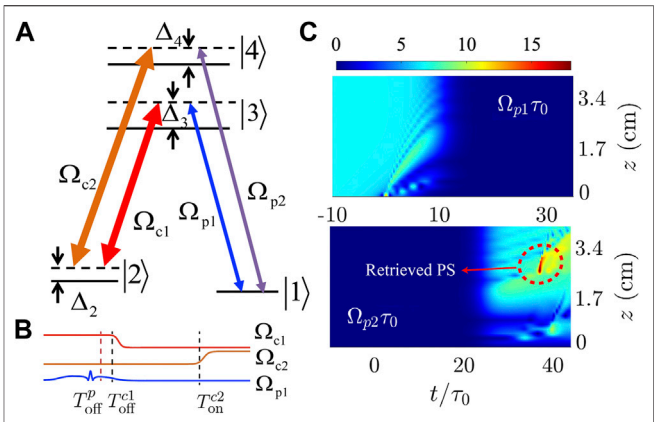

FIGURE 5 | Routing of optical Peregrine solitons. **(A)** The energy-level diagram and excitation scheme of the double-Λ-type four-level atomic system. In this configuration, two probe laser fields Ω_{p1} and Ω_{p2} drive the transitions $|1\rangle \leftrightarrow |3\rangle$ and $|1\rangle \leftrightarrow |4\rangle$, respectively; two CW control laser fields Ω_{c1} and Ω_{c2} drive the transitions $|2\rangle \leftrightarrow |3\rangle$ and $|2\rangle \leftrightarrow |4\rangle$, respectively; Δ_3 and Δ_4 are one-photon detunings, and Δ_2 is two-photon detuning. **(B)** Time sequences of the two control fields Ω_{c1}, Ω_{c2} and the probe field Ω_{p1} for realizing the soliton routing. The vertical red dashed line denotes the time $t = T^p_{\rm off}$; the vertical black dashed lines denote the times when switching off and on the control fields. **(C)** Contour maps for the routing process of the Peregrine soliton, where the upper panel is for Ω_{p1} and the lower panel is for Ω_{p2}. The Peregrine soliton is input as the probe field Ω_{p1}, but it is retrieved as the probe field Ω_{p2} (i.e., "retrieved PS" indicated by the red dashed circle in the lower panel of the figure).

with $T^p_{\rm off} < T^c_{\rm off}$. The retrieved Peregrine soliton is indicated by the red dashed circle (i.e., "Retrieved PS"). From the figure we see that the Peregrine soliton can be stored and retrieved some time later in the medium.

The steps of the storage and retrieval of the Peregrine soliton can be described as follows:

- Firstly, the control field Ω_c is switched on (to establish EIT) and the probe field (Peregrine soliton) of the form $\Omega_{p0}\tau_0 = 6.67[1 - 3.2/(1 + 4t^2/\tau_0^2)]\{0.5[(t/\tau_0 + 80)/3.0] - 0.5\tanh[(t/\tau_0 - 4)/3.0]\}$ is incident into the system (i.e., the orange line in the lower part of **Figure 3A**).
- Then, the control field is switched off at time $t = T^c_{\rm off} = 10.0\tau_0$, with the switching time of the control and probe fields setting to be $T^c_s = T^p_s = 3.0\tau_0$. The probe field (the Peregrine soliton) is thus stored in the system (i.e., it is converted into the atomic coherence σ_{21} [66, 67]).
- Lastly, the control field is switched on again at $t = T^c_{\rm on} = 20.0\tau_0$. The atomic coherence σ_{21} is converted back to the probe field, and hence the probe pulse is retrieved. Particularly, at time $t \simeq 30.3\tau_0$, the retrieved probe field manifests as a Peregrine soliton with the maximum intensity $|\Omega_p\tau_0|_{\rm max} \simeq 15.4$ at the position $z \simeq 4.1$ cm.

The efficiency of the Peregrine soliton memory can be characterized by the parameter $\eta = \int_{-\infty}^{+\infty}\left|E_p^{\rm Pere}(t)\right|^2 {\rm d}t / \int_{-\infty}^{+\infty}\left|E_p^{\rm in}(t)\right|^2 {\rm d}t$ [57, 67], where $E_p^{\rm in}(t) = E_p^{\rm in}(0, t)$ (i.e., the input Peregrine soliton) and $E_p^{\rm Pere}(t) = E_p^{\rm Pere}(L_{\rm Pere}, t)$ (i.e., the retrieved Peregrine soliton), with $L_{\rm Pere}$ ($\simeq 4.1$ cm) as the position where the Peregrine soliton is retrieved. Based on the result of **Figure 3A**, we obtain $\eta = 85.9\%$.

The fidelity of the Peregrine soliton memory can be described by the parameter ηJ^2, where J^2 describes the degree of coincidence of the wave shapes for the input and retrieved solitons, defined by the overlap integral $J^2 = \int_{-T_1}^{T_1}\left|E_p^{\rm in}(t)E_p^{\rm Pere}(t - \Delta T)\right|^2 {\rm d}t / \left[\int_{-T_1}^{T_1}\left|E_p^{\rm in}(t)\right|^2 {\rm d}t \int_{-T_1}^{T_1}\left|E_p^{\rm Pere}(t - \Delta T)\right|^2 {\rm d}t\right]$ [57, 67], where T_1 is a coefficient related to the temporal width of the Peregrine soliton (i.e., corresponding to symbol II in **Figure 2A**), and ΔT is the time interval between the peak of the input soliton pulse $E_p^{\rm in}$ and the peak of the retrieved soliton pulse $E_p^{\rm Pere}$. Here we take $\Delta T = 30.3\tau_0$ and $T_1 = 10\tau_0$. We obtain $\eta J^2 = 84.3\%$. We see that the efficiency and fidelity of the storage and retrieval of the Peregrine soliton are quite high.

The numerical result shown in **Figure 3C** is similar to that of **Figure 3A** but for $T^p_{\rm off} > T^c_{\rm off}$. In this case, the storage and retrieval of the Peregrine soliton can also be implemented; however, compared with **Figure 3A** (which is for $T^p_{\rm off} < T^c_{\rm off}$), the retrieved waveshape is little more distorted. **Figure 3D** illustrates the contour map of the Peregrine soliton in the t-z plane with $T^p_{\rm off} > T^c_{\rm off}$. One sees that the probe field has a nonzero value in the region indicated by the dashed white circle, which means that some parts of the probe field are not stored when the control field is switched off. We obtain the efficiency and fidelity of the Peregrine soliton memory for $T^p_{\rm off} > T^c_{\rm off}$ are $\eta = 77\%$ and $\eta J^2 = 65\%$, respectively. Based on these results, we conclude that

in order to get a high memory quality, the choice of $T^{p}_{\rm off} < T^{c}_{\rm off}$ is better than that of $T^{p}_{\rm off} > T^{c}_{\rm off}$.

3.2 Splitting of the Optical Peregrine Solitons

To realize an optical splitting [67] of the Peregrine soliton, we generalize the system into a four-level one with a tripod-type level configuration. Here a probe field Ω_p drives the transition $|1\rangle\leftrightarrow|3\rangle$; two CW control fields Ω_{c1} and Ω_{c2} drive respectively the transitions $|2\rangle\leftrightarrow|3\rangle$ and $|4\rangle\leftrightarrow|3\rangle$; Γ_{j3} is the decay rate from $|3\rangle$ to $|j\rangle$ ($j = 1, 2, 4$), Δ_3 and Δ_l ($l = 2, 4$) are respectively one-photon and two-photon detunings (see **Figure 4A**). The Hamiltonian of the system and the optical Bloch equations controlling the dynamics of the atoms have been presented in **Section 5 of the Supplementary Material**.

The timing sequences of the switching-off and -on of $\Omega_{cj}(t)$ for obtaining a Peregrine soliton splitter are shown in **Figure 4B**, with $T^{p}_{\rm off} < T^{c1}_{\rm off\,1} = T^{c2}_{\rm off\,1} < T^{c1}_{\rm on} < T^{c1}_{\rm off\,2} < T^{c2}_{\rm on}$. For jth control field Ω_{cj} ($j = 1, 2$), T^{cj}_{s} ($T^{cj}_{\rm on}$) is its switching-off (switching-on) time. The corresponding switching functions have been given in **Section 5 of the Supplementary Material**. When plotting the figure, we have set $\Omega_{c1}(0) = \Omega_{c2}(0) = 2\pi \times 31.8$ MHz, $T^{c1}_{\rm off\,1} = T^{c2}_{\rm off\,1} = 6.0\tau_0$, $T^{c1}_{\rm on} = 15.0\tau_0$, $T^{c1}_{\rm off\,2} = 35.0\tau_0$, $T^{c2}_{\rm on} = 45.0\tau_0$, and $T^{c1}_{s} = T^{c2}_{s} = 3.0\tau_0$.

Shown in **Figure 4C** is the numerical result on the simulation for obtaining the Peregrine soliton splitter by taking $\Omega_p\tau_0$ as a function of t/τ_0 and z (with $\tau_0 = 1.5 \times 10^{-7}$ s). The operation steps can be described as follows: 1) Firstly, the two control fields Ω_{c1} and Ω_{c2} are applied and a probe field with the waveform $\Omega_{p0}(0,t)=6.67[1-3.2/(1+4(t+5)^2/\tau_0^2)]\{0.5\tanh[(t/\tau_0+80)/3.0]-0.5\tanh[(t/\tau_0-4)/3.0]\}$ is incident to the system. 2) Then, both control fields are simultaneously switched off at time $t=T^{c1}_{\rm off\,1}=T^{c2}_{\rm off\,1}=6.0\tau_0$. Thus the probe field is stored in the two atomic coherences σ_{21} and σ_{41} simultaneously 67. 3) Later on, switching on Ω_{c1} at $t=T^{c1}_{\rm on}=15.0\tau_0$ (but Ω_{c2} is remained to be switched off), the atomic coherence σ_{21} is converted back into the probe field, and hence a new probe pulse is retrieved. At time $t \simeq 23.0\tau_0$, this retrieved probe pulse turns into a Peregrine soliton (i.e., "1st retrieved PS", indicated by a red circle in **Figure 4B**) with the maximum intensity $|\Omega_p\tau_0|_{\rm max} \simeq 15.4$ at the position z=3.7 cm. 4) By switching off Ω_{c1} at $t=T^{c1}_{\rm off\,2}=35.0\tau_0$ and switching on Ω_{c2} at $t=T^{c2}_{\rm on}=45.0\tau_0$, the atomic coherence σ_{41} converts back into the probe field; this retrieved probe field turns into another Peregrine soliton (i.e., "2nd retrieved PS", indicated by another red circle in **Figure 4B**) with the maximum intensity $|\Omega_p\tau_0|_{\rm max} \simeq 14.0$ at the position z=5.5 cm at $t \simeq 61.5\tau_0$.

In the simulation, we have taken $\Delta_2 = \Delta_4 = -2\pi \times 0.64$ MHz, $\gamma_{21} = \gamma_{41} = 2\pi \times 1.09$ kHz, with the other parameters the same as those used in **Figure 3A**. The reason for taking $\Delta_2 = \Delta_4$ and $\gamma_{21} = \gamma_{41}$ is to keep the symmetry of the tripod level configuration, which gives two nearly degenerated EITs in the system; for details, see [67]. The splitting efficiency and fidelity of the first (second) Peregrine soliton are $\eta_1 = 89.8\%$ and $\eta_1 J_1^2 = 85.4\%$ ($\eta_2 = 89.3\%, \eta_2 J_2^2 = 84.9\%$), respectively.

3.3 Routing of the Optical Peregrine Solitons

To realize all-optical routing [67, 68] of optical Peregrine solitons, we consider a four-level atomic system with a double-Λ-type level configuration. Here, two probe laser fields Ω_{p1} and Ω_{p2} drive the transitions $|1\rangle\leftrightarrow|3\rangle$ and $|1\rangle\leftrightarrow|4\rangle$, respectively; two CW control laser fields Ω_{c1} and Ω_{c2} drive the transitions $|2\rangle\leftrightarrow|3\rangle$ and $|2\rangle\leftrightarrow|4\rangle$, respectively; Δ_3 and Δ_4 are one-photon detunings, and Δ_2 is two-photon detuning (see **Figure 5A**).

The Hamiltonian of the system and the MB equations governing the dynamics of the atoms and light fields have been given in **Section 6 of the Supplementary Material**.

For simplicity, here we consider a frequency routing process, i.e., the probe field Ω_{p1} is converted into the Ω_{p2} (which has different frequency from Ω_{p1}). The time sequence of the switching off and on of Ω_{cj} for obtaining routing of Peregrine soliton is shown in **Figure 5B**, with $T^{p}_{\rm off} < T^{c1}_{\rm off} < T^{c2}_{\rm on}$, where $T^{c1}_{\rm off}$ is the switching-off time of Ω_{c1} and $T^{c2}_{\rm on}$ is the switching-on time of Ω_{c2}. The corresponding switching functions have been given in **Section 5 of the Supplementary Material**. Without loss of generality, the system parameters are set to be $\Omega_{c1} = \Omega_{c2} = 2\pi \times 31.8$ MHz, $T^{c1}_{\rm off} = 10.0\tau_0$, $T^{c2}_{\rm on} = 25.0\tau_0$, and $T^{c1}_{s} = T^{c2}_{s} = 3.0\tau_0$ (switching time).

The implementing procedure of the Peregrine soliton routing is as follows. First, by switching on the control field Ω_{c1}, the input probe field Ω_{p1} with the initial condition $\Omega_{p0}(t/\tau_0) = 6.67[1 - 3.2/(1 + 4t^2/\tau_0^2)]\{0.5\tanh[(t/\tau_0 + 80)/3.0] - 0.5\tanh[(t/\tau_0 - 4)/3.0]\}$ propagates in the system, as shown in the upper panel of **Figure 5C** as a function of propagation distance t/τ_0 and z. One sees that a trajectory of the soliton shows up before its storage. Second, by switching off Ω_{c1} at time $t = 10\tau_0$, the probe field Ω_{p1} is stored in the atomic coherence σ_{21}. Third, by switching on the control field Ω_{c2} at $t = 25\tau_0$, another probe pulse Ω_{p2} appears from the atomic coherence σ_{21}, i.e., "retrieved PS" in the lower panel of **Figure 5C**. We stress that during this routing process, the Peregrine soliton in the probe field Ω_{p1} is annihilated and a new Peregrine soliton in the probe field Ω_{p2} (which has no input) is created. Since the frequency of Ω_{p2} is different from that of Ω_{p1}, the system performs as a frequency router of the Peregrine soliton.

4 CONCLUSION

We have proposed a scheme for realizing the storage and retrieval of optical Peregrine solitons in a coherent atomic gas via EIT. We have shown that the optical Peregrine solitons with very small propagation loss, ultraslow motional velocity, and extremely low generation power can be generated in the system via EIT. We have demonstrated that such solitons can be stored, retrieved, split, and routed with high efficiency and fidelity through the manipulation of control laser fields.

The scheme can also be generalized to cases with more optical output channels through the use of more control fields, and hence the two-channel splitting and routing processes can be generalized to multiple channel ones. Furthermore, the storage and retrieval of the optical Peregrine solitons can be extended to solid materials, like on-chip optical resonator systems [69]. The research results reported here may be useful for the active control of optical Peregrine solitons and promising for potential applications in optical information processing and transmission.

DATA AVAILABILITY STATEMENT

The raw data supporting the conclusion of this article will be made available by the authors, without undue reservation.

AUTHOR CONTRIBUTIONS

GH proposed the idea and supervised the whole work. CS carried out the analytical and numerical calculation. Both authors contributed to the writing of the manuscript.

FUNDING

This work was supported by the National Natural Science Foundation of China under grant no. 11975098.

SUPPLEMENTARY MATERIAL

The Supplementary Material for this article can be found online at: https://www.frontiersin.org/articles/10.3389/fphy.2021.594680/full#supplementary-material.

REFERENCES

1. Pelinovsky E, Kharif C. *Extreme ocean waves*. Berlin: Springer (2008).
2. Akhmediev N, Ankiewicz A, Taki M. Waves that appear from nowhere and disappear without a trace. *Phys Lett A* (2009a) 373:675–8. doi:10.1016/j.physleta.2008.12.036
3. Stenflo L, Marklund M. Rogue waves in the atmosphere. *J Plasma Phys* (2010) 76:293–5. doi:10.1017/S0022377809990481
4. Efimov V, Ganshin A, Kolmakov G, McClintock P, Mezhov-Deglin L. Rogue waves in superfluid helium. *Eur Phys J Spec Top* (2010) 185:181–93. doi:10.1140/epjst/e2010-01248-5
5. Shats M, Punzmann H, Xia H. Capillary rogue waves. *Phys Rev Lett* (2010) 104:104503. doi:10.1103/PhysRevLett.104.104503
6. Chabchoub A, Hoffmann NP, Akhmediev N. Rogue wave observation in a water wave tank. *Phys Rev Lett* (2011) 106:204502. doi:10.1103/PhysRevLett.106.204502
7. Pierangeli D, Di Mei F, Conti C, Agranat AJ, DelRe E. Spatial rogue waves in photorefractive ferroelectrics. *Phys Rev Lett* (2015) 115:093901. doi:10.1103/PhysRevLett.115.093901
8. Moslem WM, Sabry R, El-Labany SK, Shukla PK. Dust-acoustic rogue waves in a nonextensive plasma. *Phys Rev E* (2011) 84:066402. doi:10.1103/PhysRevE.84.066402
9. Li BQ, Ma YL. Characteristics of rogue waves for a (2+1)-dimensional heisenberg ferromagnetic spin chain system. *J Magn Magn Mater* (2019) 474:537–43. doi:10.1016/j.jmmm.2018.10.133
10. Onorato M, Residori S, Bortolozzo U, Montina A, Arecchi F. Rogue waves and their generating mechanisms in different physical contexts. *Phys Rep* (2013) 528:47–89. doi:10.1016/j.physrep.2013.03.001
11. Dudley JM, Dias F, Erkintalo M, Genty G. Instabilities, breathers and rogue waves in optics. *Nat Photon* (2014) 8:755–64. doi:10.1038/nphoton.2014.220
12. Peregrine DH. Water waves, nonlinear schrödinger equations and their solutions. *J Aust Math Soc Ser B* (1983) 25:16–43. doi:10.1017/S0334270000003891
13. Akhmediev N, Soto-Crespo J, Ankiewicz A. Extreme waves that appear from nowhere: on the nature of rogue waves. *Phys Lett A* (2009b) 373:2137–45. doi:10.1016/j.physleta.2009.04.023
14. Shrira VI, Geogjaev VV. What makes the peregrine soliton so special as a prototype of freak waves? *J Eng Math* (2010) 67:11–22. doi:10.1007/s10665-009-9347-2
15. Ma YC. The perturbed plane-wave solutions of the cubic schrödinger equation. *Stud Appl Math* (1979) 60:43–58. doi:10.1002/sapm197960143
16. Akhmediev NN, Eleonskii VM, Kulagin NE. Exact first-order solutions of the nonlinear schrödinger equation. *Theor Math Phys* (1987) 72:809–18. doi:10.1007/BF01017105
17. Bailung H, Sharma SK, Nakamura Y. Observation of peregrine solitons in a multicomponent plasma with negative ions. *Phys Rev Lett* (2011) 107:255005. doi:10.1103/PhysRevLett.107.255005
18. Chabchoub A, Neumann S, Hoffmann NP, Akhmediev N. Spectral properties of the eregrine soliton observed in a water wave tank. *J Geophys Res* (2012) 117:C00J03. doi:10.1029/2011JC007671
19. Shemer L, Alperovich L. Peregrine breather revisited. *Phys Fluids* (2013) 25:051701. doi:10.1063/1.4807055
20. Sharma SK, Bailung H. Observation of hole peregrine soliton in a multicomponent plasma with critical density of negative ions. *J Geophys Res Space Phys* (2013) 118:919–24. doi:10.1002/jgra.50111
21. Al Khawaja U, Bahlouli H, Asad-uz-zaman M, Al-Marzoug S. Modulational instability analysis of the peregrine soliton. *Commun Nonlinear Sci Numer Simulat* (2014) 19:2706–14. doi:10.1016/j.cnsns.2014.01.002
22. Chen S, Song LY. Peregrine solitons and algebraic soliton pairs in Kerr media considering space-time correction. *Phys Lett A* (2014) 378:1228–32. doi:10.1016/j.physleta.2014.02.042
23. Dai CQ, Wang YY. Controllable combined peregrine soliton and Kuznetsov-Ma soliton in -symmetric nonlinear couplers with gain and loss. *Nonlinear Dyn* (2015) 91:715–21. doi:10.1007/s11071-015-1900-0
24. Gupta SK, Sarma AK. Peregrine rogue wave dynamics in the continuous nonlinear schrödinger system with parity-time symmetric Kerr nonlinearity. *Commun. Nonlinear Sci Numer Simulat* (2016) 36:141–7. doi:10.1016/j.cnsns.2015.11.017
25. Solli DR, Ropers C, Koonath P, Jalali B. Optical rogue waves. *Nature* (2007) 450:1054–7. doi:10.1038/nature06402
26. Solli DR, Ropers C, Jalali B. Active control of rogue waves for stimulated supercontinuum generation. *Phys Rev Lett* (2008) 101:233902. doi:10.1103/PhysRevLett.101.233902
27. Montina A, Bortolozzo U, Residori S, Arecchi FT. Non-Gaussian statistics and extreme waves in a nonlinear optical cavity. *Phys Rev Lett* (2009) 103:173901. doi:10.1103/PhysRevLett.103.173901
28. Kibler B, Fatome J, Finot C, Millot G, Dias F, Genty G, et al. The Peregrine soliton in nonlinear fibre optics. *Nat Phys* (2010) 6:790–5. doi:10.1038/NPHYS1740
29. Bonatto C, Feyereisen M, Barland S, Giudici M, Masoller C, Leite JRR, et al. Deterministic optical rogue waves. *Phys Rev Lett* (2011) 107:053901. doi:10.1103/PhysRevLett.107.053901
30. Hammani K, Kibler B, Finot C, Morin P, Fatome J, Dudley JM, et al. Peregrine soliton generation and breakup in standard telecommunications fiber. *Opt Lett* (2011) 36:112–4. doi:10.1364/OL.36.000112
31. Zaviyalov A, Egorov O, Iliew R, Lederer F. Rogue waves in mode-locked fiber lasers. *Phys Rev A* (2012) 85:013828. doi:10.1103/PhysRevA.85.013828
32. Akhmediev N, Dudley JM, Solli DR, Turitsyn SK. Recent progress in investigating optical rogue waves. *J Opt* (2013) 15:060201. doi:10.1088/2040-8978/15/6/060201
33. Bludov YV, Driben R, Konotop VV, Malomed BA. Instabilities, solitons and rogue waves in -coupled nonlinear waveguides. *J Opt* (2013) 15:064010. doi:10.1088/2040-8978/15/6/064010
34. Zhang Y, Belić MR, Zheng H, Chen H, Li C, Song J, et al. Nonlinear talbot effect of rogue waves. *Phys Rev E* (2014) 89:032902. doi:10.1103/PhysRevE.89.032902
35. Yang G, Wang Y, Qin Z, Malomed BA, Mihalache D, Li L. Breatherlike solitons extracted from the peregrine rogue wave. *Phys Rev E* (2014) 90:062909. doi:10.1103/PhysRevE.90.062909
36. Suret P, Koussaifi RE, Tikan A, Evain C, Randoux S, Szwaj C, et al. Single-shot observation of optical rogue waves in integrable turbulence using time microscopy. *Nat Commun* (2016) 7:13136. doi:10.1038/ncomms13136
37. Tikan A, Billet C, El G, Tovbis A, Bertola M, Sylvestre T, et al. Universality of the peregrine soliton in the focusing dynamics of the cubic nonlinear

schrödinger equation. *Phys Rev Lett* (2017) 119:033901. doi:10.1103/PhysRevLett.119.033901
38. Randoux S, Suret P, Chabchoub A, Kibler B, El G. Nonlinear spectral analysis of peregrine solitons observed in optics and in hydrodynamic experiments. *Phys Rev E* (2018) 98:022219. doi:10.1103/PhysRevE.98.022219
39. Xu G, Hammani K, Chabchoub A, Dudley JM, Kibler B, Finot C. Phase evolution of peregrine-like breathers in optics and hydrodynamics. *Phys Rev E* (2019a) 99:012207. doi:10.1103/PhysRevE.99.012207
40. Yang G, Li L, Jia S. Peregrine rogue waves induced by the interaction between a continuous wave and a soliton. *Phys Rev E.* (2012) 85:046608. doi:10.1103/PhysRevE.85.046608
41. Tiofack CGL, Coulibaly S, Taki M, De Bièvre S, Dujardin G. Comb generation using multiple compression points of Peregrine rogue waves in periodically modulated nonlinear Schrödinger equations. *Phys Rev A* (2015) 92:043837. doi:10.1103/PhysRevA.92.043837
42. Li J, Han J, Du Y, Dai C. Controllable behaviors of Peregrine soliton with two peaks in a birefringent fiber with higher-order effects. *Nonlinear Dyn* (2015) 82:1393–8. doi:10.1007/s11071-015-2246-3
43. Chowdury A, Kedziora DJ, Ankiewicz A, Akhmediev N. Breather-to-soliton conversions described by the quintic equation of the nonlinear Schrödinger hierarchy. *Phys Rev E* (2015) 91:032928. doi:10.1103/PhysRevE.91.032928
44. Chen S, Baronio F, Soto-Crespo JM, Liu Y, Grelu P. Chirped Peregrine solitons in a class of cubic-quintic nonlinear Schrödinger equations. *Phys Rev E* (2016) 93:062202. doi:10.1103/PhysRevE.93.062202
45. Wang L, Zhang JH, Liu C, Li M, Qi FH. Breather transition dynamics, peregrine combs and walls, and modulation instability in a variable-coefficient nonlinear Schrödinger equation with higher-order effects. *Phys Rev E* (2016) 93:062217. doi:10.1103/PhysRevE.93.062217
46. Dai CQ, Liu J, Fan Y, Yu DG. Two-dimensional localized Peregrine solution and breather excited in a variable-coefficient nonlinear Schrödinger equation with partial nonlocality. *Nonlinear Dyn* (2017) 88:1373–83. doi:10.1007/s11071-016-3316-x
47. Özkan YS, Yaşar E, Seadawy AR. On the multi-waves, interaction and Peregrine-like rational solutions of perturbed Radhakrishnan–Kundu–Lakshmanan equation. *Phys Scr* (2020) 95:085205. doi:10.1088/1402-4896/ab9af4
48. Chen S. Twisted rogue-wave pairs in the Sasa-Satsuma equation. *Phys Rev E* (2013) 88:023202. doi:10.1103/PhysRevE.88.023202
49. Chen S, Grelu P, Soto-Crespo JM. Dark- and bright-rogue-wave solutions for media with long-wave–short-wave resonance. *Phys Rev E* (2014a) 89:011201. doi:10.1103/PhysRevE.89.011201
50. Chen S, Ye Y, Soto-Crespo JM, Grelu P, Baronio F. Peregrine solitons beyond the threefold limit and their two-soliton interactions. *Phys Rev Lett* (2018) 121:104101. doi:10.1103/PhysRevLett.121.104101
51. Chen S, Pan C, Grelu P, Baronio F, Akhmediev N. Fundamental peregrine solitons of ultrastrong amplitude enhancement through self-steepening in vector nonlinear systems. *Phys Rev Lett* (2020) 124:113901. doi:10.1103/PhysRevLett.124.113901
52. Xu G, Gelash A, Chabchoub A, Zakharov V, Kibler B. Breather wave molecules. *Phys Rev Lett* (2019b) 122:084101. doi:10.1103/PhysRevLett.122.084101
53. Asgarnezhad-Zorgabad S, Berini P, Sanders BC. Polaritonic frequency-comb generation and breather propagation in a negative-index metamaterial with a cold four-level atomic medium. *Phys Rev A* (2019) 99:051802. doi:10.1103/PhysRevA.99.051802
54. Asgarnezhad-Zorgabad S, Sadighi-Bonabi R, Kibler B, Özdemir ŞK, Sanders BC. Surface-polaritonic phase singularities and multimode polaritonic frequency combs via dark rogue-wave excitation in hybrid plasmonic waveguide. *New J Phys* (2020) 22:033008. doi:10.1088/1367-2630/ab7259
55. Fleischhauer M, Imamoglu A, Marangos JP. Electromagnetically induced transparency: optics in coherent media. *Rev Mod Phys* (2005) 77:633–73. doi:10.1103/RevModPhys.77.633
56. Huang G, Deng L, Payne MG. Dynamics of ultraslow optical solitons in a cold three-state atomic system. *Phys Rev E* (2005) 72:016617. doi:10.1103/PhysRevE.72.016617
57. Chen Y, Bai Z, Huang G. Ultraslow optical solitons and their storage and retrieval in an ultracold ladder-type atomic system. *Phys Rev A* (2014b) 89:023835. doi:10.1103/PhysRevA.89.023835
58. Xu D, Chen Z, Huang G. Ultraslow weak-light solitons and their storage and retrieval in a kagome-structured hollow-core photonic crystal fiber. *Opt Express* (2017) 25:19094–111. doi:10.1364/OE.25.019094
59. Liu J, Hang C, Huang G. Weak-light rogue waves, breathers, and their active control in a cold atomic gas via electromagnetically induced transparency. *Phys Rev A* (2016) 93:063836. doi:10.1103/PhysRevA.93.063836
60. Liu J, Hang C, Huang G. Weak-light vector rogue waves, breathers, and their Stern-Gerlach deflection via electromagnetically induced transparency. *Opt Express* (2017) 25:23408–23. doi:10.1364/OE.25.023408
61. Boyd RW. *Nonlinear Optics* New York: Elsevier (2008).
62. Steck DA. *Rubidium 87 D line data* (2019) https://steck.us/alkalidata/ (Accessed August 3, 2020).
63. Newell AC, Moloney JC. Nonlinear Optics *(California*. Addison-Wesley Publishing Company (1991).
64. Kivshar YS, Luther-Davies B. Dark optical solitons: physics and applications. *Phys Rep* (1998) 298:81–197. doi:10.1016/S0370-1573(97)00073-2
65. Shou C, Huang G. Storage and retrieval of slow-light dark solitons. *Opt Lett* (2020) 45:6787–90. doi:10.1364/OL.412247
66. Mazets IE. Adiabatic pulse propagation in coherent atomic media with the tripod level configuration. *Phys Rev A* (2005) 71:023806. doi:10.1103/PhysRevA.71.023806
67. Shou C, Huang G. Slow-light soliton beam splitters. *Phys Rev A* (2019) 99:043821. doi:10.1103/PhysRevA.99.043821
68. Lemr K, Bartkiewicz K, Černoch A, Soubusta J. Resource-efficient linear-optical quantum router. *Phys Rev A* (2013) 87:062333. doi:10.1103/PhysRevA.87.062333
69. Xu Q, Sandhu S, Povinelli ML, Shakya J, Fan S, Lipson M. Experimental realization of an on-chip all-optical analogue to electromagnetically induced transparency. *Phys Rev Lett* (2006) 96:123901. doi:10.1103/PhysRevLett.96.123901

Conflict of Interest: The authors declare that the research was conducted in the absence of any commercial or financial relationships that could be construed as a potential conflict of interest.

frontiers in Physics

BRIEF RESEARCH REPORT
published: 09 April 2021
doi: 10.3389/fphy.2021.610896

Rogue Waves With Rational Profiles in Unstable Condensate and Its Solitonic Model

D. S. Agafontsev[1,2]* *and A. A. Gelash*[2,3]

[1]*P.P. Shirshov Institute of Oceanology of RAS, Moscow, Russia,* [2]*Skolkovo Institute of Science and Technology, Moscow, Russia,* [3]*Institute of Automation and Electrometry of SB RAS, Novosibirsk, Russia*

In this brief report we study numerically the spontaneous emergence of rogue waves in 1) modulationally unstable plane wave at its long-time statistically stationary state and 2) bound-state multi-soliton solutions representing the solitonic model of this state. Focusing our analysis on the cohort of the largest rogue waves, we find their practically identical dynamical and statistical properties for both systems, that strongly suggests that the main mechanism of rogue wave formation for the modulational instability case is multi-soliton interaction. Additionally, we demonstrate that most of the largest rogue waves are very well approximated–simultaneously in space and in time–by the amplitude-scaled rational breather solution of the second order.

Keywords: solitons, breathers, rogue waves, integrable systems, modulational instability

OPEN ACCESS

Edited by:
Heremba Bailung, Ministry of Science and Technology, India

Reviewed by:
Haci Mehmet Baskonus, Harran University, Turkey
Matteo Conforti, UMR8523 Physique des lasers, atomes et molécules (PhLAM), France

***Correspondence:**
D. S. Agafontsev
dmitrij@itp.ac.ru

Specialty section:
This article was submitted to Mathematical and Statistical Physics, a section of the journal Frontiers in Physics

Received: *27 September 2020*
Accepted: *20 January 2021*
Published: *09 April 2021*

Citation:
Agafontsev DS and Gelash AA (2021) Rogue Waves With Rational Profiles in Unstable Condensate and Its Solitonic Model. Front. Phys. 9:610896. doi: 10.3389/fphy.2021.610896

1 INTRODUCTION

The phenomenon of rogue waves (RWs)—unusually large waves that appear suddenly from moderate wave background–was intensively studied in the recent years. A number of mechanisms were suggested to explain their emergence, see e.g., the reviews [1–3]; with the most general idea stating that RWs could be related to breather-type solutions of the underlying nonlinear evolution equations [4–6]. Currently, ones of the most popular models for RWs are the Peregrine rational breather [7] and the higher-order rational breather [8] solutions of the one-dimensional nonlinear Schrödinger equation (1D-NLSE) of the focusing type,

$$i\psi_t + \psi_{xx} + |\psi|^2\psi = 0 \tag{1}$$

These solutions belong to a family of localized in space and time algebraic breathers, which evolve on a finite background and lead to three-fold, five-fold, seven-fold, and so on, increase in amplitude at the time of their maximum elevation. Taking specific and carefully designed initial conditions, they were reproduced in well-controlled experiments performed in different physical systems [9–13].

The 1D-NLSE is integrable in terms of the *inverse scattering transform* (IST), as it allows transformation to the so-called *scattering data*, which is in one-to-one correspondence with the wavefield and, similarly to the Fourier harmonics in the linear wave theory, changes trivially during the motion. Thanks to its properties, the scattering data can be used to characterize the wavefield. For spatially localized case, the scattering data consists of the discrete (solitons) and the continuous (nonlinear dispersive waves) parts of eigenvalue spectrum, calculated for specific auxiliary linear system. For strongly nonlinear wavefields, such as the ones where emergence of rational breathers can be expected, the solitons provide the main contribution to the energy [14] and should therefore

play the dominant role in the dynamics. In particular, as has been recently demonstrated in [15]; the modulationally unstable plane wave (the condensate) at its long-time statistically stationary state can be accurately modeled (in the statistical sense) with a certain soliton gas, designed to follow the solitonic structure of the condensate. The latter naturally raises a question of whether there is a difference between the RWs emerging in the two systems. Indeed, in a soliton gas all RWs are multi-soliton interactions by construction. Hence, if there is no significant difference, then we can draw a hypothesis that for the asymptotic stationary state of the MI (and, possibly, for other strongly nonlinear wavefields) the main mechanism of RW formation is interaction of solitons.

With the present paper, we contribute to the answer on this question by summarizing our observations of RWs for both systems. Specifically, we compute time evolution for 1,000 random realizations of the noise-induced MI of the condensate and also for 1,000 random realizations of 128-soliton solutions modeling the asymptotic state of the MI. For each realization, we analyze one largest RW emerging in the course of the evolution, thus focusing our analysis on the largest RWs. For both systems, we observe practically identical dynamical and statistical properties of the collected RWs. In particular, most of the RWs turn out to be very well approximated–simultaneously in space and in time–by the amplitude-scaled rational breather solution (RBS) of the second order. By measuring deviation between RWs and their fits with RBS as an integral of the difference in the (x, t)-space, we find that, in general, the larger the maximum amplitude of the RW, the better its convergence to the RBS of the second order (RBS2). The collected RWs for the two systems turn out to be identically distributed by their maximum amplitude and deviation from the RBS2. Additionally, we demonstrate that the observed quasi-rational profiles appear already for synchronized three-soliton interactions and discuss the next steps in the ongoing research of the RW origin.

Note that in the present paper we consider solutions of the 1D-NLSE for three different types of boundary conditions: the MI of the condensate for which we use the periodic boundary, the multi-soliton solutions with vanishing border conditions and the RBS having constant border conditions at infinity. Globally, these solutions are fundamentally different, and the different border conditions require application of separate IST techniques, see e.g., [5, 14, 16, 17]. For instance, formally our MI case corresponds to finite-band scattering data. However, the characteristic widths of the structures (RWs, solitons, RBS) are small compared to the sizes of the studied wavefields, so that the eigenvalue bands are very narrow and we neglect their difference from solitons. The similar idea was suggested in [18]; where, vice versa, the soliton gas was considered as a limit of finite-band solutions. Effectively, we assume that formation of a RW, as a local phenomenon, represents a similar process for all three cases of border conditions. As we demonstrate in the paper, this assumption is supported by the presented results, that raises an important problem that we leave for future studies–explanation of how the three models may exhibit locally similar nonlinear patterns.

2 NUMERICAL METHODS

For both the MI of the condensate and the soliton gas initial conditions, we solve **Eq. 1** numerically in a large box $x \in [-L/2, L/2]$, $L \gg 1$, with periodic boundary. We use the pseudo-spectral Runge-Kutta fourth-order method in adaptive grid with the grid size Δx set from the analysis of the Fourier spectrum of the solution; see [19] for detail. As an integrable equation, the 1D-NLSE conserves an infinite set of integrals of motion, see e.g., [14]. We have checked that the first ten integrals are conserved by our numerical scheme up to the relative errors from 10^{-10} (the first three invariants) to 10^{-6} (the 10th invariant) orders.

Without loss of generality, the initial conditions for the noise-induced MI of the condensate can be written as

$$\psi\big|_{t=0} = 1 + \varepsilon(x) \tag{2}$$

where $\varepsilon(x)$ represents a small initial noise. We use statistically homogeneous in space noise with Gaussian Fourier spectrum,

$$\varepsilon(x) = a_0 \left(\frac{\sqrt{8\pi}}{\theta L}\right)^{1/2} \sum_k e^{-k^2/\theta^2 + i\phi_k + ikx} \tag{3}$$

where a_0 is the average noise amplitude in the x-space, $k = 2\pi m/L$ is the wavenumber, $m \in \mathbb{Z}$ is integer, θ is the characteristic noise width in the k-space and ϕ_k are random phases for each k and each realization of the initial conditions; the average intensity of such noise equals to a_0^2, $\langle|\varepsilon|^2\rangle = a_0^2$. For the numerical experiment, we take the box of length $L = 256\pi$ and small initial noise, $a_0 = 10^{-5}$, with wide spectrum, $\theta = 5$. Note that these parameters match those used in [19].

To generate soliton gas, modeling the asymptotic stationary state of the noise-induced MI, we use exact 128-soliton solutions of the 1D-NLSE. More precisely, we compute the corresponding wavefields using numerical implementation of the 1D-NLSE integration technique–the so-called dressing method [20]—with 100-digits precision arithmetics, as described in [21]. Each soliton has four parameters: amplitude a_j, velocity v_j, space position x_{0j} and phase Θ_j; here $j = 1, \ldots, M$, $M = 128$, and the one-soliton solution reads as

$$\psi_s(x,t) = a \frac{\exp\left[\frac{iv}{2}(x - x_0) + \frac{i}{2}\left(a^2 - \frac{v^2}{2}\right)t + i\Theta\right]}{\cosh\frac{a(x - x_0) - avt}{\sqrt{2}}}$$

Following [15]; we distribute soliton amplitudes according to the Bohr-Sommerfeld quantization rule,

$$a_j = 2\sqrt{1 - \left(\frac{j - 1/2}{M}\right)^2} \tag{4}$$

and set soliton velocities to zero, $v_j = 0$, using uniformly-distributed soliton phases Θ_j in the interval $(0, 2\pi)$ and uniformly-distributed space position parameters x_{0j} in a narrow interval at the center of the computational box. Zero velocities mean that these multi-soliton solutions are bound-state. For the 1D-NLSE in normalization Eq. 1, the Bohr-Sommerfeld rule describes amplitudes for the bound-state solitonic content of

a rectangular box wavefield of unit amplitude $\psi = 1$ and width $L_o = \sqrt{2}\pi M$, calculated with the semi-classical Zakharov-Shabat direct scattering problem, see e.g., [14, 22, 23]. The generated 128-soliton solutions take values of unity order approximately within the interval $x \in [-L_o/2, L_o/2]$ and remain small outside of it. For more detail on the soliton gas, we refer the reader to [15]; where it has been demonstrated that its spectral (Fourier) and statistical properties match those of the long-time statistically stationary state of the MI.

For the soliton gas, we gather the RWs by simulating time evolution of the 128-soliton solutions in the interval $t \in [0, 50]$ and then collecting one largest RW for each of the 1,000 realizations of initial conditions. For time evolution, we use the same pseudo-spectral Runge-Kutta numerical scheme as for the MI of the condensate, since application of the dressing method with evolving scattering data takes too much computational time and provides the same result. The pseudo-spectral scheme uses periodic boundary conditions, so that solution $\psi(x, t)$ needs to be small near the edges of the computational box. We achieve this by taking the box of length $L = 384\sqrt{2}\pi$, so that our 128-soliton solutions are of 10^{-16} order near its edges and take values of unity order, $|\psi| \sim 1$, only within its central 1/3 part ($\equiv L_o/L$).

For the MI of the condensate, we collect the RWs similarly, but in the time interval $t \in [174, 200]$. From the one hand, the end of this interval is far enough, so that the system is sufficiently close to its asymptotic stationary state, see [19] where the same initial conditions were used. From the other hand, a chance to detect a large RW is higher in larger simulation boxes and if we wait longer. To make RW events for the two systems comparable, we impose a restriction $L^{(MI)} \cdot \Delta T^{(MI)} = L^{(SG)} \cdot \Delta T^{(SG)}$ on the lengths $L^{(MI,SG)}$ of the regions where RWs may appear and on the time intervals $\Delta T^{(MI,SG)}$ during which we wait for the largest RW. For the soliton gas, the collected RWs appear approximately in the space interval $x \in [-210, 210]$ with practically uniform distribution of their position, so that $L^{(SG)} = 420$. We believe that this property is connected with behavior of the ensemble- and time-averaged intensity $I(x) = \langle |\psi(x, t)|^2 \rangle$, which remains flat $I = 1$ inside this interval and starts to deviate from unity at its edges. For the MI, the RWs may appear anywhere within the computational box $L^{(MI)} = 256\pi$; together with the observation time for the soliton gas case $\Delta T^{(SG)} = 50$, this yields $\Delta T^{(MI)} = 26$ and the time interval $t \in [174, 200]$ for the MI.

The rational breather solution of the first order (RBS1)—the Peregrine breather [7]—reads as

$$\psi_p^{(1)}(x, t) = e^{it}\left[1 - \frac{4(1 + 2it)}{1 + 2x^2 + 4t^2}\right] \tag{5}$$

The RBS of the second order (RBS2) $\psi_p^{(2)}$ is too complex and we refer the reader to [8] where it was first found. Both solutions describe localized in space and in time perturbations that evolve on a finite background–the condensate–and lead to three-fold and five-fold increase in the overall amplitude at the time of their maximum elevation. For approximation of a RW with a RBS, we use the scaling, translation and gauge symmetries of the 1D-NLSE: indeed, if $u(x, t)$ is a solution of **Eq. 1**, then $A_0 e^{i\Theta} \cdot u(\chi, \tau)$, where $\chi = A_0(x - x_0)$, $\tau = A_0^2(t - t_0)$, and $A_0, \Theta \in \mathbb{R}$, is also a solution. Technically, we detect the maximum amplitude A of a RW together with its position x_0 and time t_0 of occurrence, and also the phase at the maximum amplitude $\Theta = \arg\psi(x_0, t_0)$, and then use the scaling coefficient $A_0 = -A/3$ for the RBS1 and $A_0 = A/5$ for the RBS2.

Note that, in general, RBS may have nonzero velocity $v \neq 0$. To account its influence, one can make a transformation $u(x, t) \to e^{ivx/2 - iv^2 t/4} \cdot u(x - vt, t)$, which also prompts a simple way to find the velocity. Indeed, at the time of the maximum elevation t_0, a RBS with zero velocity, $v = 0$, has constant phase $\arg\psi(x, t_0) = const$ in the region between the two zeros closest to the maximum amplitude. In contrast, a RBS with nonzero velocity, $v \neq 0$, has constant phase slope, $\arg\psi(x, t_0) - vx/2 = const$, in the same region. Hence, by computing the phase slope one can approximate RWs with RBS of nonzero velocity. For all the RWs studied in this paper, we have checked that taking into account velocity improves our approximations only very slightly, and for this reason we have decided to use RBS with zero velocity only.

Also note that in addition to the RBS1 and the RBS2, we have examined approximation with the RBS of the 3rd order [8]; as well. However, we have found that it works worse than either the RBS1, or the RBS2 for all 2000 examined RWs, and thereby excluded it from the analysis.

3 Rogue Waves With Rational Profiles

We start this Section with description of one RW event for the soliton gas case, and then continue with examination of RW properties for both systems–the noise-induced MI close to its asymptotic stationary state and the soliton gas representing the solitonic model of this state.

An example of one of the 10 largest RWs collected for the soliton gas case is shown in **Figure 1**. The space profile $|\psi(x, t_0)|$ and the phase $\arg\psi(x, t_0)$ at the time of the maximum elevation $t_0 \approx 39.2$ are demonstrated in **Figure 1A**, the temporal evolution of the maximum amplitude $\max_x|\psi|$—in **Figure 1B**, and the space-time representation of the amplitude $|\psi(x, t)|$ near the RW event–in **Figure 1C**. As indicated in the figures, the space profile $|\psi(x, t_0)|$ and the maximum amplitude $\max_x|\psi|$ are very well approximated by the amplitude-scaled RBS2, and the space-time representation strongly resembles that of the RBS2 as well. At the time of the maximum elevation, the RBS2 has four zeros; the RW presented in **Figure 1** also has four local minimums that are very close to zero and where the phase $\arg\psi(x, t_0)$ jumps approximately by π, see **Figure 1A**. Note that the phase is practically constant between the two local minimums closest to the maximum amplitude, as for the velocity-free RBS1 and RBS2. The described phase pattern is sometimes considered as a characteristic feature of RW formation, see [24, 25].

The deviation between a RW and its approximation with a RBS can be measured locally as

$$d_p^{(1,2)}(x, t) = \frac{|\psi - \psi_p^{(1,2)}|}{|\psi|} \tag{6}$$

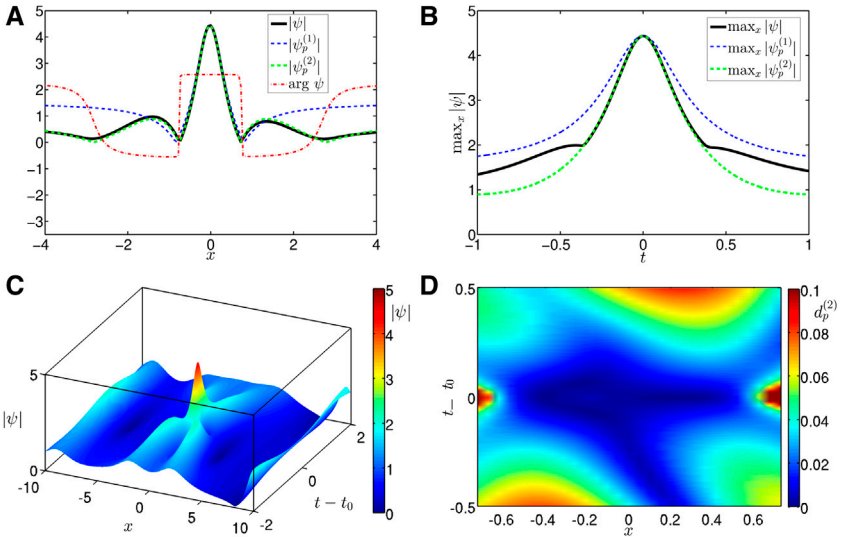

FIGURE 1 | (*Color on-line*) One of the 10 largest RWs (the coordinate of maximum amplitude is shifted to zero for better visualization) for the soliton gas case with time of occurrence $t_0 \approx 39.2$, maximum amplitude $A \approx 4.4$ and deviation **Eq. 7** from the RBS2 $\mathcal{D}_p^{(2)} \approx 0.02$: **(A)** space profile of the RW $|\psi(x,t_0)|$ at the time t_0 of its maximum elevation, **(B)** time dependency of the maximum amplitude $\max_x|\psi|$, **(C)** space-time representation of the amplitude $|\psi(x,t)|$ near the RW event, and **(D)** relative deviation **Eq. 6** between the wavefield and the fit with the RBS2 in the (x,t)-plane. In the panel **(A)**, the thick black and the thin dash-dot red lines indicate the space profile $|\psi(x,t_0)|$ and the phase $\arg\psi(x,t_0)$. In the panels **(A,B)**, the dashed blue and green lines show the fits with the RBS1 and the RBS2, respectively. In the panel **(D)**, the deviations $d_p^{(2)} \geq 0.1$ are demonstrated with constant deep red color.

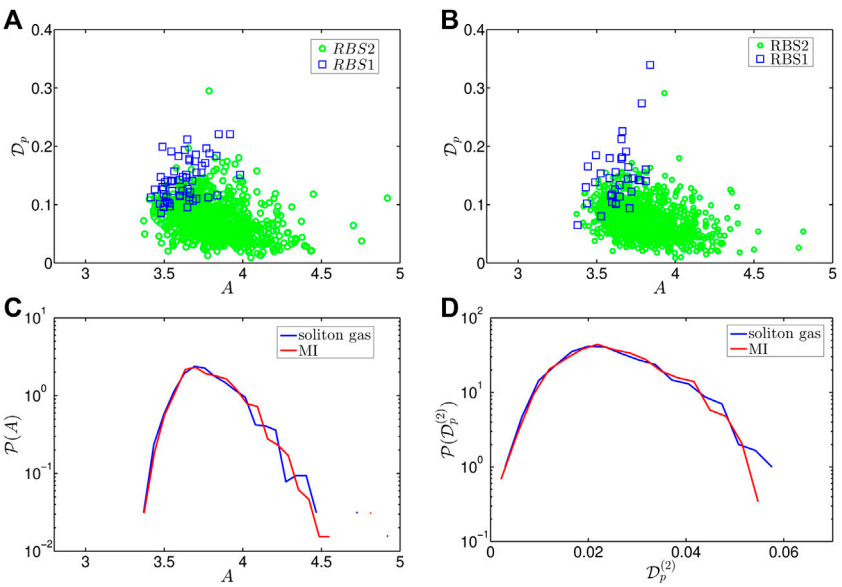

FIGURE 2 | (*Color on-line*) **(A,B)** Deviation $\mathcal{D}_p = \min\{\mathcal{D}_p^{(1)}, \mathcal{D}_p^{(2)}\}$ between RWs and their best fits with either the RBS1 or the RBS2 vs. the maximum amplitude A of the RW: **(A)** for the soliton gas and **(B)** for the MI of the condensate close to its statistically stationary state. The blue squares indicate that the best fit is achieved with the RBS1 and the green circles–with the RBS2. **(C,D)** The PDFs of **(C)** the maximum amplitude A for all the RWs and **(D)** the deviation $\mathcal{D}_p^{(2)}$ for the RWs better approximated with the RBS2, for the soliton gas (blue) and the MI of the condensate close to its statistically stationary state (red).

Figure 1D shows this deviation $d_p^{(2)}$ for the RBS2 in the (x,t)-plane: in space–between the two local minimums closest to the maximum amplitude $x \in \Omega$, and in time–in the interval $t - t_0 \in [-0.5, 0.5]$, since outside of it the maximum amplitude noticeably deviates from the fit with the RBS2 in **Figure 1C**. The deviation $d_p^{(2)}$ remains well within 5% for most of the area demonstrated in the figure, so that the RBS2 turns out to be a very good approximation for the presented RW–simultaneously in space and in time.

As an integral measure reflecting the deviation between a RW and a RBS, one can consider a quantity

$$\mathcal{D}_p^{(1,2)} = \left[\frac{\int_{x\in\Omega}\int_{t_0-\Delta T}^{t_0+\Delta T}\left|\psi-\psi_p^{(1,2)}\right|^2 dxdt}{\int_{x\in\Omega}\int_{t_0-\Delta T}^{t_0+\Delta T}\left|\psi\right|^2 dxdt}\right]^{1/2} \quad (7)$$

Here we choose the region of integration over time $t \in [t_0 - \Delta T, t_0 + \Delta T]$ from the condition that at $t_0 \pm \Delta T$ the RBS2 fit halves its maximum amplitude. Indeed, as demonstrated below, the collected RWs have maximum amplitudes roughly between 3.3 and 5, and their halving translates the waves below the RW threshold $|\psi| > 2.8$, see e.g., [19]; also, for most of the RWs, the best fit is the RBS2. For the RW presented in **Figure 1**, the interval of integration in time is $|t - t_0| \leq 0.31$ and the deviations are $\mathcal{D}_p^{(1)} \approx 0.2$ for the RBS1 and $\mathcal{D}_p^{(2)} \approx 0.02$ for the RBS2.

The quantity **Eq. 7** can be used to assess how well a RW can be approximated by a RBS. **Figure 2A** shows the minimum deviation $\mathcal{D}_p = \min\{\mathcal{D}_p^{(1)}, \mathcal{D}_p^{(2)}\}$ vs. the maximum amplitude of the RW $A = \max|\psi|$ for all 1,000 RWs collected for the soliton gas case; the RWs better approximated with the RBS1 are indicated with the blue squares and those with the RBS2—with the green circles. For 57 RWs the best fit turns out to be the RBS1—the Peregrine breather, while the other 943 RWs are better approximated by the RBS2. According to our observations, the value of the deviation **Eq. 7** below 0.05 typically means that such a RW is very well approximated with the corresponding RBS; for $0.05 \lesssim \mathcal{D}_p^{(1,2)} \lesssim 0.1$ the approximation is satisfactory, and for $\mathcal{D}_p^{(1,2)} \gtrsim 0.1$—poor. Of 57 RWs better approximated with the RBS1, only four have deviations below 0.1 and none–below 0.05; hence, approximation with the RBS1 turns out to be satisfactory at best. For the RBS2 we have completely different picture: 768 RWs show deviations from the RBS2 below 0.1 and 220—below 0.05. As demonstrated in **Figure 2A**, larger RWs are typically better approximated with the RBS2. In particular, of 143 RWs having maximum amplitude above 4, 68 have deviation from the RBS2 below 0.05, and the mean deviation for the entire group of 143 RWs is $\langle\mathcal{D}_p^{(2)}\rangle \approx 0.055$. Hence, we can conclude that the largest RWs are typically very well approximated by the RBS2.

RWs collected close to the statistically stationary state of the noise-induced MI show the same general properties as those for the soliton gas case. **Figure 2B** demonstrates very similar "clouds" of RWs approximated with either the RBS1, or the RBS2 on the diagram representing the minimum deviation $\mathcal{D}_p$ vs. the maximum amplitude A. Of 1,000 RWs in total, 36 are better approximated with the RBS1 and 964—with the RBS2. Of those better approximated with the RBS1, only three have deviations below 0.1 and none–below 0.05. Of 964 RWs better approximated with the RBS2, 792 have deviations below 0.1 and 215—below 0.05. In total, 150 RWs have amplitudes above four; out of them, 64 have deviation from the RBS2 below 0.05, and the mean deviation among the group of 150 RWs equals to $\langle\mathcal{D}_p^{(2)}\rangle \approx 0.059$.

The RWs for the two types of initial conditions turn out to be practically identically distributed by their maximum amplitude, as demonstrated in **Figure 2C** with the corresponding probability density functions (PDFs). The PDFs of the deviation $\mathcal{D}_p^{(2)}$ for the RWs better approximated by the RBS2 (green circles in **Figures 2A**,**B**) are also nearly identical, **Figure 2D**. Hence, we conclude that the largest RWs for the two systems show practically identical dynamical (resemblance with the RBS2) and statistical properties. Note that we have repeated simulations for the MI case with smaller and larger 1) computational boxes and 2) time windows for collecting the RWs. As a result, we have obtained the PDF of the maximum amplitude shifted to smaller or larger amplitudes, respectively. The nearly perfect correspondence of the two PDFs in **Figure 2C** additionally justifies the usage of the simulation parameters discussed in the previous Section.

4 DISCUSSION AND FUTURE DIRECTIONS

As we have mentioned in [21]; some two- and three-soliton collisions at the time of their maximum elevation have space profiles remarkably similar to those of the RBS1 and the RBS2. Moreover, we have presented an example of a phase-synchronized three-soliton collision, for which both the space profile and the temporal evolution of the maximum amplitude are very well approximated by the RBS2. The solitons in [21] had nonzero velocities; here we modify the two- and three-soliton examples for the case of zero velocities and also examine the local deviations $d_p^{(1,2)}(x,t)$ **Eq. 6** together with the integral deviations $\mathcal{D}_p^{(1,2)}$ **Eq. 7**.

Figure 3 shows an example of three-soliton interaction with solitons having amplitudes $a_1 = 1$, $a_2 = 1.5$ and $a_3 = 2$, zero velocities $v_j = 0$, zero space position parameters $x_{0j} = 0$ and, at the initial time $t = 0$, zero phases $\Theta_j = 0$. The space profile $|\psi(x,t_0)|$ at the time of the maximum elevation $t_0 = 0$ is remarkably similar to that of the RBS2, and the local deviation $d_p^{(2)}(x,t)$ remains well within 5% for most of the area presented in the figure as well. The integral deviation **Eq. 7** equals to $\mathcal{D}_p^{(2)} \approx 0.016$, that is even smaller than for the RW presented in **Figure 1**.

To analyze how often phase-synchronized interactions of two and three solitons of various amplitudes may lead to such quasi-rational profiles, we have created 20 two-soliton and 20 three-soliton interactions with solitons of random amplitudes, zero velocities $v_j = 0$, zero space positions parameters $x_{0j} = 0$ and phases $\Theta_j = 0$. For the two-soliton interactions, the minimum deviations from the RBS1 and the RBS2 turned out to be $\mathcal{D}_p^{(1)} \approx 0.077$ and $\mathcal{D}_p^{(2)} \approx 0.061$, and the average ones—$\langle\mathcal{D}_p^{(1)}\rangle \approx 0.14$ and $\langle\mathcal{D}_p^{(2)}\rangle \approx 0.075$, respectively. For the three-soliton case, the minimum deviations were $\mathcal{D}_p^{(1)} \approx 0.18$ and $\mathcal{D}_p^{(2)} \approx 0.003$, and the average ones—$\langle\mathcal{D}_p^{(1)}\rangle \approx 0.23$ and $\langle\mathcal{D}_p^{(2)}\rangle \approx 0.022$; the maximum deviation from the RBS2 equaled to $\mathcal{D}_p^{(2)} \approx 0.03$, that is still very good for comparison with the RBS2. Hence, we conclude that quasi-rational profiles very similar to that of the RBS2 appear already for three-soliton interactions, provided that the solitons are properly synchronized (that is, have coinciding positions and phases).

We think that the presented elementary three-soliton model might provide an explanation of RW formation inside multi-soliton solutions. The most direct way for future studies might be a demonstration of a RW for synchronized many-soliton solution. Here, however, we face a new question, that is, whether formation of a RW is a collective phenomenon that requires synchronization of all the solitons, or a "local" event that can be achieved by synchronizing of a few with arbitrary parameters of the others. Note that even the latter case represents a challenging problem. Indeed, the few solitons that generate a RW

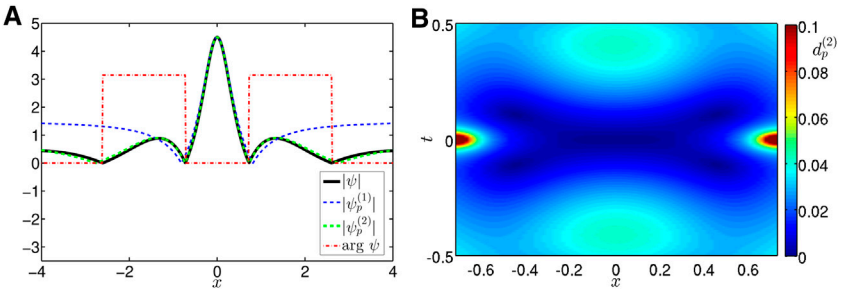

FIGURE 3 | (*Color on-line*) Synchronized three-soliton interaction of solitons having amplitudes $a_1 = 1$, $a_2 = 1.5$ and $a_3 = 2$, zero velocities $v_j = 0$, zero space positions parameters $x_{0j} = 0$ and, at the initial time $t = 0$, zero phases $\Theta_j = 0$: **(A)** space profile $|\psi(x, t_0)|$ and phase $\arg\psi(x, t_0)$ at the time of the maximum elevation $t_0 = 0$, and **(B)** relative deviation **Eq. 6** between the wavefield and the fit with the RBS2 in the (x, t)-plane. All notations are the same as in **Figures 1A,D**. The deviation **Eq. 7** from the RBS2 fit equals to $\mathcal{D}_p^{(2)} \approx 0.016$.

acquire space and phase shifts due to the presence of the remaining solitons, that should influence their optimal synchronization condition. For remote solitons, the shifts can be computed analytically using the well-known asymptotic formulas, see e.g., [14]; which however do not work for our case of a dense soliton gas where all solitons effectively interact with each other. This leaves us two options: 1) a local numerical synchronization of a small group with "trial and error" method and 2) calculation of generalized space-phase shifts for closely located solitons. Both ways seem challenging at the moment.

Also note that our study is limited with respect to statistical analysis of RWs, as we have focused on the largest RWs, while the "common" RWs may have different dynamical and statistical properties. Nevertheless, we believe that, since the largest RWs for the two systems show identical properties, the "common" RWs have identical properties too. Identification of all the RWs according to the standard criterion $A \geq 2.8$ is a nontrivial problem by itself, and we plan to return to it in the near future.

5 CONCLUSION

In this brief report we have presented our observations of RWs within the 1D-NLSE model for 1) the modulationally unstable plane wave at its long-time statistically stationary state and 2) the bound-state multi-soliton solutions representing the solitonic model of this state. Focusing our analysis on the largest RWs, we have found their practically identical dynamical and statistical properties for both systems. In particular, most of the RWs turn out to be very well approximated–simultaneously in space and in time–by the amplitude-scaled rational breather solution of the second order (RBS2), see **Figures 1**, **2** and the two sets of the collected RWs are identically distributed by their maximum amplitude and deviation from the RBS2, see **Figures 2C**,D. Additionally, we have demonstrated the appearance of quasi-rational profiles very similar to that of the RBS2 already for synchronized three-soliton interactions, see e.g., **Figure 3**.

The main messages of the present paper can be summarized as follows. First, a quasi-rational profile very similar to a RBS does not necessarily mean emergence of the corresponding rational breather, as it can be a manifestation of a multi-soliton interaction. Second, the identical dynamical and statistical properties of RWs collected for the two examined systems strongly suggest that the main mechanism of RW formation should be the same, i.e., that RWs emerging in the asymptotic stationary state of the MI (and, possibly, in other strongly nonlinear wavefields) are formed as interaction of solitons. However, more study is necessary to clarify exactly how interaction of solitons within a large wavefield may lead to formation of a RW, and we plan to continue this research in the future.

As future directions of our studies, we consider two problems. The first is about examination of whether formation of a RW in a soliton gas is a collective phenomenon that requires synchronization of all the solitons, or a "local" event that can be achieved by synchronizing of a few. The second problem relates to statistical analysis of all the RWs according to the standard criterion $A > 2.8$, in contrast to the largest RWs analyzed in this paper.

DATA AVAILABILITY STATEMENT

The raw data supporting the conclusions of this article will be made available by the authors, without undue reservation.

AUTHOR CONTRIBUTIONS

All authors contributed significantly to this work.

FUNDING

The work of DA on simulations and data analysis was supported by the state assignment of IO RAS, Grant No. 0128-2021-0003. The work of AG on generation of multi-soliton solutions and two- and three-soliton models was supported by RFBR Grant No. 19-31-60028.

ACKNOWLEDGMENTS

Simulations were performed at the Novosibirsk Supercomputer Center (NSU).

REFERENCES

1. Kharif C, and Pelinovsky E. Physical mechanisms of the rogue wave phenomenon. *Eur J Mech—B/Fluids* (2003) 22:603–34. doi:10.1016/j.euromechflu.2003.09.002
2. Dysthe K, Krogstad HE, and Müller P. Oceanic rogue waves. *Annu Rev Fluid Mech* (2008) 40:287–310. doi:10.1146/annurev.fluid.40.111406.102203
3. Onorato M, Residori S, Bortolozzo U, Montina A, and Arecchi FT. Rogue waves and their generating mechanisms in different physical contexts. *Phys Rep* (2013) 528:47–89. doi:10.1016/j.physrep.2013.03.001
4. Dysthe KB, and Trulsen K. Note on breather type solutions of the NLS as models for freak-waves. *Physica Scripta*, T82 (1999) 48. doi:10.1238/physica.topical.082a00048
5. Osborne A. *Nonlinear ocean waves and the inverse scattering transform*. Cambridge, MA: Academic Press (2010).
6. Shrira VI, and Geogjaev VV. What makes the peregrine soliton so special as a prototype of freak waves?. *J Eng Math* (2010) 67:11–22. doi:10.1007/s10665-009-9347-2
7. Peregrine DH. Water waves, nonlinear Schrödinger equations and their solutions. *J Aust Math Soc Ser B, Appl. Math* (1983) 25:16–43. doi:10.1017/s0334270000003891
8. Akhmediev N, Ankiewicz A, and Soto-Crespo JM. Rogue waves and rational solutions of the nonlinear Schrödinger equation. *Phys Rev E* (2009) 80:026601. doi:10.1103/physreve.80.026601
9. Kibler B, Fatome J, Finot C, Millot G, Dias F, Genty G, et al. The Peregrine soliton in nonlinear fibre optics. *Nat Phys* (2010) 6:790. doi:10.1038/nphys1740
10. Chabchoub A, Hoffmann NP, and Akhmediev N. Rogue wave observation in a water wave tank. *Phys Rev Lett* (2011) 106:204502. doi:10.1103/physrevlett.106.204502
11. Bailung H, Sharma SK, and Nakamura Y. Observation of Peregrine solitons in a multicomponent plasma with negative ions. *Phys Rev Lett* (2011) 107:255005. doi:10.1103/physrevlett.107.255005
12. Chabchoub A, Hoffmann N, Onorato M, and Akhmediev N. Super rogue waves: observation of a higher-order breather in water waves. *Phys Rev X* (2012) 2:011015. doi:10.1103/physrevx.2.011015
13. Chabchoub A, Hoffmann N, Onorato M, Slunyaev A, Sergeeva A, Pelinovsky E, et al. Observation of a hierarchy of up to fifth-order rogue waves in a water tank. *Phys Rev E* (2012) 86:056601. doi:10.1103/physreve.86.056601
14. Novikov S, Manakov SV, Pitaevskii LP, and Zakharov VE. *Theory of solitons: the inverse scattering method*. Berlin, Germany: Springer Science and Business Media (1984).
15. Gelash A, Agafontsev D, Zakharov V, El G, Randoux S, and Suret P. Bound state soliton gas dynamics underlying the noise-induced modulational instability. *Phys Rev Lett* (2019) 123:234102. doi:10.1103/physrevlett.123.234102
16. Belokolos ED, Bobenko AI, Enol'skii VZ, Its AR, and Matveev VB. *Algebro-geometric approach to nonlinear integrable equations*. Berlin, Germany: Springer-Verlag (1994).
17. Bobenko AI, and Klein C. *Computational approach to Riemann surfaces*. Berlin, Germany: Springer Science and Business Media (2011).
18. El GA, Krylov AL, Molchanov SA, and Venakides S. Soliton turbulence as a thermodynamic limit of stochastic soliton lattices. *Physica D: Nonlinear Phenomena* (2001) 152-153:653–64. doi:10.1016/s0167-2789(01)00198-1
19. Agafontsev DS, and Zakharov VE. Integrable turbulence and formation of rogue waves. *Nonlinearity* (2015) 28:2791. doi:10.1088/0951-7715/28/8/2791
20. Zakharov VE, and Mikhailov AV. Relativistically invariant two-dimensional models of field theory which are integrable by means of the inverse scattering problem method. *Soviet Phys JETP* (1978) 47:1017–1027.
21. Gelash AA, and Agafontsev DS. Strongly interacting soliton gas and formation of rogue waves. *Phys Rev E* (2018) 98:042210. doi:10.1103/physreve.98.042210
22. Zakharov VE, and Shabat AB. Exact theory of two-dimensional self-focusing and one-dimensional self-modulation of waves in nonlinear media. *Soviet Phys JETP* (1972) 34:62.
23. Lewis ZV. Semiclassical solutions of the Zaharov-Shabat scattering problem for phase modulated potentials. *Phys Lett A* (1985) 112:99–103. doi:10.1016/0375-9601(85)90665-6
24. Kedziora DJ, Ankiewicz A, and Akhmediev N. The phase patterns of higher-order rogue waves. *J Opt* (2013) 15:064011. doi:10.1088/2040-8978/15/6/064011
25. Xu G, Hammani K, Chabchoub A, Dudley JM, Kibler B, and Finot C. Phase evolution of Peregrine-like breathers in optics and hydrodynamics. *Phys Rev E* (2019) 99:012207. doi:10.1103/physreve.99.012207

Conflict of Interest: The authors declare that the research was conducted in the absence of any commercial or financial relationships that could be construed as a potential conflict of interest.

frontiers in Physics

ORIGINAL RESEARCH
published: 13 April 2021
doi: 10.3389/fphy.2021.622303

Directional Coherent Wave Group From an Assimilated Non-linear Wavefield

Takuji Waseda[1], Shogo Watanabe[1], Wataru Fujimoto[2], Takehiko Nose[1], Tsubasa Kodaira[1] and Amin Chabchoub[3,4]*

[1] Graduate School of Frontier Sciences, The University of Tokyo, Kashiwa, Japan, [2] Nippon Kaiji Kyokai (ClassNK), Tokyo, Japan, [3] Centre for Wind, Waves and Water, School of Civil Engineering, The University of Sydney, Sydney, NSW, Australia, [4] Marine Studies Institute, The University of Sydney, Sydney, NSW, Australia

The presence of coherent wave groups in the ocean has been so far postulated but still lacks evidence other than the indication from the radar images. Here, we attempt to reconstruct a wave field to monitor the evolution of a directional wave group based on a phase resolving two-dimensional non-linear wave model constrained by the stereo images of the ocean surface. The reconstructed wave field of around 20 wavelength squared revealed a coherent wave group compact in both propagating and transverse directions. The envelope of the wave group seems to be oriented obliquely to the propagation direction, somewhat resembling the directional soliton that was theoretically predicted and experimentally and numerically reproduced recently. A comparison with a constrained linear wave model demonstrated the coherence of the non-linear wave group that propagates for tens of wavelengths. The study elaborates a possibility of a spatially coherent short crested wave group in the directional sea.

Keywords: ocean waves, wave groups, observational tower, stereo imaging, higher-order spectral method, data assimilation, non-linear Schrödinger equation, directional envelope soliton

OPEN ACCESS

Edited by:
Xinping Zhang,
Beijing University of Technology, China

Reviewed by:
Alfred R. Osborne,
Non-linear Waves Research Corporation, United States
Filippo Bergamasco,
Ca' Foscari University of Venice, Italy
Guillaume Ducrozet,
Ecole Centrale de Nantes, France

****Correspondence:***
Takuji Waseda
waseda@k.u-tokyo.ac.jp

Specialty section:
This article was submitted to Optics and Photonics, a section of the journal Frontiers in Physics

Received: *28 October 2020*
Accepted: *24 February 2021*
Published: *13 April 2021*

Citation:
Waseda T, Watanabe S, Fujimoto W, Nose T, Kodaira T and Chabchoub A (2021) Directional Coherent Wave Group From an Assimilated Non-linear Wavefield. Front. Phys. 9:622303. doi: 10.3389/fphy.2021.622303

INTRODUCTION

Wave groups in the ocean have been recognized as early as in the 1970s in shallow and deep waters [1, 2] based on the analysis of time series data and spatial image. Concurrently, the formation of the long-crested wave groups has been postulated based on the non-linear Schrödinger equation (NLSE) and their existence was demonstrated numerically and experimentally [3, 4]. In reality, ocean waves are short-crested, but the long-crested wave envelope dynamics have been employed to explain the presence of wave groups, particularly in association with the generation mechanism of freak or rogue waves [5–7], somewhat disregarding the nature of the short-crested wind-wave field. As such, the key to understand the ocean waves, especially in the context of extremes, is to show the presence of coherent two-dimensional wave groups. A recent study by Chabchoub et al. [8] employed an innovative scheme of transforming the 2D+T NLSE into a 1D+pseudo time NLSE and vice-versa thus, allowing the application of a known solution of the long-crested (1D+T) NLSE to model a short-crested two-dimensional wave group. As a result, an oblique wave group, oriented at an angle to the propagation direction, is formed, as suggested in the theoretical study [9]. This theoretical conjecture of this short-crested wave field has been proven in an experiment in a directional wave tank [10].

However, up to now, the evidence of a coherent two-dimensional wave group in the ocean is missing. Stereo imaging of ocean waves is a promising and proven technology to capture a three-dimensional wave field [11]. The limitation is that it can only capture an area covering a few wavelengths. A new data assimilation scheme called SWEAD (Surface Wave reconstruction by Ensemble Adjoint-free Data assimilation) has been recently proposed to combine the stereo images with the phase-resolving non-linear wave model to extrapolate the surface elevation reconstructed from stereo images [12]. The validity of the scheme was demonstrated by a twin-experiment using the Higher-Order Spectral Method which is now becoming a standard tool to evaluate the phase-resolved processes based on the spectral wave model output [13–19]. HOSM is also exploited in data assimilation for RADAR observation [20, 21]. Unlike these studies that assimilates observations of the same size as the model, SWEAD incorporates observation matrix to handle observed data considerably smaller in size than the number of HOSM grids.

This paper reports the first successful implementation of the SWEAD [12] to reconstruct a wave field, which analyzes the stereo reconstructed wave field and extends the estimated wave field to an area 900 times larger (30 by 30) than the observation. By a careful look at the reconstructed wave field, a coherent wave group whose envelope is oriented obliquely to the wave propagation direction was discovered and was shown to resemble the directional soliton [8]. The ocean tower observation by the stereo camera and the data assimilation scheme is introduced in section Observation and data assimilation. The reconstructed wave field and the identified wave group therein are presented in section Observation of Coherent Wave Group. The comparison to the analytical solution and the linear wave field are discussed in section Discussion. Conclusion follows.

OBSERVATION AND DATA ASSIMILATION

Hiratsuka Tower Observation

An observation by stereo camera system was conducted at the Hiratsuka Oceanographic Experiment Station of the University of Tokyo located at the depth of 20 m, 1 km south of the Hiratsuka beach in the north of the Sagami-Bay in Japan (35.305467°N, 139.345815°E). A stereo camera system (3.92 m apart) pointing southwest is in operation since April 2017. The camera at 16 m altitude is pointing down imaging a trapezoidal area of height around 80 m (**Figure 1** left). The surface elevation was reconstructed using WASS (Waves Acquisition Stereo System) [22]. Validation of the stereo reconstructed wave field was made during a field campaign from Sep. 1 to Oct. 2, 2018 employing four different types of wave sensors (ultrasound wave gauge at the tower, two wave-riders outside of the stereo imaging region, and bottom-mounted ADCP within the stereo imaging region) [23]. The details of the stereo imaging system and the stereo reconstruction are reported therein and will be omitted from this paper.

The typical wave condition at the Hiratsuka tower is a swell system from the south. The wind-sea tends to be large for southerly wind with unlimited fetch whereas, for northerly wind, the wind-sea tends to be smaller due to limited fetch and the wave system tends to be mixed with swells propagating from the south. On Sep. 22, a swell of significant wave height ∼0.6 m and peak wave period ∼6.8 s (or ∼70 m wavelength) propagated from the south (**Figure 1** right). The wind-sea generated by the 8.1 m/s NNE wind was propagating against the swell. A small spectral peak may represent the wind-sea, but its energy was quite low. The spectra from the five sensors agree well-considering that they are not necessarily collocated. The spectrum from the ADCP measurement (magenta) appears closest to the stereo camera-based spectrum (black) as they are collocated. Sample time-series from the ADCP and the stereo camera are compared (**Figure 2**). The phases seem to match quite well but some peak values seem to deviate. This particular case was chosen for further analysis as the stereo camera images were intact.

Surface Wave Reconstruction by Ensemble Adjoint-Free Data Assimilation (SWEAD)

Surface Wave reconstruction by Ensemble Adjoint-free Data assimilation (SWEAD) was applied to the stereo images of Sep. 22, 2018. A 300 s image sequence was selected from the 20-min record and was assimilated into the phase resolving wave model. SWEAD is a scheme to reconstruct a surface wave field by assimilating observational data to a phase-resolved non-linear wave model HOSM (Higher-Order Spectral Method) [12, 24]. An efficient data assimilation scheme called the adjoint-free data assimilation (a4DVar) [25] was extended to a free surface water wave problem. The HOSM is a flexible solver of the free surface water wave in a periodic domain that can vary the order of non-linearity. As aforementioned, the method is widely used and documented; the details of the HOSM is omitted. In this study, the non-linear order of HOSM $M = 3$ was chosen such that the four-wave resonant interactions are incorporated.

The procedure of SWEAD is summarized here. The aim is to find the initial phases of the Fourier coefficients of the surface elevation $\hat{\boldsymbol{\eta}}_{\mathbf{0}}(\mathbf{k})$ whose modulus is given a priori by the directional spectra from the stereo reconstruction. Hereafter, $\hat{\boldsymbol{\eta}}_{\mathbf{0}}(\mathbf{k})$ is represented as $\mathbf{x_0}$ denoting the initial condition. The cost function $J(\mathbf{x_0})$

$$J(\mathbf{x_0}) = \frac{1}{2}\left(\mathbf{H}(\mathbf{x_0}) - \mathbf{y}\right)^{\mathbf{T}} \mathbf{R}^{-\mathbf{1}} \left(\mathbf{H}(\mathbf{x_0}) - \mathbf{y}\right) + \frac{1}{2}(\mathbf{x_0} - \mathbf{x}_b)^{\mathbf{T}} \mathbf{B}^{-\mathbf{1}} (\mathbf{x_0} - \mathbf{x}_b), \quad (1)$$

is minimized wisely circumventing the use of an adjoint model to estimate its gradient. Here, $\mathbf{H}(\mathbf{x_0})$ is the model-data projection operator, $\mathbf{y}$ is the observational data from the stereo images, and $\mathbf{R}$ is the observation error covariance. Under the framework of Gaussian statistics, the error statistics of the initial condition $\mathbf{x_0}$ is represented by the background error covariance matrix $\mathbf{B}$. The gradient of the cost function is approximated as:

$$\mathbf{P}^{\mathbf{T}} \nabla J \approx \delta \mathbf{Y}^{\mathbf{T}} \mathbf{R}^{-\mathbf{1}} \left(\mathbf{H}(\mathbf{x_0}) - \mathbf{y}\right) + \mathbf{P}^{\mathbf{T}} \mathbf{B}^{-\mathbf{1}} (\mathbf{x_0} - \mathbf{x}_b) \quad (2)$$

where the adjoint of the Jacobian matrix $\mathbf{H}$ is approximated by the perturbed ensemble model run outputs: $\mathbf{P}^{\mathbf{T}}\mathbf{H}^{\mathbf{T}} \approx \delta \mathbf{Y}^{\mathbf{T}}$, where $\mathbf{P}$ contains the orthogonal perturbation vectors and $\delta\mathbf{Y}$

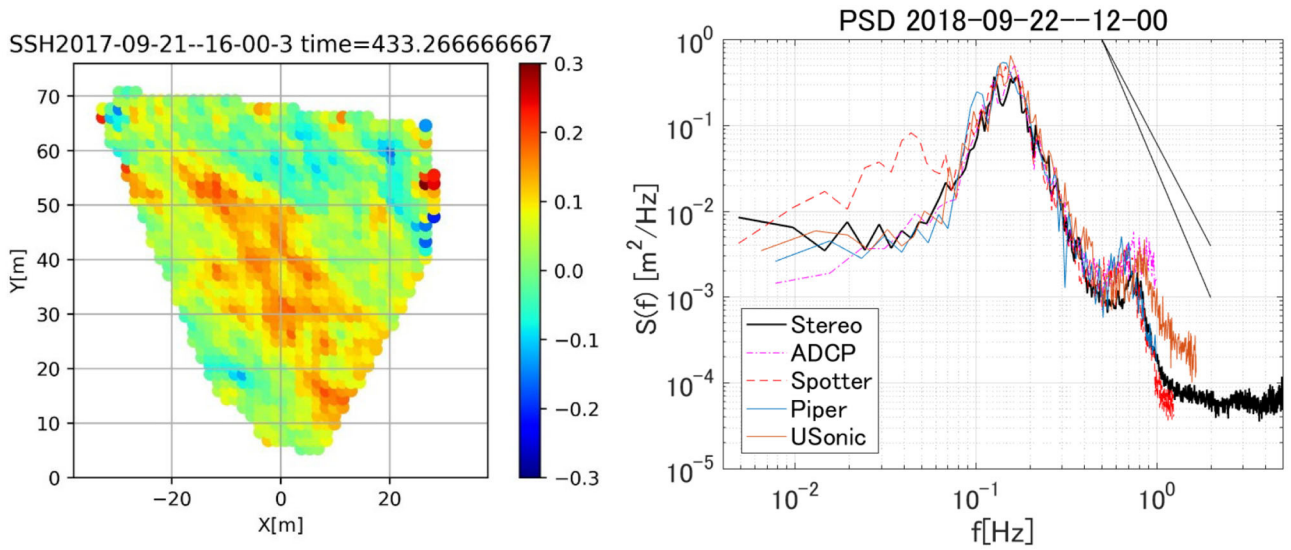

FIGURE 1 | (left) Example of the snapshot of the stereo reconstructed wave field. Note the camera is pointing southeast; (right) Wave spectra from the Stereo camera system (black), bottom-mounted ADCP (magenta), wave rider (Spotter, red), wave rider (Piper, blue), and Ultrasonic at the Hiratsuka tower (orange). The straight solid lines indicate the f^{-4} and f^{-5} slopes. The sampling rates of stereo camera system, ADCP, Spotter, Piper, and Ultrasonic wave gauges are, 10.0, 2.0, 2.5, 2.0, 3.0 Hz, respectively. The averaged periodograms were obtained with the degrees of freedom ranging between 12 and 18.

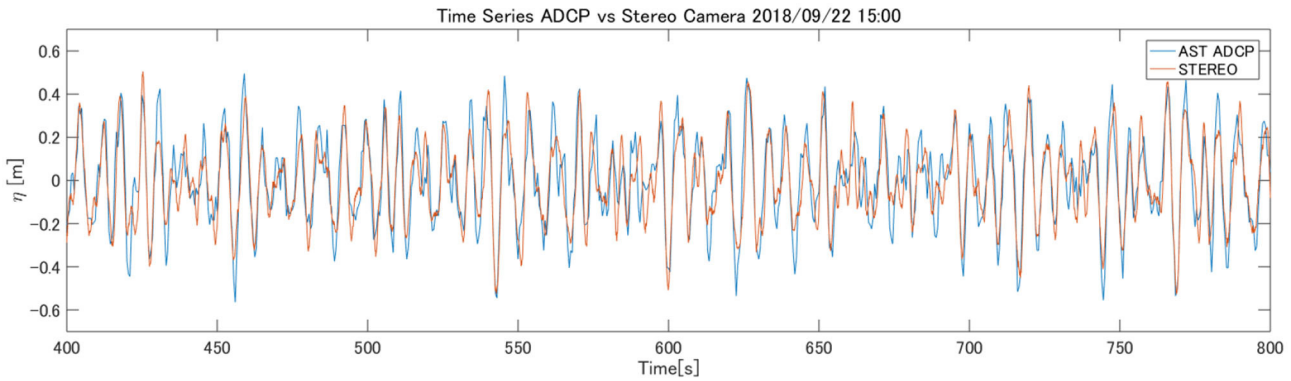

FIGURE 2 | Time series comparison of the surface elevation of the collocated ADCP (blue) and the stereo-reconstruction (red).

the associated model increments. Further simplification is made by updating the control variable as $\mathbf{x_0}+\mathbf{Ps}$ where the weighting function is determined solving equation (3) at each iteration:

$$\left(\delta\mathbf{Y}^{\mathrm{T}}\mathbf{R}^{-1}\delta\mathbf{Y}+\mathbf{P}^{\mathrm{T}}\mathbf{B}^{-1}\mathbf{P}\right)\mathbf{s}=\delta\mathbf{Y}^{\mathrm{T}}\mathbf{R}^{-1}\left(\mathbf{y}-\mathbf{H}\left(\mathbf{x_0}\right)\right)-\mathbf{P}^{\mathrm{T}}\mathbf{B}^{-1}\left(\mathbf{x_0}-\mathbf{x}_b\right). \quad (3)$$

Further improvement of the a4DVar made the method more stable. We took advantage of the spectral constraint and imposed a secant condition. Various parameters were carefully determined before the actual implementation of SWEAD. The details of these procedures are given in [12, 24].

From the stereo image analysis, the error covariance matrix $\mathbf{R}$ was estimated as $R_{ii} = \frac{\sigma_{ii}^2}{n_{ii}}$ where σ_{ii} represents the standard deviation of the stereo image estimates within a 1.5 m by 1.5 m grid, and n_{ii} is the number of samples per grid. Note that the data assimilation was made for the mean value of the surface elevation of each 1.5 m by 1.5 m grid.

The domain size of HOSM used in this study is 2.6426 km by 2.6426 km, with 1,024 times 1,024 grid points. The integration time step is 0.1 s and the integration period is 350 s following the non-linear spin-up of 50 s. For the case introduced in section Hiratsuka Tower Observation, the peak wave period of 6.8 s, the domain size corresponds to about 40 wavelengths, and the integration period to 50 wave periods. The HOSM wave field was initialized based on the spectrum from the stereo images with random phases, and the initial phases were determined conducting 400 perturbed ensemble runs that were repeated for 19 iterations minimizing the cost function [23, 26]. The

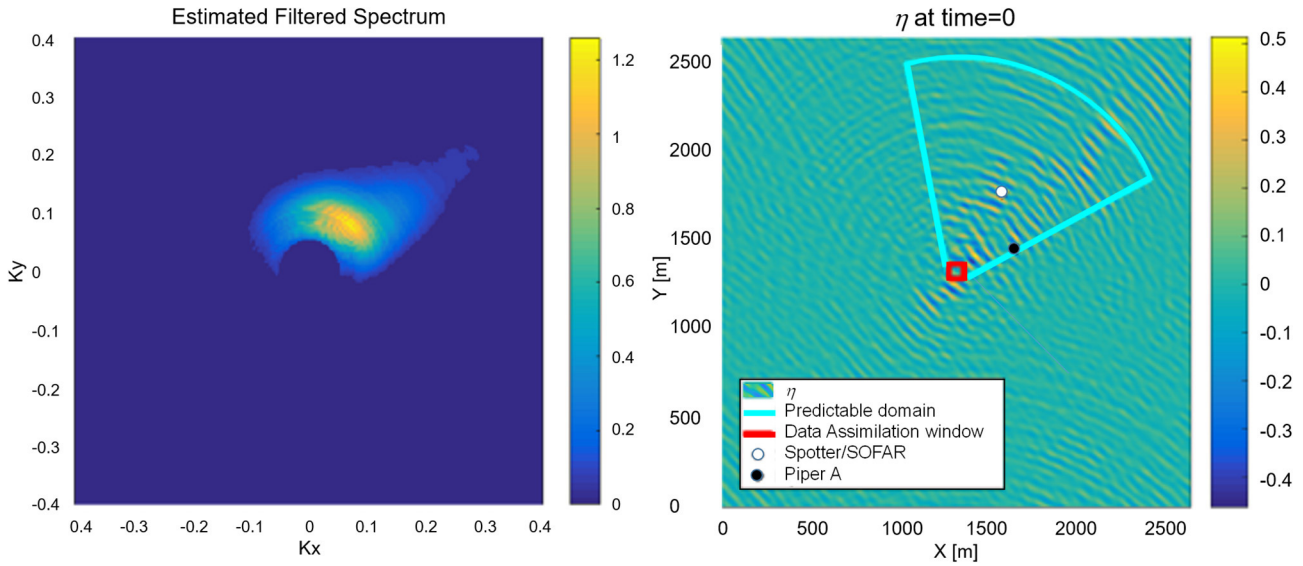

FIGURE 3 | (left) Directional spectrum estimated from the 20-min stereo image sequence. The wave numbers $\boldsymbol{k_x}$ and $\boldsymbol{k_y}$ are oriented along the image coordinate. A high-pass filter with cutoff frequency of 0.1 Hz was applied. Spectral density <5 % of the peak spectral density was removed as well. (right) Initial condition of the analysis wave field by SWEAD. The red box indicates where the stereo images were taken. The markers represent the locations of the surface wave buoys. The predictable zone for the 300 s image sequence is indicated by cyan line.

magnitude of the first term of the cost function (1) reduced by 1/7 after eight iterations and slowly reduced to about 1/10 in nineteen iterations. With the large number of ensemble members (400), one iteration took about three and half hour wall clock time using the Oakforest-PACS Supercomputer System of the University of Tokyo using 12 nodes (one node has 68 cores). The domain size (1,024 by 1,024 and 40 wavelengths square) and the number of ensemble members (400) were determined based on the original study by Fujimoto [24] in balance of the predictable region and the computational efficiency.

OBSERVATION OF COHERENT WAVE GROUP

Initial Wave Field and Reconstructed Waves

Based on the directional spectrum from the stereo imaging system (**Figure 3** left), the initial wavefield $\boldsymbol{\eta_0}(x, y)$ was estimated using SWEAD (**Figure 3**, right panel). The wave field in **Figure 3** right is mapped south-up and the dominant wave is propagating from the southwest. The directional spectrum was estimated by discrete Fourier transformation of the reconstructed wave field and was averaged over the entire 20-min image sequence. Because the directional spectrum was estimated from an area of 80 m square, waves longer than the domain size tended to be ambiguous in direction and therefore a high-pass filter was applied at 0.1 Hz. Spectral density <5 % of the peak spectral density was removed as well. Nevertheless, the directional spectrum tended to be broad in direction, and therefore, the waves tended to propagate into the stereo imaging area from all the directions. Those spurious waves appear in the initial wave field as a circular pattern. The dominant wave components are propagating from the southwest or the upper right quadrant of **Figure 3** right. It is also noticeable that there is not much energy downstream (northeast, or the lower left quadrant). This is because for the 300 s stereo reconstructed image sequence, the predictable zone [27] is restricted to a circular sector (enclosed by cyan lines in **Figure 3** right) extending to the southwest from the stereo imaging region. The waves in this area will focus on the stereo imaging domain and well-reproduced the wave record (**Figure 4**). The predictable zone was estimated for wave components with a spectral density higher than 30 % of the peak spectral density, thereby neglecting the waves coming from the opposite direction to the dominant swell. The SWEAD is not restricted to analyzing a uni-directional spectrum.

Reconstructed Directional Wave Group

From the 300 s reconstructed wave field, we have looked into the wave field upstream of the stereo imaging area within the predictable zone (**Figure 3** right). At first sight, it appears that the waves tend to form a beam where the energy is confined to a finite crest length. This is partly because SWEAD does not impose a constraint of the homogeneity of the wave energy and therefore the waves are absent from the area outside of the predictable zone. However, it is plausible that non-linearity is acting against the dispersion and thereby retaining the short crestedness of the wave train.

Notable evolution of the group-like feature was detected (**Figure 5**). The image coordinate is rotated clockwise by about 40 degrees from the original (**Figure 3**) such that the wave group is propagating from right to left. The crest line is confined in the transverse direction, and the boundary seems

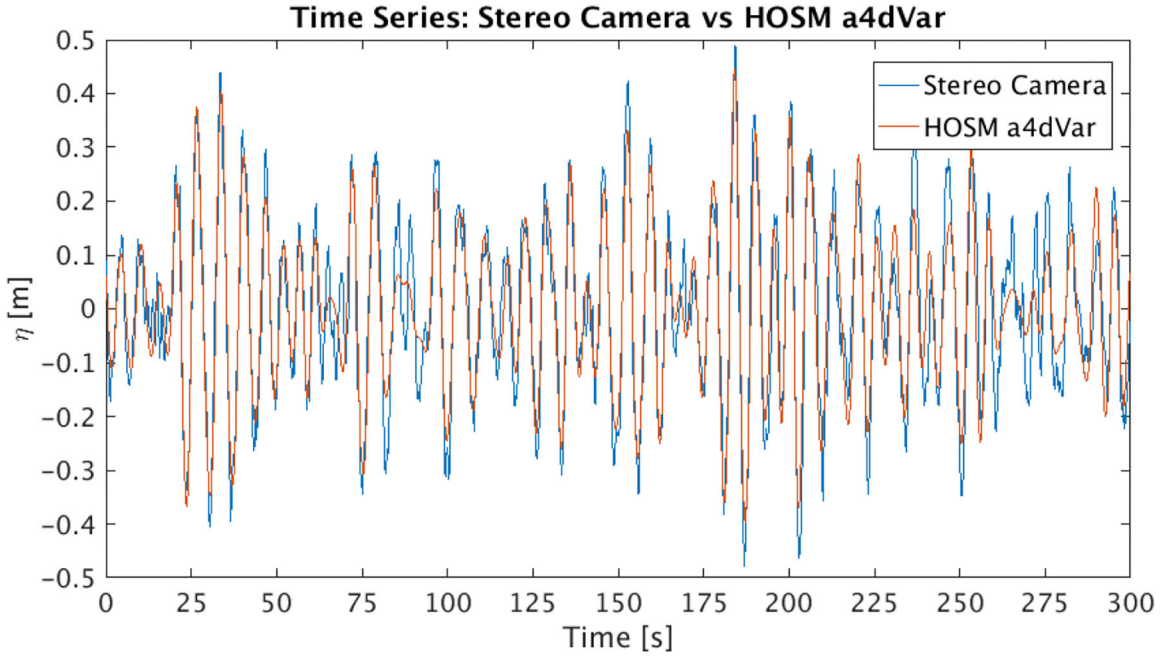

FIGURE 4 | Comparison of the surface elevation time series in the middle of the stereo imaging area; the blue line is from the stereo camera, and the red line is the reconstructed time series by SWEAD.

inclined against the propagation. The directional wave group seems coherent throughout the sequence of about 60 s shown in **Figure 5**. The animation of the evolving wave field is provided as **Supplementary Material**.

The propagation of the detected wave group is visualized by a waterfall diagram of the wave profile along a diagonal line connecting (1,300 m, 1,300 m) and (1,700 m, 1,700 m) in **Figure 3** for 80 s (**Figure 6**). The propagation of a coherent wave group is evident. The estimated propagation speed of the wave group is about 4.6 m/s which corresponds to a 5.9 s wave period. The estimated wave period roughly corresponds to the dominant wave in the observed spectrum (**Figure 1**). Unlike the directional soliton studied in Chabchoub et al. [8], the observed wave group is confined in the propagation direction as well. Long-crested envelope solitons are known to be unstable to transverse perturbation (e.g., [28]). The reconstructed wave field indicated a possible existence of a coherent directional wave group confined in both propagating and transverse directions. From the reconstructed wave field, the peak amplitude of the wave group is estimated to be around 0.5–0.6 m which corresponds to a local steepness of $A_0k_0{\sim}0.06$.

DISCUSSION

Directional Coherent Wave Group

The theoretical framework of the directional wave group follows Chabchoub et al. [8]. By applying a coordinate transformation, $T = t\cos\theta - \frac{y}{c_g}\sin\theta$, the 2D+T NLSE reduces to a 1D+T NLSE in which stable planar wave solutions exist. Then, interestingly enough, in the original coordinate, the solution appears to have a slanted envelope and the wave train becomes short-crested. The observed directional wave group somewhat resembles the directional soliton reproduced in a directional wave tank, which is parametrized as:

$$A(x,y,t) = A_0\,\mathrm{sech}\left[A_0k_0\sqrt{\frac{1}{2\left(1-3\sin^2\theta\right)}}\left\{\left(\omega_0 t\cos\theta + 2k_0 y\sin\theta\right) + 2k_0 x\cos\theta\right\}\right]\exp\left[-i\frac{\left(A_0k_0\right)^2}{2}k_0x\right] \tag{4}$$

The surface elevation field given by $\eta(x,y,t) = \mathrm{Re}\left[A(x,y,t)\exp\left\{i\left(k_0x+\omega_0t\right)\right\}\right]$ is shown as an example in **Figure 7** for the case of $\boldsymbol{\theta = -\pi/6}$. Note that the angle θ should not exceed 35.26° for the framework to be applied. The carrier wave is propagating from right to left and is short-crested in the transverse direction. However, the slanted envelope is unbounded.

The envelope of the SWEAD reconstructed directional wave group was truncated in the propagating direction as well. Mimicking the reconstructed wave field, the truncation of the wave envelope was artificially introduced to the directional

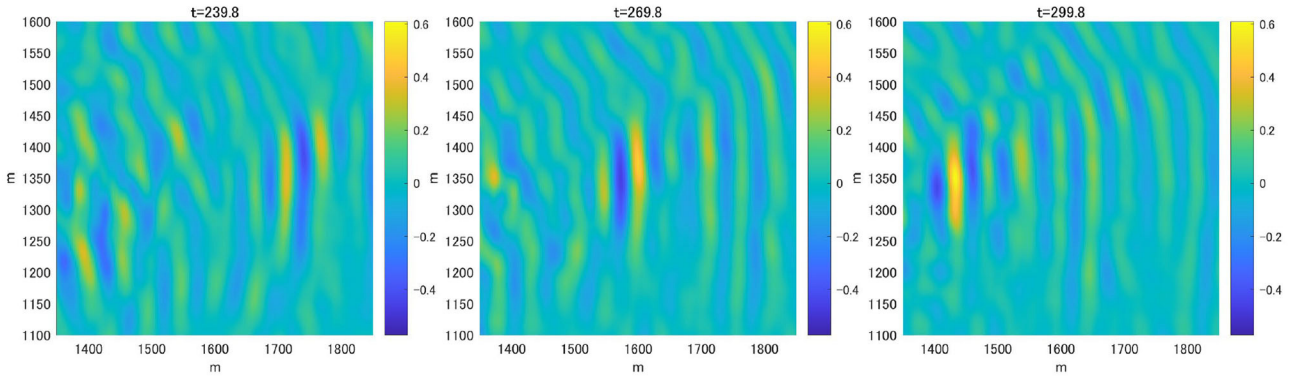

FIGURE 5 | Surface elevation contour map of the subdomain of the HOS simulation capturing a wave group. The domain covers 500 m by 500 m area, and is rotated so that the waves propagate from right to left toward the stereo imaging area. The time sequence is from left to right at 30 s interval.

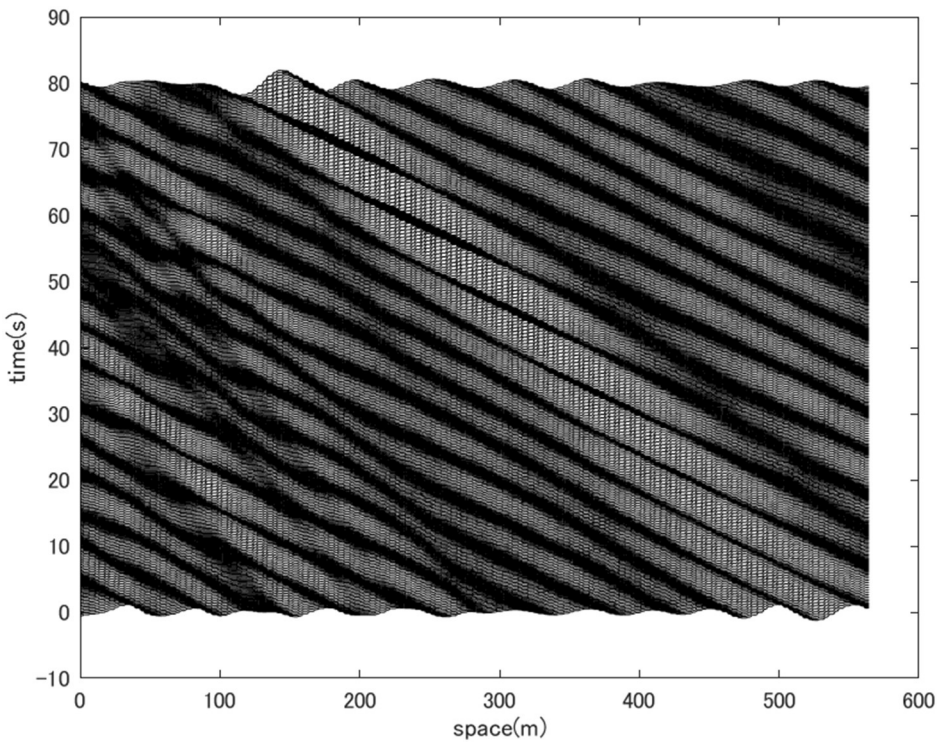

FIGURE 6 | Waterfall plots of the surface elevation profiles along a diagonal line in the wave field depicted in **Figure 3**. The line connects (1,300 m, 1,300 m) and (1,700 m, 1,700 m) and the plot is made for 80 s long. A coherent wave group is observed.

soliton solution equation (4):

$$A^{trunc.}\left(x,y,t\right) = A\left(x,y,t\right) W\left(x,t\right),$$

where,

$$W\left(x,t\right) = \begin{cases} 0 & ; x < -\frac{n\pi}{k_0} \\ \frac{k_0}{n\pi}\left(x + c_g t\right) + 1 & ; -\frac{n\pi}{k_0} \le x \le 0 \\ -\frac{k_0}{n\pi}\left(x + c_g t\right) + 1 & ; 0 \le x \le \frac{n\pi}{k_0} \\ 0 & ; x > \frac{n\pi}{k_0} \end{cases} \quad (5)$$

The $W\left(x,t\right)$ is an arbitrary function that reduces the wave energy to nil in the far-field. Here, we have chosen a triangular envelope containing n waves. The surface elevation wavefield for n=5, is shown in **Figure 8**, $\eta^{trunc.}\left(x,y,t\right) = \mathrm{Re}\left[A^{trunc.}\left(x,y,t\right)\exp\left\{i\left(k_0 x + \omega_0 t\right)\right\}\right]$. The wavefield remarkably resembles that reconstructed from the stereo images (**Figure 5**). Since $A^{trunc.}\left(x,y,t\right)$ is not a known solution of the 2D+T NLSE, in reality, its coherence due to the balance of non-linearity and dispersion remains to be tested. Nevertheless, we will show in section Comparison Against the

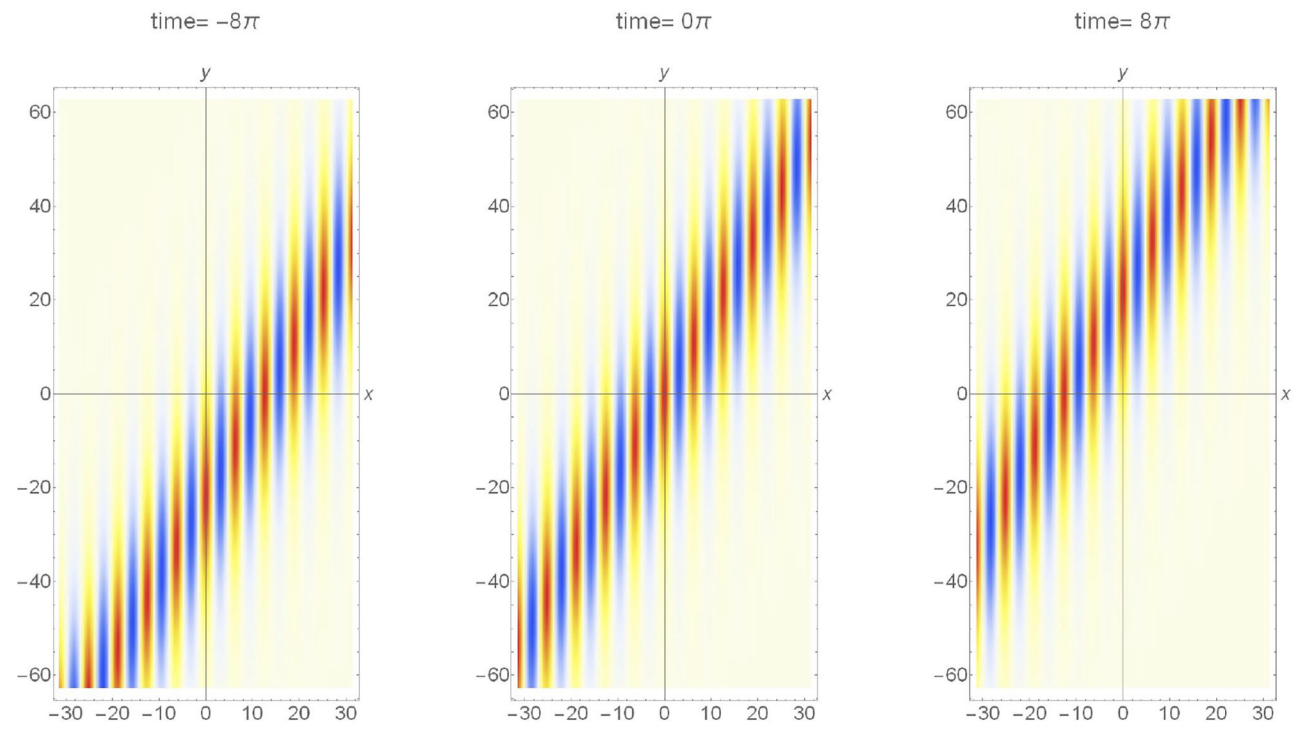

FIGURE 7 | Surface elevation map of the directional soliton [4] with obliqueness $\theta = \frac{\pi}{6}$ and the steepness $A_0 k_0 = 0.05$. The time sequence is from left to right at four-wave period interval. The wave is propagating from right to left.

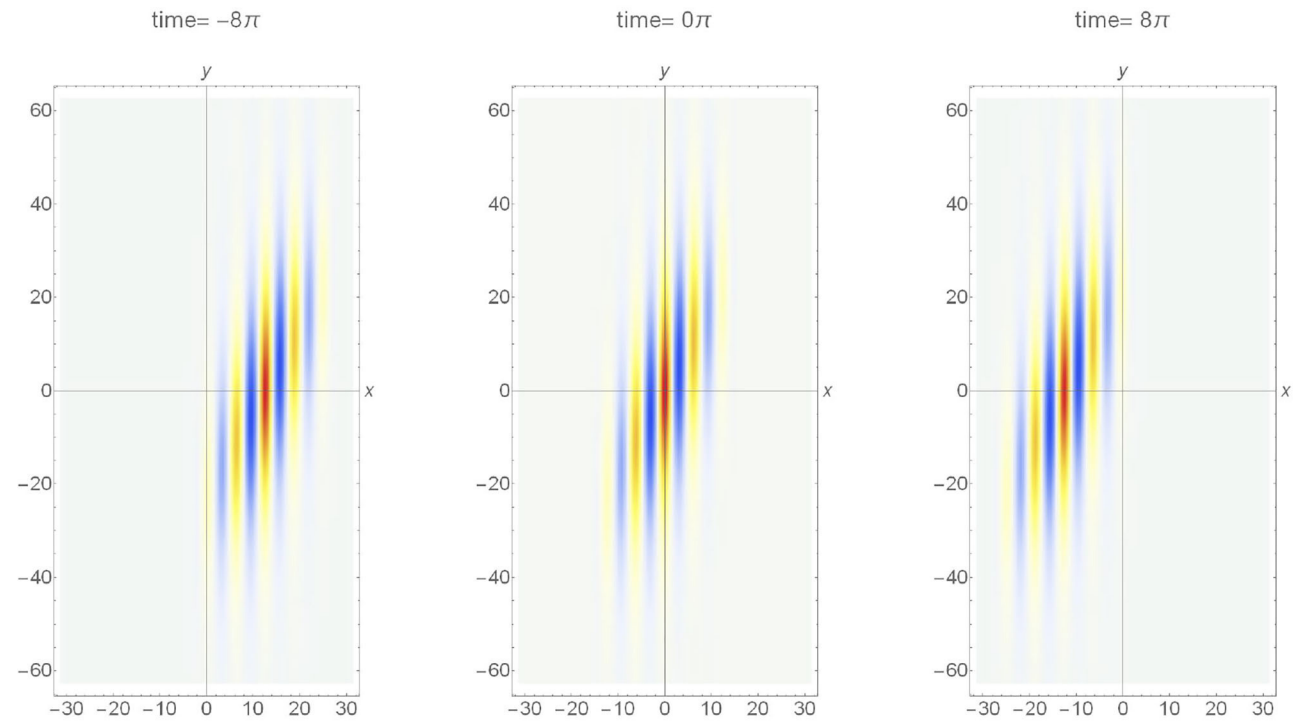

FIGURE 8 | A truncated directional soliton [5]. The number of waves in a group $n = 5$. Nomenclature is the same as **Figure 7**.

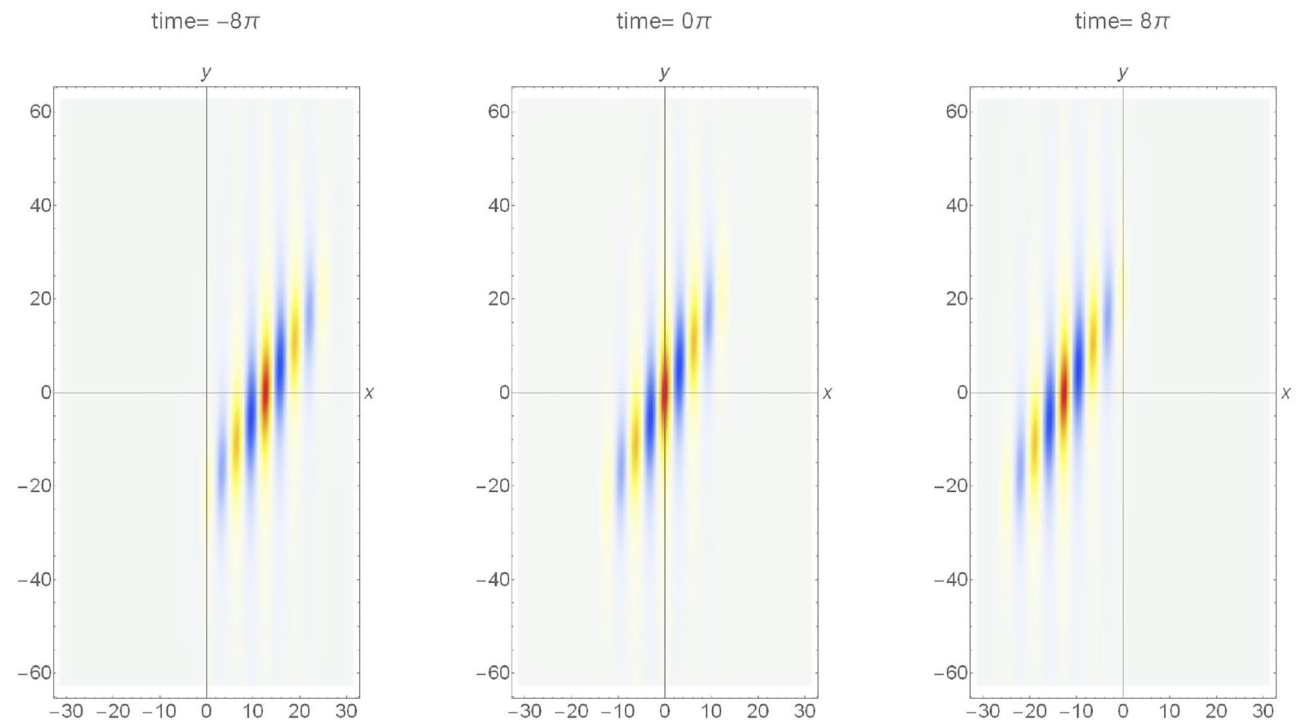

FIGURE 9 | A truncated directional Akhmediev Breather [6]. The number of waves in a group $\boldsymbol{n} = \mathbf{5}$. Nomenclature is the same as **Figure 7**.

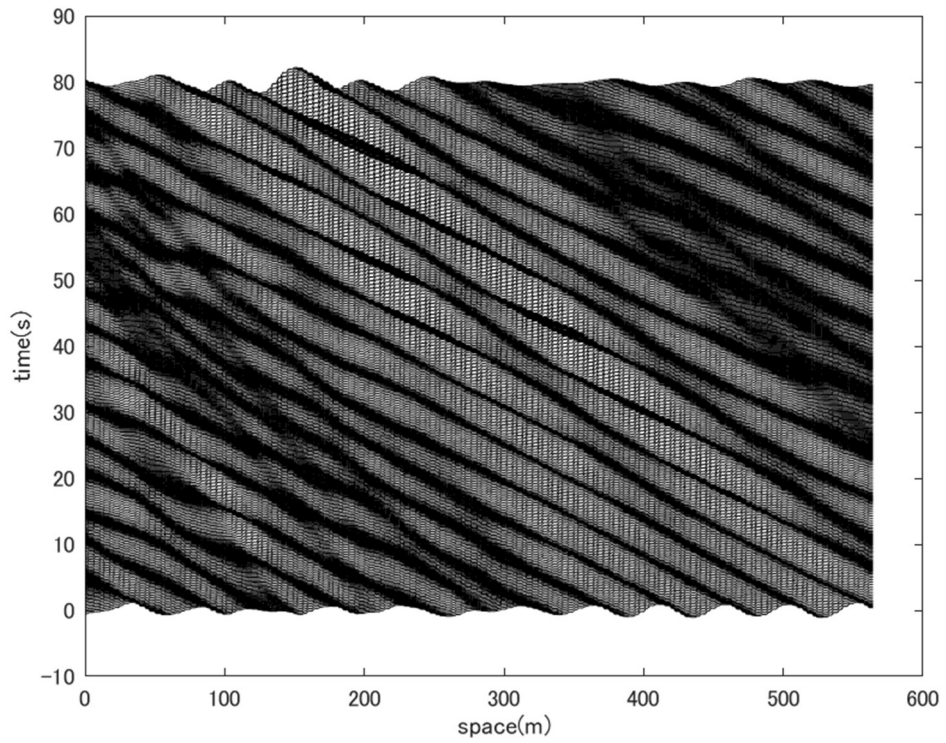

FIGURE 10 | Waterfall plots of the surface elevation profiles from an assimilated linear wave model. The wave profile is obtained along a diagonal line in the wave field depicted in **Figure 3**. The line connects (1,300 m, 1,300 m) and (1,700 m, 1,700 m) and the plot is made for 80 s long. Coherent wave group is not observed.

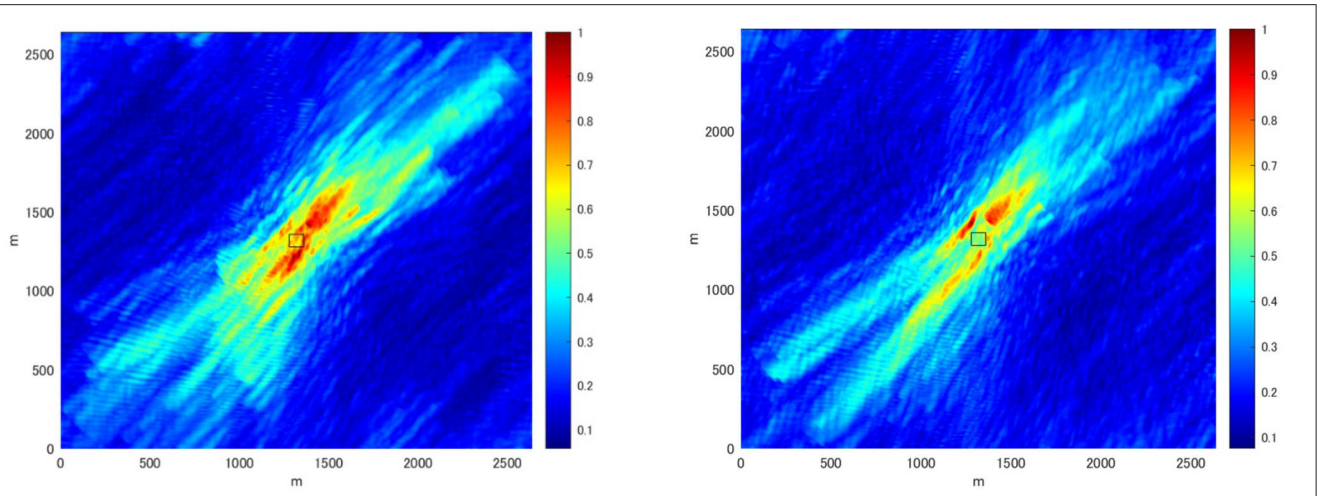

FIGURE 11 | The normalized maximum value of the surface elevation of the 300 s HOSM simulation is shown for the entire model domain (2.6426 km by 2.6426 km); in the left, non-linear ($M = 3$), and in right, linear ($M = 1$). The color map limit is from 0 to 1.0. The coherence of the wave group is depicted by the homogeneity of the maximum surface elevation along the beam. The square at the center denotes the stereo imaging area. The directional wave group was observed along 1,300 m to 1,700 m in both horizontal and vertical axes.

Linear Model, that the non-linearity was crucial in sustaining the coherence of the reconstructed directional wave group.

The directional soliton choice may be considered as too simplistic compared to other more advanced nonlinear envelope models. Examples are breathers on finite background, such as the Kuznetsov-Ma, Akhmediev or Peregrine breathers [4, 29, 30]. Given the domain limits and the absence of distinct wave focusing, we selected the envelope soliton as a reference being the fundamental stationary coherent structure allowing the nonlinear interaction with the underlying waves. Nevertheless, there is no reason not to observe how a truncated breather would look like. By applying the same coordinate transformation to the Akhmediev breather solution [29], we obtain the following expression of the diagonal breather:

$$A\left(x,y,t\right) = A_0 \exp\left[-i\left(A_0 k_0\right)^2 k_0 x\right] \left(\frac{\sqrt{2}\nu^2 \cosh\ Kx + i\sqrt{2}\sigma \sinh\ Kx}{\sqrt{2}\cosh\ Kx - \sqrt{2-\nu^2}\cos\left[\delta A_0 k_0\left(\omega_0 t\cos\theta + 2k_0 y\sin\theta + 2k_0 x\cos\theta\right)\right]}\right) \tag{6}$$

where, $\nu \equiv \delta\sqrt{1-\sin^2\theta}$, $\sigma \equiv \nu\sqrt{2-\nu^2}$, $K \equiv \left(A_0 k_0\right)^2 \sigma k_0$, and $\delta = \frac{\Omega/\omega_0}{A_0 k_0}$ representing the spectral bandwidth. Following the same steps as before, we show in **Figure 9** the surface elevation of the truncated wave train, $\eta^{trunc.}\left(x,y,t\right) = \mathrm{Re}\left[A^{trunc.}\left(x,y,t\right)\exp\left\{i\left(k_0 x + \omega_0 t\right)\right\}\right]$. We chose a small value of $\boldsymbol{\delta}$=0.0001, such that the solution approaches the Peregrine breather [30]. The resemblance of the directional Akhmediev breather to the directional soliton is striking. Although the resemblance of oblique Akhmediev/Peregrine breather, at its peak modulation, and the stationary envelope soliton is known, the implication of that to this study is noteworthy. Despite the wave field was extended to cover a large domain compared to the stereo imaging area, the domain is still not large enough to capture the full evolution of the wave group, particularly the initial disintegration of a wave train, known as the Benjamin-Feir instability [31].

Comparison Against the Linear Model

The HOSM wave field constrained by the stereo images revealed the existence of a wave group whose envelope is oblique to the propagation direction. Moreover, the analytical model of the directional envelope soliton with an artificial truncation in the propagating direction resembled the reconstructed wave group. Although this truncated directional soliton is not a known analytical solution to the 2D+T NLSE, the reconstructed wave field is a numerical solution that incorporates the third-order non-linearity and is not restricted by spectral bandwidth. To confirm that such a coherent wave field exists because of the weak non-linearity, the SWEAD was applied to the linear wave model or the HOSM simulation with $M = 1$. Note that by assimilating the stereo images, the initial condition of the linear HOSM is constrained such that the wavefield within the stereo imaging region is optimally reconstructed. What we will investigate here, however, is the difference between non-linear and linear wave models of the wave fields outside of the stereo imaging region but within the predictable region. In **Figure 10**, the evolution of the wavefield along a line connecting (1,300 m, 1,300 m) and (1,700 m, 1,700 m) of the simulated domain is shown. The coherent nature of the wave group that was found in the case of the HOSM $M = 3$ simulation has diminished with HOSM $M = 1$ despite the two solutions being strongly constrained by the same directional spectrum (**Figure 3** left).

The degree of coherence of the wave evolution becomes apparent comparing the wave fields of the entire HOSM model domain. The normalized maximum wave amplitudes are plotted in **Figure 11** for the HOSM $M = 3$ simulation (left) and the HOSM $M = 1$ simulation (right). While the reconstructed non-linear wave field (**Figure 11** left) shows a beam that extends upstream and downstream of the stereo imaging region where the energy is concentrated, the reconstructed linear wave field (**Figure 11** right) shows that the energy spreads in a broader domain. In the linear model, there are multiple beams and the energy seems to focus on the central part. If the wave groups remain coherent, it is expected that the maximum surface elevation will be homogeneous. Therefore, the high contrast of the maximum surface elevation, as seen in the linear case, implies that wave groups are not as coherent as in the non-linear case. The beam tends to weaken away from the center, and this is an artifact of the data assimilation scheme in which the predictable zone broadens away from the center. Overall, the comparison indicates that in the HOSM $M = 1$ simulation, the wave field linearly focused in the central part to reproduce the observed wave field, but coherence is less prominent than the HOSM $M = 3$ simulation. This observation is consistent with that comparing **Figures 6**, **10**.

CONCLUSION

A wave field was successfully reconstructed assimilating the stereo image sequence into a non-linear phase resolving wave model. From the reconstructed wave field, a coherent wave group was identified in which the two-dimensional wave envelope is not in alignment with the propagation direction of the carrier wave. The striking resemblance of the reconstructed directional wave group to the recently discovered directional soliton is encouraging.

The work certainly needs further improvement. Likely, the imaging area of 80 m by 80 m is not sufficient to reconstruct the wave field of the entire 2.6 km by 2.6 km model domain as the predictable region is limited by the time window of 300 s. As such, the reconstructed wave field tended to focus the energy into the stereo imaging area such that the wave field is well-reproduced within the given time window. This tendency was even more exaggerated when the linear HOSM model was used.

Nevertheless, the comparison of the non-linear and linear reconstructed wave fields elucidated the significance of the non-linearity in maintaining the coherence of the directional wave group. The kinematic properties of the wave group are realistic, with the steepness around $A_0k_0 \sim 0.06$, and contains around 5 waves in a group. This is the first time such two-dimensional coherent wave groups were identified in the ocean. The scheme of combining spatial images and non-linear wave models is promising and should be advanced by utilizing spatially wide observations such as shipborne radar images.

We were able to observe a striking similarity between the reconstructed ocean wave group with oblique NLS-type envelopes. Indeed, a truncation of the water surface elevation as modeled with an oblique form of both, envelope soliton and Akhmediev/Peregrine-type breather, by adopting the respective oblique angle, show an excellent agreement with the shape of the coherent structure in the ocean. The domain limitations were obviously a major constraint in this study for the purpose of identification of the right coherent envelope. Moreover, it was not possible to clearly identify the Benjamin-Feir instability process [31], which is a possible mechanism for the formation of ocean extreme events [7]. Nevertheless, our findings pave the way for possible soliton or breather-type rogue wave identification in the ocean [29, 32, 33]. We consequently believe that there is strong potential for observations of such pulsating envelopes in the ocean and to connect these to ocean rogue wave formations in the future.

DATA AVAILABILITY STATEMENT

The original contributions presented in this study are included in the article/**Supplementary Material**, further inquiries can be directed to the corresponding author.

AUTHOR CONTRIBUTIONS

TW, AC, and WF designed research. SW, TK, TN, AC, and TW performed research. WF, SW, TN, TK, and TW contributed new reagents and analytic tools. SW and TW analyzed data. TW, SW, TK, TN, AC, and WF wrote the paper. All authors contributed to the article and approved the submitted version.

FUNDING

TW acknowledges support from the Japan Society for the Promotion of Science KAKENHI [Grant-in-Aid for Scientific Research (A)] Grant Numbers 19H00801, 16H02429, and 25249126.

ACKNOWLEDGMENTS

Acknowledgment goes to Miguel Onorato for his insightful suggestion in the solution parametrization in the 2D+T NLSE which led us to the experimental discovery the directional soliton solution.

SUPPLEMENTARY MATERIAL

The Supplementary Material for this article can be found online at: https://www.frontiersin.org/articles/10.3389/fphy.2021.622303/full#supplementary-material

Supplementary Video 1 | Animation of the SWEAD reconstructed wave field featuring the propagation of directional wave group is provided as an AVI video.

REFERENCES

1. Sedivy DG, Thompson WC. *Ocean Wave Group Analysis (No.NPS-68SETH78091)*. Monterey: Naval Postgraduate School Monterey Calif (1978). doi: 10.5962/bhl.title.61498
2. Donelan M, Longuet-Higgins MS, Turner JS. Periodicity in whitecaps. *Nature*. (1972) 239:449. doi: 10.1038/239449a0
3. Akhmediev N, Soto-Crespo JM, Ankiewicz A. Extreme waves that appear from nowhere: on the nature of rogue waves. *Phys Lett A*. (2009) 373:2137–45. doi: 10.1016/j.physleta.2009.04.023
4. Chabchoub A, Onorato M, Akhmediev N. Hydrodynamic envelope solitons and breathers. In: *Rogue and Shock Waves in Nonlinear Dispersive Media*. Cham: Springer (2016). p. 55–87. doi: 10.1007/978-3-319-39214-1_3
5. Onorato M, Resitori S, Baronio F, editors. *Rogue and Shock Waves in Nonlinear Dispersive Media (Vol. 926)*. Hidelberg: Springer (2016). doi: 10.1007/978-3-319-39214-1
6. Dudley JM, Genty G, Dias F, Kibler B, Akhmediev N. Modulation instability, Akhmediev Breathers and continuous wave supercontinuum generation. *Opt Express*. (2019) 17:21497–508. doi: 10.1364/OE.17.021497
7. Dudley JM, Genty G, Mussot A, Chabchoub A, Dias F. Rogue waves and analogies in optics and oceanography. *Nat Rev Phys*. (2019) 1:675–89. doi: 10.1038/s42254-019-0100-0
8. Chabchoub A, Mozumi K, Hoffmann N, Babanin AV, Toffoli A, Steer JN, et al. Directional soliton and breather beams. *Proc Natl Acad Sci*. (2019) 116:9759–63. doi: 10.1073/pnas.1821970116
9. Saffman PG, Yuen HC. Stability of a plane soliton to infinitesimal two-dimensional perturbations. *Phys Fluids*. (1978) 21:1450–1. doi: 10.1063/1.862364
10. Mozumi K, Waseda T, Chabchoub A. 3D stereo imaging of abnormal waves in a wave basin. In: *International Conference on Offshore Mechanics and Arctic Engineering, Vol*. 56499. St. John's, CA: American Society of Mechanical Engineers (2015). doi: 10.1115/OMAE2015-42318
11. Benetazzo A, Barbariol F, Bergamasco F, Torsello A, Carniel S, Sclavo M. Observation of extreme sea waves in a space–time ensemble. *J Phys Oceanogr*. (2015) 45:2261–75. doi: 10.1175/JPO-D-15-0017.1
12. Fujimoto W, Waseda T. Ensemble-based variational method for nonlinear inversion of surface gravity waves. *J Atmos Ocean Technol*. (2020) 37:17–31. doi: 10.1175/JTECH-D-19-0072.1
13. West BJ, Brueckner KA, Janda RS, Milder DM, Milton RL. A new numerical method for surface hydrodynamics. *J Geophys Res*. (1987) 92:11803–24. doi: 10.1029/JC092iC11p11803
14. Toffoli A, Bitner-Gregersen E, Onorato M, Babanin AV. Wave crest and trough distributions in a broad-banded directional wave field. *Ocean Eng*. (2008) 35:1784–92. doi: 10.1016/j.oceaneng.2008.08.010
15. Bitner-Gregersen EM, Fernandez L, Lefèvre JM, Monbaliu J, Toffoli A. The North Sea Andrea storm and numerical simulations. *Nat Hazard Earth Syst Sci*. (2014) 14:1407–15. doi: 10.5194/nhess-14-1407-2014
16. Dias F, Brennan J, de León SP, Clancy C, Dudley J. Local analysis of wave fields produced from hind casted rogue wave sea states. In: *ASME 2015 34th International Conference on Ocean, Offshore and Arctic Engineering*. St. John's, CA: American Society of Mechanical Engineers (2015).
17. Trulsen K, Borge JCN, Gramstad O, Aouf L, Lefèvre JM. Crossing sea state and rogue wave probability during the Prestige accident. *J Geophys Res*. (2015) 120:7113–36. doi: 10.1002/2015JC011161
18. Fedele F, Brennan J, De León SP, Dudley J, Dias F. Real world ocean rogue waves explained without the modulational instability. *Sci Rep*. (2016) 6:27715. doi: 10.1038/srep27715
19. Fujimoto W, Waseda T, Webb A. Impact of the four-wave quasi-resonance on freak wave shapes in the ocean. *Ocean Dyn*. (2019) 69:101–21. doi: 10.1007/s10236-018-1234-9
20. Yoon S, Kim J, Choi W. An explicit data assimilation scheme for a nonlinear wave prediction model based on a pseudo-spectral method. *IEEE J Ocean Eng*. (2015) 41:112–22. doi: 10.1109/JOE.2015.2406471
21. Köllisch N, Behrendt J, Klein M, Hoffmann N. Nonlinear real time prediction of ocean surface waves. *Ocean Eng*. (2018) 157:387–400. doi: 10.1016/j.oceaneng.2018.03.048
22. Bergamasco F, Torsello A, Sclavo M, Barbariol F, Benetazzo A. WASS: an open-source pipeline for 3D stereo reconstruction of ocean waves. *Comput Geosci*. (2017) 107:28–36. doi: 10.1016/j.cageo.2017.07.001
23. Watanabe S, Fujimoto W, Nose T, Kodaira T, Davies G, Lechner D, et al. Data assimilation of the stereo reconstructed wave fields to a nonlinear phase resolved wave model. In: *International Conference on Offshore Mechanics and Arctic Engineering*. Glasgow: American Society of Mechanical Engineers (2019). doi: 10.1115/OMAE2019-95949
24. Fujimoto W. *The reproduction of freak waves by nonlinear numerical simulation* (Ph.D. Dissertation). Graduate School of Frontier Sciences, Environmental Studies Division, the University of Tokyo, Kashiwa, Japan (2017).
25. Yaremchuk M, Martin P, Koch A, Beattie C. Comparison of the adjoint and adjoint-free 4dVar assimilation of the hydrographic and velocity observations in the Adriatic Sea. *Ocean Model*. (2016) 97:129–40. doi: 10.1016/j.ocemod.2015.10.010
26. Watanabe S. *3D reconstruction of water waves by stereo imaging* (Master's Thesis). Graduate School of Frontier Sciences, Environmental Studies Division, the University of Tokyo, Kashiwa, Japan (2018).
27. Qi Y, Wu G, Liu Y, Yue D. Predictable zone for phase-resolved reconstruction and forecast of irregular waves. *Wave Motion*. (2018) 77:195–213. doi: 10.1016/j.wavemoti.2017.12.001
28. Yajima N. Stability of envelope soliton. *Prog Theor Phys*. (1974) 52:1066–7. doi: 10.1143/PTP.52.1066
29. Akhmediev NN, Ankiewicz A. *Solitons: Nonlinear Pulses and Beams*. London: Chapman and Hall (1997).
30. Peregrine DH. Water waves, nonlinear Schrödinger equations and their solutions. *ANZIAM J*. (1983) 25:16–43. doi: 10.1017/S0334270000003891
31. Benjamin TB, Feir JE. The disintegration of wave trains on deep water Part 1. Theory. *J Fluid Mech*. (1967) 27:417–30. doi: 10.1017/S002211206700045X
32. Herbst BM, Ablowitz MJ. Numerically induced chaos in the nonlinear Schrödinger equation. *Phys Rev Lett*. (1989) 62:2065. doi: 10.1103/PhysRevLett.62.2065
33. Osborne AR. Classification of homoclinic rogue wave solutions of the nonlinear Schrödinger equation. *Natural Hazards and Earth System Sciences Discussions 2.1*. (2014). p. 897–933. doi: 10.5194/nhessd-2-897-2014

Conflict of Interest: The authors declare that the research was conducted in the absence of any commercial or financial relationships that could be construed as a potential conflict of interest.

The reviewer GD declared a past co-authorship with one of the authors AC to the handling editor.

frontiers in Physics

REVIEW
published: 15 April 2021
doi: 10.3389/fphy.2021.637812

Heterodyne Optical Time Domain Reflectometer Combined With Active Loss Compensation: A Practical Tool for Investigating Fermi Pasta Ulam Recurrence Process and Breathers Dynamics in Optical Fibers

Corentin Naveau[1], *Guillaume Vanderhaegen*[1], *Pascal Szriftgiser*[1], *Gilbert Martinelli*[1], *Maxime Droques*[2], *Alexandre Kudlinski*[1], *Matteo Conforti*[1], *Stefano Trillo*[3], *Nail Akhmediev*[4] *and Arnaud Mussot*[1]*

[1]Univ. Lille, CNRS, UMR 8523-PhLAM–Physique Des Lasers Atomes Et Molécules, Lille, France, [2]Alcatel Submarine Networks, Calais, France, [3]Department of Engineering, University of Ferrara, Ferrara, Italy, [4]Optical Sciences Group, Department of Theoretical Physics, Research School of Physics, The Australian National University, Canberra, ACT, Australia

OPEN ACCESS

Edited by:
Bertrand Kibler,
UMR6303 Laboratoire Interdisciplinary Carnot De Bourgogne (ICB), France

Reviewed by:
Christophe Finot,
Université De Bourgogne, France
Miguel Gonzalez-Herraez,
University of Alcalá, Spain

***Correspondence:**
Arnaud Mussot
arnaud.mussot@univ-lille.fr

Specialty section:
This article was submitted to Optics and Photonics, a section of the journal Frontiers in Physics

Received: 04 December 2020
Accepted: 12 January 2021
Published: 15 April 2021

Citation:
Naveau C, Vanderhaegen G, Szriftgiser P, Martinelli G, Droques M, Kudlinski A, Conforti M, Trillo S, Akhmediev N and Mussot A (2021) Heterodyne Optical Time Domain Reflectometer Combined With Active Loss Compensation: A Practical Tool for Investigating Fermi Pasta Ulam Recurrence Process and Breathers Dynamics in Optical Fibers. Front. Phys. 9:637812. doi: 10.3389/fphy.2021.637812

We report recent results obtained with a novel optical fiber experimental setup based on a heterodyne optical time-domain reflectometer in the context of FPU recurrence process. Moreover, we actively compensate the dissipation of the system. We show that we can observe several FPU recurrences by monitoring the power and relative phase evolutions of the main discrete frequency components involved in the process.

Keywords: Fermi Pasta Ulam recurrence, optical fibers, modulation instability, breathers and rogue waves, heterodyne, Rayleig

1 INTRODUCTION

The Fermi-Pasta-Ulam (FPU) recurrence process describes the ability of a multimodal nonlinear system to come back to its initial state after its energy had been distributed over its modes during the evolution. It had been discovered in the 50s by Fermi and co-workers who were studying the dynamics of a chain of nonlinearly coupled oscillators [1]. The problem has been extensively studied and led to the development of a theory allowing to explain the formation of solitons by Zabusky and Kruskal in 1965 [2]. Since then, the FPU recurrence process has been especially investigated for its role in chaos [3] and for its relation with the nonlinear stage of modulation instability (MI), in the framework of nonlinear systems which can be described by the nonlinear Schrödinger equation (NLSE). In particular, it led to the development of breathers theory [4], which plays an important role in the description of rogue waves formation [5–10]. Experimentally, FPU had been observed in several fields of physics such as hydrodynamics [11] and electric transmission lines [12].

The first observation of FPU recurrence in optics has been achieved in 2001 by Van Simaeys *et al.* [13]. The main issue was to monitor the longitudinal evolution of the optical power along the fiber to confirm that the system indeed came back to its initial state. Van Simaeys *et al.* [13] succeeded via an indirect measurement method. These results attracted a lot of attention from the nonlinear scientific community with the publication of a short editorial in the prestigious Nature journal [14]. Indeed, optical fibers constitute a fantastic test bed for investigations of such complex nonlinear processes as they offer an easy tuning of initial conditions, an accurate control of fiber parameters and an accurate

characterization of the output field with sub-ten femtosecond resolution. For those reasons, this pioneering result has motivated numerous studies of FPU, breathers or rogue wave formation in fiber optics [8, 10, 15–21]. This non-exhaustive list of works highlights the strong interest for this experimental system. However, there are two main limitations in fiber optics systems. Firstly, the monitoring of the longitudinal evolution of the field is not straightforward while it is crucial in FPU recurrence investigations to unambiguously prove that the systems evolved before coming back to its initial state. Van Simaens *et al.* exploited the invariant properties of the NLSE. They used a fiber of fixed length and performed indirect distributed measurements by varying the optical power P_p instead of the distance z. This method was also used for the first observation of Peregrine soliton [16]. However, varying P_p also changes the MI frequency which scales in $\sqrt{P_p}$ so the frequency detuning of the seed has also to be varied to keep a normalized frequency detuning constant, which is not really convenient. Another set of solutions based on cut-back techniques had been reported. They are either fully destructive by cutting the fiber in several pieces [15] or by using fibers of different lengths [19] and repeating the experiments by copying the electric field characteristics to the input of the following fiber. Another approach to perform distributed measurements is the use of scattering processes, either elastic (Rayleigh) or inelastic (Brillouin), which presents the advantage of being non-invasive and offers a good resolution [22]. As an example, Brillouin optical time-domain reflectometry (OTDR) has been used [23, 24] to characterize fiber optical parametric amplifiers. Concerning OTDR based on Rayleigh scattering, it enabled the distributed measurement of one FPU recurrence via the distributed characterization of the pump and low-orders sidebands intensity when the process is coherently seeded [25] or the pump and the amplified noise intensity when it is spontaneous [26]. These options are very interesting but have the drawback to only measure power evolutions. We will see below that the knowledge of the whole electric field is crucial to accurately characterize the FPU recurrence process. The second limitation is due to dissipation, despite the ultra-low attenuation of optical fibers with the latest record of 0.1419 dB/km [27]. This is the reason why in previous experiments on FPU recurrence, most recordings had been limited to one or one and a half period of recurrence [13, 15, 23, 25, 28]. The capability to observe more than one recurrence period is of great interest to study in detail the complex dynamics of the FPU process appearing at the second compression point [29]. There is a need to develop an experimental optical fiber system enabling the monitoring of the longitudinal evolution of the electric field (phase and amplitude) without loss. Note that multiple recurrences had been observed in bulk optical systems [30], which can be considered as lossless untill a certain point, but initial conditions are trickier to tune as compared to fiber optics.

In this paper we present a review of recent results obtained with a novel optical fiber experimental setup allowing a non-invasive distributed characterization of the amplitude and phase of the main frequency components of a laser pulse train based on a heterodyne optical time domain reflectometer (HOTDR) [31]. Moreover, we implemented an active loss compensation scheme by exploiting the Raman amplification effect to get an almost fully transparent fiber [31]. Note that other groups took benefit of a recirculating loop to observe two recurrences as it was originally done in telecommunications applications to emulate long-haul fiber systems [32].

The paper is organized as follows. In the first part, we present the experimental setup. We provide detailed information on the HOTDR technique and on the active loss compensation compared to already published papers. Then we review various striking results that we recently published [33–38]. We first show a detailed characterization of the FPU recurrence, highlighting the symmetry breaking of the process [33, 35], demonstrate a record of 4 recurrences in an ultra-low loss fiber [37] and reveal the observation of A- and B-type solutions of the NLSE [36]. Then we show that a spatio-temporal evolution of the whole electrical field can be extracted from HOTDR recordings [34]. We illustrate this with the fine characterization of first and second order breathers with sub-ps resolution.

2 BASIC CONCEPTS

MI results from the amplification of weak sidebands by a strong pump wave. A numerical example is provided in **Figure 1**. As initial conditions, we used a strong pump (P_p = 450 mW), surrounded by two symmetric weak sidebands (20 dB below) located at f = 35 GHz. This frequency shift corresponds to the maximum MI gain (**Figure 1A**). These three waves are launched in the anomalous region of an optical fiber. In the early steps, the sidebands are amplified at the expense of the pump and rapidly additional side bands resulting from multiple cascaded four wave mixing processes are generated during the propagation. At about 5 km, more than twelve of these Fourier modes are generated (**Figure 1B**) and the pump is maximally depleted. This broadest spectrum corresponds to maximally compressed pulses in the temporal domain (**Figure 1C**). Then, due to the linear and nonlinear phase acquired by these waves, the energy flow is reversed back into the pump. At about 9 km, the system presents characteristics which are almost identical to initial conditions.

This behaviour is a manifestation of the FPU recurrence process. By further propagating in the fiber, the process can be repeated several times. In experiments we will aim at monitoring the evolution of the pump and sideband power evolution as well as their relative phase to characterize in detail the FPU recurrence process.

3 EXPERIMENTAL SETUP

The full experimental setup of the HOTDR we have developed is shown in **Figure 2A**. It is relatively complex and cumbersome as seen in the laboratory picture in **Figure 2B**. In the following, we will explain each element step by step.

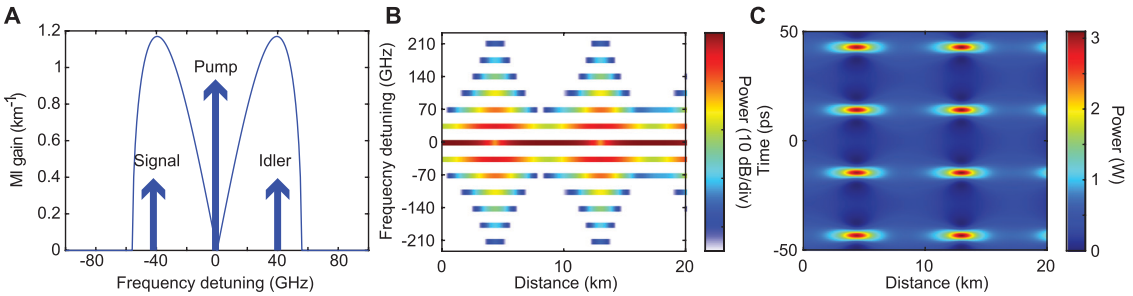

FIGURE 1 | (A) Parametric gain. **(B)** Spatio-spectral and **(C)** spatio-temporal evolutions of a modulationally unstable wave. Parameters: P_p = 450 mW, $\beta_2 = -19 \times 10^{-27}$ s^2/m, $\gamma = 1.3 \times 10^{-3}$ W/m, f = 35 GHz and the initial signal/idler (symmetric sidebands) to pump ratio is −20 dB.

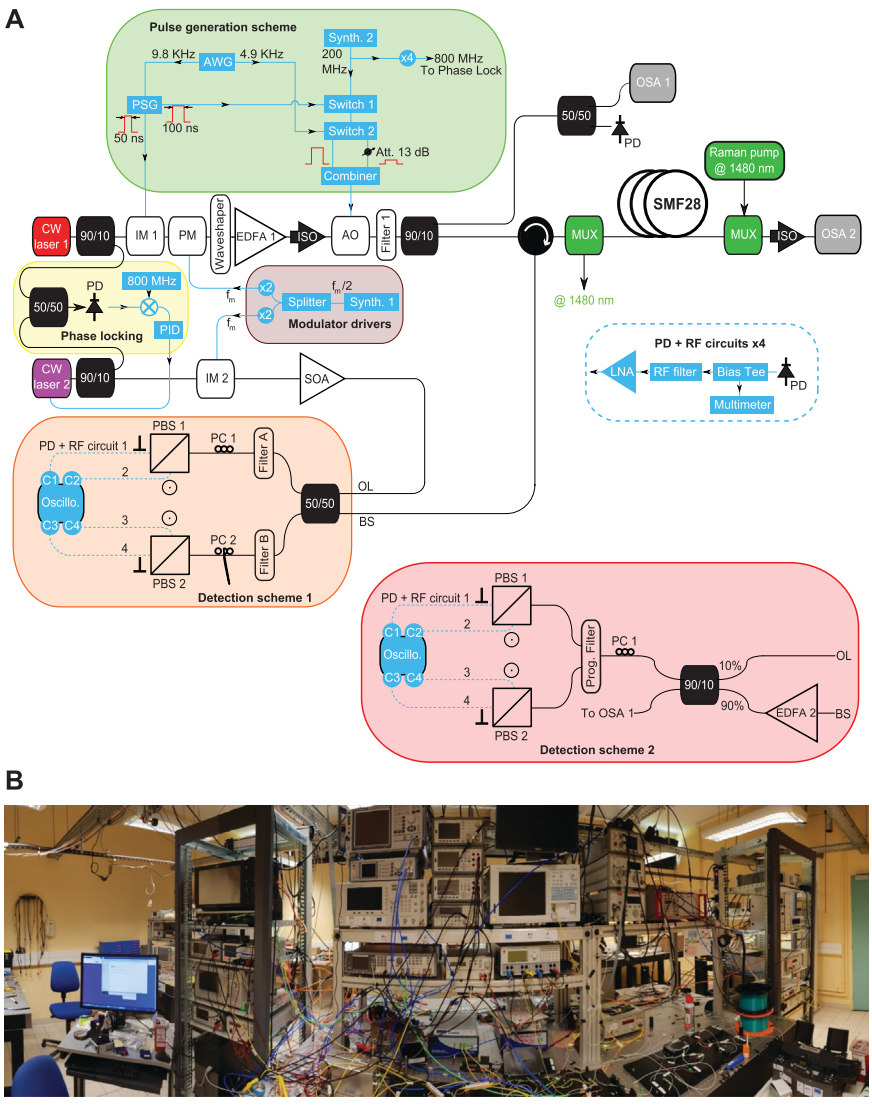

FIGURE 2 | (A) Experimental setup. Laser 1 is a narrow linewidth (100 Hz at FWHM) CW laser and laser 2 is a continuous distributed feedback laser diode. IM (1,2): intensity modulator, PM, phase modulator; AWG, arbitrary waveform generator; EDFA (1,2), erbium-doped fiber amplifier; ISO, isolator; AO, acousto-optic modulator; MUX, multiplexer or de-multiplexer; SOA, semiconductor optical amplifier; PID, proportional, integral, derivative controller; PD, photo-detector; PC, polarization controller; PBS, polarization beam splitter; RF, radio frequency; LNA, low-noize radio frequency amplifier. All instruments of the setup (including the oscilloscope) are referenced to the same 10 MHz clock. **(B)** Picture of the experiment.

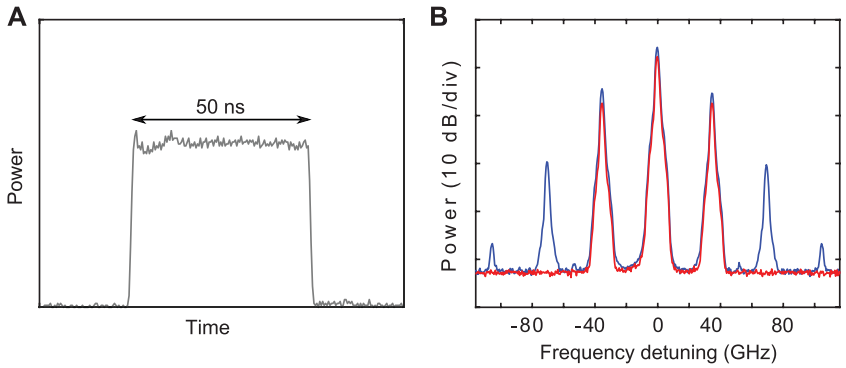

FIGURE 3 | (A) Temporal profile of the pulse. **(B)** Spectral profile of the pulses at the output of the waveshaper without any correction filter applied (blue) and with a filter applied (red).

3.1 Initial Conditions

The initial conditions we use to observe the FPU process consist of a pump and a pair of sidebands. To generate such a three-wave input, we first modulate the intensity of the CW beam delivered by laser 1 in order to get 50 ns square-shaped pulses (**Figure 3A**) at a 9.8 KHz (~ 102 ms) repetition rate (it has to be decreased when fiber length exceeds 10 *km*). To do so, an arbitrary waveform generator produces a clock at 9.8 kHz to trigger a pulse generator that delivers the RF signal driving the intensity modulator (IM1). Then, the optical pulses pass through a phase modulator (PM) to generate a frequency comb with a ~ 35 GHz line spacing. A programmable optical filter (waveshaper) with a bandwidth of 10 GHz allows us to tailor the frequency comb to select the pump, signal and idler waves and to control their relative phases. **Figure 3B** shows the spectrum at the output of the waveshaper when we do not apply any filters (blue line) and when a filter is applied to get a symmetric three waves input (red line). The unwanted harmonics are filtered out. Following the waveshaper, the pulses are amplified via an erbium-doped fiber amplifier (EDFA 1) to reach the high peak power required to trigger the FPU recurrence process (usually around 450 mW). Then the signal goes through an acousto-optic modulator with a high extinction ratio (typically higher than 50 dB) to reduce the CW background between pulses in order to mitigate the stimulated Brillouin scattering (SBS). Finally, a filter with a 1 nm bandwidth (Filter 1) removes the excess amplified spontaneous emission. The 4 GHz OSA resolution, allows us to get a signal to noise ratio of about 50 dB for the pump and 40 dB for the signal and idler (see **Figure 3B**). Finally, short squared pulses composed of a strong pump surrounded by weaker signal and idler waves with adjustable amplitude and relative phase are generated.

3.2 Local Oscillator and Phase-Locking

In order to perform phase measurements via heterodyning, the local oscillator (laser 2) has to be initially phase-locked with laser 1. To do so, we used the method described in ref. 39 based on laser difference-frequency. A 5 GHz bandwidth photodiode receives the beat note of laser 1 and 2 which is then mixed with a 800 MHz RF reference signal provided by a stable synthesizer. In order to have a beat note close to 800 MHz, the frequency of laser 2 can be coarsely tuned via its power supply. The resulting intermediate frequency goes then through a PID controller (with a response time less than 15 ns) which drives the phase of the local oscillator. The efficiency of the phase-locking can be monitored by looking at the beat signal of laser 1 and 2 on a signal analyser as shown in **Figures 4A,B**, which display the RF spectrum (with a 100 Hz resolution) of the beat signal when the locking is turned off and on, respectively. Once the lasers are phase-locked, the locking can last up to several hours. As we intend to perform measurements not only on the pump component but also on the signal/idler one, the laser 2 is modulated in intensity by IM2 to create sidebands spaced by 35 GHz so that each frequency component of interest has its own local oscillator. The RF signal driving IM2 is delivered by the same microwave source that is driving the previous phase modulator in order to ensure a fixed phase relation between them. The local oscillator is then amplified by a semiconductor optical amplifier (SOA) and the amplitude of its three main components is roughly equalized by tuning the DC bias voltage of IM2 to get similar local oscillators, as can be seen in **Figure 4C**, which shows the spectrum of the local oscillator after the SOA.

3.3 Active Loss Compensation

Linear losses have a strong influence on the FPU recurrence as illustrated in **Figure 5**. These figures display the pump and signal power evolutions for an initial signal to pump ratio of −10 dB and for $\Delta\Phi_{init} = \phi_P - \phi_S = 0$ (**Figure 5A**) or $\Delta\Phi_{init} = -\pi/2$ (**Figure 5B**) (with ϕ_P and ϕ_S the signal and pump phase respectively). We chose these specific value because they trigger the system in its two main operating regimes described by inner ($\Delta\Phi_{init} = 0$) or outer $\Delta\Phi_{init} = -\pi/2$) trajectories in the phase plane. In both cases, one can see that dissipation strongly influences the dynamic of the process. It reduces the amplitude of both pump and signal waves (**Figure 5B**) or completely disable the formation of the second recurrence (**Figure 5A**). The impact of the attenuation on the recurrent process is more or less pronounced depending on the initial relative phase, which is intrinsically linked to the complex nonlinear dynamics of the

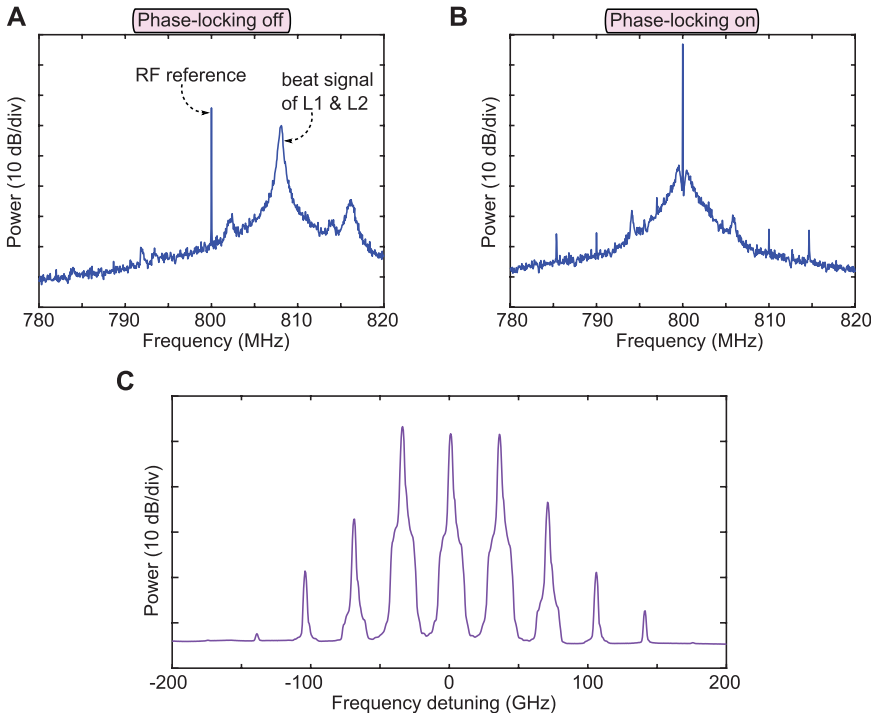

FIGURE 4 | RF spectra of the mixing of the beat signal of L1 and L2 with the 800 MHz reference when the system is **(A)** not phase-locked and **(B)** phase-locked. **(C)** Optical spectrum of the local oscillator. These three phase-locked laser lines will be used to achieve three local oscillators to analyze the pump, idler and signal waves.

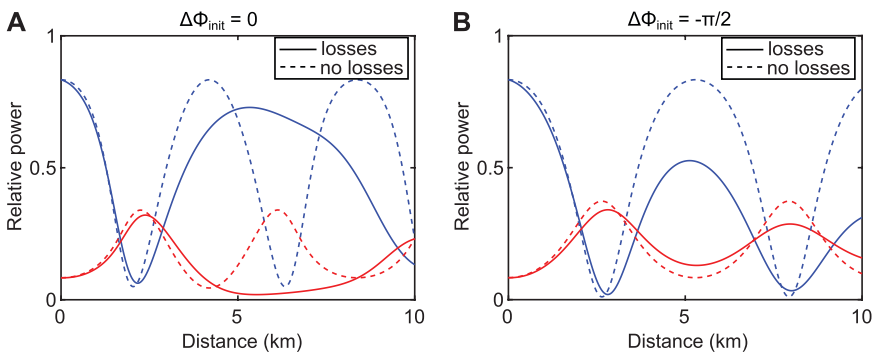

FIGURE 5 | Influence of the linear attenuation on the recurrent process. **(A)** Pump (blue lines) and signal (red lines) power evolutions for $\Delta\Phi_{init} = 0$. Solid lines correspond to the case with losses ($\alpha = 0.2$ dB/km) and dashed ones to the case without losses. **(B)** Same for $\Delta\Phi_{init} = -\pi/2$. Other parameters: $P_p = 450$ mW, $\beta_2 = -19 \times 10^{-27}$ s^2/m, $\gamma = 1.3 \times 10^{-3}$ W/m, initial signal/idler to pump ratio of −10 dB, $f = 35$ GHz.

system. It is thus necessary to compensate losses to get an almost fully transparent optical fiber to observe more than two recurrences in the two main operating mode of the system. With perfect loss compensation, the dynamics of the process is ruled by the pure NLSE and then direct comparison between experiments and theory will be achievable. Hence, we introduced a Raman amplification scheme. This idea, borrowed from the telecommunication field where distributed Raman amplification is commonly used [40], has been recently implemented successfully in a handful of nonlinear fiber optics experiments [31, 34, 41–43]. The Raman laser source is located at about 13 THz from the signal to benefit from the maximum Raman gain amplification. It counter-propagates in order to minimize the relative intensity noise transfer compared to the co-propagative case [44]. The Raman pump power is set empirically as follows. We chose the configuration where $\Delta\Phi_{init} = \pm \pi/2$ and increased the Raman pump power until the level of signal sideband at the second peak of conversion was similar to the first one. This allows to get the best overall compensation of the loss along the fiber length. It lead to very similar input and output signal power values. The efficiency of the loss compensation will be illustrated hereafter, with experimental results in excellent agreements with numerics from pure NLSE.

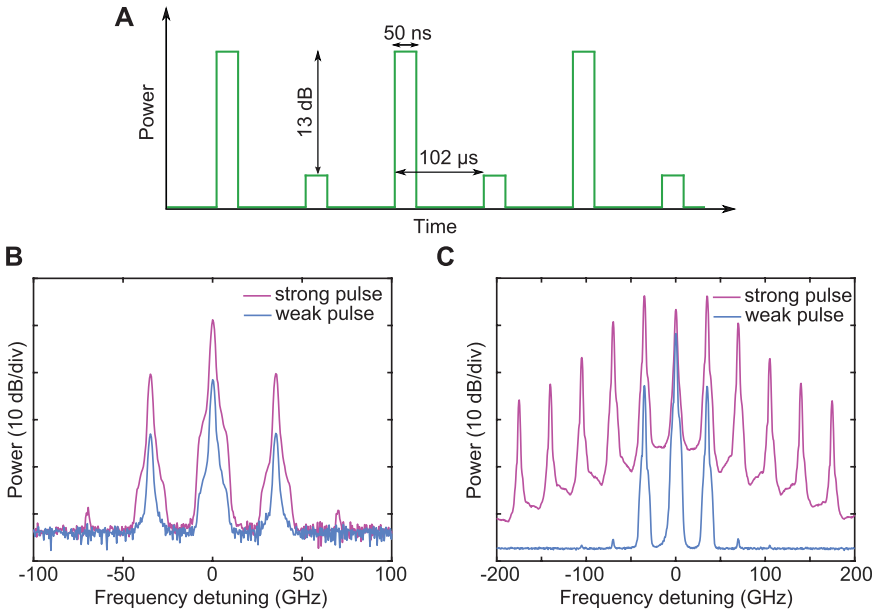

FIGURE 6 | (A) Schematic of the sequence of pulses launched into the fiber. **(B)** Spectrum of the strong (magenta lines) and weak (cyan lines) pulses at the input of the fiber and **(C)** at the output of the fiber.

3.4 Fading Suppression Technique and Signal Processing

In OTDR, it is known that a random noise in amplitude and phase is superimposed on the backscattered signal [45]. This noise, which is detrimental as it leads to jagged measurements, finds its origins in the random state of polarization of the backscattered light and a speckle-like phenomenon due to huge number of scattered waves involved in the process and/or in the thermo-mechanical fluctuations of the propagating medium. In order to avoid it, many techniques have been developed such as averaging over a huge number of backscattered signal and polarization scrambling [46, 47]. However, none of these techniques have proven to be effective and compatible with accurate distributed phase measurements in our setup. Thus, we have developed a novel method which allows us to remove effectively this additional source of noise. We made two assumptions: 1) the fading phenomenon is a purely linear effect and 2) the thermo-mechanical fluctuations have a characteristic time of a few milliseconds. Therefore, we propose the following post-processing treatment to suppress the fading. We first launch a strong 50 ns pulse into the fiber which will experience both linear and nonlinear effects. Then, 102 µs later, a weak pulse, attenuated by 13 dB, follows experiencing mostly linear effects. The attenuation is obtained via the acousto-optic modulator which is driven at half-rate clock (4.9 KHz) so that one pulse over two is attenuated as it is displayed in the schematic in **Figure 6A**. Note that the 102 µs delay between two consecutive pulses is long enough to avoid any overlapping between two backscattered signals but very short compared to the response time of the thermo-mechanical fluctuations which ensures that the linear fading effects experienced by both backscattered waves (from the strong and weak pulses) are strongly correlated. The output spectra at the input and output of the fiber of weak and strong pulses are displayed in **Figures 6B,C**. We observe that for strong pulses (magenta lines), the spectrum is composed of 11 waves in this typical example corresponding to the broadest spectrum achievable by increasing the pump power to get the first maximum compression point at the output of the fiber. In the opposite case, we observe a spectrum made of 3 main waves (cyan lines) plus weak harmonics 25 dB lower than signal/idler wave. We can thus consider that these weak pulses mainly experience linear effects. Note that we analyze each state of polarization of backscattered signals independently (which are later recombined in post-processing) thanks to the use of polarization beam splitters, thus avoiding the need of polarization scrambling. Once the heterodyned signals are logged with the four channels of the oscilloscope (two channels for each polarization states of the pump and two for those of the signal), we proceed to the following data processing. We will refer to each traces observed on the oscilloscope as $E_{Pow,Pol,Channel}(z)$ with z being the distance along the fiber (obtained simply by converting the time of flight of the backscattered wave into a distance), *Pow* can either be *Strong* (for the nonlinear pulse) or *Weak* (for the reference), *Pol* is either 1 or 2 for each polarization state and *Channel* refers to the *Pump* or *Signal*. The ratios $\frac{E_{Strong,1,Pump}(z)}{E_{Weak,1,Pump}(z)}$ and $\frac{E_{Strong,2,Pump}(z)}{E_{Weak,2,Pump}(z)}$ are calculated (the procedure is similar for the signal sideband) in order to remove all linear contributions and to cancel the fading effect in amplitude and phase[1]. Then, we used a short time fast Fourier transform (FFT) to extract phase and intensity value for each recordings. All demodulated traces are then averaged over at least one hundred

[1]Unfortunately, this removed also the linear phase due to the group velocity dispersion acquired during the propagation, which cannot be neglected as it directly impacts the dynamics of the system. The following phase term $\frac{1}{2}\beta_2(2\pi f)^2 z$ is then added later on to the measured pump-signal phase difference to get $\Delta\Phi$.

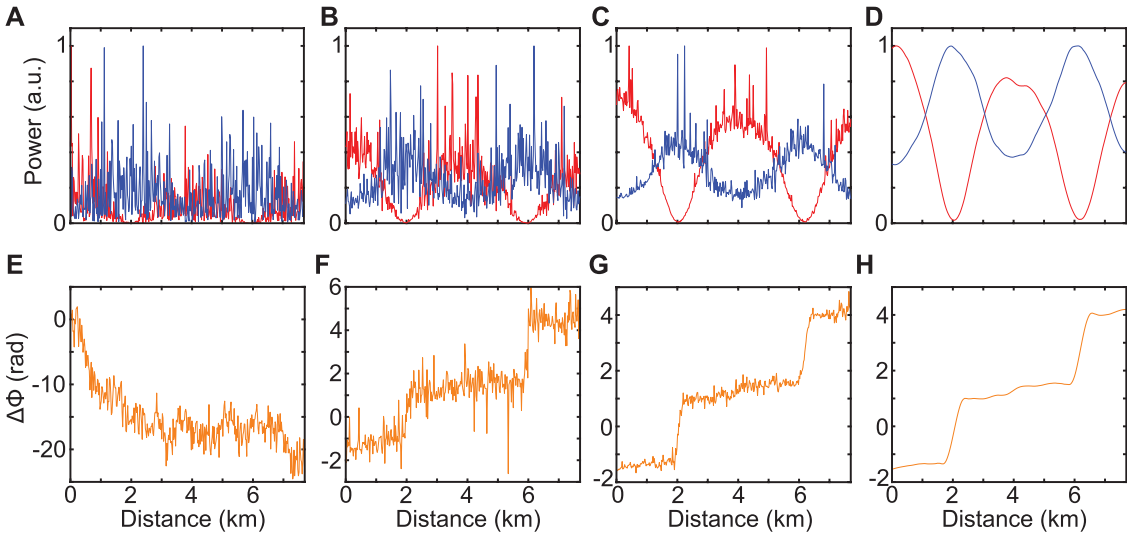

FIGURE 7 | (A) Single-shot of the pump (red line) and signal (blue line) power evolutions along the fibre when the calibration is off and **(B)** when the calibration is on. **(C)** Averaging over a hundred shots of the pump and signal power evolution when the calibration is on and **(D)** same after filtering. **(E,F,G,H)** show the relative phase evolutions corresponding to **(A–D)** respectively. All powers plot are normalised to their respective maxima.

shots to remove the noise and filtered afterward, by two types of filters: a median filter and a Savitzky-Golay filter.

The performances of our measurement technique are illustrated in **Figure 7**. **Figures 7A,E** show a single-shot of the pump and signal power evolutions (normalized to their respective maxima) and their relative phase without calibration with the reference (weak pulse). One can distinguish the exchange of energy between the pump and the signal but the measurement is very noisy and the relative phase evolution does not agree at all with the one expected. **Figures 7B,F** show the same measurements but this time with the calibration (fading removed). Although the measurements are still very noisy, one can notice almost two recurrences by looking at the power evolutions and a specific relative phase evolution with jumps around 2 km and 6 km which are approximately the positions where the direction of the power flow between the pump and the sideband reverses. After averaging over one hundred shots, we observe a significant reduction of the noise as displayed in **Figures 7C,G**. We then obtain clean traces after applying a Savitzky–Golay filter as shown in **Figures 7D,H**. All results presented in this paper passed this data processing procedure. From this experimental setup and this data processing, we can record clean phase and intensity evolutions of pump and signal waves along the fiber length and to almost perfectly compensate attenuation. In the following, we are going to present a selection of results that we obtained with our HOTDR system, which were not accessible with other setups.

4 FERMI-PASTA-ULAM RECURRENCE OBSERVATION

4.1 Evolution as a Function of the Initial Relative Phase

We first present the impact of the initial relative phase value on the dynamics of the FPU recurrence process in **Figure 8**. The experimental parameters are detailed in **Figure 8** caption. Firstly, we looked for the initial phase value allowing the system to evolve as close as possible to the separatrix (homoclinic orbit). This curve marks the border between the two main regimes of the system which consists of the inner or outer trajectories in the phase plane [29, 33, 48]. Theoretically, it corresponds to an input relative phase between the pump and the signal $\Delta\Phi_C = \cos^{-1}(\omega/2)$ from the truncated three wave model [48]. Note that, for weak input signals, the separatrix corresponds to an Akhmediev breather [4]. By finally tuning the relative phase in experiments, the closest results we got were obtained for $\Delta\Phi_{init} = 0.3\pi$ (**Figures 8A,B**), very close from the theoretical value of $\Delta\Phi_{init} = 0.29\pi$.

A single cycle of recurrence can be seen corresponding to a single loop in the right half side of the phase plane, as expected. Note that, a slight change of $\pm\, 0.02\pi$ makes the system switch o the inner or outer trajectories [33]. Then, we set the input relative phase to $\Delta\Phi_{init} = -0.42\pi$. Signal and pump power evolutions are shown in **Figure 8C** and the corresponding trajectory in the phase plane in **Figure 8D** (solid lines). As seen, the system experiences two recurrences. The pump extrema coincide with the signal ones, as expected from the theory [28, 48]. The curve in the phase plane occupies the right and left sides, showing a symmetry breaking of the FPU recurrence process due to the crossing of the semi-plane [33]. These results are in excellent agreement with numerical simulations depicted in dashed lines. Next, the relative initial phase is set to $\Delta\Phi_{init} = -0.15\pi$ to trigger the symmetric case. It is illustrated in **Figures 8E,F**. Two recurrences are still visible, but do not experience π shift as can be seen in **Figure 8F**, where only the right plane is occupied.

The global evolution is summarized in **Figure 8G**. It shows the evolution of the position of the first and second maximum compression points as a function of the initial relative phase value $\Delta\Phi_{init}$. We compared our experimental results (crosses), with theoretical predictions from Santini and Grinevitch [49] (solid lines) and numerics from the NLSE (dashed lines). The region for which the dynamics of the system corresponds to an

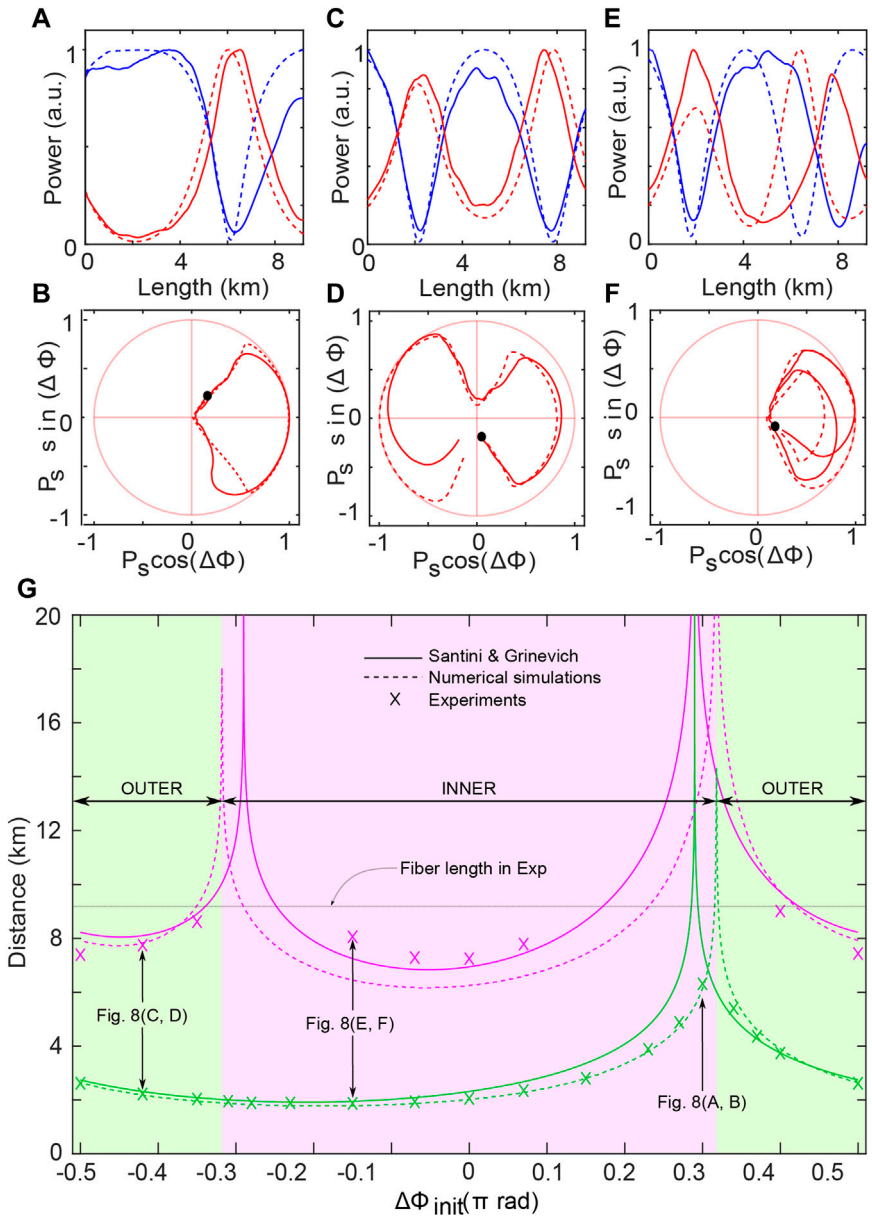

FIGURE 8 | (A,C,E) Longitudinal evolution of the pump (blue) and signal (red) powers and **(B,D,F)** their corresponding phase plane trajectories, for $\Delta\Phi_{init} = -0.42\pi$, $\Delta\Phi_{init} = -0.15\pi$ and $\Delta\Phi_{init} = 0.30\pi$. Solid lines correspond to experiments and dashed ones to numerical simulations. **(G)** Positions of the first (green) and second (magenta) pump minima. Crosses correspond to experimental recordings, dashed lines to numerical simulations from the NLSE and solid lines to the theoretical model from ref. 49. The grey line indicates the length of the fibre used in experiments. $\Delta\Phi_{init}$ was varied from $-\pi/2$ to $\pi/2$. η is the signal power normalized to its maximum value. All power plots are normalized to their maxima. Parameters: $P_p = 470$ mW, $\beta_2 = -19 \times 10^{-27}$ s^2/m, $\gamma = 1.3 \times 10^{-3}$ W/m, $L = 9.2$ km, $\omega = 1.22$ (sideband detuning from the pump of 35 GHz) and a signal/idler to pump ratio of −10.4 dB. We summarized the whole dynamics of the system including the spatio-temporal, spatio-spectral, and phase plane evolution ranging from $\Delta\Phi_{init} = -0.5\pi$ to $\Delta\Phi_{init} = 0.5\pi$ in a video available in **supplementary materials**.

outer (inner) trajectory is colored in shaded green (violet) areas, the borders correspond to the initial phase value to trigger the separatrix of the system.

As we can see, the positions of the first and the second maximum compression points diverge both for $\Delta\Phi_{init} = \Phi_\omega = 0.29\pi$. This is because this particular phase corresponds to the stable manifold of the separatrix, which entails asymptotic conversion from the input sidebands to the pump. Conversely, the position of the first maximum compression point is minimum for $\Delta\Phi_{init} = -\Phi_\omega$, which entails the most rapid growth of the sidebands to the apex. Note that the position of the second maximum compression point still diverges for this phase value since backconversion still occurs asymptotically along the separatrix. The phase $\pm\Phi_\omega$ being the critical parameter of the system,

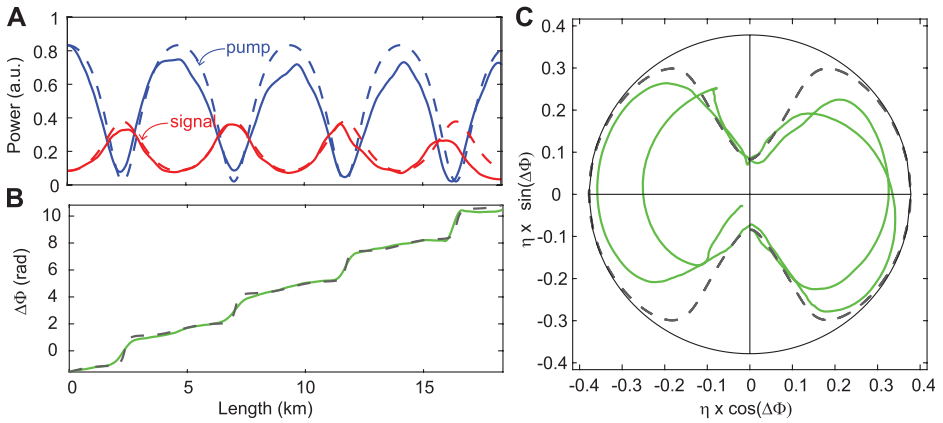

FIGURE 9 | Longitudinal evolution of **(A)** the pump (blue line) and signal (red line) powers and **(B)** their relative phase for $\Delta\Phi_{init} = -\pi/2$. **(C)** Phase-plane representation. η is the signal power normalized to the total power. Numerical simulations are shown in dashed lines and experiments in solid lines.

influences the transition from inner to outer trajectory across this phase. The relatively strong modulation used in our experiment and NLSE simulations (the sidebands contains about 15% of the total power) induces a shift of the critical phase which is here $\Delta\Phi_{c-NLSE} = \pm 0.32\pi$. The measured values of the position of the first and second recurrence are in excellent agreement with the numerical simulations and theoretical predictions [49]. Finally, our system allowed us to finely characterize the dynamics of FPU recurrence in a nonlinear system modeled by the pure NLSE and to observe two maximum compression points. More specifically, we evidenced the two main operating regimes of the system characterized by inner or outer trajectories as well as the regime very close to the one modeled by the homoclinic orbit. Detailed information on the symmetry breaking of the FPU recurrence process can be found in refs. 33 and 35.

4.2 Record Observation of 4 Recurrences in an Ultra-Low Loss Optical Fiber

In the previous section, we reported the observation of two recurrences thanks to an active compensation of the loss using a counter-propagating Raman pump. Nonetheless, much remains to be done, since at present it is not clear how far one can go in observing a higher number of recurrences. This is a preliminary step for further studies on the onset of thermalization [50] for instance. The recirculating loop architecture reported by Goosens *et al.* [32] seems to be an other option, but reported results are still limited to two recurrences. Here we show that by improving our setup it is possible to observe more than 4 recurrences. To do so, we used an ultra-low loss optical fiber developed for ultra-long-haul submarine telecommunication systems [27] with 0.147 dB/km at 1550 nm (see details in ref. 37).

Figure 9 shows an example of recordings. We set the input phase to $\Delta\Phi_{init} = -\pi/2$. This leads to phase-shifted recurrences [48] (outer trajectories). In **Figure 9A**, the power evolutions along the fiber length are represented in blue solid line for the pump and red solid line for the signal, respectively. The phase evolution is shown in **Figure 9B**. Numerics are represented in dashed lines. As seen, four recurrences have been observed, that is a record achievement [37]. These four recurrences correspond to ten nonlinear lengths in quasi-lossless optical fiber. The excellent agreement between experiments and simulations proves that the active compensation is not far from being perfect. Note that we also reported the observation of more than four recurrences in ref. 37 by triggering the regime characterized by inner trajectories ($\Delta\Phi_{init} = 0$). However, the system does not spatially evolve in a purely periodic fashion, but is rather following orbits in the infinite dimensional space that can be closer to a higher-order solution of the nonlinear Schrödinger equation [51]. It indicates that the input sideband power was a bit too high to remain close to the same trajectory. These results have been made possible due to the lowering of losses at 1550 nm by 0.05 dB/km from one side but also at the Raman pump wavelength (1450 nm) with an improvement of 0.08 dB/km. These results pave the way to study further complex problems such as the role of multiple unstable sideband pairs and the route to the thermalization using longer fiber spans.

4.3 Observation of Type-A and B Solutions of the Nonlinear Schrödinger Equation

Akhmediev breathers are exact solutions of NLSE that allow to predict for a single stage of growth to the apex and the asymptotic return to the initial state [4]. They do not allow to predict the formation of multiple FPU recurrences. Approximate solutions have been reported recently by means of finite-gap theory and asymptotic expansions to describe multiple recurrences [49]. Exact solutions have been derived by Akhmediev *et al.* and recently revisited to extract their Fourier coefficients [38]. There are two types of first-order solutions, termed type-A and type-B, according to their location in the infinite-dimensional phase space with respect

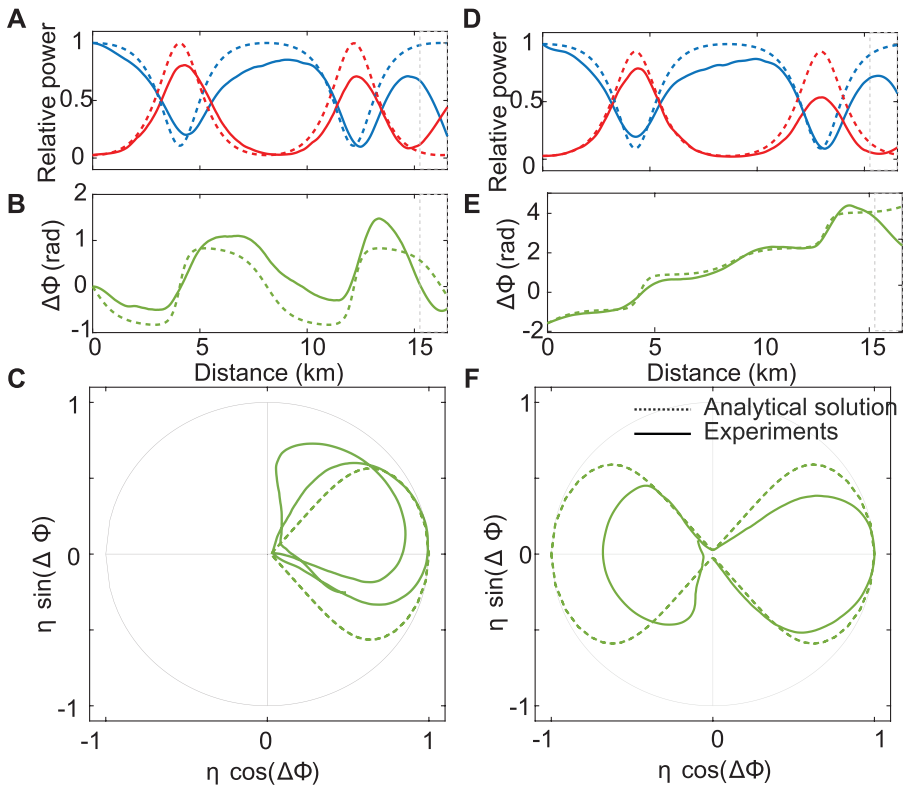

FIGURE 10 | Evolution, along the fiber, of **(A)** the pump (blue lines) and the signal (red lines) powers, **(B)** the relative phase. **(C)** Phase-plane representation. Dotted lines correspond to the B-type first-order solution of the NLSE and solid lines to the experimental data. Each component is normalized with respect to the maximum value of the analytical solution. The initial relative phase is set to $\Delta\Phi_{init} = 0$. **(D–F)** Same as **(A–C)** but for $\Delta\Phi_{init} = -\frac{\pi}{2}$ (A-type solution). η is the signal power normalized to its maximum value.

to the homoclinic orbit corresponding to the Akhmediev breather trajectory [51, 52]. Here we show that they can be observed experimentally with our experimental setup for the first time. We triggered both type-A and type-B solutions by using three initial waves and setting their relative phases to $\Delta\Phi_{init} = -\frac{\pi}{2}$ or 0, respectively [36].

First we set $\Delta\Phi_{init} = 0$ to trigger B-type solutions. Experimental results are displayed in **Figures 10A–C** in solid lines. Two maximum compression points are observed. The corresponding trajectory is limited in the right half side of the phase plane in **Figure 10C** as expected from theory [4] for B-type solutions. These results are in excellent agreement with analytical solutions (Eqs. 13–16 in ref. 4 whose parameters were determined through the perfect match condition between the initial three central waves and the experimental three-wave input). A-type solutions are then triggered by setting the initial phase to $\Delta\Phi_{init} = -\frac{\pi}{2}$. Experimental results are represented in **Figures 10D–F**. This time, the first maximum point appears in the right half side of the phase plane and the second one in the left half side. This π shift is characteristic of A-type solutions [4]. These results are also confirmed by exact solutions (dashed lines, Eqs. 13–16 in ref. 4). Detailed information can be found in ref. 36. These results highlight the fact that this system might be a fantastic test bed to observe more complex solutions, such as the rogue waves on the doubly periodic background recently derived in ref. 53.

4.4 Spatio-Temporal Characterization in Intensity and Phase

4.4.1 Principle

We saw that the measurement the phase and the intensity evolutions of different laser lines in the spectral domain was insightful and allowed the observation of new physical phenomena. However, getting the spatio-temporal evolution of the electric field would be more meaningful, providing an observation of FPU recurrence in space. This requires phase and intensity measurements with sub-picosecond resolution. Standard techniques such as frequency-resolved optical gating [54] and spectral phase interferometry for direct-electric field reconstruction [55] (a review can be found in ref. 56) provide these information with an excellent temporal resolution. Recently, new methods allowing real-time full-field characterization have been developed, based in particular on advanced time lens [21] and/or standard time lens combined with a dispersive Fourier transform technique [57] with typically sub-hundred's femtosecond resolution. However, these techniques [21, 54–58] are limited to localized measurements. Note that Xu *et al.* [59] reported recently the longitudinal full-field characterization of Peregrine-like structures using a combination of temporal and spectral measurements and a

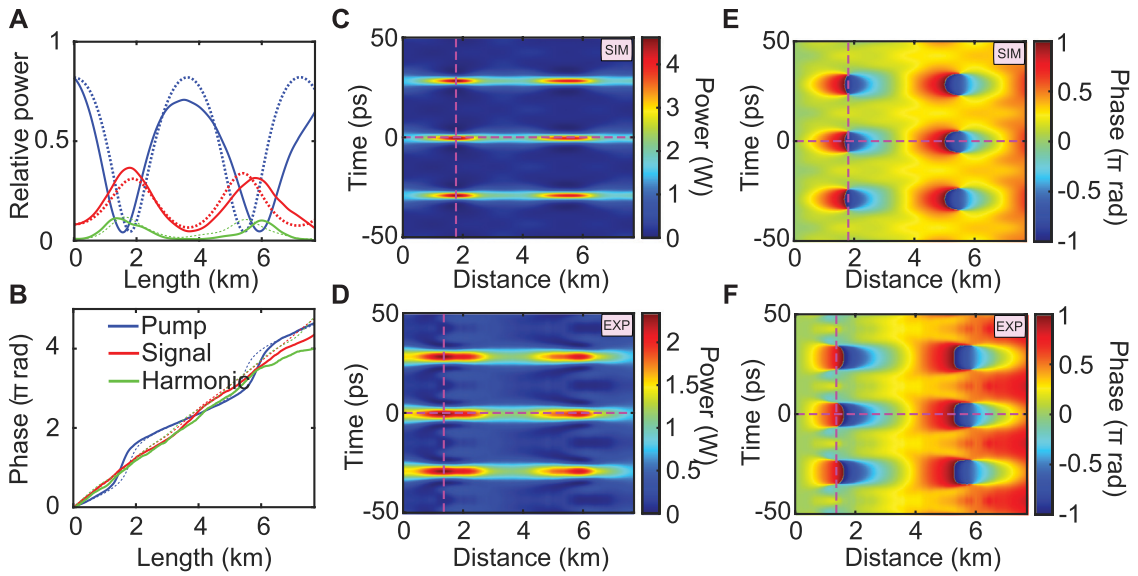

FIGURE 11 | (A, B) Power and phase of the pump, signal and first harmonic (solid lines for experiments and dashed lines for numerics). Spatio-temporal evolutions of the power and phase, **(C, E)** from numerics and **(D, F)** from experiments calculated from the inverse Fourier transform of the whole spectrum in numerics and truncated to 5 waves in experiments. Parameters: P_p = 460 mW, $\beta_2 = -19 \times 10^{-27}$ s^2/m, $\gamma = 1.3 \times 10^{-3}$ W/m, initial signal/idler to pump ratio of −10 dB and harmonics to pump ratio of −20 dB, signal/idler detuning 35 GHz from the pump, harmonics detuning 70 GHz from the pump.

reconstruction algorithm but this technique suffers from the same limitations as the cut-back one. Based on our HOTDR setup, we implemented a new method to perform fast and non-invasive full-field characterization of time-periodic pulses (i.e., with discrete line spectra) along the whole length of an optical fiber [34]. The idea is to calculate the inverse Fourier transform of the data recorded with the HOTDR setup to get the temporal characteristics of the electric field. In most investigations presented in this paper, we measured a truncated spectrum (three main spectral components, *i. e.,* the pump and signal/idler) since it was enough to get a clear description of the process. However, we remind that at maximum compression points, more than eleven spectral components appear in the spectrum in our configurations [33]. We estimated from numerics that the truncation lowers the accuracy of the recordings, specifically in regions where sharp transitions exist. By calculating the error in the sense of the mean square difference from numerics, we estimated that the error is about 13% by considering 3 waves, drops down to 3% with 5 waves and to less than 1% with 7 waves [34]. For practical reasons, we limit our recordings to 5 waves, but there is no fundamental limitations to make it with a larger number and to obtain almost perfect spatio-temporal recordings with less than 1% error [34].

4.4.2 First Order Breathers

We show here the spatio-temporal evolution of the FPU recurrence process presented in previous paragraphs. The detection of the five waves requires launching five waves at the fiber input in order to improve the signal-to-noize ratio in the heterodyne detection stage. So we launched two additional waves compared to previous experiments, but we checked numerically that they are so weak (20 dB lower than the pump), that they do not affect the dynamics of the system. We only record the evolution of the pump, signal and its first harmonic as displayed in **Figures 11A,B**. It shows the longitudinal power (**Figure 11A**) and phase evolutions (**Figure 11B**) in solid lines for experiments. The system exhibits two recurrences, in good agreement with numerical simulations depicted in dashed lines. We then calculate the spatio-temporal evolution of the field via the inverse Fourier transform from the five waves. The intensity plot is displayed in **Figure 11C** and exhibits two maximum compression points at about 1.5 km and 6 km, respectively, which are in phase, as expected (here $\Delta\Phi_{init} = 0$). This is in good overall agreement with the results obtained from numerical simulations accounting for the full spectrum and displayed in **Figure 11D**. The experimental spatio-temporal 2D-map shows broader pattern maximum compression points due to the truncation [34].

The spatio-temporal evolution of the phase of the field is displayed in **Figures 11E,F**. The experimental evolution is in very good agreement with numerical simulations, the impact of the truncation being less pronounced on the phase evolution. Noteworthy, in the temporal case (**Figure 11G**), we observe a phase jump close to π between the center of the pulses and their wings and equal to π in simulations which is one of the characteristic features of Akhmediev breathers and Peregrine soliton [8]. More details can be found in ref. 34 where we also reported the spatio-temporal evolution of the FPU recurrence when the symmetry is broken. Finally, we demonstrated that our HOTDR system enables non-invasive distributed measurements of the electric field in the temporal domain with a resolution lying in the picosecond scale with a 20 m spatial resolution.

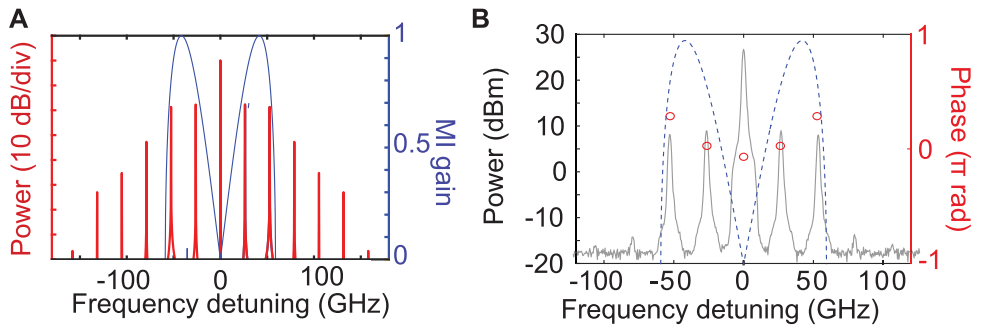

FIGURE 12 | (A) Spectrum at $\xi = 0$ from the Fourier transform from ref. 60 for $\xi_1 = \xi_2 = -2.87$ and $P_p = 500$ mW, $\beta_2 = -19 \times 10^{-27}$ s2/m, $\gamma = 1.3 \times 10^{-3}$ W/m, $\omega_1 = 2/\sqrt{5}$ and $\omega_2 = 4/\sqrt{5}$. The linear MI gain, normalized to its maximum, is superimposed in blue. **(B)** Experimental input spectrum in gray line (amplitude) and red dotes (phase). The MI gain spectrum is superimposed in dashed blue lines.

4.4.3 Second Order Breathers

Second order breathers is a family of higher order solutions of the NLSE [60]. They have already been observed in fiber optics systems by Frisquet *et al.* [18]. They are known to experience sharper edges and higher maximum powers compared to first-order solutions (e.g., the maximal normalized intensity of a first order breather is 9 while it is 25 for a second-order one). Thus, they are of great interest because they could constitute good prototypes to model extremely rare and powerful rogue waves. We will show that it is possible to record the spatio-temporal evolution of their intensity and phase with our experimental setup. The solution of the field envelope of a second-order breather is reported in ref. 60. We use the same normalized parameters in the following. In order to design the experimental initial conditions to trigger second-order breathers, we started from the analytical expression of these breathers [60] and truncated this solution to the 5 central components. We then use these 5 waves to trigger the formation of second order breathers.

We checked numerically (not shown here) that these solutions are very robust and while being excited by a truncated initial condition, they remain quasi-unchanged. We set the phase and amplitude in experiments by using the waveshaper (**Figure 2**).

As an example, we choose a solution for which signal and harmonics experience the same linear MI gain: $\xi_1 = \xi_2 = -2.87$ (and $\tau_1 = \tau_2 = 0$). In physical units, this corresponds to $\omega_1 = 2/\sqrt{5}$ and $\omega_2 = 4/\sqrt{5}$ in normalized units from ref. 60. For a total power of $P_0 = 500$ mW, $\beta_2 = -19 \times 10^{-27}$ s2/m and $\gamma = 1.3 \times 10^{-3}$ W/m this corresponds to $f_1 = 26.6$ GHz and $f_2 = 53.2$ GHz. With these parameters, the maximum compression point of this second order breather is predicted at $z = 4.41$ km. The Fourier transform of this solution $[\Psi(\xi = 0, \tau)]$ is calculated in order to get the input spectrum. This spectrum is displayed in red in **Figure 12A**. As we can see, it is composed of many sidebands with only four falling within the MI gain band (the MI gain curve is superimposed in blue): the signal and idler at frequencies $\pm f_1$ and their first harmonics at $\pm f_2 = \pm 2f_1$. These bands have indeed experience similar parametric gain. We extracted the phase and amplitude value of the 5 main components and use them as initial conditions in experiments. The input initial spectrum is shown in **Figure 12B**. Experimental results are depicted in **Figures 13C,D,G,H**. The evolution of the pump, signal and harmonic power (**Figure 13C**) are in excellent agreement with numerical simulations (solid lines in **Figure 13A**), triggered with the truncated 5 waves solution, as well as the analytical solution (dashed black lines in **Figure 13A**). The relative phase evolution is shown in **Figure 13B** (numerics and analytical solutions) and in **Figure 13D** (experiments). The agreement between experiments, numerics and analytical predictions is excellent too. It means that while initial conditions does not correspond exactly to second order solutions, it is still possible to trigger this solution. By calculating the inverse Fourier transform of these 5 waves it is possible to plot the spatio-temporal evolution of the power (**Figure 13G**) and the phase (**Figure 13H**). As seen, a sharp and powerful second-order breather can be observed. We obtained a pretty good agreement with numerical simulations (**Figures 13E,G**). The main disagreement at the maximum compression point is due to the truncation. We show that using the HOTDR setup and then calculating the inverse Fourier transform, it is possible to obtain the spatio-temporal evolution of the electric field of a second-order breather. An even better agreement would be possible by using more waves.

5 CONCLUSION

We have reviewed recent results obtained with a novel optical fiber experimental setup based on a heterodyne optical time-domain reflectometer allowing to monitor the power and relative phase evolution of the main discrete frequency components of a periodic laser pulse train. Moreover, we actively compensated fiber losses with a conter-propagating Raman pump leading to an almost fully transparent optical fiber which can be accurately modeled by the NLSE. We provided details about the experimental setup, notably about the multi-heterodyne detection technique, the phase-locking between the laser and the local oscillator, the solution we developed to suppress the fading effect, and the data processing. Then, we presented a selection of results recently

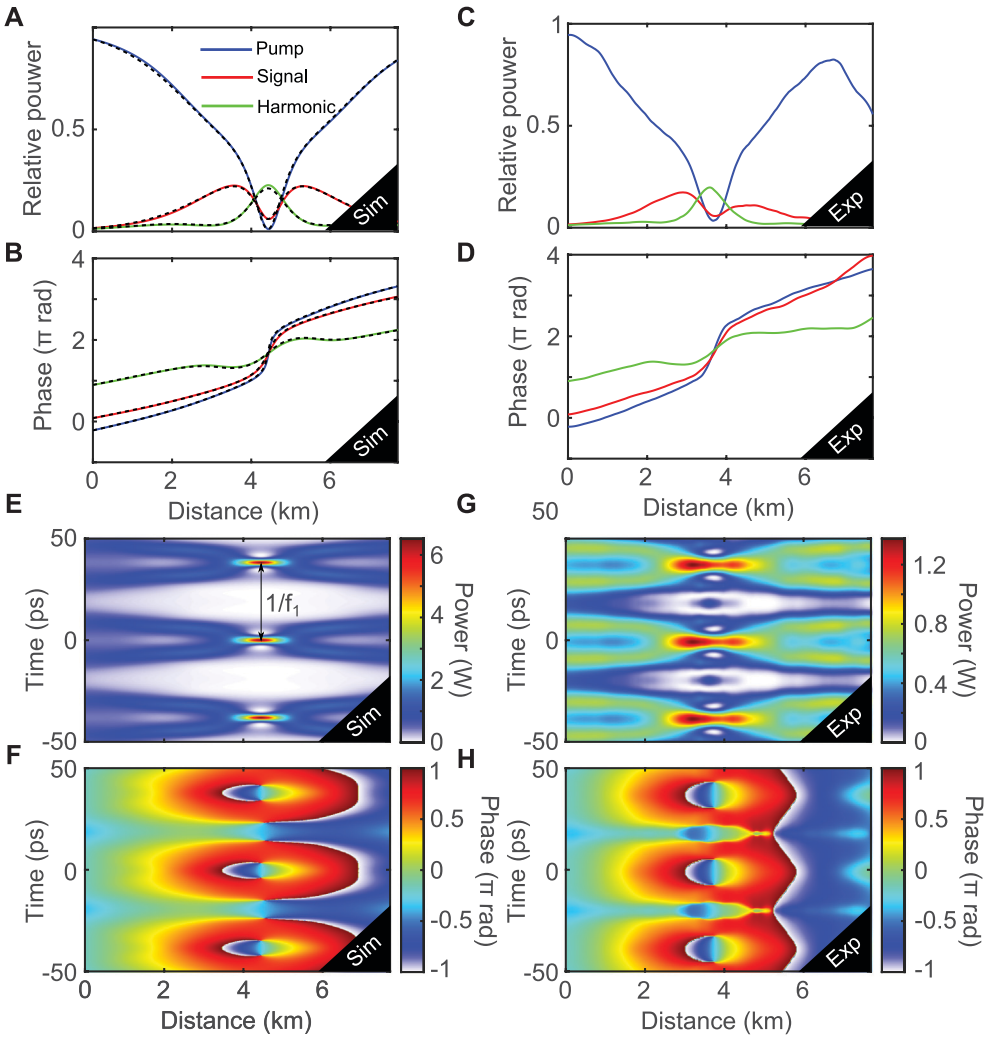

FIGURE 13 | Relative pump, signal and harmonic power and phase evolutions, respectively, from **(A,C)** numerical simulations with a five-wave input and **(B,D)** from experiments. Blue lines correspond to the pump, red ones to the signal and green ones to the harmonic. Dashed black lines in **(A,C)** correspond to the analytical solution from Theory [61]. Spatio-temporal evolution of the field power and phase **(E,G)** from numerical simulations and **(F,H)** from experiments. The spatio-temporal plot of **(F,H)** are obtained through the inverse Fourier transform of fives waves. Parameters: P_p = 470 mW, signal/idler to pump ratio of −17.7 dB, harmonics to pump ratio of −18.7 dB, φ_p = −0.68 rad, φ_s = 0.26 rad, φ_h = 2.82 rad, f_1 = 26.6 GHz and f_2 = 53.2 GHz (f_1 = 26.3 GHz and f_2 = 52.6 GHz in experiments).

obtained with this system in the context of the FPU recurrence process. It enabled the observation of several FPU recurrences for the first time, the study of their dynamics, and a direct comparison with analytical predictions from the pure NLSE. More precisely, the symmetry breaking of the FPU process has been observed by varying initial conditions, in excellent agreement with analytical predictions. Moreover, we showed by recording first harmonics in addition to the signal, idler, and pump waves it is possible to obtain the spatial evolution of the electric field of time-periodic pulses with a sub-ps resolution. We illustrated the performance of this technique by showing the power and phase evolution along the fiber of first and second-order breathers. All these results have been confirmed by numerical simulations, and remarkably with analytical solutions thanks to the efficient loss compensation scheme we developed. This original experimental setup combining dissipation compensation and non-invasive characterization of the electric field of a periodic laser pulse train is a powerful tool in nonlinear fiber optics experiments that could be implemented to investigate other nonlinear effects.

AUTHOR CONTRIBUTIONS

CN and GV performed experiments and numerical simulations. PS and AM designed the experimental setup with AK and GM. MD provided optimized optical fibers. NA, MC, and ST developed theoretical/numerical tools. All authors analyzed results and participated in the writing of the paper.

FUNDING

This work was partly supported by the Agence Nationale de la Recherche through the Equipex Fibres optiques pour les hauts flux (FLUX)through the "Programme Investissements d'Avenir", by the Ministry of Higher Education and Research, Hauts de France Council and European Regional Development Fund (ERDF) through the Contrat de Projets Etat-Region (CPER Photonics for Society, P4S), HEAFISY project and I-SITE through the FUHNKC, VERIFICO and EXAT projects and H2020 Marie Skodowska-Curie Actions (MSCA)(713694) and MEFISTA.

SUPPLEMENTARY MATERIAL

The Supplementary Material for this article can be found online at: https://www.frontiersin.org/articles/10.3389/fphy.2021.637812/full#supplementary-material.

REFERENCES

1. Fermi E, Pasta P, Ulam S, Tsingou M. Studies of the nonlinear problems. In: *Technical report*. New Mexico: Los Alamos Scientific Lab. (1955).
2. Zabusky NJ, Kruskal MD. Interaction of "solitons" in a collisionless plasma and the recurrence of initial states. *Phys Rev Lett* (1965) 15(6):240. doi:10.1103/physrevlett.15.240
3. Zabusky NJ. Fermi-Pasta-Ulam, solitons and the fabric of nonlinear and computational science: history, synergetics, and visiometrics. *Chaos* (2005) 15(1):15102. doi:10.1063/1.1861554
4. Akhmediev NN, Eleonskii VM, Kulagin NE. Exact first-order solutions of the nonlinear Schrödinger equation. *Theor Math Phys* (1987) 72(2):809–18. doi:10.1007/bf01017105
5. Solli DR, Ropers C, Koonath P, Jalali B. Optical rogue waves. *Nature* (2007) 450(7172):1054–57. doi:10.1038/nature06402
6. Akhmediev N, Soto-Crespo JM, Ankiewicz A. Extreme waves that appear from nowhere: on the nature of rogue waves. *Phys Lett* (2009) 373(25):2137–45. doi:10.1016/j.physleta.2009.04.023
7. Akhmediev N, Dudley JM, Solli DR, Turitsyn SK. Recent progress in investigating optical rogue waves. *J Optic* (2013) 15(6):060201. doi:10.1088/2040-8978/15/6/060201
8. Dudley JM, Dias F, Erkintalo M, Genty G. Instabilities, breathers and rogue waves in optics. *Nat Photon* (2014) 8(10):755–64. doi:10.1038/nphoton.2014.220
9. Akhmediev N, Kibler B, Baronio F, Belić M, Zhong WP, Zhang Y, et al. Roadmap on optical rogue waves and extreme events. *J Opt* (2016) 18(6):063001. doi:10.1088/2040-8978/18/6/063001
10. Dudley JM, Genty G, Mussot A, Chabchoub A, Dias F. Rogue waves and analogies in optics and oceanography. *Nat Rev Phys* 1(11):675–89. doi:10.1038/s42254-019-0100-0
11. Lake BM, Yuen HC, Rungaldier H, Ferguson WE. Nonlinear deep-water waves: theory and experiment. part 2. evolution of a continuous wave train. *J Fluid Mech* (1977) 83(1):49–74. doi:10.1017/S0022112077001037
12. Jäger D. Soliton propagation along periodic-loaded transmission line. *Appl Phys* (1978) 16(1):35–8. doi:10.1007/bf00931418
13. Van Simaeys G, Emplit P, Haelterman M. Experimental demonstration of the Fermi-Pasta-Ulam recurrence in a modulationally unstable optical wave. *Phys Rev Lett* (2001) 87(3):033902. doi:10.1103/PhysRevLett.87.033902
14. Akhmediev NN. Nonlinear physics. Déjà vu in optics. *Nature* (2001) 413(6853):267–8. doi:10.1038/35095154
15. Mussot A, Kudlinski A, Droques M, Szriftgiser N, Akhmediev N. Fermi-Pasta-Ulam recurrence in nonlinear fiber optics: the role of reversible and irreversible losses. *Phys Rev X* (2014) 4(1):011054. doi:10.1103/physrevx.4.011054
16. Kibler B, Fatome J, Finot C, Millot G, Dias F, Genty G, et al. The Peregrine soliton in nonlinear fibre optics. *Nat Phys* (2010) 6(10):790–5. doi:10.1038/nphys1740
17. Kibler B, Fatome J, Finot C, Millot G, Genty G, Wetzel B, et al. Observation of Kuznetsov-Ma soliton dynamics in optical fibre. *Sci Rep* (2012) 2:463. doi:10.1038/srep00463
18. Frisquet B, Kibler B, Millot G. Collision of Akhmediev breathers in nonlinear fiber optics. *Phys Rev X* (2013) 3(4):041032. doi:10.1103/physrevx.3.041032
19. Hammani K, Wetzel B, Kibler B, Fatome J, Finot C, Millot G, et al. Spectral dynamics of modulation instability described using Akhmediev breather theory. *Opt Lett* (2011) 36(11):2140–2. doi:10.1364/OL.36.002140
20. Erkintalo M, Hammani K, Kibler B, Finot C, Akhmediev N, Dudley JM, et al. Higher-order modulation instability in nonlinear fiber optics. *Phys Rev Lett* (2011) 107(25):253901. doi:10.1103/PhysRevLett.107.253901
21. Tikan A, Bielawski S, Szwaj C, Randoux S, Suret P. Single-shot measurement of phase and amplitude by using a heterodyne time-lens system and ultrafast digital time-holography. *Nat Photon* (2018) 12(4):228–34. doi:10.1038/s41566-018-0113-8
22. Thévenaz L. Review and progress in distributed fiber sensing. In: *Optical fiber sensors*. Cancun, Mexico: Optical Society of America (2006). ThC1.
23. Armand V, Alasia D, Lantz E, Maillotte H, Thévenaz L, Gonzalez-Herraez M, et al. Brillouin optical time-domain analysis of fiber-optic parametric amplifiers. *IEEE Photon Technol Lett* (2007) 19(3):179–81. doi:10.1109/LPT.2006.890039
24. Alishahi F, Vedadi A, Shoaie MA, Soto MA, Denisov A, Mehrany K, et al. Power evolution along phase-sensitive parametric amplifiers: an experimental survey. *Opt Lett* (2014) 39(21):6114–7. doi:10.1364/OL.39.006114
25. Hu X, Chen W, Lu Y, Yu Z, Chen M, Meng Z. Distributed measurement of fermi-pasta-ulam recurrence in optical fibers. *IEEE Photon Technol Lett* (2018) 30(1):47–50. doi:10.1109/lpt.2017.2773615
26. Martins HF, Martin-Lopez S, Corredera P, Salgado P, Frazão O, González-Herráez M. Modulation instability-induced fading in phase-sensitive optical time-domain reflectometry. *Opt Lett* (2013) 38(6):872–4. doi:10.1364/OL.38.000872
27. Tamura Y, Sakuma H, Morita K, Suzuki M, Yamamoto Y, Shimada K, et al. Lowest-ever 0.1419-db/km loss optical fiber. In: Optical fiber communication Conference, 2017 March 19-23, Los Angeles, CA. Optical Society of America (2017). Th5D–1.
28. Bendahmane A, Mussot A, Kudlinski A, Szriftgiser, P, Conforti M, Wabnitz S, et al. Optimal frequency conversion in the nonlinear stage of modulation instability. *Optic Express* (2015) 23(24):30861–71. doi:10.1364/OE.23.030861
29. Moon HT. Homoclinic crossings and pattern selection. *Phys Rev Lett* (1990) 64(4):412. doi:10.1103/PhysRevLett.64.412
30. Pierangeli D, Flammini M, Zhang L, Marcucci G, Agranat AJ, Grinevich PG, et al. Observation of Fermi-Pasta-Ulam-Tsingou recurrence and its exact dynamics. *Phys Rev X* (2018) 8(4):041017. doi:10.1103/physrevx.8.041017
31. Mussot A, Naveau C, Conforti M, Kudlinski A, Copie F, Szriftgiser P, et al. Fibre multi-wave mixing combs reveal the broken symmetry of Fermi-Pasta-Ulam recurrence. *Nat Photon* (2018) 12(5):303–8. doi:10.1038/s41566-018-0136-1
32. Goossens JW, Hafermann H, Jaouën Y. Experimental realization of fermi-pasta-ulam-tsingou recurrence in a long-haul optical fiber transmission system. *Sci Rep* (2019) 9(1):1–11. doi:10.1038/s41598-019-54825-4
33. Mussot A, Conforti M, Trillo S, Copie F, Alexandre K. Modulation instability in dispersion oscillating fibers. *Adv Opt Photon* (2018) 10(1):1–42. doi:10.1364/AOP.10.000001
34. Naveau C, Szriftgiser, P, Kudlinski A, Conforti M, Trillo S, Mussot A. Full-field characterization of breather dynamics over the whole length of an optical fiber. *Opt Lett* (2019) 44(4):763–6. doi:10.1364/OL.44.000763
35. Naveau C, Szriftgiser P, Kudlinski A, Conforti M, Trillo S, Mussot A. Experimental characterization of recurrences and separatrix crossing in modulation instability. *Optic Lett* (2019) 44(22):5426–9. doi:10.1364/ofc.2018.th3d.5
36. Vanderhaegen G, Szriftgiser P, Naveau C, Kudlinski A, Conforti M, Trillo S, et al. Observation of doubly periodic solutions of the nonlinear schrödinger equation in optical fibers. *Opt Lett* 45(13):3757–60. doi:10.1364/OL.394604

37. Vanderhaegen G, Szriftgiser P, Kudlinski A, Conforti M, Trillo S, Droques M, et al. 2020. Observation of four fermi-pasta-ulam-tsingou recurrences in an ultra-low-loss optical fiber, *Opt Express*. 28(12):17773–81. doi:10.1364/OE.391560
38. Conforti M, Mussot A, Kudlinski A, Trillo S, Akhmediev N. Doubly periodic solutions of the focusing nonlinear Schrödinger equation: recurrence, period doubling, and amplification outside the conventional modulation-instability band. *Phys Rev A* (2020) 101:023843. doi:10.1103/physreva.101.023843
39. Friederich F, Schuricht G, Deninger A, Lison F, Spickermann G, Haring Bolívar P, et al. Phase-locking of the beat signal of two distributed-feedback diode lasers to oscillators working in the mhz to thz range. *Optic Express* (2010) 18(8):8621–9. doi:10.1364/OE.18.008621
40. Headley C, Agrawal G. *Raman amplification in fiber optical communication systems*. 1st ed. Academic Press (2005). 392.
41. Juan Diego Ania-CastañónEllingham TJ, Ibbotson R, Chen X, Zhang L, Turitsyn SK. Ultralong raman fiber lasers as virtually lossless optical media. *Phys Rev Lett* (2006) 96:023902. doi:10.1103/physrevlett.96.023902
42. Xu G, Conforti M, Kudlinski A, Mussot A, Trillo S. Dispersive dam-break flow of a photon fluid. *Phys Rev Lett* (2017) 118(25):254101. doi:10.1103/PhysRevLett.118.254101
43. Kraych AE, Suret P, Gennady E, Randoux S. Nonlinear evolution of the locally induced modulational instability in fiber optics. *Phys Rev Lett* (2019) 122(5): 054101. doi:10.1103/physrevlett.122.054101
44. Agrawal GP. *Nonlinear fiber optics*. 5th ed. Academic Press (2012). 648.
45. Healey P. Fading in heterodyne OTDR. *Electron Lett* (1984) 20(1):30–2. doi:10.1049/el:19840022
46. Izumita H, Furukawa SI., Koyamada Y, Sankawa I. Fading noise reduction in coherent OTDR. *IEEE Photon Technol Lett* (1992) 4(2):201–3. doi:10.1109/68.122361
47. Yang G, Fan X, Wang B, Liu Q, He Z. Polarization fading elimination in phase-extracted OTDR for distributed fiber-optic vibration sensing. In: 2016 21st OptoElectronics and Communications Conference (OECC) held jointly with 2016 International Conference on Photonics in Switching (PS), 2016 July 3-7. Niigata, Japan. IEEE (2016). pages 1–3.
48. Trillo S, Wabnitz S. Dynamics of the nonlinear modulational instability in optical fibers. *Opt Lett* (1991) 16(13):986–8. doi:10.1364/ol.16.000986
49. Grinevich PG, Santini PM. The exact rogue wave recurrence in the NLS periodic setting via matched asymptotic expansions, for 1 and 2 unstable modes. *Phys Lett* (2018) 382(14):973–9. doi:10.1016/j.physleta.2018.02.014
50. Wabnitz S, Akhmediev N. Efficient modulation frequency doubling by induced modulation instability. *Opt Commun* (2010) 283(6):1152–4. doi:10.1016/j.optcom.2009.11.030
51. Kimmoun O, Hsu HC, Branger H, Li MS, Chen YY, Kharif C, et al. Modulation instability and phase-shifted Fermi-Pasta-Ulam recurrence. *Sci Rep* (2016) 6: 28516. doi:10.1038/srep28516
52. Akhmediev NN, Korneev VI. Modulation instability and periodic solutions of the nonlinear Schrödinger equation. *Theor Math Phys* (1986) 69(2):1089–93. doi:10.1007/bf01037866
53. Chen J, Pelinovsky DE, White RE. Rogue waves on the double-periodic background in the focusing nonlinear Schrödinger equation. *Phys Rev E* (Nov 2019) 100:052219. doi:10.1103/PhysRevE.100.052219
54. Rick T. *Frequency-resolved optical gating: the measurement of ultrashort laser pulses*. Springer, Boston, MA: Springer Science & Business Media (2012).
55. Iaconis C, Walmsley IA. Spectral phase interferometry for direct electric-field reconstruction of ultrashort optical pulses. *Opt Lett* (1998) 23(10):792–4. doi:10.1364/ol.23.000792
56. Walmsley IA, Dorrer C. Characterization of ultrashort electromagnetic pulses. *Adv Optic Photon* (2009) 1(2):308–437. doi:10.1364/aop.1.000308
57. Ryczkowski P, Närhi M, Billet C, Merolla JM, Genty G, Dudley JM. Real-time full-field characterization of transient dissipative soliton dynamics in a mode-locked laser. *Nat Photon* (2018) 12(4):221–7. doi:10.1038/s41566-018-0106-7
58. Cheng L, Goda K. The complete optical oscilloscope. *Nat Photon* (2018) 12(4): 190–1. doi:10.1038/s41566-018-0141-4
59. Xu G, Hammani K, Chabchoub A, Dudley JM, Kibler B, Finot C, 2019. Phase evolution of peregrine-like breathers in optics and hydrodynamics, *Phys Rev E*. 99(1):012207. doi:10.1103/PhysRevE.99.012207
60. Kedziora DJ, Ankiewicz A, Akhmediev N. Second-order nonlinear Schrödinger equation breather solutions in the degenerate and rogue wave limits. *Phys Rev E - Stat Nonlinear Soft Matter Phys* (2012) 85(6):066601. doi:10.1103/PhysRevE.85.066601
61. Devine N, Ankiewicz A, Genty G, Dudley JM, Akhmediev N. Recurrence phase shift in Fermi-Pasta-Ulam nonlinear dynamics. *Phys Lett* (2011) 375(46): 4158–61. doi:10.1016/j.physleta.2011.10.006

Conflict of Interest: The authors declare that the research was conducted in the absence of any commercial or financial relationships that could be construed as a potential conflict of interest.

frontiers in Physics

ORIGINAL RESEARCH
published: 28 April 2021
doi: 10.3389/fphy.2021.593394

Modeling Crossing Random Seas by Fully Non-Linear Numerical Simulations

Jinghua Wang[1,2], *Qingwei Ma*[3]*, *Shiqiang Yan*[3] and *Bingchen Liang*[1]

[1] School of Engineering, Ocean University of China, Qingdao, China, [2] Faculty of Engineering, National University of Singapore, Singapore, Singapore, [3] School of Mathematics, Computer Science and Engineering, City University of London, London, United Kingdom

Bimodal spectrum wave conditions, known as crossing seas, can produce extreme waves which are hostile to humans during oceanic activities. This study reports some new findings of the probability of extreme waves in deep crossing random seas in response to the variation of spectral bandwidth through fully non-linear numerical simulations. Two issues are addressed, namely (i) the impacts of the spectral bandwidth on the changes of extreme wave statistics, i.e., the kurtosis and crest exceedance probability, and (ii) the suitability of theoretical distribution models for accurately describing the wave crest height exceedance probability in crossing seas. The numerical results obtained by simulating a large number of crossing sea conditions on large spatial-temporal scale with a variety of spectral bandwidth indicate that the kurtosis and crest height exceedance probability will be enhanced when the bandwidth of each wave train becomes narrower, suggesting a higher probability of encountering extreme waves in narrowband crossing seas. Meanwhile, a novel empirical formula is suggested to predict the kurtosis in crossing seas provided the bandwidth is known in advance. In addition, the Rayleigh and second-order Tayfun distribution underestimate the crest height exceedance probability, while the third-order Tayfun distribution only yields satisfactory predictions for cases with relatively broader bandwidth regarding the wave conditions considered in this study. For crossing seas with narrower bandwidth, all the theoretical distribution models failed to accurately describe the crest height exceedance probability of extreme waves.

Keywords: crossing seas, extreme waves, kurtosis, exceedance probability, fully non-linear potential theory

OPEN ACCESS

Edited by:
Amin Chabchoub,
The University of Sydney, Australia

Reviewed by:
Alexey Slunyaev,
Institute of Applied Physics (RAS), Russia
Liang Yang,
Cranfield University, United Kingdom
Zhihua Xie,
Cardiff University, United Kingdom

***Correspondence:**
Qingwei Ma
q.ma@city.ac.uk

Specialty section:
This article was submitted to Mathematical and Statistical Physics, a section of the journal Frontiers in Physics

Received: *10 August 2020*
Accepted: *26 March 2021*
Published: *28 April 2021*

Citation:
Wang J, Ma Q, Yan S and Liang B (2021) Modeling Crossing Random Seas by Fully Non-Linear Numerical Simulations. Front. Phys. 9:593394. doi: 10.3389/fphy.2021.593394

INTRODUCTION

The need for the analysis of extreme waves arises in many branches of science and engineering, while in the practice of designing the maritime structure, extreme waves are sometimes referred to as design waves with a certain return period on the basis of statistical analysis [1]. One example is so-called rogue waves featuring twice the significant height that impose substantial threats to the survivability of engineering applications and the safety of navigation activities. And their appearances are widely reported in unidirectional seas, directional seas, and crossing seas [2]. They are conventionally believed to be rare events, however, recent studies pointed out that their probability is higher than predictions based on linear theories [3]. In unidirectional seas, one of the mechanisms indicates that their formations are induced by the third-order non-linear quasi-resonant interactions, i.e., the so-called modulational instability, and their probability is associated

with the Benjamin-Feir Index (BFI). To describe such extreme wave events, breather solutions to the third-order non-linear Schrödinger equation (NLSE) are suggested [4]. They have been successfully employed to reproduce extreme waves in laboratories [5–7] and numerical simulations [8, 9].

However, waves are short-crested in reality and a non-linear numerical analysis of several sets of observed field data in various European locations indicate that the main reason for the occurrence of extreme waves in directional seas is the constructive interference of elementary waves enhanced by second-order bound non-linearities rather than the modulation instability [10]. Therefore, breather models are usually not employed for the purpose to study extreme waves in directional seas. Nevertheless, ocean wave spectra, in some cases, are characterized by the coexistence of two wave systems in different propagating directions. This bimodal condition featuring two different spectral peaks is known as crossing seas. It has been recently pointed out that crossing seas are potentially hazardous and can create a freakish sea state where the probability of encountering rogue waves is high. For instance, a large percentage of ship accidents are reported due to bad weather conditions occurring in crossing sea states [11]. Some well-known examples are the Draupner wave [12], the Louis Majesty accident [13], and the tanker Prestige accident [14]. The properties of such extreme waves in crossing seas can differ significantly from those in non-crossing seas, e.g., experimental examination on the Draupner wave reveals that the onset and the type of wave breaking plays a significant role in creating steeper extreme waves in crossing seas [15]. Recently, some studies have suggested that extreme waves in crossing seas can be induced by modulational instability and can be represented by using a crossing breather wave model [16, 17]. Based on a stability analysis of the model, it is concluded that the occurrences of extreme waves in crossing seas are directly linked to (i) the angle between the propagating direction of two wave systems and (ii) the spectral bandwidth. Subsequently, many studies have been carried out to explore the effects of the crossing angles on extreme wave occurrences. For example, the stability analysis for two perturbed uniform wave trains implies that an extreme wave is the result of the balance between the large amplification factor and the large growth rate, so that angles between 10 and 30° are most probable for establishing a rogue wave sea [18], while the sideband growth reduces significantly at angles beyond about 40° and reaching complete stability at 60–80° [19]. Besides, Shukla et al. [20] extended the analysis to study the crossing of two wave groups with finite spectral bandwidth and found that the random-phased non-linearly interacting waves could propagate over long distances without being affected much by the modulational instability. For a wide enough spectral distribution, the formation of extreme waves might be completely suppressed.

In more realistic scenarios, e.g., random crossing seas featuring a bimodal JONSWAP (Joint North Sea Wave Project) shape spectrum, numerical results obtained by using the Euler equation suggest that the maximum value of the kurtosis, which is often adopted to indicate the probability of extreme waves, is achieved when the crossing angle is between 40 and 60° [21]. Besides, the numerical simulations based on the Schrödinger-type equation and fully non-linear potential theory model indicate that for crossing angle at near 90°, the non-linear interactions between the two crossing wave systems practically have negligible impact on the kurtosis [14]. More recently, Luxmoore et al. [22] investigated the effects of directional spreading and crossing angles on the statistics of wave crest heights. It is reported that the kurtosis and wave crest height exceedance probability are more sensitive to the variation of the directional spreading than the magnitude of the crossing angles between two crossing seas; it is also reported that reducing the directional spreading increases the kurtosis and the exceedance probabilities of extreme waves.

Though the crossing angles between two systems play an important role in the statistics of extreme waves, the question on the other hand about how the extreme wave statistics respond to the spectral bandwidth has not been studied so far. Hereby, we aim to address this issue through numerical modeling of the crossing random seas in deep water by using the Enhanced Spectral Boundary Integral (ESBI) model based on the fully non-linear potential theory [23]. In particular, we are interested in the crossing seas featuring symmetrical bimodal spectra consisting of two unidirectional random wave trains. Two questions will be answered in this study, namely (i) how the extreme wave statistics, i.e., the kurtosis and crest height exceedance probability, behave in response to the spectral bandwidth and (ii) whether the theoretical probability distribution, i.e., the Rayleigh distribution and second- and third-order Tayfun distributions, can be used to accurately describe the exceedance probability. In addition, a novel empirical formula will also be suggested to predict the kurtosis provided that the bandwidth is given in advance. The outcome of this study will contribute to gaining insight into extreme wave mechanisms in crossing seas and may offer solutions for optimizing the design and operations in ocean engineering practice.

METHODOLOGIES

Statistical Approach: Kurtosis and Wave Crest Exceedance Probability

The kurtosis is often employed to indicate the probability of extreme waves. Its mathematical form can be expressed by using the formula

$$\kappa = \frac{m_4}{m_2^2}, \tag{1}$$

where m_2 and m_4 are the second and fourth moments of the surface elevation, respectively. The Gaussian theory states that the kurtosis equals to 3. However, the non-linear effects can enhance the extreme wave probability, and therefore, kurtosis is usually larger than 3 depending on the degree of the wave non-linearities. Considering wave non-linearities up to the third order, it is reported that the kurtosis is the summation of a dynamic component due to non-linear quasi-resonant wave–wave interactions and a Stokes bound harmonic contribution [24, 25]. In a spreading sea, the former becomes a function of angular width of the directional spectrum and BFI [26, 27]. For

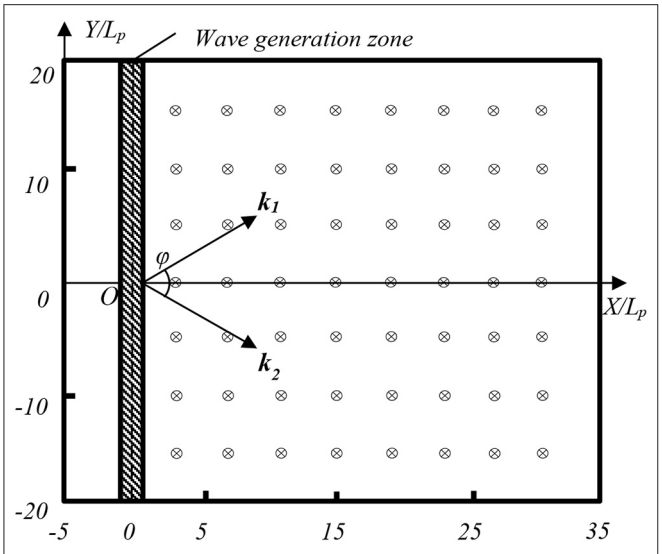

FIGURE 1 | Plan view of the computational domain used in the numerical simulations. ⊗: location of wave probe.

crossing seas consisting of two unidirectional wave trains, as studied in this paper, we employ the formula for narrowband waves to predict the kurtosis [26, 28]:

$$\tilde{\kappa} = 3 + \frac{\pi}{\sqrt{3}} BFI^2 + 24\varepsilon^2, \tag{2}$$

where *BFI* is the Benjamin-Feir index given by

$$BFI = \frac{\sqrt{2}\varepsilon}{\nu} \tag{3}$$

with wave steepness parameter $\varepsilon = k_p H_s/4$ and bandwidth parameter ν, where k_p is the peak wavenumber and H_s is the significant height as 4 times the SD (short for Standard Deviation) of the surface elevations recorded at the gauges shown in **Figure 1**. For a narrowband wave train, its spectrum can be approximated by using the Gaussian distribution with its SD as the spectral bandwidth ν. However, the bandwidth parameter ν is not explicitly defined for crossing random seas, which will be further discussed in section Kurtosis. For simplicity, this study focuses on crossing sea featuring a symmetrical bimodal spectrum so that the method by Trulsen et al. [14] is adopted to quantify the spectral bandwidth. In other words, the bandwidth of the crossing sea is characterized by one of the bimodalities, which is denoted by its half-width at half of the spectrum peak, i.e.,

$$\nu = \left(k_r - k_l\right)/(2k_p), \tag{4}$$

where k_r and k_l are corresponding wavenumbers that satisfy $S\left(k_r\right) = S\left(k_l\right) = S\left(k_p\right)/2$ and $k_r > k_p > k_l$, $S\left(k\right)$ is the wavenumber spectrum of the unidirectional sea.

On the other hand, the occurrence of extreme waves can also be depicted by the wave crest exceedance probability distribution model. For a Gaussian sea based on the linear wave theory, the exceedance probability of wave crest can be represented by the Rayleigh distribution [29]:

$$P_R = \exp\left(-8\chi^2\right), \tag{5}$$

where $\chi = H_c/H_s$, H_c is the crest height measured from the mean water level to the crest peak. It is only accurate for describing the statistics for small steepness waves where the second- and higher-order non-linear effects are insignificant. However, when the wave steepness is relatively large, the second-order non-linear effects cannot be overlooked; hence, the second-order Tayfun distribution was suggested [30]:

$$P_T^{(2)} = \exp\left[-\frac{\left(-1+\sqrt{8\sigma\chi+1}\right)^2}{2\sigma^2}\right], \tag{6}$$

where σ is one-third of the skewness of the free surface elevation. Furthermore, to accurately describe the exceedance probability considering third-order effects of narrowband waves, the third-order Tayfun distribution was proposed by incorporating the bandwidth coefficient in the steepness parameter [31]:

$$P_T^{(3)} = P_T^{(2)}\left(1+\Lambda\chi^2\left(4\chi^2-1\right)\right), \tag{7}$$

where Λ can be approximated by using $\Lambda = 8\left(\kappa-3\right)/3$ and κ is the kurtosis defined by Eq. (1) [10]. Note that though Eqs. (5)∼(7) have been employed for studying wave statistics in bimodal seas [22], they are originally derived for unimodal seas, not for crossing seas. The extent to which they are able to model the distribution of crossing seas will be examined. To do so, the key parameters such as H_s, σ, and κ in Eqs. (5)∼(7) are estimated by using the time histories recorded at wave gauges as illustrated in **Figure 1**.

Deterministic Approach: Fully Non-Linear Numerical Simulation

In this study, the ESBI method based on the fully non-linear potential theory [23] is employed to simulate crossing random seas. The details of the method are well-documented in Wang and Ma [23]. Only some key equations are briefed here for the completeness of the paper. All the dimensionless variables used in the ESBI are defined in such a way, e.g., those in length are multiplied by peak wavenumber k_p, i.e., $(\boldsymbol{X}, Z) = k_p\left(\boldsymbol{x}, z\right)$, time is multiplied by peak wave frequency ω_p, i.e., $T = \omega_p t$, velocity potential is multiplied by k_p^2/ω_p, where $\boldsymbol{x}$, z and t denote horizontal, vertical coordinates and time, respectively. The still water level is specified at Z=0. The free surface boundary conditions based on the fully non-linear potential theory can be reformulated as

$$\partial_T \boldsymbol{M} + A\boldsymbol{M} = \boldsymbol{N} \tag{8}$$

with each term expressed as

$$\boldsymbol{M} = \begin{pmatrix} KF\{\eta\} \\ K\Omega F\left\{\tilde{\phi}\right\} \end{pmatrix}, A = \begin{bmatrix} 0 & -\Omega \\ \Omega & 0 \end{bmatrix} \text{and}$$

$$\boldsymbol{N} = \begin{pmatrix} K\left(F\{V\} - KF\left\{\tilde{\phi}\right\}\right) \\ \frac{K\Omega}{2} F\left\{ \frac{\left(V+\nabla\zeta\cdot\nabla\tilde{\phi}\right)^2}{1+|\nabla\zeta|^2} - \left|\nabla\tilde{\phi}\right|^2 \right\} \end{pmatrix},$$

where ϕ and η are the velocity potential and deflection of the free surface, respectively, $\tilde{\phi}$ denotes the values of velocity potential at the surface, $F\{*\} = \int *e^{-i\boldsymbol{K}\cdot\boldsymbol{X}} d\boldsymbol{X}$ is the Fourier transform, and $F^{-1}\{*\}$ denotes the inverse transform, the wavenumber $K = |\boldsymbol{K}|$, and the frequency $\Omega = \sqrt{K}$. Eq. (8) will be used as the prognostic equation for updating the free surface and velocity potential in the time domain, and its solution can be given by

$$\boldsymbol{M}(T) = e^{-A(T-T_0)} \left[\int_{T_0}^{T} e^{A(T-T_0)} \boldsymbol{N} dT + \boldsymbol{M}(T_0) \right], \qquad (9)$$

where

$$e^{A\Delta T} = \begin{bmatrix} \cos\Omega\Delta T & -\sin\Omega\Delta T \\ \sin\Omega\Delta T & \cos\Omega\Delta T \end{bmatrix}.$$

Eq. (9) can be solved by using the fifth-order Runge–Kutta method with an adaptive time step. An energy dissipation model suggested by Xiao et al. [32] is also introduced to the ESBI to suppress breaking waves, i.e.,

$$\Lambda = \exp\left(-\left|\frac{K}{\beta}\right|^{\alpha} \right),$$

where $\alpha = 30$ and $\beta = 8$. Its effectiveness has been demonstrated and confirmed by direct comparison against laboratory measurements.

In addition, to update $\tilde{\phi}$ and η in the time domain, the vertical velocity V requires to be calculated at each time step. The evaluation of V can be achieved by using the boundary integral equation. It is decomposed into four parts depending on the degree of non-linearities. For clarity of the paper, the formulations for calculating V are summarized in the **Appendix**. The evaluation is computationally efficient, owing to the utilization of the Fast Fourier Transform. Note that the energy dissipation model is applied to both the surface elevation and velocity potential when the number of iterations for estimating the vertical velocity exceeds four times, instead of every time step as used in Xiao et al. [32]. For more details about the numerical scheme, readers can refer to Wang and Ma [23].

The ESBI model has been successfully employed to simulate the Peregrine breather and its interactions with random waves in unidirectional seas, and good agreement is achieved in comparison with the experiment measurements [9]. To verify the robustness of the ESBI model for simulating random crossing seas for the purpose in question in this study, validation is performed here by comparing with the laboratory results reported in Toffoli et al. [21]. To reproduce this crossing sea state with the same wave conditions by using the ESBI model, the computational domain covers 40-by-40 peak wavelengths and is resolved into 1,024-by-512 points in the X- and Y-directions, respectively. The selected domain size and resolution in space ensure that the Fourier modes up to 7- and 3-times peak wavenumber in the X- and Y- directions, respectively, are free of aliasing. A sensitivity test indicates that this resolution is sufficiently accurate to model the highly non-linear interactions between the two crossing wave trains for the purpose of this study. For instance, if we denote the error as the maximum difference between free surface elevation signals recorded on a probe at the same location divided by significant height, then the maximum error among all probes between the results based on the current configuration and those obtained by using 2,048-by-512 and 1,024-by-1,024 points is only about 4.3 and 5.2%, respectively. The wave generation zone is placed along the Y-direction and 5 peak wavelengths from the left boundary, while the waves are absorbed in the surrounding boundaries. The plan view of the computational domain is illustrated in **Figure 1**, where only part of the domain on the right-hand side is effectively used for the simulations. The wave gauges are deployed every 4 and 5 peak wavelengths in the X- and Y- directions, respectively, indicating that there are $8 \times 7 = 56$ gauges used in total. This will avoid the issue where using a single point observation is insufficient to investigate the extreme wave ensembles as the gauge may not always be located at the focusing point [33]. For each individual crossing sea state, four realizations are carried out by using different random number sequences as the phases for generating random waves, which is sufficient for overcoming the uncertainties due to the selection of random phases on calculating wave statistics (this will be further discussed in section Kurtosis). Meanwhile, each simulation lasts for 1,000 peak periods (equivalent to a typical 3-hour sea state), and the first 100 peak wave periods will be used for developing an established sea. We use wave surface time histories collected on the gauges where the sea state becomes equilibrium among 100–1,000 peak periods for estimating the wave statistics. It is estimated that about a total number of 10^5 waves are recorded on the chosen gauges in the domain based on an up-cross method, which is sufficient to achieve reliable statistics. Such a method to determine the total number of waves differs from that employed by Trulsen et al. [14], where spatiotemporal correlation needs to be considered. Note that the ensemble of data measured at different locations will be used to estimate the exceedance probability. For the purpose of making a comparison with theoretical probability distribution models, the condition of homogeneity and uncorrelation should hold. We compared the wave action over space and correlations of signal collected on different gauges and found that both the conditions, i.e., homogeneity and weak correlation, are affirmed, but the results are not presented in the paper for brief.

The wave condition employs the JONSWAP spectrum with a fixed peak enhancement factor $\gamma = 6$ and wave steepness $k_p H_s = 0.28$. The spreading is zero and thus each individual random wave train is unidirectional. The angle between two

crossing seas is fixed at $\varphi = 40^o$ throughout this study, which is identified as the most hazardous angle leading to the maximum kurtosis observed in the laboratory [21]. It is worth noting that this angle is not necessarily the case for a two perturbed uniform wave train as sideband growth is observed to reduce significantly at angles beyond 40° [19]. The kurtosis is then estimated by using Eq. (1) along the X-direction ($Y = 0$), i.e., the mean direction, based on the simulated free surface elevation. In addition to the laboratory results, the numerical results by using the fully non-linear Higher-Order Spectrum (HOS) method reported in Toffoli et al. [21] are also included here for comparisons, all of which are summarized in **Figure 2**. In general, the numerical results obtained by using the ESBI depict that the kurtosis gradually grows along the X- direction and becomes stabilized near the end of the computational domain. This trend agrees very well with that observed in the laboratory, namely (i) the agreement between two curves being within the confidence interval of about $\pm$ 0.2; (ii) the difference of maximum kurtosis near the end being about 0.8%; and (iii) the difference of maximum excess kurtosis being about 8%. However, there is a big deviation from those obtained by using the HOS method. The reason may be that the configuration of the HOS model is not exactly the same as those in the laboratory, e.g., periodic boundary conditions and a smaller domain size are adopted in the simulations by using the HOS method. On the other hand, by examining the significant height along the mean direction, a reduction of about 2% is observed on the last gauge at the end of the domain in comparison with the first gauge due to the usage of the energy dissipation model to suppress breaking waves. Nevertheless, the agreement between the results obtained by using the ESBI and those from the experiment implies that the ESBI model with the current configurations can be reliably used for the purpose of this study.

RESULTS AND DISCUSSIONS

To investigate the effects of the spectral bandwidth on extreme wave statistics in crossing seas, the JONSWAP spectrum is employed with selected values for peak enhancement factor among $\gamma = 1 \sim 9$. This range basically covers the majority of the cases from the broadband to narrowband seas [1]. Note that the larger γ is, the narrower the spectrum is. The bandwidth parameter ν is estimated based on Eq. (4) and its values are summarized in **Table 1**. Other configurations are the same as those explained in section Methodologies. Selected snapshots of the free surface elevation in space are extracted at the end of the simulation and they are displayed in **Figure 3**. It shows that at this selected time instance, the number of extreme waves observed in the crossing sea of narrow bandwidth is larger than those in the relatively broadband sea.

TABLE 1 | Peak enhancement factor against spectral bandwidth.

γ	1	1.3	1.6	2	3	4	6	9
ν	0.49	0.39	0.31	0.25	0.19	0.16	0.14	0.11

Kurtosis

Kurtosis was selected in this study for the indication of extreme wave probability as it has been known that the non-linear four-wave interactions are one of the primary causes of rogue waves, and there is a strong correlation between the kurtosis and the strength of four-wave interactions [24]. Prior to investigating the effects of spectral bandwidth on kurtosis, it is of interest to examine whether the kurtosis is enhanced or not due to the crossing of two wave trains. For that examination, the simulations of non-crossing unidirectional random waves with $k_pH_s = 0.28$ and $\gamma = 6$ were performed, and the values of kurtosis along $Y = 0$ are shown in **Figure 2**. It is observed that the kurtosis for non-crossing seas grows in a similar trend to that of the crossing seas, i.e., it gradually increases along $Y = 0$ and becomes stabilized after propagating a distance of about 23 peak wavelengths. However, the excess part of the stabilized kurtosis near the end of the computational domain for the non-crossing seas was 36.8% smaller than that of the crossing seas. This is not surprising as the crossing sea state can produce higher steepness waves in comparison with non-crossing seas [15]. Consequently, the probability of observing extreme waves during the crossing increases; hence, the kurtosis will be enhanced. It should also be pointed out that as the crossing seas are established by two unidirectional wave trains, the kurtosis monotonically increases with distance to the asymptotic value and will not drop afterward without change of computational conditions, which is in contrast to the "overshoot" phenomenon observed in the spreading waves, where the dynamic excess kurtosis will vanish at a large distance due to energy spreads directionally [27]. In addition, to address that the kurtosis obtained by the fully non-linear model is induced by third- and higher-order non-linearities, another group of simulations of crossing seas with the wave condition $k_pH_s = 0.28$ and $\gamma = 6$ were performed by restricting the estimation of the vertical velocity in the ESBI model up to the second order, i.e., $V = V_1 + V_2$. And the second term of N in Eq. (8) is set to zero. By doing so, the non-linear effects beyond the second order were ignored in the numerical simulation, which is similar to the approach of the second-order HOS model employed in Fedele et al. [10]. The numerical results showed that the stabilized kurtosis is 3.14, which basically agreed with the theoretical prediction based on Eq. (2) without the dynamic part, i.e., $\tilde{\kappa} = 3 + 24\varepsilon^2 \approx 3.12$. It implies that Eq. (2) without the dynamic part can be approximately used to predict the excess kurtosis due to the bound waves obtained by using the numerical model without the third- and higher-order non-linear terms. Otherwise, the kurtosis estimated using the results from the fully non-linear model exhibits larger values due to the contribution of the third- and higher-order non-linearities.

The rest of this section discusses the effects of spectral bandwidth on the kurtosis of crossing random seas. The kurtosis is firstly estimated by Eq. (1) using the surface time histories collected on probes along the center line of the domain $Y = 0$, and the results are summarized in **Figure 4**. It shows that the kurtosis increases along X-direction and is subjected to a deceleration, and then becomes stabilized toward the end of the domain. The values observed near the end of the domain are all larger than 3, indicating that the non-linearities play an

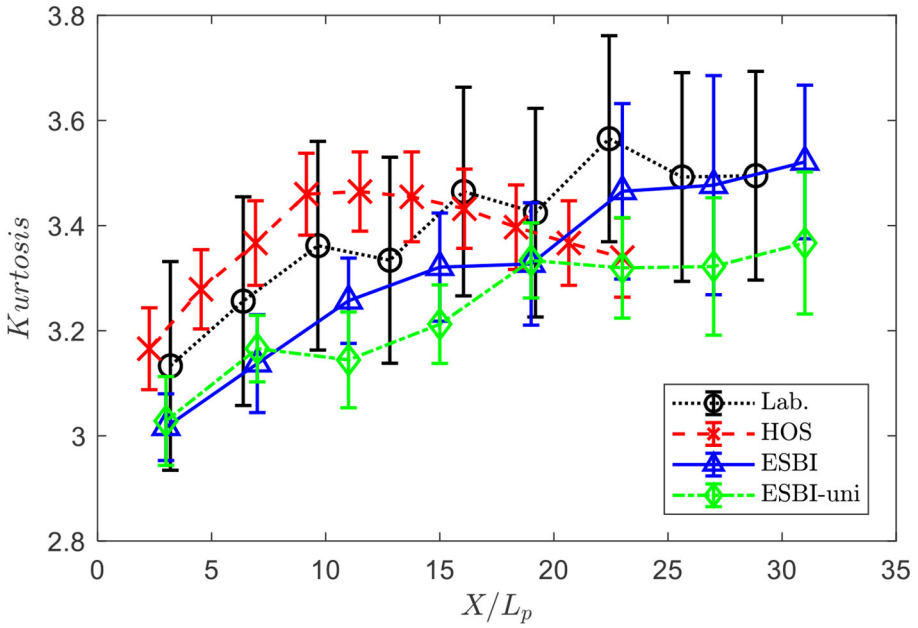

FIGURE 2 | Kurtosis along the center line of the domain $Y = 0$. "Lab.": Laboratory experiment results; "HOS": Numerical results by using the HOS method; "ESBI": Numerical results by using the ESBI method for crossing sea; "ESBI-uni": Numerical results by using ESBI for non-crossing unidirectional sea.

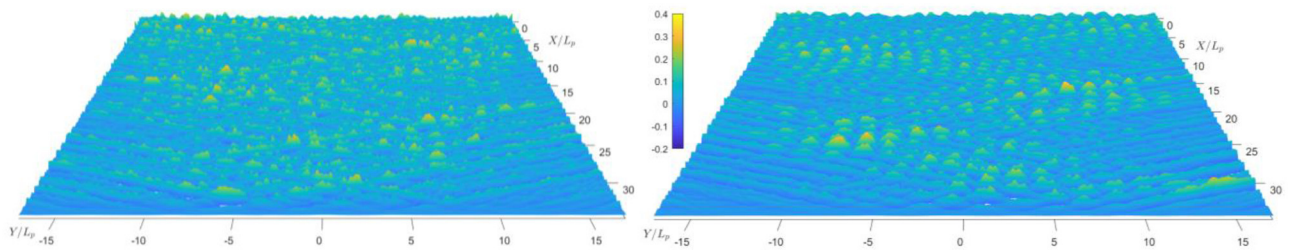

FIGURE 3 | Selected snapshot of the free surface spatial distribution in **(A)** broadband sea and **(B)** narrowband sea.

important role in the formation of extreme waves in the crossing sea. In addition, the growth rate among each curve depends on the spectral bandwidth and, in general, it is faster for narrow bandwidth. Meanwhile, the stabilized kurtosis near the end of the domain also implied that narrower bandwidth yields relatively higher values of kurtosis. This finding basically agrees with that reported based on a stability analysis of crossing perturbed Stokes wave trains, which claims that narrow spectral bandwidth leads to higher amplification of the wave amplitude [18]. It should be noted that the development of unstable waves of small growth rate will be constrained by the computational domain size and so they may not develop into large waves. This is particularly important for the study of two crossing perturbed uniform wave trains [18]. However, this study aims to generate an established crossing random sea where the stabilized statistics are of interest. To demonstrate that the domain size employed in this study is sufficient for achieving stabilized statistics, a group of simulations is performed in a larger domain of 80-by-40 peak wavelengths with the same grid size for the case $\gamma = 6$. It is found that the kurtosis does not increase further beyond the maximum distance $X/L_p = 31$ along $Y = 0$. For instance, it is found that the average kurtosis within the section $23 \leq X/L_p \leq 31$ is 3.49 in the current domain, which is very close to the average kurtosis of 3.51 within the section $23 \leq X/L_p \leq 47$ in the larger domain. Therefore, we can justify that the kurtosis has reached the equilibrium stage within the distance $23 \leq X/L_p \leq 31$ of the current domain.

Apart from examining the kurtosis along the centerline, it is also important to examine the stabilized kurtosis after it reaches equilibrium. To do that, the kurtosis is estimated via Eq. (1) by using the surface time histories collected on the gauges within the section $23 \leq X/L_p \leq 31$, and the stabilized kurtosis takes the mean value and then is averaged over four realizations. In

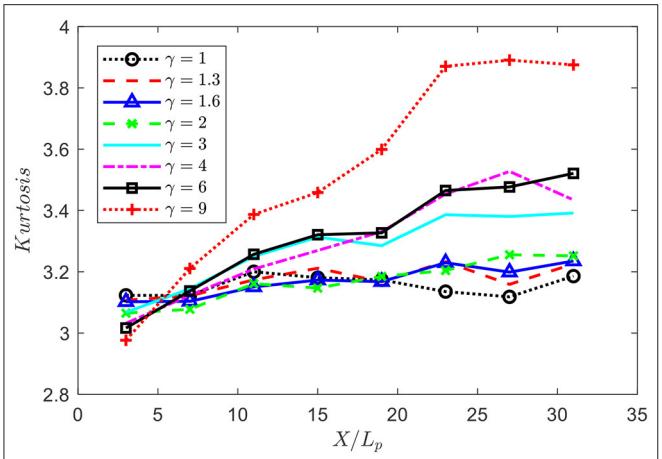

FIGURE 4 | Kurtosis along the center line of the domain $Y = 0$ for cases with different bandwidth.

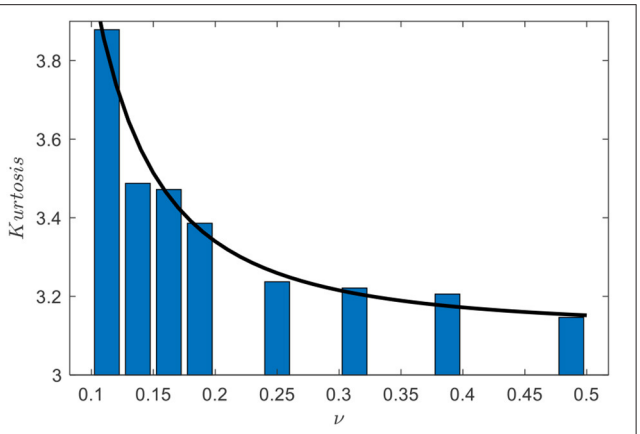

FIGURE 5 | Average kurtosis against spectral bandwidth. Bars represent the values estimated by using Eq. (1); Lines represent fitted results by Eq. (11).

order to demonstrate the sufficiency of the realization number, a fifth realization has also been performed and it is found that the maximum error of stabilized kurtosis between using four and five realizations is about 0.4% among all bandwidths. Therefore, four realizations are sufficient for the purpose of this study, while the results afterward are obtained based on five realizations for a more reliable analysis. The results of stabilized kurtosis against the spectral bandwidth are summarized in **Figure 5**. The figure shows that the stabilized kurtosis decreases as the spectral bandwidth becomes wider. Furthermore, it is also noted that the variation of the stabilized kurtosis drops faster for narrower bandwidth and is subject to a deceleration toward broader bandwidth. Its maximum corresponding to the narrowest bandwidth, i.e., $\nu = 0.11$ ($\gamma = 9$), is about 3.88, which is much larger than 3, i.e., the Gaussian sea indicator. It implies that the probability of extreme waves due to the non-linear interactions between two crossing seas can be significant in the area where crossing is evident. And the chance of encountering an extreme wave is much higher than the predicted probability based on the linear theory.

Next, to predict the kurtosis for crossing seas provided that the bandwidth is given, the relationship between kurtosis and spectral bandwidth is to be established. However, Eqs. (2)∼(4) cannot be directly used in crossing seas as there is no unique way to quantify the bandwidth. For example, many studies have suggested estimating the spectral bandwidth for unidirectional seas by using, e.g., the peakedness parameter introduced by Goda [34], zeroth, first and second moment of the spectrum [29], renormalized SD of the spectrum [22, 24], or the half-width at half the peak value of the spectrum [14]. Each method produces bandwidth values in a certain range and they can be empirically converted to each other [24, 35]. Nevertheless, to achieve this goal, here, we refer to Eqs. (2)∼(4) and examine whether they can be improved to approximate the values of kurtosis reported in **Figure 5**. According to Eq. (2), as the wave steepness and angle of crossing are fixed, one expects the variation of the predicted excess kurtosis is in proportion to the inverse of ν^2, i.e.,

$$\tilde{\kappa} - \sigma \propto \frac{1}{\nu^2}, \tag{10}$$

where σ is expected to be a constant larger than 3 as it includes the non-linear Stokes contribution. Based on that, the least squares method is performed to fit the values of kurtosis in **Figure 5**, and the relationship between kurtosis and spectral bandwidth can then be established by using the following formula:

$$\kappa' = 3.116 + \frac{0.009}{\nu^2}, \quad X/L_p \geq 21 \tag{11}$$

The curve of fitted values κ' is displayed in **Figure 5**, which agrees very well with those calculated directly from using the fully non-linear simulation results. The suggested formula has successfully captured the variation of the kurtosis subject to the changes of the bandwidth, while the maximum error is about 5%. The good agreement reveals that Eq. (11) modified based on Eqs. (2)∼(4) works very well for the cases being studied here. Heuristically, the usage of the spectral bandwidth for predicting the kurtosis may be extended in crossing seas with wave conditions not limited in this study. Note that Eq. (11) can only be used for predicting the stabilized kurtosis in the region where waves attain equilibrium or are fully developed. The variation of kurtosis during the translational stage is not the focus of this study as it is induced by the unrealistic assumption of the initial Gaussian wave field [27] for wave generation and does not provide practical value.

Wave Crest Exceedance Probability

In this section, the exceedance probability of the crest height is estimated by using the surface elevation time histories collected on gauges within the section $23 \leq X/L_p \leq 31$ over five realizations with a down-crossing method performed in the time domain (with a sampling rate of 40 points per peak period) and comparisons are made against the theories based on Eqs. (5)∼(7). It should be pointed out that such a way to

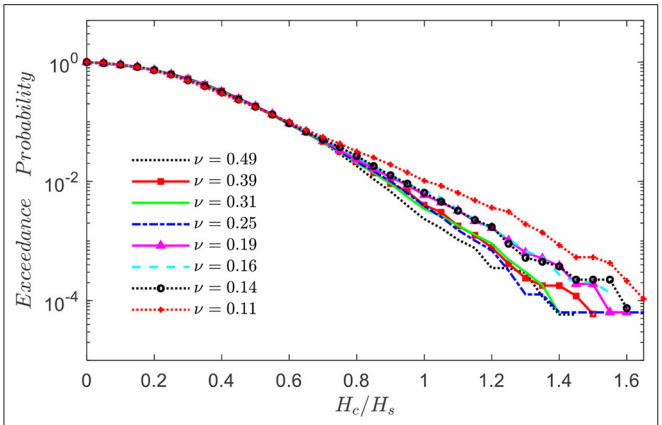

FIGURE 6 | Wave crest exceedance probability estimated by using fully non-linear numerical results.

ensemble crest height over spatial measurements is equivalent to the averaged exceedance probability over the selected gauges. Note that the values of kurtosis as used by Eq. (7) are those presented in **Figure 5**, i.e., those estimated directly from using the fully non-linear simulation results. It means that the theoretical results by Eq. (7) consider a certain degree of fully non-linear effects. To verify the effects of bandwidth on the exceedance probability, the numerical results are summarized and displayed in **Figure 6**. It indicates that the probability of the extreme waves as described by the tail of the distribution generally increases as the spectral bandwidth becomes narrower. This is consistent with the findings regarding the kurtosis in section Kurtosis. It is also depicted in **Figure 6**, when the spectral bandwidth becomes extremely narrow, e.g., $\nu \leq 0.19$, the exceedance probability obtained from the numerical results starts to exhibit a higher tail moving toward a straight asymptote in the semi-logarithm scale. This is unusual and worth to be further investigated comprehensively. Nevertheless, it can be concluded that the probability of observing an extreme wave in the crossing sea is enhanced if the spectral bandwidth reduces.

In addition, to discuss the suitability of theoretical distribution models for describing the crest height exceedance probability, the predictions based on Eqs. (5)∼(7) and those obtained from numerical results are summarized in **Figure 7**. It can be noted that both the Rayleigh distribution and second-order Tayfun distribution underestimate the wave crest exceedance probability in all the cases being studied here, which is also reported in a study with experiments conducted in a laboratory [22]. Therefore, it can be concluded that the Rayleigh distribution based on the linear wave theory and the Tayfun distribution of second-order cannot be used to accurately describe the crest exceedance probability in crossing sea state with the wave conditions discussed in this study. This basically agrees with the findings by Fedele et al. [36] using space-time measurements in crossing sea states consisting of swell and wind waves. On the other hand, for relatively wider spectral bandwidth, as shown in **Figures 7A,B**, the third-order Tayfun distribution is generally in good agreement with the numerical results, though slightly overestimates the probability in the range $H_c/H_s < 1$. However, the discrepancy between the numerical results and third-order Tayfun theoretical distribution becomes evident for relatively narrower bandwidth as shown in **Figures 7C,D**. In particular, the difference becomes dramatic in the range $H_c/H_s > 1.2$, which is often used as one of the criteria to justify whether an extreme is a rogue wave (the other condition $H/H_s > 2$ must also be met to be identified as a rogue wave, where H is the crest to trough height). For example, it is noticed that for those cases with relatively narrower bandwidth, the third-order Tayfun distribution significantly underestimates the exceedance probability at the tail of the distribution. Therefore, the third-order Tayfun distribution may not be suitable for studying the crest exceedance probability for the crossing wave conditions with narrow bandwidths, even for the average peakedness condition of a JONSWAP sea, i.e., $\gamma = 3$.

CONCLUSIONS

This study discusses the effects of spectral bandwidth on the extreme wave statistics in deep crossing seas, in particular, the kurtosis and wave crest exceedance probability, through fully non-linear numerical simulations on a large spatial-temporal scale of 40 × 40 peak wavelengths in domain size and 1,000 peak periods in time. Each of the two random wave trains is unidirectional based on the JONSWAP spectrum with a peak enhancement factor in the range 1–9. The free surface time histories are collected on selected wave probes deployed in the computational domain where the waves attain equilibrium and are used for reliable estimation of the kurtosis and exceedance probability. Verification of the numerical model is performed against laboratory experiments while the robustness of the numerical model is demonstrated by the good agreement observed with measurements with a confidence interval of ±0.2 for averaged kurtosis, while errors of maximum kurtosis and maximum excess kurtosis were about 0.8 and 8%, respectively.

The results reveal that the excess part of the stabilized kurtosis for the non-crossing seas is about 40% smaller than that of the crossing seas. This is due to the fact that the crossing sea state creates higher steepness waves [15], and the probability of observing extreme waves increases as a consequence, hence, enhancing the kurtosis in the crossing seas. Besides, it is concluded that the kurtosis will become smaller when the spectral bandwidth of each individual random wave train in crossing seas increases, and its variation subjects to a deceleration toward broader bandwidth. The maximum kurtosis observed in this study is about 3.88, which is much higher than the Gaussian sea indicator, i.e., $\kappa = 3$. It is evidenced that the non-linearities play an important role in the enhancement of the kurtosis in crossing seas. Besides, a novel empirical formula for predicting the stabilized kurtosis by using the spectral bandwidth is proposed where the coefficients are derived through fitting the numerical values. The formula suggests that the excess kurtosis is proportional to the inverse of the square of bandwidth. Meanwhile, the good agreement between the fitted and numerical results with a maximum error of about 5% is encouraging,

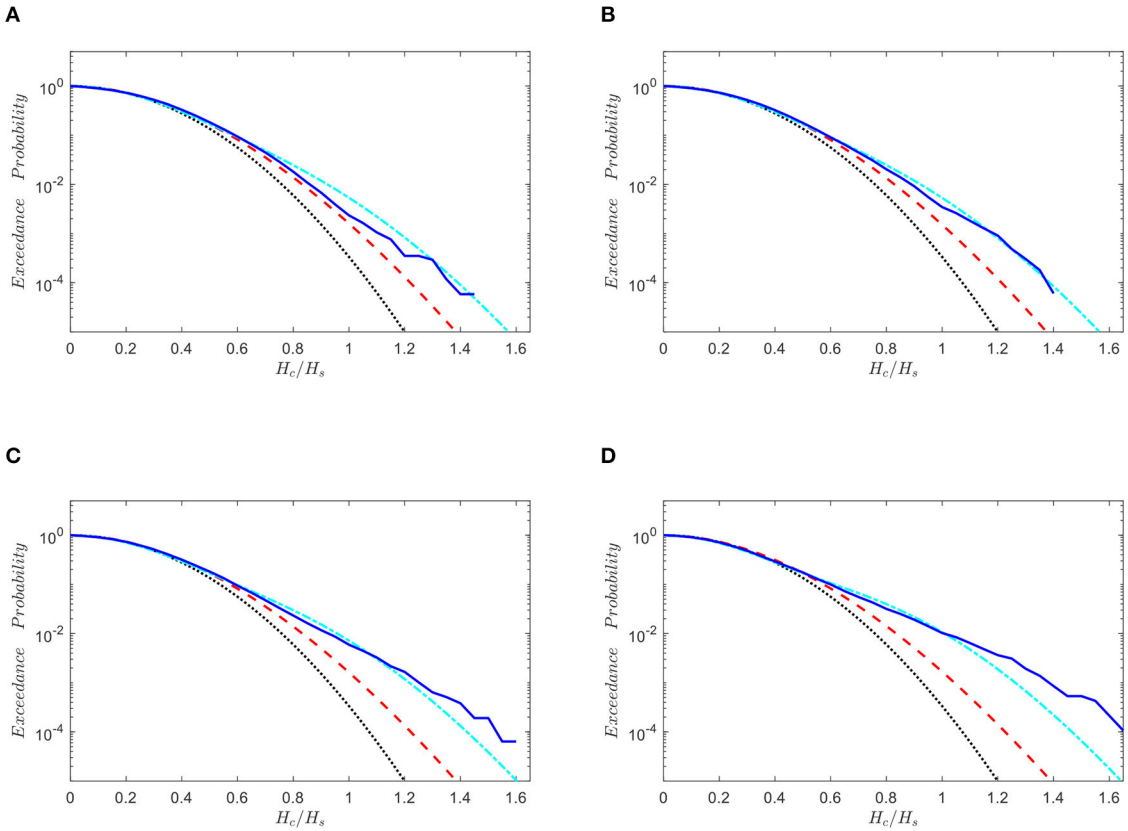

FIGURE 7 | Wave crest exceedance probability. "···": P_R, Rayleigh distribution; "—":$P_T^{(2)}$, second-order Tayfun distribution; "· — · — ·": $P_T^{(3)}$, third-order Tayfun distribution; "–": Numerical results based on ESBI. **(A)** $\nu = 0.49$ ($\gamma = 1$). **(B)** $\nu = 0.31$ ($\gamma = 1.6$). **(C)** $\nu = 0.19$ ($\gamma = 3$). **(D)** $\nu = 0.11$ ($\gamma = 9$).

which implies that the suggested formula has the potential to be extended for other wave conditions not considered in this study, but it requires careful calibration.

Furthermore, the study also shows that the crest height exceedance probability of extreme waves grows as a result of narrower bandwidth. Comparisons between the numerical results and theoretical distributions, i.e., the Rayleigh distribution, second- and third-order Tayfun distribution, are also carried out. It is found that the Rayleigh and second-order Tayfun distribution significantly underestimate the exceedance probability regardless of the spectral bandwidth. Thus, neither of them can be used to accurately predict the crest exceedance probability in crossing seas if the wave conditions are similar to those reported in this study, i.e., initial steepness $k_pH_s = 0.28$ and crossing angle $\varphi = 40^o$. Meanwhile, the third-order Tayfun distribution can successfully describe the exceedance probability for cases of relatively broader bandwidth, e.g., $\gamma \leq 1.6$; however, it underestimates the tail of the distribution when the bandwidth becomes narrower. Therefore, the suitability of third-order Tayfun distribution for crossing seas depends on the magnitude of the bandwidth, which needs to be investigated quantitatively. However, these conclusions are arrived at using the results for crossing seas. This does not negate the suitability of their application in non-crossing (or uni-modal) seas.

Nevertheless, it should be noted that this study only covers some cases in a broad class of situations, e.g., the crossing sea in this study features a symmetrical bimodal spectrum, which is composed of two unidirectional random wave trains that are identical in terms of the significant height, peak wavenumber, and bandwidth. Therefore, the conclusions above hold only for the cases reported in this study and may not be true for other cases beyond the wave conditions considered here, namely the initial steepness k_pH_s not being equal to 0.28, the crossing angle not being 40^o, spreading angle of each wave train not being 0, and the spectral shape not being able to be described by the JONSWAP spectrum. Studies will be carried out in the future to investigate the extreme wave properties in two crossing seas subject to the variation of other wave parameters such as wave steepness, crossing angle, etc., and spreading will also be considered in order to identify the most influential factor on the extreme wave statistic. The correlation between the wave steepness and crossing angle needs to be considered as well, as the integral steepness varies largely with the crossing condition subject to cyclonic winds [37]. Note that the scaling should be taken into consideration for predicting the variation of kurtosis

during the translational stage. Eq. (11) cannot be used for this purpose. That being said, this formula is an implication that the kurtosis is inversely proportional to the spectral bandwidth. In addition, Ruban [38], in a recent study, pointed out that the formation of extreme waves also depends on the orientation of the wavefronts to the direction of the group, while the highest amplification happens at about 18–28° degrees. To address this issue in crossing seas, the effects of various angles between the wavefront and group direction of each individual random wave train on excitation of extreme waves during crossing will also be taken into consideration in the future study.

DATA AVAILABILITY STATEMENT

The raw data supporting the conclusions of this article will be made available by the authors, without undue reservation.

AUTHOR CONTRIBUTIONS

JW was responsible for conceptualization, methodology, analysis, and writing. QM was responsible for data curation, writing, and editing. SY was responsible for writing and reviewing. BL was responsible for reviewing. All authors contributed to the article and approved the submitted version.

FUNDING

JW and BL show gratitude to the sponsorship provided by NSFC, China (51679223, 51739010). QM and SY acknowledge the financial support of EPSRC, UK (EP/L01467X/1, EP/T00424X/1, EP/T026782/1), and DST-UKIERI project (DST-UKIERI-2016-17-0029).

ACKNOWLEDGMENTS

JW acknowledges the host of Prof. Philip L.-F. Liu at Faculty of Engineering, National University of Singapore, where this research was conducted. The authors would like to thank the very insightful comments of three reviewers.

SUPPLEMENTARY MATERIAL

The Supplementary Material for this article can be found online at: https://www.frontiersin.org/articles/10.3389/fphy.2021.593394/full#supplementary-material

REFERENCES

1. Goda Y. *Random Seas and Design of Maritime Structures.* 3rd edn. Singapore: World scientific (2010).
2. Kharif C, Pelinovsky E, Slunyaev A. *Rogue Waves in the Ocean.* Berlin: Springer-Verlag (2009).
3. Ruban V, Kodama Y, Ruderman M, Dudley J, Grimshaw R, McClintock PVE, et al. Rogue waves–towards a unifying concept?: Discussions and debates. *Eur Phys J Special Top.* (2010) 185:5–15. doi: 10.1140/epjst/e2010-01234-y
4. Akhmediev N, Ankiewicz A, Taki M. Waves that appear from nowhere and disappear without a trace. *Phys Lett A.* (2009) 373:675–8. doi: 10.1016/j.physleta.2008.12.036
5. Chabchoub A, Hoffmann NP, Akhmediev N. Rogue wave observation in a water wave tank. *Phys Rev Lett.* (2011) 106:204502. doi: 10.1103/PhysRevLett.106.204502
6. Chabchoub A, Hoffmann N, Onorato M, Slunyaev A, Sergeeva A, Pelinovsky E, et al. Observation of a hierarchy of up to fifth-order rogue waves in a water tank. *Phys Rev E.* (2012) 86:056601. doi: 10.1103/PhysRevE.86.056601
7. Chabchoub A. Tracking breather dynamics in irregular sea state conditions. *Phys Rev Lett.* (2016) 117:144103. doi: 10.1103/PhysRevLett.117.144103
8. Slunyaev A, Pelinovsky E, Sergeeva A, Chabchoub A, Hoffmann N, Onorato M, et al. Super-rogue waves in simulations based on weakly nonlinear and fully nonlinear hydrodynamic equations. *Phys Rev E.* (2013) 88:012909. doi: 10.1103/PhysRevE.88.012909
9. Wang J, Ma QW, Yan S, Chabchoub A. Breather rogue waves in random seas. *Phys Rev Appl.* (2018) 9:014016. doi: 10.1103/PhysRevApplied.9.014016
10. Fedele F, Brennan J, Ponce de León S, Dudley J, Dias F. Real world ocean rogue waves explained without the modulational instability. *Sci Rep.* (2016) 6:27715. doi: 10.1038/srep27715
11. Toffoli A, Lefèvre JM, Monbaliu J, Bitner-Gregersen E. Dangerous sea-states for marine operations. In: *Proceedings of the 14th International Offshore and Polar Engineering Conference*. Toulon (2004).
12. Adcock TAA, Taylor PH, Yan S, Ma QW, Janssen PAEM. Did the draupner wave occur in a crossing sea? *Proc R Soc London A: Mathematical Phys Eng Sci.* (2011) 467:3004–21. doi: 10.1098/rspa.2011.0049
13. Cavaleri L, Bertotti L, Torrisi L, Bitner-Gregersen E, Serio M, Onorato M. Rogue waves in crossing seas: The Louis Majesty accident. *J Geophys Res Oceans.* (2012) 117:1–8. doi: 10.1029/2012JC007923
14. Trulsen K, Nieto-Borge JC, Gramstad O, Aouf L. Crossing sea state and rogue wave probability during the prestige accident. *J Geophys Res Oceans.* (2015) 120:7113–36. doi: 10.1002/2015JC011161
15. McAllister ML, Draycott S, Adcock TAA, Taylor PH, van den Bremer TS. Laboratory recreation of the Draupner wave and the role of breaking in crossing seas. *J Fluid Mech.* (2019) 860:767–86. doi: 10.1017/jfm.2018.886
16. Onorato M, Osborne AR, Serio M. Modulational instability in crossing sea states: a possible mechanism for the formation of freak waves. *Phys Rev Lett.* (2006) 96:014503. doi: 10.1103/PhysRevLett.96.014503
17. Shukla PK, Kourakis I, Eliasson B, Marklund M, Stenflo L. Instability and evolution of nonlinearly interacting water waves. *Phys Rev Lett.* (2006) 97:094501. doi: 10.1103/PhysRevLett.97.094501
18. Onorato M, Proment D, Toffoli A. Freak waves in crossing seas. *Eur Phys J Special Topics.* (2010) 185:45–55. doi: 10.1140/epjst/e2010-01237-8
19. Steer JN, McAllister ML, Borthwick AG, Van Den Bremer TS. Experimental observation of modulational instability in crossing surface gravity wavetrains. *Fluids.* (2019) 4:105. doi: 10.3390/fluids4020105
20. Shukla PK, Marklund M, Stenflo L. Modulational instability of nonlinearly interacting incoherent sea states. *JETP Lett.* (2007) 84:645–9. doi: 10.1134/S0021364006240039
21. Toffoli A, Bitner-Gregersen EM, Osborne AE, Serio E, Monbaliu J, Onorato M. Extreme waves in random crossing seas: laboratory experiments and numerical simulations. *Geophys Res Lett.* (2011) 38:6. doi: 10.1029/2011GL046827
22. Luxmoore JF, Ilic S, Mori N. On kurtosis and extreme waves in crossing directional seas: a laboratory experiment. *J Fluid Mech.* (2019) 876:792–817. doi: 10.1017/jfm.2019.575
23. Wang J, Ma QW. Numerical techniques on improving computational efficiency of spectral boundary integral method. *Int J Numer Methods Eng.* (2015) 102:1638–69. doi: 10.1002/nme.4857
24. Janssen PA. Nonlinear four-wave interactions and freak waves. *J Phys Oceanogr.* (2003) 33:863–84. doi: 10.1175/1520-0485(2003)33<863:NFIAFW>2.0.CO;2

25. Janssen PA. On some consequences of the canonical transformation in the Hamiltonian theory of water waves. *J Fluid Mech.* (2009) 637:1–44. doi: 10.1017/S0022112009008131
26. Mori N, Janssen PA. On kurtosis and occurrence probability of freak waves. *J Phys Oceanogr.* (2006) 36:1471–83. doi: 10.1175/JPO2922.1
27. Fedele F. On the kurtosis of deep-water gravity waves. *J Fluid Mech.* (2015) 782:25–36. doi: 10.1017/jfm.2015.538
28. Janssen PA, Bidlot JR. *On the Extension of the Freak Wave Warning System and Its Verification.* s.l.:European Centre for Medium-Range Weather Forecasts, Reading (2009).
29. Longuet-Higgins MS. On the joint distribution of wave periods and amplitudes in a random wave field. *Proc R Soc Lond.* (1983) 389:241–58. doi: 10.1098/rspa.1983.0107
30. Tayfun M. Narrow-band nonlinear sea waves. *J Geophys Res Oceans.* (1980) 85:1548–52. doi: 10.1029/JC085iC03p01548
31. Tayfun MA, Fedele F. Wave-height distributions and nonlinear effects. *Ocean Eng.* (2007) 34:1631–49. doi: 10.1016/j.oceaneng.2006.11.006
32. Xiao W, Liu Y, Wu G, Yue DKP. Rogue wave occurrence and dynamics by direct simulations of nonlinear wave-field evolution. *J Fluid Mech.* (2013) 720:357–92. doi: 10.1017/jfm.2013.37
33. Benetazzo A, Ardhuin F, Bergamasco F, Cavaleri L, Guimarães PV, Schwendeman M, et al. On the shape and likelihood of oceanic rogue waves. *Sci Rep.* (2017) 7:8276. doi: 10.1038/s41598-017-07704-9
34. Goda Y. Numerical experiments on wave statistics with spectral simulation. *Report Port Harbour Res Inst.* (1970) 9:3–57.
35. Mori N, Onorato M, Janssen PA. On the estimation of the kurtosis in directional sea states for freak wave forecasting. *J Phys Oceanogr.* (2011) 41:1484–97. doi: 10.1175/2011JPO4542.1
36. Fedele F, Benetazzo A, Gallego G, Shih PC, Yezzi A. Space–time measurements of oceanic sea states. *Ocean Model.* (2013) 70:103–15. doi: 10.1016/j.ocemod.2013.01.001
37. Holthuijsen LH, Powell MD, Pietrzak JD. Wind and waves in extreme hurricanes. *J Geophys Res Oceans.* (2012) 117:C09003. doi: 10.1029/2012JC007983
38. Ruban VP. Enhanced rise of rogue waves in slant wave groups. *JETP Lett.* (2011) 94:177–81. doi: 10.1134/S0021364011150100

Conflict of Interest: The authors declare that the research was conducted in the absence of any commercial or financial relationships that could be construed as a potential conflict of interest.

frontiers in Physics

ORIGINAL RESEARCH
published: 30 April 2021
doi: 10.3389/fphy.2021.633890

On the Stabilization of Breather-type Solutions of the Damped Higher Order Nonlinear Schrödinger Equation

C. M. Schober and A. L. Islas*

Department of Mathematics, University of Central Florida, Orlando, FL, United States

Spatially periodic breather solutions (SPBs) of the nonlinear Schrödinger (NLS) equation are frequently used to model rogue waves and are typically unstable. In this paper we study the effects of dissipation and higher order nonlinearities on the stabilization of N-mode SPBs, $1 \leq N \leq 3$, in the framework of a damped higher order NLS (HONLS) equation. We observe the onset of novel instabilities associated with the development of critical states resulting from symmetry breaking in the damped HONLS system. We develop a broadened Floquet characterization of instabilities of solutions of the NLS equation by showing that instabilities are associated with degenerate complex elements of not only the discrete, but also the continuous Floquet spectrum. As a result, the Floquet criteria for the stabilization of a solution of the damped HONLS centers around the elimination of all complex degenerate elements of the spectrum. For a given initial N-mode SPB, a short-time perturbation analysis shows that the complex double points associated with resonant modes split under the damped HONLS while those associated with nonresonant modes remain closed. The corresponding /damped HONLS numerical experiments corroborate that instabilities associated with nonresonant modes persist on a longer time scale than the instabilities associated with resonant modes.

Keywords: spatially periodic breathers, rogue waves, modulational instability, higher order nonlinear Schrödinger, Floquet spectrum

OPEN ACCESS

Edited by:
Amin Chabchoub,
The University of Sydney, Australia

Reviewed by:
Petr Grinevich,
Steklov Mathematical Institute, Russia
Xing Lu,
Beijing Jiaotong University, China

****Correspondence:***
C. M. Schober
cschober@ucf.edu

Specialty section:
This article was submitted to Mathematical and Statistical Physics, a section of the journal Frontiers in Physics

Received: *26 November 2020*
Accepted: *08 February 2021*
Published: *30 April 2021*

Citation:
Schober CM and Islas AL (2021) On the Stabilization of Breather-type Solutions of the Damped Higher Order Nonlinear Schrödinger Equation. Front. Phys. 9:633890. doi: 10.3389/fphy.2021.633890

1 INTRODUCTION

In one of his foundational studies, Stokes established the existence of traveling nonlinear periodic wave trains in deep water [1]. The stability of these waves was resolved when Benjamin and Feir proved that in sufficiently deep water the Stokes wave is modulationally unstable. Small perturbations of Stokes waves were found to lead to exponential growth of the side bands [2, 3]. More recently, modulational instability (MI) of the background state is considered to play a prominent role in the development of rogue waves in oceanic sea states, nonlinear optics, and plasmas [4–9].

The nonlinear Schrödinger (NLS) equation (when $\varepsilon, \gamma = 0$ in **Eq. 1**) is one of the simplest models for studying phenomena related to MI; as such, special solutions of the NLS equation are regarded as prototypes of rogue waves. Among the more tractable "rogue wave" solutions of the NLS equation are the rational solutions (with the Peregrine breather being the lowest order) and the spatially periodic breathers (SPBs) which are constructed as heteroclinic orbits of modulationally unstable Stokes waves [10–12]. In the case of the Stokes waves with N unstable modes (UMs), the associated SPBs can be of dimension $M \leq N$ and are referred to as M-mode SPBs; the single mode SPB is the Akhmediev breather [13]. For more realistic sea states with non-uniform backgrounds, heteroclinic orbits of unstable N-phase solutions have been used to describe rogue waves [14–16].

For theoretical and practical purposes it is important to understand the stability of the SPBs with respect to small variations in initial data and small perturbations of the NLS equation. Using the squared eigenfunction connection between the Floquet spectrum of the NLS equation and the linear stability problem, the SPBs were shown to be typically unstable [17]. The effects of damping on deep water wave dynamics, even when weak, can be significant and in many instances must be included in models to enable accurate predictions of laboratory and field data [18–22].

In a recent study the authors examined the stabilization of symmetric SPBs using the linear damped NLS equation (a near-integrable system that preserves even symmetry of solutions) [23]. The route to stability for these damped SPBs was determined by appealing to the Floquet spectral theory of the NLS equation. Degenerate complex elements of the periodic spectrum (referred to as complex double points) are associated with instabilities of the solution and may split under perturbation to the system. In the restricted subspace of even solutions complex double points can reform as time evolves. The damped solutions were found to be unstable as long as complex double points were present in the spectral decomposition of the data (either by persisting or reforming). A key issue in analyzing the route to stability is determining which complex double points in the spectrum of the SPB are split by damping. For an initial SPB with a given mode structure, perturbation analysis showed that only the complex double points associated with resonant modes split under damping while those associated with nonresonant modes remained closed [23].

The evolution of deep water waves is described only to leading order by the NLS equation. A more accurate description of the wave dynamics is provided by the Dysthe equation, obtained by extending the asymptotic analysis used to derived the NLS equation to fourth order. The Dysthe equation has been shown to accurately predict laboratory data for a wider range of wave parameters than the NLS equation [24, 25, 26]. Gramstad and Trulsen brought the Dysthe equation into Hamiltonian form obtaining a new higher order NLS (HONLS) equation (**Eq. 1** with $\gamma = 0$) [27]. Damped versions of the HONLS equation have successfully described ocean swell and frequency downshift of wave trains on deep water [28, 29].

In this paper we examine the competing effects of dissipation and higher order nonlinearities on the routes to stability of the N-mode SPBs in the framework of the linear damped HONLS equation over a spatially periodic domain:

$$iu_t + u_{xx} + 2|u|^2u + i\varepsilon\left(\frac{1}{2}u_{xxx} - 8|u|^2u_x - 2iu\left[\mathcal{H}\left(|u|^2\right)\right]_x\right) + i\gamma u = 0 \tag{1}$$

where $u(x,t)$ is the complex envelope of the wave train, $\mathcal{H}\{f(x)\} = \frac{1}{\pi}\int_{-\infty}^{\infty}\frac{f(\xi)}{x-\xi}d\xi$ is the Hilbert transform of f, and $0 < \varepsilon, \gamma \ll 1$. The initial data used in the numerical experiments is generated using exact SPB solutions of the integrable NLS equation. The SPBs are over Stokes waves with N unstable modes (referred to as the N-UM regime) for $1 \le N \le 3$. We interpret the damped HONLS (near-integrable) dynamics by appealing to the NLS Floquet spectral theory.

The higher order nonlinearities in **Eq. 1** break the even symmetry of both the initial data and the equation. This raises several interesting questions regarding the damped HONLS equation. Which integrable instabilities are excited by the damped HONLS flow and which elements of the Floquet spectrum are associated with these instabilities? What are the routes to stability under damping; i.e., what remnants of integrable NLS structures are detected in the damped HONLS evolution?

In the present study we observe the onset of novel instabilities as a result of symmetry breaking and the development of critical states in the damped HONLS flow which were nonexistent in the previously examined damped NLS system with even symmetry. Significantly, we determine these instabilities are associated with degenerate complex elements of both the periodic and continuous spectrum, i.e., with both complex "double points" and complex "critical points", respectively. This association was not previously recognized. With regard to teminology, although double points are among the critical points of Δ, in this paper we exclusively call degenerate complex periodic spectrum where $\Delta = \pm 2$ "double points" and reserve the term "critical points" for degenerate complex spectrum where $\Delta \neq \pm 2$.

The paper is organized as follows. In **Section 2** we present elements of the NLS Floquet spectral theory which we use to distinguish instabilities in the numerical experiments. Whether higher phase solutions, such as the even 3-phase solution given in **Eq. 8**, are unstable with respect to general noneven perturbations and what the Floquet "signature" is of the possible instabilities, has been an open question. The closest stability results we are aware of are for the elliptic solutions of the focusing NLS equation [30]. We numerically show an even 3-phase solution of the NLS equation is unstable with respect to generic perturbations of initial data and find the relevant element of the Floquet spectrum associated with the instability in order to develop a broadened Floquet characterization of instabilities of the NLS equation.

A brief overview of the SPB solutions of the NLS is provided at the end of **Section 2** before numerically examining their stabilization under the damped HONLS flow in **Section 3**. The Floquet decompositions of the numerical solutions are computed for $0 \le t \le 100$. Complex double points are initially present in the spectrum. If one of the complex double points present initially splits due to the damped HONLS perturbation, the subsequent evolution involves repeated formation and splitting of complex critical points (not double points) which we correlate with the observed instabilities. The Floquet spectral analysis is complemented by an examination of the growth of small perturbations in the SPB initial data under the damped HONLS flow. We determine that the instabilities saturate and the solutions stabilize once all complex double points and complex critical points vanish in the spectral decomposition of the perturbed flow. Variations in the spectrum under the HONLS flow are correlated with deformations of certain NLS solutions to determine the routes to stability for the damped HONLS SPBs.

In **Section 4**, *via* perturbation analysis, we examine splitting of the complex double points, present in the SPB initial data, under

the damped HONLS flow. We find that for short time, the complex double points associated with modes that resonate with the SPB structure split producing disjoint asymmetric bands, while the complex double points associated with nonresonant modes remain closed, substantiating the initial spectral evolutions observed in the numerical experiments. The nonresonant double points are observed to remain closed for the duration of the experiments, beyond the time-frame of the short time analysis, even though the solution evolves as a damped asymmetric multi-phase state. In this study resonances have a stabilizing effect; the instabilities of nonresonant modes persist on a longer time scale than the instabilities associated with resonant modes.

2 ANALYTICAL FRAMEWORK

The nonlinear Schrödinger equation (when $\varepsilon, \gamma = 0$ in **Eq. 1**) arises as the solvability condition of the Zakharov-Shabat (Z-S) pair of linear systems [31]:

$$\mathcal{L}(u)\phi = \lambda\phi, \qquad \mathcal{L}(u) = \begin{pmatrix} i\partial_x & u \\ -u^* & -i\partial_x \end{pmatrix} \tag{2}$$

$$\phi_t = \begin{pmatrix} -2i\lambda^2 + i|u|^2 & 2i\lambda u - u_x \\ 2i\lambda u^* + u_x^* & 2i\lambda^2 - i|u|^2 \end{pmatrix}\phi \tag{3}$$

where λ is the spectral parameter, ϕ is a complex vector valued eigenfunction, and $u(x,t)$ is a solution of the NLS equation itself. Associated with an L−periodic NLS solution is it's Floquet spectrum

$$\sigma(u) := \{\lambda \in \mathbb{C} | \mathcal{L}\phi = \lambda\phi, |\phi| \; bounded \; \forall x\} \tag{4}$$

Given a fundamental matrix solution of the Z-S system, Φ, one defines the Floquet discriminant as the trace of the transfer matrix across one period L, $\Delta(u,\lambda) = Trace[\Phi(x+L,t;\lambda)\Phi^{-1}(x,t;\lambda)]$. The Floquet spectrum has an explicit representation in terms of the discriminant:

$$\sigma(u) := \{\lambda \in \mathbb{C} | \Delta(u,\lambda) \in \mathbb{R}, -2 \le \Delta(u,\lambda) \le 2\} \tag{5}$$

The Floquet discriminant $\Delta(\lambda)$ is analytic and is a conserved functional of the NLS equation. As such, the spectrum $\sigma(u)$ of an NLS solution is invariant under the time evolution.

The spectrum consists of the entire real axis and curves or "bands of spectrum" in the complex λ plane ($\mathcal{L}(u)$ is not self-adjoint). The periodic/antiperiodic points (abbreviated here as periodic points) of the Floquet spectrum are those at which $\Delta = \pm 2$. The endpoints of the bands of spectrum are given by the simple points of the periodic spectrum $\sigma^s(u) = \{\lambda_j^s \big| \Delta(\lambda_j) = \pm 2, \partial\Delta/\partial\lambda \neq 0\}$. Located within the bands of spectrum are two important spectral elements:

1. Critical points of spectrum, λ_j^c, determined by the condition $\partial\Delta/\partial\lambda = 0$.
2. Double points of periodic spectrum $\sigma^d(u) = \{\lambda_j^d \big| \Delta(\lambda_j^d) = \pm 2, \partial\Delta/\partial\lambda = 0, \partial^2\Delta/\partial\lambda^2 \neq 0\}$.

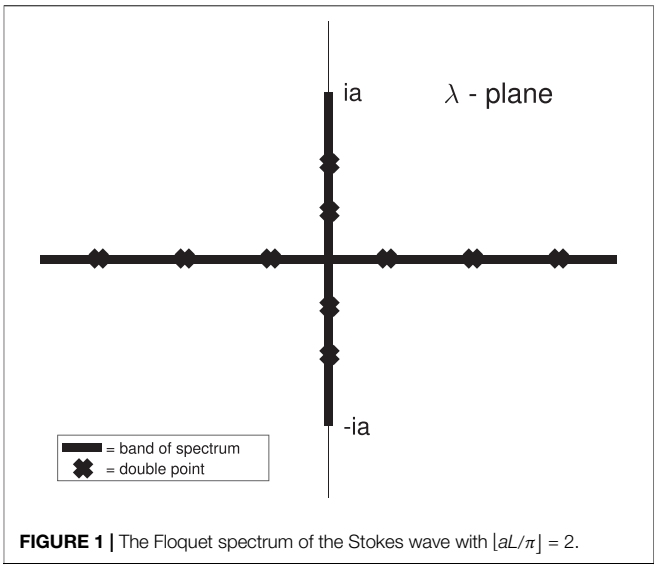

FIGURE 1 | The Floquet spectrum of the Stokes wave with $\lfloor aL/\pi \rfloor = 2$.

Double points are among the critical points of Δ. However, in this paper, we exclusively call the degenerate periodic spectrum where $\Delta = \pm 2$ "double points" and reserve the term "critical points" for degenerate elements of the spectrum where $\Delta \neq \pm 2$.

The Floquet spectrum can be used to represent a solution in terms of a set of nonlinear modes where the structure and stability of the modes are determined by the band-gap structure of the spectrum. Simple periodic points are associated with stable active modes. The location of the double points is particularly important. Real double points correspond to zero amplitude inactive nonlinear modes. On the other hand, complex double points are associated with degenerate, potentially unstable, nonlinear modes with either positive or zero growth rate. When restricted to the subpace of even solutions, exponential instabilities of a solution are associated with complex double points in the spectrum [32].

A concrete example illustrating the correspondence between complex double points in the spectrum and linear instabilities is the Stokes wave solution $u_a(t) = ae^{i(2a^2t+\phi)}$. For small perturbations of the form $u(x,t) = u_a(t)[1+\varepsilon(x,t)]$, $|\varepsilon| \ll 1$, one finds ϵ satisfies the linearized NLS equation

$$i\varepsilon_t + \varepsilon_{xx} + 2|a|^2(\varepsilon + \varepsilon^*) = 0 \tag{6}$$

Representing ϵ as a Fourier series with modes $\varepsilon_j \propto e^{i\mu_j x + \sigma_j t}$, $\mu_j = 2\pi j/L$, gives $\sigma_j^2 = \mu_j^2(4|a|^2 - \mu_j^2)$. As a result, the jth mode is unstable if $0 < (j\pi/\mathrm{L})^2 < |a|^2$. The number of UMs is the largest integer M such that $0 < M < |a|L/\pi$.

The Floquet discriminant for the Stokes wave is $\Delta = 2\cos(\sqrt{a^2+\lambda^2}\,L)$. The Floquet spectrum consists of continuous bands $\mathbb{R} \cup [-ia, ia]$ and a discrete part containing $\lambda_0^s = \pm i|a|$ and the infinte number of double points

$$\left(\lambda_j^d\right)^2 = \left(\frac{j\pi}{L}\right)^2 - a^2, \quad j \in \mathbb{Z}, \quad j \neq 0 \tag{7}$$

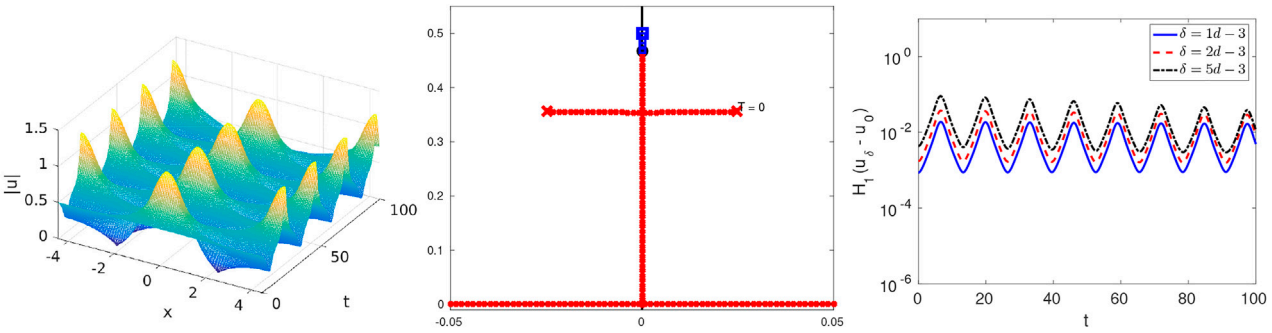

FIGURE 2 | NLS cross state: **(A)** $|u_0(x,t)|$ for $0 \le t \le 100$, **(B)** it's spectrum at $t = 0$, **(C)** $\eta(t)$ for $u_\delta(x,0) = u_0(x,0) + \delta g_1(x)$.

as shown in **Figure 1**. Note that the condition for λ_j^d to be complex is precisely the condition for the jth Fourier mode ε_j to be unstable. The remaining λ_j^d for $|j| > M$ are real double points.

As the NLS spectrum is symmetric under complex conjugation, we subsequently only display the spectrum in the upper half λ-plane.

2.1 A Broadened Floquet Spectral Characterization of Instabilities

Earlier work on perturbations of the NLS equation dealt primarily with solutions with even symmetry whose instabilities were identified solely *via* complex double points [33, 34]. In general, imposing symmetry on a solution restricts it's dynamical behavior and may suppress instabilities. In the current damped HONLS experiments we find instabilities arise due to the asymmetry of the system that are not captured by complex double points. Although complex double points, if present in the damped HONLS flow, still identify instabilities, we need to develop a broader Floquet spectral characterization of instabilities to capture the instabilities of generic solutions.

A clue as to which new spectral elements are associated with instabilities in the full solution space of the NLS equation is provided by considering generic perturbations of initial data for even solutions of the NLS equation. One of the simplest solutions to examine is the following even 3-phase solution of the NLS equation [13],

$$u_0(x,t) = a e^{2ia^2 t} \frac{\sqrt{\frac{\kappa}{1+\kappa}}\, cn\left(\frac{ax}{\sqrt{\kappa}}, \sqrt{\frac{1-\kappa}{2}}\right) dn\left(\frac{a^2 t}{\kappa}, \kappa\right) + i\kappa\, sn\left(\frac{a^2 t}{\kappa}, \kappa\right)}{\sqrt{2}\kappa\left[1 - \sqrt{\frac{\kappa}{1+\kappa}}\, cn\left(\frac{ax}{\sqrt{\kappa}}, \sqrt{\frac{1-\kappa}{2}}\right) cn\left(\frac{a^2 t}{\kappa}, \kappa\right)\right]} \quad (8)$$

With respect to t the solution has a double frequency; a frequency determined by the exponential function and a modulation frequency determined by the elliptic functions. **Equation 8** describes an even standing wave, periodic in space and time, arising as the degeneration of a 3-phase solution due to symmetry in it's spectrum. The spatial period L and temporal period T are functions of $\mathcal{K}_x\left(\sqrt{\frac{1-\kappa}{2}}\right)$ and $\mathcal{K}_t(\kappa)$, respectively, where $\mathcal{K}$ is the complete elliptic integral of the first kind. As $\kappa \to 1$ in **Eq. 8**, $T \to \infty$ and $u_0(x,t) \to U^{(1)}(x,t)$, the SPB given in **Eq. 10** associated with one complex double point.

The surface and Floquet spectrum for $u_0(x,t)$ are shown in **Figures 2A,B**. The spectrum forms an even "cross" state with two bands of spectrum in the upper half plane with endpoints given by the simple periodic spectrum $\lambda_0 = 0.5i$ and $\lambda_1^{\pm} = 0.35i \pm \alpha$. These two bands intersect transversally at λ^c on the imaginary axis. Since $\partial\Delta/\partial\lambda = 0$ at transverse intersections of bands of continuous spectrum, λ^c is a critical point. There are no complex double points in $\sigma[u_0(x,t)]$.

To numerically address the stability of the cross state **Eq. 8** with respect to initial data we consider small perturbations (both symmetric and asymmetric) of the following form:

$$u_\delta(x,0) = u_0(x,0) + \delta g_k(x), \quad k = 1,2$$

where $g_1(x) = e^{i\phi}\cos\mu x$, $g_2(x) = e^{i\phi_1}\cos\mu x + re^{i\phi_2}\sin\mu x$, and $\delta = 10^{-3}, \ldots, 5\times 10^{-3}$. We examine 1) the Floquet spectrum of $u_\delta(x,t)$ as compared with $u_0(x,t)$ and 2) the growth of the perturbations as δ is varied. We consider a solution $u(x,t)$ of the NLS equation to be stable if for every $\varepsilon > 0$ there exists a $\delta > 0$ such that if $\|u_\delta(x,0) - u(x,0)\|_{H^1} < \delta$, then $\|u_\delta(x,t) - u(x,t)\|_{H^1} < \varepsilon$, for all t. Therefore, to determine whether u and u_δ stay close as time evolves, we monitor the evolution of the difference

$$\eta(t) = \|u_\delta(x,t) - u(x,t)\|_{H^1} \quad (9)$$

where $\|f\|_{H^1}^2 = \int_{-L/2}^{L/2} (|f_x|^2 + |f|^2)dx$.

Symmetric Perturbations of Initial Data

As ϕ and δ are varied, the surface and spectrum for $u_\delta(x,t)$ for perturbation $g_1(x)$ are qualitatively the same as in **Figures 2A,B**. The endpoints of the band of spectrum, $\sigma^s(u_\delta)$, are slightly shifted maintaining even symmetry. Due to analyticity of Δ, λ^c does not split under even perturbations and the spectrum is not topologically different. **Figure 2C** shows the evolution of $\eta(t)$ for even perturbations $u_\delta(x,0) = u_0(x,0) + \delta g_1(x)$. The small osciallations in $\eta(t)$, typical in Hamiltonian systems, do not grow. The Floquet spectrum and the evolution of $\eta(t)$ show that when restricted to the subspace of even solutions, $u_0(x,t)$ is stable.

Asymmetric Perturbations of Initial Data

The surface and spectrum of $u_\delta(x,t)$ for $u_\delta(x,0) = u_0(x,0) + 0.05\sin\mu x$ are shown in **Figures 3A,B**. A topologically different

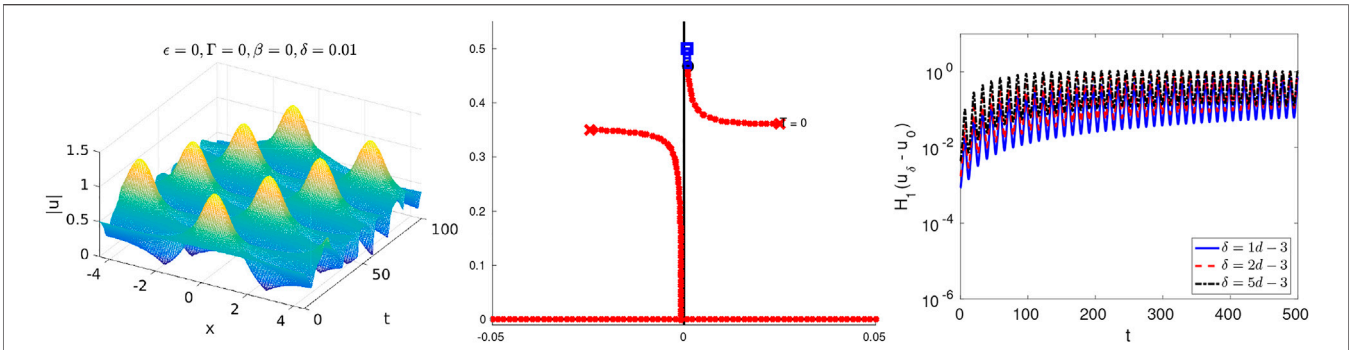

FIGURE 3 | NLS noneven 3-phase solution: **(A)** $|u_\delta(x,t)|$ for $0 \le t \le 100$, **(B)** it's spectrum at $t = 0$, **(C)** $\eta(t)$ for $u_\delta(x,0) = u_0(x,0) + \delta g_2(x)$.

spectral configuration is obtained and the waveform is a modulated right traveling wave. The critical point λ^c has split into $\lambda^c_\pm$ and the two disjoint bands of spectrum form a "right" state: the upper band with endpoints λ^s_0 and $\lambda^+_{1,\delta}$ in the right quadrant and the lower band with endpoint $\lambda^-_{1,\delta}$ extending to the real axis in the left quadrant. On the other hand, if e.g., $u_\delta(x,0) = u_0(x,0) + 0.05(\cos\mu x + e^{i\pi/3}\sin\mu x)$, the waveform is a modulated left traveling wave. In this case the orientation of the bands of spectrum is reversed, forming a "left" state with the upper band in the left quadrant and the lower band in the right quadrant. As the parameters in $g_2(x)$ are varied these are the two possible noneven spectral configurations for $u_\delta(x,t)$. The perturbation analysis in **Section 4** is related and shows noneven perturbations of the SPB split complex double points into left and right states.

Figure 3C shows $\eta(t)$ grows to $\mathcal{O}(1)$ for asymmetric perturbations $u_\delta(x,0) = u_0(x,0) + \delta g_2(x)$. Clearly $u_\delta(x,t)$ does not remain close to $u_0(x,t)$ for these perturbations. We associate the transverse complex critical points with instabilities arising from symmetry breaking which are not excited when evenness is imposed. The exact nature of the instability associated with complex critical points is under investigation. The current damped HONLS experiments in **Section 3** corroborate the significance of transverse critical points λ^c in identifying instabilities in the unrestricted solution space.

2.2 Spatially Periodic Breather Solutions of the NLS Equation

A variety of dressing methods can be used to derive new nontrivial solutions to integrable equations [see [35] for applications of the Darboux transformation to generate solutions of generalized NLS models]. Here we use the Bäcklund-gauge transformation (BT) for the NLS equation [36] to generate the heteroclinic orbits of a spatially periodic unstable NLS potential $u(x,t)$ with complex double points, λ^d_j, in its Floquet spectrum. Given a Stokes wave $u_a(t)$ with N complex double points, a single BT of $u_a(t)$ at λ^d_j yields the one mode SPB, $U^{(j)}(x,t)$, associated with the jth UM, $1 \le j \le N$. Introducing $\mu_j = 2\pi j/L$, $\sigma_j = -2i\mu_j\lambda_j$, $\cos p_j = \mu_j/2a$, and $\tau_j = (\rho - \sigma_j t)$ one obtains [13, 33]:

$$U^{(j)}(x,t) = a e^{2ia^2 t}\left(\frac{i\sin 2p_j \tanh\tau_j + \cos 2p_j - \sin p_j \cos(\mu_j x + \beta)\sec h\tau_j}{1 + \sin p_j \cos(\mu_j x + \beta)\sec h\,\tau_j}\right) \tag{10}$$

$U^{(j)}(x,t)$ exponentially approaches a phase shift of the Stokes wave, $\lim_{t\to\pm\infty} U^{(j)}(x,t) = a e^{2ia^2 t + \alpha_\pm}$, at a rate depending on λ^d_j. **Figures 4A,B** show the amplitudes of two distinct single mode SPBs, $U^{(1)}(x,t)$ and $U^{(2)}(x,t)$ over a Stokes waves with $N = 2$ UMs. $U^{(1)}(x,t)$ and $U^{(2)}(x,t)$ are both unstable as the BT based at λ_j saturates the instability of the jth UM while the other instabilities of the background persist.

When the Stokes wave posesses two or more UMs, the BT can be iterated to obtain multi mode SPBs. For example, the two-mode SPB with wavenumbers μ_i and μ_j, obtained by applying the BT successively at complex λ^d_i and λ^d_j, is of the following form:

$$U^{(i,j)}(x,t;\rho,\tau) = a\, e^{2ia^2 t}\frac{N(x,t;\rho,\tau)}{D(x,t;\rho,\tau)} \tag{11}$$

The exact formula is provided in [11]. The parameters ρ and τ determine the time at which the first and second modes become excited, respectively. **Figure 4C** shows the amplitude of the "coalesced" two mode SPB $U^{(1,2)}(x,t;\rho,\tau)$ $(\rho = -2,\ \tau = -3)$ over a Stokes waves with $N = 2$ UMs where the two modes are excited simultaneously.

An important property of the Bäcklund transformation: The BT is isospectral, i.e., $\sigma[u_a(t)] = \sigma[U^{(j)}(x,t)] = \sigma[U^{(i,j)}(x,t)]$. For example, the Stokes wave with $N = 2$ UMs (given in **Figure 1**) and each of the SPBs shown in **Figure 4A–C** share the same Floquet spectrum.

3 NUMERICAL INVESTIGATION OF ROUTES TO STABILITY OF SPBS IN THE DAMPED HIGHER ORDER NLS EQUATION

In our examination of the even 3-phase solution in **Section 2** we found that when evenness is relaxed novel instabilities arise which are associated with complex critical points. Armed with this result, in this section we return to the questions posed at the outset of our study: 1) Which integrable instabilities are excited by the damped HONLS flow and what is the Floquet criteria for

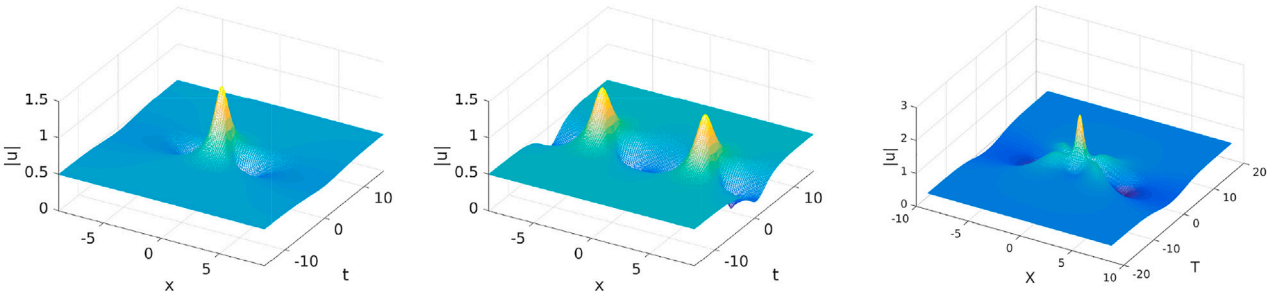

FIGURE 4 | SPBs over a Stokes wave with $N = 2$ UMs, $a = 0.5, L = 4\sqrt{2}\pi$: Amplitudes of **(A–B)** single mode SPBs $|U^{(1)}(x,t,\rho)|$ and $|U^{(2)}(x,t,\rho)|$ ($\rho = \beta = 0$) and **(C)** 2-mode SPB $|U^{(1,2)}(\rho,\tau)|$.

their saturation? 2) What remnants of integrable NLS structures are detected in the damped HONLS evolution?

The notation used in this section is as follows: 1) The "N UM regime" refers to the range of parameters a and L for which the underlying Stokes wave initially has N unstable modes. 2) The initial data used in the numerical experiments is generated using exact SPB solutions of the integrable NLS equation. The perturbed SPBs are indicated with subscripts: $U^{(j)}_{\varepsilon,\gamma}(x,t)$ refers to the solution of the damped HONLS **Eq. 1** for one-mode SPB initial data $U^{(j)}(x,0)$. Likewise $U^{(i,j)}_{\varepsilon,\gamma}(x,t)$ is the solution to **Eq. 1** for iterated SPB initial data.

The damped HONLS equation is solved numerically using a high-order spectral method due to Trefethen [37]. The integrator uses a Fourier-mode decomposition in space with a fourth-order Runge-Kutta discretization in time. The number of Fourier modes and the time step used depends on the complexity of the solution. For example, for initial data in the three UM regime, $N = 1024$ Fourier modes are used with time step $\Delta t = 7.5 \times 10^{-5}$. As a benchmark the first three global invariants of the HONLS equation, the energy $E = \int_0^L |u|^2 dx$, momentum $P = i\int_0^L (u^* u_x - u u_x^*) dx$, and Hamiltonian

$$H = \int_0^L \Big\{ -i|u_x|^2 + i|u|^4 - \frac{\varepsilon}{4}\left(u_x u_{xx}^* - u_x^* u_{xx}\right) + 2\varepsilon|u|^2\left(u^* u_x - u u_x^*\right) + i\varepsilon|u|^2\left[\mathcal{H}\left(|u|^2\right)\right]_x \Big\} dx$$

are preserved with an accuracy of $\mathcal{O}(10^{-12})$ for $0 \le t \le 100$. The invariant for the damped HONLS system, the spectral center $k_m = -P/2E$, is preserved with an accuracy of at least $\mathcal{O}(10^{-12})$ in the experiments.

Nonlinear mode decomposition of the damped HONLS flow: At each time t we compute the spectral decomposition of the damped HONLS data using the numerical procedure developed by Overman et. al. [34]. After solving system **Eq. (2)**, the discriminant Δ is constructed. The zeros of $\Delta \pm 2$ are determined using a root solver based on Müller's method and then the curves of spectrum filled in. The spectrum is calculated with an accuracy of $\mathcal{O}(10^{-6})$ which is sufficient given the perturbation parameters ϵ and γ used in the numerical experiments are $\mathcal{O}(10^{-2})$.

Notation used in the spectral plots: The periodic spectrum is indicated with a large × when $\Delta = -2$ and a large box when $\Delta = 2$. The continuous spectrum is indicated with small × when the Δ is negative and a small box when Δ is positive.

Interpreting the damped HONLS flow via the NLS spectral theory: A tractable example which illustrates the use of the Floquet spectrum to interpret near integrable dynamics is the spatially uniform solution (there is no depenence on ϵ) of the damped HONLS **Eq. 1**,

$$u_{a,\gamma}(t) = a e^{-\gamma t} e^{i\left(|a|^2 \frac{\left(1-e^{-2\gamma t}\right)}{\gamma}\right)} \tag{12}$$

At a given time $t = t_*$ the nonlinear spectral decomposition of **Eq. 12** can be explicitly determined by substituting $u_{a,\gamma}(t_*)$ into $\mathcal{L}(u)\phi = \lambda\phi$. We find the periodic Floquet spectrum consists of $\lambda_0^s = \pm i a e^{-\gamma t_*}$ and infinitely many double points

$$\left(\lambda_j^d\right)^2 = \left(\frac{j\pi}{L}\right)^2 - e^{-2\gamma t_*} a^2, \quad j \in \mathbb{Z}, \quad j \neq 0 \tag{13}$$

where λ_j^d is complex if $\left(\frac{j\pi}{L}\right)^2 < e^{-2\gamma t_*} a^2$. Under the damped HONLS evolution the endpoint of the band of spectrum λ_0^s and the complex double points λ_j^d move down the imaginary axis and then onto the real axis. Similarly, at $t = t_*$, a linearized stability analysis about $u_{a,\gamma}(t_*)$ shows the growth rate of the jth mode $\sigma_j^2 = \mu_j^2\left(4e^{-2\gamma t_*} a^2 - \mu_j^2\right)$. Thus the number of complex double points and the number of unstable modes diminishes in time due to damping. As a result, $u_{a,\gamma}(t)$ stabilizes when the growth rate $\sigma_1 = 0$, i.e., when $\lambda_1^d = 0$, giving $t_* = \ln(aL/\pi)/\gamma$.

Saturation time of the instabilities: Since the association of complex critical points with instabilities is a new result, we supplement the spectral analysis with an examination of the saturation time of the instabilities for the damped SPBs $U^{(j)}_{\varepsilon,\gamma}(x,t)$ and $U^{(j,k)}_{\varepsilon,\gamma}(x,t)$ as follows: we examine the growth of small asymmetric perturbations in the initial data of the following form,

$$U^{(j)}_{\varepsilon,\gamma,\delta}(x,0) = U^{(j)}(x,0) + \delta f_k(x)$$

and

$$U^{(i,j)}_{\varepsilon,\gamma,\delta}(x,0) = U^{(i,j)}(x,0) + \delta f_k(x)$$

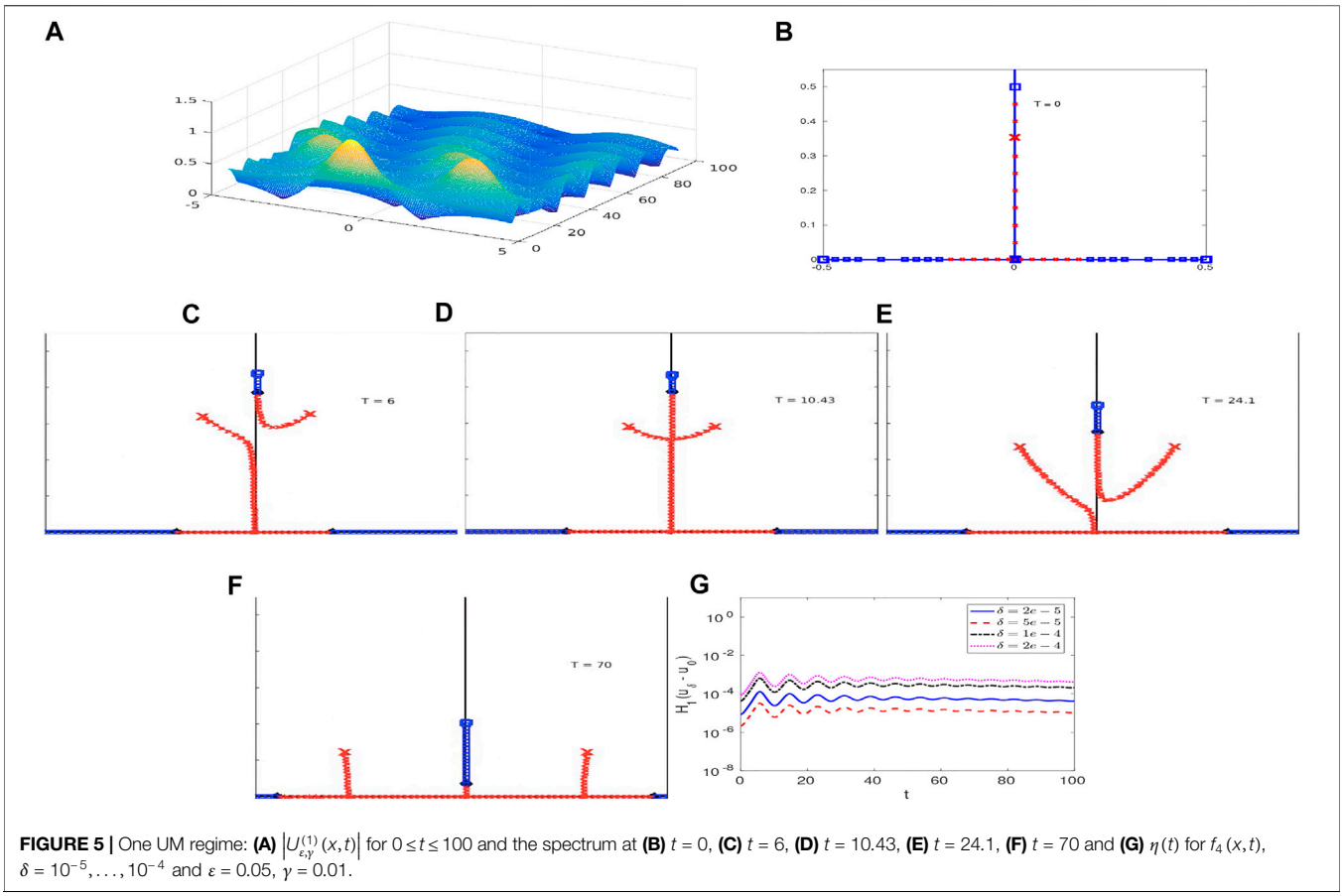

FIGURE 5 | One UM regime: **(A)** $\left|U^{(1)}_{\varepsilon,\gamma}(x,t)\right|$ for $0 \le t \le 100$ and the spectrum at **(B)** $t = 0$, **(C)** $t = 6$, **(D)** $t = 10.43$, **(E)** $t = 24.1$, **(F)** $t = 70$ and **(G)** $\eta(t)$ for $f_4(x,t)$, $\delta = 10^{-5}, \ldots, 10^{-4}$ and $\varepsilon = 0.05$, $\gamma = 0.01$.

where.

i. $f_k(x) = \cos \mu_k x + r_k e^{i\phi_k} \sin \mu_k x$, $\mu_k = 2\pi k/L$, $1 \le k \le 3$,
ii. $f_4(x) = r(x)$, $r(x) \in [0,1]$ is random noise.

To determine the closeness of $U^{(j)}_{\varepsilon,\gamma}(x,t)$ and $U^{(j)}_{\varepsilon,\gamma,\delta}(x,t)$ as time evolves we monitor the evolution of $\eta(t)$, as given by **Eq. 9**. We consider the solution to have stabilized under the damped HONLS flow once $\eta(t)$ saturates.

In the damped HONLS numerical experiments we obtain a new criteria for the saturation of instabilities: $\eta(t)$ saturates and the SPB stabilizes once damping eliminates all complex double points and complex critical points in the spectrum.

3.1 Damped HONLS SPB in the One Unstable Mode Regime

$U^{(1)}_{\varepsilon,\gamma}(x,t)$ in the one UM regime

We begin by considering $U^{(1)}_{\varepsilon,\gamma}(x,t)$ for $\varepsilon = 0.05$ and $\gamma = 0.01$ in the one UM regime with initial data generated using **Eq. 10** with $j = 1$, $a = 0.5$ and $L = 2\sqrt{2}\pi$. **Figure 5A** shows the surface $\left|U^{(1)}_{\varepsilon,\gamma}(x,t)\right|$ for $0 < t < 100$.

The evolution of the Floquet spectrum for $U^{(1)}_{\varepsilon,\gamma}(x,t)$ is as follows: At $t = 0$, the spectrum in the upper half plane consists of a single band of spectrum with end point at $\lambda^s_0 = 0.5i$, indicated by a large "box", and one imaginary double point at $\lambda^d_1 = 0.3535i$, indicated by a large "×" (**Figure 5B**). Under the damped HONLS λ^d_1 splits asymmetrically forming a right state, with the upper band of spectrum in the right quadrant and the lower band in the left quadrant, consistent with the short time perturbation analysis in **Section 4**. The right state is clearly visible at $t = 6$ in **Figure 5C** with the waveform characterized by a single damped modulated mode traveling to the right. The spectrum persists in a right state with the separation distance between the two bands varying until $t = 10.43$, **Figure 5D**, when a cross state forms with an embedded critical point indicating an instability. Subsequently the critical point splits into a right state. As damping continues the band in the right quadrant widens, **Figure 5E**, and the vertex of the loop eventually touches the origin at $t \approx 27.5$. The spectrum then has three bands emanating off the real axis, with endpoints $\lambda^-_1, \lambda^s_0, \lambda^+_1$ which, as damping continues, diminish in amplitude and move away from the imaginary axis, **Figure 5F**.

Figure 5G shows the evolution of $\eta(t)$ for $U^{(1)}_{\varepsilon,\gamma}(x,t)$ using f_4 and $\delta = 10^{-5}, \ldots, 10^{-4}$. The saturation of $\eta(t)$ at $t \approx 16$ is consistent with the Floquet criteria that the solution stabilizes after complex double points and complex critical points are eliminated in the damped HONLS flow.

From the spectral analysis of $U^{(1)}_{\varepsilon,\gamma}(x,t)$ in the one UM regime, we find it may be characterized as a continuous

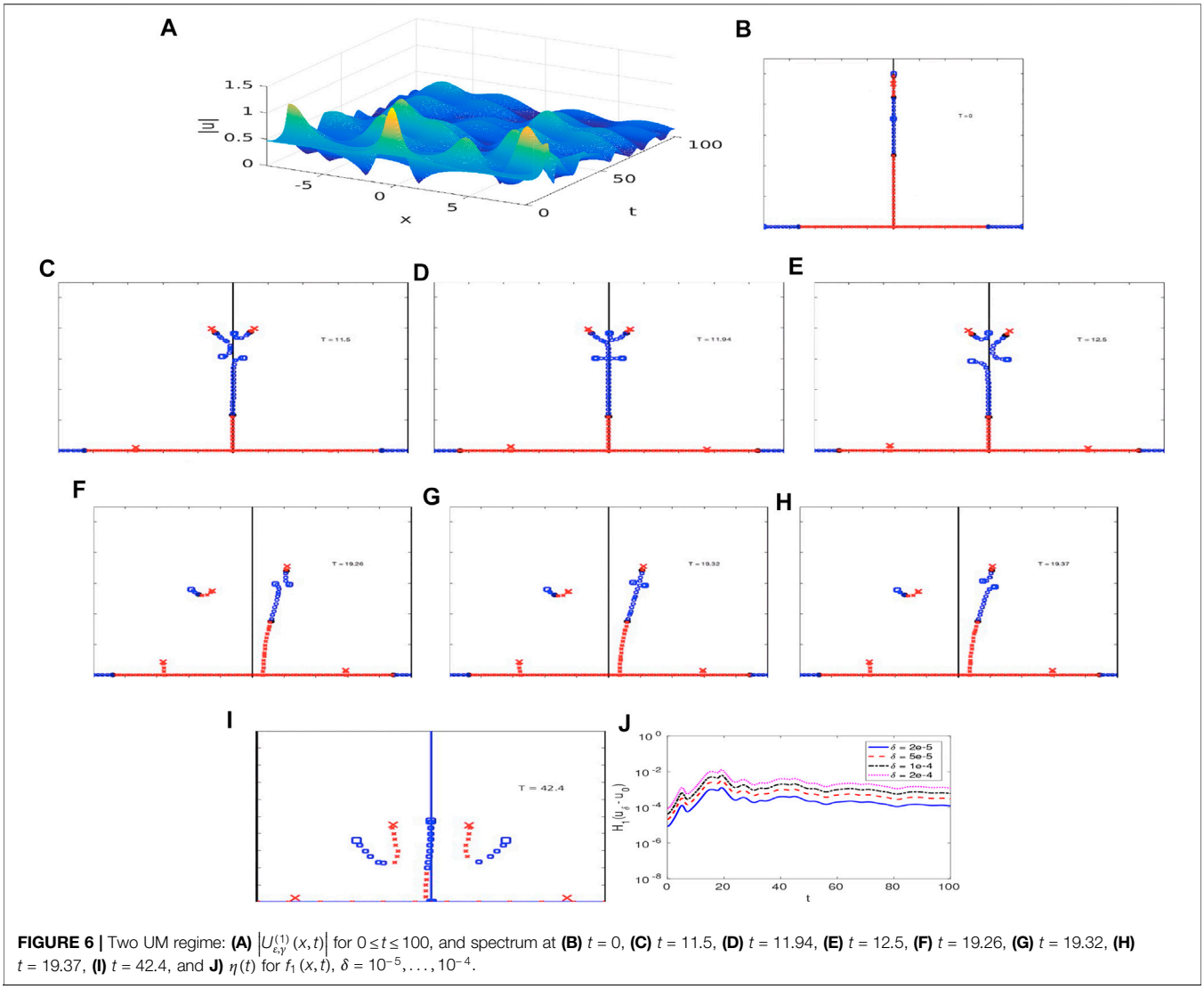

FIGURE 6 | Two UM regime: **(A)** $\left|U^{(1)}_{\varepsilon,\gamma}(x,t)\right|$ for $0 \le t \le 100$, and spectrum at **(B)** $t = 0$, **(C)** $t = 11.5$, **(D)** $t = 11.94$, **(E)** $t = 12.5$, **(F)** $t = 19.26$, **(G)** $t = 19.32$, **(H)** $t = 19.37$, **(I)** $t = 42.4$, and **J)** $\eta(t)$ for $f_1(x,t)$, $\delta = 10^{-5}, \ldots, 10^{-4}$.

deformation of a noneven generalization of the 3-phase solution, the right state, given by **Eq. 8**. The amplitude of the oscillations of $U^{(1)}_{\varepsilon,\gamma}(x,t)$ decreases and the frequency increases until small fast oscillations about the damped Stokes wave, visible in **Figure 5A**, are obtained.

An alternate approach to studying the effect of small damping (or gain) on the one mode SPB is to consider the evolution of asymmetric initial data in the neighborhood of the SPB under the linearly damped NLS equation. Using the finite gap method of the periodic NLS equation [38], the solution is analytically approximated to leading order with a sum of SPBs shifted in space and time. The quantitative agreement between the leading order analytical formula and the corresponding numerical experiments was found to be good [21]. It is interesting to note that, although we use exact SPB initial data under the linearly damped HONLS equation, with different damping values, the asymmetric evolution of the Floquet spectral data is qualitatively consistent with the numerical experiments described in [21].

3.2 Damped HONLS SPBs in the Two Unstable Mode Regime

For the two UM regime we let $a = 0.5$, $L = 4\sqrt{2}\pi$ and consider the two distinct perturbed single mode SPBs $U^{(1)}_{\varepsilon,\gamma}(x,t)$ and $U^{(2)}_{\varepsilon,\gamma}(x,t)$ and the perturbed iterated SPB $U^{(1,2)}_{\varepsilon,\gamma}(x,t)$. The damped HONLS perturbation parameters are $\varepsilon = 0.05$ and $\gamma = 0.01$.

$U^{(1)}_{\varepsilon,\gamma}(x,t)$ in the two UM regime

Figure 6A shows the surface $\left|U^{(1)}_{\varepsilon,\gamma}(x,t)\right|$ for $0 < t < 100$ for initial data given by **Eq. 10** with $j = 1$. The Floquet spectrum at $t = 0$ is given in **Figure 6B**. The end point of the band of spectrum at $\lambda^s_0 = 0.5i$ is indicated by a "box". There are two complex double points at $\lambda^d_1 = 0.4677i$ and $\lambda^d_2 = 0.3535i$, indicated by a "×" and "box", respectively. For $t > 0$ both double points split asymmetrically: λ^d_1, the complex double point at which $U^{(1)}(x,t)$ is constructed, splits at leading order into $\lambda^{\pm}_1$ such that a right state forms with the first mode traveling to the right. The second double point λ^d_2 splits at higher order into $\lambda^{\pm}_2$ such

that a left state forms with the second mode traveling to the left. These disjoint asymmetric bands of spectrum are consistent with the short time perturbation analysis in **Section 4** for damped HONLS data of the form **Eq. 18**.

This spectral configuration is representative of the spectrum during the initial stage of it's evolution and is still observable in **Figure 6C** at $t = 11.5$. A sequence of bifurcations occur at $t \approx 11.94$, **Figure 6D**, when two complex critical points emerge in rapid succession in the spectrum, indicating instabilities associated with both nonlinear modes. Subsequently both complex critical points split, **Figure 6E**, with the upper band in the left quadrant and the second band in the right quadrant corresponding to a damped waveform with the first mode traveling to the left and the second mode traveling to the right.

The bifurcation at $t = 11.94$ corresponds to transitioning through the remnant of an unstable 5-phase solution (with two instabilities) of the NLS equation. The bands eventually become completely detached from the imaginary axis and a second complex critical point forms at $t = 19.32$. The bifurcation sequence is shown in **Figure 6F–H**. The main band emanating from the real axis then reestablishes itself close to the imaginary axis, **Figure 6I**, and the spectrum settles into a configuration corresponding to a stable 5 phase solution. The bands move apart and downwards and hit the real axis with no further development of complex critical points. From the Floquet spectral perspective, once damping eliminates complex critical points in the spectrum at approximately $t \approx 20$, $U^{(1)}_{\varepsilon,\gamma}(x,t)$ stabilizes.

Figure 6J shows the evolution of $\eta(t)$ for $U^{(1)}_{\varepsilon,\gamma}(x,t)$ with f_2 for $\delta = 10^{-5}, \ldots, 10^{-4}$. The perturbation f_2 is chosen in the direction of the unstable mode associated with λ_2^d. $\eta(t)$ stops growing by $t \approx 20$, confirming the instabilities associated with the complex critical ponts and time of stabilization obtained from the nonlinear spectral analysis.

For $U^{(1)}_{\varepsilon,\gamma}(x,t)$ in the 2-UM regime, both λ_1^d and λ_2^d resonate with the perturbation. The route to stability is characterized by the appearance of the double cross state of the NLS and the proximity to this state is significant in organazing the damped HONLS dynamics. Once stabilized, $U^{(1)}_{\varepsilon,\gamma}(x,t)$ may be characterized as a continuous deformation of a stable 5-phase solution.

$U^{(2)}_{\varepsilon,\gamma}(x,t)$ in the two UM regime

We now consider $U^{(2)}_{\varepsilon,\gamma}(x,t)$ whose initial data is given by **Eq. 10** with $j = 2$. Although $U^{(1)}(x,t)$ and $U^{(2)}(x,t)$ are both single mode SPBs over the same Stokes wave, their respective routes to stability under damping are quite different. Notice in **Figure 7A** the surface of $\left|U^{(2)}_{\varepsilon,\gamma}(x,t)\right|$ for $0 \le t \le 100$ is a damped modulated traveling state, exhibiting regular behavior, in contrast to the irregular behavior of $\left|U^{(1)}_{\varepsilon,\gamma}(x,t)\right|$ in the two UM regime.

The spectrum of $U^{(2)}_{\varepsilon,\gamma}$ at $t = 0$ is the same as in **Figure 6B**. Under perturbation λ_2^d immediately splits asymmetrically into $\lambda_2^{\pm}$ with the upper band in the right quadrant and the lower band in the left quadrant, while the first double point λ_1^d (indicated by the large "×") does not split. **Figure 7B** clearly shows that at $t = 6$ damping has only split λ_2^d, i.e., the double point at which the SPB $U^{(2)}$ is constructed. In fact λ_1^d does not split for the duration of the damped HONLS evolution, $0 \le t \le 100$. In **Figure 7C**, by $t = 11$, the two bands have aligned forming a cross state with a complex critical point at the transverse intersection of the bands while λ_1^d is still intact and has simply translated down the imaginary axis.

The complex critical point subsequently splits with the upper band of spectrum again in the right quadrant, **Figure 7D**. Complex critical points do not reappear in the spectrum. At $t = 27.4$ the vertex of the upper band of spectrum touches the real axis **Figure 7E**. As damping continues λ_1^d moves down the imaginary axis and the two bands move away from the imaginary axis with diminishing amplitude. In **Figure 7F** the complex double point λ_1^d has moved almost all the way down the imaginary axis. At $t \approx 72$, $\lambda_1^d = 0$ and complex double points do not arise in the subsequent spectral evolution.

We find $\eta(t)$ grows until $t = t_s \approx 80$, **Figure 7G**, consistent with the expectation that $U^{(2)}_{\varepsilon,\gamma}$ will stabilize once all complex critical points and complex double points vanish in the spectrum. Until λ_1^d moves onto the real axis, perturbations to the initial data $U^{(2)}_{\varepsilon,\gamma,\delta}$ can excite the first mode associated with λ_1^d causing $U^{(2)}_{\varepsilon,\gamma}$ and $U^{(2)}_{\varepsilon,\gamma,\delta}$ to grow apart.

Why doesn't the HONLS perturbation split λ_1^d when given $U^{(2)}(x,0)$ initial data? In **Section 4**, for short time, a suitable linearization of the damped HONLS SPB data is found to be given by **Eq. 19** for $j = 1, 2$, respectively where $\tilde{\varepsilon} = \tilde{\varepsilon}(\varepsilon, \gamma)$. The perturbation analysis shows that at leading order damping asymmetrically splits only the double point λ_2^d associated with $U^{(2)}(x,0)$. The endpoint of spectrum, λ_0^s, decreases in amplitude and the rest of the double points simply move along curves of continuous spectrum without splitting. The resonant modes which correspond to λ_{2m}^d split asymmetrically at higher order $\mathcal{O}(\tilde{\varepsilon}^m)$. The splitting of λ_l^d, $l \neq 2m$, is zero and is termed "closed".

The spectral evolution for $U^{(2)}_{\varepsilon,\gamma}(x,t)$ in the 2 UM regime is reminiscent of the spectral evolution of $U^{(1)}_{\varepsilon,\gamma}(x,t)$ in the one UM regime. There is an important difference though: The nearby cross state that appears in the spectral decomposition of $U^{(2)}_{\varepsilon,\gamma}(x,t)$ has two different types of instabilites: the instability associated with the complex critical point (potentially a phase instability) and the exponential instability associated with the (nonresonant) complex double point λ_1^d. The numerical results suggest that when nonresonant modes are present in the damped HONLS, their instabilities persist and organize the dynamics on a longer time scale. As λ_1^d remains closed for $t < t_s$, $U^{(2)}_{\varepsilon,\gamma}(x,t)$ can be characterized as a continuous deformation of a noneven generalization of the degenerate 3 phase solution given by **Eq. 8** (the parameter values change due to doubling the period L; i,e., a j–th mode excitation with period L becomes a $2j$–th mode excitation with period $2L$.)

$U^{(1,2)}_{\varepsilon,\gamma}(x,t)$ in the two UM regime

Figure 8A shows the surface $\left|U^{(1,2)}_{\varepsilon,\gamma}(x,t)\right|$ for $0 < t < 100$ for initial data obtained from **Eq. 11** by setting $\rho = 0$ and $\tau = -2$, $a = 0.5$. The spectrum of $U^{(1,2)}_{\varepsilon,\gamma}$ at $t = 0$ is given by **Figure 6B**. As we've seen in the previous examples, once complex double points split they do not reform in the perturbed system; if they are present in the spectral decomposition of the damped HONLS, it is because the modes corresponding to λ_j^d didn't resonate under perturbation. Here both double points λ_1^d and λ_2^d split at

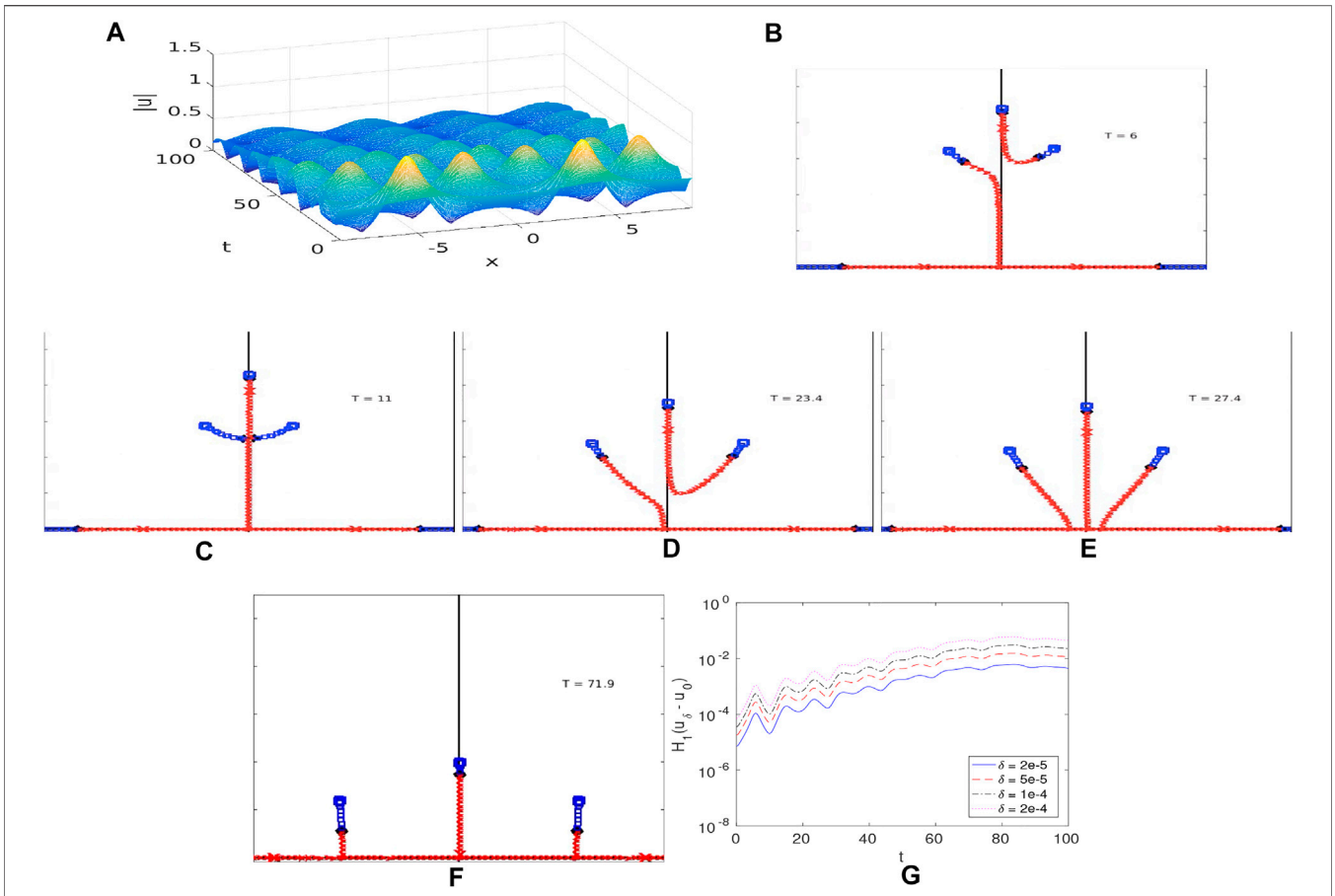

FIGURE 7 | Two UM regime: **(A)** $\left|U^{(2)}_{\varepsilon,\gamma}(x,t)\right|$ for $0 \le t \le 100$ and Spectrum at **(B)** $t = 6$, **(C)** $t = 11$, **(D)** $t = 23.4$, **(E)** $t = 27.4$, **(F)** $t = 71.9$, and **(G)** $\eta(t)$ for $f_1(x,t)$, $\delta = 10^{-5}, \ldots, 10^{-4}$ and $\gamma = 0.01$.

leading order under the damped HONLS perturbation. **Figure 8B** shows for short time ($t = 1.5$) the spectrum has a band gap structure indicating the first mode travels to the right and the second travels to the left. As time evolves the bands shift and align and **Figure 8C** shows at $t \approx 15.9$ two bands in the right quadrant intersect with an embedded complex critical point. The critical point splits with one band moving back toward the imaginary axis. There are now two bands detached from the primary band and evolving towards the real axis, **Figures 8D,E**. Complex critical points do not appear for $t > 15.9$.

Figure 8F shows $\eta(t)$ for the example under consideration ($\rho = 0, \tau = -2$) when $f_1(x,t), \delta = 10^{-5}, \ldots, 10^{-4}$. We find $\eta(t)$ saturates at $t_s \approx 20$ indicating $U^{(1,2)}_{\varepsilon,\gamma}$ has stabilized. For $t > t_s$ $U^{(1,2)}_{\varepsilon,\gamma}$ is characterized as a continuous deformation of a stable NLS five-phase solution. The numerically observed initial splitting of complex double points λ^d_1 and $\lambda^{\bar{d}}_2$ is consistent with the perturbation analysis of damped HONLS SPB data (19).

Among the two mode SPBs in the 2 UM regime, the one of highest amplitude due to coalescence of the modes appeared to be more robust [17]. An interesting observation is obtained if we examine the evolution of spectrum and of $\eta(t)$ using the initial data for the special coalesced two mode SPB, generated from **Eq. 11** by setting $\rho = 0.665$, $\tau = 1$, and $a = 0.5$. For the coalesced case, complex critical points form 4 times for $0 < t < 45$ in the damped HONLS system. **Figure 8G** shows $\eta(t)$ saturates for $t \approx 50$. A comparison with the results of the non-coalesced two mode SPB given above indicate that remnants of the coalesced $U^{(1,2)}$ and it's instabilities influence the damped HONLS dynamics over a longer time period, suggesting enhanced robustness with respect to perturbations of the NLS equation.

3.3 Damped SPBs in the Three Unstable Mode Regime

The parameters used for the three UM regime are $a = 0.7$ and $L = 4\sqrt{2}\pi$. The damped HONLS perturbation parameters are $\varepsilon = 0.05$ and $\gamma = 0.01$. We present the results of two damped HONLS SPBs, $U^{(2)}_{\varepsilon,\gamma}(x,t)$ and $U^{(2,3)}_{\varepsilon,\gamma}(x,t)$, which exhibit an interesting or new feature. The evolutions of the other damped HONLS SPBs in the three UM regime in the three UM regime are discussed in relation to these cases.

$U^{(2)}_{\varepsilon,\gamma}(x,t)$ in the three UM regime

The surface $\left|U^{(2)}_{\varepsilon,\gamma}(x,t)\right|$ for initial data given by **Eq. 10** with $j = 2$ is shown in **Figure 9A** for $0 < t < 100$. Notice in the 3 UM regime $U^{(2)}_{\varepsilon,\gamma}(x,t)$ exhibits regular behavior and is a damped modulated

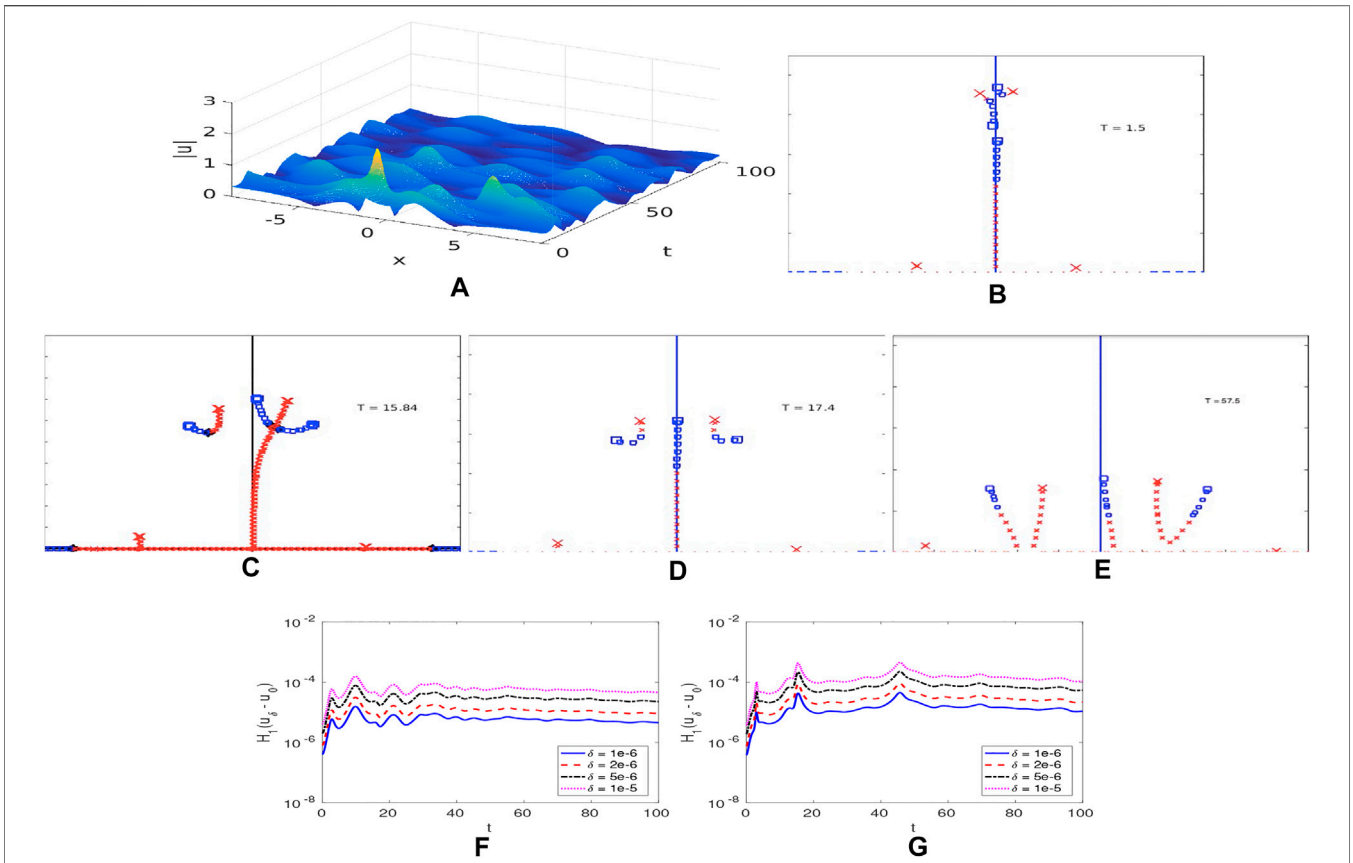

FIGURE 8 | Two UM regime: **(A)** $\left|U^{(1,2)}_{\varepsilon,\gamma}(x,t)\right|$ for $0 \le t \le 100$ and spectrum at **(B)** $t = 1.5$, **(C)** $t = 15.84$, **(D)** $t = 17.4$, **(E)** $t = 57.5$, and $\eta(t)$ for $U^{(1,2)}_{\varepsilon,\gamma}(x,t)$ with $f_1(x,t)$ when **(F)** $\rho = 0, \tau = -2$ (the uncoalesced SPB), **(G)** $\rho = 0.665, \tau = 1$ (the coalesced SPB).

right traveling wave as was $U^{(2)}_{\varepsilon,\gamma}(x,t)$ in the 2 UM regime. The spectrum at $t = 0$ is given in **Figure 9B**. The end point of the band of spectrum, $\lambda^s_0 = 0.7i$ is indicated by a "box". There are three complex double points at $\lambda^d_1 = 0.677i$, $\lambda^d_2 = 0.604i$, and $\lambda^d_3 = 0.456i$ indicated by an "×", "box" and "×", respectively. Under the damped HONLS perturbation the complex double point at which $U^{(2)}_{\varepsilon,\gamma}(x,t)$ is constructed, λ^d_2, splits into a right state as shown in **Figure 9C**. The complex double points λ^d_1 and λ^d_3 remain closed; λ^d_1 lies on the upper band in the right quadrant and λ^d_3 lies on the lower band. Transverse cross states with embedded complex critical points form frequently in the spectrum until $t \approx 68$, e.g., a cross state is shown at $t = 36.6$ in **Figure 9D**. **Figures 9E,F** show the complex double points persist on the bands of spectrum until damping sufficiently diminishes the amplitude of the background and the complex double points reach the real axis at $t \approx 85$. In **Figure 9G** $\eta(t)$ saturates at $t = t_s \approx 90$. Due to the presence of the complex double points for $t < t_s$, $U^{(2)}_{\varepsilon,\gamma}(x,t)$ can be viewed as a continuous deformation of an unstable 3 phase solution (with two instabilities). As discussed previously, the instabilities associated with the nonresonant modes persist longer than for the resonant modes.

In the 3 UM regime the behavior of the SPB $U^{(3)}_{\varepsilon,\gamma}(x,t)$ is similar to $U^{(2)}_{\varepsilon,\gamma}(x,t)$. In this case λ^d_3 initially splits asymmetrically into the right state (which we've now seen frequently in the initial damped HONLS system when only one mode is activated). The double points λ^d_1 and λ^d_2 do not split, they move along the band of spectrum created by λ^s_0 and λ^+_3. As a result $U^{(3)}_{\varepsilon,\gamma}(x,t)$ stabilizes only when λ^d_1 and λ^d_2 become real, at $t \approx 140$. As in the previous cases, it is striking that the prediction from a short time perturbation analysis that certain double points remain closed, holds for the duration of the experiments (even while the solution evolves as a perturbed degenerate 3-phase state (with two instabilities). In contrast, for $U^{(1)}_{\varepsilon,\gamma}(x,t)$ the higher order nonlinearities and damping excite all the modes. The solution is characterized by the formation of complex critical points and irregular behavior before stabilizing at $t \approx 40$.

$U^{(2,3)}_{\varepsilon,\gamma}(x,t)$ in the three UM regime

Figure 10A shows the surface $\left|U^{(2,3)}_{\varepsilon,\gamma}(x,t)\right|$ for $0 < t < 100$ for initial data given by **Eq. 11** with $i, j = 2, 3$.

The spectrum at $t = 0$ is as in **Figure 9B**. The perturbation initially splits the double points λ^d_2 and λ^d_3 into $\lambda^{\pm}_2$ and $\lambda^{\pm}_3$ that correspond to a left and right modulated traveling modes, respectively. The new feature here is that the first complex double point, λ^d_1, splits at higher order into $\lambda^{\pm}_1$ (see the analysis in **Section 4** showing that a multi-mode perturbation in a higher UM regime introduces new resonances not seen with

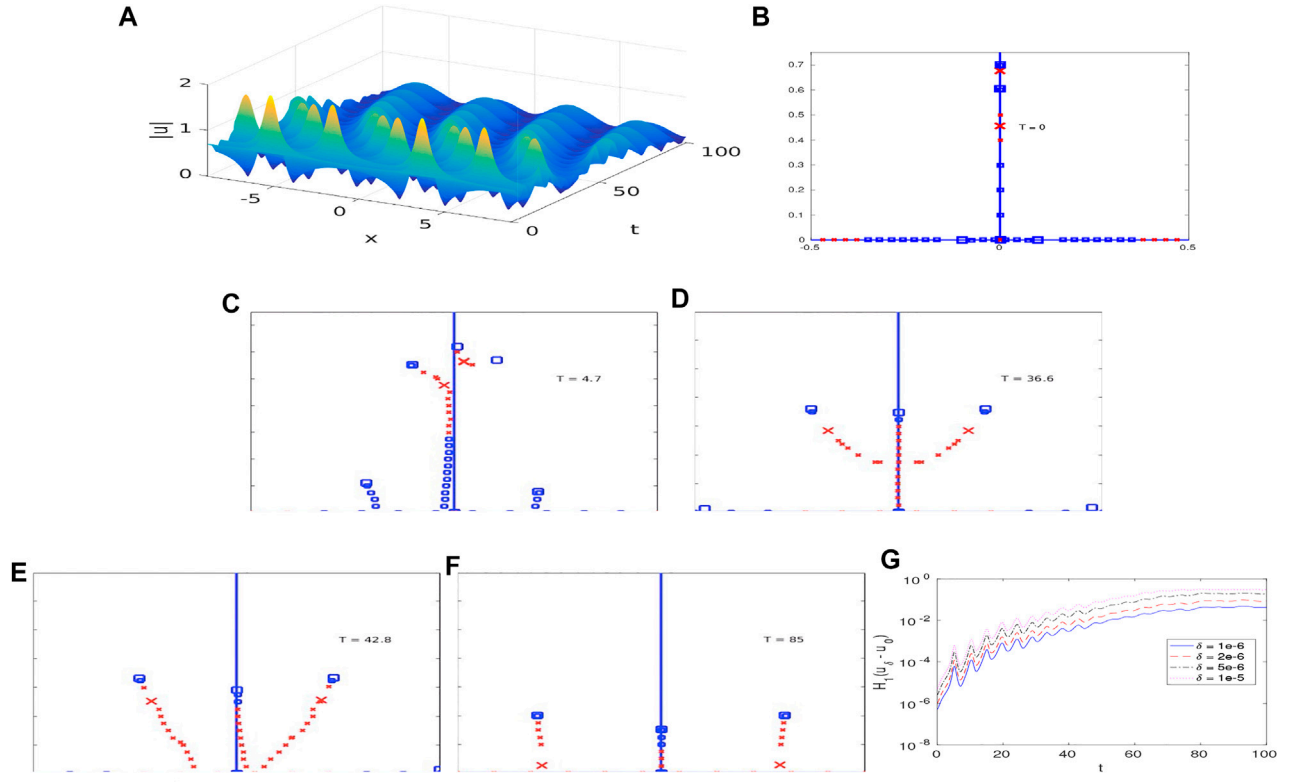

FIGURE 9 | Three UM regime: **(A)** $\left|U^{(2)}_{\varepsilon,\gamma}(x,t)\right|$ for $0 \le t \le 100$ and Spectrum at **(B)** $t = 0$, **(C)** $t = 4.7$, **(D)** $t = 36.6$, **(E)** $t = 42.8$, **(F)** $t = 85$ and **(G)** $\eta(t)$ for $f_1(x,t)$, $\delta = 10^{-6}, \ldots, 10^{-5}$.

single mode perturbations). The higher order splitting is visible in **Figure 10B** at $t = 10.5$.

Complex double points are not observed in the spectral evolution for $t > 0$.The formation of complex critical points in the spectrum occurs frequently as shown, for example, in **Figure 10C** and **Figure 10D**. Since the amplitude of the background state at $a = 0.7$ is initially very close to the 4 UM regime, in this example we observe that nearby real double points are noticeably split by the perturbation. **Figure 10E** shows the spectrum at $t = 68.4$ when the last complex critical point forms. This is reflected in **Figure 10G** which shows $\eta(t)$ saturates at $t_s \approx 68$. Each of the bursts of growth in $\eta(t)$ can be correlated with a complex critical point crossing. As time evolves disspiation diminshes the strength of the instability captured by the complex critical points or complex double points. $U^{(2,3)}_{\varepsilon,\gamma}(x,t)$ exhibits quite rich and compex dynamics before damping saturates the instabilities and it's behavior is not easy to characterize as when dealing with the perturbed SPBs in the $N = 1, 2$ UM regimes. For $t > t_s$ the evolution of $U^{(2,3)}_{\varepsilon,\gamma}(x,t)$ may be characterized as a continuous deformation of a stable 7-phase solution (**Figure 10F**).

As a comparison, $U^{(1,2)}_{\varepsilon,\gamma}(x,t)$ and $U^{(1,3)}_{\varepsilon,\gamma}(x,t)$ exhibit shorter term irregular behavior with all the dominant modes excited and they stabilize at $t \approx 15, 18$. respectively. $U^{(2,3)}_{\varepsilon,\gamma}(x,t)$ was observed to take longer to stabilize due to the higher order splitting in λ^d_1.

The exact nature of the instability associated with complex critical points in under investigation. They may be weaker than the exponential instabilities associated with complex double points but the evolution of $U^{(2,3)}_{\varepsilon,\gamma}(x,t)$ illustrates their cumulative impact can be significant.

4 PERTURBATION ANALYSIS

While examining the route to stability of the SPBs under the damped HONLS several novel results arose. One feature was that the instabilities of nonresonant modes persist longer than the instabilities of the resonant modes. We are interested in the fate of complex double points under noneven perturbations induced by HONLS as they characterize the SPB. Following the perturbation analysis in [39] used to determine the $\mathcal{O}(\varepsilon)$ splitting of double points for single mode perturbations, we carry the analysis to higher order for noneven multi mode perturbations of the SPBs. We find 1) additional modes resonate with the perturbation and 2) complex double points associated with nonresonant modes remain closed.

To obtain linearized initial conditions for the one and two mode SPBs we use the Hirota formulation of the SPBs [40]. For example for the one mode SPB one obtains,

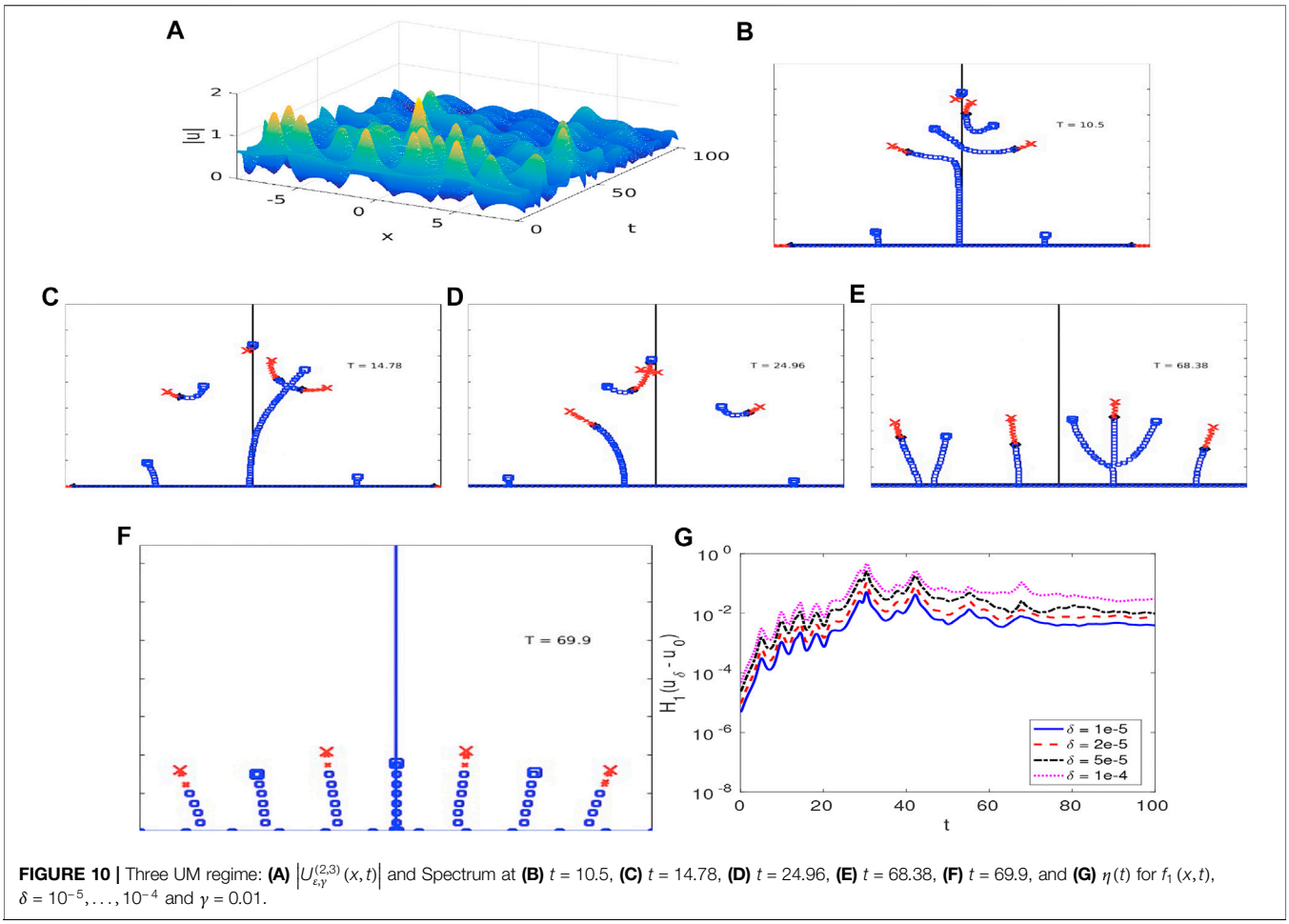

FIGURE 10 | Three UM regime: **(A)** $\left|U_{\epsilon,\gamma}^{(2,3)}(x,t)\right|$ and Spectrum at **(B)** $t = 10.5$, **(C)** $t = 14.78$, **(D)** $t = 24.96$, **(E)** $t = 68.38$, **(F)** $t = 69.9$, and **(G)** $\eta(t)$ for $f_1(x,t)$, $\delta = 10^{-5}, \ldots, 10^{-4}$ and $\gamma = 0.01$.

$$u^{(j)}(x,t) = ae^{2ia^2t}\frac{1 + 2e^{2i\theta_j+\Omega_j t+\gamma}\cos\mu_j x + A_{12}e^{2\left(2i\theta_j+\Omega_j t+\gamma\right)}}{1 + 2e^{\Omega_j t+\gamma}\cos\mu_j x + A_{12}e^{2\left(\Omega_j t+\gamma\right)}} \tag{14}$$

where $\mu_j = 2\pi j/L$, $\Omega_j = \mu_j\sqrt{4a^2-\mu_j^2}$, $\sin\theta_j = \mu_j/2a$, $A_{12} = \sec^2\theta_j$, and γ is an arbitrary phase.

The appropriate linearized initial conditions for the one and two mode SPBs, $u^{(i)}(x,0)$ and $u^{(i,j)}(x,0)$ respectively, are obtained by choosing t and γ such that $\tilde{\varepsilon}_s = 4i\sin\theta_s\, e^{\Omega_s t+\gamma}$, $s = i, j$, are small. After neglecting second-order terms we obtain:

$$u^{(j)}(x,0) = a\left(1 + \tilde{\varepsilon}_j e^{i\theta_j}\cos\mu_j x\right) \tag{15}$$

$$u^{(i,j)}(x,0) = a\left(1 + \tilde{\varepsilon}_i\, e^{i\theta_i}\cos\mu_i x + \tilde{\varepsilon}_j\, e^{i\theta_j}\cos\mu_j x\right) \tag{16}$$

The damped HONLS yields the following noneven first order approximation for small time,

$$u^{(j)}(x,h) = a\left[1 + \tilde{\varepsilon}_j\left(e^{i\theta_j}\cos\mu_j x + r_j e^{i\phi_j}\sin\mu_j x\right)\right] \tag{17}$$

$$u^{(i,j)}(x,h) = a\Big[1 + \tilde{\varepsilon}_i\left(e^{i\theta_i}\cos\mu_i x + r_i\, e^{i\phi_i}\sin\mu_i x\right) + \tilde{\varepsilon}_j\left(e^{i\theta_j}\cos\mu_j x + r_j e^{i\phi_j}\sin\mu_j x\right)\Big] \tag{18}$$

where $\theta_s \neq \phi_s$ and $a, \tilde{\varepsilon}_s, r_s$ are functions of h and the damped HONLS parameters ϵ and γ, for $s = i, j$. For simplicity we set $\varepsilon = \tilde{\varepsilon}_s$ and suppress their explicit dependence on ε, γ:

$$\begin{aligned} u &= a + \varepsilon\left[e^{i\theta_i}\cos\mu_i x + r_i e^{i\phi_i}\sin\mu_i x + Q\left(e^{i\theta_j}\cos\mu_j x + r_j e^{i\phi_j}\sin\mu_j x\right)\right] \\ &= a + \varepsilon u^{(1)} \end{aligned} \tag{19}$$

where $r_s \neq 0$ and Q can be 0 or 1, depending on whether a one or two mode SPB is under consideration.

Since $\Delta(\lambda, u)$ and the eigenfunctions $v_n = \begin{bmatrix} v_{n1} \\ v_{n2} \end{bmatrix}$ are analytic functions of their arguments, at the double points λ_n we assume the following expansions:

$$v_n = v_n^{(0)} + \varepsilon v_n^{(1)} + \varepsilon^2 v_n^{(2)} + \cdots \tag{20}$$

$$\lambda_n = \lambda_n^{(0)} + \varepsilon\lambda_n^{(1)} + \varepsilon^2\lambda_n^{(2)} + \cdots \tag{21}$$

Substituting these expansions into **Eq. 25** we obtain the following:

$$\mathcal{O}(\varepsilon^0): \quad \mathcal{L}v_n^{(0)} = 0 \tag{22}$$

$$\mathcal{O}(\varepsilon^1): \quad \mathcal{L}v_n^{(1)} = \begin{bmatrix} -i\lambda_n^{(1)}v_{n1}^{(0)} + u^{(1)}v_{n2}^{(0)} \\ -i\lambda_n^{(1)}v_{n2}^{(0)} + u^{(1)*}v_{n1}^{(0)} \end{bmatrix} \equiv F \tag{23}$$

$$\mathcal{O}(\varepsilon^2): \quad \mathcal{L}v_n^{(2)} = \begin{bmatrix} -i\lambda_n^{(1)}v_{n1}^{(1)} - i\lambda_n^{(2)}v_{n1}^{(0)} + u^{(1)}v_{n2}^{(1)} \\ -i\lambda_n^{(1)}v_{n2}^{(1)} - i\lambda_n^{(2)}v_{n2}^{(0)} + u^{(1)*}v_{n1}^{(1)} \end{bmatrix} \equiv G \quad (24)$$

where

$$\mathcal{L} = \begin{bmatrix} \partial/\partial x + i\lambda_n^{(0)} & -a \\ -a & -\partial/\partial x + i\lambda_n^{(0)} \end{bmatrix} \quad (25)$$

The leading order **Eq. 22** provides the spectrum for the Stokes wave. At the double points $\lambda_n^{(0)}$ the two dimensional eigenspace is spanned by the eigenfunctions

$$\phi_n^{\pm} = e^{\pm ik_n x}\begin{bmatrix} 1 \\ \frac{i}{a}(\pm k_n + \lambda_n) \end{bmatrix} \quad (26)$$

where $(\lambda_n^{(0)})^2 = k_n^2 - a^2, k_n = n\pi/L$, and the general solution is given by

$$v_n^{(0)} = A^+\phi_n^+ + A^-\phi_n^-$$

4.1 First Order Results

For periodic v, the solvability condition for the system $\mathcal{L}v = F = \begin{bmatrix} F_1 \\ F_2 \end{bmatrix}$ is given by the orthogonality condition

$$\int_0^L (F_1 w_1^* + F_2 w_2^*) = 0$$

for all w in the nullspace of the Hermitian operator

$$\mathcal{L}^H = \begin{bmatrix} -\partial/\partial x - i\lambda_n^* & -a \\ -a & \partial/\partial x - i\lambda_n^* \end{bmatrix}$$

At the double points the nullspace of $\mathcal{L}^H$ is spanned by the eigenfunctions $\begin{bmatrix} \phi_{n2}^{\pm} \\ \phi_{n1}^{\pm} \end{bmatrix}^*$ and the orthogonality condition becomes

$$\int_0^L (F_1\phi_{n2}^{\pm} + F_2\phi_{n1}^{\pm})dx = 0 \quad (27)$$

Applying this orthogonality condition to **Eq. 23** yields the system of equations

$$\begin{bmatrix} T_+ & T \\ T & T_- \end{bmatrix}\begin{bmatrix} A^+ \\ A^- \end{bmatrix} = 0$$

where

$$T = 2\lambda_n^{(0)}\lambda_n^{(1)}/a \quad (28)$$

$$T_{\pm} = -\frac{1}{2}\begin{cases} \left(\frac{\pm k_n + \lambda_n}{a}\right)^2\left(e^{i\theta_n} \pm ir_n e^{i\phi_n}\right) - \left(e^{-i\theta_n} \pm ir_n e^{-i\phi_n}\right) & n = i,j \\ 0 & n \neq i,j \end{cases} \quad (29)$$

Non trivial solutions $A^{\pm}$ are obtained only at the complex double points λ_n, $n = i, j$ at which the SPB was constructed providing the first order correction

$$\left(\lambda_n^{(1)}\right)^2 = \begin{cases} \frac{a^2}{4\lambda_n^2}[\sin(\omega_n + \theta_n)\sin(\omega_n - \theta_n) \\ \quad + r_n^2\sin(\omega_n + \phi_n)\sin(\omega_n - \phi_n) \quad n = i,j \\ \quad + ir_n\sin(\phi_n - \theta_n)\sin 2\omega_n] \\ 0 \qquad\qquad\qquad\qquad\qquad\qquad n \neq i,j \end{cases} \quad (30)$$

where $\tan\omega_n = \mathrm{Im}(\lambda_n^{(0)})/k_n$ and $\theta_s \neq \phi_s \pm n\pi$ for $s = i, j$. As a result $\lambda_n^{(1)} = \pm r^{1/2}e^{ip/2}$ where $0 < p < 2\pi$ and the double point splits asymmetrically in any direction. Examining Δ in a neighborhood of $u^{(0)}$ we find that when $u^{(1)}$ resonates with a particular mode, the band of continuous spectrum along the imaginary axis splits asymmetrically into two disjoint bands in the upper half plane. The other double points do not experience an $\mathcal{O}(\varepsilon)$ correction.

The spectral configuration is determind by the location of $\lambda_n^{(\pm)} = \lambda^{(0)} + \varepsilon\lambda^{(1)}$. λ_n^+ determines the speed and direction of the associated phase. For example, in the one complex double point regime there are only two spectral configurations associated with noneven perturbation: 1) For $0 < p < \pi$, Re $\lambda^+ > 0$ and the upper band of spctrum lies in the first quadrant. The wave form is characterized by a single modulated mode traveling to the right. 2) For $\pi < p < 2\pi$, Re $\lambda^+ < 0$, the upper band of spectrum is in the second quadrant, and the wave form is characterized by a single modulated mode traveling to the left.

As observed in the damped HONLS numerical experiments, the spectrum evolves between two distinct configurations when the continuous spectrum develops a complex critical point (not double point) due to the formation of transverse bands which then splits.

4.2 Second Order Results

Determining the $\mathcal{O}(\varepsilon^2)$ corrections to the double points λ_n for $n \neq i, j$, requires determining the eigenfunctions at $\mathcal{O}(\varepsilon)$. When $\lambda_n^{(1)} = 0$ the right hand side of **Eq. 23** simplifies to

$$\mathcal{L}v_n^{(1)} = \mathcal{F} = \begin{bmatrix} 0 & u^{(1)} \\ u^{(1)*} & 0 \end{bmatrix}v_n^{(0)} = \begin{bmatrix} u^{(1)}(A^+\phi_{n2}^+ + A^-\phi_{n2}^-) \\ u^{(1)*}(A^+\phi_{n1}^+ + A^-\phi_{n1}^-) \end{bmatrix}$$

where $\phi_n^{\pm}$ is given by **Eq. 26**. We assume $v_n^{(1)} = v_n^{(0)} + \sum_n^{(1)}$ where

$$\begin{aligned}\sum_n^{(1)} = {} & A_i e^{i(k_n+\mu_i)x} + B_i e^{i(k_n+\mu_i)x} + C_i e^{-i(k_n-\mu_i)x} + D_i e^{-i(k_n+\mu_i)x} \\ & + A_j e^{i(k_n+\mu_j)x} + B_j e^{i(k_n-\mu_j)x} + C_j e^{-i(k_n-\mu_j)x} + D_j e^{-i(k_n+\mu_j)x}\end{aligned} \quad (31)$$

Substituting $\sum_n^{(1)}$ into **Eq. 23** we find the coefficient vectors to be (with $n \neq s$, $s = i, j$)

$$A_s = \frac{A^+/2}{\mu_s^2 + 2k_n\mu_s}\begin{bmatrix} \frac{1}{a}\left[2(\cos\theta_s - \sin\phi_s)a^2 + \left(e^{i\theta_s} + ie^{i\phi_s}\right)(k_n + \lambda_n)\mu_s\right] \\ i\left[2(\cos\theta_s - \sin\phi_s)(k_n + \lambda_n) + \left(e^{i\theta_s} - ie^{i\phi_s}\right)\mu_s\right] \end{bmatrix}$$

$$B_s = \frac{A^+/2}{\mu_s^2 - 2k_n\mu_s}\begin{bmatrix} \frac{1}{a}\left[2(\cos\theta_s - \sin\phi_s)a^2 - \left(e^{i\theta_s} + ie^{i\phi_s}\right)(k_n + \lambda_n)\mu_s\right] \\ i\left[2(\cos\theta_s - \sin\phi_s)(k_n + \lambda_n) - \left(e^{i\theta_s} - ie^{i\phi_s}\right)\mu_s\right] \end{bmatrix}$$

$$C_s = \frac{A^-/2}{\mu_s^2 - 2k_n\mu_s}\begin{bmatrix} \frac{1}{a}\left[2(\cos\theta_s - \sin\phi_s)a^2 + \left(e^{i\theta_s} + ie^{i\phi_s}\right)(-k_n + \lambda_n)\mu_s\right] \\ i\left[2(\cos\theta_s - \sin\phi_s)(-k_n + \lambda_n) + \left(e^{i\theta_s} - ie^{i\phi_s}\right)\mu_s\right] \end{bmatrix}$$

$$D_s = \frac{A^-/2}{\mu_s^2 + 2k_n\mu_s}\begin{bmatrix} \frac{1}{a}\left[2(\cos\theta_s - \sin\phi_s)a^2 - \left(e^{i\theta_s} + ie^{i\phi_s}\right)(-k_n + \lambda_n)\mu_s\right] \\ i\left[2(\cos\theta_s - \sin\phi_s)(-k_n + \lambda_n) - \left(e^{i\theta_s} - ie^{i\phi_s}\right)\mu_s\right] \end{bmatrix}$$

With $\nu_n^{(1)}$ in hand, applying the orthogonality condition to **Eq. 24** yields the system

$$\begin{bmatrix} \alpha_n^+ & \lambda_n^{(2)} - \beta_n \\ \lambda_n^{(2)} - \beta_n & \alpha_n^- \end{bmatrix} \begin{bmatrix} A^+ \\ A^- \end{bmatrix} = 0 \tag{32}$$

giving an $\mathcal{O}(\varepsilon^2)$ correction of the form

$$\left(\lambda_n^{(2)} - \beta_n\right)^2 = \begin{cases} \alpha_n^+ \alpha_n^- & n = 2i, 2j, i+j, j-i \\ 0 & \textit{for all other cases} \end{cases} \tag{33}$$

Consequently only the double points $\lambda_n^{(0)}$ with $n = 2i, 2j, i+j$, or $j-i$ experience an $\mathcal{O}(\varepsilon^2)$ splitting. All other double points experience an $\mathcal{O}(\varepsilon^2)$ translation. This calculation can be carried to higher order $\mathcal{O}(\varepsilon^m)$. In the simpler case of a damped single mode SPB, $U_{\varepsilon,\gamma}^{(j)}(x,t)$, only $\lambda_n^{(0)}$ corresponding to the resonant mode $n = mj$ will split at order $\mathcal{O}(\varepsilon^m)$ whereas the splitting is zero for $\lambda_n^{(0)}$, $n \neq mj$ [41].

For the two mode damped SPB $U_{\varepsilon,\gamma}^{(2,3)}$ in the 3 UM regime we find λ_2^d and λ_3^d will split at $\mathcal{O}(\varepsilon)$. The mode associated with $\lambda_1^{(0)}$ resonates also with $u^{(1)}$ at $\mathcal{O}(\varepsilon^2)$. All 3 complex double points split, in contrast with the one mode $U_{\varepsilon,\gamma}^{(2)}$ where $\lambda_1^{(0)}$ and $\lambda_3^{(0)}$ do not split.

5 CONCLUSIONS

In this paper we investigated the route to stability for even N-mode SPB solutions of the NLS equation in the framework of a damped HONLS equation using the Floquet spectral theory of the NLS equation. We found novel instabilities emerging in the symmetry broken solution space of the damped HONLS which are not captured by complex double points in the Floquet spectrum. We developed a broadened Floquet characterization of instabilities by examining the stability of an even 3-phase solution of the NLS equation with respect to noneven perturbations. We found the transverse complex critical point in its spectrum is associated with an instability which is not excited when evenness is imposed.

The association of instabilities excited by symmetry breaking with complex critical points of the Floquet spectrum was corroborated by the numerical experiments. If one of the complex double points present at $t = 0$ splits in the damped HONLS system, the subsequent spectral evolution involves repeated formation and splitting of complex critical points (not double points) which we correlated with the observed instabilities.

In the numerical study we presented experiments using fixed values of the perturbation parameters ϵ and γ. As these parameters are varied fewer or more critical points may form and the time the damped HONLS solution stabilizes may vary but the following interesting results are independent of their specific value: 2) Instabilities excited by symmetry breaking are associated with complex critical points. 2) Solutions stabilize once damping eliminates all the complex critical points and complex double points in the spectral deomposition of the damped HONLS data. 3) Only certain modes resonate with the damped HONLS perturbation. Resonant modes aid in stabilizing the solution. If nonresonant modes are present, their instabilities persist and appear to organize the dynamics on a longer timescale.

Each burst of growth in $\eta(t)$ can be correlated with the emergence of a complex critical point. The numerics suggest the instabilities associated with complex critical points may be weaker than those associated with complex double points. Even so the exact nature of the instability warrants further investigation. As demonstrated by the evolution of $U_{\varepsilon,\gamma}^{(2,3)}(x,t)$ their cumulative impact can be significant.

Via a short time perturbation analysis we find that resonant complex double points split producing disjoint asymmetric bands, while the nonresonant complex double points remain closed as they move along the bands of spectrum, corroborating the initial spectral evolutions observed in the numerical experiments. Further, the nonresonant double points remain closed for the duration of the experiments, beyond the time-frame of the short time analysis, even though the solution evolves as a damped asymmetric multi-phase state.

DATA AVAILABILITY STATEMENT

The original contributions presented in the study are included in the article/Supplementary Material, further inquiries can be directed to the corresponding author.

AUTHOR CONTRIBUTIONS

CS was responsible for the theoretical framework, calculations, and the writing of the manuscript. CS and AI performed the numerical simulations. Both authors approve the manuscript.

FUNDING

This work was partially supported by Simons Foundation, Grant No. #527565.

REFERENCES

1. Stokes GG. On the theory of oscillatory waves. *Trans Cambridge Philos Soc* (1847) 8:441–73.
2. Benjamin TB, Feir JE. The disintegration of wave trains in deep water. *J Fl Mech* (1967) 27:417–30. doi:10.1017/s002211206700045x
3. Zakharov VE. Stability of periodic waves of finite amplitude on the surface of a deep fluid. *J Appl Mech Tech Phys* (1968) 9:190–4. doi:10.1007/BF00913182
4. Peregrine D. Water waves, nonlinear Schrödinger equations and their solutions. *J Austral Math Soc Ser B* (1983) 25:16–43. doi:10.1017/s0334270000003891
5. Dysthe KB, Trulsen K. Note on breather type solutions of the NLS as models for freak-waves. *Physica Scripta* (1999) T82:48–52. doi:10.1238/physica.topical.082a00048
6. Kibbler B, Fatome J, Finot C, Millot G, Dias F, Genty G, et al. The Peregrine soliton in nonlinear fibre optics. *Nat Phys* (2010) 6:790–5. doi:10.1038/nphys1740
7. Kharif C, Pelinovsky E, Slunyaev A. *Rogue waves in the ocean*. Berlin Heidelberg: Springer-Verlag (2009).

8. Onorato M, Residori S, Bortolozzo U, Montina A, Arecchi FT. Rogue waves and their generating mechanisms in different physical contexts. *Phys Rep* (2013) 528:47–89. doi:10.1016/j.physrep.2013.03.001
9. Solli DR, Ropers C, Koonath P, Jalali B. Optical rogue waves. *Nature* (2007) 450: 1054–7. doi:10.1038/nature06402
10. Osborne A, Onorato M, Serio M. The nonlinear dynamics of rogue waves and holes in deep-water gravity wave train. *Phys Lett A* (2000) 275:386–93. doi:10.1016/s0375-9601(00)00575-2
11. Calini A, Schober CM. Homoclinic chaos increases the likelihood of rogue wave formation. *Phys Lett A* (2002) 298:335–49. doi:10.1016/s0375-9601(02)00576-5
12. Akhmediev N, Soto-Crespo JM, Ankiewicz A. Extreme waves that appear from nowhere: on the nature of rogue waves. *Phys Lett A* (2009) 373:2137–45. doi:10.1016/j.physleta.2009.04.023
13. Akhmediev NN, Eleonskii VM, Kulagin NE. Exact first-order solutions of the nonlinear Schrödinger equation. *Theor Math Phys (Ussr)* (1987) 72:809–18. doi:10.1007/bf01017105
14. Calini A, Schober CM. Characterizing JONSWAP rogue waves and their statistics *via* inverse spectral data. *Wave Motion* (2017) 71:5–17. doi:10.1016/j.wavemoti.2016.06.007
15. Chen J, Pelinovsky D. Rogue periodic waves of the focusing nonlinear Schrödinger equation. *Proc Math Phy Eng Sci* (2018) 474:20170814. doi:10.1098/rspa.2017.0814
16. Chen J, Pelinovsky DE, White RE. Rogue waves on the double-periodic background in the focusing nonlinear Schrödinger equation. *Phys Rev E* (2019) 100:052219. doi:10.1103/physreve.100.052219
17. Calini A, Schober CM. Numerical investigation of stability of breather-type solutions of the nonlinear Schrödinger equation. *Nat Hazards Earth Syst Sci* (2014) 14:1431–40. doi:10.5194/nhess-14-1431-2014
18. Segur H, Henderson D, Carter J, Hammack J, Li C, Pheiff D, et al. Stabilizing the benjamin-feir instability. *J Fluid Mech* (2005) 539:229–71. doi:10.1017/s002211200500563x
19. Chabchoub A, Hoffmann NP, Akhmediev N. Rogue wave observation in a water wave tank. *Phys Rev Lett* (2011) 106:1–4. doi:10.1103/physrevlett.106.204502
20. Fotopoulos G, Frantzeskakis DJ, Karachalios NI, Kevrekidis PG, Koukouloyannis V, Vetas K. Extreme wave events for a nonlinear Schrödinger equation with linear damping and Gaussian driving. *Commun Nonlinear Sci Numer Simul* (2019) 82: 105058. doi:10.1016/j.cnsns.2019.105058
21. Coppini F, Grinevich PG, Santini PM. Effect of a small loss or gain in the periodic nonlinear Schrödinger anomalous wave dynamics. *Phys Rev E* (2020) 101:032204. doi:10.1103/physreve.101.032204
22. Kimmoun O, Hsu HC, Branger H, Li MS, Chen YY, Kharif C, et al. Modulation instability and phase-shifted Fermi-Pasta-Ulam recurrence. *Sci Rep* (2016) 6: 28516. doi:10.1038/srep28516
23. Schober CM, Islas AL. The routes to stability of spatially periodic solutions of the linearly damped NLS equation. *The Eur Phys J Plus* (2020) 135:1–20. doi:10.1140/epjp/s13360-020-00660-w
24. Dysthe K. Note on a modification to the nonlinear Schrödinger equation for deep water. *Proc R Soc London Ser A Math Phys Sci* (1979) 369:105–14. doi:10.1098/rspa.1979.0154
25. Lo E, Mei CC. A numerical study of water wave modulation based on a higher-order nonlinear Schrödinger equation. *J Fluid Mech* (2020) 150:395–416. doi:10.1017/s0022112085000180
26. Ablowitz MJ, Herbst B, Schober CM. Long-time dynamics of the modulational instability of deep water waves. *Physica D* (2001) 152-153:416–33. doi:10.1016/s0167-2789(01)00183-x
27. Gramstad O, Trulsen K. Hamiltonian form of the modified nonlinear Schrödinger equation for gravity waves on arbitrary depth. *J Fluid Mech* (2011) 670:404–26. doi:10.1017/s0022112010005355
28. Zaug C, Carter JD. Dissipative models of swell propagation across the Pacific. *arXiv*. Preprint: arXiv:2005.06635. doi:10.1002/essoar.10503175.1
29. Carter JD, Henderson D, Butterfield I. A comparison of frequency downshift models of wave trains on deep water. *Phys Fluids* (2019) 31:013103. doi:10.1063/1.5063016
30. Deconinck B, Segal BL. The stability spectrum for elliptic solutions to the focusing NLS equation. *Physica D* (2017) 346:1–19. doi:10.1016/j.physd.2017.01.004
31. Zakharov VE, Shabat AB. Exact theory of two-dimensional self-focusing and onedimensional self-modulation of waves in nonlinear media. *Soviet Phys JETP* (1972) 34:62–9.
32. Ercolani N, Forest MG, McLaughlin DW. Geometry of the modulational instability. iii. homoclinic orbits for the periodic Sine-Gordon equation. *Physica D* (1990) 43:349–84. doi:10.1016/0167-2789(90)90142-c
33. McLaughlin DW, Overman EA. Whiskered tori for integrable pdes and chaotic behavior in near integrable pdes. *Surv Appl Math* (1995) 1:83–203. doi:10.1007/978-1-4899-0436-2_2
34. Overman EA, II, McLaughlin DW, Bishop AR. Coherence and chaos in the driven damped Sine-Gordon equation: measurement of the soliton spectrum. *Physica D* (1986) 19:1–14. doi:10.1016/0167-2789(86)90052-7
35. Lu X, Ma WX, Yu J, Khalique CM. Solitary waves with the Madelung fluid description: a generalized derivative nonlinear Schrödinger equation. *Commun Nonlinear Sci Numer Simul* (2016) 31:40–6. doi:10.1016/j.cnsns.2015.07.007
36. Sattinger DH, Zurkowski VD. Gauge theory of BÄcklund transformations. ii. *Physica D Nonlinear Phenom* (1987) 26:225–50. doi:10.1016/0167-2789(87)90227-2
37. Trefethen LN. *Spectral methods*. Philadelphia: SIAM (2000).
38. Grinevich PG, Santini PM. The finite gap method and the analytic description of the exact rogue wave recurrence in the periodic NLS Cauchy problem. *Nonlinearity* (2018) 31:5258–308. doi:10.1088/1361-6544/aaddcf
39. Ablowitz MJ, Herbst BM, Schober CM. Computational chaos in the nonlinear Schrödinger equation without homoclinic crossings. *Physica A* (1996) 228: 212–35. doi:10.1016/0378-4371(95)00434-3
40. Hirota R. *Lecture notes in mathematics*. New York, NY: Springer-Verlag (1976), 515.
41. Ablowitz MJ, Schober CM. Effective chaos in the nonlinear Schrödinger equation. *Contemp Math* (1994) 172:253. doi:10.1090/conm/172/01808

Conflict of Interest: The authors declare that the research was conducted in the absence of any commercial or financial relationships that could be construed as a potential conflict of interest.

frontiers in Physics

ORIGINAL RESEARCH
published: 25 August 2021
doi: 10.3389/fphy.2021.633549

The Peregrine Breather on the Zero-Background Limit as the Two-Soliton Degenerate Solution: An Experimental Study

Amin Chabchoub[1,2,3]*, *Alexey Slunyaev*[4,5], *Norbert Hoffmann*[6,7], *Frederic Dias*[8,9], *Bertrand Kibler*[10], *Goëry Genty*[11], *John M. Dudley*[12] *and Nail Akhmediev*[13]

[1]Hakubi Center for Advanced Research, Kyoto University, Kyoto, Japan, [2]Disaster Prevention Research Institute, Kyoto University, Kyoto, Japan, [3]Center for Wind, Waves and Water, School of Civil Engineering, The University of Sydney, Sydney, NSW, Australia, [4]Department of Nonlinear Geophysical Processes, Institute of Applied Physics RAS, Nizhny Novgorod, Russia, [5]Laboratory of Dynamical Systems and Applications, National Research University Higher School of Economics, Nizhny Novgorod, Russia, [6]Dynamics Group, Hamburg University of Technology, Hamburg, Germany, [7]Department of Mechanical Engineering Imperial College London, London, United Kingdom, [8]School of Mathematics and Statistics, University College Dublin, Dublin, Ireland, [9]ENS Paris-Saclay, CNRS, Centre Borelli, Université Paris-Saclay, Gif-sur-Yvette, France, [10]Laboratoire Interdisciplinaire Carnot de Bourgogne (ICB), UMR 6303 CNRS-Université Bourgogne Franche-Comté, Dijon, France, [11]Photonics Laboratory, Physics Unit, Tampere University, Tampere, Finland, [12]Institut FEMTO-ST, Université Bourgogne Franche-Comté CNRS UMR 6174, Besançon, France, [13]Department of Theoretical Physics, Research School of Physics, The Australian National University, Canberra, ACT, Australia

OPEN ACCESS

Edited by:
Jürgen Vollmer,
Universität Leipzig, Germany

Reviewed by:
Oreste Piro,
University of the Balearic Islands, Spain
Reinaldo Roberto Rosa,
National Institute of Space Research (INPE), Brazil

***Correspondence:**
Amin Chabchoub
chabchoub.amin.8w@kyoto-u.ac.jp

Specialty section:
This article was submitted to Interdisciplinary Physics, a section of the journal Frontiers in Physics

Received: *25 November 2020*
Accepted: *28 July 2021*
Published: *25 August 2021*

Citation:
Chabchoub A, Slunyaev A, Hoffmann N, Dias F, Kibler B, Genty G, Dudley JM and Akhmediev N (2021) The Peregrine Breather on the Zero-Background Limit as the Two-Soliton Degenerate Solution: An Experimental Study. Front. Phys. 9:633549. doi: 10.3389/fphy.2021.633549

Solitons are coherent structures that describe the nonlinear evolution of wave localizations in hydrodynamics, optics, plasma and Bose-Einstein condensates. While the Peregrine breather is known to amplify a single localized perturbation of a carrier wave of finite amplitude by a factor of three, there is a counterpart solution on zero background known as the degenerate two-soliton which also leads to high amplitude maxima. In this study, we report several observations of such multi-soliton with doubly-localized peaks in a water wave flume. The data collected in this experiment confirm the distinctive attainment of wave amplification by a factor of two in good agreement with the dynamics of the nonlinear Schrödinger equation solution. Advanced numerical simulations solving the problem of nonlinear free water surface boundary conditions of an ideal fluid quantify the physical limitations of the degenerate two-soliton in hydrodynamics.

Keywords: degenerate soliton, Peregrine breather on the zero-background limit, rogue waves, nonlinear waves, wave hydrodynamics

INTRODUCTION

The Peregrine breather (PB) [1] is a fundamental wave envelope solution of the nonlinear Schrödinger equation (NLSE) localized both in space and time, yielding a three-fold amplification of the initial amplitude at the point of maximum localization. These unique characteristics have led the PB to be generally considered as a potential backbone model allowing to describe the emergence of extreme events in several physical systems [2, 3]. Although the PB existence was originally predicted in the early eighties [1], it took about 3 decades to observe this particular wave envelope in a laboratory environment [4–6]. These initial studies have attracted significant attention and led to many follow-up studies related to PB dynamics and its peculiar physical properties [7–14]. The initial or boundary conditions

leading to the PB excitation require to impose a small perturbation on top of a plane wave background. Recently, generic features of PB dynamics on a stationary dnoidal background have been presented [15]. The regular background solution represents only one limiting case of the exact family of NLSE dnoidal solutions while the other limit is the envelope soliton on zero-background [16, 17]. This allows a more general construction of Peregrine-type coherent structures on different type of stationary backgrounds. The respective evolution in time and space can be described by an exact solution [18].

In this paper, we experimentally investigate the PB dynamics in the zero background limit, which can be also associated with the degenerate case of two soliton interaction, resulting in an amplitude amplification factor of two at the point of maximum localization [19]. The laboratory experiments, conducted in different water wave flumes, are in excellent agreement with the theory when the carrier steepness is moderate. We recall that the carrier wave steepness, being physically the product of wavenumber and wave amplitude and mathematically the expansion parameter in the weakly nonlinear approximation of the water wave problem [3], is a nonlinearity indicator of wave field. Otherwise, deviations from the symmetric envelope shapes are inevitable due to the physical limitations of the NLSE approach to describe broadband and highly nonlinear processes in water waves. The numerical simulations based on the higher-order spectral method (HOSM), which accurately solves the nonlinear water wave problem, quantify the limitations in the evolution of the hydrodynamic degenerate soliton on the water surface. The HOSM results predict a recurrent focusing behavior, not anticipated by the NLSE, when the carrier wave steepness is substantial. We believe that our results will have a significant impact in nonlinear dynamics as well as integrable systems and improve fundamental understanding of extreme wave formation in a variety of nonlinear media.

Higher-Order Solitons on Zero Background and the Case of Degeneracy

The NLSE for surface gravity waves is the simplest nonlinear evolution equation that takes into account the interplay between dispersion and nonlinearity in the evolution of a narrowband wave field. Assuming unidirectional propagation of the wave field in infinite water depth, the wave envelope evolution equation reads [20]

$$i\left(\frac{\partial\psi}{\partial t}+c_g\frac{\partial\psi}{\partial x}\right)+\frac{\omega}{8k^2}\frac{\partial^2\psi}{\partial x^2}+\frac{\omega k^2}{2}|\psi|^2\psi=0, \tag{1}$$

where $\psi(x, t)$ is the complex wave envelope, x is the spatial coordinate along the wave propagation, and t represents time. The parameters ω and k are the carrier cyclic wave frequency and wavenumber, respectively. The latter are constrained by the gravitational acceleration g-dependent deep-water dispersion equation

$$\omega^2=gk, \tag{2}$$

and the envelope is assumed to propagate with the group velocity $c_g=\frac{\partial\omega}{\partial k}=\frac{\omega}{2k}$.

The NLSE is a partial differential equation that belongs to the family of integrable evolution equations [21]. Its exact solutions provide physically relevant models for investigating the dynamics of nonlinear coherent wave groups in controlled laboratory environments. The fields of its application are hydrodynamics, optics and Bose-Einstein condensates. It is common to use the dimensionless form of **Eq. 1** for simplicity, particularly when aiming for the derivation of exact solutions,

$$i\frac{\partial\Psi}{\partial T}+\frac{\partial^2\Psi}{\partial X^2}+2|\Psi|^2\Psi=0, \tag{3}$$

which is obtained by introducing the following transformations

$$X=2k\left(x-c_gt\right),\quad T=\frac{\omega}{2}t,\quad \Psi=\frac{k}{\sqrt{2}}\psi. \tag{4}$$

One of the most-fundamental solutions of the NLSE is an isolated and stationary sech-shape nonlinear wave group on zero-background known as envelope soliton, which can be considered as a mode of a nonlinear system remaining unchanged with propagation [22]. At the same time, interactions and collisions between envelope solitons are elastic [23, 24]. The number of solitons contained in a localized initial condition remains fixed during the follow up evolution. The zero-velocity soliton solution with an amplitude of one can be written as

$$\Psi_S(X,T)=\mathrm{sech}\,(X)\ \exp\,(iT). \tag{5}$$

The initial-value problem for the NLSE can be solved with the help of the inverse scattering technique (IST) [21, 25, 26]. More complex (higher-order) structures containing multiple solitons can be also constructed using the Darboux transformation [27] or dressing method [28]. Each envelope soliton in these superpositions is unambiguously characterized by the pair of its two key parameters: the amplitude and the velocity. The NLSE solution describing the dynamics of two envelope solitons with fixed amplitudes 0.5 and 1.5, zero-velocities and located at the same position $X = 0$, is known as the Satsuma-Yajima breather [29]

$$\Psi_{S_2}(X,T)=4\frac{\cosh 3X+3\cosh X\ \exp\ 8iT}{\cosh 4X+4\cosh 2X+3\ \cos\ 8T}\exp\,(iT). \tag{6}$$

This solution is periodic in T and can be used for pulse nonlinear wave group compression. At $T = 0$, this solution takes the form of a soliton with twice the amplitude of a single soliton of the same width, i.e. $\Psi_{S_2}(X,0)=2\,\mathrm{sech}(X)=2\,\Psi_S(X,0)$. However, this initial condition changes with propagation and evolves towards a self-compression, i.e., breathing process [29]. Such solutions also play a key role in the formation of significant irreversible spectral broadening and the creation of supercontinua as a result of soliton fission [30, 31]. Generally, when the parameters of the two envelope solitons become close, the distance between them increases and they repel each other, moving away towards infinity. Due to this fact, for more than

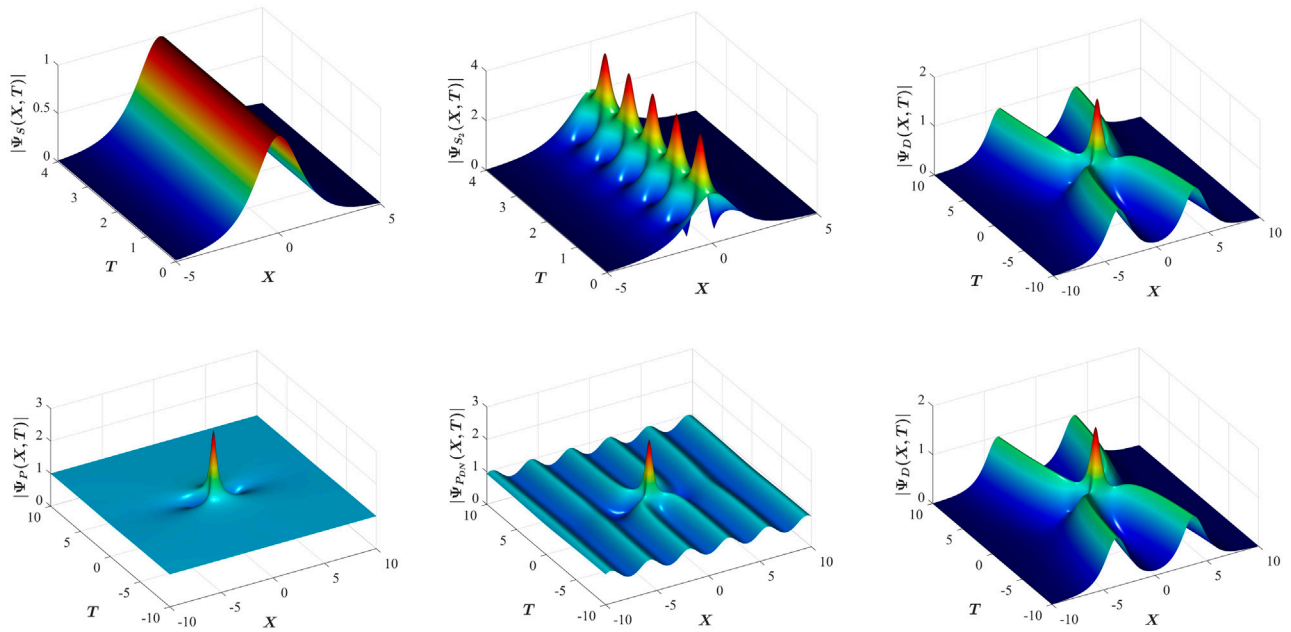

FIGURE 1 | Spatio-temporal evolution of solitons on finite and zero-background. **Top left**: single envelope soliton. **Top middle**: Higher-order soliton of order 2. **Top right**: Degenerate two-solution solution. **Bottom left**: Peregrine breather. **Bottom middle**: Peregrine breather on a dnoidal background. **Bottom right**: Degenerate two-soliton solution.

2 decades since the development of the IST, the two-soliton solution of the NLSE with exactly the same parameters has been considered as non-existent. Overcoming this controversy, the solution has been reported in [1, 19]. Such solution is the degenerate two-soliton solution, as finding it requires considering the special limit when their amplitudes and velocities tend to the same limiting values. It is represented by a mixed semi-rational semi-hyperbolic functions

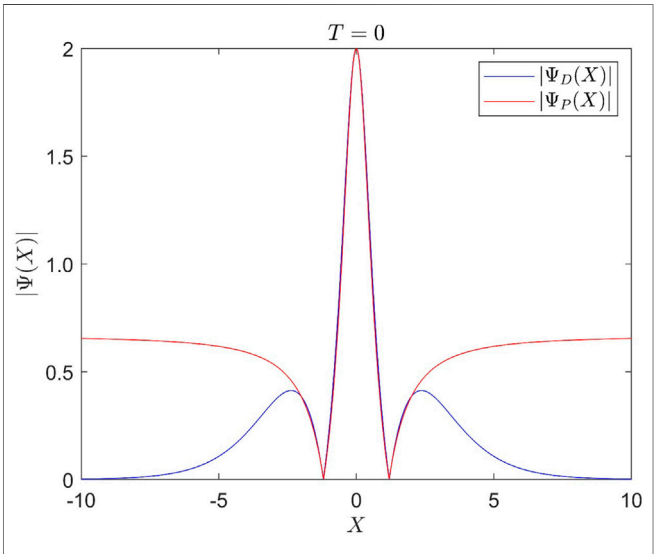

FIGURE 2 | The amplitude rescaled Peregrine breather envelope shape vs. degenerate two-soliton solution profile at $T = 0$.

$$\Psi_D(X,T) = 4\frac{X\sinh X - \cosh X - 2iT\cosh X}{\cosh 2X + 1 + 2X^2 + 8T^2}\exp(iT). \quad (7)$$

Here, the subindex D refers to the degenerate case. More specifically, the solution (**Eq. 7**) describes the interaction of two envelope solitons with unit amplitudes and with their center of mass located at $X = 0$. The envelope $|\Psi_D|$ in (**Eq. 7**) is symmetric with respect to the change of the sign of either X or T. Note that the solution (**Eq. 7**) may be generalized using the invariant transforms of the NLSE, i.e., arbitrary phase, scaling and Galilean transforms. In the reduced form (**Eq. 7**), it does not contain any free parameters. The degenerate solution (**Eq. 7**) describes two "attracting" envelope solitons when $T < 0$. When $T = 0$, the two solitons are superimposed and form an extreme event with an amplitude at the point of collision twice that the amplitude of the isolated solitons. At large times $T \gg 1$, the solution (**Eq. 7**) describes the two envelope solitons which slowly walk away from each other after the collision. Each of them can be approximated as a quasi-single-soliton solution. The opposite velocities of the two solitons reduce when $T \to \infty$.

What at first sight seems to be just a mathematical artifact has in fact a particular physical relevance. Indeed, the central part of the degenerate solution (**Eq. 7**) can be considered as the PB on the zero-background limit. The comparison is relevant because the solution (**Eq. 7**) is semi-rational while PB is a rational solution. Representing hyperbolic functions $\cosh X$ and $\cosh 2X$ in the central part of the solution as an expanded series in X can reduce it to a rational approximation similar to the PB. On the other hand, the PB can be excited on top of exact dnoidal solutions, parameterized as

$\Psi_{\mathrm{dn}}(X,T) = \mathrm{dn}(X,m)\exp(i[2-m^2]T)$; $0 \le m \le 1$ see [15, 18]. Such one-parameter family of modulated wave envelopes is steady and the parameter m determines two edge cases [16, 17]. One limiting case of this one-parameter family of stationary dnoidal solutions is the regular background ($m = 0$) and the other limit is the envelope soliton ($m = 1$). This second limit leads to the formation of the degenerate soliton solution. The transformation is controlled by an additional free parameter–modulus of the dn function. The role of this parameter in the highly nontrivial process of degenerate soliton formation can be seen from **Figure 7** in [15]. The latter process admits several stages of PB transformation. A significantly simplified version of the process can be seen from **Figure 1** (see bottom panels from left to right). Here, the classical Peregrine solution on finite background is transformed to the degenerate solution on zero background with one intermediate step in the form of the PB on the modulated DN-wave background (referring to the semicircle in the λ-plane in **Figure 2** of [15]).

The Peregrine Solution

$$\Psi_P(x,t) = \left(-1 + \frac{4 + 16iT}{1 + 4X^2 + 16T^2}\right)\exp(2iT) \tag{8}$$

has been found to be present in multi-soliton solutions [32]. On the other hand, the degenerate two-soliton solution (**Eq. 7**) can represent Peregrine-type dynamics with zero condensate. This becomes more evident when considering the type of localization around the point of maximum amplitude. In fact, the shape of the extreme wave at $T = 0$ does resemble the shape of the Peregrine breather.

This can be seen from **Figure 2**, where the degenerate two-soliton solution at $T = 0$ is compared with the shape of the Peregrine breather at $T = 0$ multiplied by the factor 2/3 in order to equalize the maximal amplitudes.

The agreement between the two profiles is remarkably good within the interval between the zeros.

Even though the dynamics of the degenerate two-soliton solution creates a smaller wave amplification than the Peregrine breather (2 rather than 3), it is still a rapidly forming extreme event. We should also take into account the difference between the backgrounds. Thus, such solutions can be responsible for the occurrence of extreme wave events, which are very similar to the PB.

LABORATORY EXPERIMENTS

The physical experiments have been conducted in two different water wave facilities: Hamburg University of Technology and the University of Sydney flumes, as described in [7, 33], respectively. Although both facilities are different when considering their size and type of wave generators (flap- and piston-type, respectively), the experimental procedures are similar. The wave generator is programmed to create the temporal surface elevation as described by the NLSE solution at fixed position x^* to first-order in steepness

$$\eta_{\text{wave maker}}(x^\star, t) = \mathrm{Re}\left(\psi(x^*, t)\exp\left[i(\omega t - kx^*)\right]\right). \tag{9}$$

Note that wave makers are calibrated by means of a transfer function, which is specific for each type of wave maker, to properly generate the carrier wave amplitudes and frequency as specified by **Eq. 9** and any other pre-defined time-series. Since the maximal compression occurs at $x^\star = 0$, a negative value for x^* has to be chosen in order to observe the nonlinear soliton interaction and the gradual breather-type focusing process in the wave facility. The larger $|x^\star|$, the more the two solitons move away from each other. The second-order Stokes correction is considered when comparing the collected data with the theoretical NLSE predictions at the respective gauge location x_g^*, that is

$$\eta\left(x_g^*, t\right) = \mathrm{Re}\Big(\psi\left(x_g^*, t\right)\exp\left[i\left(\omega t - kx_g^*\right)\right] + \frac{1}{2}k\psi^2\left(x_g^*, t\right)\exp\left[2i\left(\omega t - kx_g^*\right)\right]\Big). \tag{10}$$

Note also that when programming the wave maker to produce the surface elevation to first-order in steepness according to (9), results are expected to be identical as the bound waves (higher-order Stokes harmonics) are immediately generated within half a wavelength due to the intrinsic feature of the nonlinearity in the description of water waves. Moreover, fixing two key physical parameters, namely wave amplitude a and the carrier frequency $f = \frac{\omega}{2\pi}$ are sufficient to determine all physical features of the surface elevation. The choice for the specific values of the carrier amplitude and frequency is restricted to the stroke and frequency range specifications of the wave generator. The wave steepness ka, which is an indicator for the nonlinearity of the carrier wave, can be easily determined using

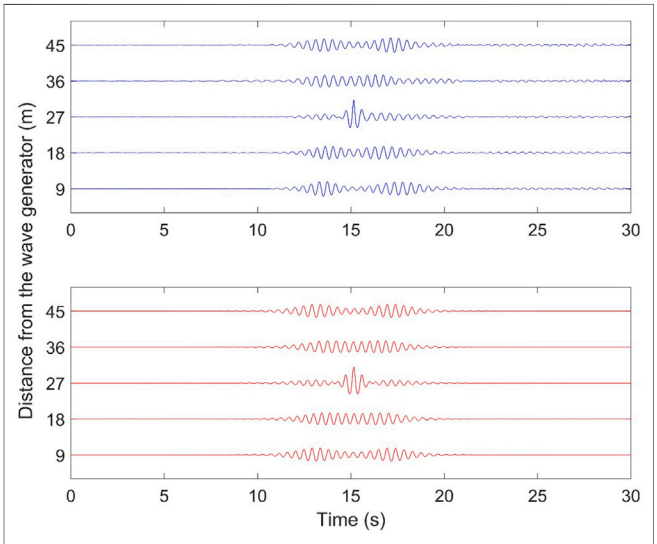

FIGURE 3 | Experimental observation of a degenerate soliton for $a = 0.006$ m, $ka = 0.12$ and $x^* = -27$ m as measured in the Hamburg University of Technology flume. **Top**: Water surface as measured by the wave gauges. **Bottom**: NLSE predictions at the same physical locations using **Eq. 10**.

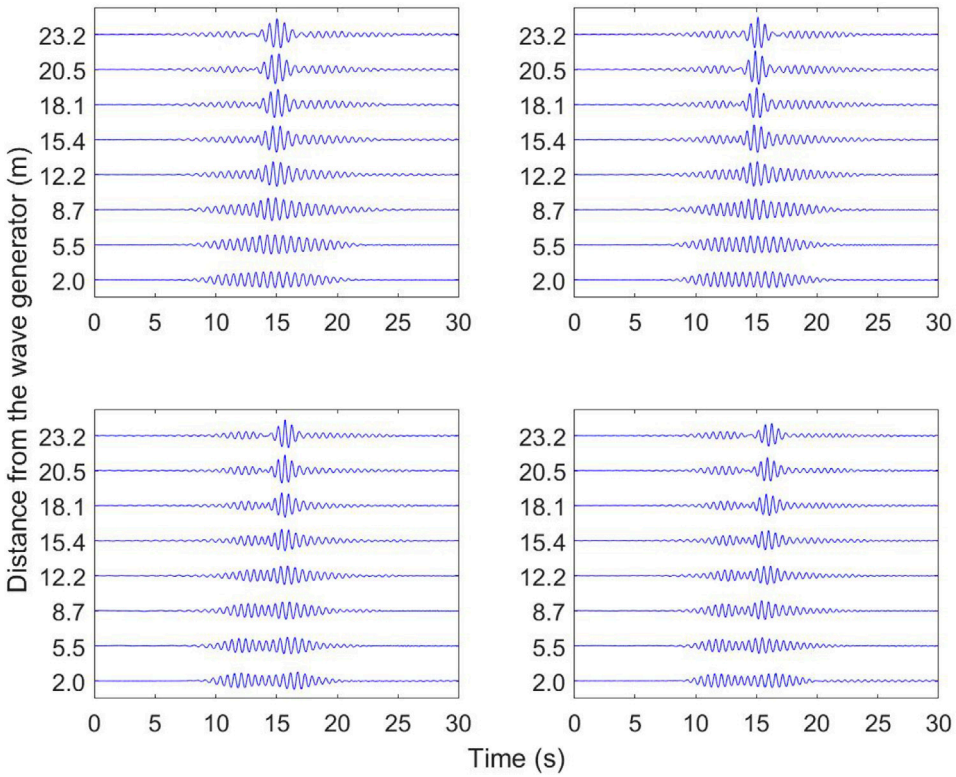

FIGURE 4 | Experimental observation of a degenerate soliton for a = 0.01 m and x^* = −23 m with varying steepness values as measured in the University of Sydney flume. **Top left**: ka = 0.10. **Top right**: ka = 0.11. **Bottom left**: ka = 0.12. **Bottom right**: ka = 0.13.

the dispersion relation (**Eq. 2**). One crucial step consists in scaling the solution $\Psi(X, T)$ to a dimensional form $\psi(x, t)$ satisfying **Eq. 1**. Considering a scaling with respect to the space- or time-NLSE does not have a major impact on the evolution of the degenerate solution in a water wave flume [34]. Finally, capacitance wave gauges are installed along the flume to collect the temporal variation of the water surface at different locations in the direction of wave propagation. Note that a wave-absorbing installation is placed opposite to the wave maker to ensure a wave field propagation free of reflections. Exact schematics of both facilities can be found in [5, 33]. A graphical guide to better understand the origin of the data as measured by the wave gauges along the flume can be found in [35].

The first experiment reported here aims to demonstrate the evolution of the solution over a significantly large distance of 45 m in order to observe the nonlinear and solution-specific interaction between the two envelope solitons yielding an extreme localization. On the other hand, the evolution in the Hamburg University of Technology flume was restricted to 15 m (when taking out the beach installation, effectively 12 m). To overcome this limitation, the reflection-free wave measurement at 9 m was re-injected to the wave generator four times mimicking continuation of the wave propagation. The results of these tests are shown in **Figure 3**.

These results are a clear confirmation of degenerate soliton dynamics on the water surface. Note the excellent agreement in the distinct dynamics with the theoretical prediction, especially considering the total evolution distance of about 144 times the value of the wavelength.

There are obvious limitations of the NLSE model for water waves [36–38]. In fact, when waves become steep, the spectral broadening reduces the ability of the NLSE to accurately describe the wave hydrodynamics. However, this strongly depends on the initial carrier steepness and the bandwidth of the wave train [39].

The next series of tests have been conducted at the University of Sydney wave flume. These addressed the role of wave steepness on the collision process. Several tests have been conducted by gradually increasing the wave steepness from 0.10 to 0.13 with a 0.01 step for the same carrier amplitude of 0.01 m. The four examples of evolution of the degenerate solution at different steepness values are shown in **Figure 4**.

We can clearly notice that the increase of carrier steepness distorts the *clean* and ideal evolution of the NLSE solution, particularly when the carrier steepness values exceed 0.13 in these laboratory tests. Consequently, the soliton interaction becomes asymmetric with a distortion of the envelope shape at the peak.

These restrictions can be accurately addressed and quantified numerically by solving the Euler equations as is discussed in the next section.

NUMERICAL SIMULATIONS

The numerical simulation is performed within the framework of the potential Euler equations using the High-Order Spectral Method (HOSM) following [40]. The HOSM simulations include 2^{10} grid

points in the physical space and a twice larger number in the Fourier domain. The iterations in time are performed with the help of a split-step Fourier procedure. The order of nonlinearity is set to $M = 6$. This corresponds to the solution that is accurate of up to 7-wave nonlinear interactions. The initial-value problem is solved in a periodic spatial domain. The wave steepness is the only physical parameter which controls the wave evolution. The steepness is determined by the quantity ka, where a is the amplitude of the envelope solitons long before they start to collide.

With the purpose of comparing the results of the simulations with the NLSE solution (**Eq. 7**), the computed surface evolution was transformed to the co-moving dimensionless variables (**Eq. 4**) as used in the NLSE. It is then re-scaled to provide the unit amplitudes of the envelope solitons when these are detached at $T \to -\infty$, according to the transformations similar to (**Eq. 4**)

$$X = 2ak\left(x - c_g t\right), \quad T = a^2\frac{\omega}{2}t, \quad \Psi = \frac{k}{\sqrt{2}}\frac{\eta}{a} \tag{11}$$

Note that in **Eq. 11** the function $\Psi(X, T)$ is now real-valued. Three cases of the wave steepness were simulated, which correspond to $ka = 0.05$, $ka = 0.10$ and $ka = 0.15$. In all these cases, the initial condition is specified according to the solution (**Eq. 8**). The dimensionless time is chosen to be $T_0 \approx -12$. This choice corresponds to the situation when solitons already exhibit partial overlap as can be seen in **Figure 5**. This overlap seeds the interaction process in the simulations.

The physical time of the start of the simulation t_0 depends on the wave steepness, see **Eq. 11**. In fact, it corresponds to about 340 wave periods in the steepest case shown in the right panel of **Figure 5**, and to about 3,000 periods in the small-amplitude case shown in the left panel of **Figure 5**. In order to initiate the simulation of the HOSM code, the surface displacement and the surface velocity potential are calculated from $\psi(x, -t_0)$ with a more precise definition than **Eq. 10**, using the third-order asymptotic solution for nonlinear modulated waves, see [41]. Only the cases without wave breaking were simulated, thus, no filters are required to take into account wave breaking effects.

Six runs of the numerical simulations were performed with different complex phases of the initial condition $\psi(x, -t_0)$, for several wave steepness conditions. The envelope $\Psi_{env}(X, T)$ is calculated as the maximal values of Ψ among these six simulations at every X and T. The surface displacements of the initial conditions are plotted in **Figure 5** with respect to two versions of the dimensionless space and amplitude variables.

A false color representation of the evolution of each degenerate soliton envelope in time and space is shown in **Figure 6**.

The intersection of the white dashed lines corresponds to the point in time and space where the maximum wave is expected within the NLSE framework. Qualitatively, the evolution of waves with small steepness $ka = 0.05$ (see **Figure 6** left panel) is similar to the one obtained from the NLSE theory (**Figure 1** right panel) and in the laboratory experiment (**Figure 3**). In the simulations, the two solitary groups separated initially collide, form an extreme event and then separate again restoring their soliton shape. However, the strongly nonlinear simulation results in faster propagation of the wave groups and slightly quicker formation of the large wave (yellow dot). Interestingly, the amplitudes of the solitons after the separation are slightly different: the amplitude of the leading group is larger. The described features of the strongly nonlinear simulation become more pronounced when the steepness is larger than $ka = 0.1$ (**Figure 6**, middle panel).

Indeed, when the steepness further increases, $ka = 0.15$, the new recurrence effects are becoming more apparent (**Figure 6** right panel). Moreover, when the two soliton groups merge, they form a bound state similar to the bi-soliton described in [1, 29]. However, in contrast to the bi-soliton, the interaction here is asymmetric. The two subsequent extreme events are still large in amplitude in this type of recurrent dynamics. **Figure 7** shows the time evolution of the maxima of the wave elevation for the three simulations shown in **Figure 6**.

After a few beating cycles, the solitary groups finally decouple. At the end of the interaction process the leading soliton has a higher amplitude than the trailing one. After the three collisions, the envelope solitons are completely separated. The groups emerged after the third collision are not stationary. The leading soliton reveals the breathing dynamics (this can be seen in **Figure 7** for $T > 20$). The second solitary group spreads decaying in amplitude. Thus, the water wave dynamics of very steep degenerate solitons shows the survival of only one (leading) soliton. Its amplitude increases while the energy of the other group reduces.

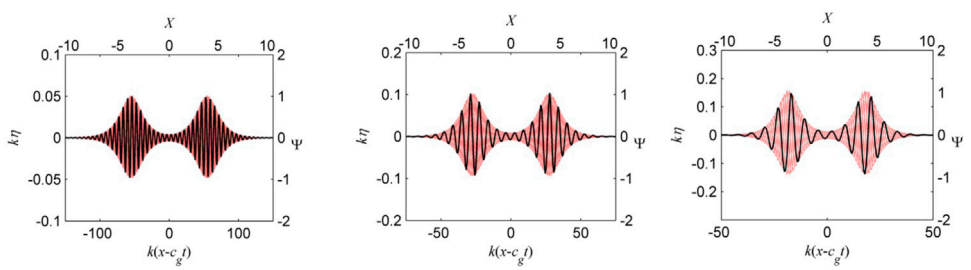

FIGURE 5 | Initial conditions for the numerical simulations of the degenerate soliton. **Left panel**: $ka = 0.05$. **Middle panel**: $ka = 0.1$. **Right panel**: $ka = 0.15$. The axes show the physical scaled coordinate and surface displacement (y-axis **left**), the standard NSLE coordinate $X = k(x - c_g t)$ (x-axis) and the complex amplitude $\Psi = \frac{k}{\sqrt{2}}\frac{\eta}{a}$ (y-axis **right**).

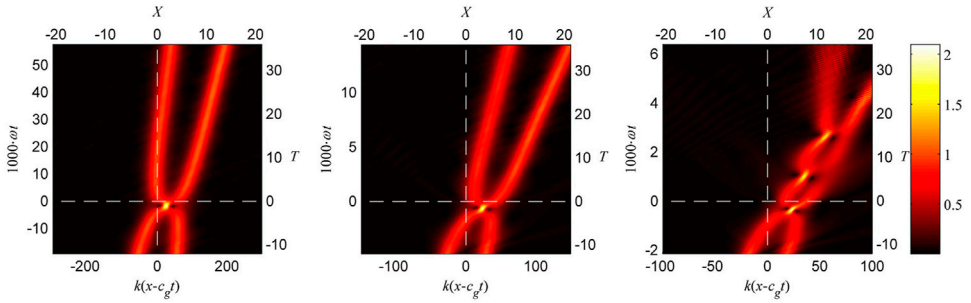

FIGURE 6 | Numerical simulations of the Euler equations of the degenerate soliton for different steepness values of the initial condition: $ka = 0.05$ on the **left panel**, $ka = 0.1$ on the **middle panel**, and $ka = 0.15$ on the **right panel**. The color-coded evolution of the wave envelope Ψ_{env} is shown.

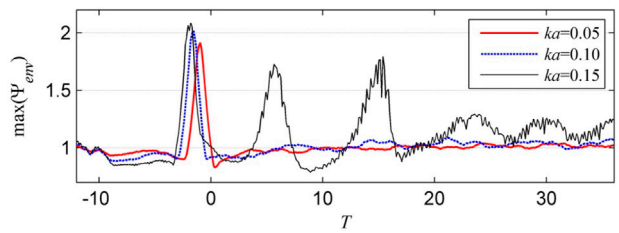

FIGURE 7 | Evolution of the wave maxima in the numerical simulations shown in **Figure 6**.

The extreme wave groups with highest amplitude which arise in the course of the wave dynamics are shown in **Figure 8**.

In contrast to the envelopes shown in **Figure 5**, these wave profiles possess strong back-to-front asymmetry. Some alteration of the central feature with maximal amplitude, when the wave steepness grows, may be noticed as well. This difference from the experimental observations is most-probably caused by dissipative effects [17]. The maximum water elevation is slightly smaller than anticipated by the NLSE solution for $\Psi = 2$ (marked by the dotted red lines in **Figure 8**) in the smaller wave steepness case, shown in **Figure 8** (left panel). However, this limit is slightly exceeded in the case of larger wave steepness shown in **Figure 8** right panel. The wave groups in **Figure 8** possess noticeable vertical asymmetry in the steeper cases (**Figure 8** middle and right panels) due to the bound (phase-locked) waves. While the wave crest exceeds the value of $\Psi = 2$ in the steepest wave case (**Figure 8** right panel), the deepest wave trough is well under the level of the NLSE solution. We emphasize that the wavelength of the carrier wave is assumed to be sufficiently large so that the capillary effects may be neglected while being small enough to satisfy the deep-water condition. We also report the evolution of the normalized and spatial Fourier transform of the three simulated evolutions, i.e., $ka = 0.05$, $ka = 0.1$ and $ka = 0.15$, in **Figure 9** to complete the picture.

The evolution of the Fourier modes confirms the characteristic evolution features of the degenerate two-soliton when the steepness is $ka = 0.05$, thus, being very small. This appears to be the case for $ka = 0.1$. On the other hand, deviations start to occur with the gradual increase of carrier wave steepness. For $ka = 0.15$ a noticeable beating, i.e. recurrent breathing process, can be noted.

CONCLUSION

We have reported for the first time the experimental observation of the *degenerate* soliton interaction in nonlinear physics. This coherent structure can be considered to be a PB on the zero-background limit. The experimental data and numerical simulations are both in excellent agreement for small and moderate carrier wave steepness values while deviations in form of beatings are observed for strongly nonlinear regimes. This fact confirms the accuracy of the

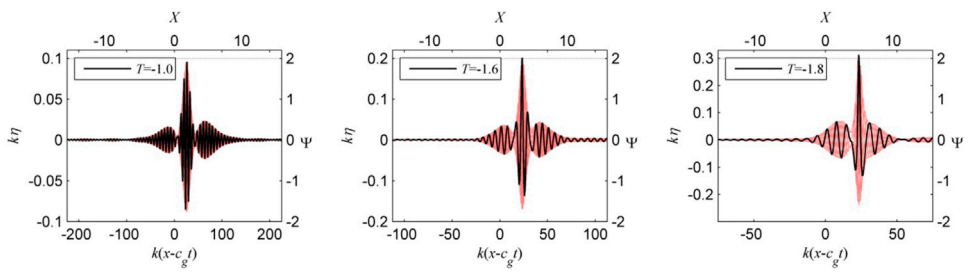

FIGURE 8 | Extreme events with highest amplitude during the evolution presented in **Figure 6**.

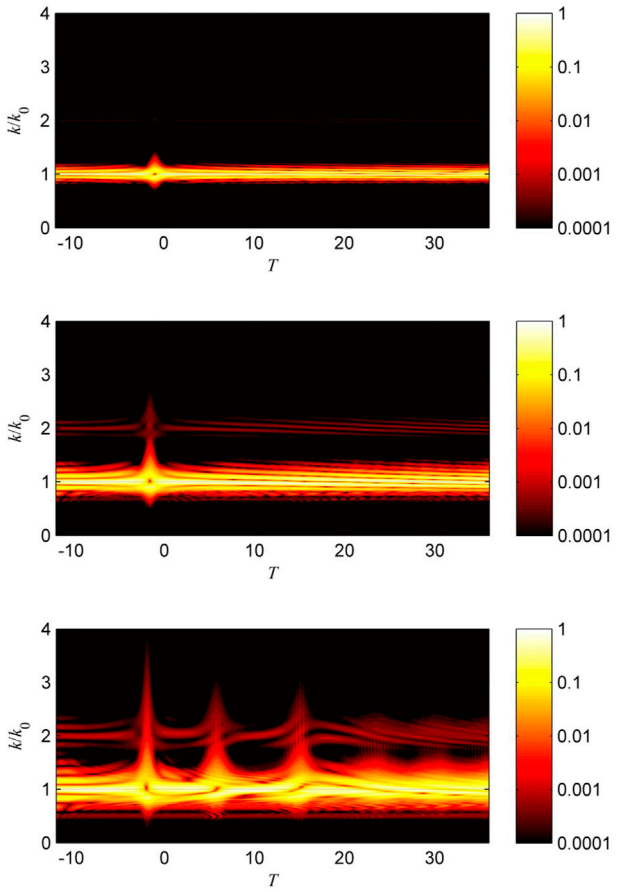

FIGURE 9 | Evolution of the spatial Fourier transform in the cases ka = 0.05 **(A)**, ka = 0.10 **(B)** and ka = 0.15 **(C)** as in **Figure 6**. The decimal logarithm of the normalized Fourier power is in the range from 1 down to 10^{-4}.

NLSE in the description of extreme wave events for a wide range of reasonable carrier wave parameters in nonlinear dispersive wave guides. Moreover, we anticipate motivated studies related to further exploration of such distinct degenerate soliton dynamics in optics and quantum physics. We also believe that the degenerate soliton solution may play a substantial role in the spontaneous formation [42, 43] identification of doubly-localized extreme wave events using data-driven methods [44]. Future studies will be devoted to higher-order soliton degeneracy beyond the collision of two solitons. This will in our opinion further improve our understanding of the role of integrable systems and nonlinear wave interaction in the formation of rogue waves.

DATA AVAILABILITY STATEMENT

The raw data supporting the conclusion of this article will be made available by authors, upon reasonable request.

AUTHOR CONTRIBUTIONS

AC conducted the experiments in the water wave flumes. AS performed the HOSM simulations. All Authors designed the experiments, analysed the data and interpreted results, and took part in writing the manuscript.

FUNDING

AS was partially supported by Laboratory of Dynamical Systems and Applications NRU HSE, of the Ministry of Science and Higher Education of the Russian Federation Grant 075-15-2019-1931; and by the Grant 21-55-15008 of the Russian Foundation for Basic Research. BK and JD acknowledge support from the French National Research Agency (EUR EIPHI ANR-17-EURE-0002 and PIA2/ISITE-BFC, ANR-15-IDEX-03, "Breathing Light" and "Nextlight" projects, and ANR-20-CE30-0004 "OPTIMAL" project). FD acknowledges support from the European Research Council (ERC-2018-AdG 833125 HIGHWAVE).

ACKNOWLEDGMENTS

AC acknowledges Zachary Benitez and Theo Gresley-Daines for technical support. AS acknowledges support from the International Visitor Program of The University of Sydney.

REFERENCES

1. Peregrine DH. Water Waves, Nonlinear Schrödinger Equations and Their Solutions. *J Aust Math Soc Ser B, Appl. Math* (1983) 25:16–43. doi:10.1017/s0334270000003891
2. Shrira VI, and Geogjaev VV. What Makes the Peregrine Soliton So Special as a Prototype of Freak Waves? *J Eng Math* (2010) 67:11–22. doi:10.1007/s10665-009-9347-2
3. Dudley JM, Genty G, Mussot A, Chabchoub A, and Dias F. Rogue Waves and Analogies in Optics and Oceanography. *Nat Rev Phys* (2019) 1:675–89. doi:10.1038/s42254-019-0100-0
4. Kibler B, Fatome J, Finot C, Millot G, Dias F, Genty G, et al. The Peregrine Soliton in Nonlinear Fibre Optics. *Nat Phys* (2010) 6:790–5. doi:10.1038/nphys1740
5. Chabchoub A, Hoffmann NP, and Akhmediev N. Rogue Wave Observation in a Water Wave Tank. *Phys Rev Lett* (2011) 106:204502. doi:10.1103/physrevlett.106.204502
6. Bailung H, Sharma SK, and Nakamura Y. Observation of Peregrine Solitons in a Multicomponent Plasma with Negative Ions. *Phys Rev Lett* (2011) 107:255005. doi:10.1103/physrevlett.107.255005
7. Chabchoub A, Hoffmann N, Onorato M, and Akhmediev N. Super Rogue Waves: Observation of a Higher-Order Breather in Water Waves. *Phys Rev X* (2012) 2:011015. doi:10.1103/physrevx.2.011015
8. Chabchoub A, and Akhmediev N. Observation of Rogue Wave Triplets in Water Waves. *Phys Lett A* (2013) 377:2590–3. doi:10.1016/j.physleta.2013.07.027
9. Klein M, Clauss GF, Rajendran S, Guedes Soares C, and Onorato M. Peregrine Breathers as Design Waves for Wave-Structure Interaction. *Ocean Eng* (2016) 128:199–212. doi:10.1016/j.oceaneng.2016.09.042

10. Chabchoub A. Tracking Breather Dynamics in Irregular Sea State Conditions. *Phys Rev Lett* (2016) 117:144103. doi:10.1103/physrevlett.117.144103
11. Randoux S, Suret P, Chabchoub A, Kibler B, and El G. Nonlinear Spectral Analysis of Peregrine Solitons Observed in Optics and in Hydrodynamic Experiments. *Phys Rev E* (2018) 98:022219. doi:10.1103/physreve.98.022219
12. Xu G, Hammani K, Chabchoub A, Dudley JM, Kibler B, and Finot C. Phase Evolution of Peregrine-like Breathers in Optics and Hydrodynamics. *Phys Rev E* (2019) 99:012207. doi:10.1103/physreve.99.012207
13. Chabchoub A, Mozumi K, Hoffmann N, Babanin AV, Toffoli A, Steer JN, et al. Directional Soliton and Breather Beams. *Proc Natl Acad Sci USA* (2019) 116:9759–63. doi:10.1073/pnas.1821970116
14. Michel G, Bonnefoy F, Ducrozet G, Prabhudesai G, Cazaubiel A, Copie F, et al. Emergence of Peregrine Solitons in Integrable Turbulence of Deep Water Gravity Waves. *Phys Rev Fluids* (2020) 5:082801. doi:10.1103/physrevfluids.5.082801
15. Kedziora DJ, Ankiewicz A, and Akhmediev N. Rogue Waves and Solitons on a Cnoidal Background. *Eur Phys J Spec Top* (2014) 223:43–62. doi:10.1140/epjst/e2014-02083-4
16. Dysthe KB, and Trulsen K. Note on Breather Type Solutions of the NLS as Models for Freak-Waves. *Physica Scripta* (1999) T82:48. doi:10.1238/physica.topical.082a00048
17. Magnani M, Onorato M, Gunn D, Rudman M, Kibler B, Akhmediev N, et al. Experimental Realization of Periodic Deep-Water Wave Envelopes with and without Dissipation. *Water Waves* (2019) 2:113–22. doi:10.1007/s42286-019-00015-8
18. Chen J, and Pelinovsky DE. Rogue Periodic Waves of the Focusing Nonlinear Schrödinger Equation. *Proc R Soc A* (2018) 474:20170814. doi:10.1098/rspa.2017.0814
19. Akhmediev N, and Ankiewicz A. Spatial Soliton X-Junctions and Couplers. *Opt Commun* (1993) 100:186–92. doi:10.1016/0030-4018(93)90577-r
20. Zakharov VE. Stability of Periodic Waves of Finite Amplitude on the Surface of a Deep Fluid. *J Appl Mech Tech Phys* (1968) 9:190–4. doi:10.1007/bf00913182
21. Zakharov VE, and Shabat AB. Exact Theory of Two-Dimensional Self-Focusing and One-Dimensional Self-Modulation of Waves in Nonlinear media. *Sov Phys JETP* (1972) 34:62–9.
22. Yuen HC, and Lake BM. Nonlinear Dynamics of Deep-Water Gravity Waves. *Adv Appl Mech* (1982) 22:67–229. doi:10.1016/s0065-2156(08)70066-8
23. Slunyaev A, Clauss GF, Klein M, and Onorato M. Simulations and Experiments of Short Intense Envelope Solitons of Surface Water Waves. *Phys Fluids* (2013) 25:067105. doi:10.1063/1.4811493
24. Slunyaev A, Klein M, and Clauss GF. Laboratory and Numerical Study of Intense Envelope Solitons of Water Waves: Generation, Reflection from a wall and Collisions. *Phys Fluids* (2017) 29:047103. doi:10.1063/1.4979524
25. Ablowitz MJ, Kaup DJ, Newell AC, and Segur H. The Inverse Scattering Transform-Fourier Analysis for Nonlinear Problems. *Stud Appl Math* (1974) 53:249–315. doi:10.1002/sapm1974534249
26. Osborne AR. Nonlinear Ocean Wave and the Inverse Scattering Transform. *Scattering* (2010) 637–66. Academic Press. doi:10.1016/b978-012613760-6/50033-4
27. Akhmediev N, and Ankiewicz A. *Solitons: Nonlinear Pulses and Beams*. Springer (1997).
28. Zakharov VE, and Gelash AA. Nonlinear Stage of Modulation Instability. *Phys Rev Lett* (2013) 111:054101. doi:10.1103/physrevlett.111.054101
29. Satsuma J, and Yajima N. B. Initial Value Problems of One-Dimensional Self-Modulation of Nonlinear Waves in Dispersive media. *Prog Theor Phys Suppl* (1974) 55:284–306. doi:10.1143/ptps.55.284
30. Dudley JM, and Genty G. Supercontinuum Light. *Phys Today* (2013) 66:29–34. doi:10.1063/pt.3.2045
31. Chabchoub A, Hoffmann N, Onorato M, Genty G, Dudley JM, and Akhmediev N. Hydrodynamic Supercontinuum. *Phys Rev Lett* (2013) 111:054104. doi:10.1103/physrevlett.111.054104
32. Tikan A, Billet C, El G, Tovbis A, Bertola M, Sylvestre T, et al. Universality of the Peregrine Soliton in the Focusing Dynamics of the Cubic Nonlinear Schrödinger Equation. *Phys Rev Lett* (2017) 119:033901. doi:10.1103/physrevlett.119.033901
33. Xu G, Chabchoub A, Pelinovsky DE, and Kibler B. Observation of Modulation Instability and Rogue Breathers on Stationary Periodic Waves. *Phys Rev Res* (2020) 2:033528. doi:10.1103/physrevresearch.2.033528
34. Chabchoub A, and Grimshaw R. The Hydrodynamic Nonlinear Schrödinger Equation: Space and Time. *Fluids* (2016) 1:23. doi:10.3390/fluids1030023
35. Gomel A, Chabchoub A, Brunetti M, Trillo S, Kasparian J, and Armaroli A. Stabilization of Extreme Wave Events by Phase Space Manipulation. *Phys Rev Lett* (2021) 126:174501. doi:10.1103/physrevlett.126.174501
36. Dysthe KB. Note on a Modification to the Nonlinear Schrödinger Equation for Application to Deep Water Waves. *Proc R Soc Lond A. Math Phys Sci* (1979) 369:105–14. doi:10.1098/rspa.1979.0154
37. Slunyaev A, Pelinovsky E, Sergeeva A, Chabchoub A, Hoffmann N, Onorato M, et al. Super-rogue Waves in Simulations Based on Weakly Nonlinear and Fully Nonlinear Hydrodynamic Equations. *Phys Rev E* (2013) 88:012909. doi:10.1103/physreve.88.012909
38. Shemer L, and Alperovich L. Peregrine Breather Revisited. *Phys Fluids* (2013) 25:051701. doi:10.1063/1.4807055
39. Waseda T, Fujimoto W, and Chabchoub A. On the Asymmetric Spectral Broadening of a Hydrodynamic Modulated Wave Train in the Optical Regime. *Fluids* (2019) 4:84. doi:10.3390/fluids4020084
40. West BJ, Brueckner KA, Janda RS, Milder DM, and Milton RL. A New Numerical Method for Surface Hydrodynamics. *J Geophys Res* (1987) 92:11803–24. doi:10.1029/jc092ic11p11803
41. Slunyaev A, Pelinovsky E, and Guedes Soares C. Reconstruction of Extreme Events through Numerical Simulations. *J Offshore Mech Arctic Eng* (2014) 136:011302. doi:10.1115/1.4025545
42. Suret P, El Koussaifi R, Tikan A, Evain C, Randoux S, Szwaj C, et al. Single-shot Observation of Optical Rogue Waves in Integrable Turbulence Using Time Microscopy. *Nat Commun* (2016) 7:1–8. doi:10.1038/ncomms13136
43. Närhi M, Wetzel B, Billet C, Toenger S, Sylvestre T, Merolla JM, et al. Real-time Measurements of Spontaneous Breathers and Rogue Wave Events in Optical Fibre Modulation Instability. *Nat Commun* (2016) 7:1–9. doi:10.1038/ncomms13675
44. Salmela L, Tsipinakis N, Foi A, Billet C, Dudley JM, and Genty G. Predicting Ultrafast Nonlinear Dynamics in Fibre Optics with a Recurrent Neural Network. *Nat Machine Intelligence* (2021) 3:344–54. doi:10.1038/s42256-021-00297-z

Conflict of Interest: The authors declare that the research was conducted in the absence of any commercial or financial relationships that could be construed as a potential conflict of interest.

frontiers in Physics

REVIEW
published: 27 September 2021
doi: 10.3389/fphy.2021.599767

Peregrine Soliton as a Limiting Behavior of the Kuznetsov-Ma and Akhmediev Breathers

Natanael Karjanto *

Department of Mathematics, University College, Natural Science Campus, Sungkyunkwan University, Suwon, South Korea

This article discusses a limiting behavior of breather solutions of the focusing nonlinear Schrödinger equation. These breathers belong to the family of solitons on a non-vanishing and constant background, where the continuous-wave envelope serves as a pedestal. The rational Peregrine soliton acts as a limiting behavior of the other two breather solitons, i.e., the Kuznetsov-Ma breather and Akhmediev soliton. Albeit with a phase shift, the latter becomes a nonlinear extension of the homoclinic orbit waveform corresponding to an unstable mode in the modulational instability phenomenon. All breathers are prototypes for rogue waves in nonlinear and dispersive media. We present a rigorous proof using the ϵ-δ argument and show the corresponding visualization for this limiting behavior.

Keywords: nonlinear Schrödinger equation, Kuznetsov-Ma breather, Akhmediev soliton, Peregrine soliton, modulational instability, rogue waves, homoclinic orbit, limiting behavior

OPEN ACCESS

Edited by:
Bertrand Kibler, UMR6303 Laboratoire Interdisciplinaire Carnot de Bourgogne (ICB), France

Reviewed by:
Gang Xu, The University of Auckland, New Zealand
Efstathios Charalampidis, California Polytechnic State University, United States

***Correspondence:**
Natanael Karjanto
natanael@skku.edu

Specialty section:
This article was submitted to Mathematical and Statistical Physics, a section of the journal Frontiers in Physics

Received: *28 August 2020*
Accepted: *18 January 2021*
Published: *27 September 2021*

Citation:
Karjanto N (2021) Peregrine Soliton as a Limiting Behavior of the Kuznetsov-Ma and Akhmediev Breathers. Front. Phys. 9:599767. doi: 10.3389/fphy.2021.599767

1 INTRODUCTION

Although the study of wave phenomena traces its history back to the time of Pythagoras, research on nonlinear and rogue waves has attracted great scientific interest recently, both theoretically and experimentally. In particular, the focusing nonlinear Schrödinger (NLS) equation and its exact analytical solutions that belong to the family of soliton on constant background have been adopted as models and prototypes for rogue wave phenomena. The purpose of this article is to provide an overview of the relationship between these soliton solutions in this context. It also fills the gap in the details of limiting behavior. While the connection is well-known, the rigorous proof seems to be absent, and the visualizations found in the literature are incomplete. We will present this connection of the limiting behavior both analytically and visually. This introduction section covers a brief history of the NLS equation, exact solutions of the NLS equation, and a literature review on rogue waves.

1.1 A Brief Historical Background of the Nonlinear Schrödinger Equation

The NLS equation is a nonlinear evolution equation that models slowly varying envelope dynamics of a weakly nonlinear quasi-monochromatic wave packet in dispersive media. The model has an infinite set of conservation laws and belongs to a completely integrable system of nonlinear partial differential equations. It has a wide range of applications in various physical settings, such as surface water waves, nonlinear optics, plasma physics, superconductivity, and Bose-Einstein condensates (BEC) [1–8].

Among early derivations of the NLS equation were found in nonlinear optics [9, 10], plasma physics [11–15], and hydrodynamics [16–18]. In BEC, the NLS equation with the non-zero potential term is known as the Gross-Pitaevskii equation [19, 20]. In superconductivity, the time-independent

NLS equation resembles some similarities with a simplified $(1+1)$-D form of the Ginzburg-Landau equation [21]. A further overview and extensive discussion of the NLS equation can be found in [7, 22–26].

1.2 Exact Solutions of the Nonlinear Schrödinger Equation

There are various techniques to derive analytical solutions of the NLS equation, among others, are the phase-amplitude algebraic ansatz [27–30], the Hirota method [31–34], nonlinear Fourier transform of inverse scattering transform (IST) [6, 35–40], symmetry reduction methods [41], variational formulation and displaced phase-amplitude equations [42–44]. Another derivation using IST with asymmetric boundary conditions is given in [45].

Throughout this article, we adopt the following $(1+1)$D, focusing-type of the NLS equation in a standard form:

$$iq_t + q_{xx} + 2|q|^2 q = 0, \qquad q(x,t) \in C. \tag{1}$$

Usually, the variables x and t denote the space and time variables, respectively. The simplest-solution is called the "plane-wave" or "continuous-wave" solution: $q(x,t) = q_0(t) = e^{2it}$. Another simple solution with a vanishing background is known as the "bright soliton" or "one-soliton solution", given as follows:

$$q(x,t) = q_S(x,t) = a\,\mathrm{sech}\,(ax - 2abt + \theta_0)e^{i\left(bx + \left(a^2 - b^2\right)t + \phi_0\right)}, \quad a, b, \theta_0, \phi_0 \in \mathbb{R}. \tag{2}$$

We focus our discussion on the family of exact solutions with constant and non-vanishing background, also called "breather soliton solutions" [46]. There are three types of breather, and all of them are considered as weakly nonlinear prototypes for freak waves. Other solutions of the NLS equation include cnoidal wave envelopes that can be expressed in terms of the Jacobi elliptic functions and can be derived using the Hirota bilinear transformation, theta functions, or with some clever algebraic ansatz [30, 47].

In this subsection, the coverage follows the historical order of the time when the breathers were found. Furthermore, the term "breather" and "soliton" can be used interchangeably in this article, and they can also appear as a single term "breather soliton". All of them refer to the same object, i.e., the exact analytical solutions of the NLS equation with a non-vanishing, constant pedestal, or background of continuous-wave solution.

1.2.1 The Kuznetsov-Ma Breather

The first found solution is called the "Kuznetsov-Ma breather", where Kuznetsov derived it for the first time in the 1970s [48]. The original Russian version of his paper was published as a preprint in 1976 by the Institute of Automation and Electrometry of the Siberian Branch of the USSR (now Russian) Academy of Sciences in Novosibirsk. This preprint was then reproduced in English and appeared in the Proceedings of the 13th International Conference on Phenomena in ionized Gases and Plasma, held in East Berlin, German Democratic Republic, on 12–17 September 1977 [49].

Although some authors stated that Kawata and Inoue, as well as Ma, also derived this solution independently, understanding the history behind its development might change our perspective [50, 51]. Between 1976 and 1977, Evgenii A. Kuznetsov met Tutomu Kawata (also spelled Tsutomu, 川田 勉) many times because the latter was a postdoctoral researcher in the Landau Institute for Theoretical Physics in Chernogolovka, near Moscow, under the mentorship of Professor Vladimir E. Zakharov. Kuznetsov personally gave Kawata his preprint on the soliton solution of the NLS equation. Furthermore, although Yan-Chow Ma has never really met with Kuznetsov, Ma was surely aware of Kuznetsov's paper. In his work [51], Ma has cited another Kuznetsov's paper that was written together with Alexander V. Mikhailov on the stability of stationary waves using the Korteweg-de Vries (KdV) equation [49, 52].

Although the term "Kuznetsov-Ma soliton" has been introduced earlier [53], we will adopt and use the terminology "Kuznetsov-Ma breather" throughout this article. When the breather dynamics were observed experimentally for the first time in optical fibers by Kibler and collaborators, this term is getting popular since then [54]. We denote it as q_{M}, and it is explicitly given by

$$q(x,t) = q_{\mathrm{M}}(x,t) = e^{2it}\left(\frac{\mu^3\cos(\rho t) + i\mu\rho\sin(\rho t)}{2\mu\cos(\rho t) - \rho\cosh(\mu x)} + 1\right), \tag{3}$$

where $\rho = \mu\sqrt{4+\mu^2}$. The Kuznetsov-Ma breather does not represent a traveling wave. It is localized in the spatial variable x and periodic in the temporal variable t, and hence some authors also called it as the "temporal periodic breather" [55].

A minor typographical error found in Kawata and Inoue's paper [50] has been corrected by Gagnon [56]. Kawata and Inoue [50], as well as Ma [51], derived the Kuznetsov-Ma breather solution using the IST for finite boundary conditions at $x \to \pm\infty$. The derivation using a direct method of Bäcklund transformation can be found in [57, 58], where the former analyzed solitary waves in the context of an optical bistable ring cavity.

Defining the amplitude amplification factor (AF) as the quotient of the maximum breather amplitude and the value of its background [43], we obtain that the amplitude amplification for the Kuznetsov-Ma breather is always larger than the factor of three, and it is explicitly given by

$$\mathrm{AF}_{\mathrm{M}}(\mu) = 1 + \sqrt{4+\mu^2}, \quad \mu > 0. \tag{4}$$

The function is bounded below and is increasing as the parameter μ also increases. The plot of this AF can be found in [43, 44], and different expressions of the AF for this breather also appear in [59–62].

The Kuznetsov-Ma breather finds applications as a rogue wave prototype in nonlinear optics [30, 54, 63] and deep-water gravity waves [38, 39, 61, 64]. A numerical comparison of the Kuznetsov-Ma breather indicated that a qualitative agreement was reached in the central part of the corresponding wave packet and on the real

face of the modulation [59]. The stability analysis of the Kuznetsov-Ma breather using a perturbation theory based on the IST verified that although the soliton is rather robust with respect to dispersive perturbations, damping terms strongly influence its dynamics [65].

The dynamics of the Kuznetsov-Ma breather in a microfabricated optomechanical array showed an excellent agreement between theory and numerical calculations [66]. The spectral stability analysis of this breather has been considered using the Floquet theory [67]. The mechanism of the Kuznetsov-Ma breather has been discussed and two distinctive mechanisms are paramount: modulational instability and the interference effects between the continuous-wave background and bright soliton [68]. New scenarios of rogue wave formation for artificially prepared initial conditions using the Kuznetsov-Ma and superregular breathers in small localized condensate perturbations are demonstrated numerically by solving the Zakharov-Shabat eigenvalue problem [69].

A higher-order Kuznetsov-Ma breather can be derived using the Hirota method and utilized in studying soliton propagation with an influence of small plane-wave background [70, 71]; or using the bilinear method [72].

1.2.2 The Akhmediev Soliton

The second one is called the Akhmediev-Eleonskiĭ-Kulagin breather and was found in the 1980s [27–29]. In short, we simply call it the "Akhmediev soliton" and denote it as q_{A}. This breather is localized in the temporal variable t and is periodic in the spatial variable x, and it can be written explicitly as follows:

$$q(x,t) = q_{\mathrm{A}}(x,t) = e^{2it}\left(\frac{\nu^3\cosh(\sigma t) + i\nu\sigma\sinh(\sigma t)}{2\nu\cosh(\sigma t) - \sigma\cos(\nu x)} - 1\right). \quad (5)$$

Here, the parameter ν, $0 \le \nu < 2$ denotes a modulation frequency (or wavenumber) and $\sigma(\nu) = \nu\sqrt{4-\nu^2}$ is the modulation growth rate. The colleagues from nonlinear optics prefer calling this soliton "instanton" [73, 74] instead of "breather" since it breathes only once [75]. Other names for this solution include "modulational instability" [30], "homoclinic orbit" [34, 76], "spatial periodic breather" [55], and "rogue wave solution" [39].

The amplitude amplification for the Akhmediev soliton is at most of the factor of three, and it is explicitly given by

$$\mathrm{AF}_{\mathrm{A}}(\nu) = 1 + \sqrt{4-\nu^2}, \quad 0 < \nu < 2. \quad (6)$$

This function is bounded above and below, $1 < \mathrm{AF}_{\mathrm{A}} < 3$, and is decreasing for an increasing value of the modulation parameter ν. Although the maximum growth rate occurs for $\nu = \sqrt{2}$, the maximum AF occurs when $\nu \to 0$, when the Akhmediev breather becomes the Peregrine soliton. To the best of our knowledge, this expression was introduced by Onorato et al. in their study on freak wave generation in random ocean waves where this AF depends on the wave steepness and number of waves under the envelope [77]. The plot for this AF can be found in [43, 78, 79]. Some variations in the AF expression for this soliton also appear in [59–62, 80, 81].

The Akhmediev soliton is rather well-known due to its characteristics being a nonlinear extension of linear modulational instability. This instability is also known as sideband (or Bespalov-Talanov) instability in nonlinear optics [82–84], or Benjamin-Feir instability in water waves [17, 85]. Some authors studied the modulational instability in plasma physics [11, 86–88] and in BEC [89–94]. Modulational instability is defined as the temporal growth of the continuous-wave NLS solution due to a small, side-band modulation, in a monochromatic wave train. A geometric condition for wave instability in deep water waves is given in [95] and for a historical review of modulational instability, see [96].

It has been shown numerically and experimentally that the modulated unstable wave trains grow to a maximum limit and then subside. In the spectral domain, the wave energy is transferred from the central frequency to its sidebands during the wave propagation for a certain period, and then it is recollected back to the primary frequency mode [97–101]. It turns out that the long-time evolution of these unstable wave trains leads to a sequence of modulation and demodulation cycles, known as the Fermi-Pasta-Ulam-Tsingou (FPUT) recurrence phenomenon [102, 103]. Although the FPUT recurrence using the NLS model has been observed experimentally in surface gravity waves in the late 1970s [98], it took more than 2 decades for the phenomenon to be successfully recovered in nonlinear optics [104].

Since the modulational instability extends nonlinearly to the Akhmediev soliton, it is no surprise that the former is considered as a possible mechanism for the generation of rogue waves while the latter acts as one prototype [105–107]. For wave trains with amplitude and phase modulation, there is a competition between the nonlinearity and dispersive factors. After the modulational instability occurs, the growth predicted by linear theory is exponential, and the nonlinear effect in the form of the Akhmediev soliton takes over before the wave trains return to the stage similar to the initial profiles with a phase-shift difference [64, 108]. On the other hand, Biondini and Fagerstrom argued that the major cause of modulational instability in the NLS equation is not the breather soliton solutions per se, but the existence of perturbations where discrete spectra are absence [109].

Experimental attempts on deterministic rogue wave generation using the Akhmediev solitons suggested that the symmetric structure is not preserved and the wave spectrum experiences frequency downshift even though wavefront dislocation and phase singularity are visible [43, 110–114]. A numerical calculation of rogue wave composition can be described in the form of the collision of Akhmediev breathers [115]. Another comparison of the Akhmediev breathers with the North Sea Draupner New Year and the Sea of Japan Yura wave signals also show some qualitative agreement [116]. The characteristics of the Akhmediev solitons have also been observed experimentally in nonlinear optics [117].

A theoretical, numerical, and experimental report of higher-order modulational instability indicates that a relatively low-frequency modulation on a plane-wave induces pulse splitting

at different phases of evolution [118]. Second-order breathers composed of nonlinear combinations of the Kuznetsov-Ma breather and Akhmediev soliton reveal the dependence of the wave envelope on the degenerate eigenvalues and differential shifts [119]. Similar higher-order Akhmediev solitons visualized in [118, 119] have been featured earlier in [43, 120] and similar illustrations can also be found in [60, 121–127].

1.2.3 The Peregrine Soliton

The third one is called the "Peregrine soliton", also known as the "rational solution" [128]. This soliton is localized in both spatial and temporal variables (x, t) and is written as follows (denoted as q_{P}):

$$q(x,t) = q_{\mathrm{P}}(x,t) = e^{2it}\left(\frac{4(1+4it)}{1+16t^2+4x^2} - 1\right). \tag{7}$$

This solution is neither a traveling wave nor contains free parameters. Johnson called it a "rational-cum-oscillatory solution" [129]. Others referred to it as the "isolated Ma soliton" [130], an "explode-decay solitary wave" [131], the "rational growing-and-decaying mode" [71], the "algebraic breather" [132], or the "fundamental rogue wave solution" [124].

The amplitude amplification for the Peregrine soliton is exactly of factor three, and this can be obtained by taking the limit of the parameters toward zero in the previous two breathers:

$$\mathrm{AF_P} = \lim_{\mu \to 0} \mathrm{AF_M}(\mu) = 3 = \lim_{\nu \to 0} \mathrm{AF_A}(\nu). \tag{8}$$

Although the other two breather solitons are also proposed as rogue wave prototypes, some authors argued that the Peregrine soliton is the most likely freak wave event due to its appearance from nowhere and disappearance without a trace [79] as well as its closeness to all initial supercritical humps of small uniform envelope amplitude [133]. Some numerical and experimental studies may support this reasoning.

Henderson et al. studied numerically unsteady surface gravity wave modulations by comparing the fully nonlinear and NLS equations [130]. For steep-waves, their computations produced striking similarities with the Peregrine soliton. On the other hand, Voronovich et al. confirmed numerically that the bottom friction effect, even when it is small in comparison to the nonlinear term, could hamper the formation of a breather freak wave at the nonlinear stage of instability [134]. Investigations on linear stability demonstrated that the Peregrine soliton is unstable against all standard perturbations, where the analytical study is supported by numerical evidence [135–138].

An important breakthrough in the study of rogue waves is the observation of the Peregrine soliton in nonlinear media. In nonlinear optics, the existence of strongly localized temporal and spatial peaks on a non-vanishing background, which indicates near-ideal Peregrine soliton characteristics, was successfully implemented for the first time in optical fiber generating femtosecond pulses in 2010 [139]. Not long after that, the Peregrine soliton was also observed experimentally for the first time in a water wave tank [140]. A comparison between the predictions from the theoretical model and the measurement results exhibits an excellent qualitative agreement in terms of wave signal pattern, its amplification factor, and its symmetric structure. Another successful experimental observation of the Peregrine solitons is reported in ion-acoustic waves of a multicomponent plasma with negative ions when the density of negative ions is equal to the critical value [141].

A sequence of related experimental studies using the Peregrine soliton demonstrated reasonably good qualitative agreement with the theoretical prediction. Some discrepancies occur in the modulational gradients, spatiotemporal symmetries, and for larger steepness values [142], as well as the frequency downshift [143]. Interestingly, Chabchoub et al. shown further experimentally that the dynamics of the Peregrine soliton and its spectrum characteristics persist even in the presence of wind forcing with high velocity [144]. By selecting a target location and determining an initial steepness, an experiment using the Peregrine soliton of wave interaction with floating bodies during extreme ocean condition has also been successfully implemented [145].

The Peregrine soliton also finds applications in the evolution of the intrathermocline eddies, also known as the oceanic lenses [146]. It appeared as a special case of stationary limit in the solutions of the spinor BEC model [147], and it was observed experimentally emerging from the stochastic background in deep-water surface gravity waves [148].

Nonlinear spectral analysis using the finite gap theory showed that the spectral portraits of the Peregrine soliton represent a degenerate genus two of the NLS equation solution [149]. Higher-order Peregrine solitons in terms of quasi-rational functions are derived in [150]. Higher-order Peregrine solitons up to the fourth-order using a modified Darboux transformation has been presented with applications in rogue waves in the deep ocean and high-intensity rogue light wave pulses in optical fibers [151]. Super rogue waves modeled with higher-order Peregrine soliton with an amplitude amplification factor of five times the background value are observed experimentally in a water-wave tank [122].

1.3 A Literature Review on Rogue Waves

There are various excellent reviews on rogue wave phenomena based on the NLS equation as a mathematical model and its corresponding breather solitons. Onorato et al. covered rogue waves in several physical contexts including surface gravity waves, photonic crystal fibers, laser fiber systems, and 2D spatiotemporal systems [60]. Dudley et al. reviewed breathers and rogue waves in optical fiber systems with an emphasis on the underlying physical processes that drive the appearance of extreme optical structures [125]. They reasoned that the mechanisms driving rogue wave behavior depend very much on the system. Residori et al. presented physical concepts and mathematical tools for rogue wave description [62]. They highlighted the most common features of the phenomenon include large deviations of wave amplitude from the Gaussian statistics and large-scale symmetry breaking. Chen et al. discussed rogue waves in scalar, vector, and multidimensional systems [152] while Malomed and Mihalache surveyed some theoretical and experimental studies on nonlinear waves in optical and matter-wave media [153].

Rogue waves come from and are closely related to modulational instability with resonance perturbation on continuous background [154]. A comparison of breather solutions of the NLS equation with emergent peaks in noise-seeded modulational instability indicated that the latter clustered closely around the analytical predictions [155]. "Superregular breathers" is the term coined indicating creation and annihilation dynamics of modulational instability, and the evidence of the broadest group of these superregular breathers in hydrodynamics and optics has been reported [156]. An interaction between breather and higher-order rogue waves in a nonlinear optical fiber is characterized by a trajectory of localized troughs and crests [157].

Breather soliton solutions find several applications, among others in beam-plasma interactions [158], in the transmission line analog of nonlinear left-handed metamaterials [159], in a nonlinear model describing an electron moving along the axis of deformable helical molecules [160], and in the mechanisms underlying the formation and real-time prediction of extreme events [161]. Additionally, optical rogue waves also successfully simulated in the presence of nonlinear self-image phenomenon in the near-field diffraction of plane waves from lightwave grating, known as the Talbot effect [162].

Since the definitions of "rogue waves" and "extreme events" are varied, a roadmap for unifying different perspectives could stimulate further discussion [163]. Theoretical, numerical, and experimental evidence of the dissipation effect on phase-shifted FPUT dynamics in a super wave tank, which is related to modulational instability, can be described by the breather solutions of the NLS equation [164]. Since the behavior of a large class of perturbations characterized by a continuous spectrum is described by the identical asymptotic state, it turns out that the asymptotic stage of modulational instability is universal [165]. Surprisingly, the long-time asymptotic behavior of modulationally unstable media is composed of an ensemble of classical soliton solutions of the NLS equation instead of the breather-type solutions [166].

General N-solitonic solutions of the NLS equation in the presence of a condensate derived using the dressing method describe the nonlinear stage of the modulational instability of the condensate [167]. Rogue waves on a periodic background in the form of cnoidal functions that exhibit modulational instability not only generalize the Peregrine's soliton but also potentially stimulate further discussion [168]. Recently, both theoretical description and experimental observation of the nonlinear mutual interactions between a pair of copropagative breathers are presented and it is observed that the bound state of breathers exhibits a behavior similar to a molecule with quasiperiodic oscillatory dynamics [169].

The paper will be presented as follows. After this introduction, **Section 2** discusses rigorous proof for the limiting behavior of the breather wave solutions using the ϵ-δ argument. The limiting behavior will continue in **Section 3**, where we cover it from the visual viewpoint. We present the corresponding contour plots for various values of parameters and the parameterization sketches of the non-rapid oscillating complex-valued breather amplitudes. Finally, **Section 4** concludes our discussion and provide remarks for potential future research.

2 LIMITING BEHAVIOR

This section provides rigorous proof of the limiting behavior of breather wave solutions using the ϵ-δ argument. We have the following theorem:

Theorem 1. The Peregrine soliton is a limiting case for both the Kuznetsov-Ma breather and Akhmediev soliton:

$$\lim_{\mu\to 0} q_{\mathrm{M}}(x,t) = q_{\mathrm{P}}(x,t) = \lim_{\nu\to 0} q_{\mathrm{A}}(x,t). \tag{9}$$

We split the proof into four parts, and each limit consists of two parts corresponding to the real and imaginary parts of the solitons.

Proof. The following shows that the limit for the real parts of the Kuznetsov-Ma breather and Peregrine soliton is correct, i.e.,

$$\lim_{\nu\to 0} \mathrm{Re}\{q_{\mathrm{M}}(x,t)\} = \mathrm{Re}\{q_{\mathrm{P}}(x,t)\}.$$

For each $\varepsilon > 0$, there exists $\delta = \sqrt{(\varepsilon+2)^2 - 4} > 0$ such that if $0 < \mu < \delta$, then $\left|\mathrm{Re}\{q_{\mathrm{M}}\} - \mathrm{Re}\{q_{\mathrm{P}}\}\right| < \varepsilon$. We know that since

$$\frac{\cosh\mu(x-x_0)}{\cos\rho(t-t_0)} \geq 1 \quad \text{for all } (x,t) \in \mathbb{R}^2,$$

it then implies

$$\rho\frac{\cosh\mu(x-x_0)}{\cos\rho(t-t_0)} - 2\mu \geq \rho - 2\mu,$$

It follows that

$$\begin{aligned}
\left|\mathrm{Re}\{q_{\mathrm{M}}\} - \mathrm{Re}\{q_{\mathrm{P}}\}\right| &= \left| \frac{\mu^3}{\rho\dfrac{\cosh\nu(x-x_0)}{\cos\rho(t-t_0)} - 2\mu} \right. \\
&\quad \left. - \frac{4}{1+16(t-t_0)^2+4(x-x_0)^2} \right| \\
&\leq \left| \frac{\mu^3}{\rho-2\mu} - 4 \right| = \left| \sqrt{\mu^2+4} - 2 \right| \\
&\leq \sqrt{\delta^2+4} - 2 \\
&= \sqrt{\left(\sqrt{(\varepsilon+2)^2-4}\right)^2 + 4} - 2 = \varepsilon.
\end{aligned}$$

The following verifies that the limit for the imaginary parts of the Kuznetsov-Ma breather and Peregrine soliton is accurate, i.e.,

$$\lim_{\nu\to 0} \mathrm{Im}\{q_{\mathrm{M}}(x,t)\} = \mathrm{Im}\{q_{\mathrm{P}}(x,t)\}.$$

For each $\varepsilon > 0$, there exists $\delta = \sqrt{-10 + 2\sqrt{25 + 4\varepsilon/|t-t_0|}} > 0$ such that if $0 < \mu < \delta$, then $\left|\mathrm{Im}\{q_{\mathrm{M}}\} - \mathrm{Im}\{q_{\mathrm{P}}\}\right| < \varepsilon$. We can write the imaginary parts of q_{M} and q_{P} as follows

$$\mathrm{Im}\{q_{\mathrm{M}}\} = \frac{\mu\rho}{\rho\dfrac{\cosh\mu(x-x_0)}{\sin\rho(t-t_0)} - 2\mu\cot\rho(t-t_0)} \leq \frac{\mu\rho^2|t-t_0|}{\rho-2\mu},$$

$$\mathrm{Im}\{q_{\mathrm{P}}\} = \frac{16(t-t_0)}{1+16(t-t_0)^2+4(x-x_0)^2} \leq 16|t-t_0|,$$

It follows that

$$\begin{aligned}\left|\mathrm{Im}\{q_{\mathrm{M}}\}-\mathrm{Im}\{q_{\mathrm{P}}\}\right| &= \left|\frac{\mu\rho}{\rho\dfrac{\cosh\mu(x-x_0)}{\sin\rho(t-t_0)}-2\mu\cot\rho(t-t_0)} - \frac{16(t-t_0)}{1+16(t-t_0)^2+4(x-x_0)^2}\right| \\ &\le \left|\frac{\mu\rho^2}{\rho-2\mu}-16\right||t-t_0| \\ &= \left|\left(\mu^2+4\right)\left(\sqrt{\mu^2+4}+2\right)-16\right||t-t_0| \\ &< \left|\left(\delta^2+4\right)\left(\frac{\delta^2}{4}+4\right)-16\right||t-t_0| \\ &= \left|\frac{\delta^4}{4}+5\delta^2\right||t-t_0| = \varepsilon.\end{aligned}$$

In what follows, we present the limit of the real part of the Akhmediev soliton as $\nu\to 0$ is indeed the real part of the Peregrine soliton, i.e.,

$$\lim_{\nu\to 0}\mathrm{Re}\{q_{\mathrm{A}}(x,t)\} = \mathrm{Re}\{q_{\mathrm{P}}(x,t)\}.$$

For each $\varepsilon>0$, there exists $\delta=\sqrt{\varepsilon/3}>0$ such that if $0<\nu<\delta<2$, then $\left|\mathrm{Re}\{q_{\mathrm{A}}\}-\mathrm{Re}\{q_{\mathrm{P}}\}\right|<\varepsilon$. We know that since

$$-1\le\frac{\cos\nu(x-x_0)}{\cosh\sigma(t-t_0)}\le 1 \qquad \text{for all } (x,t)\in\mathbb{R}^2,$$

it then implies

$$2\nu-\sigma\le 2\nu-\sigma\frac{\cos\nu(x-x_0)}{\cosh\sigma(t-t_0)}.$$

We also have $1+16(t-t_0)^2+4(x-x_0)^2\ge 1$ for all $(x,t)\in\mathbb{R}^2$. Furthermore, since $0\le\sqrt{4-\nu^2}\le 2$, $0\le 2-\sqrt{4-\nu^2}\le 2$,

$$\begin{aligned}&\frac{1}{4}\le\frac{2-\sqrt{4-\nu^2}}{\nu^2}\le\frac{1}{2},\\ &\frac{1}{2}\le\frac{1}{4}+\frac{2-\sqrt{4-\nu^2}}{\nu^2}\le\frac{3}{4},\\ &\text{and}\quad \frac{2-\sqrt{4-\nu^2}}{4\nu^2}\ge\frac{1}{4\delta^2},\end{aligned}$$

it follows that

$$\begin{aligned}\left|\mathrm{Re}\{q_{\mathrm{A}}\}-\mathrm{Re}\{q_{\mathrm{P}}\}\right| &= \left|\frac{\nu^3}{2\nu-\sigma\dfrac{\cos\nu(x-x_0)}{\cosh\sigma(t-t_0)}} - \frac{4}{1+16(t-t_0)^2+4(x-x_0)^2}\right| \\ &\le \left|\frac{\nu^3}{2\nu-\sigma}+4\right| = \left|\frac{1}{\dfrac{(2-\sqrt{4-\nu^2})}{\nu^2}}+\frac{1}{\dfrac{1}{4}}\right| \\ &= \frac{\left|\dfrac{1}{4}+\dfrac{(2-\sqrt{4-\nu^2})}{\nu^2}\right|}{\left|\dfrac{(2-\sqrt{4-\nu^2})}{4\nu^2}\right|} \le \frac{3}{4}\left(4\delta^2\right) = 3\left(\sqrt{\frac{\varepsilon}{3}}\right)^2 = \varepsilon.\end{aligned}$$

In what follows, we demonstrate that the limit of the imaginary part of the Akhmediev soliton becomes the imaginary part of the Peregrine soliton, i.e.,

$$\lim_{\nu\to 0}\mathrm{Im}\{q_{\mathrm{A}}(x,t)\} = \mathrm{Im}\{q_{\mathrm{P}}(x,t)\}.$$

For each $\varepsilon>0$, there exists $\delta=\sqrt{\varepsilon/4}>0$ such that if $0<\nu<\delta<2$, then $\left|\mathrm{Im}\{q_{\mathrm{A}}\}-\mathrm{Im}\{q_{\mathrm{P}}\}\right|<\varepsilon$. We can write the imaginary parts of q_{A} and q_{P} as follows

$$\begin{aligned}\mathrm{Im}\{q_{\mathrm{A}}\} &= \frac{\nu\sigma\tanh\sigma(t-t_0)}{2\nu-\sigma\dfrac{\cos\nu(x-x_0)}{\cosh\sigma(t-t_0)}} \le \frac{\nu\sigma^2|t-t_0|}{2\nu-\sigma},\\ \mathrm{Im}\{q_{\mathrm{P}}\} &= \frac{16(t-t_0)}{1+16(t-t_0)^2+4(x-x_0)^2} \le 16|t-t_0|.\end{aligned}$$

Since $2+\sqrt{4-\nu^2}\le 4$ and $(4-\nu^2)\le 4+\delta^2/|t-t_0|$, it follows that

$$\begin{aligned}\left|\mathrm{Im}\{q_{\mathrm{A}}\}-\mathrm{Im}\{q_{\mathrm{P}}\}\right| &= \left|\frac{\nu\sigma\tanh\sigma(t-t_0)}{2\nu-\sigma\dfrac{\cos\nu(x-x_0)}{\cosh\sigma(t-t_0)}} - \frac{16(t-t_0)}{1+16(t-t_0)^2+4(x-x_0)^2}\right| \\ &\le \left|\frac{\nu\sigma^2}{2\nu-\sigma}-16\right||t-t_0| \\ &= \left|\left(4-\nu^2\right)\left(2+\sqrt{4-\nu^2}\right)-16\right||t-t_0| \\ &< \left|4\left(4+\frac{\delta^2}{|t-t_0|}\right)-16\right||t-t_0| \\ &= 4\delta^2 = 4\left(\sqrt{\frac{\varepsilon}{4}}\right)^2 = \varepsilon.\end{aligned}$$

We have completed the proof.

In the following section, we will visualize the limiting behavior of the breather solutions as they approach toward the Peregrine soliton.

3 LIMITING BEHAVIOR VISUALIZED

In this section, we will visually confirm the limiting behavior of the Kuznetsov-Ma and Akhmediev breathers toward the Peregrine soliton as both parameter values approach zero. **Subsection 3.1** presents the contour plots of the amplitude modulus, and **Subsection 3.2** discusses the spatial and temporal parameterizations of the breathers. We select several parameter values in sketching the plots. **Figure 1** displays the chosen parametric values for both breather solutions, where they can be visualized in the complex-plane for the parameter pair (μ,ν).

3.1 Contour Plot

In this subsection, we observe the contour plots of the amplitude modulus of the breather and how the changes in the parameter values affect the envelope's period and wavelength. Similar contour plots have been presented in the context of

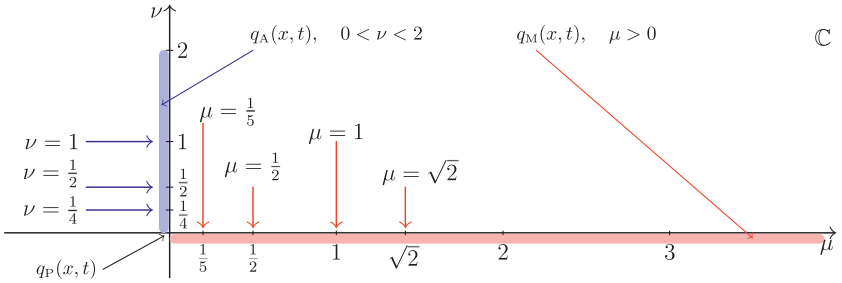

FIGURE 1 | Selected parametric values ν and $\mu = i\nu$ displayed in the complex plane for the Kuznetsov-Ma breather and Akhmediev soliton visualized in this section.

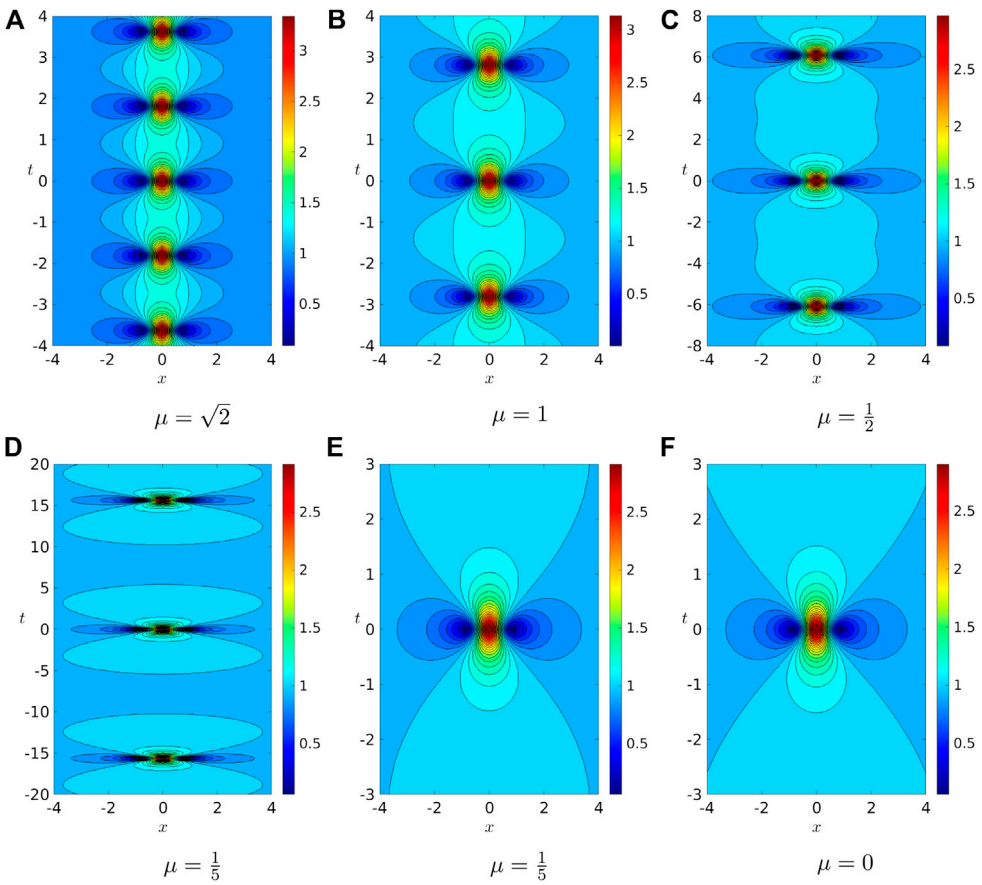

FIGURE 2 | Contour plots for the moduli of the Kuznetsov-Ma breather for **(A)** $\mu = \sqrt{2}$, **(B)** $\mu = 1$, **(C)** $\mu = 0.5$, **(D)** $\mu = 0.2$, **(E)** also $\mu = 0.2$ but a zoom-in version, and **(F)** $\mu = 0$, which gives the Peregrine soliton. Notice that the contour plots (e) and (f) are qualitatively nearly identical.

electronegative plasmas with Maxwellian negative ions [170]. In particular, the contour plot of the Peregrine soliton is also displayed in [142].

Figures 2A-E display the contour plots of the Kuznetsov-Ma breather for several values of parameters μ: $\sqrt{2}, 1, 1/2$, and $1/5$. **Figure 2E** is a zoom-in version of the same contour plot given in **Figure 2D**. **Figure 2F** is the final stop when we let the parameter $\mu \to 0$, for which the Kuznetsov-Ma breather turns into the Peregrine soliton. It is interesting to note that for $\mu = 1/5$, the contour plot is nearly identical to the one from the Peregrine soliton, as we can observe by qualitatively comparing panels (E) and (F) of **Figure 2**.

Let $T_{\rm M}$ denote the temporal envelope period for the Kuznetsov-Ma breather, then we know that in general, $T_{\rm M} = 2\pi/\rho$. For $\mu \to \infty$, $T_{\rm M} \to 0$ and vice versa, for $\mu \to 0$, $T_{\rm M} \to \infty$. For any given value of $\mu > 0$, $T_{\rm M}$ can be easily calculated. Here are some examples. For $\mu = \sqrt{2}$, $T_{\rm M} = \pi/\sqrt{3} \approx 1.814$ and we display five periods in **Figure 2A** along the temporal axis t. For $\mu = 1$, $T_{\rm M} = 2\pi/\sqrt{5} \approx 2.81$ and for the same time interval as in panel (A), we can only capture three periods along the

TABLE 1 | Exact values of the temporal envelope period T_M and their approximate values for selected parameter values μ corresponding to the Kuznetsov-Ma breather.

Parameter values				Temporal envelope period	
μ (exact)	**μ (decimal)**	**ρ (exact)**	**ρ (approximation)**	**T_M (Exact)**	**T_M (Approximation)**
1/5	0.2	$\sqrt{101}/25$	0.402	$50\pi/\sqrt{101}$	15.630
1/2	0.5	$\sqrt{17}/4$	1.031	$8\pi/\sqrt{17}$	6.096
1	1.0	$\sqrt{5}$	2.236	$2\pi/\sqrt{5}$	2.810
$\sqrt{2}$	1.414	$2\sqrt{3}$	3.464	$\pi/\sqrt{3}$	1.814

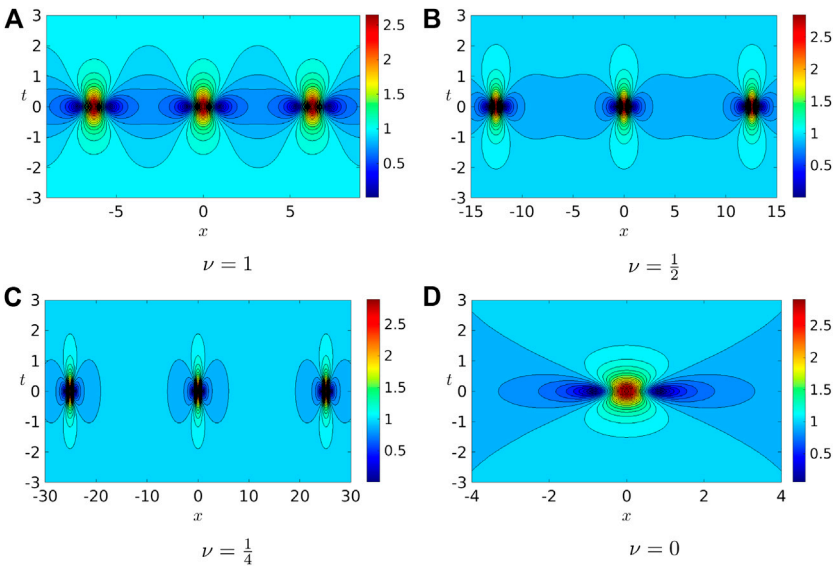

FIGURE 3 | Contour plots for the moduli of the Akhmediev breather for **(A)** $\nu = 1$, **(B)** $\nu = 0.5$, and **(C)** $\nu = 0.25$, as well as **(D)** the Peregrine soliton.

TABLE 2 | Exact values of the spatial envelope wavelength L_A and their approximate values for selected parameter values ν corresponding to the Akhmediev soliton.

Parameter values				Spatial envelope wavelength	
ν (exact)	**ν (decimal)**	**σ (exact)**	**σ (approximation)**	**L_A (Exact)**	**L_A (Approximation)**
1/4	0.25	$3\sqrt{7}/16$	0.496	8π	25.133
1/2	0.5	$\sqrt{15}/4$	0.968	4π	12.566
1	1.0	$\sqrt{3}$	1.732	2π	6.283

temporal axis t, as shown in **Figure 2B**. Furthermore, for $\mu = 1/2$, $T_M = 8\pi/\sqrt{17} \approx 6.1$ and we need to extend almost twice the length in the time interval in order to capture at least three periods. **Figure 2C** shows this contour plot. Finally, for $\mu = 1/5$, $T_M = 50\pi/\sqrt{101} \approx 15.63$. As we can observe in **Figure 2D**, extending the length of time interval to around 40 units is sufficient to capture at least three periods, albeit the detail around maximum and minimum is hardly visible. **Table 1** displays selected parameter values of the Kuznetsov-Ma breather and their corresponding temporal envelope periods T_M.

Figures 3A–C display the contour plot of the Akhmediev soliton for selected values of its parameters ν: 1, 1/2, and 1/4. **Figure 3D** shows the contour plot of the Peregrine soliton, which occurs as the final destination when letting the parameter $\nu \to 0$. **Figure 3D** is identical to **Figure 2F**, the only difference lies in the length-scale of both horizontal and vertical axes. Similar to the previous case, zooming-in the contour plot for $\nu = 1/4$ in **Figure 3C** will yield a qualitatively nearly identical contour plot with the Peregrine soliton shown in the panel (D). (It is not shown in the figure.)

Let L_A denote the spatial envelope wavelength for the Akhmediev soliton, then for $0 < \nu < 2$, $L_A = 2\pi/\nu$, which gives $L_A > \pi$. For $\nu \to 2$, $L_A \to \pi$, and as $\nu \to 0$, $L_A \to \infty$. **Table 2** displays selected values of the parameter ν and their corresponding spatial envelope wavelength L_A for the Akhmediev soliton. For $\nu = 1$, $L_A = 2\pi$ and the spatial length of 20 units in **Figure 3A** is sufficient to capture three envelope wavelength. For $\nu = 1/2$, $L_A = 4\pi$ and the spatial length of 40 units in **Figure 3B** is required to capture at least three envelope wavelength. For $\nu = 1/4$, $L_A = 8\pi$ and the spatial length of 60 units in **Figure 3C** is needed to capture at least three

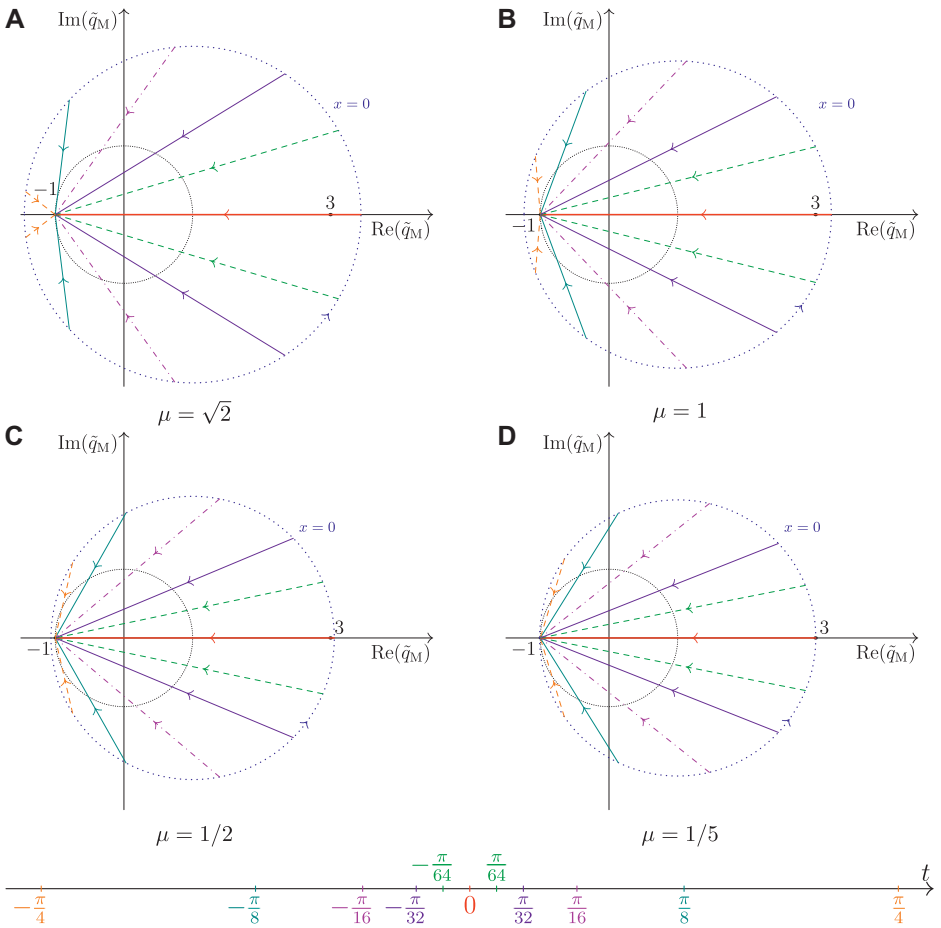

FIGURE 4 | Parameterization of the non-rapid-oscillating complex-valued amplitude of the Kuznetsov-Ma breather $\tilde{q}_\mathrm{M}$ in the spatial variable x, $x \geq 0$, for different values of temporal variable t and different values of the parameter μ: **(A)** $\mu = \sqrt{2}$, **(B)** $\mu = 1$, **(C)** $\mu = 1/2$, and **(D)** $\mu = 1/5$. The selected values of t are $t = 0$ (solid red), $t = \pm\pi/64$ (dashed green), $t = \pm\pi/32$ (solid purple), $t = \pm\pi/16$ (dash-dotted magenta), $t = \pm\pi/8$ (solid cyan), and $t = \pm\pi/4$ (dashed orange).

envelope wavelength. The details around maxima and minima are hardly visible for the latter.

3.2 Parameterization in Spatial and Temporal Variables

In this subsection, we write the breather solutions as $q_\mathrm{X}(x,t) = q_0(t)\,\tilde{q}_\mathrm{X}(x,t)$, where $q_0(t)$ is the plane-wave solution and $\mathrm{X} = \{\mathrm{M}, \mathrm{A}, \mathrm{P}\}$. Since the plane-wave solution gives a fast-oscillating effect, we only consider the non-rapid oscillating part of the breathers $\tilde{q}_\mathrm{X}$ for the parameterization visualization. In the subsequent figures, we present both spatial and temporal parameterizations of the Kuznetsov-Ma breather, Akhmediev, and Peregrine solitons. A similar description has been briefly covered and discussed in [30, 61, 63, 164]. This article does not only complements and supplements but also provides detailed explanations to those references. Additionally, note that the unit circle centered at the origin appeared in each panel of **Figures 4–7** (dotted black circle) corresponds to the phase of the continuous-wave pedestal, i.e., the manifold of the breathers for $x \to \pm\infty$ or $t \to \pm\infty$ [30].

Figure 4 displays the parameterization of the non-rapid oscillating Kuznetsov-Ma breather $\tilde{q}_\mathrm{M}$ in the spatial variable x for different values of the temporal variable t and parameter μ. Different panels indicate different parameter values μ and for each panel, different curves, for which in this particular case, they are merely straight lines, indicate different time t. For all cases, we consider $x \geq 0$ due to the symmetry nature of the breathers. The straight-line trajectories move inwardly focused from the dotted blue circle at $x = 0$ toward $(-1, 0)$ as $x \to \infty$. The situation is simply reversed for $x < 0$: the path of trajectories move outwardly defocused as x progresses from $(-1, 0)$ at $x \to -\infty$ toward the dotted blue circle at $x = 0$. At the bottom of these four panels, we also present the t-axis and corresponding values of the selected values of t for $-T_\mathrm{M}/2 < -\pi/4 \leq t \leq \pi/4 < T_\mathrm{M}/2$. The trajectories in the upper-part and lower-part of the complex-plane correspond to the positive and negative values of t, respectively. We observe that the trajectories shift faster in space around $t = 0$ than around $t = \pm T_\mathrm{M}/2 = \pm\pi/\rho$.

In particular, for $t = n\pi/\rho$, $n \in \mathbb{Z}$, $\tilde{q}_\mathrm{M}$ reduces to a real-valued function, i.e., $\mathrm{Im}(\tilde{q}_\mathrm{M}) = 0$ for all $\mu > 0$. Hence, the parameterized curve is a straight line at the real-axis. For $t = 2n\pi/\rho, n \in \mathbb{Z}$, this is shown by

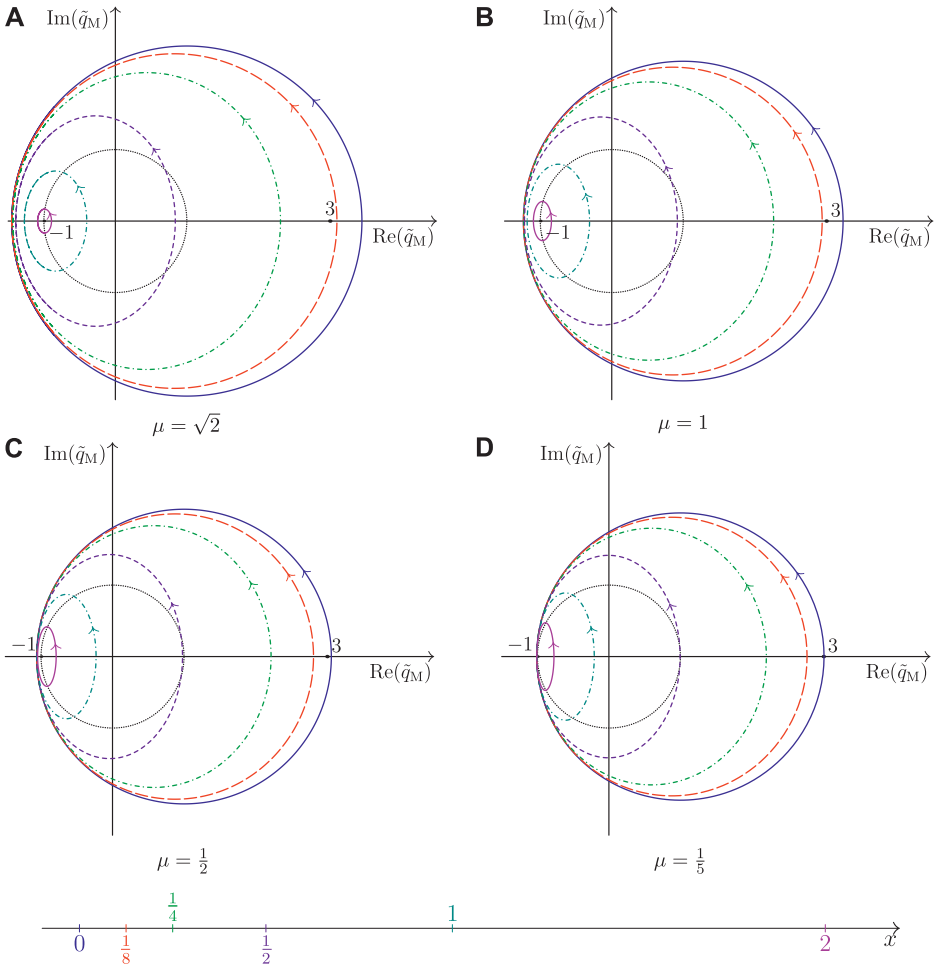

FIGURE 5 | Parameterization of the non-rapid oscillating complex-valued amplitude of the Kuznetsov-Ma breather $\tilde{q}_\mathrm{M}$ in the temporal variable t $(-\pi/\rho < t < \pi/\rho)$ for different values of spatial variable x: $x = 0$ (solid blue), $x = 1/8$ (long-dashed red), $x = 1/4$ (dash-dotted green), $x = 1/2$ (dashed purple), $x = 1$ (dash-dotted cyan), and $x = 2$ (solid magenta) and different values of the parameter μ: **(A)** $\mu = \sqrt{2}$, **(B)** $\mu = 1$, **(C)** $\mu = 1/2$, and **(D)** $\mu = 1/5$.

the horizontal solid red line lying on the real axis moving from a point larger than $\mathrm{Re}(\tilde{q}_\mathrm{M}) = 3$ to $\mathrm{Re}\,(\tilde{q}_\mathrm{M}) = -1$ for $x > 0$. The represented case $t = 0$ is displayed in **Figure 4** while the case $t = \pi/\rho$ is not shown in the figure. Indeed, from **(3)**, we obtain the following limiting values for $n \in \mathbb{Z}$:

$$\lim_{x \to 0} q_\mathrm{M}(x, 2n\pi/\rho) = 1 + \sqrt{\mu^2 + 4}, \quad \text{and} \quad \lim_{x \to 0} q_\mathrm{M}(x, (2n+1)\pi/\rho) = 1 - \sqrt{\mu^2 + 4}. \tag{10}$$

Additionally, $\lim_{x \to \pm\infty} q_M(x, n\pi/\rho) = -1$. Using a similar analysis, vertical straight lines at $\mathrm{Re}\,(\tilde{q}_\mathrm{M}) = -1$ can be obtained by taking the values of $t = (n + 1/2)\pi/\rho$, for $n \in \mathbb{Z}$. The line direction from the positive and negative regions of $\mathrm{Im}\,(\tilde{q}_\mathrm{M})$ is downward and upward toward $(-1, 0)$ for even and odd values of $n \in \mathbb{Z}$, respectively.

Figure 5 displays the sketch of the non-rapid-oscillating Kuznetsov-Ma breather $\tilde{q}_\mathrm{M}$ in the complex-plane parameterized in the temporal variable t for different values of the spatial variable x and parameter μ. For each case, t is taken for one temporal envelope period, i.e., $-T_\mathrm{M}/2 = -\pi/\rho < t < \pi/\rho = T_\mathrm{M}/2$. Instead of a set of straight lines, the trajectories form the shape of elliptical curves. For each $x = x_0 \in \mathbb{R}$, the ellipse is centered at $(c(x_0), 0)$ with semi-minor axis $a(x_0)$ and semi-major axis $b(x_0)$, where

$$a(x_0) = \frac{\mu\rho \cosh(\mu x_0)}{d(x_0)} \tag{11}$$

$$b(x_0) = \frac{\rho \cosh(\mu x_0)}{\sqrt{d(x_0)}} \tag{12}$$

$$c(x_0) = \frac{2\mu^2}{d(x_0)} - 1 \tag{13}$$

$$d(x_0) = 2\cosh(2\mu x_0) + \mu^2 - 2. \tag{14}$$

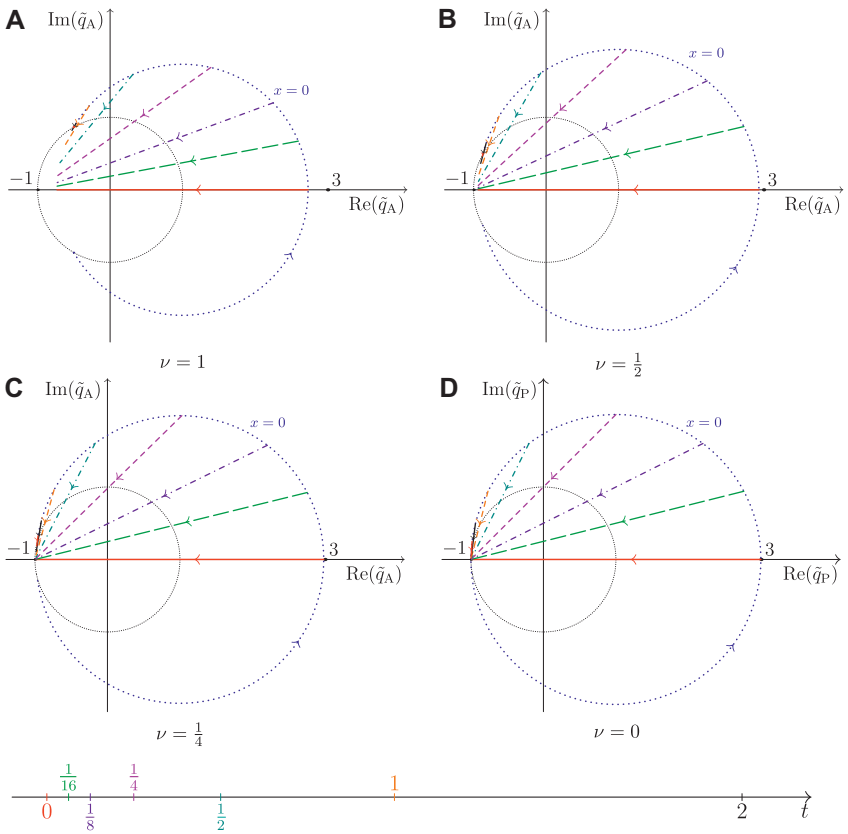

FIGURE 6 | Parameterization of the non-rapid oscillating complex-valued amplitude $\tilde{q}$ in the spatial variable x for different values of temporal variable t: $t = 0$ (solid red), $t = 1/16$ (long-dashed green), $t = 1/8$ (dash-dotted purple), $t = 1/4$ (dash magenta), $t = 1/2$ (dash-dotted cyan), $t = 1$ (dashed orange), $t = 2$ (solid black), and $t = 4$ (solid red), and modulation frequencies of the Akhmediev solitons **(A)** $\nu = 1$ $(0 \le x \le \pi)$, **(B)** $\nu = 1/2$ $(0 \le x \le 2\pi)$, **(C)** $\nu = 1/4$ $(0 \le x \le 4\pi)$, and **(D)** $\nu = 0$, $x \ge 0$ (Peregrine soliton).

The special case of a circle is obtained for $x_0 = 0$ with the radius $r = \sqrt{\mu^2 + 4}$ centered at $(1, 0)$. All curves move in the counterclockwise direction for increasing t. For $x > 0$, the larger the values of x, the smaller the ellipses become. The situation is the opposite for $x < 0$: smaller values of x (but largely negatives in its absolute value sense) correspond to smaller ellipses in the complex plane. Due to its spatial symmetry, only the plots for positive values of x are displayed. The axis below the figure panels shows the selected x values for a better overview of the variable scaling: $x = 0$, 1/8, 1/4, 1/2, 1, and $x = 2$.

In **Figure 4**, the starting points of the trajectories for $x = 0$ are shrinking as μ decreases, as indicated by the dotted blue exterior circles. For the same interval of time t, these initial points also tend to be absorbed toward the right-hand side of the exterior circles while they focus toward $(-1, 0)$. As we can observe in panels (A) and (B), the trajectories at $t = \pm \pi/4$ originate from the left-hand side of the exterior circles for $\mu \ge 1$. A similar pattern was no longer observed as the values of μ get smaller, as we can see in panels (C) and (D). Meanwhile, the circles and ellipses are getting smaller in **Figure 5** for decreasing values of μ. Except for the circles that are always centered at $(1, 0)$, the centers of the ellipses shift toward the left-hand side of the blue exterior circle near $(-1, 0)$ as μ decreases.

Figure 6 displays the sketch in the complex-plane of the non-rapid-oscillating Akhmediev soliton $\tilde{q}_\mathrm{A}$ [panels (A)-(C)] and Peregrine soliton $\tilde{q}_\mathrm{P}$ [panel (D)] parameterized in the spatial variable x for different values of the temporal variable t and parameter ν. We only display the trajectories corresponding to the positive values of t, the trajectories for the negative values of t are simply the reflection over the horizontal axis $\mathrm{Re}\,(\tilde{q}_\mathrm{P}) = 0$. The t-axis below the panels indicate the chosen values of t displayed in the figure. Similar to the trajectories for the Kuznetsov-Ma breather when they are parameterized in the spatial variable x, the trajectories for the Akhmediev soliton parameterized in x are also collections of straight lines shifting in the counterclockwise direction for increasing values of t. Different from the previous case, these straight lines are periodic in x. The experimental results of deterministic freak wave generation using the spatial NLS equation showed that instead of straight lines, we obtained non-degenerate Wessel curves, suggesting that the periodic lines might be perturbed during the downstream evolution [43, 113].

For each panel, we only sketch the trajectories for an interval of half the spatial envelope wavelength, i.e., $0 \le x \le L_\mathrm{A}/2 = \pi/\nu$. For this limited space interval, the direction of the lines is moving inwardly focused, from the dotted-blue exterior circle for $x = 0$ to some values in the left-part of the complex-plane near $\mathrm{Re}\,(\tilde{q}_\mathrm{A}) = -1$. As the value of x progresses,

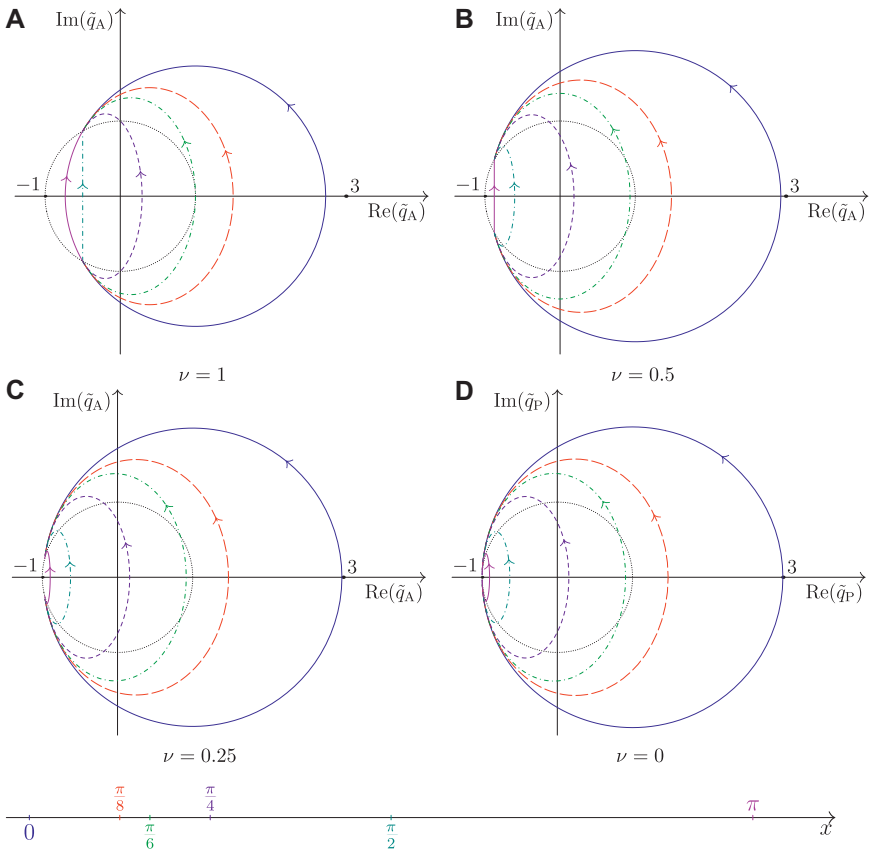

FIGURE 7 | Parameterization of the non-rapid oscillating complex-valued amplitude $\tilde{q}$ in the temporal variable t $(-\infty < t < \infty)$ for different values of spatial variable x: $x = 0$ (solid blue), $x = \pi/8$ (long-dashed red), $x = \pi/6$ (dash-dotted green), $x = \pi/4$ (dashed purple), $x = \pi/2$ (dash-dotted cyan), and $x = \pi$ (solid magenta), and modulation frequencies of the Akhmediev solitons **(A)** $\nu = 1$, **(B)** $\nu = 0.5$, **(C)** $\nu = 0.25$, and **(D)** $\nu \to 0$ (the Peregrine soliton).

$L_\mathrm{A}/2 = \pi/\nu \leq x \leq L_\mathrm{A} = 2\pi/\nu$, the trajectories bounce back toward the initial points by following the identical paths. They then travel in the same manner periodically as $x \to \pm\infty$. For a decreasing value of the parameter ν, the endpoint of these lines tends to focus around the region near $(-1, 0)$, as we can observe in **Figures 6A–C**. For the Peregrine soliton, the trajectories are not periodic as $L_\mathrm{A} \to \infty$, and they tend to $(-1, 0)$ for $x \to \pm\infty$, as can be seen in **Figure 6D**.

In **Figure 6**, a prominent difference in the trajectories for different values of the parameter ν is its lengths. The length of the trajectories is increasing for decreasing values of ν. While the starting points for the Kuznetsov-Ma breathers are shrinking, for this family of Akhmediev solitons, they are expanding as $\nu \to 0$ until the dotted blue exterior circle reaches a radius of 2 unit length. Moreover, the endpoints for larger values of ν stop at some points where their real values become negative but still larger than −1. These endpoints eventually approach $(-1, 0)$ as $\nu \to 0$.

Figure 7 displays the sketch of the non-rapid-oscillating part of the Akhmediev soliton $\tilde{q}_\mathrm{A}$ [panels (A)-(C)] and Peregrine soliton $\tilde{q}_\mathrm{P}$ [panel (D)] in the complex-plane parameterized in the temporal variable t for different values of the spatial variable x and parameter ν. The values of t run from $t \to -\infty$ to $t \to +\infty$, and we only sketch the positive values of x. The plots for the negative values of x are identical and are not shown due to the symmetry property of the soliton. The x-axis below the panels shows the selected values of x ranging from $x = 0$ to $x = \pi$. For $\tilde{q}_\mathrm{A}$, the trajectories are composed of circular sectors, elliptical sectors, and straight lines instead of closed curves like circles or ellipses. Since this soliton is a nonlinear extension of the modulational instability, the trajectories for each value of the parameter ν, $0 < \nu < 2$, are the corresponding homoclinic orbit for an unstable mode, and the presence of a phase shift prevents closed-path trajectories [30, 34, 76, 164].

The circular sectors are attained for $x = 0$ and the straight lines occur at $x = (n + 1/2)\pi/\nu, n \in \mathbb{Z}$, $n \in \mathbb{Z}$. Trajectories at other locations yield the elliptical sectors. The initial and final points are not identical, and this indicates a phase shift in the soliton. Let $\phi_{+\infty}$ and $\phi_{-\infty}$ be the phases for $x \to \pm\infty$, respectively. Let also $\Delta\phi = \phi_{+\infty} - \phi_{-\infty}$ be the difference between the phases at $x = +\infty$ and $x = -\infty$, then we have the following phase relationships:

$$\tan\phi_{\pm\infty} = \pm\frac{\sigma}{\nu^2 - 1}, \tag{15}$$

$$\text{and} \qquad \Delta\phi = 2\arctan\left(\frac{\sigma}{\nu^2 - 1}\right). \tag{16}$$

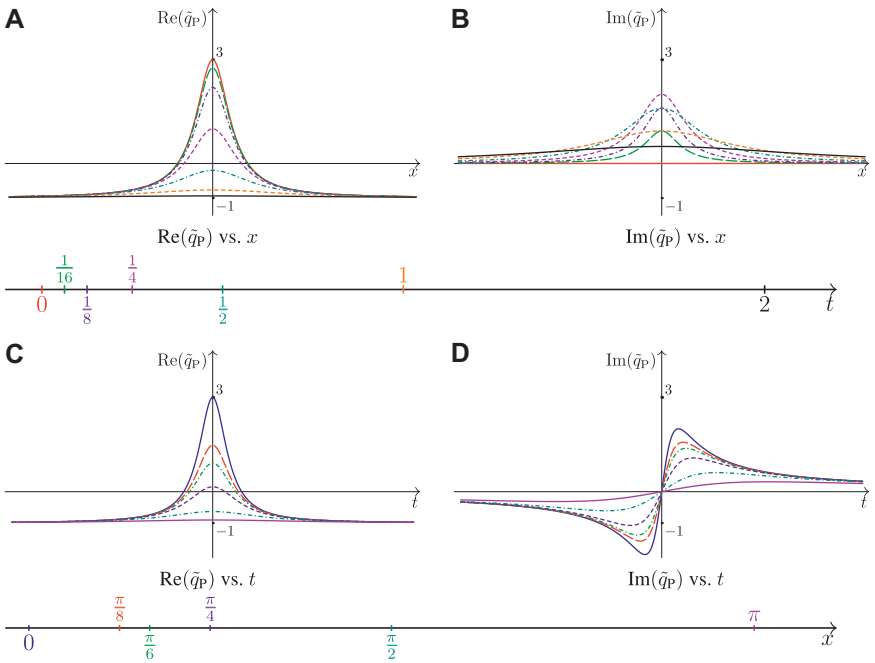

FIGURE 8 | Plots of the real and imaginary parts of the non-rapid oscillating complex-valued amplitude for the Peregrine soliton with respect to the spatial and temporal variables, x (upper panels) and t (lower panels), respectively. For upper panels **(A)** and **(B)**, various curves indicates different time: $t = 0$ (solid red), $t = 1/16$ (long-dashed green), $t = 1/8$ (dash-dotted purple), $t = 1/4$ (dash magenta), $t = 1/2$ (dash-dotted cyan), $t = 1$ (dashed orange), and $t = 2$ (solid black). For lower panels **(C)** and **(D)**, different curves indicates different positions: $x = 0$ (solid blue), $x = \pi/8$ (long-dashed red), $x = \pi/6$ (dash-dotted green), $x = \pi/4$ (dashed purple), $x = \pi/2$ (dash-dotted cyan), and $x = \pi$ (solid magenta).

For the Peregrine soliton, the trajectories of time parameterization in the complex-plane are either a circle (for $x = 0$) or ellipses (for other values of $x \neq 0$). The circle is centered at $(1, 0)$ with radius $r = 2$. Let $x = x_0 \in \mathbb{R}$ be the position for the Peregrine soliton, then the ellipse has the length of semi-minor axis $a(x_0)$, the length of semi-major axis $b(x_0)$, and is centered at $(c(x_0), 0)$, where

$$a(x_0) = \frac{2}{1 + 4x_0^2}, \tag{17}$$

$$b(x_0) = \frac{2}{\sqrt{1 + 4x_0^2}}, \tag{18}$$

$$\text{and} \quad c(x_0) = a(x_0) - 1. \tag{19}$$

Nearly all trajectories in **Figure 7** follow the right-hand side paths instead of the left-hand side. For decreasing values of ν, the trajectories are generally expanding in size, except for the curve at $x = \pi$ that becomes a straight line when the parameter value changes from $\nu = 1$ to $\nu = 1/2$. When the values of ν is further decreased, the trajectories at $x = \pi$ become an elliptical sector and an ellipse for $\nu = 1/4$ and $\nu = 0$, respectively.

Figure 8 should be viewed in connection to **Figures 6D**, **7D**. It displays the plots of the real and imaginary parts of the non-rapid-oscillating complex-valued amplitude for the Peregrine soliton $\tilde{q}_\text{P}$ with respect to x and t, which are presented in the upper and lower panels, respectively. For the former, different curves correspond to selected values of time $t \in \{0, 1/16, 1/8, 1/4, 1/2, 1, 2\}$. For the latter, different curves correspond to selected values of position $x \in \{0, \pi/8, \pi/6, \pi/4, \pi/2, \pi\}$. The phase difference in the time parameterization of $\tilde{q}_\text{P}$ is discernible from the behavior of $\text{Im}(\tilde{q}_\text{P})$ as $t \to \pm\infty$. While $\lim_{x \to \pm\infty} \text{Re}(\tilde{q}_P) = -1$, the quantity for $\lim_{x \to \pm\infty} \text{Im}(\tilde{q}_P)$ takes positive and negative values, respectively.

4 CONCLUSION

We have considered the exact analytical breather solutions of the focusing NLS equation, where the wave envelopes at infinity have a nonzero but constant background. These solutions have been adopted as weakly nonlinear prototypes for freak waves in dispersive media due to their fine agreement with various experimental results. We have provided not only a brief historical review of the breathers but also covered some recent progress in the field of rogue wave modeling in the context of the NLS equation.

In particular, we have discussed the Peregrine soliton as a limiting case of the Kuznetsov-Ma breather and Akhmediev soliton. We have verified rigorously using the ε-δ argument that as each of the parameter values from these two breathers is approaching zero, they reduce to the Peregrine soliton. We have also presented this limiting behavior visually by depicting the contour plots of the

breather amplitude modulus for selected parameter values. We displayed the parameterization plots of the non-rapid-oscillating complex-valued breather amplitudes both spatially and temporally.

The trajectories for the spatial parameterization in the complex-plane exhibit a set of straight lines for all the breathers. From $x \to -\infty$ to $x \to +\infty$, the paths are passed twice for the Kuznetsov-Ma breather and are elapsed many times infinitely for the Akhmediev soliton due to its spatial periodic characteristics. The trajectories in the complex plane for the parameterization in the temporal variable of the Kuznetsov-Ma breather and Peregrine soliton feature a periodic circle and a set of periodic ellipses due to its temporal symmetry. For the Akhmediev soliton, on the other hand, the path does not only turn into circle and ellipse sectors but also becomes straight lines as it travels from $t \to -\infty$ to $t \to +\infty$, featuring homoclinic orbits with a phase shift.

DATA AVAILABILITY STATEMENT

The original contributions presented in the study are included in the article/Supplementary Material, further inquiries can be directed to the corresponding author.

AUTHOR CONTRIBUTIONS

The author confirms being the sole contributor of this work and has approved it for publication.

DEDICATION

The author would like to dedicate this article to his late father Zakaria Karjanto (Khouw Kim Soey, 許金瑞) who not only taught him the alphabet, numbers, and the calendar in his early childhood but also cultivated the value of hard work, diligence, discipline, perseverance, persistence, and grit. Karjanto Senior was born in Tasikmalaya, West Java, Japanese-occupied Dutch East Indies on 1 January 1944 (Saturday Pahing) and died in Bandung, West Java, Indonesia on 18 April 2021 (Sunday Wage).

ACKNOWLEDGMENTS

The author wishes to thank Bertrand Kibler, Amin Chabchoub, and Heremba Bailung for the invitation to contribute to the article collection "Peregrine Soliton and Breathers in Wave Physics: Achievements and Perspectives" and Marlena Radomska from the Production Team of Frontiers in Physics for her excellent and outstanding administrative assistance. The author also acknowledges E. (Brenny) van Groesen, Mark Ablowitz, Constance Schober, Frederic Dias, Roger Grimshaw, Panayotis Kevrekidis, Boris Malomed, Evgenii Kuznetsov, Nail Akhmediev, Alfred Osborne, Miguel Onorato, Gert Klopman, René Huijsmans, Andonowati, Stephan van Gils, Guido Schneider, Anthony Roberts, Shanti Toenger, Omar Kirikchi, Ardhasena Sopaheluwakan, Hadi Susanto, Alexander Iskandar, Agung Trisetyarso, Ade Irma Suriajaya, and Defrianto Pratama for fruitful discussion.

REFERENCES

1. Osborne AR. *Nonlinear Ocean Wave and the Inverse Scattering Transform*. Cambridge, MA: Academic Press (2010).
2. Debnath L. *Nonlinear Partial Differential Equations for Scientists and Engineers*. Berlin, Germany: Springer Science + Business Media (2012).
3. Agrawal GP. *Nonlinear Fiber Optics*. 5th ed. Cambridge, MA: Academic Press (2012).
4. Kivshar YS, and Agrawal GP. *Optical Solitons: From Fibers to Photonic Crystals*. Cambridge, MA: Academic Press (2003).
5. Infeld E, and Rowlands G. *Nonlinear Waves, Solitons and Chaos*. 2nd ed. Cambridge, United Kingdom: Cambridge University Press (2000).
6. Newell AC. *Solitons in Mathematics and Physics*. Philadelphia, PA: SIAM (1985).
7. Sulem C, and Sulem PL. *The Nonlinear Schrödinger Equation: Self-Focusing and Wave Collapse*. Berlin, Germany: Springer-Verlag (1999).
8. Kevrekidis PG, Frantzeskakis DJ, and Carretero-González R. *Emergent Nonlinear Phenomena in Bose-Einstein Condensates: Theory and Experiment*. Berlin, Germany: Springer Science + Business Media (2007).
9. Chiao RY, Garmire E, and Townes CH. Self-trapping of Optical Beams. *Phys Rev Lett* (1964) 13:479–82. doi:10.1103/physrevlett.13.479
10. Kelley PL. Self-focusing of Optical Beams. *Phys Rev Lett* (1965) 15: 1005–1008. doi:10.1103/physrevlett.15.1005
11. Taniuti T, and Washimi H. Self-trapping and Instability of Hydromagnetic Waves along the Magnetic Field in a Cold Plasma. *Phys Rev Lett* (1968) 21: 209–212. doi:10.1103/physrevlett.21.209
12. Karpman VI, and Krushkal EM Modulated Waves in Nonlinear Dispersive Media. *Soviet Phys JETP* (1969) 28:277. doi:10.1007/3-540-46629-0_2
13. Taniuti T, and Yajima N. Perturbation Method for a Nonlinear Wave Modulation. I. *J Math Phys* (1969) 10:1369–1372. doi:10.1063/1.1664975
14. Asano N, Taniuti T, and Yajima N. Perturbation Method for a Nonlinear Wave Modulation. II. *J Math Phys* (1969) 10:2020–2024. doi:10.1063/1.1664797
15. Tappert FD, and Varma CM. Asymptotic Theory of Self-Trapping of Heat Pulses in Solids. *Phys Rev Lett* (1970) 25:1108–1111. doi:10.1103/physrevlett.25.1108
16. Benney DJ, and Newell AC The Propagation of Nonlinear Wave Envelopes. *J Math Phys* (1967) 46:133–139. doi:10.1002/sapm1967461133
17. Zakharov VE. Stability of Periodic Waves of Finite Amplitude on the Surface of a Deep Fluid. *J Appl Mech Tech Phys* (1968) 9:190–194. doi:10.1007/BF00913182
18. Hasimoto H, and Ono H. Nonlinear Modulation of Gravity Waves. *J Phys Soc Jpn* (1972) 33:805–811. doi:10.1143/jpsj.33.805
19. Gross EP. Structure of a Quantized Vortex in Boson Systems. *Il Nuovo Cimento* (1955–1965) 20:454–477. doi:10.1007/BF02731494
20. Pitaevskii LP. Vortex Lines in an Imperfect Bose Gas. *Soviet Phys JETP* (1961) 13:451–454.
21. Ginzburg VL, and Landau LD. *On the Theory of Superconductivity*. *On Superconductivity and Superfluidity*. Berlin Heilderberg, Germany: Springer (2009). 113–137.
22. Malomed BA. Nonlinear Schrödinger Equation. In: A Scott, editor. *Encyclopedia of Nonlinear Science*. New York, NY: Routledge (2005). 639–643.
23. Ablowitz M, and Prinari B. Nonlinear Schrodinger Systems: Continuous and Discrete. *Scholarpedia* (2008) 3:5561. doi:10.4249/scholarpedia.5561
24. Huang J. Nonlinear Schrödinger Equation. In: B Lembrikov, editor. *Nonlinear Optics: Novel Results in Theory and Applications*. London, UK and Rijeka, Croatia: IntechOpen (2018). 11–29.
25. Karjanto N. The Nonlinear Schrödinger Equation: A Mathematical Model with its Wide Range of Applications. In: V Simpao and H Little, editors. *Understanding the Schrödinger Equation: Some (Non)Linear Perspectives*. Hauppauge, New York: Nova Science Publishers (2020). 135–179. Accessible online at arXiv, preprint arXiv:1912.10683.

26. Fibich G. *The Nonlinear Schrödinger Equation: Singular Solutions and Optical Collapse*. Cham, Switzerland: Springer (2015).
27. Akhmediev NN, Eleonskiĭ VM, and Kulagin NE. Generation of Periodic Trains of Picosecond Pulses in an Optical Fiber: Exact Solutions. *Soviet Phys JETP* (1985) 62:894–899.
28. Akhmediev NN, and Korneev VI. Modulation Instability and Periodic Solutions of the Nonlinear Schrödinger Equation. *Theor Math Phys* (1986) 69:1089–1093. doi:10.1007/bf01037866
29. Akhmediev NN, Eleonskii VM, and Kulagin NE. Exact First-Order Solutions of the Nonlinear Schrödinger Equation. *Theor Math Phys* (1987) 72:809–818. doi:10.1007/bf01017105
30. Akhmediev NN, and Ankiewicz A. *Solitons: Nonlinear Pulses and Beams*. London, United Kingdom: Chapman & Hall (1997).
31. Hirota R. A New Form of Backlund Transformations and its Relation to the Inverse Scattering Problem. *Prog Theor Phys* (1974) 52:1498–1512. doi:10.1143/ptp.52.1498
32. Hirota R. Direct Method of Finding Exact Solutions of Nonlinear Evolution Equations. In: *Bäcklund Transformations, the Inverse Scattering Method, Solitons, and Their Applications*. *Lecture Notes in Mathematics*, 515. Berlin, Germany: Springer (1976). 40–68. doi:10.1007/bfb0081162
33. Hirota R, and Satsuma J. A Variety of Nonlinear Network Equations Generated from the Bäcklund Transformation for the Toda Lattice. *Prog Theor Phys Suppl* (1976) 59:64–100. doi:10.1143/ptps.59.64
34. Ablowitz MJ, and Herbst BM. On Homoclinic Structure and Numerically Induced Chaos for the Nonlinear Schrödinger Equation. *SIAM J Appl Math* (1990) 50:339–351. doi:10.1137/0150021
35. Zakharov VE, and Shabat AB. Exact Theory of Two-Dimensional Self-Focusing and One-Dimensional Self-Modulation of Waves in Nonlinear Media. *Soviet Phys JETP* (1972) 34:62.
36. Zakharov VE, and Shabat AB. Interaction between Solitons in a Stable Medium. *Soviet Phys JETP* (1973) 37:823–828.
37. Ablowitz MJ, and Segur H. *Solitons and the Inverse Scattering Transform*. Philadelphia, PA: SIAM (1981).
38. Osborne AR, Onorato M, and Serio M. The Nonlinear Dynamics of Rogue Waves and Holes in Deep-Water Gravity Wave Trains. *Phys Lett A* (2000) 275:386–393. doi:10.1016/s0375-9601(00)00575-2
39. Osborne AR. The Random and Deterministic Dynamics of 'Rogue Waves' in Unidirectional, Deep-Water Wave Trains. *Mar Structures* (2001) 14:275–293. doi:10.1016/s0951-8339(00)00064-2
40. Biondini G, and Kovačič G. Inverse Scattering Transform for the Focusing Nonlinear Schrödinger Equation with Nonzero Boundary Conditions. *J Math Phys* (2014) 55:031506. doi:10.1063/1.4868483
41. Olver PJ. *Applications of Lie Groups to Differential Equations*. 2nd ed. Berlin, Germany: Springer Science + Business Media (1993).
42. van Groesen E, A ndonowati, and Karjanto N. Displaced Phase-Amplitude Variables for Waves on Finite Background. *Phys Lett A* (2006) 354:312–319. doi:10.1016/j.physleta.2006.02.037
43. Karjanto N. *Mathematical Aspects of Extreme Water Waves (Enschede and Zutphen, the Netherlands: The University of Twente and Wöhrmann Print Service)*. [PhD thesis] (2006). Accessible online at arXiv, preprint arXiv: 2006.00766.
44. Karjanto N, and van Groesen E. Derivation of the NLS Breather Solutions Using Displaced Phase-Amplitude Variables. In: S Wahyuni, IE Wijayanti, and D Rosadi, editors. Proceedings of SEAMS-GMU Conference 2007. Indonesia: Applied Mathematics (Department of Mathematics, Gadjah Mada University (2007). 357–368. Accessible online at arXiv, preprint arXiv:1110.4704.
45. Demontis F, Prinari B, Van Der Mee C, and Vitale F. The Inverse Scattering Transform for the Focusing Nonlinear Schrödinger Equation with Asymmetric Boundary Conditions. *J Math Phys* (2014) 55:101505. doi:10.1063/1.4898768
46. Dysthe KB, and Trulsen K. Note on Breather Type Solutions of the NLS as Models for Freak-Waves. *Physica Scripta* (1999) T82:48. doi:10.1238/physica.topical.082a00048
47. Chow KW. A Class of Exact, Periodic Solutions of Nonlinear Envelope Equations. *J Math Phys* (1995a) 36:4125–4137. doi:10.1063/1.530951
48. Kuznetsov EA. Solitons in a Parametrically Unstable Plasma. *Akademiia Nauk SSSR Doklady* (1977) 236:575–577. English translation: *Soviet Physics Doklady* **22** (1977) 507–508.
49. Kuznetsov EA. *Personal Communication* (2020).
50. Kawata T, Inoue H, Adachihara H, McLaughlin DW, Moloney JV, and Newell AC. Solitary Waves as Fixed Points of Infinite-dimensional Maps for an Optical Bistable Ring Cavity: Analysis. *J Math Phys* (1988) 29:63–85. doi:10.1063/1.528136
51. Ma Y-C. The Perturbed Plane-Wave Solutions of the Cubic Schrödinger Equation. *Stud Appl Math* (1979) 60:43–58. doi:10.1002/sapm197960143
52. Kuznetsov EA, and Mikhailov AV. Stability of Stationary Waves in Nonlinear Weakly Dispersive Media. *Zhurnal Eksperimentalnoi I Teoreticheskoi Fiziki* ***67*** (1974). p. 1717–1727. English translation: *Soviet Physics JETP* **40**(2)1975855859.
53. Slunyaev A. Nonlinear Analysis and Simulations of Measured Freak Wave Time Series. *Eur J Mech - B/Fluids* (2006) 25:621–635. doi:10.1016/j.euromechflu.2006.03.005
54. Kibler B, Fatome J, Finot C, Millot G, Genty G, Wetzel B, et al. Observation of Kuznetsov-Ma Soliton Dynamics in Optical Fibre. *Scientific Rep* (2012) 2:463. doi:10.1038/srep00463
55. Grimshaw R, Pelinovsky D, Pelinovsky E, and Talipova T. Wave Group Dynamics in Weakly Nonlinear Long-Wave Models. *Physica D: Nonlinear Phenomena* (2001) 159:35–57. doi:10.1016/s0167-2789(01)00333-5
56. Gagnon L. Solitons on a Continuous-Wave Background and Collision between Two Dark Pulses: Some Analytical Results. *J Opt Soc Am B* (1993) 10:469–74. doi:10.1364/josab.10.000469
57. Adachihara H, McLaughlin DW, Moloney JV, and Newell AC. Solitary Waves as Fixed Points of Infinite-dimensional Maps for an Optical Bistable Ring Cavity: Analysis. *J Math Phys* (1988) 29:63–85. doi:10.1063/1.528136
58. Mihalache D, Lederer F, and Baboiu D-M. Two-parameter Family of Exact Solutions of the Nonlinear Schrödinger Equation Describing Optical-Soliton Propagation. *Phys Rev A* (1993) 47:3285–3290. doi:10.1103/physreva.47.3285
59. Clamond D, Francius M, Grue J, and Kharif C. Long Time Interaction of Envelope Solitons and Freak Wave Formations. *Eur J Mech - B/Fluids* (2006) 25:536–553. doi:10.1016/j.euromechflu.2006.02.007
60. Onorato M, Residori S, Bortolozzo U, Montina A, and Arecchi FT. Rogue Waves and Their Generating Mechanisms in Different Physical Contexts. *Phys Rep* (2013) 528:47–89. doi:10.1016/j.physrep.2013.03.001
61. Chabchoub A, Kibler B, Dudley JM, and Akhmediev N. Hydrodynamics of Periodic Breathers. *Phil Trans R Soc A* (2014) 372:20140005. doi:10.1098/rsta.2014.0005
62. Residori S, Onorato M, Bortolozzo U, and Arecchi FT. Rogue Waves: a Unique Approach to Multidisciplinary Physics. *Contemp Phys* (2017) 58:53–69. doi:10.1080/00107514.2016.1243351
63. Akhmediev NN, and Wabnitz S. Phase Detecting of Solitons by Mixing with a Continuous-Wave Background in an Optical Fiber. *J Opt Soc Am B* (1992) 9:236–242. doi:10.1364/josab.9.000236
64. Kharif C, Pelinovsky E, Talipova T, and Slunyaev A. Focusing of Nonlinear Wave Groups in Deep Water. *JETP Lett* (2001) 73:170–175. doi:10.1134/1.1368708
65. Garnier J, and Kalimeris K. Inverse Scattering Perturbation Theory for the Nonlinear Schrödinger Equation with Non-vanishing Background. *J Phys A: Math Theor* (2011) 45:035202. doi:10.1088/1751-8113/45/3/035202
66. Xiong H, Gan J, and Wu Y. Kuznetsov-Ma Soliton Dynamics Based on the Mechanical Effect of Light. *Phys Rev Lett* (2017) 119:153901. doi:10.1103/physrevlett.119.153901
67. Cuevas-Maraver J, Kevrekidis PG, Frantzeskakis DJ, Karachalios NI, Haragus M, and James G. Floquet Analysis of Kuznetsov-Ma Breathers: A Path towards Spectral Stability of Rogue Waves. *Phys Rev E* (2017) 96:012202. doi:10.1103/physreve.96.012202
68. Zhao LC, Ling L, and Yang ZY. Mechanism of Kuznetsov-Ma Breathers. *Phys Rev E* (2018) 97:022218. doi:10.1103/physreve.97.022218
69. Gelash A. Formation of Rogue Waves from a Locally Perturbed Condensate. *Phys Rev E* (2018) 97:022208. doi:10.1103/physreve.97.022208
70. Bélanger N, and Bélanger P-A. Bright Solitons on a CW Background. *Opt Commun* (1996) 124:301–308. doi:10.1016/0030-4018(95)00659-1
71. Tajiri M, and Watanabe Y. Breather Solutions to the Focusing Nonlinear Schrödinger Equation. *Phys Rev E* (1998) 57:3510–3519. doi:10.1103/physreve.57.3510
72. Chow KW. Solitary Waves on a Continuous Wave Background. *J Phys Soc Jpn* (1995) 64:1524–1528. doi:10.1143/jpsj.64.1524

73. Rajaraman R. *Solitons and Instantons: An Introduction to Solitons and Instantons in Quantum Field Theory*. Amsterdam, Netherlands: Elsevier/North Holland (1982).
74. Falkovich G, Kolokolov I, Lebedev V, and Migdal A. Instantons and Intermittency. *Phys Rev E* (1996) 54:4896–907. doi:10.1103/physreve.54.4896
75. Turitsyn SK, Bale BG, and Fedoruk MP. Dispersion-managed Solitons in Fibre Systems and Lasers. *Phys Rep* (2012) 521:135–203. doi:10.1016/j.physrep.2012.09.004
76. Calini A, and Schober CM. Homoclinic Chaos Increases the Likelihood of Rogue Wave Formation. *Phys Lett A* (2002) 298:335–349. doi:10.1016/s0375-9601(02)00576-5
77. Onorato M, Osborne AR, Serio M, and Damiani T. Occurrence of Freak Waves from Envelope Equations in Random Ocean Wave Simulations. In: *Rogue Waves 2000*. editors M Olagnon and M Prevosto, (Brest, France: IFREMER, French Research Institute for Exploitation of the Sea). (2001). 11.
78. Karjanto N, van Groesen E, and Peterson P. Investigation of the Maximum Amplitude Increase from the Benjamin-Feir Instability. *J Indonesian Math Soc* (2002) 8:39.
79. Akhmediev N, Ankiewicz A, and Taki M. Waves that Appear from Nowhere and Disappear without a Trace. *Phys Lett A* (2009) 373:675–678. doi:10.1016/j.physleta.2008.12.036
80. Onorato M, Proment D, and Toffoli A. Triggering Rogue Waves in Opposing Currents. *Phys Rev Lett* (2011) 107:184502. doi:10.1103/physrevlett.107.184502
81. Slunyaev AV, and Shrira VI. On the Highest Non-breaking Wave in a Group: Fully Nonlinear Water Wave Breathers versus Weakly Nonlinear Theory. *J Fluid Mech* (2013) 735:203–248. doi:10.1017/jfm.2013.498
82. Bespalov VI, and Talanov VI. Filamentary Structure of Light Beams in Nonlinear Liquids. *Soviet Phys JETP Lett* (1966) 3:307–312.
83. Ostrovskii L. Propagation of Wave Packets and Space-Time Self-Focusing in a Nonlinear Medium. *Soviet Phys JETP* (1967) 24:797–800.
84. Karpman VI. Self-modulation of Nonlinear Plane Waves in Dispersive Media. *JETP Lett* (1967) 6:277.
85. Benjamin TB, and Feir JE. The Disintegration of Wave Trains on Deep Water Part 1. Theory. *J Fluid Mech* (1967) 27:417–30. doi:10.1017/s002211206700045x
86. Tam CKW. Amplitude Dispersion and Nonlinear Instability of Whistlers. *Phys Fluids* (1969) 12:1028–1035. doi:10.1063/1.2163663
87. Hasegawa A. Observation of Self-Trapping Instability of a Plasma Cyclotron Wave in a Computer Experiment. *Phys Rev Lett* (1970) 24:1165–1168. doi:10.1103/physrevlett.24.1165
88. Hasegawa A. Theory and Computer Experiment on Self-Trapping Instability of Plasma Cyclotron Waves. *Phys Fluids* (1972) 15:870–881. doi:10.1063/1.1693996
89. Robins NP, Zhang W, Ostrovskaya EA, and Kivshar YS. Modulational Instability of Spinor Condensates. *Phys Rev A* (2001) 64:021601. doi:10.1103/physreva.64.021601
90. Konotop V, and Salerno M. Modulational Instability in Bose-Einstein Condensates in Optical Lattices. *Phys Rev A* (2002) 65:021602. doi:10.1103/physreva.65.021602
91. Smerzi A, Trombettoni A, Kevrekidis P, and Bishop A. Dynamical Superfluid-Insulator Transition in a Chain of Weakly Coupled Bose-Einstein Condensates. *Phys Rev Lett* (2002) 89:170402. doi:10.1103/physrevlett.89.170402
92. Baizakov BB, Konotop VV, and Salerno M. Regular Spatial Structures in Arrays of Bose Einstein Condensates Induced by Modulational Instability. *J Phys B: Mol Opt Phys* (2002) 35:5105–5119. doi:10.1088/0953-4075/35/24/312
93. Salasnich L, Parola A, and Reatto L Modulational Instability and Complex Dynamics of Confined Matter-Wave Solitons. *Phys Rev Lett* (2003) 91:080405. doi:10.1103/physrevlett.91.080405
94. Theocharis G, Rapti Z, Kevrekidis P, Frantzeskakis D, and Konotop V. Modulational Instability of Gross-Pitaevskii-type Equations in 1 + 1 Dimensions. *Phys Rev A* (2003) 67:063610. doi:10.1103/physreva.67.063610
95. Lighthill MJ. Contributions to the Theory of Waves in Non-linear Dispersive Systems. *IMA J Appl Math* (1965) 1:269–306. doi:10.1093/imamat/1.3.269
96. Zakharov VE, and Ostrovsky LA. Modulation Instability: The Beginning. *Physica D: Nonlinear Phenomena* (2009) 238:540–548. doi:10.1016/j.physd.2008.12.002
97. Yuen HC, and Lake BM. Nonlinear Deep Water Waves: Theory and Experiment. *Phys Fluids* (1975) 18:956–960. doi:10.1063/1.861268
98. Lake BM, Yuen HC, Rungaldier H, and Ferguson WE. Nonlinear Deep-Water Waves: Theory and Experiment. Part 2. Evolution of a Continuous Wave Train. *J Fluid Mech* (1977) 83:49–74. doi:10.1017/s0022112077001037
99. Yuen HC, and Ferguson WE, Jr. Relationship between Benjamin-Feir Instability and Recurrence in the Nonlinear Schrödinger Equation. *Phys Fluids* (1978a) 21:1275–1278. doi:10.1063/1.862394
100. Yuen HC, and Ferguson WE, Jr. Fermi-Pasta-Ulam Recurrence in the Two-Space Dimensional Nonlinear Schrödinger Equation. *Phys Fluids* (1978b) 21:2116–2118. doi:10.1063/1.862122
101. Yuen HC, and Lake BM. Instabilities of Waves on Deep Water. *Annu Rev Fluid Mech* (1980) 12:303–334. doi:10.1146/annurev.fl.12.010180.001511
102. Fermi E, Pasta P, Ulam S, and Tsingou M. *Studies of the Nonlinear Problems*. Technical Report No. LA-1940. New Mexico: Los Alamos Scientific Laboratory (1955). doi:10.2172/4376203
103. Janssen PAEM. Modulational Instability and the Fermi-Pasta-Ulam Recurrence. *Phys Fluids* (1981) 24:23–26. doi:10.1063/1.863242
104. Van Simaeys G, Emplit P, and Haelterman M. Experimental Demonstration of the Fermi-Pasta-Ulam Recurrence in a Modulationally Unstable Optical Wave. *Phys Rev Lett* (2001) 87:033902. doi:10.1103/physrevlett.87.033902
105. Janssen PAEM. Nonlinear Four-Wave Interactions and Freak Waves. *J Phys Oceanogr* (2003) 33:863–884. doi:10.1175/1520-0485(2003)33863
106. Dysthe K, Krogstad HE, and Müller P. Oceanic Rogue Waves. *Annu Rev Fluid Mech* (2008) 40:287–310. doi:10.1146/annurev.fluid.40.111406.102203
107. Kharif C, Pelinovsky E, and Slunyaev A. *Rogue Waves in the Ocean*. Berlin, Germany: Springer Science + Business Media (2009).
108. Slunyaev A, Kharif C, Pelinovsky E, and Talipova T. Nonlinear Wave Focusing on Water of Finite Depth. *Physica D: Nonlinear Phenomena* (2002) 173:77–96. doi:10.1016/s0167-2789(02)00662-0
109. Biondini G, and Fagerstrom E. The Integrable Nature of Modulational Instability. *SIAM J Appl Math* (2015) 75:136–163. doi:10.1137/140965089
110. Huijsmans RH, Klopman G, Karjanto N, and Andonowati. Experiments on Extreme Wave Generation Using the Soliton on Finite Background. in *Rogue Waves 2004* (Brest, France: IFREMER, French Research Institute for Exploitation of the Sea) editors M. Olagnon and M. Prevosto. (2005). 10. Accessible online at arXiv, preprint arXiv:1110.5119
111. van Groesen E, Andonowati, and Karjanto N. Deterministic Aspects of Nonlinear Modulation Instability. in *Rogue Waves 2004* (Brest, France: IFREMER, French Research Institute for Exploitation of the Sea) editors. M Olagnon and M Prevosto. (2005). 12. Accessible online at arXiv, preprint arXiv:1110.5120
112. Andonowati, Karjanto N, and van Groesen E. Extreme Wave Phenomena in Down-Stream Running Modulated Waves. *Appl Math Model* (2007) 31:1425–1443. doi:10.1016/j.apm.2006.04.015
113. Karjanto N, and van Groesen E. Qualitative Comparisons of Experimental Results on Deterministic Freak Wave Generation Based on Modulational Instability. *J Hydro-environment Res* (2010) 3:186–192. doi:10.1016/j.jher.2009.10.008
114. Karjanto N, and van Groesen E. Note on Wavefront Dislocation in Surface Water Waves. *Phys Lett A* (2007b) 371:173–179. doi:10.1016/j.physleta.2007.06.064
115. Akhmediev N, Soto-Crespo JM, and Ankiewicz A. Extreme Waves that Appear from Nowhere: on the Nature of Rogue Waves. *Phys Lett A* (2009) 373:2137–2145. doi:10.1016/j.physleta.2009.04.023
116. Chabchoub A, Vitanov N, and Hoffmann N. Experimental Evidence for Breather Type Dynamics in Freak Waves. *Proc Appl Math Mech* (2010) 10:495–496. doi:10.1002/pamm.201010240
117. Dudley JM, Genty G, Dias F, Kibler B, and Akhmediev N. Modulation Instability, Akhmediev Breathers and Continuous Wave Supercontinuum Generation. *Opt Express* (2009) 17:21497–21508. doi:10.1364/oe.17.021497
118. Erkintalo M, Hammani K, Kibler B, Finot C, Akhmediev N, Dudley JM, et al. Higher-order Modulation Instability in Nonlinear Fiber Optics. *Phys Rev Lett* (2011) 107:253901. doi:10.1103/physrevlett.107.253901
119. Kedziora DJ, Ankiewicz A, and Akhmediev N. Second-order Nonlinear Schrödinger Equation Breather Solutions in the Degenerate and Rogue Wave Limits. *Phys Rev E* (2012) 85:066601. doi:10.1103/physreve.85.066601
120. Karjanto N, and van Groesen E. Mathematical Physics Properties of Waves on Finite Background. In: SP Lang and SH Bedore, editors. *Handbook of Solitons: Research, Technology and Applications*. Hauppauge, NY: Nova Science Publishers) (2009). 501–539.
121. Branger H, Chabchoub A, Hoffmann N, Kimmoun O, Kharif C, and Akhmediev N. Evolution of a Peregrine Breather: Analytical and Experimental Studies. In: Presented in the 13th Hydrodynamics Days (Saint-Venant Hydrodynamic Laboratory, Île des Impressionnistes, Chatou, Seine River. France): Yvelines department, Île-de-France region

(2012). 12. The typographical error contained in the English version of the title has been corrected in this reference.
122. Chabchoub A, Hoffmann N, Onorato M, and Akhmediev N. Super Rogue Waves: Observation of a Higher-Order Breather in Water Waves. *Phys Rev X* (2012) 2:011015. doi:10.1103/physrevx.2.011015
123. Calini A, and Schober CM. Observable and Reproducible Rogue Waves. *J Opt* (2013) 15:105201. doi:10.1088/2040-8978/15/10/105201
124. Ling L, and Zhao LC. Simple Determinant Representation for Rogue Waves of the Nonlinear Schrödinger Equation. *Phys Rev E* (2013) 88:043201. doi:10.1103/physreve.88.043201
125. Dudley JM, Dias F, Erkintalo M, and Genty G. Instabilities, Breathers and Rogue Waves in Optics. *Nat Photon* (2014) 8:755–764. doi:10.1038/nphoton.2014.220
126. Chabchoub A, and Fink M. Time-reversal Generation of Rogue Waves. *Phys Rev Lett* (2014) 112:124101. doi:10.1103/physrevlett.112.124101
127. Bilman D, and Miller PD. A Robust Inverse Scattering Transform for the Focusing Nonlinear Schrödinger Equation. *Comm Pure Appl Math* (2019) 72:1722–1805. doi:10.1002/cpa.21819
128. Peregrine DH. Water Waves, Nonlinear Schrödinger Equations and Their Solutions. *J Aust Math Soc Ser B, Appl. Math* (1983) 25:16–43. doi:10.1017/s0334270000003891
129. Johnson RS. *A Modern Introduction to the Mathematical Theory of Water Waves*. Cambridge, United Kingdom: Cambridge University Press (1997).
130. Henderson KL, Peregrine DH, and Dold JW. Unsteady Water Wave Modulations: Fully Nonlinear Solutions and Comparison with the Nonlinear Schrödinger Equation. *Wave Motion* (1999) 29:341–361. doi:10.1016/s0165-2125(98)00045-6
131. Nakamura A, and Hirota R A. New Example of Explode-Decay Solitary Waves in One-Dimension. *J Phys Soc Jpn* (1985) 54:491–499. doi:10.1143/jpsj.54.491
132. Yan Z. Nonautonomous "rogons" in the Inhomogeneous Nonlinear Schrödinger Equation with Variable Coefficients. *Phys Lett A* (2010) 374:672–679. doi:10.1016/j.physleta.2009.11.030
133. Shrira VI, and Geogjaev VV. What Makes the Peregrine Soliton So Special as a Prototype of Freak Waves? *J Eng Math* (2010) 67:11–22. doi:10.1007/s10665-009-9347-2
134. Voronovich VV, Shrira VI, and Thomas G. Can Bottom Friction Suppress "Freak Wave" Formation? *J Fluid Mech* (2008) 604:263–296. doi:10.1017/s0022112008001171
135. Klein C, and Haragus M. Numerical Study of the Stability of the Peregrine Solution. *Ann Math Sci Appl* (2017) 2:217–239. doi:10.4310/amsa.2017.v2.n2.a1
136. Muñoz C Instability in Nonlinear Schrödinger Breathers. *Proyecciones* (2017) 36:653–683. doi:10.4067/s0716-09172017000400653
137. Calini A, Schober CM, and Strawn M. Linear Instability of the Peregrine Breather: Numerical and Analytical Investigations. *Appl Numer Math* (2019) 141:36–43. doi:10.1016/j.apnum.2018.11.005
138. Klein C, and Stoilov N. Numerical Study of the Transverse Stability of the Peregrine Solution. *Stud Appl Math* (2020) 145:36–51. doi:10.1111/sapm.12306
139. Kibler B, Fatome J, Finot C, Millot G, Dias F, Genty G, et al. The Peregrine Soliton in Nonlinear Fibre Optics. *Nat Phys* (2010) 6:790–795. doi:10.1038/nphys1740
140. Chabchoub A, Hoffmann NP, and Akhmediev N. Rogue Wave Observation in a Water Wave Tank. *Phys Rev Lett* (2011) 106:204502. doi:10.1103/physrevlett.106.204502
141. Bailung H, Sharma SK, and Nakamura Y. Observation of Peregrine Solitons in a Multicomponent Plasma with Negative Ions. *Phys Rev Lett* (2011) 107:255005. doi:10.1103/physrevlett.107.255005
142. Chabchoub A, Akhmediev N, and Hoffmann N. Experimental Study of Spatiotemporally Localized Surface Gravity Water Waves. *Phys Rev E* (2012) 86:016311. doi:10.1103/physreve.86.016311
143. Shemer L, and Alperovich L. Peregrine Breather Revisited. *Phys Fluids* (2013) 25:051701. doi:10.1063/1.4807055
144. Chabchoub A, Hoffmann N, Branger H, Kharif C, and Akhmediev N. Experiments on Wind-Perturbed Rogue Wave Hydrodynamics Using the Peregrine Breather Model. *Phys Fluids* (2013) 25:101704. doi:10.1063/1.4824706
145. Onorato M, Proment D, Clauss G, and Klein M. Rogue Waves: From Nonlinear Schrödinger Breather Solutions to Sea-Keeping Test. *PLOS One* (2013) 8:e54629. doi:10.1371/journal.pone.0054629
146. Yurova A. A Hidden Life of Peregrine's Soliton: Rouge Waves in the Oceanic Depths. *Int J Geom Methods Mod Phys* (2014) 11:1450057. doi:10.1142/s0219887814500571
147. Li S, Prinari B, and Biondini G. Solitons and Rogue Waves in Spinor Bose-Einstein Condensates. *Phys Rev E* (2018) 97:022221. doi:10.1103/physreve.97.022221
148. Cazaubiel A, Michel G, Lepot S, Semin B, Aumaître S, Berhanu M, et al. Coexistence of Solitons and Extreme Events in Deep Water Surface Waves. *Phys Rev Fluids* (2018) 3:114802. doi:10.1103/physrevfluids.3.114802
149. Randoux S, Suret P, Chabchoub A, Kibler B, and El G. Nonlinear Spectral Analysis of Peregrine Solitons Observed in Optics and in Hydrodynamic Experiments. *Phys Rev E* (2018) 98:022219. doi:10.1103/physreve.98.022219
150. Gaillard P. Multi-parametric Deformations of Peregrine Breathers Solutions to the NLS Equation. *Adv Res* (2015) 4:346–364. doi:10.9734/air/2015/16827
151. Akhmediev N, Ankiewicz A, and Soto-Crespo JM. Rogue Waves and Rational Solutions of the Nonlinear Schrödinger Equation. *Phys Rev E* (2009c) 80:026601. doi:10.1103/physreve.80.026601
152. Chen S, Baronio F, Soto-Crespo JM, Grelu P, and Mihalache D. Versatile Rogue Waves in Scalar, Vector, and Multidimensional Nonlinear Systems. *J Phys A: Math Theor* (2017) 50:463001. doi:10.1088/1751-8121/aa8f00
153. Malomed BA, and Mihalache D. Nonlinear Waves in Optical and Matter-Wave Media: A Topical Survey of Recent Theoretical and Experimental Results. *Rom J Phys* (2019) 64:106.
154. Zhao L-C, and Ling L. Quantitative Relations between Modulational Instability and Several Well-Known Nonlinear Excitations. *J Opt Soc Am B* (2016) 33:850–856. doi:10.1364/josab.33.000850
155. Toenger S, Godin T, Billet C, Dias F, Erkintalo M, Genty G, et al. Emergent Rogue Wave Structures and Statistics in Spontaneous Modulation Instability. *Scientific Rep* (2015) 5:10380. doi:10.1038/srep10380
156. Kibler B, Chabchoub A, Gelash A, Akhmediev N, and Zakharov VE. Superregular Breathers in Optics and Hydrodynamics: Omnipresent Modulation Instability beyond Simple Periodicity. *Phys Rev X* (2015) 5:041026. doi:10.1103/physrevx.5.041026
157. Liu XS, Zhao LC, Duan L, Gao P, Yang ZY, and Yang WL. Interaction between Breathers and Rogue Waves in a Nonlinear Optical Fiber. *Chin Phys Lett* (2018) 35:020501. doi:10.1088/0256-307x/35/2/020501
158. Veldes G, Borhanian J, McKerr M, Saxena V, Frantzeskakis D, and Kourakis I. Electromagnetic Rogue Waves in Beam-Plasma Interactions. *J Opt* (2013) 15:064003. doi:10.1088/2040-8978/15/6/064003
159. Shen Y, Kevrekidis P, Veldes G, Frantzeskakis D, DiMarzio D, Lan X, et al. From Solitons to Rogue Waves in Nonlinear Left-Handed Metamaterials. *Phys Rev E* (2017) 95:032223. doi:10.1103/physreve.95.032223
160. Albares P, Díaz E, Cerveró JM, Domínguez-Adame F, Diez E, and Estévez P. Solitons in a Nonlinear Model of Spin Transport in Helical Molecules. *Phys Rev E* (2018) 97:022210. doi:10.1103/physreve.97.022210
161. Farazmand M, and Sapsis TP. Extreme Events: Mechanisms and Prediction. *Appl Mech Rev* (2019) 71. doi:10.1115/1.4042065
162. Zhang Y, Belić MR, Zheng H, Chen H, Li C, Song J, et al. Nonlinear Talbot Effect of Rogue Waves. *Phys Rev E* (2014) 89:032902. doi:10.1103/physreve.89.032902
163. Akhmediev N, Kibler B, Baronio F, Belić M, Zhong WP, Zhang Y, et al. Roadmap on Optical Rogue Waves and Extreme Events. *J Opt* (2016) 18:063001. doi:10.1088/2040-8978/18/6/063001
164. Kimmoun O, Hsu H, Branger H, Li M, Chen YY, Kharif C, et al. Modulation Instability and Phase-Shifted Fermi-Pasta-Ulam Recurrence. *Scientific Rep* (2016) 6:28516. doi:10.1038/srep28516
165. Biondini G, and Mantzavinos D. Universal Nature of the Nonlinear Stage of Modulational Instability. *Phys Rev Lett* (2016) 116:043902. doi:10.1103/physrevlett.116.043902
166. Biondini G, Li S, and Mantzavinos D Oscillation Structure of Localized Perturbations in Modulationally Unstable Media. *Phys Rev E* (2016) 94:060201. doi:10.1103/physreve.94.060201
167. Gelash AA, and Zakharov VE. Superregular Solitonic Solutions: a Novel Scenario for the Nonlinear Stage of Modulation Instability. *Nonlinearity* (2014) 27:R1–38. doi:10.1088/0951-7715/27/4/r1
168. Chen J, and Pelinovsky DE. Rogue Periodic Waves of the Focusing Nonlinear Schrödinger Equation. *Proc R Soc A* (2018) 474:20170814. doi:10.1098/rspa.2017.0814
169. Xu G, Gelash A, Chabchoub A, Zakharov V, and Kibler B. Breather Wave Molecules. *Phys Rev Lett* (2019) 122:084101. doi:10.1103/physrevlett.122.084101

170. El-Tantawy S, Wazwaz A, and Ali Shan S. On the Nonlinear Dynamics of Breathers Waves in Electronegative Plasmas with Maxwellian Negative Ions. *Phys Plasmas* (2017) 24:022105. doi:10.1063/1.4975090

Conflict of Interest: The author declares that the research was conducted in the absence of any commercial or financial relationships that could be construed as a potential conflict of interest.

Publisher's Note: All claims expressed in this article are solely those of the authors and do not necessarily represent those of their affiliated organizations, or those of the publisher, the editors and the reviewers. Any product that may be evaluated in this article, or claim that may be made by its manufacturer, is not guaranteed or endorsed by the publisher.

frontiers | Frontiers in Physics

ORIGINAL RESEARCH
published: 08 July 2022
doi: 10.3389/fphy.2021.611797

Role of Homoclinic Breathers in the Interpretation of Experimental Measurements, With Emphasis on the Peregrine Breather

Alfred R. Osborne *

Nonlinear Waves Research Corporation, Alexandria, VA, United States

A class of generalized homoclinic solutions of the nonlinear Schrödinger (NLS) equation in 1+1 dimensions is studied. These are homoclinic breathers that are shown to be derivable from the ratio of Riemann theta functions for the genus-2 solutions of the nonlinear Schrödinger equation. We discuss how these solutions behave in the homoclinic limit for which a fundamental parameter ε goes to zero, $\varepsilon \to 0$ (such that two points of simple spectrum converge to double points at some particular lambda-plane eigenvalue). The homoclinic solutions cover the entire lambda plane (the Riemann surface of the NLS equation) and are given in terms of simple trigonometric functions. When the spectral eigenvalues converge to the carrier amplitude in the lambda plane we have the Peregrine breather. While the Peregrine solution is often called a soliton, it is in reality a breather, albeit occurring at the "singular point" corresponding to the carrier eigenvalue in the lambda plane and consequently "breathes" only once in its lifetime. The Peregrine breather separates small-amplitude modulations below the carrier from large amplitude modulation above the carrier. This fact means that the Peregrine breather has a "central" role in the lambda plane characterization of the NLS nonlinear spectrum. The Akhmediev breather occurs somewhat below the carrier (and is therefore a small-amplitude modulation) and the Kuznetsov-Ma breather occurs above the carrier (and is therefore a large-amplitude modulation). The general homoclinic solutions can be constructed everywhere in the lambda plane and are shown to be a useful tool to interpret the nonlinear Fourier spectrum of space and time series recorded in the laboratory and ocean environment. Nonlinear filtering is suggested as a way to extract breather trains from experimental time series. The generalized homoclinic breathers can be thought of as "extreme wave packets" or "rogue wave" solutions of water waves for scientific and engineering applications in various fields of physics including physical oceanography and nonlinear optics.

Keywords: nonlinear Schrödinger equation, homoclinic solutions, Akhmediev breather, Peregrine breather, Kuznetsov-Ma breather, rogue waves, freak waves

OPEN ACCESS

Edited by:
Amin Chabchoub,
The University of Sydney, Australia

Reviewed by:
Nail Akhmediev,
Australian National University, Australia
Xing Lu,
Beijing Jiaotong University, China

***Correspondence:**
Alfred R. Osborne
alosborne@protonmail.com

Specialty section:
This article was submitted to Mathematical and Statistical Physics, a section of the journal Frontiers in Physics

Received: *29 September 2020*
Accepted: *30 April 2021*
Published: *08 July 2022*

Citation:
Osborne AR (2022) Role of Homoclinic Breathers in the Interpretation of Experimental Measurements, With Emphasis on the Peregrine Breather. Front. Phys. 9:611797. doi: 10.3389/fphy.2021.611797

INTRODUCTION

The nonlinear Schrödinger equation in one-space and one-time dimensions (1+1) has been a useful, but simple model for the study of nonlinear waves in many fields of study, including physical oceanography, ocean engineering and nonlinear optics [1–6]. The general periodic/quasiperiodic solutions of NLS equation consist of ratios of Riemann theta functions that have differing phases [7–9]. The general Riemann (nonlinear) spectrum is described parametrically by the Riemann matrix. The diagonal elements of the Riemann matrix are the Stokes wave solutions of NLS and the off-diagonal elements describe the interactions among Stokes waves. When spectral components have a Benjamin-Feir parameter greater than one, then two Stokes modes will phase lock with one another, thereby creating a breather, i.e., a wave packet that "breathes" up and down during its evolution. The maximum amplitude of a breather during its nonlinear motion has a central enhanced carrier wave that is often referred to as a "rogue" or "freak" wave. The work of Peregrine identified one particular breather of exceptional simplicity: The ratio of two low degree polynomials. Peregrine called such solutions "sudden steep events" although the field of nonlinear waves has chosen the term "breathers" instead, due to the naming convention used in early theoretical work (see for example [10]). The field has grown tremendously in the past 30 years because it has captured the imagination of a large number of investigators interested in freak wave behavior in ocean waves and in nonlinear optics.

There are a large number of "coherent structures" in the nonlinear Schrödinger equation. For example in shallow water there are Stokes waves, dark solitons and "ghost" or "fossil" wave packets. In deep water there are also Stokes waves, bright solitons and breathers. Deep-water breathers are essentially phase-locked Stokes waves or solitons. The general solutions of the Schrödinger equation are determined from the ratio of multidimensional Riemann theta functions and these solutions contain all of the special cases of coherent structures just mentioned. Furthermore, it is known that the multidimensional theta function solutions can be reduced to the so-called *N*-soliton limit of NLS equation. How then does the Peregrine breather fit into all of this mathematical physics? The answer is that the above multidimensional solutions can be reduced to the so-called general homoclinic solutions, which occur in the soliton limit, by introducing periodic/quasiperiodic boundary conditions. The general homoclinic solutions can then be reduced to the Akhmediev, Peregrine and Kuznetzov-Ma breathers as special cases. Of course there is a continuous range of homoclinic solutions that provide a broad spectrum of breathers. Experimentally, if one is studying a quasiperiodic, multidimensional simulation or space/time series measurement of ocean waves, then it is not easy to pick out by eye from a seemingly random wave train what the actual coherent modes are. This has lead to a guessing game of trying to decide what particular modes are present in a selected time series measurement. This conundrum has led to the implementation of nonlinear Fourier methods for analyzing data [5], [11–13]. While details of this latter topic are treated elsewhere, the main goal of the present paper is to discuss the role that coherent structures play in solutions of the NLS equation and in the analysis of data. In this way one is able to identify their particular spectral signature in the nonlinear Fourier scheme, thus enabling experimentalists to better understand the physics of coherent structures in measured ocean waves.

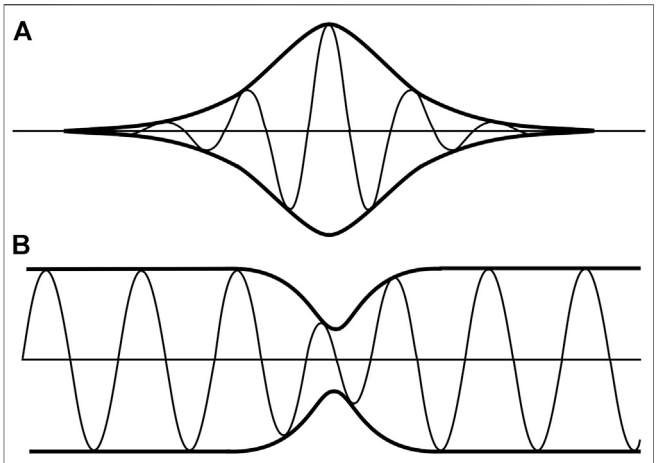

FIGURE 1 | (A) A deep water envelope or bright soliton of the NLS equation (the thin line is the surface wave elevation and the thick line is the modulus of the envelope of NLS equation) and **(B)** a shallow water dark soliton (where the thin line is the surface elevation and the thick line is the modulus of the envelope of NLS equation).

The goal of this paper is to investigate a large general class of rogue wave breather solutions previously studied by [14, 15] and how they can be derived from Riemann theta functions. Herein I describe a simple breather solution that parametrically depends on a single eigenvalue that lies on the imaginary axis of the Riemann spectrum or so-called lambda plane (the Riemann surface) of the 1+1 NLS equation. Three particular eigenvalues give the most well known breathers used in the field today and due to [16, 17]; and [14, 18].

The results given herein have implications on the modern theoretical and experimental study of coherent structures and breather trains in both one and two dimensions. Recent exciting studies of nonlinear waves and their coherent properties for the ocean and laboratory have been made by a number of authors, including [5], [11], [19–26]. A central goal of this paper is to show how to use generalized homoclinic solutions to analyze space/time series data together with the Zakharov-Shabat eigenvalue problem, as described by Osborne and co-workers [5], [11], [12].

INTEGRABILITY AND COHERENT STRUCTURES FOR 1D WATER WAVES

We consider water wave solutions of the nonlinear Schrödinger (NLS) equation

$$iu_t + u_{xx} + 2\sigma|u|^2 u = 0 \tag{1}$$

The parameter σ sigma can be ± 1. The plus sign ($\sigma = +1$) occurs for deep-water waves such that $kh > 1.363$ where the modulational instability exists and the Benjamin-Feir instability governs the nonlinear wave dynamics. In shallow

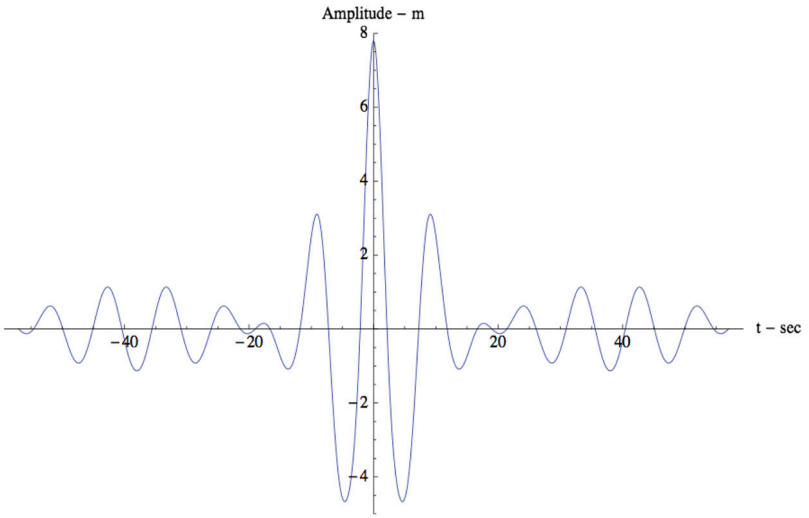

FIGURE 2 | Breather solution of the nonlinear Schrödinger equation at the moment when it reaches maximum amplitude.

water ($\sigma = -1$, where $kh < 1.363$) the wave solutions are always stable. Detailed discussions of the NLS equation in terms of the theory of the inverse scattering method are given elsewhere [27], [9] (applications to ocean waves are given in [5]).

NLS equation has well-known coherent structures including Stokes waves, bright solitons, dark solitons and breathers. From the point of view of the mathematical physics a single Stokes wave or soliton is a genus-1 solution of the nonlinear Schrödinger equation. Cases for bright and dark solitons are shown in **Figure 1**. The bright soliton solutions are associated with infinite line boundary conditions, while the dark solution solutions are related to a finite condition at infinity (or periodic boundary conditions). Thus Stokes waves are single-degree of freedom solutions and for the increasing nonlinear limit they morph these into soliton solutions (for the periodicity requirement often used in the study of water waves means that soliton trains are a feature of the method). Breathers are formed from the phase locking of two Stokes waves in the genus-2 case, an example of which is shown in **Figure 2**.

Of course a great deal of effort has been made to determine if the methods of soliton physics can be useful in the study of coherent structures in ocean waves. This is an important issue because the usual paradigm for nonlinear ocean waves is that for the 4-wave interactions where ocean waves are assumed to be weakly interacting sine waves. Thus a new approach, which is able to determine the behavior of nonlinear ocean waves from the point of view of their coherent structures, is a significant step beyond current understanding of quasilinear methods. Of course one has to extend the approach beyond one dimension to the two-dimensional equations such as NLS and its subsequent orders of approximation [28–31] equations. We are focused here on the 1D case where we attempt to bring together the complete set of ideas with regard to both infinite-line boundary conditions and periodic boundary conditions for the NLS equation. We are interested in the Stokes waves, soliton and breather solutions of the equation. Thus considerations with regard to infinite-line inverse scattering theory and the periodic solutions of inverse scattering theory are addressed. Why study IST? Because it provides one approach to study methods that allow one to nonlinearly Fourier analyze data to understand the role of coherent structures in ocean wave data [5], [11], [12].

SPECIAL AND GENERAL SOLUTIONS OF THE NLS EQUATION

We discuss the special solution of the NLS equation, which are known to have homoclinic solutions. These include soliton solutions for both the shallow and deep-water NLS equations and for the deep-water theta function solutions.

Dark Soliton Solutions in Shallow Water

Given the nonlinear Schrödinger equation in shallow water, with complex solution $u(x, t)$

$$iu_t + u_{xx} - 2|u|^2 u = 0 \tag{2}$$

[32] first wrote down the Dark soliton solutions of **Eq. 2**. This is written as the ratio of two functions:

$$u(x,t) = a\frac{g(x,t)}{f(x,t)}e^{-2ia^2t} \tag{3}$$

where

$$f = \sum_{\mu_1=0}^{1}\sum_{\mu_2=0}^{1} e^{\sum_{j>k}^{N}\mu_i\mu_j A_{ij}+\sum_{i=1}^{N}\mu_i\left(k_i x-\Omega_i t+\gamma_i\right)}$$

$$g = \sum_{\mu_1=0}^{1}\sum_{\mu_2=0}^{1} e^{\sum_{j>k}^{N}\mu_i\mu_j A_{ij}+\sum_{i=1}^{N}\mu_i\left(k_i x-\Omega_i t+\gamma_i+2i\phi_i\right)} \tag{4}$$

where

$$A_{ij} = \ln\left[\frac{\sin\left(\frac{1}{2}\left(\phi_j - \phi_k\right)\right)}{\sin\left(\frac{1}{2}\left(\phi_j + \phi_k\right)\right)}\right]^2$$
$$k_j = 2a\sin\phi_j$$
$$\Omega_j = \pm k_j\left(4a^2 - k_j^2\right)^{1/2}$$

Here γ_j are arbitrary constants.

A dark, or more correctly a gray, soliton is shown in **Figure 1B**. These are the single soliton solutions modes of the above multisoliton solution, which individually have the form:

$$|u(x,t)|^2 = \rho^2 - \frac{k^2/4}{\cosh^2\left[\frac{1}{2}(kx - \Omega t)\right]}$$

Bright Soliton Solutions in Deep Water

The nonlinear Schrödinger equation for deep water, with complex solution $\psi(x,t)$

$$iu_t + u_{xx} + 2|u|^2 u = 0 \tag{5}$$

[33] derived the bright N-soliton packet solutions of **Eq. 5**. We seek a solution as the ratio of two functions:

$$u(x,t) = \frac{G(x,t)}{F(x,t)} \tag{6}$$

At this stage we can "separate the variables" and set

$$\begin{aligned} &i(G_t F - GF_t) + \mu(G_{xx}F - 2G_x F_x + GF_{xx}) = 0 \\ &2\left(FF_{xx} - F_x^2\right) - |G|^2 = 0 \end{aligned} \tag{7}$$

From the second of **Eq. 7** get

$$|\psi|^2 = \frac{GG^*}{F^2} = 2\partial_{xx}\ln F \tag{8}$$

At this point the N-soliton solution arises as before by suitable exponential expansions:

$$F = \sum_{\mu_1=0}^{1}\sum_{\mu_2=0}^{1}\ldots\sum_{\mu_N=0}^{1} D_1(\mu_1,\mu_2)e^{\sum_{1\le i<j}\mu_i\mu_j A_{ij} + \sum_{i=1}^{2N}\mu_i\left(k_i x - \Omega_i t + \phi_i\right)} \tag{9}$$

$$G = \sum_{\mu_1=0}^{1}\sum_{\mu_2=0}^{1}\ldots\sum_{\mu_N=0}^{1} D_2(\mu_1,\mu_2)e^{\sum_{1\le i<j}\mu_i\mu_j A_{ij} + \sum_{i=1}^{2N}\mu_i\left(k_i x - \Omega_i t + \phi_i\right)}$$

where

$$k_{i+N} = k_i^* \quad \Omega_{i+N} = \Omega_i^* \quad \phi_{i+N} = \phi_i^*; \quad \Omega_i = -ik_i^2 \quad i = 1, 2\ldots N$$
$$A_{ij} = \ln\left[\frac{1}{2}\left(k_i + k_j\right)^{-2}\right] \text{ for} = 1, 2\ldots N \text{ and } j = N+1, N+2\ldots 2N$$
$$A_{ij} = \ln\left[\frac{1}{2}\left(k_i - k_j\right)^{-2}\right] \text{ for} = N+1, N+2\ldots 2N \text{ and } j = N+1, N+2\ldots 2N$$

and

$$D_1(\mu_1,\mu_2) = \begin{cases} 1 & \text{when } \sum_{i=1}^{N}\mu_i = \sum_{i=1}^{N}\mu_{i+N} \\ 0 & \text{otherwise} \end{cases}$$

$$D_2(\mu_1,\mu_2) = \begin{cases} 1 & \text{when } 1 + \sum_{i=1}^{N}\mu_{i+N} = \sum_{i=1}^{N}\mu_i \\ 0 & \text{otherwise} \end{cases}$$

This formulation gives the multisoliton solutions of the NLS equation for bright solitons on the infinite line.

A single bright soliton packet solution that has the form:

$$u(x,t) = a\,\mathrm{sech}\left[a\left|\frac{\nu}{2\mu}\right|^{1/2}(x - Vt)\right]e^{i\left(\frac{\nu}{2\mu}x - \frac{V^2}{4\mu}t + \frac{1}{2}\nu a^2 t\right)}$$

Here V is an arbitrary group speed and a is an arbitrary amplitude. This solution can be seen in **Figure 1A** above.

Stokes Wave Solutions With Riemann Theta Functions for Periodic Boundary Conditions

The Riemann theta function solution of the NLS equation for deep water **Eq. 5** is given by [9], [5]:

$$u(x,t) = A\frac{\theta(x,t|\boldsymbol{\tau},\delta^-)}{\theta(x,t|\boldsymbol{\tau},\delta^+)}e^{2iA^2 t} \tag{10}$$

The $\theta(x,t|\boldsymbol{\tau},\delta)$ are generalized Fourier series known as N-dimensional Riemann theta functions:

$$\begin{aligned} \theta(x,t|\tau,\delta^{\pm}) &= \\ &= \sum_{m_1=-\infty}^{\infty}\sum_{m_2=-\infty}^{\infty}\ldots\sum_{m_N=-\infty}^{\infty}\exp i\left[\sum_{n=1}^{N}m_n K_n x + \sum_{n=1}^{N}m_n\Omega_n t\right. \\ &\left. + \sum_{n=1}^{N}m_n\delta_n^{\pm} + \sum_{j=1}^{N}\sum_{k=1}^{N}m_j m_k\tau_{jk}\right] \end{aligned} \tag{11}$$

where the K_n are wavenumbers, the Ω_n are frequencies, the $\delta_n^{\pm}$ are phases and τ_{mn} is the Riemann matrix, in which the diagonal elements correspond to Stokes waves and the off-diagonal elements refer to nonlinear interactions amongst the Stokes waves.

An important case is for the 2 × 2 period matrix, $\boldsymbol{\tau}$, which implies that $N = 2$, a case considered in detail by [8]. For $N = 2$ the theta function has the form:

$$\begin{aligned} \theta(x,t|\boldsymbol{\tau},\boldsymbol{\delta}^{\pm}) = \sum_{m_1=-\infty}^{\infty}\sum_{m_2=-\infty}^{\infty}\exp i&\left[\sum_{n=1}^{2}m_n K_n x + \sum_{n=1}^{2}m_n\Omega_n t\right. \\ &\left. + \sum_{n=1}^{2}m_n\delta_n^{\pm} + \sum_{j=1}^{2}\sum_{k=1}^{2}m_j m_k\tau_{jk}\right] \end{aligned} \tag{12}$$

The parameters in the theta function are given by [5]:

- Expansion Parameters and Riemann Sheet Indices

$$\begin{aligned} \varepsilon_1 &= \varepsilon_o e^{i\theta} & \varepsilon_2 &= \varepsilon_1^* \\ \sigma_1 &= 1 & \sigma_2 &= -1 \end{aligned} \tag{13}$$

- Spectral Eigenvalue

$$\lambda_1 = \lambda_R + i\lambda_I \qquad \lambda_2 = \lambda_1^* \tag{14}$$

- Spectral Wavenumber

$$K_1 = -2\sqrt{A^2 + \lambda_1^2} \qquad K_2 = -2\sqrt{A^2 + \lambda_2^2} \tag{15}$$

- Spectral Frequency

$$\Omega_1 = 2\lambda_1 K_1 \qquad \Omega_2 = 2\lambda_2 K_2 \tag{16}$$

- Period Matrix

$$\tau_{11} = \frac{1}{2} + \frac{i}{\pi}\ln\left(\frac{K_1^2}{\varepsilon_1}\right) \quad \tau_{12} = \frac{i}{2\pi}\ln\left(\frac{1 + \lambda_1\lambda_2 + \frac{1}{4}K_1K_2}{1 + \lambda_1\lambda_2 - \frac{1}{4}K_1K_2}\right) \tag{17}$$

$$\tau_{21} = \tau_{12} \qquad \tau_{22} = \frac{1}{2} + \frac{i}{\pi}\ln\left(\frac{K_2^2}{\varepsilon_2}\right) \tag{18}$$

- Phases

$$\begin{aligned}
\delta_1^+ &= \pi + i\ln\left(\lambda_1 - \frac{1}{2}K_1\right) + i\ln\left(\sigma_1\lambda_1 + \frac{1}{2}K_1\right)\\
\delta_1^- &= \pi + i\ln\left(\lambda_1 + \frac{1}{2}K_1\right) + i\ln\left(\sigma_1\lambda_1 + \frac{1}{2}K_1\right)\\
\delta_2^+ &= \pi + i\ln\left(\lambda_2 - \frac{1}{2}K_2\right) + i\ln\left(\sigma_2\lambda_2 - \frac{1}{2}K_2\right)\\
\delta_2^- &= \pi + i\ln\left(\lambda_2 + \frac{1}{2}K_2\right) + i\ln\left(\sigma_2\lambda_2 - \frac{1}{2}K_2\right)
\end{aligned} \tag{19}$$

Use of the above formulas in the theta function provides a simple way to compute the breather trains for the particular case of a modulated plane wave carrier.

Homoclinic Solutions

There are several ways the general homoclinic solutions can be derived. These are listed below:

1) The general methods of [14, 17, 18] and [16]. These are the classical approaches, are well known and will not be discussed further here.
2) From dark 2-soliton solutions (2)–(4). This has been discussed by [34] in considerable detail (see also [15]). The method begins with the dark N-soliton solutions as discuss above (3), (4). This approach provides an important connection between the dark solitons and homoclinic solutions.
3) From Stokes wave solutions with Riemann Theta Functions for periodic boundary conditions. These solutions can be used to determine the homoclinic solutions by letting the parameter $\varepsilon \to 0$, as given by [35]. Likewise we can take the theta function solutions in the soliton limit to determine the deep-water N-soliton solution (5)–(9).
4) From bright 2-soliton solutions (5)–(9), by invoking periodic boundary conditions for the deep-water NLS **Eq. 5** we can directly compute the homoclinic solution.

All of the above methods provide keen insight into the generalized homoclinic solutions (see *Generalized Homoclinic Solution* below) and their relationship to the inverse scattering transform. Why however do we care about homoclinic solutions from a physical standpoint?

- (a) For large oceanic wave fields the breathers tend to have spectral components clustered about the peak of the spectrum, and hence are homoclinic. Homoclinicity is a found in Mother Nature for extreme sea states and the homoclinic solutions are good physical approximations for the Fourier components in time series data.
- (b) Homoclinic solutions are simple, i.e., they are written in terms of trigonometric functions, not in terms of theta functions.
- (c) The simple homoclinic formulas are the "nonlinear Fourier modes" that are associated with each of the largest modes in the nonlinear spectrum. Since these modes have parameters that can be determined from time series by solving the Zakharov-Shabat eigenvalue problem for periodic boundary conditions [5], we know that the homoclinic modes uniquely describe each breather train in the measured time series. Therefore one might think of locating each measured breather train and comparing it with the homoclinic solution for the appropriate nonlinear Fourier component.

Let us now look at the generalized homoclinic solution of 1+1 NLS and discuss some of its properties.

GENERALIZED HOMOCLINIC SOLUTION

The nonlinear Schrödinger equation in deep water is given by **Eq. 5**. Herein, we are interested in spatially periodic boundary conditions ($u(x,t) = u(x+L,t)$) for which a large class of homoclinic solutions whose derivations are discussed above in *Integrability and Coherent Structures for 1D Water Waves*, and which are given by [14, 15, 34]:

$$u(x,t) = a\left(\frac{1 - 2\cos(Kx)e^{\Omega t - 2i\phi + \gamma} + Ae^{2\Omega t - 4i\phi + 2\gamma}}{1 - 2\cos(Kx)e^{\Omega t + \gamma} + Ae^{2\Omega t + 2\gamma}}\right)e^{2ia^2 t} \tag{20}$$

where

$$\Omega = K\sqrt{4a^2 - K^2}\,(\text{Frequency}) \tag{21}$$

$$K = 2a\sin\phi\,(\text{Wavenumber}) \tag{22}$$

$$L = \frac{2\pi}{K} = \frac{\pi}{a\sin\phi}\,(\text{Wavelength}) \tag{23}$$

$$A = \sec^2\phi = \frac{1}{\cos^2\phi} \tag{24}$$

Here a is the amplitude of the carrier wave. Notice that the parameter γ may be interpreted as just a temporal phase shift and could just as well be omitted. However, I use γ to keep the maximum of the waveform at the origin, $u_{\max} = u(0,0)$. The presence of the parameter ϕ is the only difference between the numerator and denominator and is fundamental for describing modulational solutions of the NLS equation.

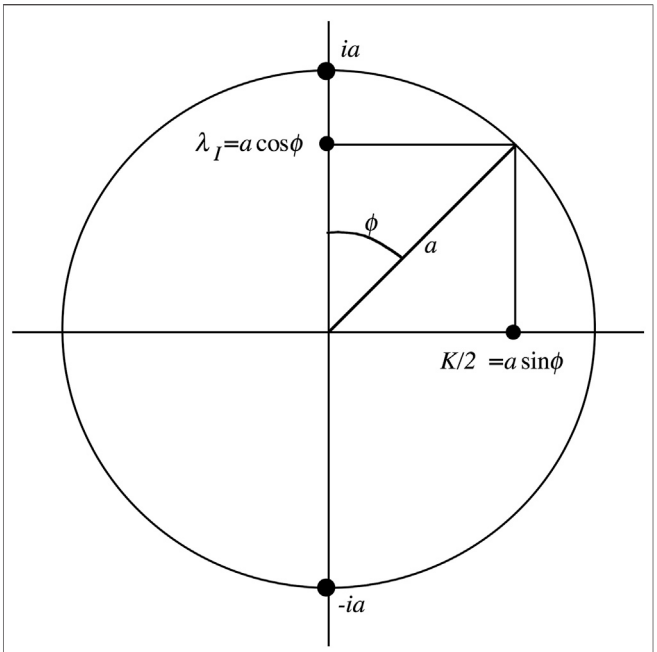

FIGURE 3 | The λ-plane in the inverse scattering transform for solutions of the NLS equation. This is the spectral domain in which homoclinic breathers live. Here the eigenvalue λ_I lies on the interval between the origin and the carrier (0, ia).

Some observations are in order here with respect to relating the above solution to the inverse scattering transform (IST) that I discuss further in *Comments on Data Analysis*. Clearly ϕ must be related to the periodic IST eigenvalue[1] in the so-called λ-plane, where the Floquet problem for the Zakharov-Shabat eigenvalue problem is solved. Recall that the wavenumber is related to λ by the following relation (this is just the IST loop integral to leading order in the parameter ε [5]):

$$K = 2\sqrt{a^2 + \lambda^2} \tag{25}$$

Here the eigenvalue has real and imaginary parts, so that $\lambda = \lambda_R + i\lambda_I$ where

$$\lambda_I = a\cos\phi,\ \lambda_R = 0 \tag{26}$$

Then

$$K = 2\sqrt{a^2 - \lambda_I^2} = 2a\sqrt{1 - \cos^2\phi} = 2a\sin\phi \tag{27}$$

So we have the wavenumber in the λ-plane eigenvalue and the relation $\lambda_I = a\cos\phi$ results. The frequency can be written

$$\Omega = K\sqrt{4a^2 - K^2} = 2a^2\sin(2\phi) = 2K\lambda_I \tag{28}$$

Then

$$A = \frac{1}{\cos^2\phi} = \left(\frac{a}{\lambda_I}\right)^2 \quad L = \frac{2\pi}{K} = \frac{\pi}{a\sin\phi} = \frac{2\pi}{2\sqrt{a^2 - \lambda_I^2}} \tag{29}$$

[1]Associated with the Floquet problem for the Zakharov-Shabat eigenvalue problem.

Also

$$\tan\phi = \frac{K}{2\lambda_I} = \frac{2\sqrt{a^2 - \lambda_I^2}}{2\lambda_I} \tag{30}$$

A graph of the λ-plane below the carrier amplitude *ia* is given in **Figure 3**.

Assume $\Omega t + \gamma = \Omega(t + \gamma/\Omega) = \Omega\tau$, where $\tau = (t + \gamma/\Omega)$, we find

$$u(x,\tau) = a\left(\frac{1 - 2\cos(Kx)e^{\Omega\tau - 2i\phi} + Ae^{2\Omega\tau - 4i\phi}}{1 - 2\cos(Kx)e^{\Omega\tau} + Ae^{2\Omega\tau}}\right)e^{2ia^2t} \tag{31}$$

Thus the parameter γ introduces only a temporal phase shift that can be removed.

The most general form for the homoclinic solution below the carrier is then given by:

$$u(x,t) = a\left[\frac{1 - 2e^{\gamma - 2i\phi + 2a^2\sin(2\phi)t}\cos(2a\sin\phi x) + \sec^2\phi e^{2\gamma - 4i\phi + 4a^2\sin(2\phi)t}}{1 - 2e^{\gamma + 2a^2\sin(2\phi)t}\cos(2a\sin\phi x) + \sec^2\phi e^{2\gamma + 4a^2\sin(2\phi)t}}\right]e^{2ia^2t} \tag{32}$$

Note that ϕ is the IST phase and γ is seen in the role of an amplitude-multiplying factor in the initial modulation. Now use

$$\theta(t) = 2a^2\sin(2\phi)t \tag{33}$$

The *primordial time* is given by the following (set $\varepsilon = e^{2a^2\sin 2\phi\, t}$, then expand as a Taylor series in ε as $t \to -\infty$):

$$u(x,t) \simeq a\left[1 + 4\varepsilon e^{\gamma}\sin\phi e^{i\left(\frac{\pi}{2} - \phi\right)}\cos(2a\sin\phi x)\right]e^{2ia^2t} \tag{34}$$

This corresponds to a small-amplitude modulation back at the "initial" time or initial condition where the motion is generated. **Equation 34** is useful as an initial condition for the motion of a wave maker in a laboratory experiment. The subsequent wave motion evolves into a breather train as the waves propagate down the wave tank.

The higher genus solutions of the NLS equation found by Matveev and colleagues [36][37] correspond to the case $N = 4$, and have a four-by-four Riemann matrix. Similar solutions have been developed by [15]. I will address these "multi component" solutions in detail with relation to the periodic IST in a later paper. These solutions are very important because they constitute homoclinic "superbreathers" in the solutions of the NLS equation.

It is worthwhile noting that the generalized homoclinic solutions of the NLS equation are wonderful in their own right and can be easily applied to problems in the physics of nonlinear wave propagation, to engineering, etc. However, when we analyze complex oceanic time series we are generally faced with hundreds or thousands of nonlinear modes. Thus the methods of Fourier analysis from inverse scattering theory must be applied to obtain the full nonlinear spectrum. In the case where the time series is described by a "rogue sea" then most of the energy in the spectrum will be "clustered" about the peak of the spectrum, and these modes consequently will be homoclinic. This means that we can combine generalized homoclinic solutions with the breather modes from time series analysis using the Zakharov-Shabat eigenvalue problem.

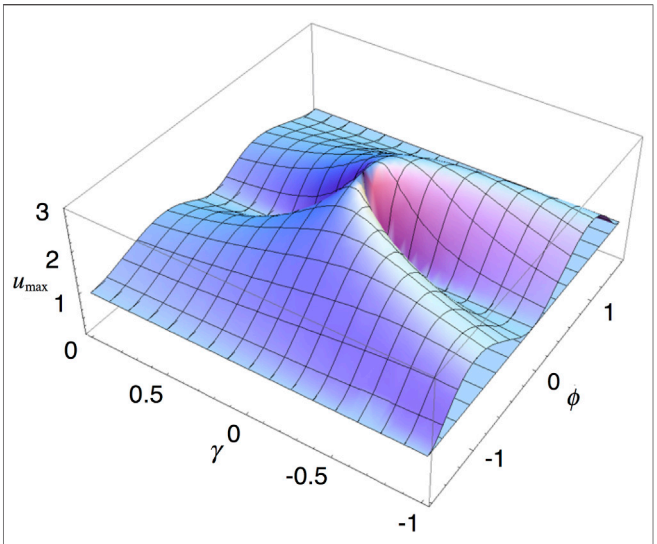

FIGURE 4 | Graph of the rogue wave maximum, $u_{max} = |u(0,0)|(\phi,\gamma)$, as a function of ϕ, γ.

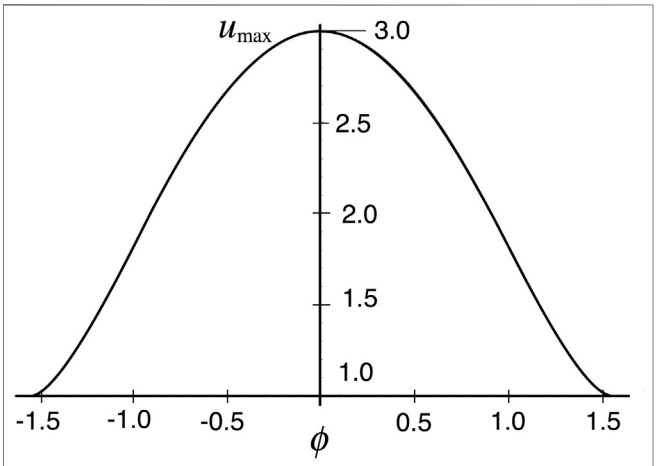

FIGURE 5 | Graph of the largest freak waves as a function of the parameter ϕ, $u_{max} = |\psi(0,0)|(\phi,0)$, for $\gamma = 0$.

THE AKHMEDIEV BREATHER SOLUTION

To obtain the Akhmediev breather we set $\lambda_I = ia/\sqrt{2}$ where

$$\phi = \frac{\pi}{4}, \quad \gamma = \frac{1}{2}\ln\left(\frac{1}{2}\right) \tag{35}$$

Equation 32 then reduces to the Akhmediev breather [16]:

$$u(x,t) = -ia\left[\frac{\cos\left(\sqrt{2}\,a\,x\right)\operatorname{sech}\left(2a^2t\right) + \sqrt{2}i\tanh\left(2a^2t\right)}{\sqrt{2} - \cos\left(\sqrt{2}\,a\,x\right)\operatorname{sech}\left(2a^2t\right)}\right]e^{2ia^2t} \tag{36}$$

The *primordial form* is given by as $t \to -\infty$:

$$u(x,t) \simeq -ia\left[1 + \sqrt{2}\,\varepsilon(1+i)\cos\left(\sqrt{2}\,ax\right)\right]e^{2ia^2t} \tag{37}$$

This is the small amplitude Cauchy initial condition for a particular solution. The factor $-i$ is an arbitrary, non-physical, phase shift for the NLS equation, give by $-\pi/2$.

THE EXTREME FREAK WAVE

The largest wave happens for $\phi \sim \Delta\phi << 1$, which occurs at $x = t = 0$, hence we compute from **Eq. 32**:

$$|u(0,0)|(\phi,\gamma) = \sqrt{1 + \frac{4e^{\gamma}\sin^2 2\phi}{1 + 2e^{2\gamma} - 4e^{\gamma}\cos^2\phi + \cos 2\phi}} \tag{38}$$

A graph of this function is given in **Figure 4**: $|u(0,0)|(\phi,\gamma)$ as a function of ϕ, γ. The maximum value is found at $\gamma = 0$

$$\left|\psi(0,0)\right|(\phi,0) = \sqrt{5 + 4\cos 2\phi} \tag{39}$$

This is shown in **Figure 5**. Note that the maximum value occurs at the coordinate values $\gamma = \phi = 0$. Furthermore, an important observation is that **Eq. 32** is indeterminate for $\phi = 0$. This singularity occurs for the Peregrine breather, where the maximum amplitude is 3 and therefore we hereafter assume $\phi > 0$.

THE PEREGRINE BREATHER

The Peregrine breather happens in the limit that the spatial periodicity tends to infinity $L \to \infty$, at the same time the wavenumber tends to 0. The infinite period limit occurs for $\phi \to 0$. We then obtain

$$u(x,\tau) = a\left[\frac{1 - 2e^{-2i\phi + 2a^2\sin(2\phi)\tau}\cos(2a\sin\phi x) + \sec^2\phi e^{-4i\phi + 4a^2\sin(2\phi)\tau}}{1 - 2e^{2a^2\sin(2\phi)\tau}\cos(2a\sin\phi x) + \sec^2\phi e^{4a^2\sin(2\phi)\tau}}\right]e^{2ia^2t} \tag{40}$$

Here we have used

$$\tau = \left(t + \frac{\gamma}{\Omega}\right) = \left(t + \frac{\gamma}{2a^2\sin(2\phi)}\right) = t + \gamma_o \tag{41}$$

The shift in time occurs on both γ and ϕ:

$$\gamma_o = \frac{\gamma}{2a^2\sin(2\phi)} \tag{42}$$

For the limit $\gamma \to 0$ we can expand both the denominator and numerator to *second order* in ϕ. After simplifying we get the standard form for the Peregrine breather:

$$u(x,t) = a\left[1 - \frac{4\left(1 + 4ia^2t\right)}{1 + 16a^4t^2 + 4a^2x^2}\right]e^{2ia^2t} \tag{43}$$

THE KUZNETSOV-MA BREATHER

We now look at the plane region which lies above the carrier, as depicted in **Figure 6**. Therefore **Eq. 6** becomes (use $\lambda = i\lambda_I$, $ia \le \lambda_I < \infty$, and $\lambda_I = a\cos(i\phi) = a\cosh\phi$):

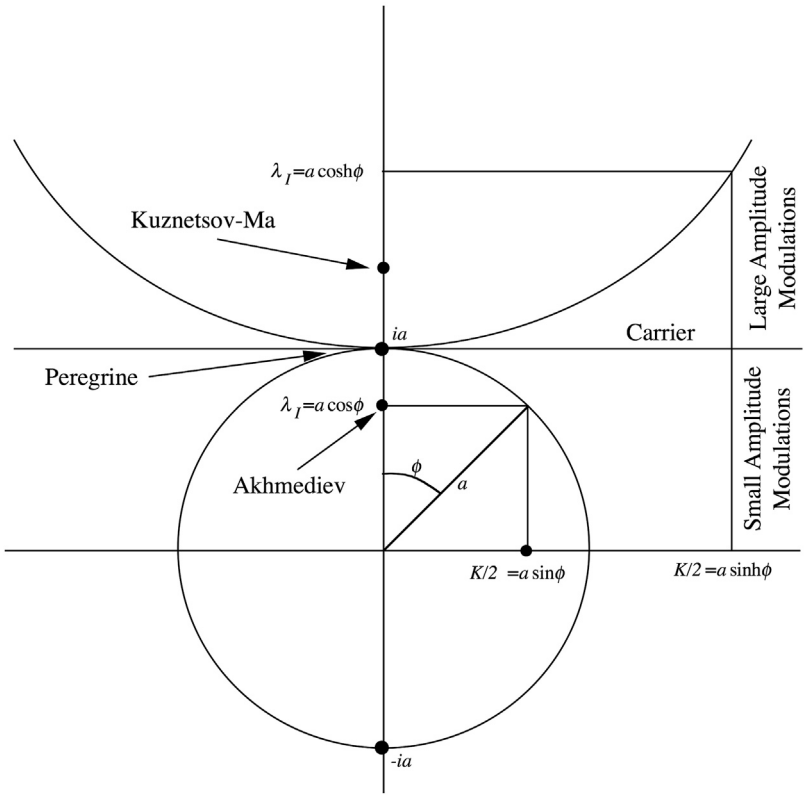

FIGURE 6 | Parameters for the homoclinic solution of the NLS equation above the carrier in the lambda plane, i.e., where λ_I can be seen to lie on the interval $(ia, i\infty)$. This diagram makes clear the regions of small-amplitude modulations below the carrier and the region of large-amplitude modulations above the carrier.

$$K \to 2\sqrt{a^2 + \lambda^2} = 2i\sqrt{\lambda_I^2 - a^2} = 2ia\sinh\phi \tag{44}$$

This means further:

$$\Omega \to K\sqrt{4a^2 - K^2} = 2ia^2\sinh(2\phi) \tag{45}$$

We make the following transformation $\phi \to i\phi$, $K \to iK$ and $\Omega \to i\Omega$ to obtain the solution above the carrier in the lambda plane. This solution corresponds to a large amplitude modulation:

$$u(x,t) = -ia\left(\frac{1 - 2\cosh(Kx)e^{i\Omega t + 2\phi + \gamma} + Ae^{2i\Omega t + 4\phi + 2\gamma}}{1 - 2\cosh(Kx)e^{i\Omega t + \gamma} + Ae^{2i\Omega t + 2\gamma}}\right)e^{2ia^2 t} \tag{46}$$

The Kuznetsov-Ma breather [18], [14] occurs for $\lambda_I = ia\sqrt{2}$ and is given by:

$$u(x,t) = a\left[1 + \frac{2\left(\cos\left[4\sqrt{2}a^2 t\right] + i\sqrt{2}\sin\left[4\sqrt{2}a^2 t\right]\right)}{\cos\left[4\sqrt{2}a^2 t\right] + \sqrt{2}\cosh[2ax]}\right]e^{2ia^2 t} \tag{47}$$

The maximum value of the Kuznetsov-Ma waveform is $u_{\max}(0, \pi/(4\sqrt{2}\,a^2)) = 1 + 2\sqrt{2} \cong 3.828$. The period in time T is given by

$$T = \frac{\pi}{2\sqrt{2}a^2} \tag{48}$$

We now consider the interval $(-\pi/(2\sqrt{2}\,a^2), 0)$ in time, where the initial waveform occurs, leading to a:

$$u(x,t) = a\left[1 + \frac{2}{1 + \sqrt{2}\cosh[2ax]}\right]e^{2ia^2 t} \tag{49}$$

For $a = 1$, $x = 0$ we see that this large amplitude initial condition has amplitude 1.828. In a wave tank experiment we thus have a large amplitude initial condition for all waves with spectral parameters above the carrier. This contrasts to the cases below the carrier, which have small amplitude initial conditions.

COMMENTS ON DATA ANALYSIS

We have seen how the homoclinic solutions of the NLS equation are constructed and further how these reduce to the particular forms for the Akhmediev, Peregrine and Kuznetsov-Ma breathers. The general formula for the homoclinic solution **Eqs 20–24** describes a single nonlinear Fourier component of the inverse scattering method for some complete "potential" of the NLS equation. This statement means: Given a space or time series that describes an energetic sea state in which there are many large breather packets, each packet is then approximately homoclinic and is therefore given in the space/time domain by

Eqs 20–24. This provides a simple alternative to Riemann theta functions to describe, in an experimental context, the actual space/time dynamics of each breather train in the nonlinear spectrum in the absence of the other breathers. Consequently one can think of the homoclinic breather **Eqs 20–24** as a simple road to an approximate filtering algorithm in which single breathers can be extracted from a measured wave train and then subsequently graphed as a single component. We now give an experimental overview of how one then interprets the spectrum for a particular time series.

Structure of the Nonlinear Spectrum

One strong point of the nonlinear Fourier analysis approach is that the solutions of the nonlinear wave equations are given very generally by Riemann theta functions. This means that one can "least squares fit" theta functions to measured time series to determine the Riemann spectral parameters, essentially in a fashion similar to that for ordinary periodic Fourier analysis. In the present case however one solves the Floquet problem for the Zakharov-Shabat eigenvalue problem to determine the spectral parameters [5]. The nonlinear parameters to be determined include the Riemann matrix, frequencies and phases of the nonlinear spectral components. Nonlinear Fourier analysis has coherent structures, so that the data can be analyzed in terms of Stokes waves, solitons, breathers and superbreathers. The Stokes waves constitute the diagonal elements of the Riemann matrix and the off-diagonal elements are the nonlinear interactions. The Stokes waves may be small enough that they are essentially sine waves, or they may be so large that they form solitons. If the Stokes waves are large enough (such that the Benjamin-Feir parameter is greater than 1), they nonlinearly couple or phase lock to each other to become breathers. This perspective contrasts with the usual assumption that ocean waves consist of weakly interacting sine waves, which we now know is valid only for very small ocean waves [5]. In modern times, however, we have the option of using nonlinear Fourier analysis to describe ocean waves as they really are, i.e., as huge numbers of nonlinearly interacting coherent structures.

Understanding the full physical behavior of coherent structures on the many aspects of ocean wave dynamics therefore plays an important role in modern research. The influence of coherency on wind wave modeling, data analysis, and computation of wave forces on ships and offshore structures are some of the reasons for improving our knowledge of the nonlinear dynamics of ocean waves with coherent structures.

It is worthwhile discussing briefly the structure of the spectrum of the NLS equation in deep-water ocean waves, primarily because deep water constitutes most (over 99%) of the ocean. In deep water the NLS equation coherent structure solutions consist of Stokes waves, (bright) soliton wave packets, breather wave trains and superbreathers. A typical ocean wave train in terms of these structures is given in **Figure 7**. This simple representation of a nonlinear spectrum has arisen from a large number of time series measurements and subsequent analysis by nonlinear Fourier methods [5], [11], [12]. Thus we see in **Figure 7** a nonlinear spectrum that is generated by wind on waves in a generic fashion: The shape of the spectrum consists of nonlinear wave components that are solutions of the NLS equation that are generated by Mother Nature in the real world environment. To interpret the spectrum it is worthwhile noting that the larger the spectral components are the more nonlinear they are. The larger components generally occur about the peak of the spectrum. The continuous black line in **Figure 7** is a typical ocean wave spectrum such as that described by the Pierson-Moskowitz or JONSWAP power spectra. The points (black and red dots) are the components of the nonlinear ocean wave spectrum. The dots are "points of simple spectrum" from the Zakharov-Shabat eigenvalue problem [38]. The larger the components are, the greater is the nonlinearity.

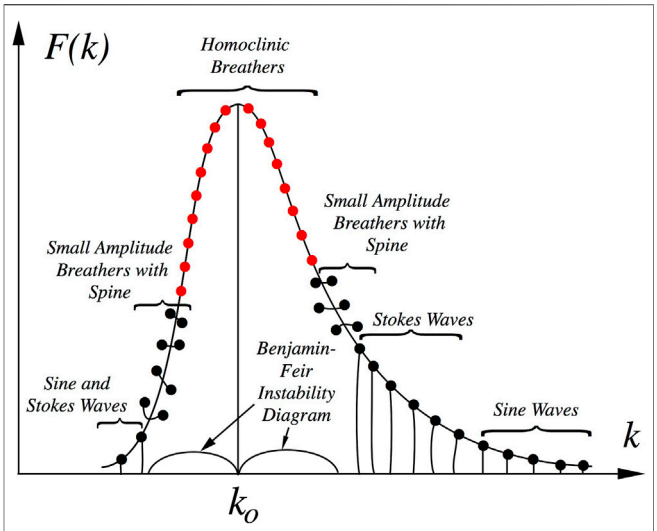

FIGURE 7 | Schematic of typical nonlinear wavenumber spectrum for deep-water ocean waves. For a large amplitude sea state the spectral energy is dominated by the largest breathers, which are essentially homoclinic (red dots).

Referring to **Figure 7** the character of the nonlinear components is given by a mathematical object called a spine, which is a line of spectrum that either descends to the frequency axis from a point of spectrum, or connects two points of simple spectrum above the frequency axis. The components with spines that descend to the frequency axis are sine or Stokes waves. The low amplitude tails of the spectrum typically contains small-amplitude sine waves while slightly larger components (slightly nearer the peak of the spectrum) are Stokes waves. The frequency band about the peak of the spectrum has the components that are most nonlinear: Here the spines are seen to connect two points of simple spectrum, corresponding to small or medium amplitude breathers. The red dots are "double points", i.e., two points of simple spectrum that nearly coincide and thus the spines are too short to be visible: These are the homoclinic breathers in the spectrum. In a large sea state these homoclinic breathers are clustered about the spectral peak and energetically dominate the nonlinear wave motion [39], [12]. Sea states of densely packed

breathers are referred to as "breather turbulence" and consequently characterize a "rogue sea" condition.

The double lobed curves, shown at the bottom of the graph on the frequency axis, are centered about the peak of the spectrum at the carrier wavenumber k_o. This double lobe constitutes the "instability diagram" of the Benjamin-Feir instability region: Spectral points within this band of spectrum are breathers. Once again the red dots are the homoclinic breathers. They are the biggest and baddest of the breather packets and are sources of rogue waves in the sea state. When the largest breather packets reach their maximum amplitudes during their breathing cycles the central wave is often viewed as a rogue wave. The wave trains that characterize the nonlinear waves for each red dot are the homoclinic solutions of **Eqs 20–24** discussed above in this paper. Therefore, for anyone wanting to study nonlinear waves these homoclinic solutions can be very important for a full understanding of the most energetic coherent structures in the spectrum, i.e., those that are sources of rogue waves in a "rogue sea." Breathers consist of two phase locked Stokes waves with a 2 × 2 Riemann spectrum and we see they have a homoclinic limit, **Eqs 20–24**. Superbreathers consist of three or four (or more) phase locked Stokes waves and they too have a homoclinic limit. Up to now breathers are ubiquitous spectral components in measured ocean wave time series [40], [11], [12]. Superbreathers have yet to be found in ocean wave measurements up to now.

How can a spectrum of wind waves of the type shown in **Figure 7** be generated by wind in the ocean? Beginning with a calm sea state the wind starts to blow and the initial small amplitude waves have the form of a random sea state that has a rough spectral shape similar to the solid curve in **Figure 7**. At this stage it is found that the nonlinear wave components are essentially sine waves. After the wind brings up the sea state slightly more we find the spectrum consists of sine waves that interact weakly with one another. Further injection of wind energy into the sea state we find that the nonlinear components near the peak of the spectrum become Stokes waves. Further energy input forces couples of Stokes waves near the peak to phase lock with each other creating breather trains. For a fully "nonlinearly saturated" sea state most of the energy near the peak of the spectrum is dominated by breather trains. We have found that in Currituck Sound the breathers are quite dense and 30-min time series have over 200 breathers, suggesting that "breather turbulence" might be a proper way to describe these types of energetic sea states which might also be called "rogue seas."

It might be tempting to try and describe ocean waves in terms of a few simple breather trains and it would seem reasonable to think of large breathers as rare events. However, for ocean waves it has been found that for extreme sea states the breathers are highly dense and each breather has its own shape and dynamical properties. For example their maximum heights are random statistical variables, and so to are their rise times. Thus breathers as nonlinear Fourier modes are drastically different from simple weakly interacting sine waves. It is also worthwhile noting that while the nonlinear Schrödinger equation has many complex types of nonlinear Fourier modes, it is unclear how those modes might be distributed in a particular physical situation. Only through experimental measurements and their subsequent analysis by nonlinear Fourier analysis, can we begin to understand the true physical behavior of nonlinear ocean waves and what their nonlinear spectra are. We now understand that the old paradigm of weakly interacting sine waves is no longer tenable. However, the full consequences of large sea states dominated by coherent structures are still to be fully understood. The implications of such a new scenario on all aspects of living and working in the ocean will only slowly become better understood as the new paradigm is exploited to better understand nonlinear stochastic wave motion with coherent structures.

Fossil Breathers and Ghost Packets in Shallow Water

We would like to briefly discuss the possible existence of "fossil" breathers in shallow water. What are these special solutions of the shallow water NLS equation? Suppose that one has a deep-water breather that is propagating toward shore over decreasing water depth. At some point it will pass the depth where $Kh = 1.363$ and the breather train will no longer be Benjamin-Feir unstable. What happens physically to the breather packet if it is placed in shallow water, where the sign of the nonlinear terms of NLS equation changes? One still, momentarily, has a wave packet that has essentially the same shape as the precursor deep-water breather. However, in shallow water the packet now has a real frequency, not the imaginary frequency for BF unstable dynamics in deep water. This new shallow water packet, still phase locked as in the deep-water case, will therefore propagate shoreward with a fixed shape, i.e., it no longer breathes. The packet will undergo wave transformation (changes in shape) as it propagates into even shallower water. Under the right conditions each of the large waves in the packet will roll over and break and possibly create good conditions for surfing. We call this shallow water packet (before roll over and breaking) a "fossil" breather because it contains in its nonlinear Fourier parameters all the information necessary to compute the properties of the original breather back in "primordial" time far offshore, perhaps even in terms of a far away storm. Thus shallow water measurements of fossil breathers should provide understanding of the incoming flux of breathers from deep water. The fossil breathers are "ghosts" of the past breathers, which are now dead and gone once the BF instability no longer dominates their dynamics. Figuratively speaking their breathing has been switched off at the transition from deep to shallow water, at $Kh = 1.363$, where they effectively die and propagate shoreward as ghost breathers out of the past. Theoretically the simplest way to understand how this happens is to study the theta function solution of the NLS equation for the case $N = 2$, the topic of a future paper.

CONCLUSION

A discussion of the general homoclinic solutions of the 1+1 NLS equation is given and a several ways to derive them are discussed. This work sets the stage for using the homoclinic solution to help analyze and understand experimental data from laboratory and oceanic measurements of nonlinear waves. Analysis of space/time series data using the Zakharov-Shabat eigenvalue problem are given elsewhere. What has been found in these data analyses is that for high amplitude sea states the spectrum is energetically dominated by breather states that are very nearly in the homoclinic limit. This experimentally determined idea then provides motivation for this paper in which we treat the homoclinic spectral components as being represented by **Eqs 20–24**, expressions which are valid for any mode anywhere in the lambda plane. This provides a heuristic interpretation of experimental data for energetic sea states as being a linear superposition of homoclinic breathers plus interactions amongst these breathers. Such an interpretation suggests that new filtering procedures could be used to extract individual breather modes from time series. Details of the application of this procedure to data will be given in future papers.

DATA AVAILABILITY STATEMENT

The original contributions presented in the study are included in the article/supplementary material, further inquiries can be directed to the corresponding author.

AUTHOR CONTRIBUTIONS

The author confirms being the sole contributor of this work and has approved it for publication.

FUNDING

This work has been supported by Tom Drake of the Office of Naval Research of the United States.

ACKNOWLEDGMENTS

The author thanks the referees for their positive comments.

REFERENCES

1. Akhmediev N, and Pelinovsky E. Discussion and Debate: Rogue Waves – towards a Unifying Concept?. *Eur Phys J Spec Top* (2010) 185(Issue 1). doi:10.1140/epjst/e2010-01233-0
2. Kharif C, Pelinovsky E, and Slunyaev A. *Rogue Waves in the Ocean*. Berlin: Springer-Verlag (2009).
3. Olagnon M, and Athanassoulis GA. *Rogue Waves 2000*. Brest: Ifremer (2000).
4. Olagnon M, and Prevost M. *Rogue Waves 2008*. Brest: Ifremer (2008).
5. Osborne AR. Rogue Waves: Classification, Measurement and Data Analysis, and Hyperfast Numerical Modeling. *Eur Phys J Spec Top* (2010) 185:225–45. doi:10.1140/epjst/e2010-01251-x
6. Pelinovsky E, and Kharif C. *Extreme Ocean Waves*. Berlin: Springer-Verlag (2008).
7. Kotljarov VP, and Its AR. *Dopovidi Akad Nauk UkRSR., Ser A* (1976) 11: 965–8.
8. Tracy ER, and Chen HH. Nonlinear Self-Modulation: An Exactly Solvable Model. *Phys Rev A* (1988) 37:815–39. doi:10.1103/physreva.37.815
9. Belokolos ED, Bobenko AI, Enolskii VZ, Its AR, and Matveev VB. *Algebro-Geometric Approach to Nonlinear Integrable Equations*. Berlin: Springer-Verlag (1994).
10. Lamb GL. *Elements of Soliton Theory*. New York: John Wiley & Sons (1980).
11. Costa A, Osborne AR, Resio DT, Alessio S, Chirivì E, Saggese E, et al. Soliton Turbulence in Shallow Water Ocean Surface Waves. *PRL* (2014) 113:108501. doi:10.1103/physrevlett.113.108501
12. Osborne AR, Resio DT, Costa A, Ponce de León S, and Chirivì E. Highly Nonlinear Wind Waves in Currituck Sound: Dense Breather Turbulence in Random Ocean Waves. *Ocean Dyn* (2018) 69:187–219. doi:10.1007/s10236-018-1232-y
13. Osborne AR. Nonlinear Fourier Analysis: Rogue Waves in Numerical Modeling and Data Analysis. *J Mar Sci Eng* (2020). in press. doi:10.1115/omae2020-18850
14. Ma Y-C. The Perturbed Plane-Wave Solutions of the Cubic Schrödinger Equation. *Stud Appl Math* (1979) 60:43–58. doi:10.1002/sapm197960143
15. Ablowitz MJ, and Clarkson PA. *Solitons, Nonlinear Evolution Equations and Inverse Scattering*. Cambridge: Cambridge University Press (1991). doi:10.1017/cbo9780511623998
16. Akhmediev N. *Teoreticheskaya I Matematicheskaya Fizika* (1986) 69(2): 189–94.
17. Peregrine DH. Water Waves, Nonlinear Schrödinger Equations and Their Solutions. *J Aust Math Soc Ser B, Appl. Math* (1983) 25:16–43. doi:10.1017/s0334270000003891
18. Kuznetsov E. Solitons in a Parametrically Unstable Plasma. *Sov Phys Dokl* (1977) 22:507–8.
19. Toffoli A, Onorato M, Bitner-Gregersen EM, and Monbaliu J. Development of a bimodal structure in ocean wave spectra. *J Geophys Res Oceans* (2010) 115: C03006.
20. Toffoli A, Bitner-Gregersen EM, Osborne AR, Serio M, Monbaliu J, and Onorato M. Extreme Waves in Random Crossing Seas: Laboratory Experiments and Numerical Simulations. *Geophys Res Lett* (2011) 38:L06605.
21. Chabchoub A, Hoffmann NP, and Akhmediev N. Rogue Wave Observation in a Water Wave Tank. *Phys Rev Lett* (2011) 106:204502. doi:10.1103/physrevlett.106.204502
22. Islas AL, and Schober CM. Predicting Rogue Waves in Random Oceanic Sea States. *Phys Fluids* (2005) 17:031701. doi:10.1063/1.1872093
23. Pinho UF, and Babanin AV. Emergence of Short Crestedness in Originally Unidirectional Nonlinear Waves. *Geophys Res Lett* (2015) 42:4110–5.
24. Mozumi K, Waseda T, and Chabchoub A. 3D Stereo Imaging of Abnormal Waves in a Wave basin. In ASME 2015 34th International Conference on Ocean, Offshore and Arctic Engineering. New York: Am Soc Mechanical Engineers (2015) (Accessed May 31, 2015). doi:10.1115/omae2015-42318
25. Sanina EV, Suslov SA, Chalikov D, and Babanin AV. Detection and Analysis of Coherent Groups in Three-Dimensional Fully-Nonlinear Potential Wave fields. *Ocean Model* (2016) 103:73–86. doi:10.1016/j.ocemod.2015.09.012
26. Chabchoub A, Mozumi K, Hoffmann N, Babanin AV, Toffoli A, Steer JN, et al. Directional Soliton and Breather Beams. *Proc Natl Acad Sci U S A* (2019) 116(20):9759–63. doi:10.1073/pnas.1821970116
27. Abramowitz M, and Stegun IA, 55. United States: National Bureau of Standards, Applied Mathematics Series, U.S. Dept. of Commerce (1964). Handbook of Mathematical Functions
28. Dysthe KB. Note on a Modification to the Nonlinear Schrödinger Equation for Application to Deep Water Waves. *Proc R Soc Lond A* (1979) 369(–114).
29. Trulsen K, and Dysthe KB. A Modified Nonlinear Schrödinger Equation for Broader Bandwidth Gravity Waves on Deep Water. *Wave Motion* (1996) 24: 281–9. doi:10.1016/s0165-2125(96)00020-0
30. Zakharov VE. Stability of Periodic Waves of Finite Amplitude on the Surface of a Deep Fluid. *J Appl Mech Tech Phys USSR* (1968) 2:190.

31. Yuen HC, and Lake BM. Nonlinear Dynamics of Deep-Water Gravity Waves. *Adv Appl Mech* (1982) 22:67–229. doi:10.1016/s0065-2156(08)70066-8
32. Hirota R. "Direct Methods in Soliton Theory," in *Solitons* RK Bullough and PJ Caudry, editors, 17. Berlin-Heidelberg-New York: Springer-Verlag (1980). p. 157–176. doi:10.1007/978-3-642-81448-8_5
33. Hirota R. Exact Envelope-soliton Solutions of a Nonlinear Wave Equation. *J Math Phys* (1973) 14:805–9. doi:10.1063/1.1666399
34. Herbst BM, and Ablowitz MJ. Numerically Induced Chaos in the Nonlinear Schrödinger Equation. *Phys Rev Lett* (1989) 62:2065–8. doi:10.1103/physrevlett.62.2065
35 Osborne AR. Classification of Homoclinic Rogue Wave Solutions of the Nonlinear Schrödinger Equation. *Nat Hazards Earth Syst Sci Discuss* 2 (2014). 897–933.
36. Dubard P, Gaillard P, Klein C, and Matveev VB. On Multi-Rogue Wave Solutions of the NLS Equation and Positon Solutions of the KdV Equation. *Eur Phys J Spec Top* (2010) 185:247–58. doi:10.1140/epjst/e2010-01252-9
37. Dubard P, and Matveev VB. Multi-rogue Waves Solutions to the Focusing NLS Equation and the KP-I Equation. *Nat Hazards Earth Syst Sci* (2011) 11:667–72. doi:10.5194/nhess-11-667-2011
38. Osborne AR. Deterministic and Wind/Wave Modeling: A Comprehensive Approach to Deterministic and Probabilistic Descriptions of Ocean Waves. In Proceedings of the 31st International Conference on Ocean, Offshore and Arctic Engineering OMAE2012 June 10-15. Rio de Janeiro, Brazil (2012).
39. Osborne AR. Advances in Nonlinear Waves with Emphasis on Aspects for Ship Design and Wave Forensics. In Proceedings of the ASME 2013 32nd International Conference on Ocean, Offshore and Arctic Engineering OMAE2013 June 9-14. France: Nantes (2013). doi:10.1115/omae2013-10873
40. Osborne AR, Nonlinear Ocean Waves and the Inverse Scattering Transform. *Acad Press, Int Geophys Ser* 97 (2010). p. 944.

Conflict of Interest: Author AO was employed by the company Nonlinear Waves Research Corporation.

Advantages of publishing in Frontiers

OPEN ACCESS
Articles are free to read for greatest visibility and readership

FAST PUBLICATION
Around 90 days from submission to decision

HIGH QUALITY PEER-REVIEW
Rigorous, collaborative, and constructive peer-review

TRANSPARENT PEER-REVIEW
Editors and reviewers acknowledged by name on published articles

Frontiers
Avenue du Tribunal-Fédéral 34
1005 Lausanne | Switzerland

Visit us: www.frontiersin.org
Contact us: frontiersin.org/about/contact

REPRODUCIBILITY OF RESEARCH
Support open data and methods to enhance research reproducibility

DIGITAL PUBLISHING
Articles designed for optimal readership across devices

FOLLOW US
@frontiersin

IMPACT METRICS
Advanced article metrics track visibility across digital media

EXTENSIVE PROMOTION
Marketing and promotion of impactful research

LOOP RESEARCH NETWORK
Our network increases your article's readership